RECEIVED BY DTIE FEB 3 1969

CONFIDENTIAL

This report has been prepared under Contract AT(29-2)-2062 with the U.S. Atomic Energy Commission

IND2062-12-8
C92A, M-3679, 59th Edition.
AEC Research and Development Report

TID-24922

MASTER

UNCLASSIFIED

SNAP 29
POWER SUPPLY SYSTEM
NINTH QUARTERLY PROGRESS REPORT

IND2062-12-8

January 1969

NOTICE
This report was prepared as an account of work sponsored by the United States Government Neither the United States nor the United States Energy Research and Development Administration, nor any of their employees nor any of their contractors, subcontractors or their employees makes any warranty express or implied or assumes any legal liability or responsibility for the accuracy, completeness or usefulness of any information, apparatus product or process disclosed or represents that its use would not infringe privately owned rights

CLASSIFICATION CANCELLED
OR CHANGED TO
BY AUTHORITY OF D.O.E.
BY L. Tokar DATE 11/2/71
Exempt from CCRP Re-review Requirements
(per 7/22/82 Duff/Caudle memorandum)
NK 5/9/05

This document contains information affecting the National Defense of the United States within the meaning of the Espionage Laws, Title 18, U.S.C., Sections 793 and 794, the transmission or revelation of which in any manner to an unauthorized person is prohibited by law.

Group 3
Downgraded at 12 year intervals;
not automatically declassified.

LEGAL NOTICE

This report was prepared as an account of Government sponsored work Neither the United States, nor the Commission, nor any person acting on behalf of the Commission

A Makes any warranty or representation, expressed or implied, with respect to the accuracy, completeness, or usefulness of the information contained in this report, or that the use of any information, apparatus, method, or process disclosed in this report may not infringe privately owned rights, or

B Assumes any liabilities with respect to the use of, or for damages resulting from the use of any information, apparatus, method, or process disclosed in this report

As used in the above, "person acting on behalf of the Commission" includes any employee or contractor of the Commission, or employee of such contractor, to the extent that such employee or contractor of the Commission, or employee of such contractor prepares, disseminates, or provides access to, any information pursuant to his employment or contract with the Commission, or his employment with such contractor

DISTRIBUTION OF THIS DOCUMENT IS UNLIMITED

ISOTOPES
NUCLEAR SYSTEMS DIVISION
A TELEDYNE COMPANY

DISTRIBUTION OF THIS DOCUMENT IS LIMITED
To Government Agencies and their Contractors

DISCLAIMER

This report was prepared as an account of work sponsored by an agency of the United States Government. Neither the United States Government nor any agency Thereof, nor any of their employees, makes any warranty, express or implied, or assumes any legal liability or responsibility for the accuracy, completeness, or usefulness of any information, apparatus, product, or process disclosed, or represents that its use would not infringe privately owned rights. Reference herein to any specific commercial product, process, or service by trade name, trademark, manufacturer, or otherwise does not necessarily constitute or imply its endorsement, recommendation, or favoring by the United States Government or any agency thereof. The views and opinions of authors expressed herein do not necessarily state or reflect those of the United States Government or any agency thereof.

DISCLAIMER

Portions of this document may be illegible in electronic image products. Images are produced from the best available original document.

UNCLASSIFIED

LEGAL NOTICE

This report was prepared as an account of Government sponsored work. Neither the United States, nor the Commission, nor any person acting on behalf of the Commission:

A. Makes any warranty or representation, expressed or implied, with respect to the accuracy, completeness, or usefulness of the information contained in this report, or that the use of any information, apparatus, method, or process disclosed in this report may not infringe privately owned rights; or

B. Assumes any liabilities with respect to the use of, or for damages resulting from the use of any information, apparatus, method, or process disclosed in this report.

As used in the above, "person acting on behalf of the Commission" includes any employee or contractor of the Commission, or employee of such contractor, to the extent that such employee or contractor of the Commission, or employee of such contractor prepares, disseminates, or provides access to, any information pursuant to his employment or contract with the Commission, or his employment with such contractor.

[illegible]

FOREWORD

This is the Ninth Quarterly Progress Report prepared under Contract AT(29-2)-2062. It covers the progress of the Isotopes, Inc., Nuclear Systems Division on the SNAP 29 program and is prepared for the United States Atomic Energy Commission.

The report covers the period from October 1, 1968 through December 31, 1968.

BLANK

CONTENTS

		Page
	Legal Notice	ii
	Foreword	iii
	Contents	v
	Summary	vii
I.	Introduction	I-1
II.	Radioisotope Thermoelectric Generator System--Control Point 1000	II-1
	A. Summary of Significant Accomplishments	II-1
	B. RTG Heat Source (Isotopic) Subsystem--Control Point 1100	II-3
	C. Heat Source (Electrical) Subsystem--Control Point 1200	II-49
	D. Thermoelectric Modules Subsystem--Control Point 1300	II-50
	E. Thermal Control Subsystem--Control Point 1500	II-85
	F. Heat Pipe Heat Rejection Subsystem--Control Point 1800	II-89
	G. RTG Housing Structural Subsystem--Control Point 1900	II-101
	H. References	II-109
III.	Systems Evaluation and Integration--Control Point 3200	III-1
	A. Summary of Significant Accomplishments	III-1
	B. System Interface Evaluation--Control Point 3210	III-1
	C. System Test Integration--Control Point 3240	III-2
IV.	Reliability--Control Point 3230	IV-1
	A. Summary of Significant Accomplishments	IV-1
	B. Reliability Planning and System Analysis--Control Point 3231	IV-1
	C. Design Evaluation and Approval--Control Point 3232	IV-8
V.	Aerospace Ground Equipment System--Control Point 2000	V-1
VI.	Safety Evaluation and Integration--Control Point 3300	VI-1
	A. Summary of Significant Accomplishments	VI-1
	B. Safety Evaluation and Integration--Control Point 3310	VI-1
	C. Aerodynamic Analyses and Test--Control Point 3320	VI-2
	D. Impact and Burial Tests and Analyses--Control Point 3330	VI-30
VII.	Mound Laboratory Effort in Support of SNAP 29	VII-1
	A. Program Summary	VII-1
	B. Work Accomplished	VII-1

CONTENTS (continued)

Page

Appendices

A. I^2R Losses for Copper Flame-Sprayed Pads A-1
B. Thermoelectric Data for TAGS (TEDP-00-10A) and SnTe (TEDP-00-27) Thermoelectric Elements B-1
C. Selection of 2N-TAGS/SnTe Thermoelectric Couple Bonding Procedure C-1
D. T/E Couple Development, Experimental Data D-1
E. Heat Pipe Design Selection E-1
F. Pretest Thermal Analyses of Heat Rejection Subsystem Manufacturing Checkout Unit Test Series F-1
G. Design Evaluation of Rene 41 Fuel Block Support Beams G-1
H. TRW Platinum-Rhodium Clad Development Program H-1

SUMMARY

A. RADIOISOTOPE THERMOELECTRIC GENERATOR SYSTEM

The SNAP 29 Task Force Final Report was issued (INSD-2062-4002).

The burnup heat source design was completed.

The nickel heater block design was modified to enlarge the heater holes to accommodate the heater cartridges.

Preparations were completed for placing S/N 003, 005 and the LTM back on test.

Preparations for the cold end ΔT test were completed.

The NaK diaphragm life test successfully completed 90 days of operation.

Twenty NaK/argon accumulators have been received from the vendor.

The T/E module side skin design has been improved to eliminate weld assembly problems.

Diagnostic disassembly of modules S/N 001, 002 and 004 was completed.

Couple development of 2N-TAGS/SnTe is near completion. The TAGS element fabrication process has been qualified.

Fabrication of the first set of thermal control shutters was completed.

Final documentation of the heat pipe design selection was completed.

Trial runs in the full-scale radiator bonding fixture were initiated.

Design of the RTG test stand was completed.

Fabrication of components of the RTG structure was completed.

Fabrication and checkout of the three portable test consoles for use in system and module testing was completed.

B. SYSTEM EVALUATION AND INTEGRATION

The GFE survey was completed and a letter summarizing the transfer action was transmitted to the AEC.

The three systems test consoles for checking out the four-module RTG were completed.

C. RELIABILITY

The impact of the reduced rate of expenditures imposed on the SNAP 29 program and its effect on the scope of the reliability program and tasks has been evaluated.

The ability of the RTG four-module configuration to meet the load voltage requirements specified by contract documents has been substantiated through preparation of voltage-current and power-current characteristics for the generator at beginning and end of life.

An analysis and reliability prediction for the heat rejection subsystem has been initiated.

The analysis of the qualification lot of the selected SNAP 29 2N-TAGS/SnTe couple has been completed.

D. AEROSPACE GROUND EQUIPMENT

Due to program redirection, effort on AGE design has been deferred until later in the program.

E. SAFETY EVALUATION AND INTEGRATION

Re-entry and abort trajectory and heating rates were obtained for various burn-up element configurations and a fuel matrix.

Final wind tunnel test reports on the intact heat source have either been issued or completed on the following tests: free flight, low density force and moment, forced oscillation and the rotating force and damping.

F. MOUND LABORATORY EFFORT IN SUPPORT OF SNAP 29

Two capsulette mechanical seal designs have been found to produce a gas-tight seal.

Two polonium metal distribution tests were completed.

I. INTRODUCTION

The purpose of the SNAP 29 program is to develop and demonstrate a radioisotope thermoelectric generator (RTG) system that meets the following objectives:

(1) The Radioisotope Thermoelectric Technology by fabricating and electrically operating, for 114 days, two groundbased RTG preprototype units which utilize a modular concept design that is capable of:

  (a) Intact re-entry of the fuel capsules for the intact heat source or capsule burnup in the case of the burn-up type of re-entry

  (b) Fuel containment as required to meet safety criteria.

(2) The Aerospace Ground Equipment Technology by fabricating and operating AGE demonstration units.

The SNAP 29 radioisotope thermoelectric generator (RTG) system is made up of:

(1) A heat source subsystem

(2) Thermoelectric module subsystem

(3) Thermal control subsystem

(4) Heat rejection subsystem

(5) Structures subsystem.

Integrated aerospace ground equipment (AGE) is provided for transportation, storage and installation of the isotopic heat source into the prototype RTG on a simulated launch pad and system checkout.

The SNAP 29 development program consists of five major tasks:

(1) Radioisotope Thermoelectric Generator System--Control Point 1000

(2) Aerospace Ground Equipment System--Control Point 2000

(3) Program Management and Control--Control Point 3100

(4) Systems Evaluation and Integration--Control Point 3200

(5) Safety Evaluation and Integration--Control Point 3300.

Chapter II presents the status of development for the radioisotope thermoelectric generator system (Control Point 1000). The RTG system consists of six subsystems:

(1) CP 1100--RTG Heat Source (Isotopic)

(2) CP 1200--Heat Source (Electrical)

(3) CP 1300--Thermoelectric Modules

(4) CP 1500--Thermal Control

(5) CP 1800--Heat Pipe Heat Rejection

(6) CP 1900--Structures

Chapter III relates to systems evaluation and integration (Control Point 3200).

Reliability is presented in Chapter IV.

Chapter V concerns the development of the aerospace ground equipment (CP 2000).

Safety evaluation and integration (CP 3300) are treated under Chapter VI.

Chapter VII represents the Mound Laboratory effort in support of SNAP 29.

Figure I-1 represents the present schedule as proposed in the current program plan (MND-2062-400).

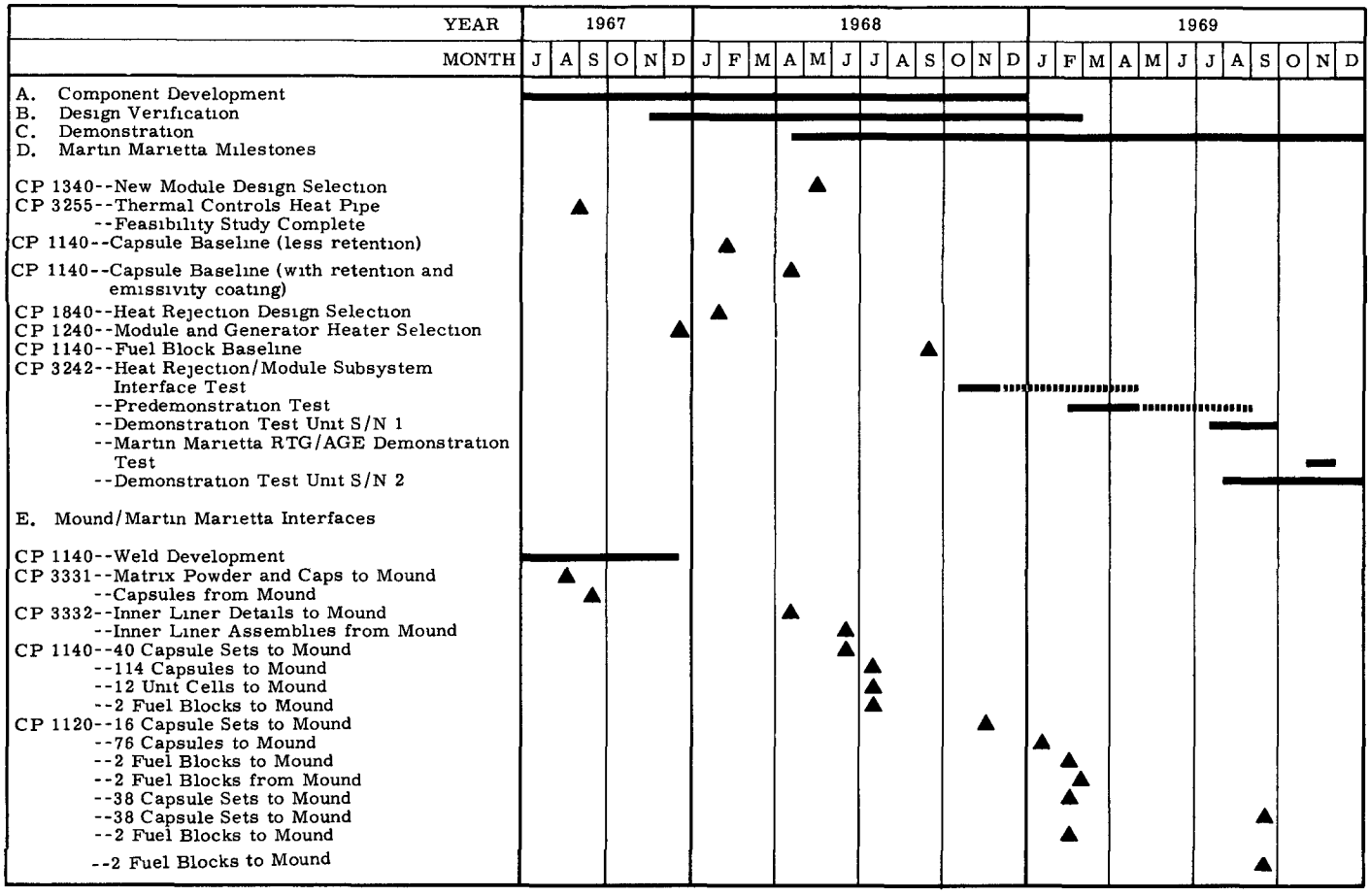

FIG. I-1. SNAP 29 MILESTONE SCHEDULE

II. RADIOISOTOPE THERMOELECTRIC GENERATOR SYSTEM--CONTROL POINT 1000

The SNAP 29 RTG system goal is to demonstrate the radioisotope thermoelectric technology by fabricating and electrically operating, for 114 days, two ground-based RTG preprototype units which utilize a modular concept design. The heat source shall be capable of:

(1) Intact re-entry of the fuel capsules for the intact heat source, or capsule burnup in the case of the burn-up type of re-entry

(2) Fuel containment as required to meet safety criteria.

The system design life of 114 days includes a 90-day duration orbital mission. In order to more effectively accomplish the design, a control point system has been established which breaks the RTG into its major subsystems. The control point breakdown is defined in the following:

CP 1100--Isotopic Heat Source Subsystem

CP 1200--Electrical Heat Source Subsystem

CP 1300--Thermoelectric Module Subsystem

CP 1500--Thermal Control Subsystem

CP 1800--Heat Pipe Heat Rejection Subsystem

CP 1900--RTG Housing Structural Subsystem

The first phase of the program consists of design and development testing on a subsystem level in order to generate sufficient data to establish required design modifications prior to initiation of the second phase. On the basis of design and development tests, further design refinements will be effected to optimize the system design toward the stated goal. These changes will appear in the preprototype system configuration, which will demonstrate the capability of the RTG on a system level and affirm the applicability of the system to flight hardware.

A. SUMMARY OF SIGNIFICANT ACCOMPLISHMENTS

1. Isotopic Heat Source Subsystem--Control Point 1100

During the past quarter, the following items have been completed:

The SNAP 29 Task Force Final Report was issued (INSD-2062-4002)

The burn-up heat source design was completed

2. Electrical Heat Source--Control Point 1200

The nickel heater block design was modified to enlarge the heater holes to accommodate the heater cartridges.

3. Thermoelectric Module Subsystem--Control Point 1300

The following items were completed during this quarter:

Preparations were completed for placing S/N 003, 005 and LTM on test again.

Preparations for the cold and ΔT tests.

The NaK diaphragm life test successfully completed 90 days of operation.

Twenty NaK/argon accumulators have been received from the vendor.

The T/E module side skin design has been improved to eliminate weld assembly problems.

Diagnostic disassembly of Modules S/N 001, 002 and 004 was completed.

The 2N-TAGS/SnTe couple development is near completion. The TAGS element fabrication process has been qualified.

Fabrication of the first set of thermal control shutters was completed.

5. Heat Pipe Rejection Subsystem--Control Point 1800

The two items that were completed during the past quarter were:

Final documentation of the heat pipe design selection was completed.

Trial runs in the full-scale radiator bonding fixture were initiated.

6. RTG Housing Structural Subsystem--Control Point 1900

The following lists the work accomplished under Control Point 1900 during the past quarter·

Design of the RTG test stand was completed.

Fabrication of components of the RTG structure was completed.

Fabrication and checkout of the three portable test consoles for use in system and module testing was completed.

B. RTG HEAT SOURCE (ISOTOPIC) SUBSYSTEM-- CONTROL POINT 1100

The objective of this task is to design, develop, procure material, fabricate and test an isotopic heat source capable of meeting the following requirements:

(1) To provide sufficient thermal energy to the thermoelectric modules subsystem for the generation of the required power.

(2) To be capable of intact re-entry of the fuel capsules for the intact heat source, or capsule burnup in the case of the burn-up type of re-entry.

(3) To provide fuel containment as required to meet safety criteria.

The development program for the heat source will consist of the following sequential phases:

CP 1140--Materials and Component Development

CP 1130--Design Verification

CP 1120--Demonstration Unit

1. Intact Heat Source Design

Direction was received from USAEC to terminate in-house engineering, fabrication and procurement effort related to the intact heat source. Prior to this direction, no new design effort was initiated on the intact heat source, but only those items were performed which were necessary to maintain efforts already in progress. The following specific items were accomplished to maintain fabrication and procurement activities already underway at that time.

(1) Procurement requirements imposed on the capsule liner material supplier were relaxed. This was necessary because design modifications had rendered the supplier unable to comply strictly with the original requirements.

(2) Drawing 466A1141056 of a dummy fuel capsule was revised to incorporate improved brazing and fixturing techniques.

(3) Freeze orders were written where applicable to stop component fabrication and procurement.

2. Burn-up Heat Source Design

The heat source design concept which was generated last quarter was circulated by the Task Force for review and comment. Comments were received from Mound and Sandia personnel which provided a basis for the first of a series of design modifications. A detail preliminary design was completed of the fuel element and all its components, and a heat source assembly drawing was generated. A list of these drawings is provided in Table II-1.

TABLE II-1

Completed Heat Source Drawings

Number	Name	Issue Dates Original	Latest
466A1141060	Element Assembly	11/11	11/19
466A1141061	Capsule Assembly	10/29	11/20
466A1141062	Inner Liner and Liner Details	9/16	11/15
466A1141063	Heat Shield Assembly	10/3	11/6
466A1141064	Spacer	10/8	11/13
466A1141065	Capsulette	11/21	11/21

An attempt was made to delineate all system requirements on the drawings to ensure that the resulting product performs as expected. Such things as thermal inventory tolerances, thermal distribution, radioactive contamination levels, gas-fill control and component temperature limitations have been included in notes on the appropriate drawings. The same subject may not be considered in other documents, such as the Mound/Isotopes Interface Plan or the Mound-prepared SNAP 29 Product Specification. Design effort will be expended in the future to ensure that there are no conflicts between the system requirements delineated on the drawings and overlapping requirements imposed in other documents by other organizations or agencies.

A meeting was held at Isotopes on October 17 with Superior Tube Corporation personnel, at which time their response to the cobalt-base alloy material specification, 466A1030024, and related purchase requisitions was obtained. Comments were received from other tubing suppliers and Isotopes manufacturing personnel in an effort to resolve procurement and fabrication problems before they actually occur. Since that time, a nickel-base alloy material specification, 466A1030025, has been prepared, and the same approach is being taken in exploring suppliers and fabricators for possible problems relating to materials availability and component fabrication. A price and availability study has been initiated to permit quick action once procurement go-ahead is received from the customer.

The design of specific components follows.

a. Capsulette

The minimum number of capsulettes per capsule has been determined to be seven based on fuel handling considerations at Mound Laboratory. Verbal agreement has been obtained from Mound that this number will be incorporated into the final design. The corresponding capsulette length is 1.83 inches.

It is recognized that Mound will have complete design and procurement responsibility for the capsulettes. The capsulette design shown on Isotopes Drawing 466A1141065-009 delineates only those items which are felt to be necessary to ensure correct operation of the heat source subsystem. In this sense it satisfies the requirements of an interface drawing and should require joint approval by Mound and Isotopes. Discussion of this and other component drawings has already taken place by telephone. Additional meetings and discussions will be scheduled between the two organizations in the future.

Since responsibility for the capsulette design has been transferred to Mound, the test effort that was originally planned for the conical lip seal concept has now been discontinued. Two specimens have been reworked since the last report to increase the angular mismatch between the sealing surfaces from two to five degrees. One of the sealing surfaces in each specimen was plated with soft nickel to enhance its sealing action. The specimens were tested at progressively increased torque, but no seal was effected on either specimen. One of the specimens underwent plastic deformation when the cap was tightened and the nickel plating inside the lip separated from its substrate (see Fig. II-1). The results are now being summarized in a topical report. No further work in this area is anticipated.

b. Capsule

Helium, for thermal conduction, is desired within the inner liner and in the annular gap between the inner liner and liner. This will be achieved by performing assembly and welding operations in a helium environment.

The presence of the gas fill eliminates the need for high emissivity coatings on the capsule walls. The application of a high emissivity stable oxide coating would have resulted in loss of dimensional integrity (warping) of fabricated parts.

c. Heat shield

An end closure design has been selected in which a seal weld is used to contain helium as in the capsule/heat shield interface. This came about because thermal calculations showed capsule operating temperatures without a conductive gas interface to be excessive. The recommendation to seal weld the ends of the heat shield has been made by the Task Force. Mound personnel are planning to install a welder in their final assembly position (Box 10) to perform the required seal weld.

It should be noted that the two heat shield ends shown in Drawing 466A1141063 are dissimilar so aerodynamic symmetry is not maintained. This was discussed with aerodynamic analysis personnel, and it is felt that perfect symmetry is not a requirement. The question whether the first end closure should be performed by Mound or Isotopes has yet to be resolved.

Since the acceptance of the seal welded end closure, there are no vacuum gaps within the fuel element. Heat transfer from wall to wall will occur through gas conduction. No intermediate coatings will be required to enhance radiative heat transfer.

A detailed comparison was made of the properties of Haynes-25 and Inconel 625 superalloys (see Memo Report 52). Inconel 625 was selected based on its superior welding and aging characteristics and its lower density.

d. Spacer

A preliminary design was completed (Drawing 466A1141064) for a tubular spacer for use between the fuel capsules. The spacer length of 1.88 inches will provide the necessary separation between the capsules to concentrate their thermal output over the active area of the thermoelectric modules. Other features provided by the spacer are a programmed weak spot to limit the axial forces applied to the capsule during possible overtorquing of the heat shield end caps or unforeseen thermal expansion and impact attenuation during end-on impact. Tubing used in the spacer design has dimensions identical to that used in the inner liner, and the same material is used.

FIG. II-1. PLASTIC DEFORMATION AND NICKEL PLATING SEPARATED FROM SUBSTRATE

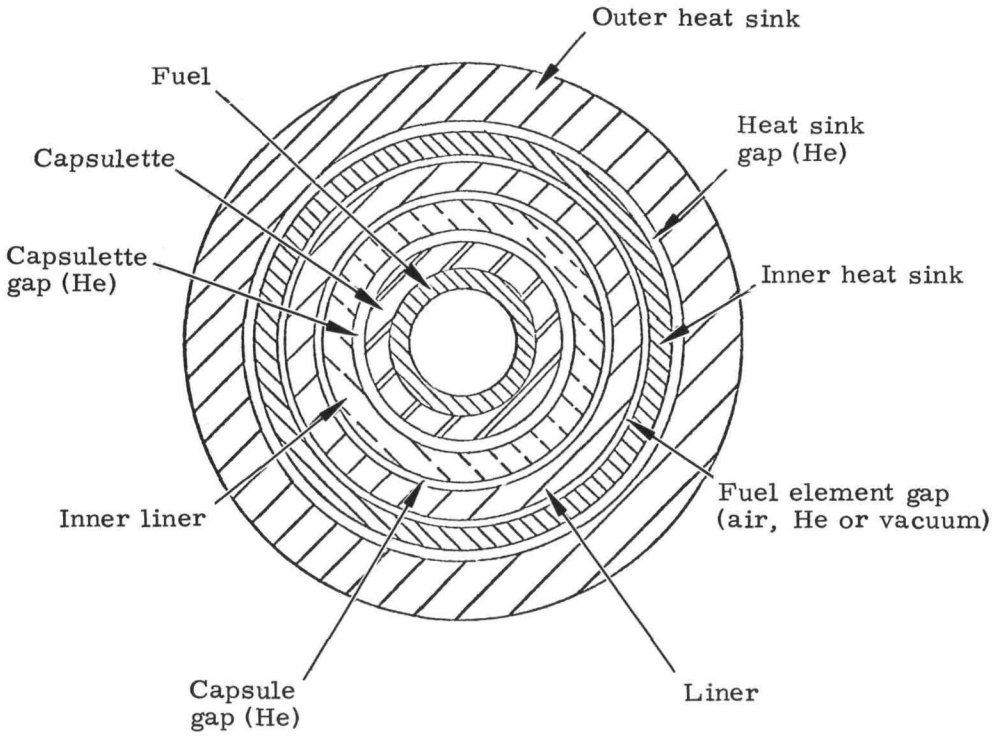

FIG. II-2. FUEL ELEMENT

e. Heat source considerations

Detailed heat shield weight calculations were made for 12, 13 and 14 fuel elements per heat source. The results are tabulated. It is seen that considerable weight can be saved by using a larger number of (thinner) fuel elements. Thirteen elements per heat source were selected based on minimum heat shield thickness requirements for protection from a possible fireball environment.

No. of Elements	Nominal Element Diameter (in.)	Nominal Heat Shield Wall Thickness (in.)	Heat Shield Weights	
			Element (lb)	Total (lb/heat source)
12	1.300	0.200	7.17	86.0
13	1.200	0.150	5.25	68.2
14	1.100	0.100	3.48	48.7

A comparison was made between loading individual fuel elements and loading the entire heat source during the RTG fueling operation. This was done because manipulation of the burn-up heat source may be difficult due to its increased weight. It was concluded that manipulation of a single heat source is the best approach, even if power assist devices are required (see Report 4002-38).

f. Solid propellant burn test specimen

Two fuel element test specimens have been designed for use in the solid propellant burn test. One of these (NSK-984) utilizes stainless steel tubing to simulate annular capsule and heat shield walls. The other (NSK-983) utilizes the actual materials of the fuel element design. Both specimens have internal heaters for preheating the specimen prior to ignition of the solid propellant. Each specimen has thermocouple instrumentation to obtain the temperature history of each tube wall. It was found that pressurization of the specimen could not be achieved without compromising other features such as reliability so specimens will be operated with air at atmospheric pressure in all annular spaces. A specimen holder and thermal insulation will also be provided for the convenience of test personnel and for protection of the power and instrumentation leads.

Discussions have been generated in which the stainless steel and superalloy specimens were compared. Since the superalloy melt temperature is somewhat lower than that for stainless steel, longer melt times are expected for the stainless steel specimen. However, both specimens provide a basis on which to check out the analytical model for use in subsequent predictions. Since both specimens are filled with air instead of pressurized helium, neither provides an exact simulation of the actual fuel element. The fabrication cost of the stainless steel specimen components is approximately one fifth that of the corresponding superalloy parts.

3. Operational Thermal Analysis--Burn-up System

A preliminary thermal analysis for beginning of life (Day 30) was performed for the burn-up fuel element (ref. Fig. II-2) using helium exclusively in all gaps except outside the liner where air and vacuum were also considered. The purpose of this analysis was to determine initial steady state component temperatures in space for a heat source utilizing 13 fuel elements (i.e. 26 capsules, each with 615 watts(t) at Day 30 in conjunction with 2N-SnTe/TAGS diaphragm thermoelectric modules.

Fuel element dimensions are given in Table II-2. For this analysis, maximum gaps were used and it was assumed that the fuel uniformly coats the lateral interior surface of the capsulette.

TABLE II-2

Fuel Element Dimensions

Component	Thickness (in.)	Diameters (in.) Outside	Inside
Outer heat sink	0.0925	$1.200^{+0.000}_{-0.005}$	$1.015^{+0.005}_{-0.000}$
Inner heat sink	0.0565	$1.000^{+0.000}_{-0.005}$	$0.887^{+0.004}_{-0.000}$
Liner	$0.027^{+0.003}_{-0.003}$	--	$0.813^{+0.003}_{-0.000}$
Inner liner	0.0215	$0.795^{+0.000}_{-0.003}$	$0.752^{+0.004}_{-0.000}$
Capsulette	0.020	$0.741^{+0.001}_{-0.001}$	$0.701^{+0.001}_{-0.001}$

Results of the analysis are shown in Table II-3. Although both the air and helium cases are acceptable, the all helium-filled design is preferable. These temperatures are several hundred degrees below the level at which fuel compatibility problems occur or at which creep-strain problems occur on the liner.

TABLE II-3

Temperatures at BOL for a 26-Capsule Burn-up Heat Source Design

Component	Temperature (°F)	T (°F)	Temperature (°F)	T (°F)	Temperature (°F)	T (°F)
Outer heat sink	1460		1460		1460	
0.0125-inch heat sink gap	He	37	He	37	He	37
Inner heat sink	1497		1497		1497	
0.0135-inch fuel element gap	Vac	208	Air	113	He	47
Strength liner	1705		1610		1544	
0.012-inch capsule gap	He	42	He	42	He	42
Inner liner	1747		1652		1586	
0.008-inch capsulette gap	He	30	He	30	He	30
Capsulette	1777		1682		1616	

Similar work was performed on a 12-fuel element heat source (i.e., 24 capsules) and is reported in Report 4002-27, CDI. In addition to the gas fills considered for the 13-fuel element heat source, air and vacuum fills between the inner and outer heat sinks and outside the liner were investigated. These results are presented in Table II-4.

Case 7 (vacuum in both the heat sink and fuel element gaps) is unacceptable on both the capsulette (fuel compatibility) and liner (creep-strain problem). Cases 5 and 6 (vacuum outside liner, helium or air between heat sinks) are marginal. However, a multidimensional analysis would probably eliminate these two cases because of local thermal effects (presence of shutters, circumferential conduction toward the shutters and T/E modules). In addition, inability to achieve an emissivity of 0.8 inside the fuel element would cause all capsule temperatures in Cases 3 through 7 to rise (see Section B-1), a trend that would also reject Cases 5 and 6. Cases 1 through 4 would be acceptable approaches for normal steady state operation. As discussed, the all-helium filled design has been selected using 13 fuel elements.

4. Thermal Effect of Emissivity in Fuel Element

A beginning-of-life (Day 30) thermal analysis was performed to determine the effect of emissivity (on the outer surface of the liner and the inner surface of the inner heat shield) on capsule component temperatures. The burn-up design considered was that of 13 fuel elements (26 capsules) and a split superalloy heat sink with helium between the sinks. The work was reported in Report 4002-41. The outer and inner heat sinks will operate at 1460° and 1490° F, respectively. Capsule component temperatures are given in Fig. II-3 for various effective emissivities.

The critical temperature is that on the capsulette for fuel compatibility reasons. (Liner temperatures are not as critical for creep strain.) Since some margin on capsulette temperature will be necessary because of locally higher temperatures (due to shutter and other three-dimensional effects), an effective emissivity of ~0.7 will be required. With this value, actual emissivities on the order of 0.8 are required. The ability of an oxide coating to provide this initially is from marginal to not possible. In addition, the stability of the oxide surface in vacuum is questionable (Report 4002-44). The use of an externally applied high emissive coating, such as iron titanate, may not be an acceptable approach because of difficulty in applying it on the inner surface of the inner heat shield and because of decontamination difficulty with the capsule.

5. N-series Thermal Analysis (Mound Test Specimen)

Mound Laboratory requested Isotopes to perform a thermal analysis of a double-walled Haynes-25 test capsule for use in a pending compatibility test (N-series). The purpose of the analysis was to determine what ambient air or capsule surface temperature is required to obtain 1000° C on the inner liner in the vicinity of the fuel (GdPo/Ta matrix). This work is reported in Report 4002-57, CDI.

Six containers are to be loaded in a furnace with two control specimens for the 50- to 150-day compatibility test. A sketch of the test setup is given in Fig. II-4. As shown in the sketch, the eight capsules are placed in a Haynes-25 pan and inserted into a 2-1/2-inch ID alumina tube. The tube is placed in a furnace and air surrounds the specimens.

Figure II-5 is a dimensioned cross section of a single test specimen. Figure II-6 is the same specimen divided into 72 nodes for thermal analysis as follows:

TABLE II-4

Temperatures at BOL for 24-Capsule Burn-up Concept Heat Source

Component	Case 1		Case 2		Case 3		Case 4		Case 5		Case 6		Case 7	
	Temp (°F)	T	Temp (°F)	T	Temp (°F)	T	Temp (°F)	T	Temp (°F)	T	Temp (°F)	T	Temp (°F)	T
Outer heat sink	1460		1460		1460		1460		1460		1460		1460	
0.0125-inch heat sink gap	Air	104	He	39	Air	104	He	39	Air	104	He	39	Vac	205
Inner heat sink	1564		1499		1564		1499		1564		1499		1665	
0.0135-inch fuel element gap	He	38	He	40	Air	116	Air	121	Vac	196	Vac	220	Vac	179
Strength member	1602		1539		1680		1620		1760		1719		1844	
0.012-inch capsule gap	He	48	He	48	He	48	He	48	He	48	He	48	He	48
Liner	1650		1587		1728		1668		1808		1767		1892	
0.007-inch capsulette gap	He	28	He	28	He	28	He	28	He	28	He	28	He	28
Capsulette	1678		1615		1756		1696		1836		1795		1920	

CONFIDENTIAL

CONFIDENTIAL

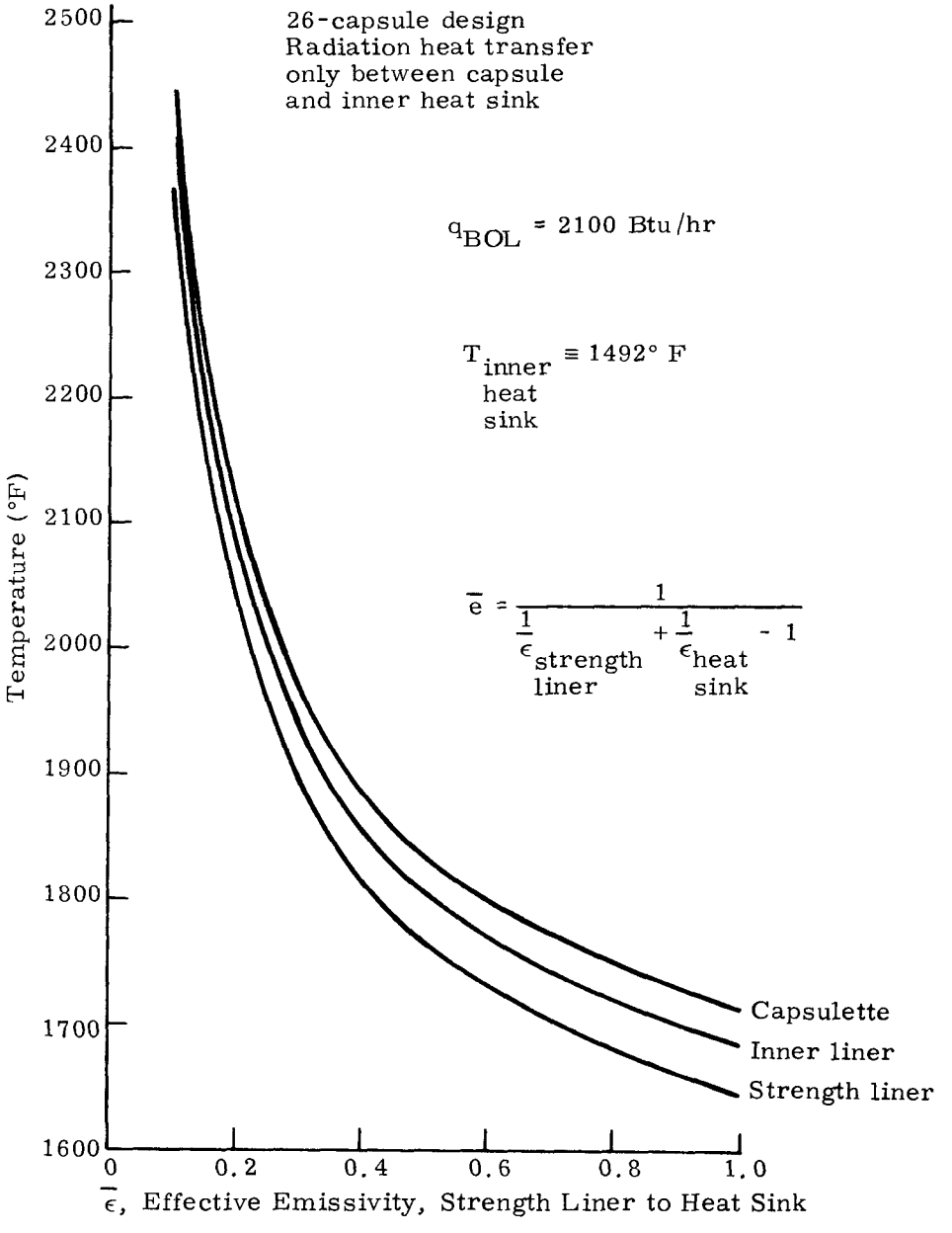

FIG. II-3. CAPSULE COMPONENT TEMPERATURES VERSUS STRENGTH LINER TO HEAT SINK EFFECTIVE EMISSIVITY

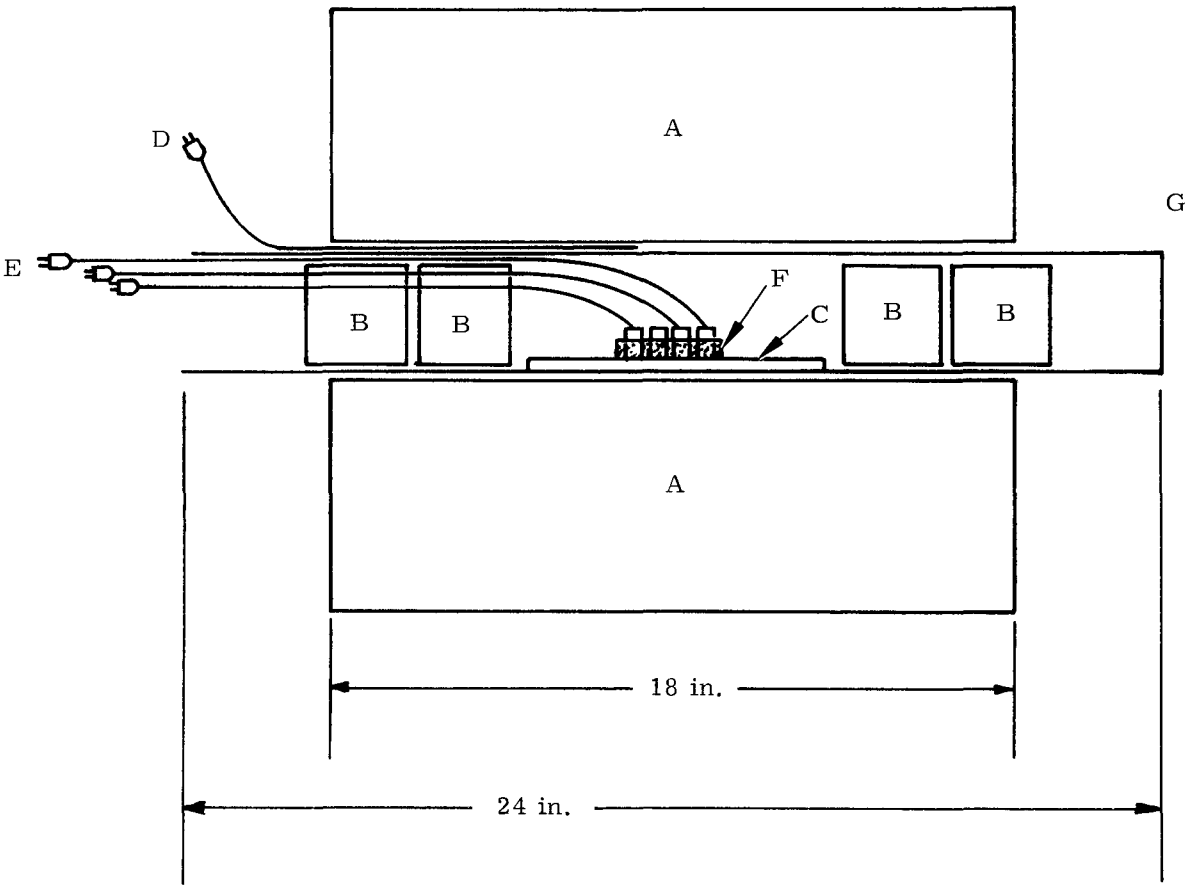

A. Pt-wound furnace
B. Ceramic plugs
C. Ceramic base
D. Thermocouple for power control
E. Thermocouples attached to 3 capsules. Actual temperature control will be based on 1 thermocouple
F. Haynes-25 pan (well oxidized) 2-1/2 in. long x 2 in. wide x 1/2 in. deep
G. 2-1/2 in. ID alumina tube

Loading will involve 8 capsules placed 2 deep, about 1/8 in. apart.

FIG. II-4. COMPATIBILITY TEST SETUP

CONFIDENTIAL

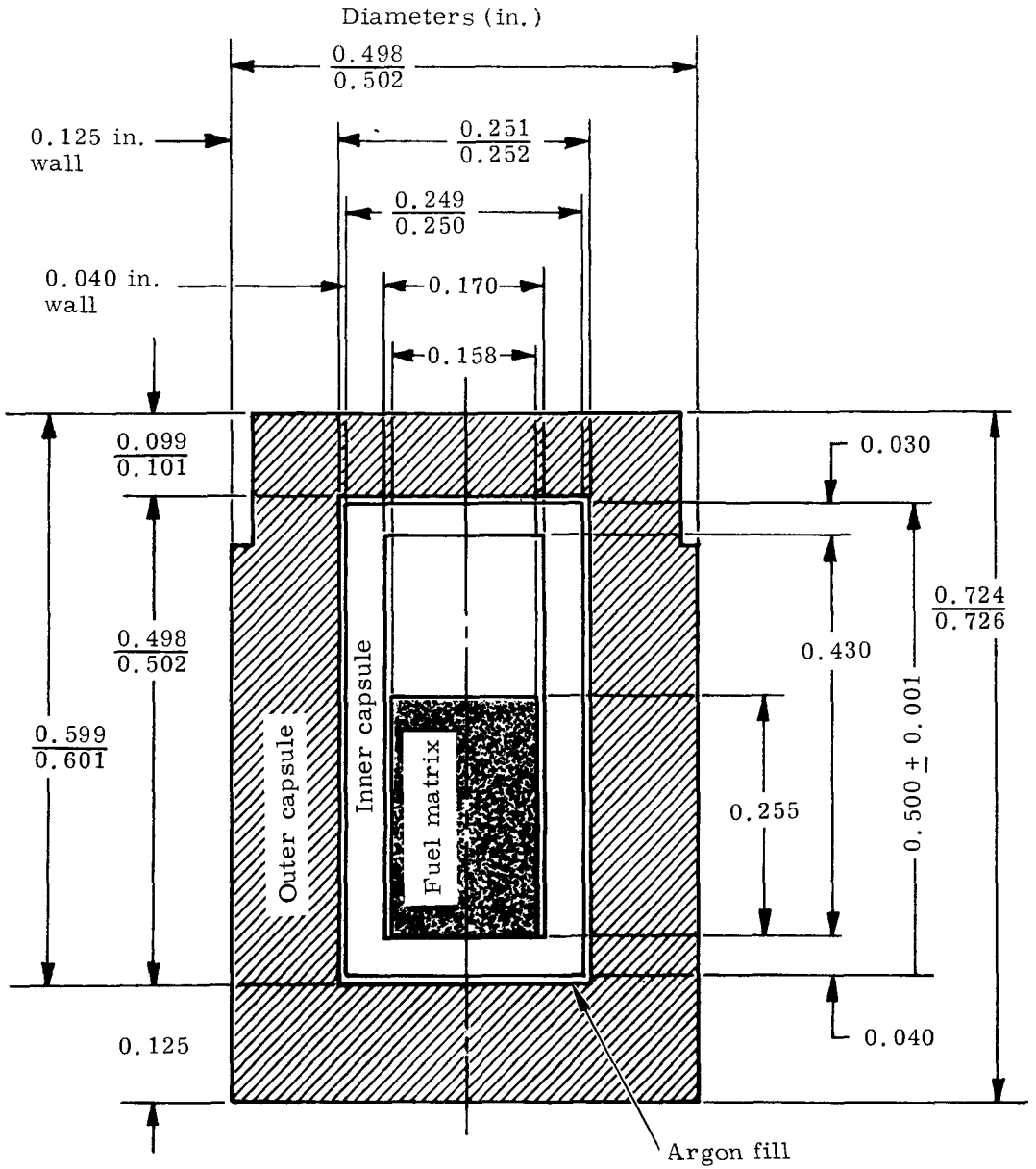

FIG. II-5. TEST CAPSULE

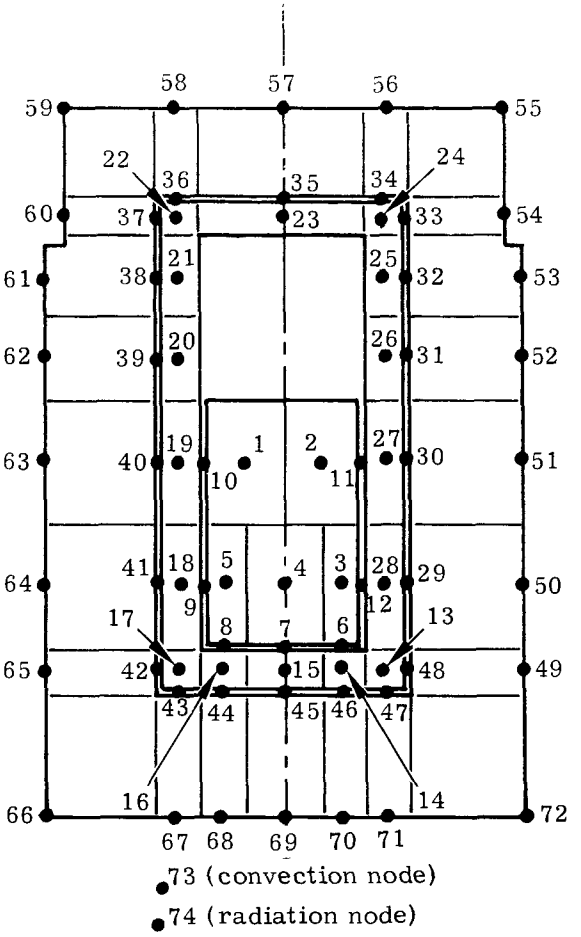

FIG. II-6. THERMAL ANALYSIS MODEL

CONFIDENTIAL

Item	Nodes
Fuel	1 to 5
Argon between fuel and inner liner	6 to 12
Inner liner	13 to 28
Argon between liners	29 to 48
Outer liner	49 to 72

Node 73 is a boundary node for convection while Node 74 is a boundary node for radiation. All nodes to the left of the centerline on Fig. II-6 are centers for nodal segments that occupy one-fourth of the capsule in the -direction. Those to the right of the centerline are modeled for segments occupying the other three-fourths of the capsule. This nodal breakdown was used to permit analysis of a capsule adjacent to others in the Haynes-25 pan. Such a capsule will effectively be insulated for radiation (not convection) for ~25% of its lateral area. The emissivity of the Haynes-25 outer liner and pan is 0.80 (oxidized). A heat transfer coefficient for material convection of 0.74 Btu/ft^2-hr-°F was determined.

Three Po-210 fuel inventories were examined: 3.47 watts, the maximum initial inventory of any capsule; 2.27 watts, the minimum initial inventory; and 1.00 watt, the minimum inventory possible for any capsule at Day 150.

A summary of cases investigated is given in Table II-5. In all cases, the Linearized Matrix Theory Heat Transfer Program was used to obtain the solution.

TABLE II-5

Cases Investigated

Case	Fuel Inventory (watts)	Lateral Surface Radiating Heat to Boundary (%)	Gap Between Liners (in.)	Remarks
1	2.27	100	None	Minimum initial inventory; minimum gap; maximum heat rejection area. Case gives minimum initial temperatures
2	3.47	100	None	Maximum initial inventory
3	3.47	75	None	Shows effect of radiating area
4	3.47	75	0.0015	Case uses maximum possible gap; gives maximum initial temperatures
5	1.00	100	None	Minimum inventory at Day 150; minimum temperatures possible at Day 150. Inventory based on 2.27-watt inventory at Day 0.

Detailed temperature results for all cases in Table II-5 are presented in Report 4002-57, CDI. Table II-6 is a summary and depicts temperatures for each of the five cases at top center (Node 57) and midpoint (Node 63) on the outer capsule, at the bottom (Node 15) of the inner capsule (maximum capsule temperature point) and on the boundary (Nodes 73 and 74). The boundary is defined as the Haynes-25 pan, the alumina tube or the air. Also shown on Table II-6 is the difference between the boundary temperature and the maximum liner temperature.

TABLE II-6

Selected Temperature Results

Case	Boundary Nodes 73 & 74(2) (°F)	(°C)	Node 57(2) (°F)	(°C)	Node 63(2) (°F)	(°C)	Node 15(2) (°F)	(°C)	Difference Between Boundary and Node 15 (°F)	(°C)
1	1815	991	1825	996	1828	998	1834	1001	19	10
2	1800	982	1815	991	1820	993	1829	998	29	16
3	1795	979	1814	990	1821	994	1829	998	34	19
4	1779	971	1800	982	1806	986	1833	1001	54	30
5	1825	996	1829	999	1831	999	1833	1001	8	5

(1) See Table II-10 for case identification

(2) See Fig. II-19 for nodal identification

For a compatibility experiment, the lowest liner temperature must be considered the limit of demonstrated experimental evidence. Thus, Case 1 predicts that the capsule loaded with 2.27 watts will have a maximum liner temperature 10° C above the ambient air temperature in the tube; Case 2 predicts that the capsule loaded with 3.47 watts could operate as low as 16° C above ambient. Case 4 predicts that the 3.47-watt capsule will, at most, be 30° C above ambient. Case 3 shows that the effect of insulating part of the lateral area of a capsule (due to adjacent fueled capsules) is not large. Case 5, which is the lowest possible situation at Day 150, shows an ambient-to-liner difference of only 5° C. From the other cases, it is clear that the temperature difference is nearly proportional to fuel loading, and hence the 150 Day result for higher inventories will be about half of the initial difference.

The conclusion of this study is that for conservatism, it is necessary to control with the 10° C difference between the air and the maximum liner temperature. After 150 days this temperature difference will be 5° C.

6. Thermal Analysis of Mound Test Capsule for Po Metal Hot Spot Test

An analysis was performed to determine the steady-state temperature distribution of the Mound fuel capsule used in the first polonium metal hot spot test at Mound Laboratory. Details of the Mound capsule are shown in Fig. II-7. The capsule is fueled with ~1 gram (144 watts) of polonium metal and was tested in a vacuum environment.

Three fuel distributions within the capsule were investigated:

(1) Uniform coating of the bottom end cap

(2) Uniform coating of the bottom end cap and the lower portion of the side wall

(3) Uniform coating of the entire internal surface.

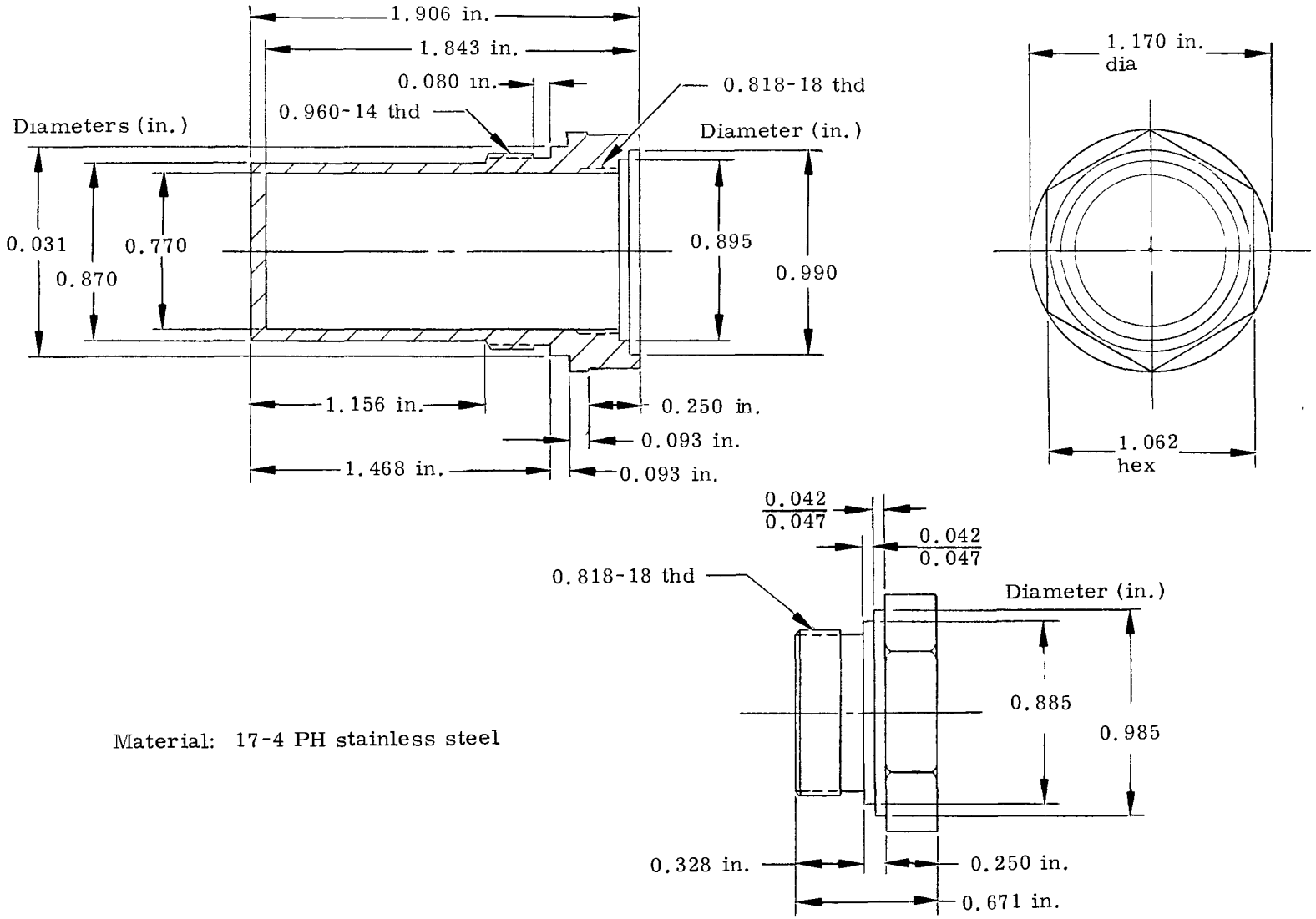

Material: 17-4 PH stainless steel

FIG. II-7. MOUND TEST CAPSULE

The thermal models associated with each of these fuel distributions are shown in Figs. II-8 through II-10. The specific cases analyzed are listed in Table II-7. In all cases, the capsule was assumed to be in radiation equilibrium with a 70° F ambient environment. The effect of internal radiation was investigated for the case of an emissivity of 0.8 on both the inner and outer surfaces with the fuel coating only the bottom end cap (i.e., Case 4). This case was treated conservatively in that multiple reflections among the internal nodes were not considered. Instead, Nodes 6 through 16 were given an unity absorption factor and connected to a sink which was assigned a temperature (namely, 700° F) which was slightly higher than the average temperature of Nodes 22 through 26 determined from the results of the analogous case (Case 3) with no internal radiation. Internal convection, along with the effect of evaporization and condensation of the fuel, was neglected in the analysis. In addition, all contained vapors were assumed to be transparent and nonheat generating.

The Linearized Matrix Inversion Steady State Heat Transfer Program (KN340A) was used for the analyses.

TABLE II-7

Summary of Cases Analyzed

Case	Capsule Emissivity	Fuel Distribution	Internal Radiation
1	0.2	Bottom end cap	No
2	0.5	Bottom end cap	No
3	0.8	Bottom end cap	No
4	0.8	Bottom end cap	Yes (ϵ = 0.8)
5	0.8	Nodes 6 thru 14	No
6	0.8	Entire inner surface	No

Temperature distributions for the cases analyzed are shown in Figs. II-11 through II-16. Temperatures at various points on the test capsule are also summarized in Table II-8. Temperature gradients as large as 1600° F arise between the bottom and top end cap when the fuel is uniformly distributed over only the bottom end cap. Results from the case where internal radiation was considered indicate that this mechanism would decrease the hot spot temperatures by at most 300° F. Consequently, since large temperature gradients will still remain, a hot spot would readily be detected visually if the fuel agglomerates on the bottom end cap. Note that the temperatures of Nodes 22 to 44 are approximately 70° F lower with internal radiation than they were with no internal radiation. This is due to the manner in which internal radiation was treated in the analysis. As mentioned in the analysis, Nodes 6 to 16 were connected to a 700° F sink and multiple reflections among the internal nodes was not taken into account. In reality, the temperature of Nodes 22 to 44 would increase slightly due to internal radiation.

Capsule temperatures and the temperature gradient were decreased significantly for the remaining two fuel distributions. The gradient associated with the uniform coating of the fuel on the bottom and part of the side of the capsule is still quite large (~800° F) so that the hot spot temperatures would readily be detected by proper thermocouple instrumentation.

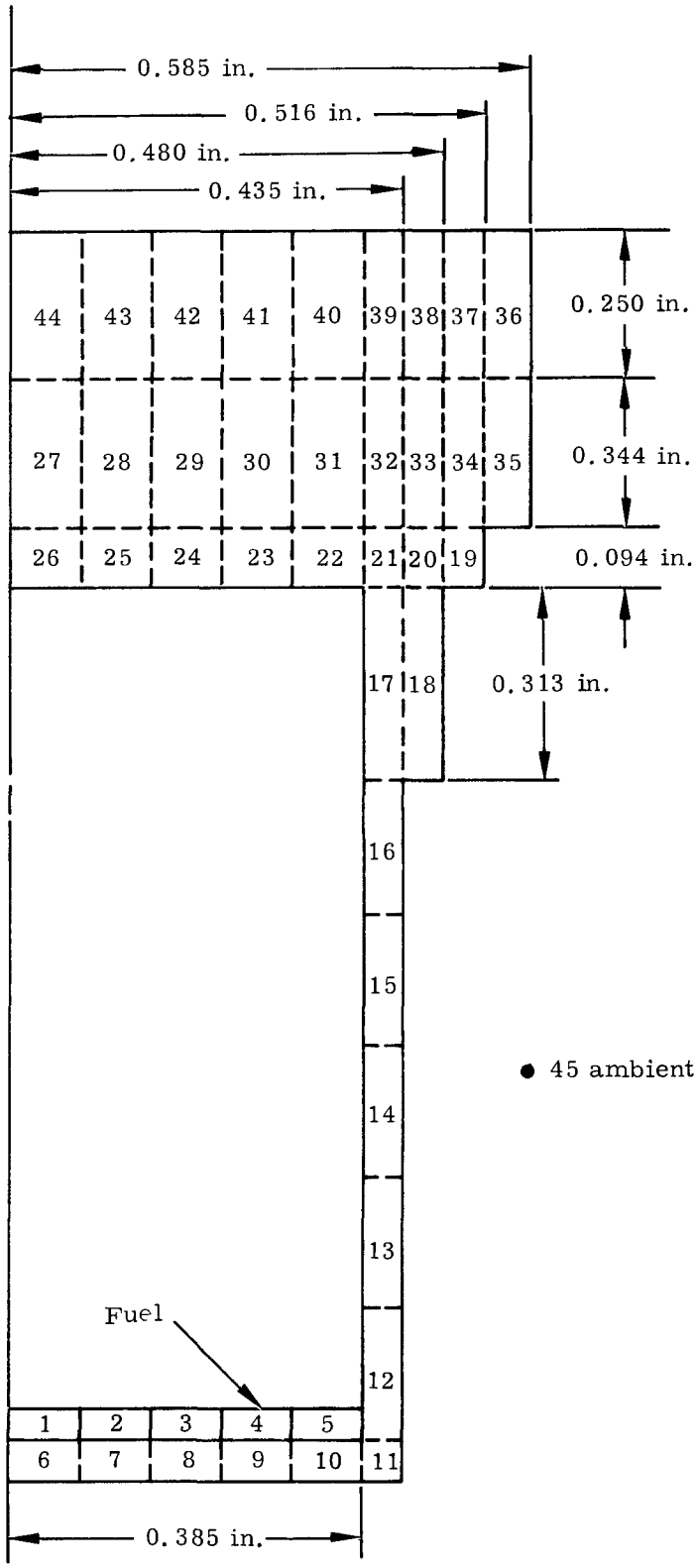

FIG. II-8. THERMAL MODEL FOR FUEL ON BOTTOM END CAP

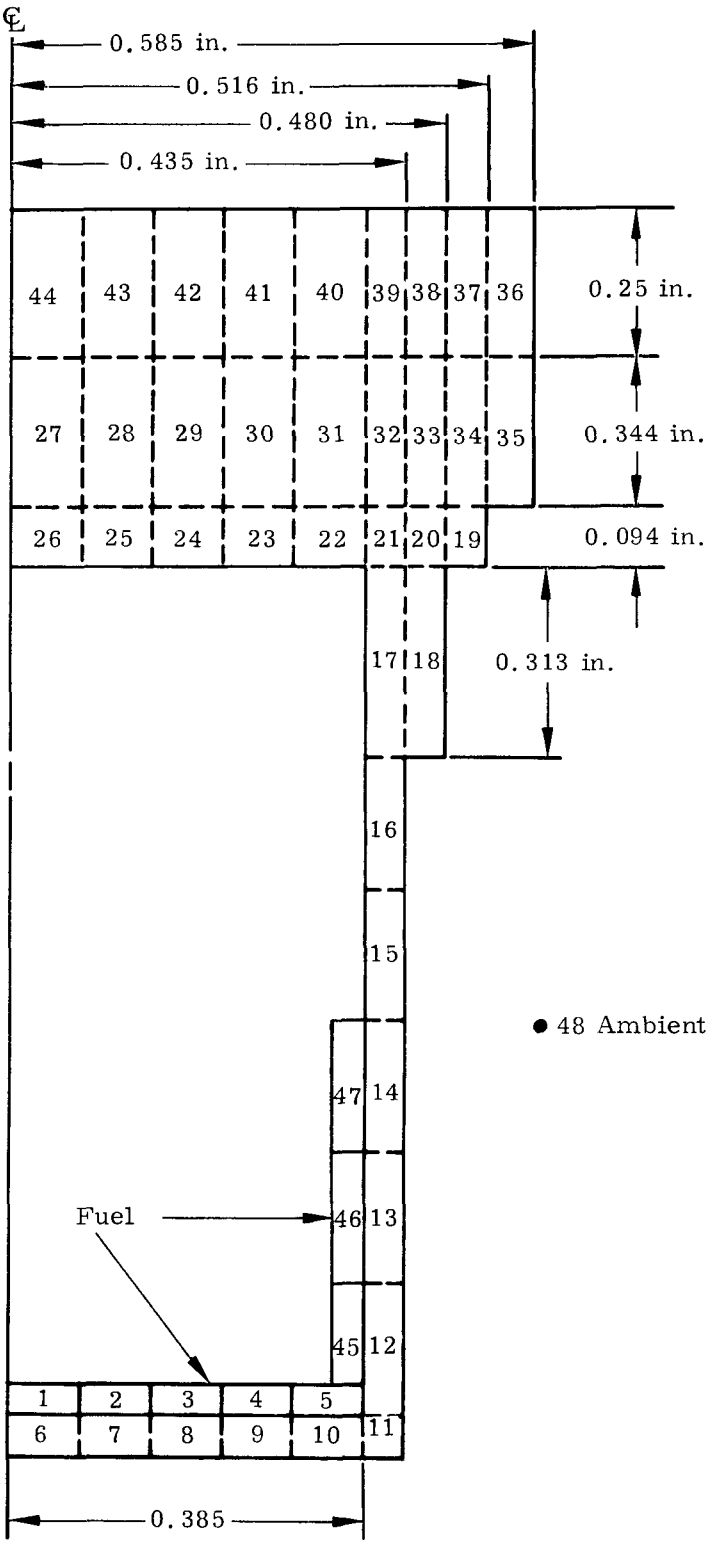

FIG. II-9. THERMAL MODEL FOR FUEL ON BOTTOM AND LOWER SIDE

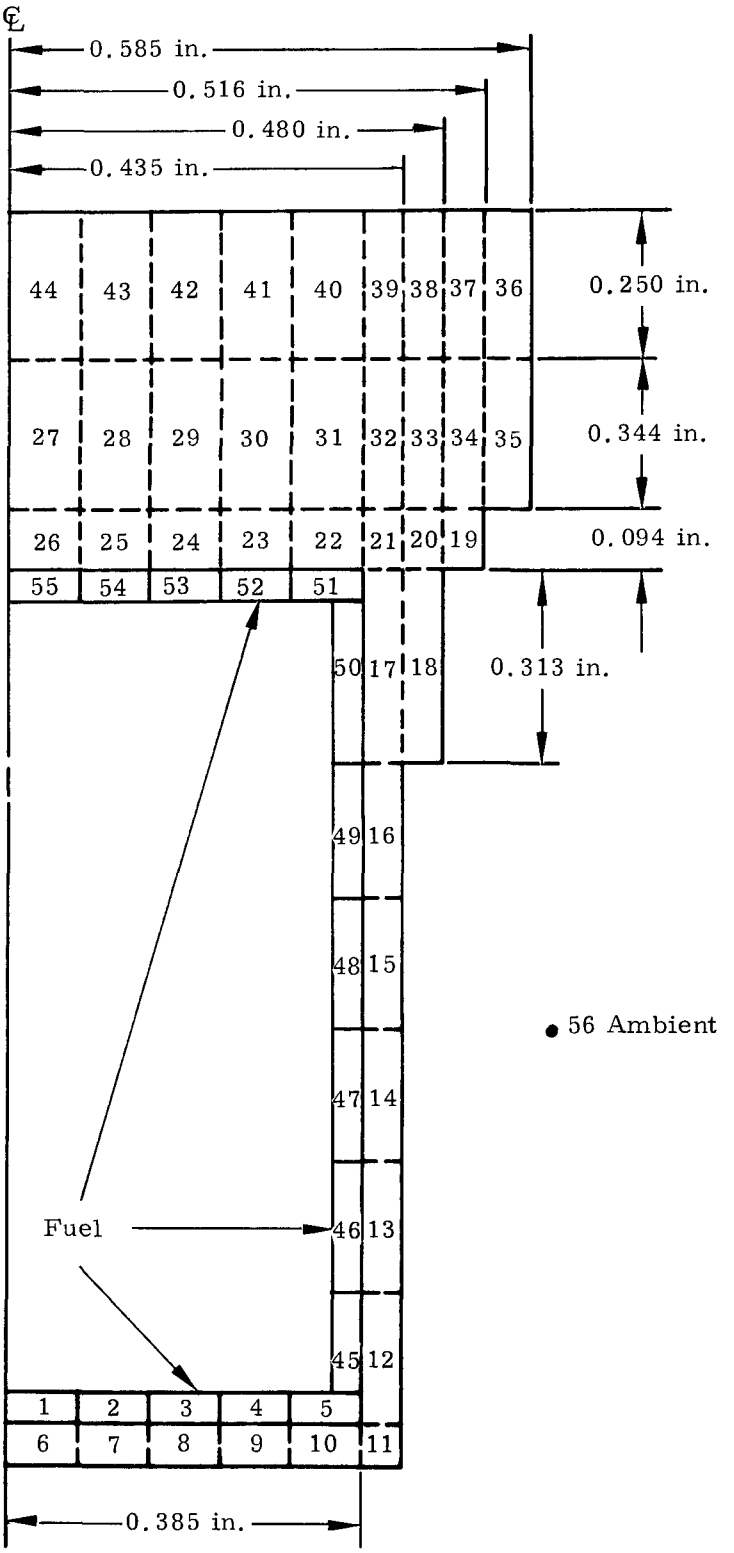

FIG. II-10. THERMAL MODEL FOR FUEL UNIFORMLY DISTRIBUTED

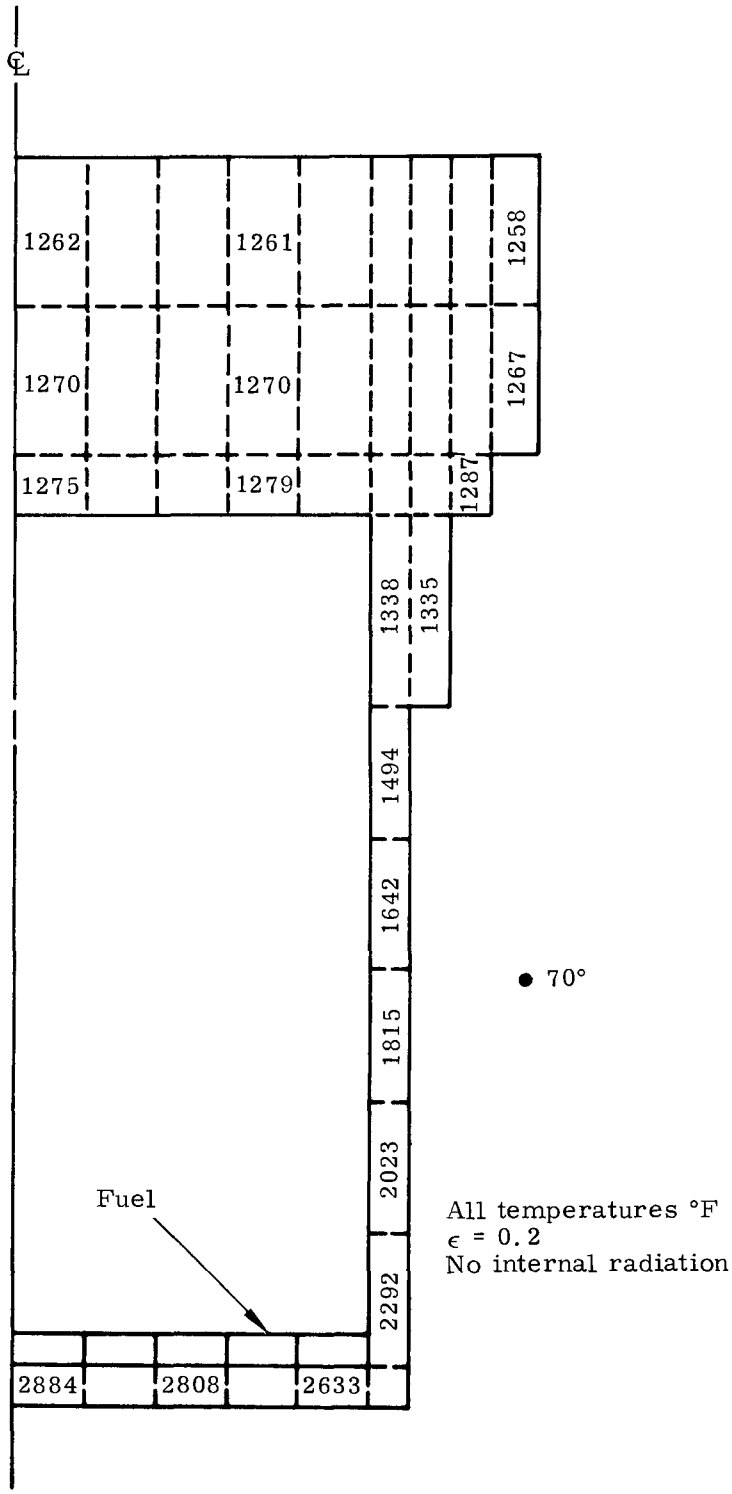

FIG. II-11. TEMPERATURES FOR FUEL ON BOTTOM END CAP

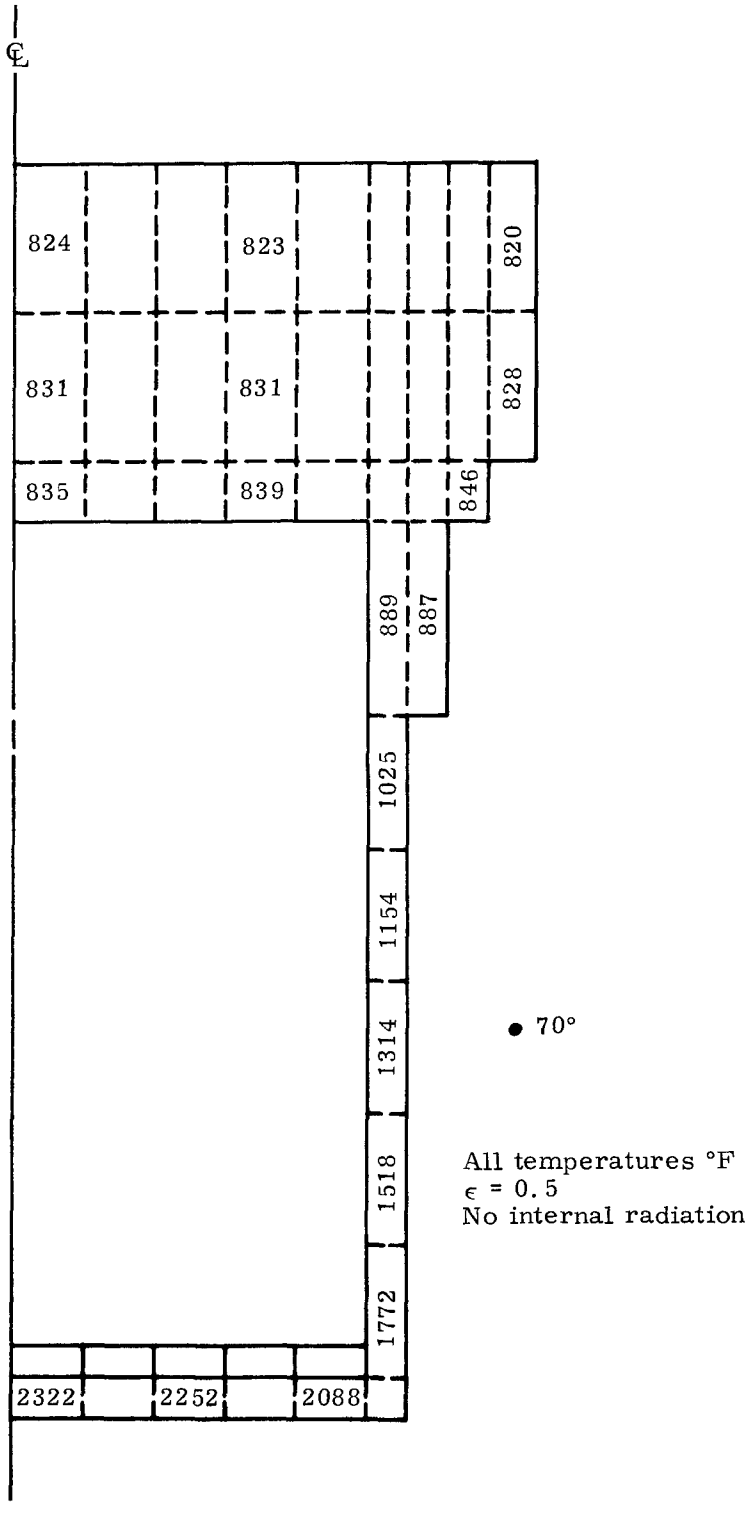

FIG. II-12. TEMPERATURES FOR FUEL ON BOTTOM END CAP

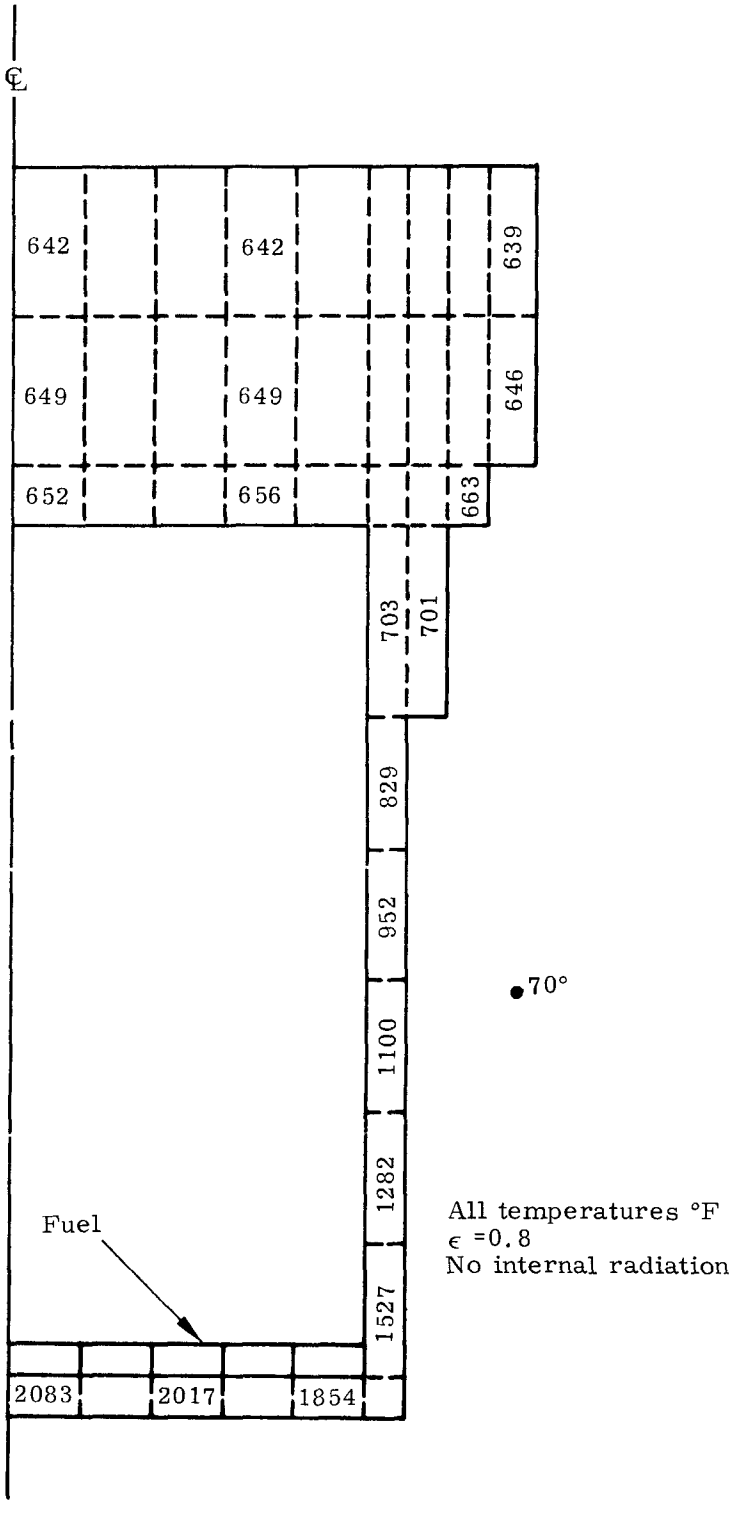

FIG. II-13. TEMPERATURES FOR FUEL ON BOTTOM END

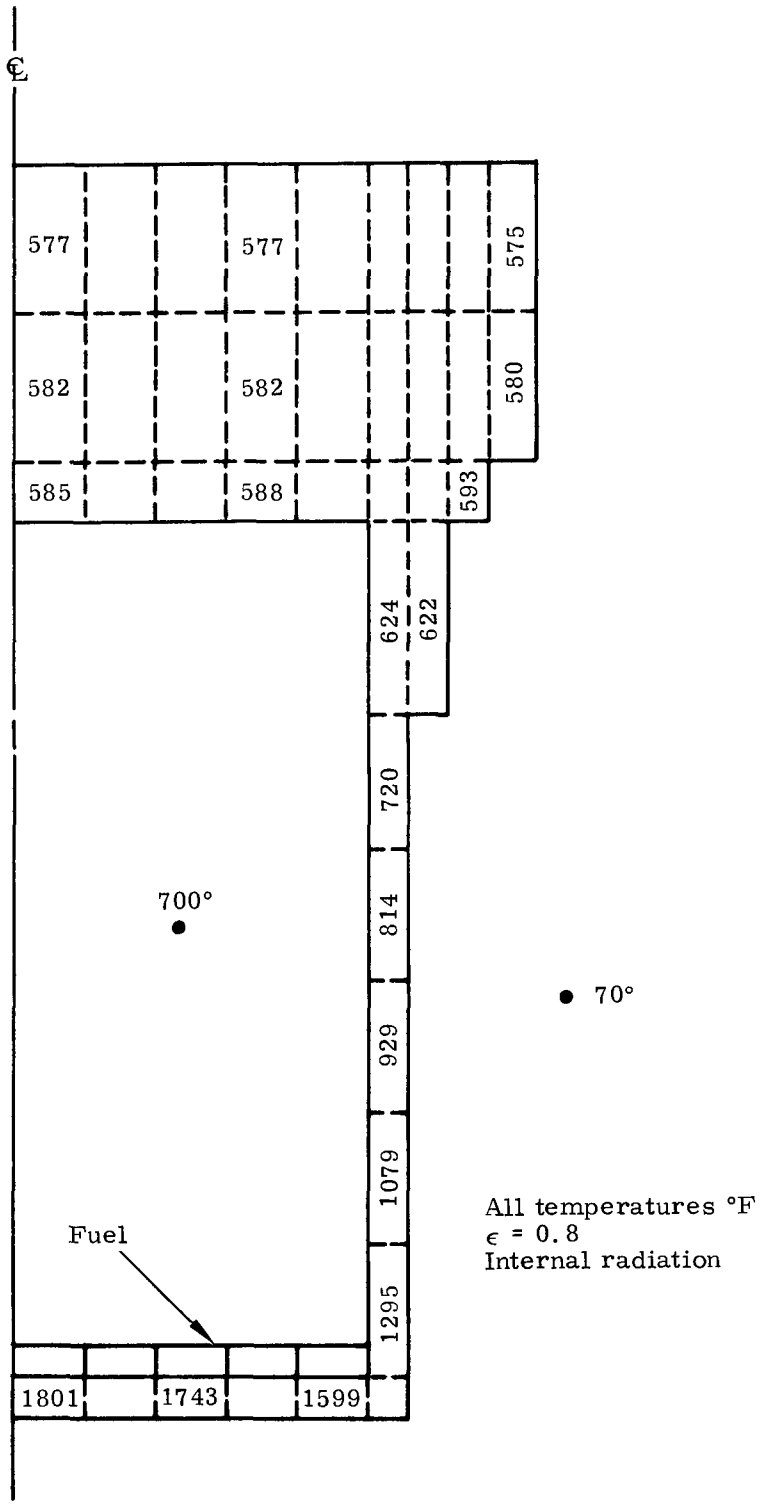

FIG. II-14. TEMPERATURES FOR FUEL ON BOTTOM END CAP

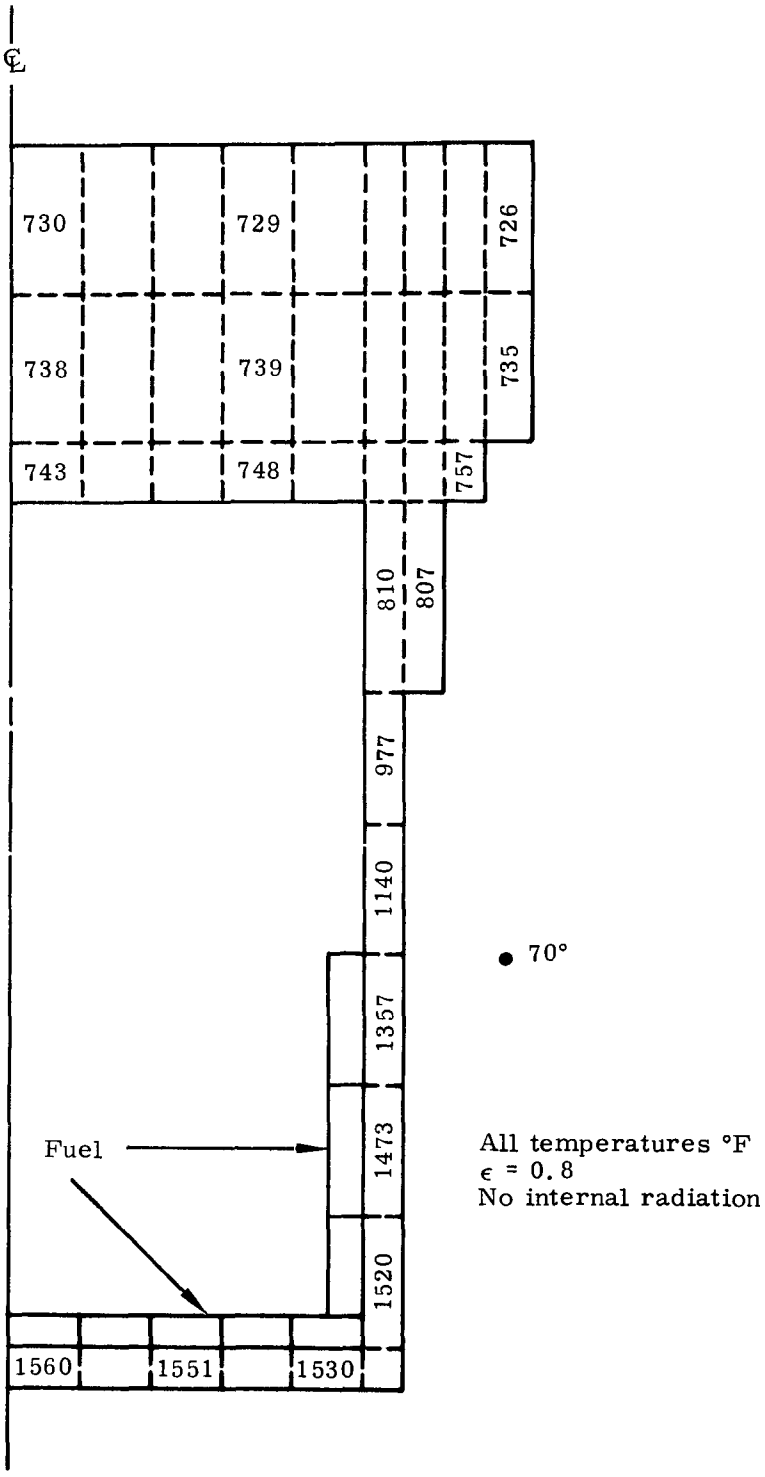

FIG. II-15. TEMPERATURES FOR FUEL ON BOTTOM AND LOWER SIDE

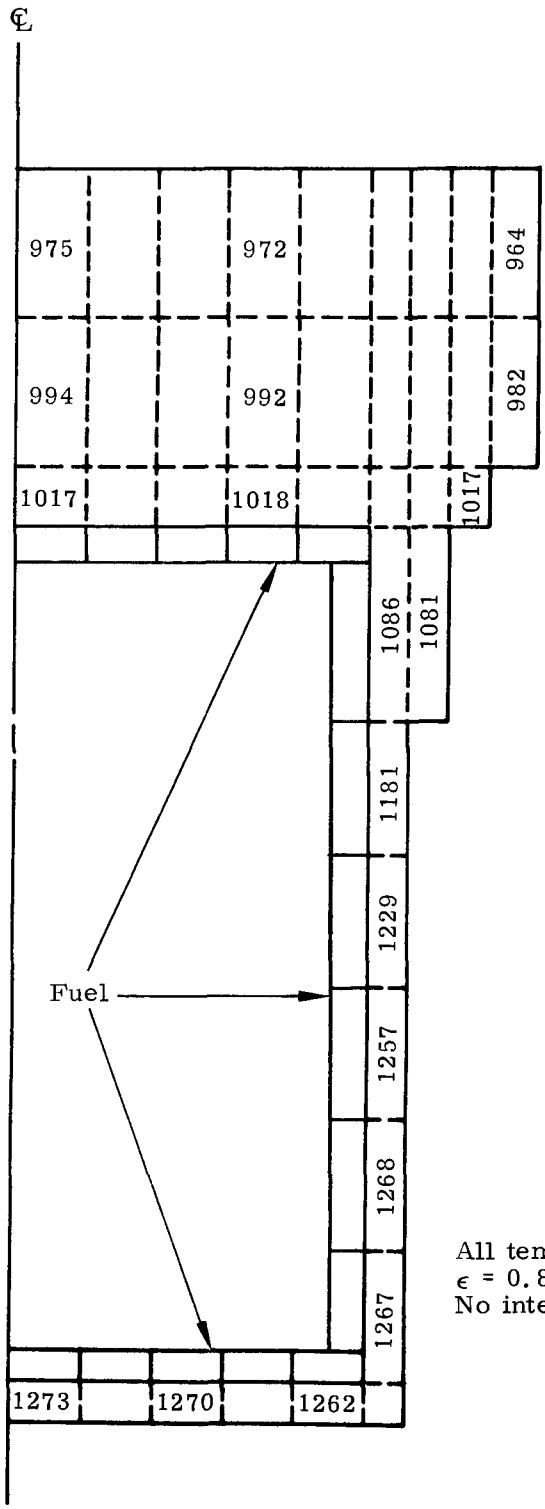

FIG. II-16. TEMPERATURES FOR UNIFORM FUEL DISTRIBUTION

TABLE II-8

Summary of Capsule Temperatures (°F)

Case*	Node 6	Node 12	Node 15	Node 19	Node 36
1	2884	2292	1642	1287	1258
2	2322	1772	1154	846	820
3	2083	1527	952	663	639
4	1801	1295	814	593	575
5	1560	1520	1140	757	726
6	1273	1267	1229	1017	964

*See Table II-7.

Conclusions which can be derived from the results are as follows:

(1) The magnitude of the temperatures and the temperature gradient that arise when the fuel is on the bottom end cap are such that the hot spot should be readily detected visually. This also holds true for the case where the fuel coats the bottom and lower part of the side of the capsule.

(2) Internal radiation will alleviate hot spot temperatures to the extent that melting of the capsule should not occur if the fuel uniformly coats the bottom end cap (the melting range of 17-4 PH steel is 2560° to 2625° F). However, if the fuel were to agglomerate on the bottom end cap this conclusion would probably not hold.

(3) Uniform coating of the inside of the test capsule could produce gradients of several hundred degrees Fahrenheit with the asymmetric test capsule used.

7. Capsule Meteoroid Penetration

Two capsule meteoroid penetration studies were performed to determine the no-penetration probability of a proposed SNAP 29 burn-up capsule (1.2-inch OD) for 90-day operation in space. The individual studies predicted the probability of no penetration through various thicknesses of the following heat shield materials:

(1) Type 301 stainless steel (Report 4002-35)

(2) Inconel 625 (Report 4002-60).

Both the current accepted and proposed new criteria (both by Aerospace Corporation) were used in determining the no-penetration probability.

The 90-day no-penetration probability is plotted versus outer heat shield thickness for the Type 301 stainless steel and Inconel 625 heat shields in Figs. II-17 and II-18, respectively. For the current split heat sink design (0.092 inch thick outer heat shield), the probability of no-penetration for either criteria was ~0.9985 for the Type 301 stainless steel and 0.999 for the Inconel 625. The no-penetration reliability should be considered along with other reliabilities in the generator to determine whether or not the required RTG overall mission reliability of 0.98 is being met.

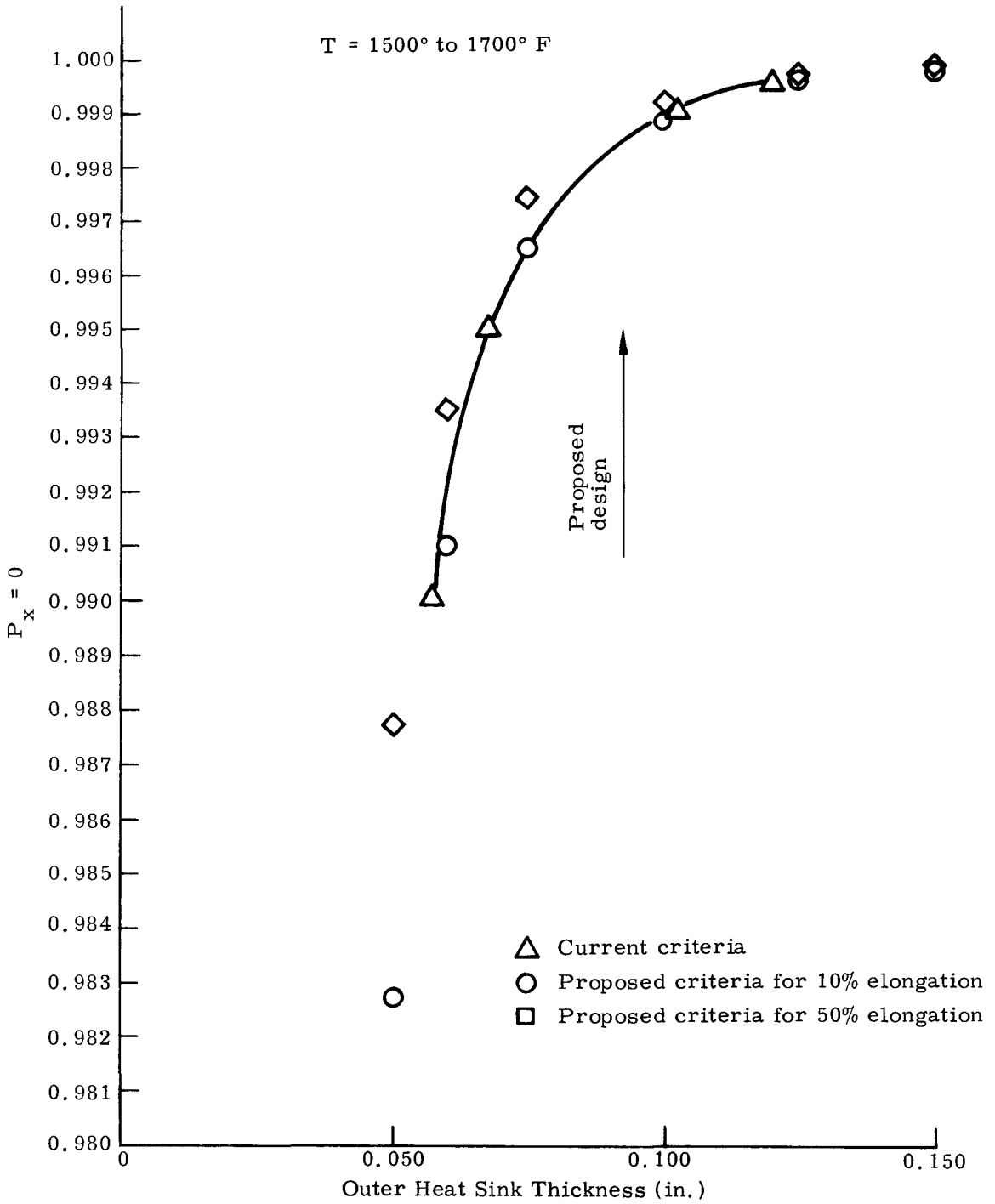

FIG. II-17. NO-PENETRATION PROBABILITIES FOR BURN-UP HEAT SOURCE MADE OF TYPE 301 STAINLESS STEEL

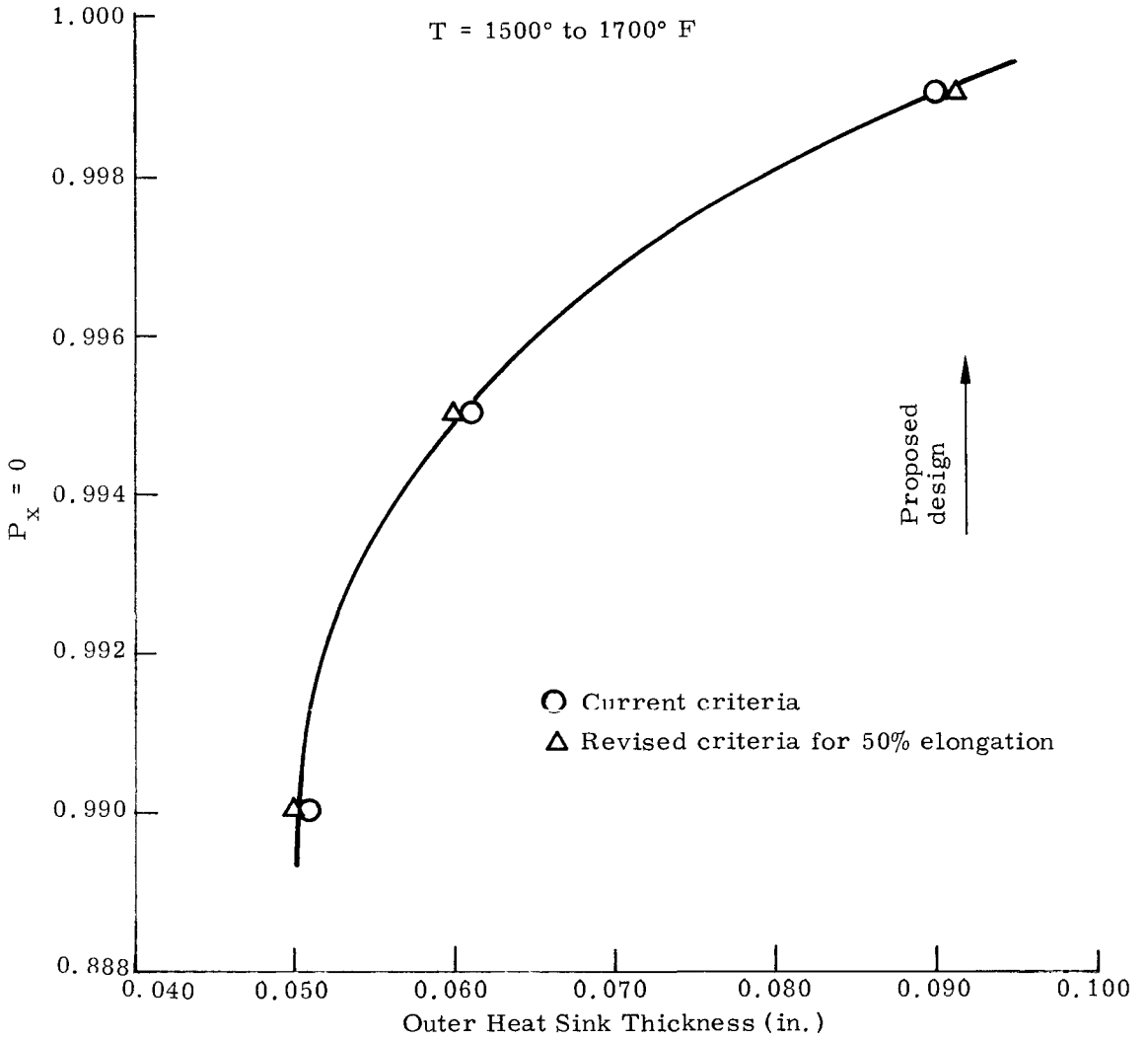

FIG. II-18. NO-PENETRATION PROBABILITIES FOR BURN-UP HEAT SOURCE MADE OF INCONEL 625

8. Heat Source Thermal Analysis

View factors and absorption (β) factors associated with radiant interchange between the fuel elements and the closed shutters (EOL) have been determined (Report 1140-420). The half unit cell model used in the analysis is shown in Fig. II-19.

The view factors were determined using the CONFAC II computer program. A utilization report (Report NSD-PB-7651) for using CONFAC II on the IBM 360/44 to determine view factors between planar surfaces has been documented in this quarter. The view factors which were calculated for the SNAP 29 heat source are listed in Table II-9.

TABLE II-9

Summary of SNAP 29 Heat Source View Factors

Fuel Element--Hot Plate, Diaphragm Module

	View Factors*							
i	F_{i-1}	F_{i-2}	F_{i-3}	F_{i-7}	F_{i-8}	F_{i-9}	F_{i-15}	F_{i-16}
1				0.29589	0.26883	0.41120	0.01193	0.01193
2				0.04777	0.15651	0.77268	0.01152	0.01152
3					0.02049	0.95834	0.01024	0.01024
7	0.09573	0.01539			0.20900	0.66100	0.01143	0.01443
8	0.13914	0.08098	0.01061	0.34890		0.39768	0.01196	0.01196
9	0.08167	0.15000	0.18500	0.41300	0.14900		0.01121	0.01121
15	0.09652	0.06958	0.01113	0.27979	0.18322	0.36618		0.00024
16	0.09652	0.06958	0.01113	0.27979	0.18322	0.36618	0.00024	

Fuel Element--Closed Shutters

i	F_{i-4}	F_{i-5}	F_{i-6}	F_{i-10}	F_{i-11}	F_{i-12}	F_{i-13}	F_{i-14}
4				0.96045	0.01673	0.00110	0.01075	0.01075
5				0.80800	0.07340	0.09260	0.01301	0.01301
6				0.52546	0.11245	0.33331	0.01428	0.01428
10	0.09885	0.08248	0.05417		0.08711	0.65348	0.01197	0.01197
11	0.00866	0.03797	0.05821	0.43879		0.42746	0.01423	0.01423
12	0.00014	0.01191	0.04365	0.81657	0.10515		0.01219	0.01219
13	0.00816	0.04057	0.05892	0.41306	0.11101	0.37181		0.00054
14	0.00816	0.04057	0.05892	0.41306	0.11101	0.37181	0.00054	

*See Fig. II-19 for view factor subscripts.

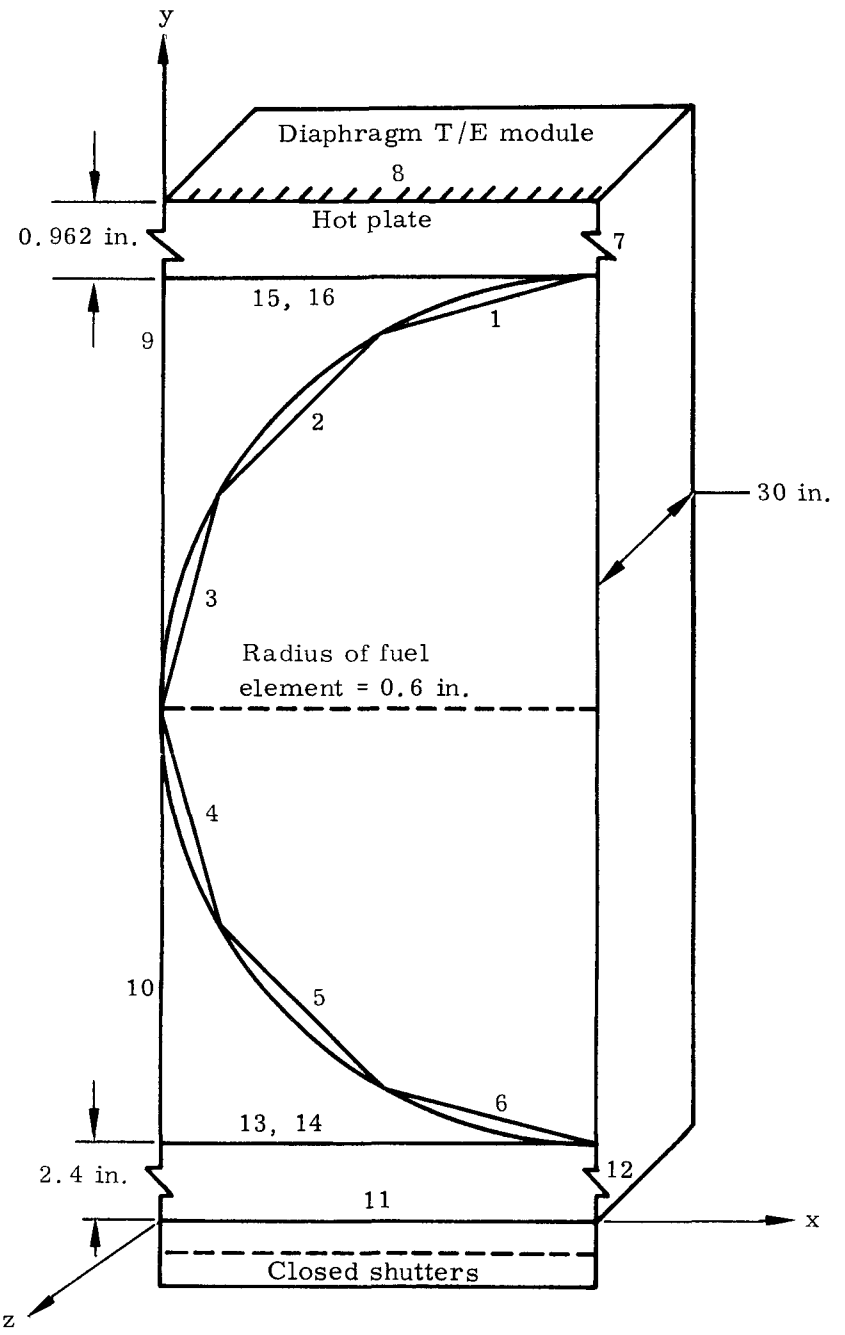

FIG. II-19. HALF-UNIT CELL MODEL FOR SNAP 29 HEAT SOURCE

The absorption factors were determined from the view factors for appropriate emissivities using the IRBETA code. The fuel elements and the hot plate have a high emissivity coating (calcium titanate or iron titanate), while the inside of the shutters will be bare Haynes-25 (after a short period of space operation). The absorption factors will be used ultimately in a parametric thermal analysis of the heat source. Therefore absorption factors were calculated for a representative range of values of the emissivities of the radiating surfaces. A summary of the various values of emissivity for which the absorption factors were calculated is presented in Table II-10. The heat source absorption factors associated with the various values of emissivity are summarized in Table II-11. The absorption factor values on the T/E side of the heat source are applicable to any time from launch pad to EOL; those on the shutter side of the heat source apply only to EOL since only then are the shutters closed.

TABLE II-10

Summary of Emissivities Used to Determine
SNAP 29 Heat Source Absorption Factors

Fuel Element--Hot Plate

Case No.	Fuel Element Emissivity*	Hot Plate Emissivity*
1a	0.85	0.85
1b	0.80	0.80
1c	0.75	0.75
1d	0.75	0.85
1e	0.75	0.80
1f	0.70	0.85
1g	0.70	0.80
1h	0.70	0.75
1i	0.65	0.85
1j	0.65	0.80
1k	0.65	0.75
1l	0.60	0.85
1m	0.60	0.80

Fuel Element--Closed Shutters

Case No.	Fuel Element Emissivity*	Bare Haynes-25 Emissivity**
2a	0.85	0.25
2b	0.85	0.30
2c	0.85	0.35
2d	0.80	0.25
2e	0.80	0.30
2f	0.80	0.35
2g	0.75	0.25
2h	0.75	0.30
2i	0.75	0.35
2j	0.70	0.25
2k	0.70	0.30
2l	0.70	0.35
2m	0.65	0.25
2n	0.65	0.30
2o	0.65	0.35
2p	0.60	0.25
2q	0.60	0.30
2r	0.60	0.35

*Gray, J. H. III, "Capsule Cladding, Fuel Block, and Hot Plate Emittance Coating Evaluation," Report 1140-360 (revised version), 8/13/68.

**De Santis, V. J., "Total Hemispherical Emittance of Oxidized Heat Resistant Alloys," General Electric R 64SD60, 8/64.

TABLE II-11

Summary of SNAP 29 Heat Source Absorption Factors

Fuel Element--Hot Plate

Case No.*	Absorption Factors**															
	β_{1-1}	β_{1-2}	β_{1-3}	β_{1-8}	β_{2-1}	β_{2-2}	β_{2-3}	β_{2-8}	β_{3-1}	β_{3-2}	β_{3-3}	β_{3-8}	β_{8-1}	β_{8-2}	β_{8-3}	β_{8-8}
1a	0.155	0.156	0.168	0.525	0.162	0.189	0.212	0.442	0.179	0.216	0.246	0.363	0.277	0.228	0.182	0.319
1b	0.159	0.159	0.170	0.517	0.165	0.190	0.211	0.439	0.180	0.216	0.244	0.365	0.272	0.226	0.183	0.325
1c	0.163	0.162	0.172	0.508	0.168	0.191	0.210	0.436	0.182	0.215	0.241	0.367	0.268	0.225	0.184	0.330
1d	0.146	0.148	0.160	0.553	0.153	0.179	0.201	0.474	0.170	0.205	0.233	0.399	0.257	0.216	0.177	0.360
1e	0.155	0.155	0.166	0.532	0.161	0.185	0.206	0.456	0.176	0.210	0.237	0.384	0.263	0.220	0.181	0.346
1f	0.141	0.144	0.155	0.568	0.149	0.173	0.194	0.491	0.165	0.198	0.225	0.419	0.247	0.208	0.173	0.382
1g	0.149	0.151	0.161	0.547	0.156	0.179	0.199	0.473	0.171	0.204	0.229	0.404	0.252	0.213	0.177	0.367
1h	0.158	0.158	0.167	0.525	0.164	0.186	0.205	0.454	0.177	0.209	0.234	0.387	0.258	0.218	0.181	0.353
1i	0.135	0.139	0.150	0.584	0.143	0.167	0.187	0.510	0.159	0.191	0.217	0.440	0.235	0.201	0.169	0.405
1j	0.144	0.146	0.156	0.563	0.151	0.173	0.192	0.492	0.165	0.197	0.221	0.425	0.241	0.206	0.173	0.390
1k	0.152	0.153	0.162	0.541	0.158	0.180	0.198	0.473	0.172	0.202	0.226	0.408	0.247	0.211	0.177	0.375
1l	0.130	0.133	0.144	0.601	0.138	0.160	0.180	0.530	0.153	0.184	0.208	0.463	0.224	0.193	0.164	0.430
1m	0.138	0.140	0.150	0.581	0.145	0.167	0.185	0.512	0.159	0.189	0.213	0.447	0.230	0.198	0.168	0.415

*See Table II-10 for case numbers.

**See Fig. II-19 for β factor subscripts.

CONFIDENTIAL

CONFIDENTIAL

TABLE II-11 (continued)

Summary of SNAP 29 Heat Source Absorption Factors

Fuel Element--Closed Shutters

Case No.*	Absorption Factors**															
	β_{4-4}	β_{4-5}	β_{4-6}	β_{4-11}	β_{5-4}	β_{5-5}	β_{5-6}	β_{5-11}	β_{6-4}	β_{6-5}	β_{6-6}	β_{6-11}	β_{11-4}	β_{11-5}	β_{11-6}	β_{11-11}
2a	0.290	0.284	0.280	0.151	0.282	0.279	0.280	0.165	0.272	0.274	0.283	0.177	0.262	0.287	0.314	0.142
2b	0.282	0.275	0.271	0.176	0.274	0.270	0.270	0.192	0.263	0.264	0.272	0.206	0.254	0.279	0.306	0.165
2c	0.275	0.267	0.262	0.200	0.266	0.261	0.260	0.218	0.255	0.254	0.262	0.234	0.248	0.272	0.297	0.188
2d	0.287	0.281	0.278	0.160	0.279	0.276	0.277	0.173	0.270	0.271	0.280	0.185	0.260	0.284	0.310	0.151
2e	0.279	0.272	0.268	0.186	0.270	0.267	0.267	0.202	0.260	0.261	0.269	0.216	0.253	0.276	0.301	0.175
2f	0.271	0.264	0.259	0.211	0.262	0.258	0.257	0.229	0.252	0.251	0.258	0.244	0.246	0.268	0.292	0.199
2g	0.283	0.278	0.275	0.169	0.276	0.273	0.274	0.183	0.267	0.268	0.276	0.194	0.259	0.281	0.305	0.160
2h	0.275	0.269	0.265	0.197	0.267	0.263	0.263	0.212	0.257	0.257	0.265	0.226	0.251	0.272	0.296	0.186
2i	0.267	0.260	0.255	0.223	0.258	0.254	0.253	0.240	0.248	0.248	0.254	0.256	0.243	0.264	0.287	0.211
2j	0.280	0.274	0.272	0.180	0.273	0.270	0.271	0.193	0.264	0.265	0.273	0.205	0.257	0.278	0.300	0.171
2k	0.271	0.265	0.261	0.209	0.263	0.259	0.259	0.224	0.254	0.254	0.261	0.238	0.248	0.268	0.290	0.199
2l	0.262	0.256	0.251	0.236	0.254	0.250	0.249	0.253	0.244	0.244	0.250	0.268	0.240	0.260	0.281	0.224
2m	0.275	0.270	0.268	0.192	0.269	0.266	0.267	0.205	0.260	0.261	0.269	0.217	0.254	0.274	0.295	0.183
2n	0.266	0.260	0.257	0.223	0.259	0.255	0.255	0.237	0.250	0.250	0.256	0.251	0.245	0.264	0.284	0.212
2o	0.257	0.251	0.247	0.251	0.249	0.245	0.244	0.267	0.240	0.239	0.245	0.282	0.237	0.255	0.275	0.239
2p	0.271	0.266	0.264	0.206	0.264	0.262	0.263	0.219	0.256	0.257	0.264	0.230	0.252	0.269	0.289	0.197
2q	0.261	0.255	0.253	0.238	0.254	0.250	0.250	0.252	0.245	0.245	0.251	0.265	0.242	0.259	0.278	0.228
2r	0.252	0.245	0.242	0.267	0.244	0.240	0.239	0.284	0.235	0.234	0.239	0.298	0.233	0.249	0.268	0.256

*See Table II-10 for case numbers.

**See Fig. II-19 for β factor subscripts.

CONFIDENTIAL

CONFIDENTIAL

A two-dimensional (r,θ) half-unit cell thermal model of the SNAP 29 heat source which will be used in conjunction with the linearized matrix inversion code to perform the parametric steady-state thermal analysis has been checked out. This work will be documented in the next reporting period.

9. Thermal Inventory Tolerance of SNAP 29 Burn-up Heat Source Capsulettes

The following equation describes the fuel inventory loaded into a capsulette:

$$q/\text{capsulette} = q_{1\text{desired}} \pm \text{accuracy of gamma probe technique} + \text{undershoot or overshoot from } q_{1\text{desired}}$$

In this equation, $q_{1\text{desired}}$ is a discrete value. The accuracy of the gamma count technique is $\pm$ 10%. It is obviously desirable to minimize the undershoot or overshoot in this equation to achieve a high number of successfully loaded liners.

a. Liners

For liners the fuel inventory is described by:

$$q/\text{liner} = q_{2\text{desired}} \pm \text{accuracy of calorimetry} + \text{undershoot or overshoot from } q_{2\text{desired}}.$$

If calorimetry is accurate to $\pm$ 2% and $\pm$ 10% tolerance on the liners is to be held, then the loading variation of liners must be held (as measured by calorimetry) to $\pm$ 8%. This implies that more than the actual number of required capsulettes (182) may have to be fueled.

b. Heat source

For the entire heat source,

$$q/\text{heat source} = q_{3\text{desired}} \pm 5\% \text{ (based on liner calorimetry data only).}$$

This value of 5% includes the 2% calorimetry error on liners. (Thus the indicated q must be $\pm$ 3%.) Since $\pm$ 5% is tighter than $\pm$ 10% required on liners, the possibility arises of having to produce more than 26 capsules. A tradeoff exists between tightening the liner tolerance, and thus having to produce more capsulettes, and producing additional liners.

10. Heat Source Stress Analyses

A majority of the structural analysis effort during the past reporting period was provided in support of the Task Force assignment to evaluate a burn-up heat source. This effort included a stress evaluation of the capsule liner under elevated temperatures and a load environment associated with isotope decay and the resulting helium generation. A dynamics analysis was required to aid in the choice of heat sink material. Not only must a heat sink design meet required thermal capability but must also withstand the environment associated with liftoff shock vibration.

The stress analysis consisted of evaluating the capability of the structural liner for both abort conditions and operational environment. Assuming 26 capsules with a nominal fuel loading of ~161 watts/in.^{3}, a critical liner temperature was found

for both design conditions. For mission operation of 90 days plus a launch pad hold time, the critical temperature is ~1820° F. This is based upon the creep-strain characteristics of the Haynes-25. The second environment examined consisted of an ascent abort which implies a fireball followed by a residual fire. The critical fireball temperature based upon short time loading response was approximately 2160° F.

A residual fire temperature versus time was also studied to evaluate system capability. Fire temperatures of 2000° to 2150° F were included for extended periods of time. Details of these evaluations may be obtained from Reports 4002-27 and 4002-39.

Whether the heat source is designed for burn-up or intact re-entry, a structural problem of some significance is centered about the load carrying capability of the liner end caps. Report 4002-53 provides a specimen design for a burst test program and proposes loading histories to simulate both operational and abort environments. Too little is known with regard to weldment efficiency based upon metal crystalline structure and joint geometry (especially as concerned with a potential stress riser). Thus, the test program is required to demonstrate operational capability as well as to define the limitations with respect to a fireball environment.

A spacer of Haynes-25 is included within a fuel element to separate the two fuel capsules. The spacer is designed with a convolution so that axial loads from restraint of thermal expansion will not be excessive. An analysis is provided in Report 4002-53.

Maximum loading on the inner and outer heat shield is a result of random vibration environment. The design criteria for random vibration was based upon Compartment 2A of the Titan IIID launch vehicle as a representative example. With this environment including an operational temperature of ~1500° F, a large number of heat resistant alloys were examined. In addition to strength characteristics, the materials were evaluated for availability, welding and machining characteristics. Considering all variables, Haynes-25 and Inconel 625 became leading candidates.

Assuming each fuel element is simply supported at the support frame, the natural frequency of a fuel element at temperature is about 72 to 115 cps. This variation is dependent upon the amount of effective weight and effective rigidity of the fuel element. This is difficult to determine with accuracy since the configuration is made up of concentric shells.

11. Fireball Thermal Analyses

a. Solid vs split heat shield designs

During a launch pad abort fireball, the critical design parameter is the peak temperature of the liner. By fabricating the heat shield in the form of two concentric shells separated by a gap, the liner will be further insulated from the fireball heating, thus reducing the required heat shield thickness. The double shell construction is referred to as the split heat shield design. The reduced thickness permitted with the split heat shield design reduces the total heat source weight and increases the reliability of burn-up during re-entry. An additional advantage of a split heat shield design is that the inner shield, which is considerably cooler than the outer shield during the early stages of the fireball, adds to the impact strength of the fuel element. The element must withstand ground impact after falling from its position on the vehicle during a launch pad abort.

The peak liner temperature is shown in Fig. II-20 as a function of heat shield thickness for both solid and split designs. The heat shield materials initially considered were Rene' 41 and Type 301 stainless steel. Although neither material is part of the present design, the resulting trends should be valid.

It can be seen from Fig. II-20 that for a given heat shield thickness, the peak liner temperature is considerably less for a split design than for a solid one. The transient nature of the temperature response results in a maximum liner temperature for a split shield thickness of approximately 0.200 inch. This maximum occurs due to the increased surface recession for the lesser thicknesses. Since the peak liner temperature is a function of the heat shield cooling rate following the duration of the fireball stem, the remaining heat shield mass is an important parameter.

The degree of surface recession is difficult to predict due to the complex nature of melting and melt flow. Assuming a liquid propellant residual fire, the liner temperature limit (2150° F) will not be exceeded with a split heat shield design provided the liner is not exposed to the transient portion of the fireball. It is estimated that a 0.150 inch thick split shield should be adequate to prevent exposure of the liner.

b. Haynes-25 and Inconel 625 heat shield designs

The design fireball has been defined by the SNAP 29 Task Force as the liquid propellant fire plus 25% of the solid propellants. Both liquid and solid propellant residual fires are under consideration. The estimated residual fire temperatures are 1825° and 3220° F for the liquid and solid cases, respectively.

Two heat shield materials, Haynes-25 and Inconel 625, have been analyzed for exposure to the launch pad abort fireball/residual fire environment. Both designs consisted of a 0.050-inch thick inner shield and a 0.100-inch thick outer shield separated by a uniform, 0.010-inch wide, helium-filled gap.

The temperature histories for various components of the Haynes-25 heat shield design are shown in Fig. II-21 for the liquid propellant residual fire. The peak liner temperature is 2090° F. The temperature histories for the Inconel 625 design are shown in Fig. II-22. The peak liner temperature for this design is 2045° F. The primary reason for the lower temperature associated with Inconel 625 is that its melting temperature is ~90° F less than that of Haynes-25.

The temperature histories for the Haynes-25 heat shield design in the fireball with a solid propellant residual fire are shown in Fig. II-23. Since the residual fire temperature is above the melt temperature of the heat shield for an extended length of time, the fuel element will completely melt. The X's in Fig. II-23 indicate the times at which the particular components have completely melted. The entire element melts about 1.5 minutes after the initiation of the fireball. The liner temperature exceeds its pressure containment limit (~2150° F) in about 15 seconds. A similar response could be expected for the Inconel 625 design.

c. Error analysis

The fireball error analysis of peak liner temperature has begun. The thermal analysis parameters fall into three general categories: heat input, material properties and design variables. The heat input variables include liftoff time and residual fire temperature. The material properties under consideration are conductivity, specific heat, density, melt temperature, latent heat, and internal and external surface emissivities. The design parameters are fuel inventory, initial temperature and gap widths.

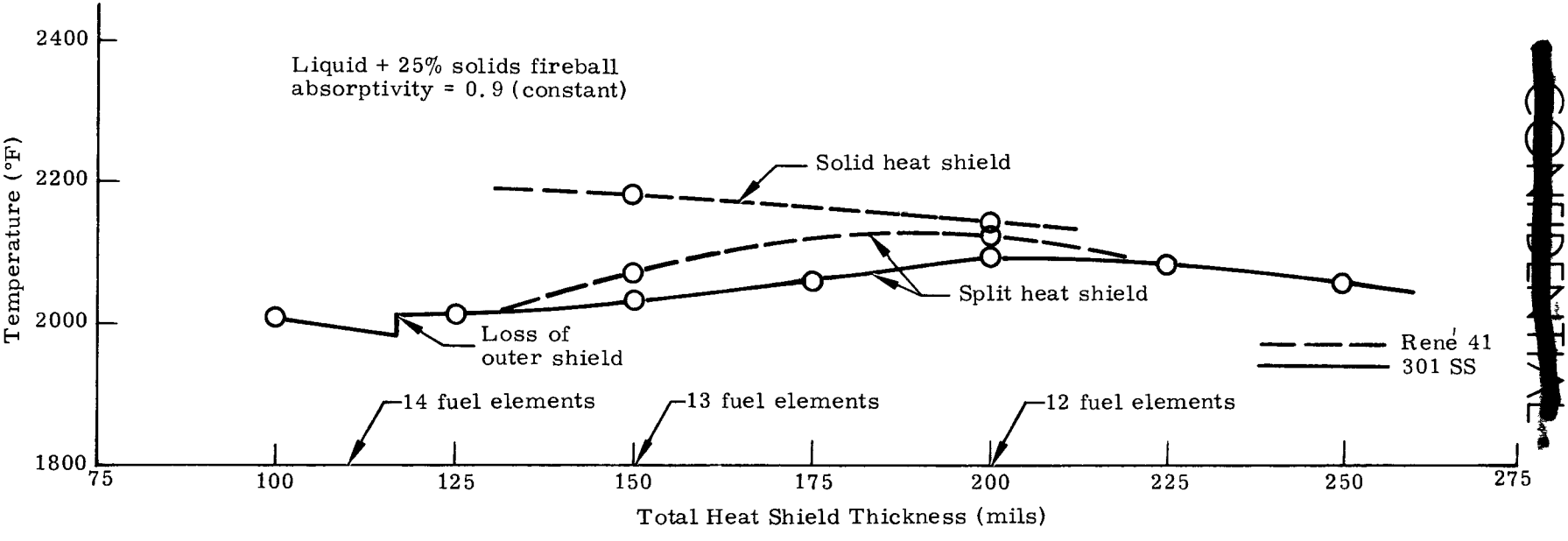

FIG. II-20. HEAT SHIELD THICKNESS VARIATION

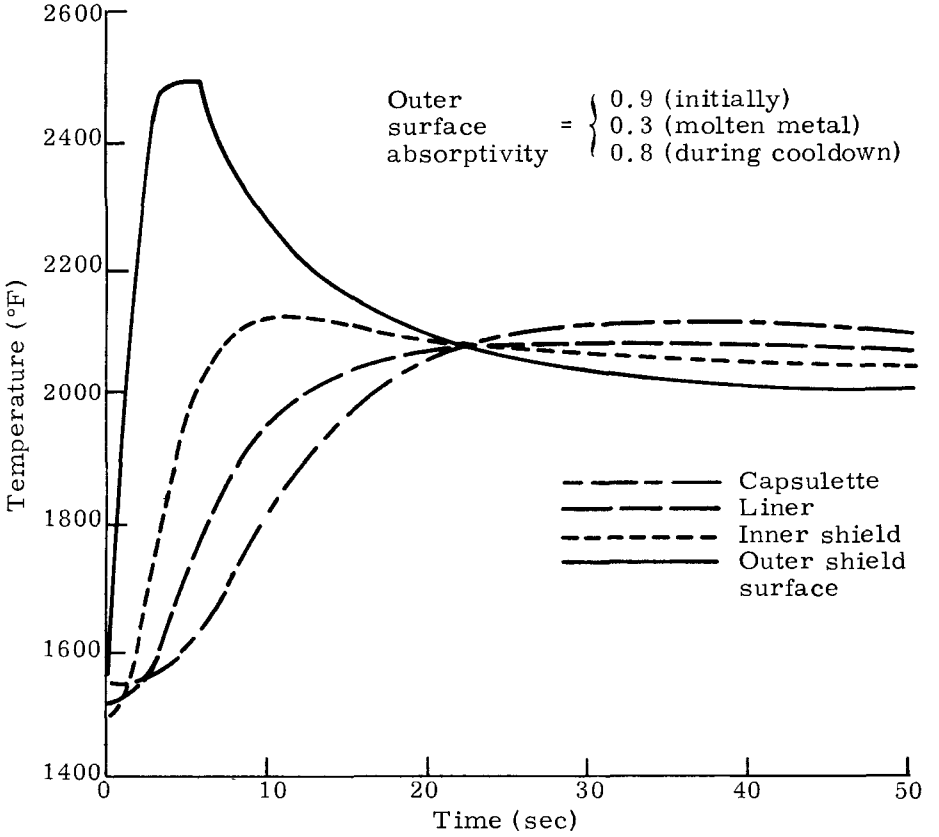

FIG. II-21. FIREBALL TEMPERATURE HISTORIES FOR LIQUID PROPELLANT RESIDUAL FIRE; HAYNES-25 HEAT SHIELD

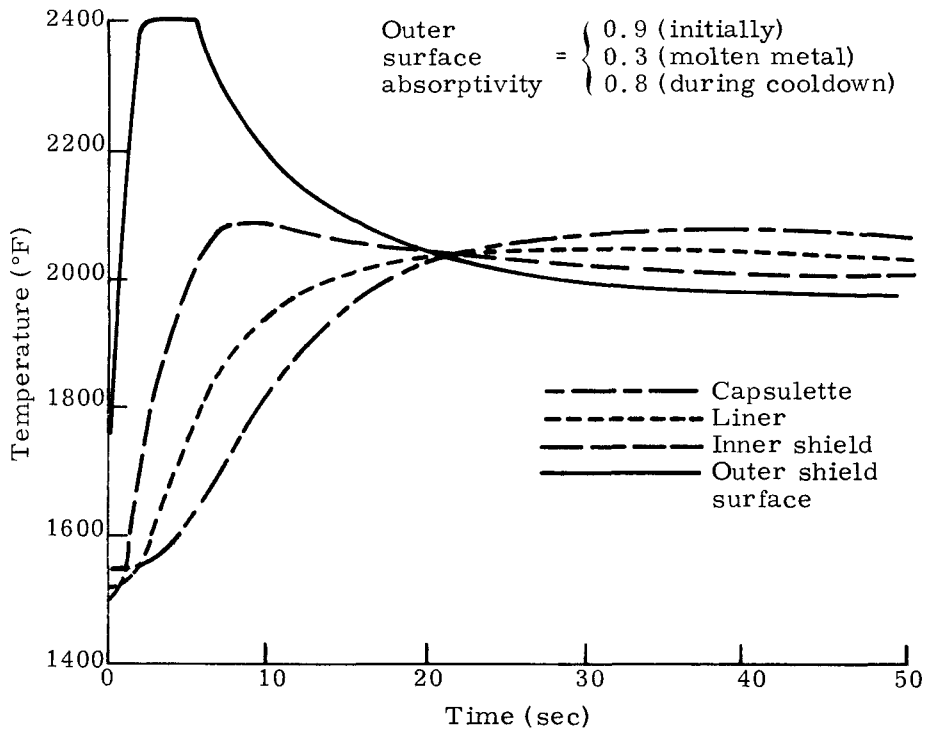

FIG. II-22. FIREBALL TEMPERATURE HISTORIES FOR LIQUID PROPELLANT RESIDUAL FIRE; INCONEL 625 HEAT SHIELD

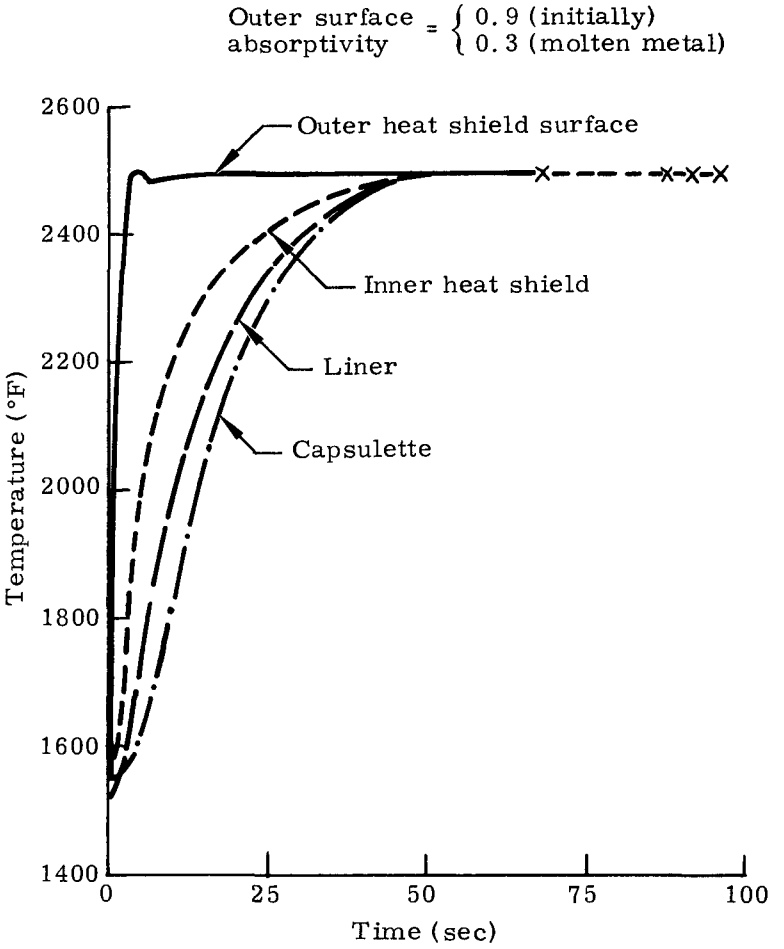

FIG. II-23. FIREBALL TEMPERATURE HISTORIES FOR SOLID PROPELLANT RESIDUAL FIRE; HAYNES-25 HEAT SHIELD

Although all of the limits on parameter variations have not yet been established, a preliminary analysis is underway to determine the most critical parameters. Thus-far, the heat input variables appear to be most significant. There is ~90° F difference in peak liner temperature corresponding to the difference between the mean and $+3\sigma$ (design fireball) liftoff times. At present, the liquid propellant residual fire temperature is assumed to be 1825° F. A 200° F increase in this temperature results in a 105° F increase in peak liner temperature. This increase puts the peak liner temperature of the Inconel 625 heat shield design at its pressure containment limit of 2150° F. The actual range of residual fire temperature has not been established.

d. Solid propellant burn test specimen analysis

For the proposed solid propellant burn tests, a specimen representing the fuel element is desired. In the limited time available, however, the design tubing dimensions and materials will be difficult to obtain. Therefore, the use of a more readily available material, such as stainless steel, may be required. An analysis has been conducted to compare the effects of the predicted solid propellant fire environment on specimens of both the design materials (prototype) and stainless steel to the effects on the actual fuel element design.

The thermal response of the actual design to a 3218° F solid propellant fire is shown in Fig. II-24. The predicted responses of the prototype and stainless steel test specimens are shown in Figs. II-25 and II-26, respectively. Based on the time required to melt the liner, the prototype specimen response is 10% longer, and the stainless steel specimen response is 22% longer than the actual fuel element. The 10% increase for the prototype specimen is due to the presence of air instead of helium in the specimen gaps. The 22% increase for the stainless steel specimen is due to the air gaps plus the higher melting temperature of stainless steel.

A series of preliminary solid propellant burn tests will be conducted to define the thermal environment. For these tests, quick response specimens in the form of hollow cylinders will be used. An analysis was conducted to determine the response time for various specimen wall thicknesses. A 1.0-inch OD Type 301 stainless steel specimen was examined. Figure II-27 shows the time required for the surface to reach melt temperature (2600° F) as a function of wall thickness. Both coated (ϵ = 0.5) and uncoated (ϵ = 0.85) specimens were considered. For a 65-mil wall, the response time is about 15 seconds for a coated specimen and 25 seconds for an uncoated specimen.

12. Ascent Abort

Trajectory data for six ascent abort conditions have been generated by the Aerophysics Group, utilizing a typical Titan III boost trajectory with a modified Agena upper stage. These six assumed aborts, usually occurring at the time of discrete functional events during the ascent, are listed in Table II-12. Only Cases 4, 5 and 6 result in appreciable heating of the fuel elements and were the only cases analyzed.

Both Haynes-25 and Inconel 625 heat shield designs were examined for exposure to these three ascent abort cases. The individual fuel elements were assumed to be exposed at the time of the abort. A side-on roll element orientation, for which the average overall heating should be least, was examined. Nominal predicted heating rates were used.

CONFIDENTIAL

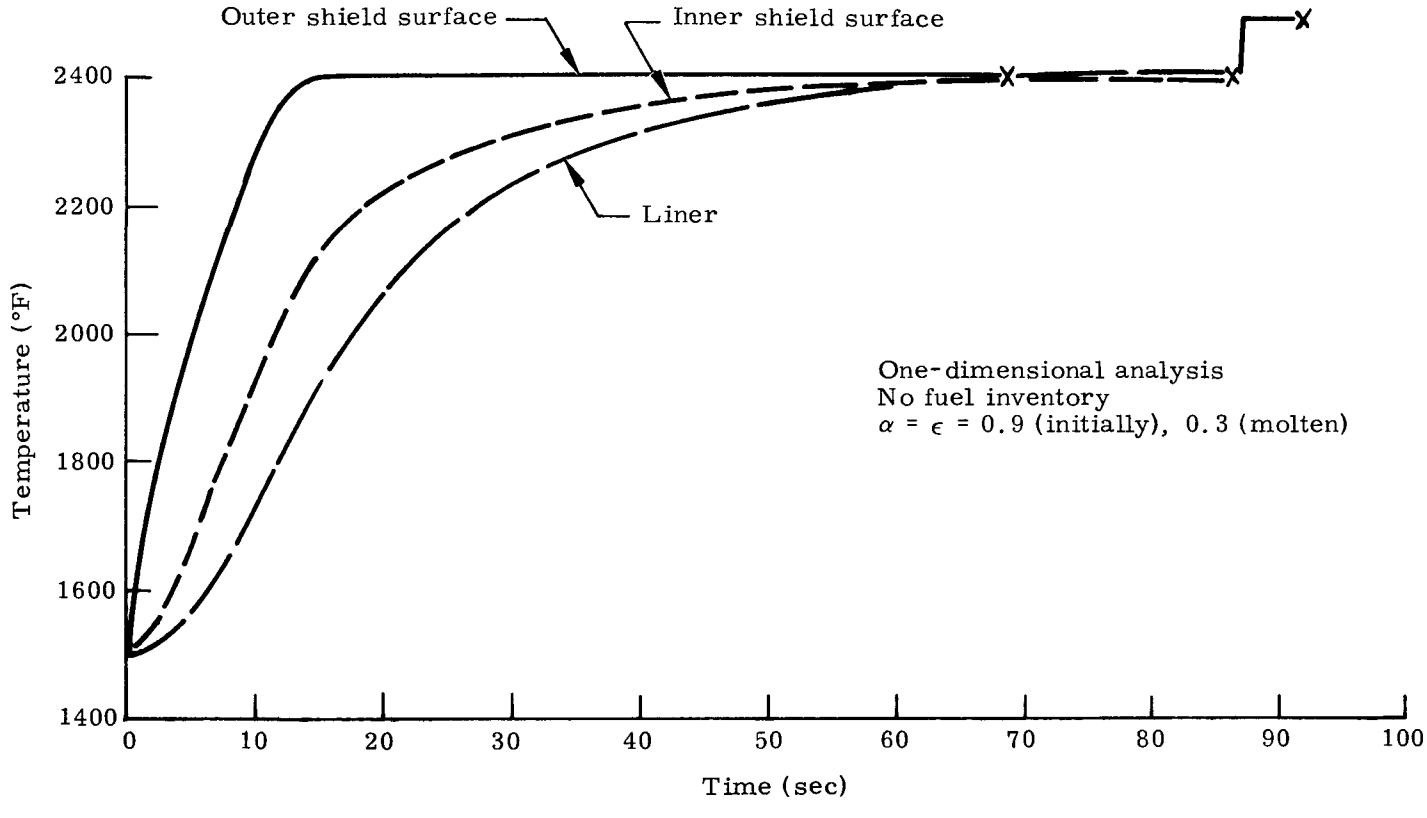

FIG. II-24. SNAP 29 BURN-UP DESIGN TEMPERATURE RESPONSE EXPOSURE TO SOLID PROPELLANT FIRE (3218° F)

CONFIDENTIAL

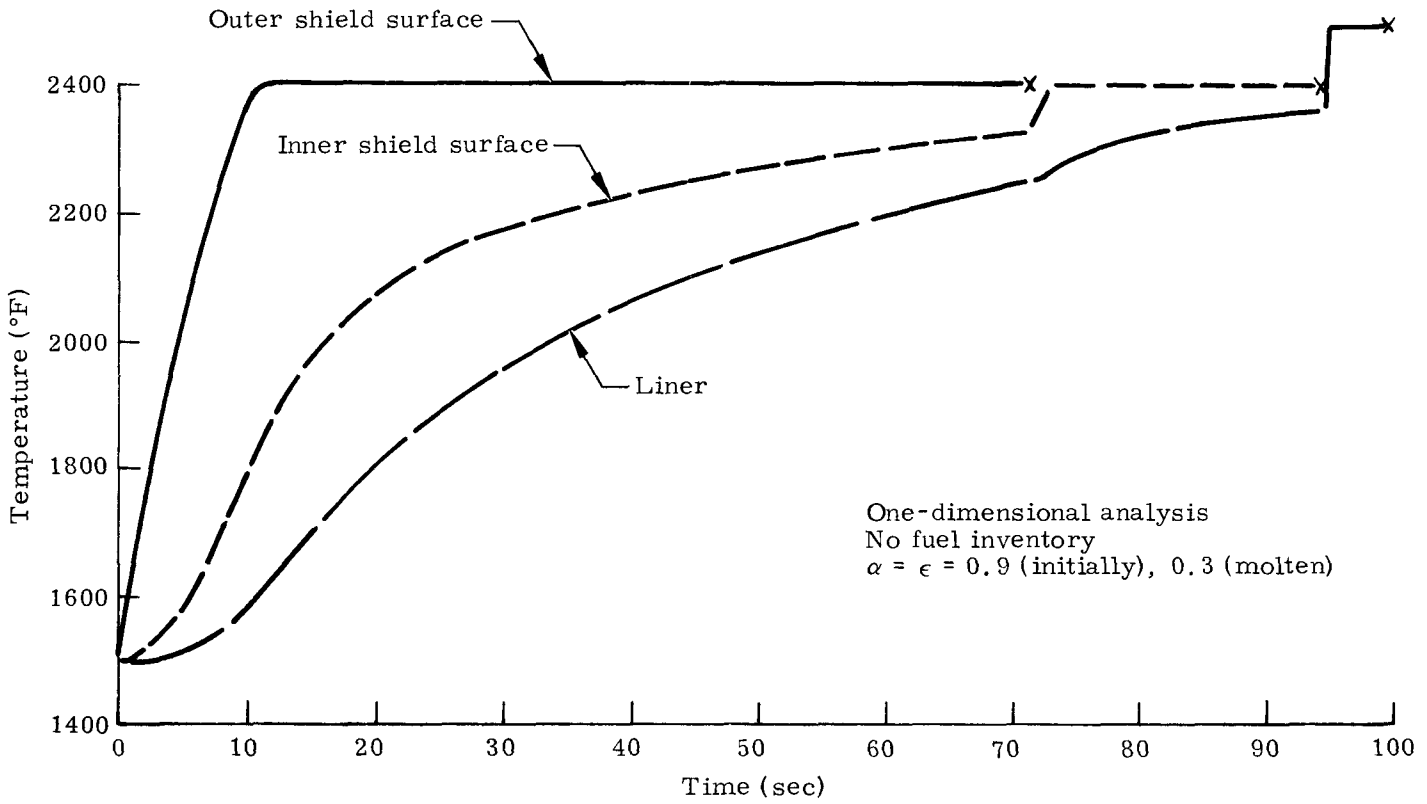

FIG. II-25. PROTOTYPE SPECIMEN TEMPERATURE RESPONSE FOR EXPOSURE TO SOLID PROPELLANT FIRE (3218° F) PREHEATED TO 1500° F WITH AIR IN GAPS

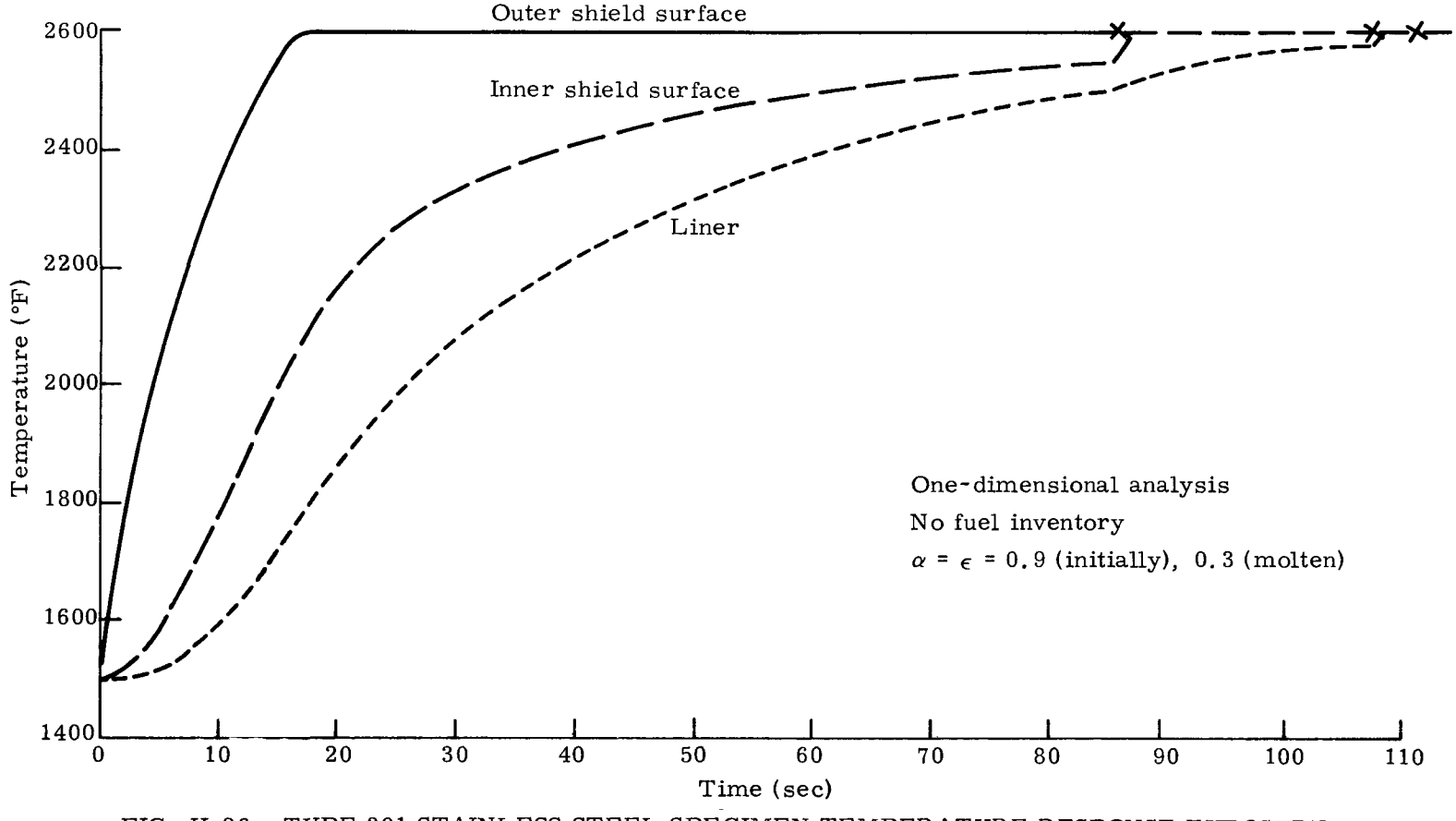

FIG. II-26. TYPE 301 STAINLESS STEEL SPECIMEN TEMPERATURE RESPONSE EXPOSURE TO SOLID PROPELLANT FIRE (3218° F) PREHEATED TO 1500° F WITH AIR IN GAPS

CONFIDENTIAL

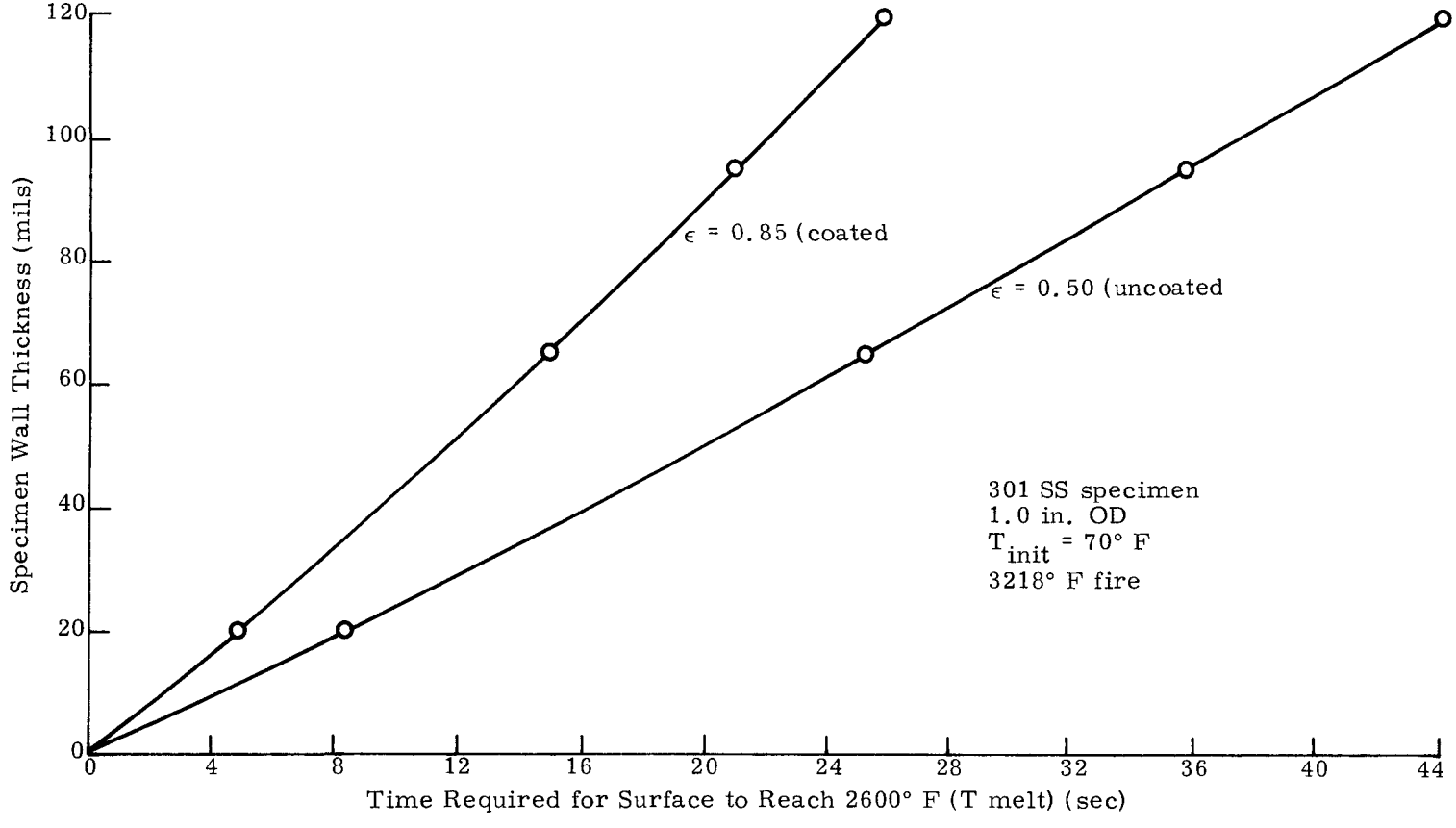

FIG. II-27. PRELIMINARY SOLID PROPELLANT TEST SPECIMEN RESPONSE

TABLE II-12

Ascent Abort Conditions

Abort No.	Event	Time from Launch (sec)	Velocity (fps)	Flight Path Angle (deg)	Altitude (1000 ft)
1	Maximum dynamic pressure	56	1,508	53.3	35.5
2	Stage I start	119.26	4,750	23.2	140
3	Jettison Fair T-111D		9,008	9.2	281
4	Stage II start	258.23	13,324	8.2	357
5	During Stage II burn	300	14,596	5.6	423
6	Stage III start	481.2	22,180	2.0	570

The results are summarized in Tables II-13 and II-14. Each table shows the time and altitude at which various fuel element components either melt or reach their peak temperature. No melting occurs for either design for abort Case 4 (Stage II start). For Case 5 (during Stage II burn), the surface of the Inconel 625 heat shield reaches the melt temperature, but very little recession occurs. However, the pressure containment temperature limit (2150° F) of the liner is exceeded for both heat shield materials. For Case 6 (Stage III start), both designs completely melt. The altitude of burnup is 184,000 feet for the Haynes-25 design and 188,000 feet for Inconel 625.

TABLE II-13

SNAP 29 Burn-up Ascent Abort Analysis
Haynes-25 Heat Shield

Abort No.	Fuel Element Component	Peak Temperature (°F)	Time from Abort (sec)	Altitude (1000 ft)
4	Heat shield surface	2050	250	132
	Outer shield	2050	250	132
	Inner shield	1970	255	124
	Liner	1950	265	108
	Capsulette	1980	270	102
5	Heat shield surface	2330	250	136
	Outer shield	2330	250	136
	Inner shield	2220	255	124
	Liner	2190	260	116
	Capsulette	2210	265	108
6	Heat shield surface	Melt	426	225
	Outer shield	Melt	434	205
	Inner shield	Melt	439	195
	Liner	Melt	441	190
	Capsulette	Melt	444	184

TABLE II-14

SNAP 29 Burn-up Ascent Abort Analysis
Inconel 625 Heat Shield

Abort No.	Fuel Element Component	Peak Temperature (°F)	Time from Abort (sec)	Altitude (1000 ft)
4	Heat shield surface	2095	250	132
	Outer shield	2095	250	132
	Inner shield	2009	255	124
	Liner	1987	260	116
	Capsulette	2010	265	108
5	Heat shield surface	2405*	252-259	128-117
	Outer shield	2405	252-259	128-117
	Inner shield	2329	260	116
	Liner	2282	260	116
	Capsulette	2300	265	108
6	Heat shield surface	Melt	422	237
	Outer shield	Melt	431	214
	Inner shield	Melt	435	204
	Liner	Melt	438	197
	Capsulette	Melt	442	188

*Melt temperature of Inconel 625

The results of this preliminary analysis indicate a potential hazard associated with ascent aborts. Partial burnup of the fuel element or pressure failure of the liner could be expected for certain cases. Whether or not these failures can occur below a safe fuel release altitude will be determined by further analysis. Other element orientations and variations in heating rates and recession criteria must be examined. Also, the minimum allowable release altitude must be determined.

13. Re-entry

Re-entry thermal analysis of the Haynes-25 heat shield design at end-of-life was conducted for initial flight path angles of -3.0 and 0.1 degrees. A side-on roll re-entry mode, for which the average overall heating should be least, was examined. Results were obtained using the nominally predicted heating rates and using 50% of the predicted rates. The individual fuel elements were assumed to be exposed at the initial altitude of 400,000 feet with an initial velocity of 25,690 fps.

The results of the analysis are presented in Table II-15. The capsulettes melt prior to peak heating for the nominal heating cases. The altitude of burnup is 227,000 feet for -3.0 degrees and 259,000 feet for -0.1 degree. Burnup also occurs for the 50% heating cases, although the altitude is less than 200,000 feet. Burnup would be marginal for heating rates slightly less than 50% of the predicted levels.

TABLE II-15

Snap 29 Burn-up EOL Re-entry Haynes-25 Heat Shield

Initial Flight Path Angle (deg)	Nominal Heating Rate (%)	Time and Altitude of Burnup*			
		Heat Shields		Strength Liner	Capsulette
		Outer	Inner		
-3.0	100	120 sec 242,000 ft	125 237,000	128 232,000	132 227,000
-3.0	50	147 207,000	155 197,000	161 190,000	172 175,000
-0.1	100	977 267,000	985 263,000	990 261,000	997 259,000
-0.1	50	1054 225,000	1065 214,000	1073 205,000	1086 193,000

*Peak heating occurs at 144 seconds (212,000 ft) for -3.0 degrees, and 1055 seconds (224,000 ft) for -0.1 degree.

C. HEAT SOURCE (ELECTRICAL) SUBSYSTEM--CONTROL POINT 1200

The objective of this task is the development and qualification of electrical heat sources for the thermoelectric module and generator which simulate the thermal characteristics of the isotopic heat source. The task is divided into the following subtasks:

CP 1240--Heat Source (Electrical) Subsystem, Component Development

CP 1230--Heat Source (Electrical) Subsystem, Design Verification

Effort was continued during this reporting period on the component development of the electrical heat source for the T/E modules and of the generator electric heat source.

WORK ACCOMPLISHED

During this reporting period, the design effort consisted of liaison with Manufacturing during the fabrication of the electrical heat source. As a result of an out-of-tolerance condition on a number of procured electrical heaters, the nickel heater block design was modified to enlarge the heater holes to accommodate the heater cartridge. Fabrication of the heater blocks has been slightly hampered by the need for frequent sharpening of the gun drills.

D. THERMOELECTRIC MODULES SUBSYSTEM--CONTROL POINT 1300

The objective of this task is to develop a thermoelectric module subsystem which will withstand the predicted dynamic conditions and produce the required power output over the mission life with high reliability.

The thermoelectric module subsystem is designed, fabricated, inspected and tested under this task. The basic philosophy in the module development program is to develop module components on an individual basis and then integrate the components into module assemblies. The assembled modules will then be subjected to performance testing for reliability data and design verification. Modules will be fabricated and acceptance tested for use in preprototype RTG units. Commensurate with this philosophy, the work effort has been broken down into the following control points:

CP 1340--T/E Module Subsystem, Component Development

CP 1330--T/E Module Subsystem, Design Verification and Preprototype

WORK ACCOMPLISHED

1. T/E Module Performance Testing

As reported in the Eighth Quarterly, the two 2N-3P modules (S/N 003 and 005) and the large TAGS module, (LTM) were removed from test late in the prior reporting period in order to make water test loop repairs and modification. No additional analysis efforts were accomplished on the 2N-3P modules during this quarter. However, data reduction of the LTM data was extended to include all of the testing time prior to the test loop shutdown. Results of that analysis indicate that the module power output shows no degradation after ~4125 hours of operation.

During this period, preparations were begun to place the LTM and S/N 003 and 005 back on test. The insulation in the S/N 003 and 005 test fixtures was modified to be identical to that of the LTM. In addition, all thermocouples in the modules were rechecked prior to closing their respective test fixtures. This examination indicated that all thermocouples (except one) inside the 2N-3P modules had approximately the same resistance from thermocouple lead to electrical circuit as recorded during the final stage of module assembly. However, the thermocouples on the hot junction of the LTM indicated an increase in resistance during the operational life of the module. This observation leads to the questioning of the validity of the hot junction temperature indication of the LTM. Further visual examination of the chromel-alumel thermocouples on the external surfaces of the modules resulted in the replacement of thermocouples on the hot plate of all three modules. Due to the lack of confidence in the hot junction temperature measurement of the LTM, additional thermocouples were placed on the LTM hot plate, and will be used in conjunction with prior test data to aid in the assessment of the indicated hot junction temperatures on the LTM. A portable loop is being prepared to supply coolant water to these three modules since, due to program plan changes, the steady state water test loop modifications will not be completed and the loop will not be used in future module testing. All future module tests beyond S/N 003, 005 and the LTM will consist of integral T/E module/heat pipe heat rejection systems. Testing of S/N 003 and 005 and the LTM will begin in January 1969.

2. T/E Module Cold End ΔT Test

During this period, planning and preparation for a test to evaluate the thermal and structural interactions between the thermoelectric couples and the T/E module cold end hardware was accomplished. The objectives of the test are:

(1) To evaluate the ΔT through the module cold end.

(2) To evaluate the solder bond of the couples to the heat sink

(3) To evaluate the thermo-structural integrity of the flame-sprayed circuitry.

(4) To evaluate the structural response of the thermoelectric couples to induced thermal stresses under simulated thermal operational conditions.

The test configuration consists of a simulated heat sink and hot plate. These are beryllium plates with top and bottom Haynes-25 sheets brazed together. Nickel tubes, to be used for coolant, are brazed into the heat sink. The heat sink is spray coated with nickel aluminide, aluminum oxide and copper pads, (Fig. II-28). Couples, in the Min-K insulation, are bonded to the copper pads as shown in Fig. II-29. The couples used in the test specimen consist of 80 2N-3P couples and 10 2N-TAGS/SnTe couples of the SNAP 29 design configuration. The heat sink is cooled by a portable water loop circulating coolant through a manifold integral with the heat sink plate. This test is scheduled for initiation early in the next reporting period.

3. T/E Module Hot Plate and Heat Sink Subassembly Brazing

During this reporting period, additional brazed assemblies were fabricated. These assemblies were made to provide a hot plate and heat sink for the cold end ΔT test and to provide a heat sink for use in developing processes for soldering heat pipes to the module cold end. They were also designed to supplement prior brazing experience in this area in terms of verifying temperature/time cycle repeatability and resultant braze quality. On one of these assemblies, cracks appeared in the 0.012 inch Haynes-25 sheet that was brazed to the beryllium hot plate. It is standard practice to braze a hot plate and heat sink assembly simultaneously.

A hot plate is comprised of a beryllium plate with one brazed 12-mil Haynes-25 sheet and one brazed 30-mil Haynes-25 sheet. The heat sink plate is beryllium with 12- and 24-mil Haynes-25 faces. The plates are so oriented in the braze fixture (Fig. II-30a) that the two 12-mil face sheets bear against one another through a thin slip sheet. Figure II-30b is a photo of the assembled braze fixture.

It was noted that the cracking condition was present only in the 12-mil face of the hot plate. Figure II-31 shows the crack condition. Note that the cracking occurred primarily in a nearly symmetrical pattern of elliptical shape in the center of the plate. Only one additional crack was located beyond the basic pattern on the long edge of the sheet. It was also noted that the cracks were oriented at ~90 degrees to the sheet rolling direction. In an attempt to identify the cause of the problem, the following action items were performed:

(1) Photographic record of defects

(2) Zyglo inspection of hot plate surface and as-received material

(3) Dye check of hot plate surface

(4) Hardness check of hot plate surface, (X pattern)

(5) Hardness check of heat sink surface, (X pattern). This part brazed simultaneously with hot plate, contains 0.012 inch H-25 sheet from same heat as defective part

(6) X-ray inspect hot plate, attempt to pick-up cracks

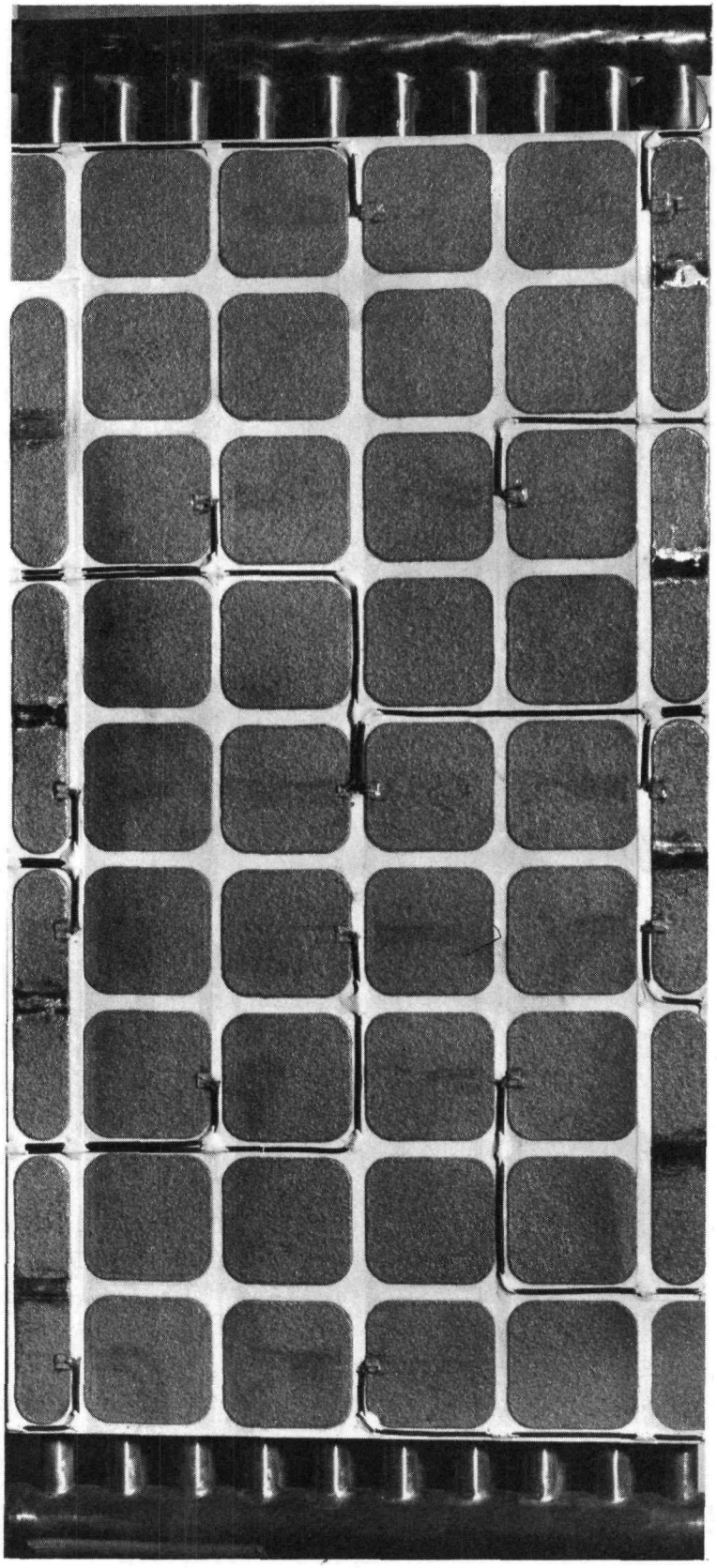

FIG. II-28. COLD END ΔT TEST HEAT SINK SPECIMEN WITH FLAME-SPRAYED COPPER PADS

CONFIDENTIAL

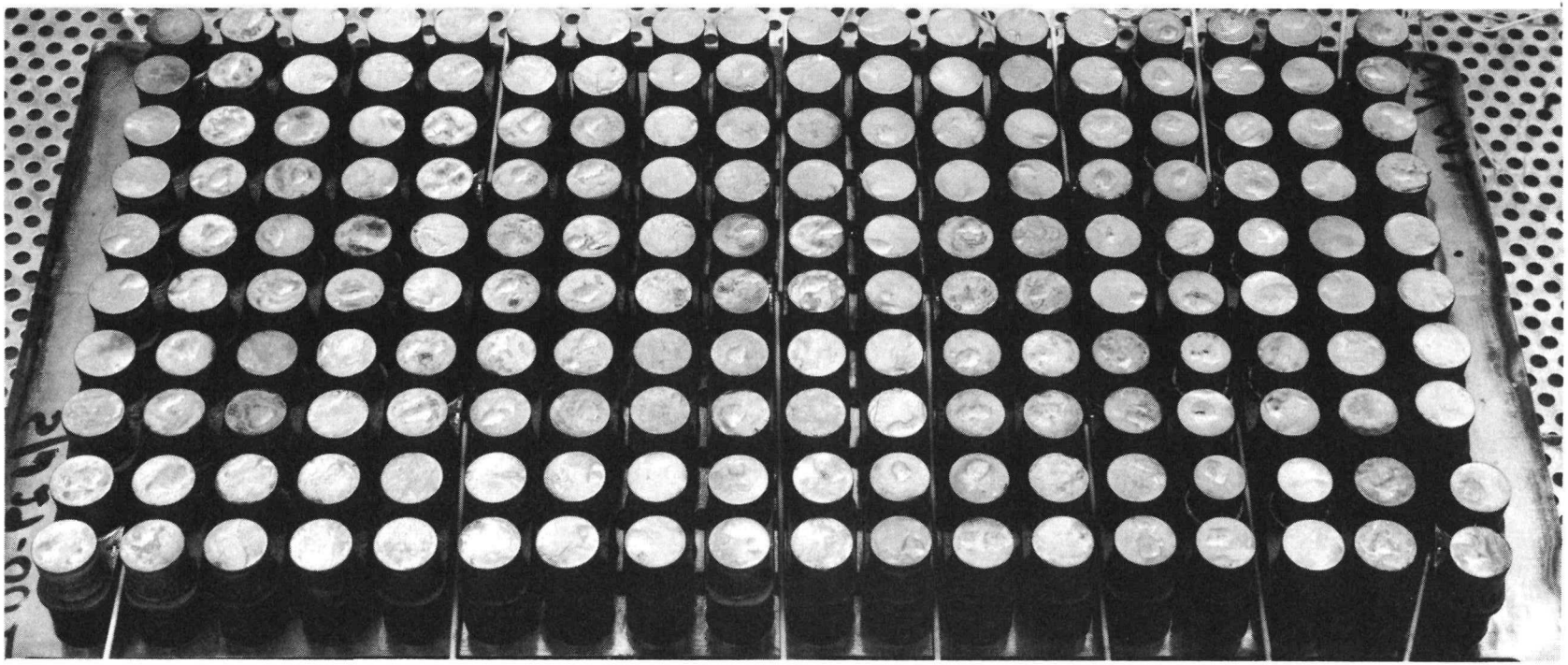

FIG. II-29. COLD END ΔT TEST COUPLES MOUNTED ON BONDING TOOL PRESSURE PLATE. (NOTE PRETINNED COLD END CAPS)

CONFIDENTIAL

CONFIDENTIAL

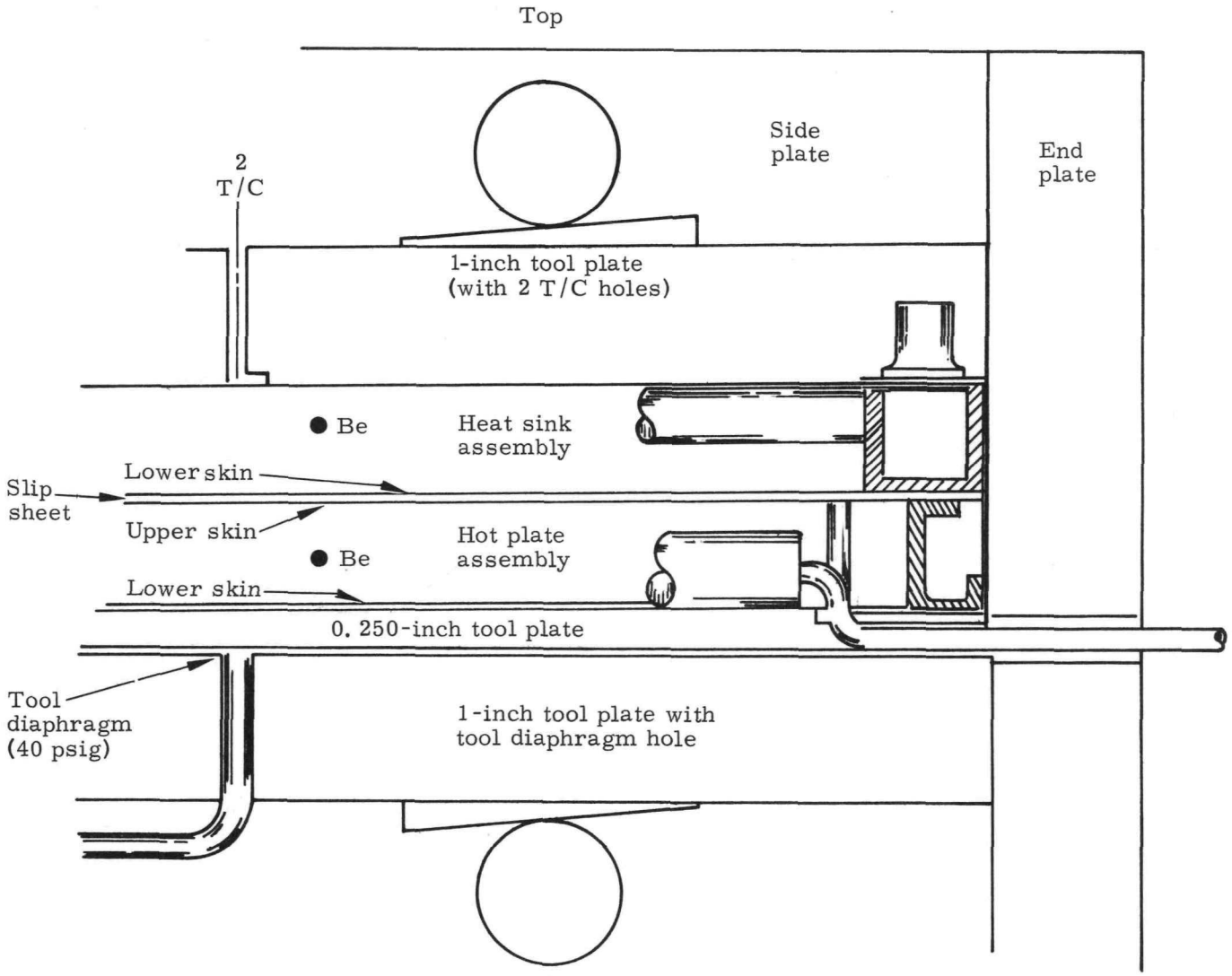

FIG. II-30a. T/E MODULE Be/HAYNES-25 PLATE BRAZING FIXTURE

CONFIDENTIAL

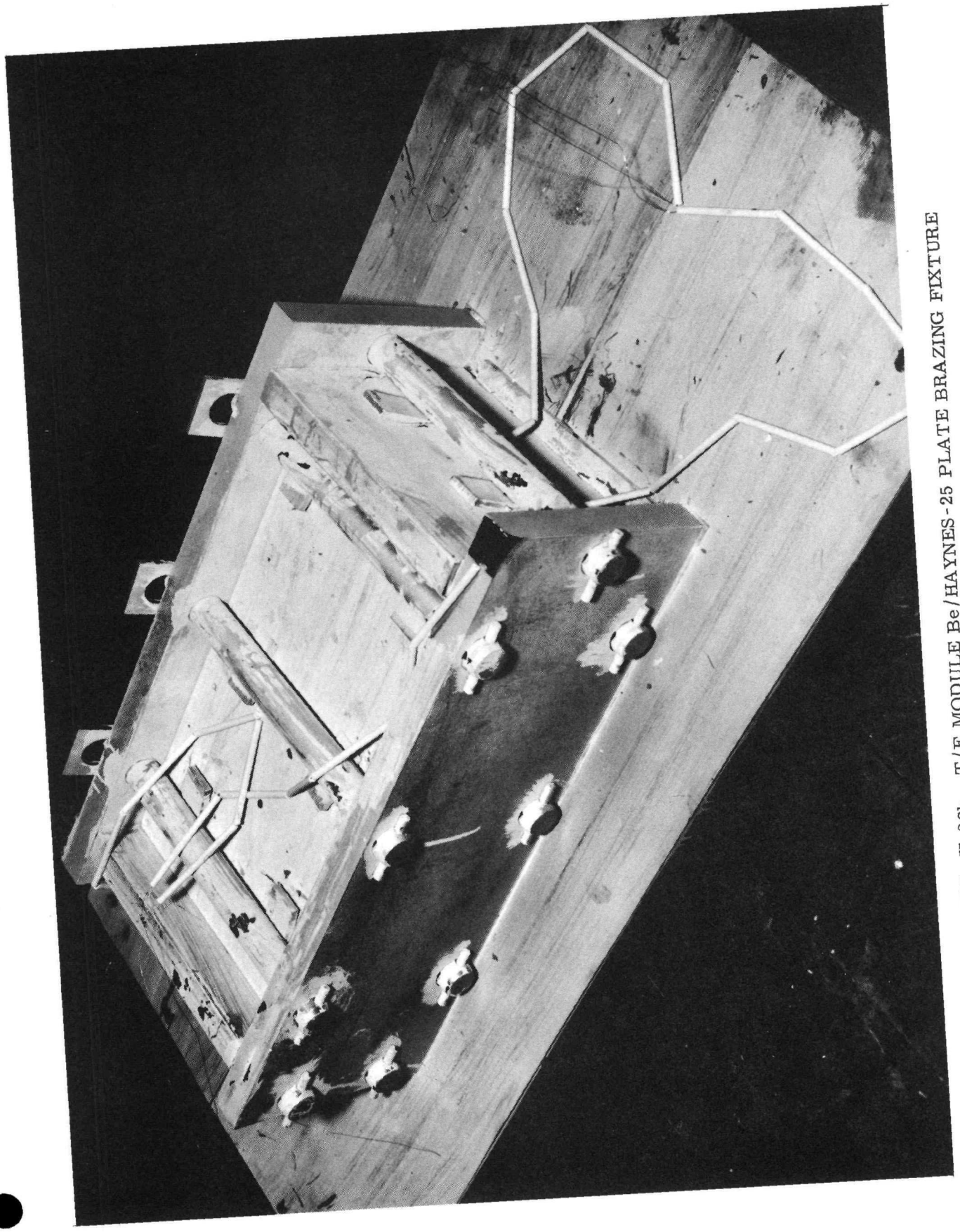

FIG. II-30b. T/E MODULE Be/HAYNES-25 PLATE BRAZING FIXTURE

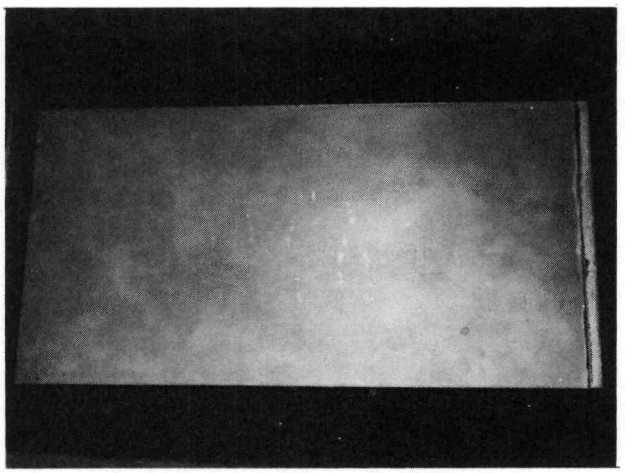

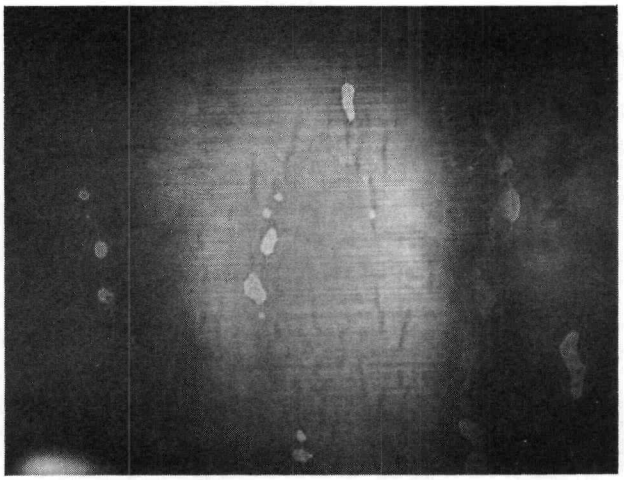

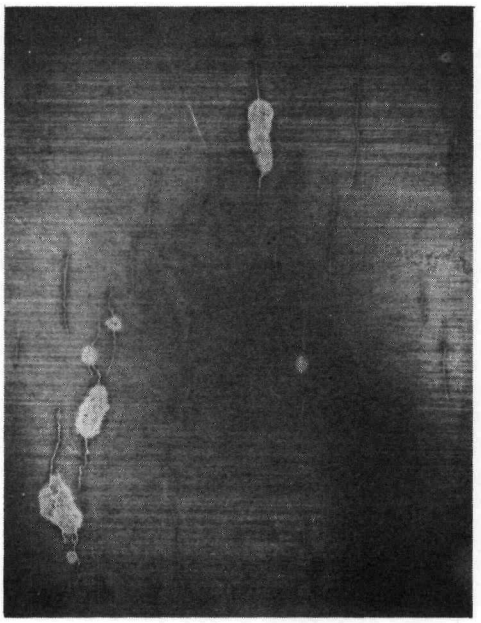

FIG. II-31. HAYNES-25/Be BRAZED HOT PLATE WITH CRACKS

(7) Verify by test whether hot plate 0.012 inch sheet is Haynes-25

(8) Metallographic inspection on piece of as-brazed material

(9) Ultrasonic inspection on both surfaces of hot plate to evaluate braze interfaces

(10) Section brazed hot plate and perform metallographic inspection

(11) For as-received material heat which was used for this part:

(a) Perform hardness check

(b) Perform metallographic analysis

(c) Make six tensile specimens to obtain stress/strain curves--three parallel to roll direction, three perpendicular to roll direction

(d) Trace and record disposition of all other material taken from this heat. Inspect all parts and pieces for evidence of cracks

(12) Review all fabrication processes experienced by subject part to verify complete compliance with applicable specifications

(13) Review material procurement history and material certification sheets for conformance with specifications

(14) Contact Union Carbide to discuss problem.

Both Zyglo and dye check examinations on the brazed and as-received material (Haynes-25) revealed only the cracks which were visible to the naked eye on the 12-mil hot plate face sheet. In several cracks it was apparent that the sterling silver braze alloy had flowed through the cracks in its molten state. The silver had filled the cracks so that they were difficult to identify even under fluorescent dye penetrant inspection. Hardness checks on the brazed cracked sheet and as-received material revealed no out of specification condition. It was initially suspected that the orientation of the cracks relative to the roll direction might indicate a cold working condition of a localized nature in the sheet during the mill process. This theory was not supported by the investigation.

X-ray inspection identified some of the known cracks but was not particularly useful in supplementing the investigations. The cracked sheet was identified as Haynes-25 by testing for the presence of cobalt. Ultrasonic inspection was performed on the cracked surface in addition to the other plate surfaces. Results of the ultrasonic trace revealed no apparent relationship between the braze defects and the cracking. Figure II-32 is a composite sketch superimposing the apparent unbrazed areas as per ultrasonic inspection, (shaded areas) and the crack pattern on the hot plate, (dashed line shows boundary of cracked area). Also shown are areas where the plate was sectioned for metallographic inspection. Tensile test specimens were fabricated to examine the parallel and cross roll direction stress/strain characteristics (at room temperature) of the as-received material lot from which the cracked sheet was taken. Again, no condition was identified which could have caused cracking since the yield, ultimate and elongation values were in accordance with applicable specifications. A trace of the disposition of all Haynes-25 material from this particular lot revealed that pieces were used in prior brazing operations and did not reveal any cracks. (These particular runs varied from the

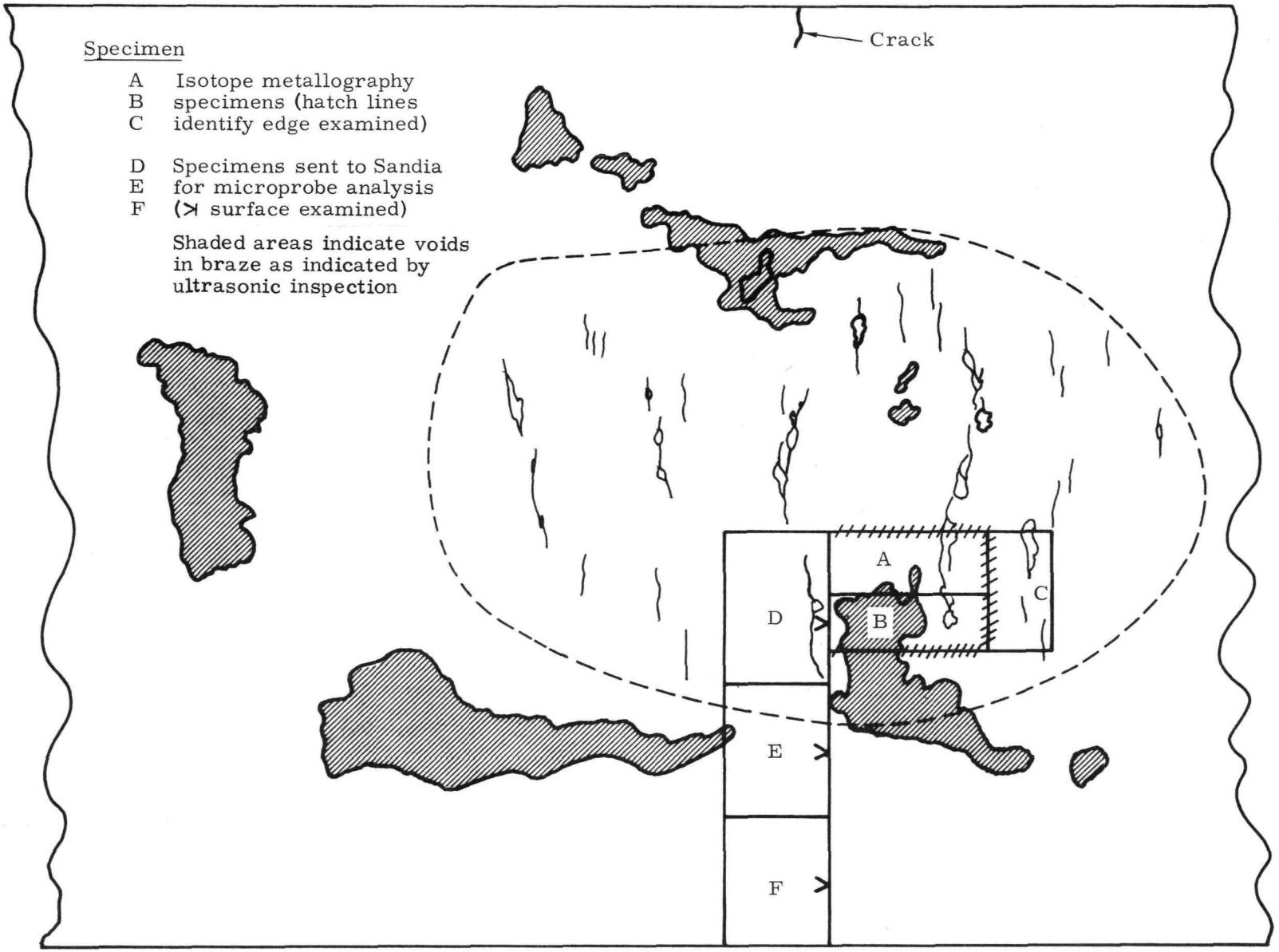

FIG. II-32. HOT PLATE CRACK PATTERN AND ULTRASONIC TRACE

CONFIDENTIAL

CONFIDENTIAL

offending one in that the 40 psig pressure was not applied to the fixtured parts.) Examination of manufacturing records, (logs and strip chart records of braze furnace temperature versus time) revealed no evidence of irregularities or deviation from process requirements.

Three sets of samples from the failed hot plate were metallographically examined. There were as follows:

(1) A 1/8-inch wide strip of 0.012 inch Haynes-25 sheet cut from the edge of the assembly. This strip was not cracked but most of it was not bonded to the beryllium.

(2) Three cross sections of the complete assembly out of the center cracked region. Cross Section A was through a crack, Cross Section B was through an area which had been indicated as unbonded by ultrasonic test, and Cross Section C was at 90 degrees to A and B.

(3) A cross section of the complete assembly near the edge, well away from the failed region, which ultrasonic test had indicated to be well bonded.

Figures II-33, II-34 and II-35 show cross sections of the 0.012-inch thick Haynes-25 sheet with the Haynes-25 at the bottom of the picture. Figure II-33, which is unetched, shows a diffusion layer adjacent to the Haynes-25 which contains cracks. Figure II-34, which has been selectively etched for silver, indicates little or no silver in this diffusion layer. This is seen by comparing the unattacked condition of the diffusion layer with the etched condition of the layer below the Haynes-25 which is braze material that has flowed around the edge of the Haynes-25 sheet. Figure II-35 shows the same cross section selectively etched for beryllium and indicates that the diffusion layer is beryllium rich. Figures II-36 and EE-37 compare the grain size in the Haynes-25 sheet which has been subjected to the brazing cycle with the grain size in the as-received sheet. They indicate that no significant grain growth has occurred during the brazing cycle.

Figures II-38, II-39 and II-40 show the full cross section of the failed assembly. Figures II-38 and II-39 show the same type of diffusion zone between the Haynes-25 and the braze layer as was shown by previous figures. This zone is shown by selective etching to be beryllium rich. Figures II-38 and II-39 also show a penetration of braze material through the Haynes-25 sheet. There is no evidence of gross chemical reaction in the vicinity of this penetration. Figures II-38 and II-39 also show that the lack of bonding indicated by ultrasonic test occurred between the diffusion layer and the Haynes-25.

Figure II-40 shows a cross section in the failed area etched to show the Haynes-25 grain boundaries. The beryllium has been etched completely away and shows clearly that the failure through the Haynes-25 sheet is intergranular. Again, there is no evidence of gross chemical reaction accompanying the penetration.

Figure II-41 shows a full cross section sample away from the failed area. It is to be noted that the same diffusion layer is present between the Haynes-25 and the braze material. However, in this sample a sound bond is seen between the diffusion zone and the Haynes-25.

Measurements of the diffusion layer thickness and the remaining Haynes-25 thickness were made with a calibrated monocular eyepiece. These measurements are summarized in Table II-16. The first seven measurements were made on samples used to develop the brazing process, while the last six measurements were

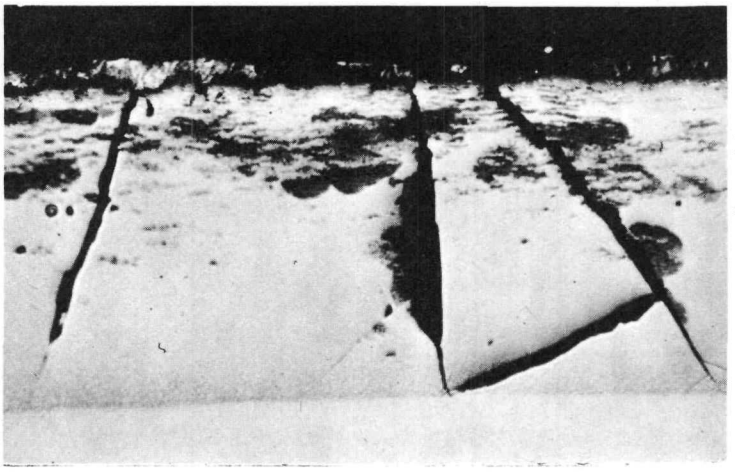

FIG. II-33. BRAZED SAMPLE SHOWING DIFFUSION ZONE PLUS HAYNES-25. AS-POLISHED; MAGNIFICATION--500X

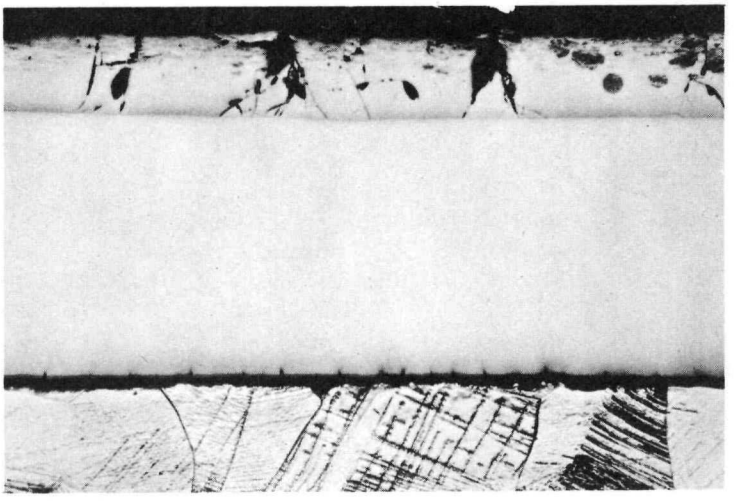

FIG. II-34. BRAZED SAMPLE SHOWING DIFFUSION ZONE PLUS HAYNES-25. ETCHED FOR 5 SECONDS WITH Ag SOLDER ETCHANT. ETCHANT-- $NH_4OH + H_2O_2$; MAGNIFICATION--150X

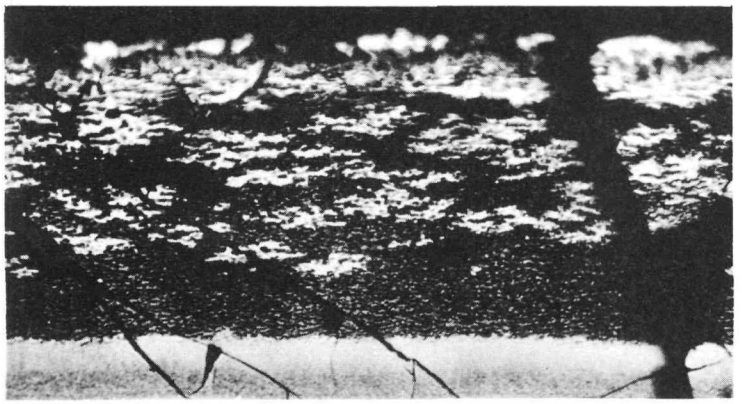

FIG. II-35. BRAZED SAMPLE SHOWING DIFFUSION ZONE PLUS HAYNES-25 ETCHED FOR 10 SECONDS WITH Be ETCHANT. ETCHANT--HF + ALCOHOL; MAGNIFICATION--500X

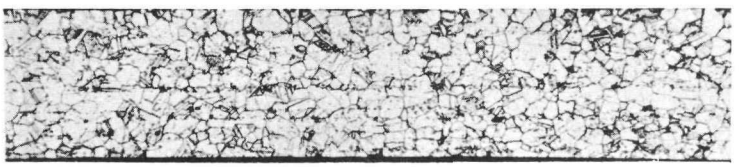

FIG. II-36. HAYNES-25 BRAZED SAMPLE; ASTM GRAIN SIZE = 6.5. ETCHANT--MIXED ACIDS: MAGNIFICATION--75X

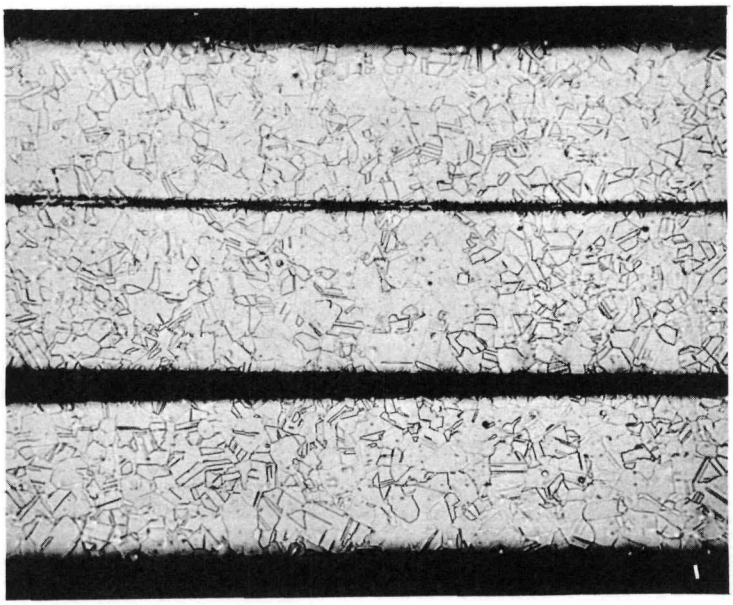

FIG. II-37. HAYNES-25 AS-RECEIVED SHEET; ASTM GRAIN SIZE = 6.5. ETCHANT--MIXED ACIDS; MAGNIFICATION--75X

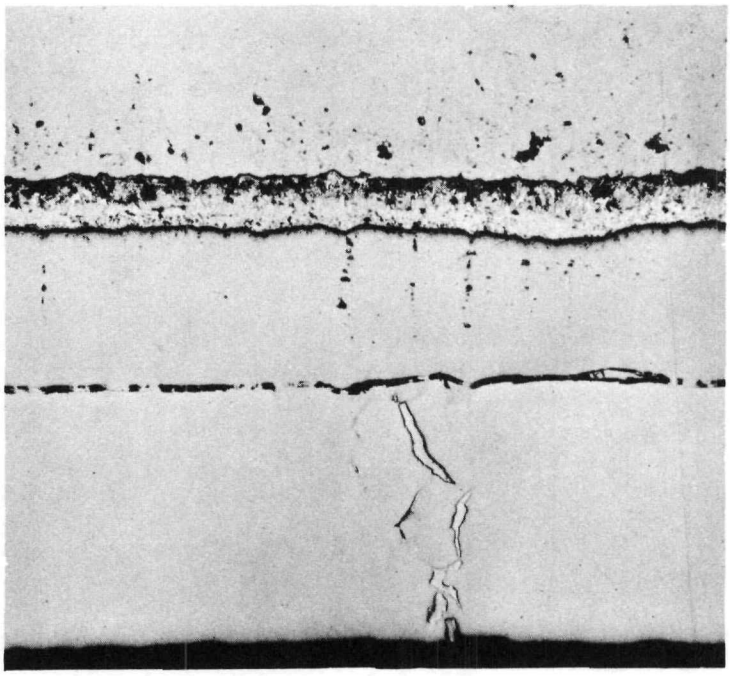

FIG. II-38. BRAZED HEAT SINK SAMPLE B SHOWING FAILURE AREA, DIFFUSION LAYER PLUS HAYNES-25. AS-POLISHED: MAGNIFICATION--150X

CONFIDENTIAL

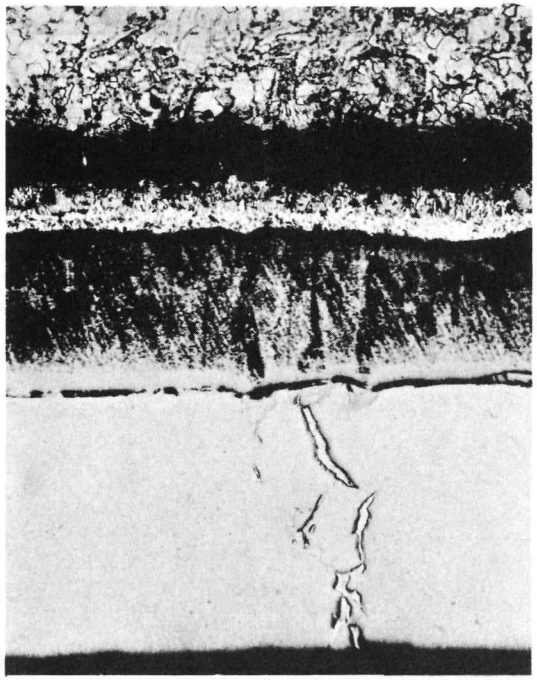

FIG. II-39. BRAZED HEAT SINK SAMPLE B SHOWING FAILURE AREA, DIFFUSION LAYER PLUS HAYNES-25. ETCHED WITH Be ETCHANT FOR 10 SECONDS. ETCHANT--HF + ALCOHOL; MAGNIFICATION--150X

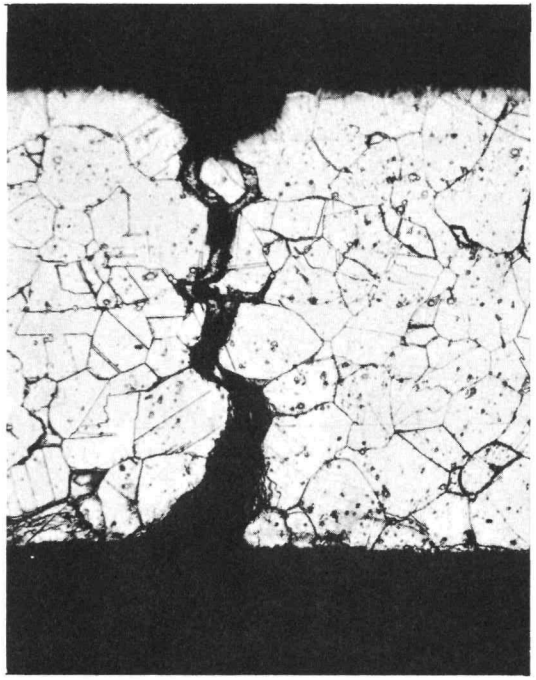

FIG. II-40. BRAZED HEAT SINK SAMPLE A SHOWING FAILURE AREA. ETCHED HEAVILY FOR HAYNES-25 GRAIN BOUNDARIES. ETCHANT--MIXED ACIDS; MAGNIFICATION--150X

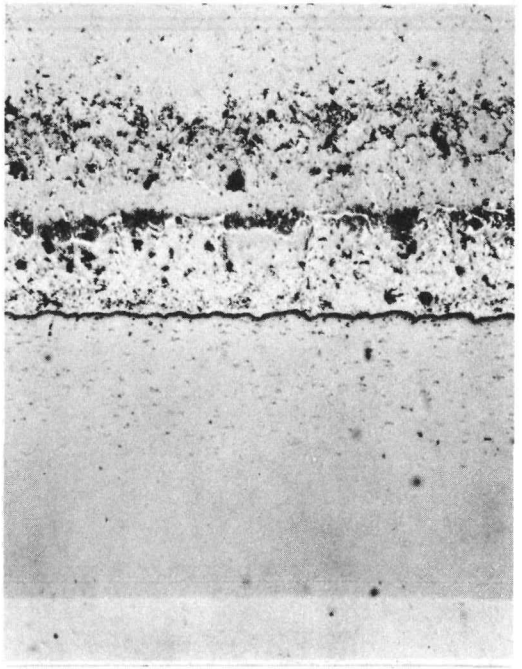

FIG. II-41. HAYNES-25, 0.012 INCH THICK, Ag BRAZED TO Be SHOWING GOOD BOND AREA. AS-POLISHED; MAGNIFICATION--250X

CONFIDENTIAL

made on cross section samples through the failed area of the brazed assembly. Three important conclusions can be drawn from these measurements.

(1) In only one case (205-minute development sample) is any reduction in the original Haynes-25 thickness evident during brazing, and even in this case the thickness reduction averages only about 0.0015 inch. This indicates that the diffusion zone forms primarily by beryllium diffusing through the braze material, and its presence should not noticeably affect the mechanical properties of the Haynes-25 skin.

(2) The thickness of the diffusion zone is essentially uniform from sample to sample and essentially the same on the side of the 0.030-inch thick Haynes-25 as it is on the side of the 0.012-inch thick Haynes-25. This indicates that its thickness is determined by brazing time and temperature.

(3) This thickness of the diffusion zone in the brazed assembly samples when compared with the diffusion zone thicknesses of the developmental samples indicates that the brazed assembly was above the critical temperature for diffusion (1400° F) for approximately 205 minutes. This is in distinct disagreement with the measured time which was approximately 100 minutes.

TABLE II-16

Thickness Measurements

Sample	Haynes-25 Thickness (in.)	Beryllium Diffusion Zone Thickness
Process Development Sample		
27mm	0.0120	0.00025
27 mm	0.0122	0.0001 (max)
93 mm	0.0120	0.0001
93 mm	0.0123	0.0004
205 mm	0.0110	0.0050
205 mm	0.0113	0.0055
205 mm	0.0093	0.0055
Brazed Assembly		
Sample A	0.0118	0.007
Sample A	0.0296	0.0045
Sample B	0.012	0.0065
Sample B	0.030	0.007
Sample C	0.012	0.0065
Sample C	0.030	0.007

It must be concluded that the metallographic examinations performed disclosed no direct evidence of the cause of cracking of the Haynes-25 skin.

Samples of the subject block were sent to Sandia Corporation for their independent evaluation, (metallography, ultrasonic, electron microprobe). To date, results of the Sandia evaluation have not identified the cause of the cracks. The results of the Isotopes investigation are inconclusive with regard to identifying the source of cracks in the Haynes-25 sheet. Since the crack phenomenon had not been encountered in the past and since it only occurred in one of the four Haynes-25 faces brazed simultaneously, an attempt was made to duplicate the failure under identical conditions. The results of the repeated braze operation were negative in that no cracks were evident on any of the faces of the hot plate and heat sink assemblies. Figure II-42 shows the plates as brazed after the duplication run. At present, the cause of the crack formation has not been identified. The brazing program will continue as originally planned since no evidence has been uncovered to indicate that this isolated incident is process related. Quality control checks will be made on all future parts in order to identify any recurrence of cracks. Most recently a braze operation was performed on two heat sink parts to provide additional hardware for heat pipe soldering development and to optimize the furnace operation in order to minimize time above 1400° F in the brazing process. By increasing heat up rates, the time above 1400° F for this run was held to 72 minutes, a substantial improvement over prior runs, (~90 to 100 minutes). The necessary process changes have been effected. No evidence of cracks was found on these parts. The desirability of decreasing time above 1400° F stems from data obtained during braze development and subsequent verification runs which show a relationship between time above 1400° F and the formation and growth of an apparently brittle intermetallic zone in the beryllium. The extent of this zone diminishes with decreasing time above 1400° F. Based on the limited data obtained to date, this zone, though not fully characterized, does not appear detrimental to the structural performance of the joint since analysis predicts low working stresses in the braze area and prior testing of a hot plate brazement resulted in no failure of the joint under environmental conditions of temperature and pressure.

In order to provide an increased capability for evaluating ultrasonic inspection results in the future, an ultrasonic test standard will be fabricated. Figure II-43 shows a sketch of the standard which will have discrete geometric braze defects built in during the brazing operation. This standard will be made with actual module hot plate components and will be ultrasonically tested simultaneously with each brazement to provide a comparison with known defects.

4. Diaphragm Development

Figure II-52 of the Eighth Quarterly Progress Report shows a cutaway sketch of the test set up for the NaK diaphragm life test. Figure II-44 of this report is a photograph of the actual test arrangement. As of 12/31/68, this test completed 91 days of successful operation. During this period, pressure has remained at a nominal 40.5 psig and the average ΔT through the diaphragm is 3° F. Average recorded temperature of the bottom of the diaphragm is ~1125° F. Table II-17 shows the typical life test data acquired to date. Figure II-45 shows thermocouple locations on the diaphragm faces and heater block. Testing of the NaK diaphragm will continue on an extended life basis during the next reporting period.

The NaK-filled diaphragm design includes a NaK/argon accumulator to maintain constant pressure in the system under changing volumetric capacities of the diaphragm due to thermal and structural effects, (Fig. II-51, Eighth Quarterly Report). The accumulator was designed and fabricated in accordance with SNAP 29 Procurement Specification 466S48002 by Robertshaw Controls Company, Fulton Sylphon Division,

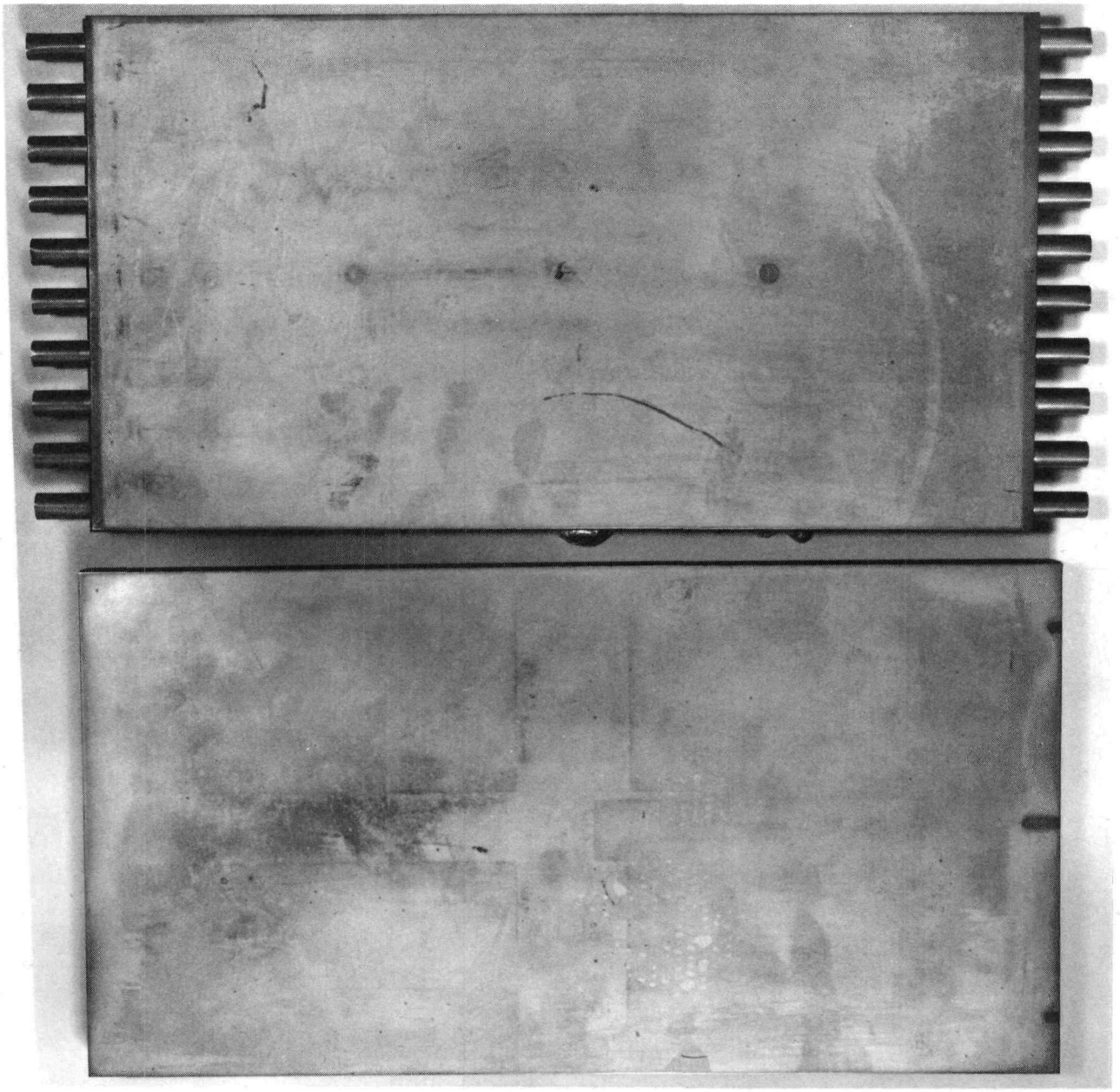

FIG. II-42. BRAZED HOT PLATE AND HEAT SINK AFTER ATTEMPT TO DUPLICATE CRACKING

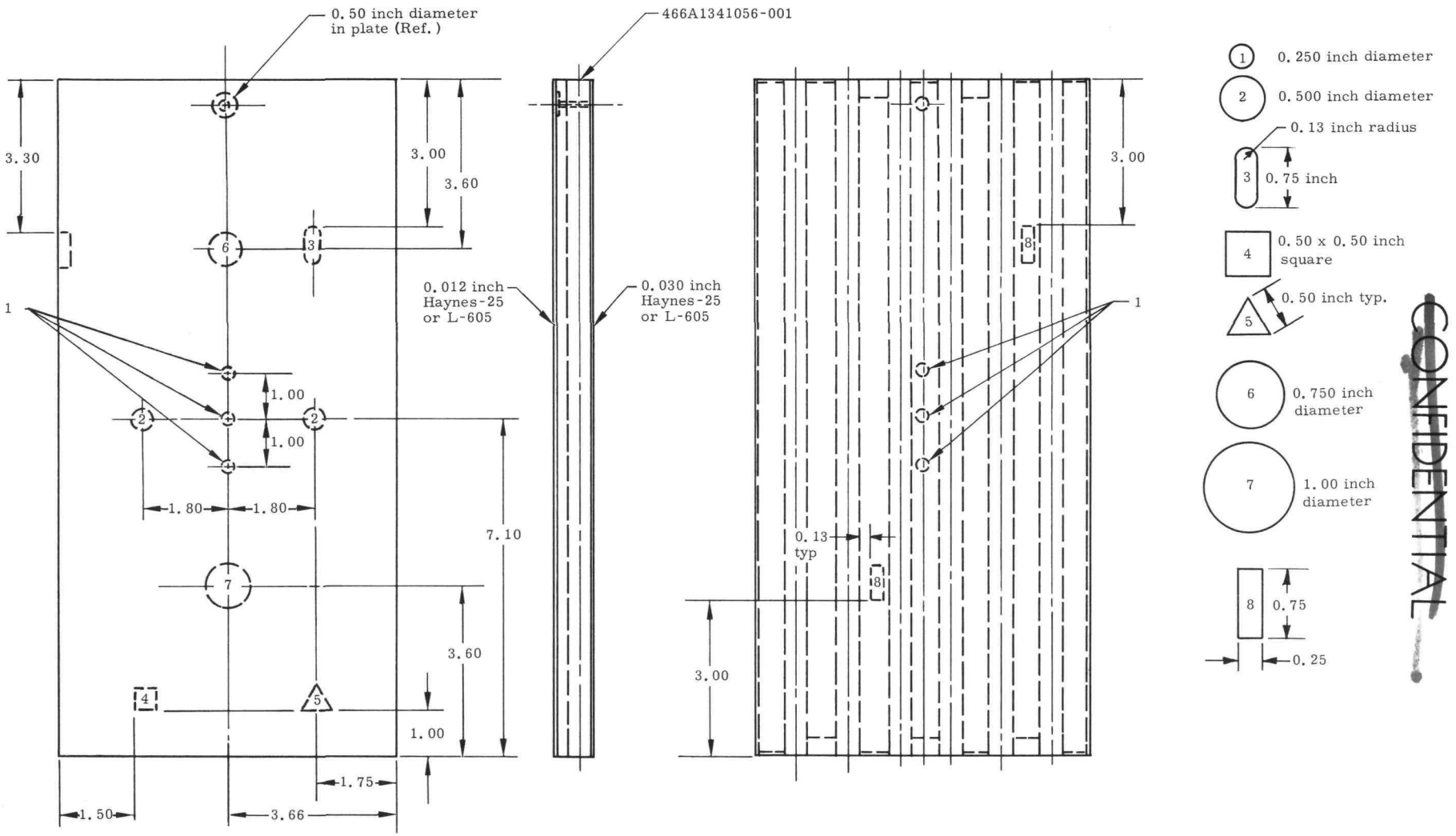

FIG. II-43. ULTRASONIC INSPECTION STANDARD

CONFIDENTIAL

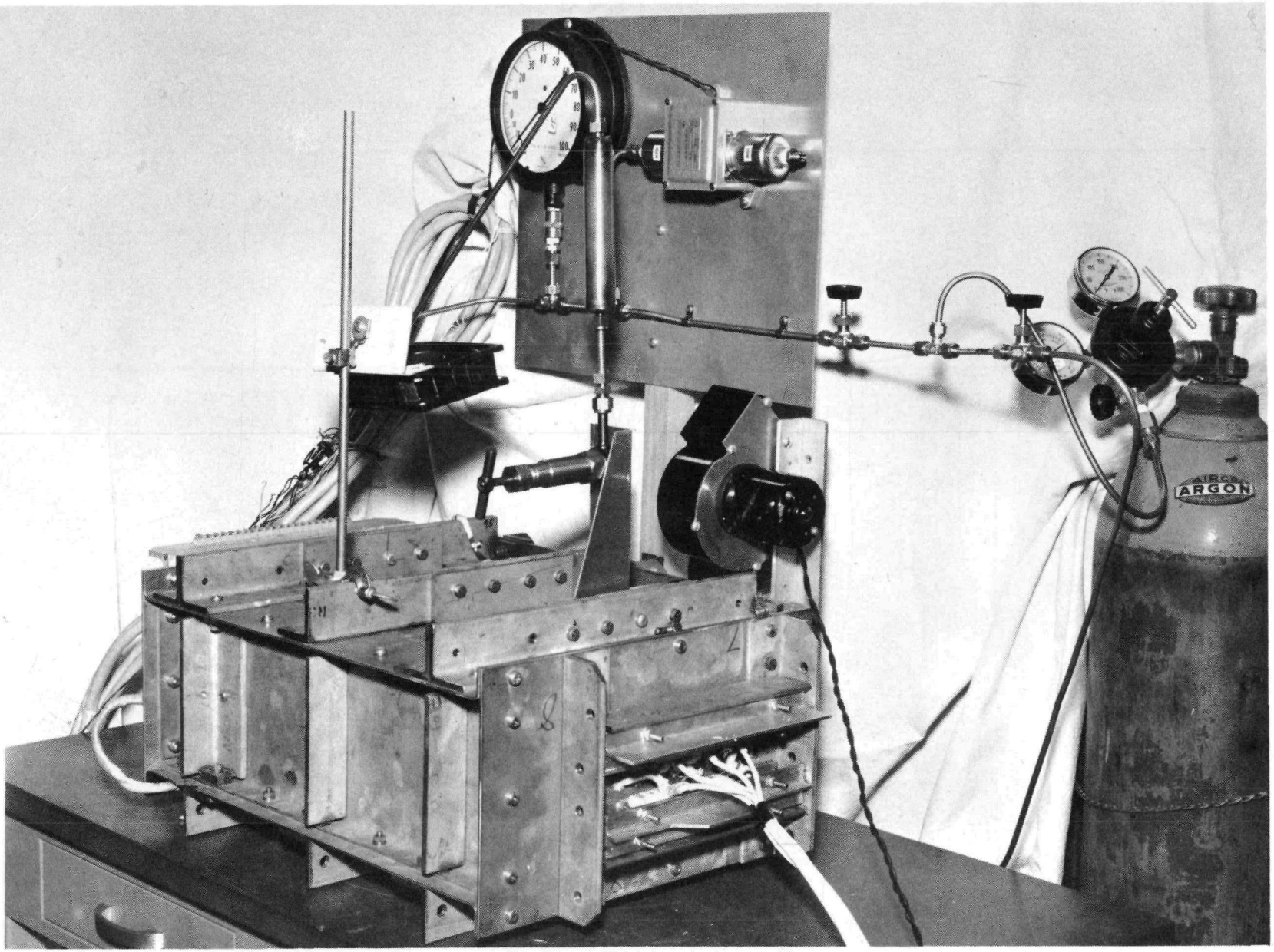

FIG. II-44. NaK DIAPHRAGM LIFE TEST SETUP

CONFIDENTIAL

CONFIDENTIAL

TABLE II-17

SNAP 29 NaK Diaphragm Life Test Data Summary

	TC No.	5001	5002	5003	5004	5005	5006	5007	5008	5009	1	2	3	4	5	6	7	8	9	10	11	12	13	14	15	16	17	18	19	20
		Heater Block (°F)									Bottom of Diaphragm (°F)												Top of Diaphragm (°F)							
Date	Time																													
10-7-68	0830	1884	1126	1156	1165	1134	1160	1181	1140	1106	1106	1175	1157	1134	1127	1171	1148	1153	1156	1131	1198	Out	1106	1072	1156	1131	1124	1172	1146	1149
11-4-68	0955	1167	1113	1141		1119	1140	1162	1128	1093	1089	1062	1141	1122	1112	1158	1133	1141	1142	1119	1089	Out	1086	1058	1140	1120	1108	1161	1136	1136
12-2-68	0830	1172	1117	1146				1168	1132	1100	1093	1063	1145	1127	1116	1162	1139	1147	1147	1122	1092	Out	1089	1060	1143	1123	1109	1164	1139	1142
12-30-68	0945	1183	1127	1157	1167	1134	1157	1180	1142	1106	1103	1072	1158	1135	1127	1174	1148	1156	1158	1132	1102	Out	1103	1068	1156	1132	1123	1175	1148	1151

	TC No.	21	22	23	24							Δ TC T									
		Top of Diaphragm				Power In	Average Heater Block	Average of Diaphragm		ΔT Average Top and Bottom	Pressure	1-13	2-14	3-15	4-16	5-17	6-18	7-19	8-20	9-21	10-22	11-23
Date	Time	(°F)	(°F)	(°F)	(°F)	(watts)	(°F)	Bottom (°F)	Top (°F)	(°F)	(psig)	(°F)	(°F)	(°F)	(°F)	(°F)	(°F)	(°F)	(°F)	(°F)	(°F)	(°F)
10-7-68	0830	1155	1132	1048	1045	912	1150	1132	1124	8	40.1	0	3	1	3	3	-1	-1	4	1	-1	0
11-4-68	0955	1141	1121	1088	1032	880	1135	1119	1111	10	40.0	4	4	1	2	5	-3	-3	5	1	-2	1
12-2-68	0830	1146	1126	1088	1037	904	1139	1123	1114	13	39.1	4	3	2	4	7	-2	1	5	1	-4	4
12-30-68	0945	1156	1132	1098	1043	912	1150	1133	1124	9	39.5	0	4	2	3	4	-1	0	5	2	0	4

CONFIDENTIAL

CONFIDENTIAL

Bottom of diaphragm T/C	Top of diaphragm T/C	Top of Heater Block T/C
1	13	5006
2	14	5002
3	15	5007
4	16	5003
5	17	5006 5005
6	18	5001 5007
7	19	5001
8	20	5001 5003
9	21	5004
10	22	5008
11	23	5001
12	24	5009

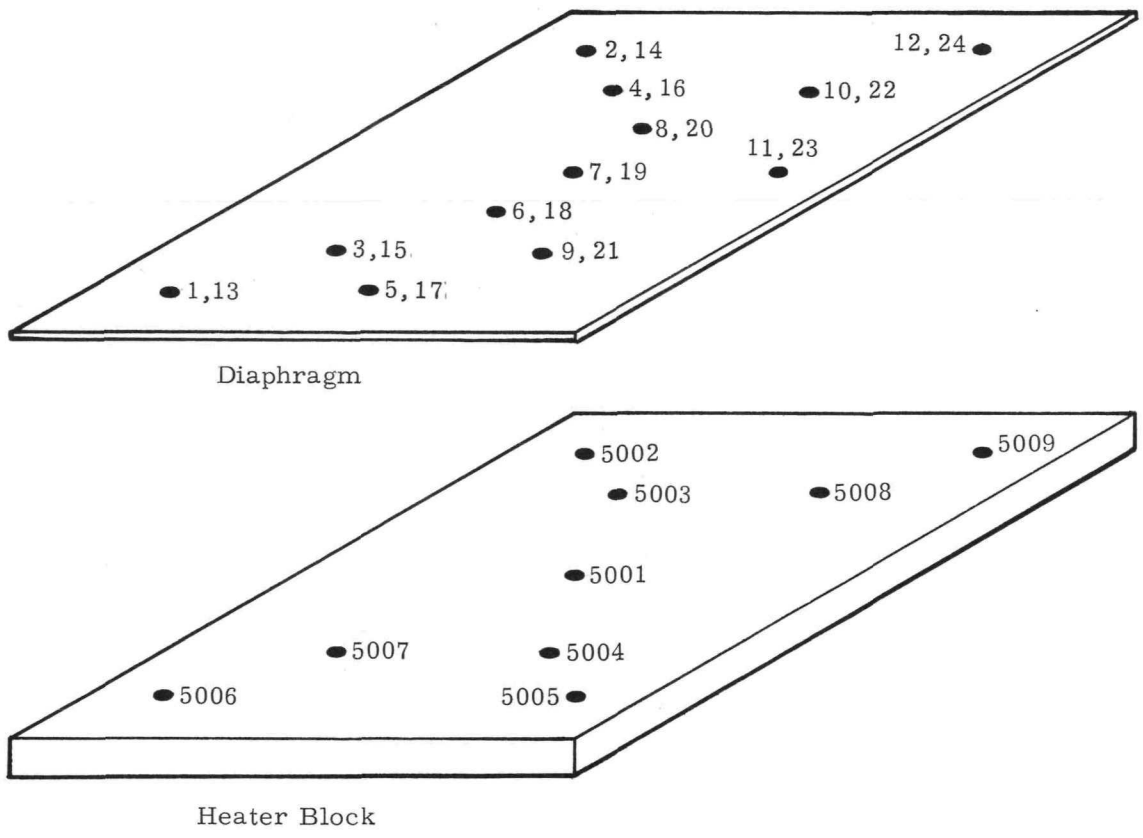

FIG. II-45. NaK DIAPHRAGM THERMOCOUPLE LOCATIONS

CONFIDENTIAL

Knoxville, Tennessee. All units have been delivered during this reporting period and have been accepted. It is planned to initiate a life test on one of the accumulators during the next reporting period. Figure II-46 shows a NaK/argon accumulator.

5. T/E Module Side Skin Design Development

The original concept of a one piece wraparound 0.012 inch Haynes-25 side skin TIG welded to the hot plate and heat sink frames was found to result in brittle weldments with high residual stresses due to excessive heat required to accomplish a weld to the high mass plate frames. This condition was the cause of repeated leakage in the side skins during performance testing of the piston heat sink modules. The proposed design modification to eliminate this problem was to retain the side skin configuration and replace TIG welding with EB welds. Side skin EB weld development work performed during this period revealed that although higher quality welds can be consistently attained, the use of a wraparound single piece side skin introduces new problems when used in conjunction with EB welding. On a mocked up module frame/side skin weld sample, a weld burnthrough was encountered at three of the eight corner locations where the side skin bends around the frames. The problem results from the difficulty in maintaining complete faying surface contact in bending the 12-mil side skin around the sharp frame corner. Rounding the frame corners will not allow a sound, continuous EB weld. It was necessary to patch these burnthrough areas with TIG welds which successfully produced a leak proof seal. Another potential problem exists in that should an EB weld burnthrough occur on the flat sides of the frame/side skin weld due to current surge, it would again be necessary to provide a TIG weld patch. The undesirability of TIG welding in this application has already been pointed out. An alternate design has been evolved which replaces the continuous 12-mil sheet side skin with four flat slab sides consisting of a basic 12-mil sheet with 24-mil weld land areas. This eliminates the corner bends and provides added thickness in all weld zones. The added thickness will reduce the post-weld buckling previously experienced and improve the possibility of the side skins being repaired by TIG welding should leaks be detected in the EB weld. This technique involves EB welding the slabs to the plate frames and joining the slabs at the corners by TIG welding. TIG welding is acceptable at the corners since the heat input required to weld two 24-mil sheets is minimal. A weld sample of the modified configuration was fabricated and successfully leak checked. Figure II-47 shows the sample in various stages of assembly. Note the titanium foil weld shield which prevents the corner TIG weld from being contaminated by the Min-K insulation constituents. Presently, two methods of fabricating the slab side skins with weld lands are under consideration:

(1) Diffusion bond a 12-mil sheet with a cutout to a 12-mil solid sheet. This method was used in the weld sample and proved successful. The diffusion bond, while not 100%, proved adequate.

(2) Eliminate the diffusion bond by removing material from a 24-mil sheet by electrical discharge machining (EDM). This method is presently under evaluation.

6. Flame Sprayed Circuitry Analysis and Development

During this period a study was completed analysing the results of measurements of sprayed copper pad resistance values. This was done as a function of pad thickness in terms of the internal I^2R losses in the module circuitry.

On a module basis at nominal operating conditions, (28 amperes and 375° F,) the I^2R losses are 2.40 watts for 0.012-inch thick pads and 1.23 watts for 0.020-inch

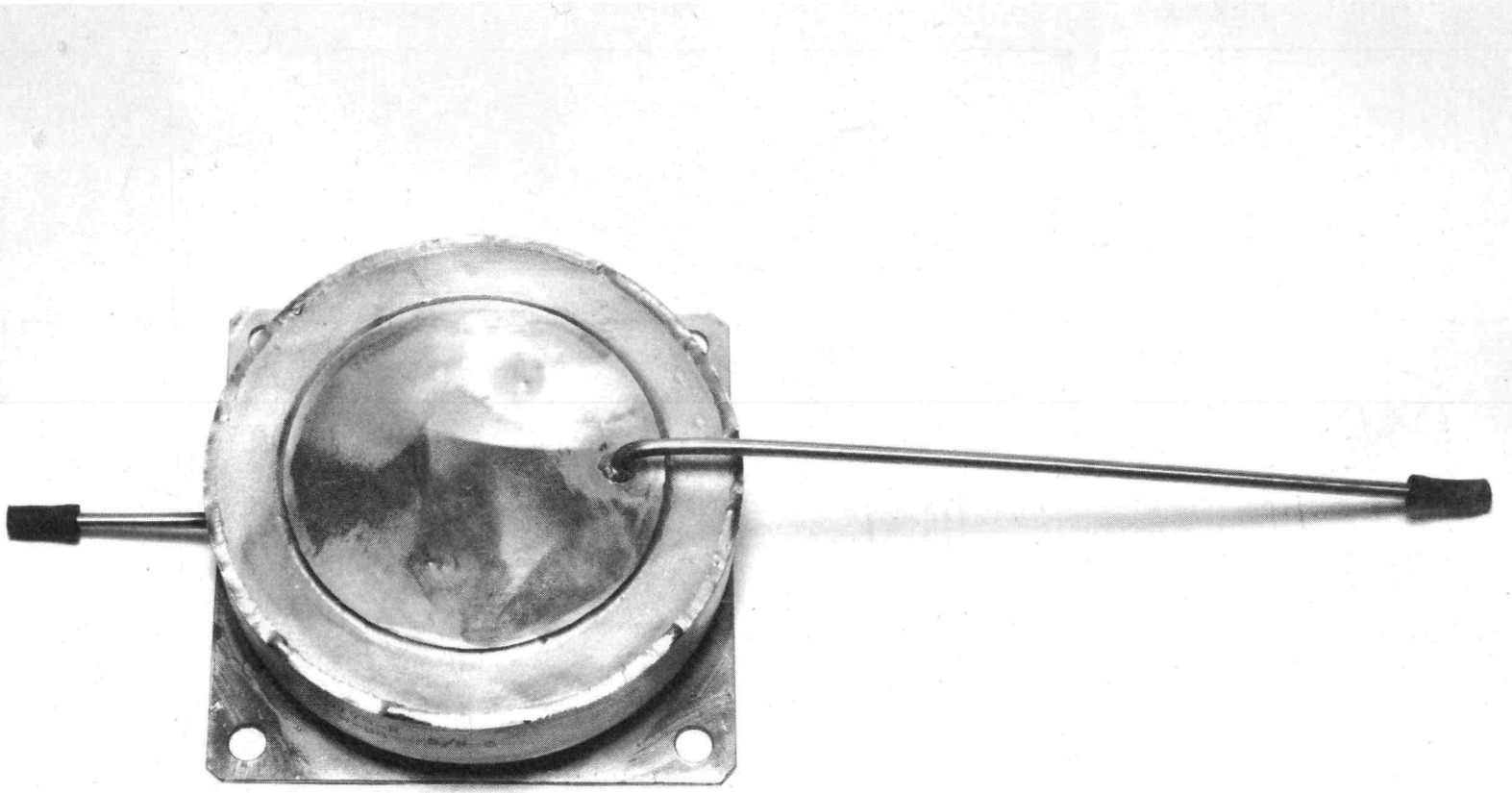

FIG. II-46. NaK/ARGON ACCUMULATOR

CONFIDENTIAL

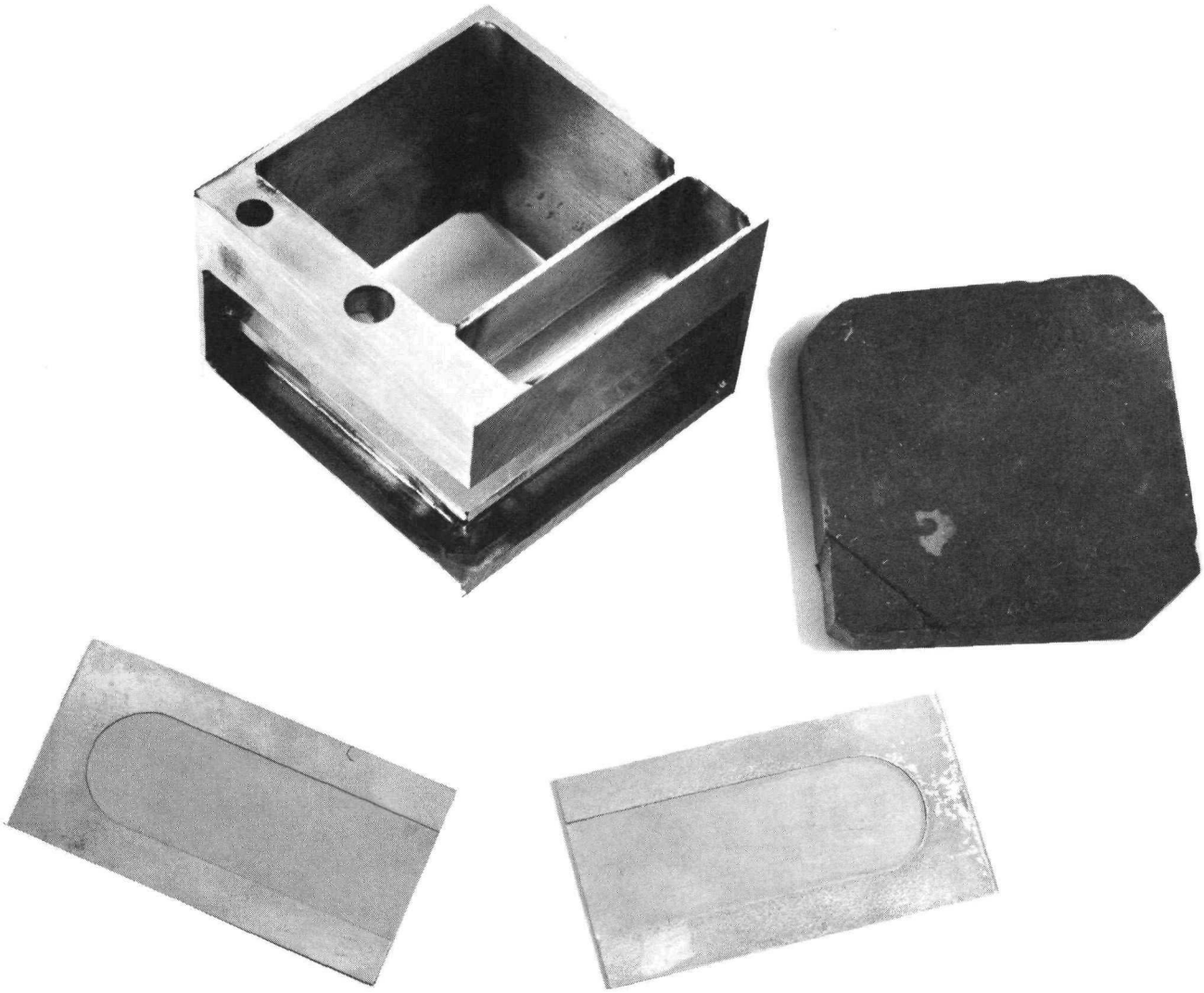

FIG. II-47a. WELD SAMPLES FOR SIDE SKIN DESIGN MODIFICATION

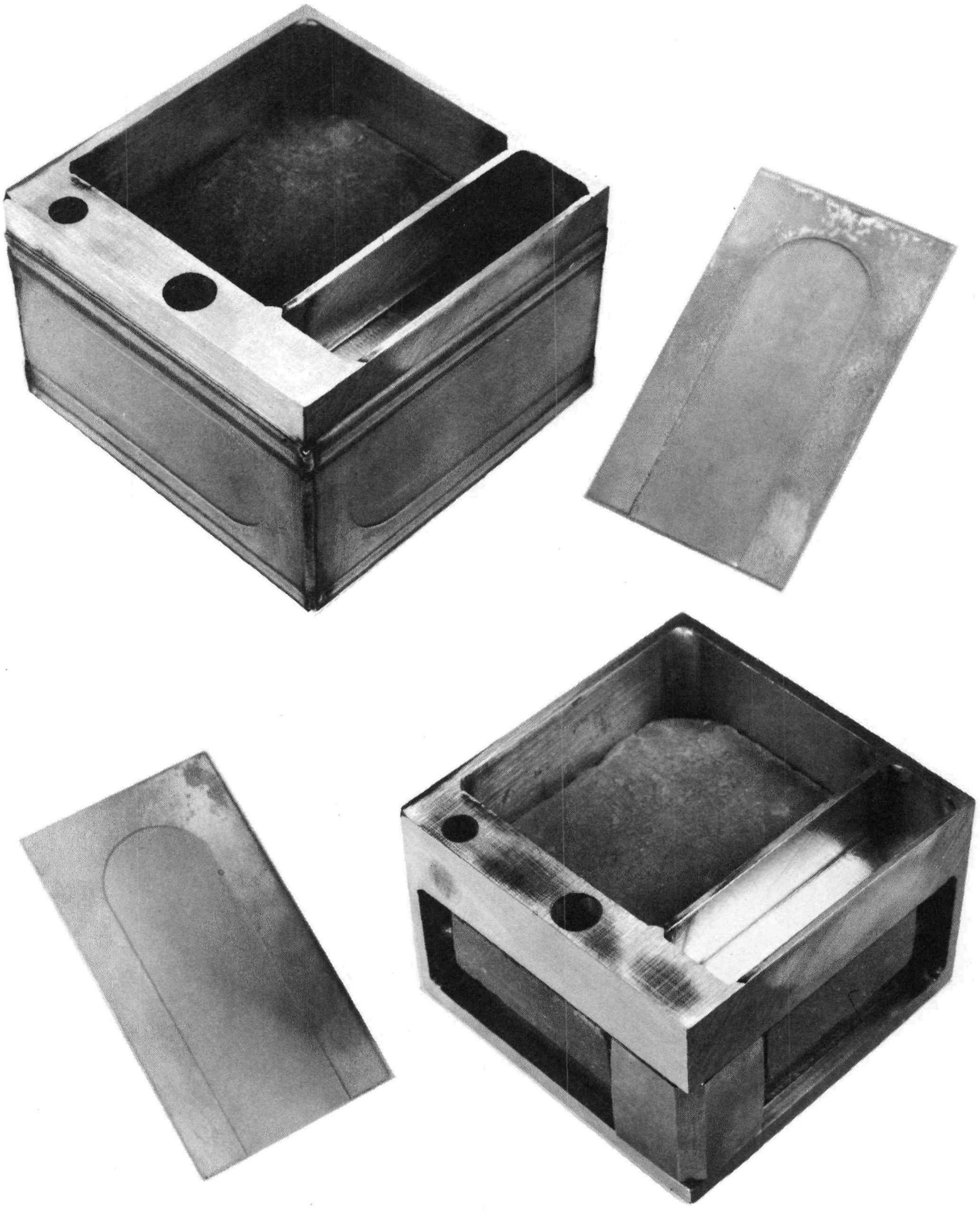

FIG. II-47b. WELD SAMPLES FOR SIDE SKIN DESIGN MODIFICATION

thick pads. Therefore, an increase in I^2R losses of 1.17 watts/module is experienced between the 0.020- and 0.012-inch thick copper flame-sprayed pads at the nominal TAGS operating condition. It was also determined that a pad thickness of approximately 0.035 inch optimizes the specific power of the SNAP 29 system. Since the SNAP 29 module uses 0.015-inch thick pads, the specific power of the 0.012-inch pads was examined and found to be 1% less than optimum power. It was concluded that little penalty in specific power will result if the thickness of the copper flame-sprayed pads is less than the optimum thickness but greater than 0.012 inch. The complete analysis is presented as Appendix A of this document.

Development work conducted during this reporting period relative to flame spraying 0.015 inch copper pads to the cold end hardware surface revealed a tendency for the long connector pads between adjacent rows of pads to lift up at the edges. It was found that by spraying a thin (0.002 inch) layer of pure zinc between the aluminum oxide and copper pad that this tendency was eliminated. Mechanical pull tests indicated about a 40% increase in interface bond strength between the copper and the aluminum oxide substrate with the zinc interlayer. Specimens are currently undergoing metallographic examination. If further confirmation of bond integrity is obtained, this technique will be adopted.

7. Diagnostic Disassembly of T/E Modules

Diagnostic disassembly of piston heat sink modules S/N 001, 002 and 004 was completed during this period. The predominant failure mode of the couples was an unbonding of the P leg at the hot shoe. Some discoloration was noted in modules which had developed leaks during testing. Disassembly of S/N 002 indicated a tolerance problem between the length of the couple legs and the insulation thickness. Impressions of the cold strap pattern appeared in the Min-K 1301 at locations (Figs. II-48a and II-48b) which resulted in the inability to attain a good cold end bond in these locations. As a result of this, design tolerances were reviewed for the couple leg length and insulation thickness and modifications were made to prevent a recurrence of this problem. Table II-18 presents a summary of the condition of the couples as determined after disassembly.

TABLE II-18

T/E Couple Condition After Module Disassembly

	Quantity		
Condition	S/N 001	S/N 002	S/N 004
Unbonded P element hot end	70	89	65
Unbonded N element hot end	12	0	8
Unbonded N and P element hot end	4	0	9
Broken P element	3	0	1
Broken N element	0	0	0
Cracked P element	0	0	0
Cracked N element	2	0	0
Intact couples	11	1	8

Each of the modules exhibited in varying degrees, poor quality solder bonds at the cold end (Fig. II-49). Some of this can be attributed to the previously discussed mismatch between insulation thickness and couple length. An additional remedy to

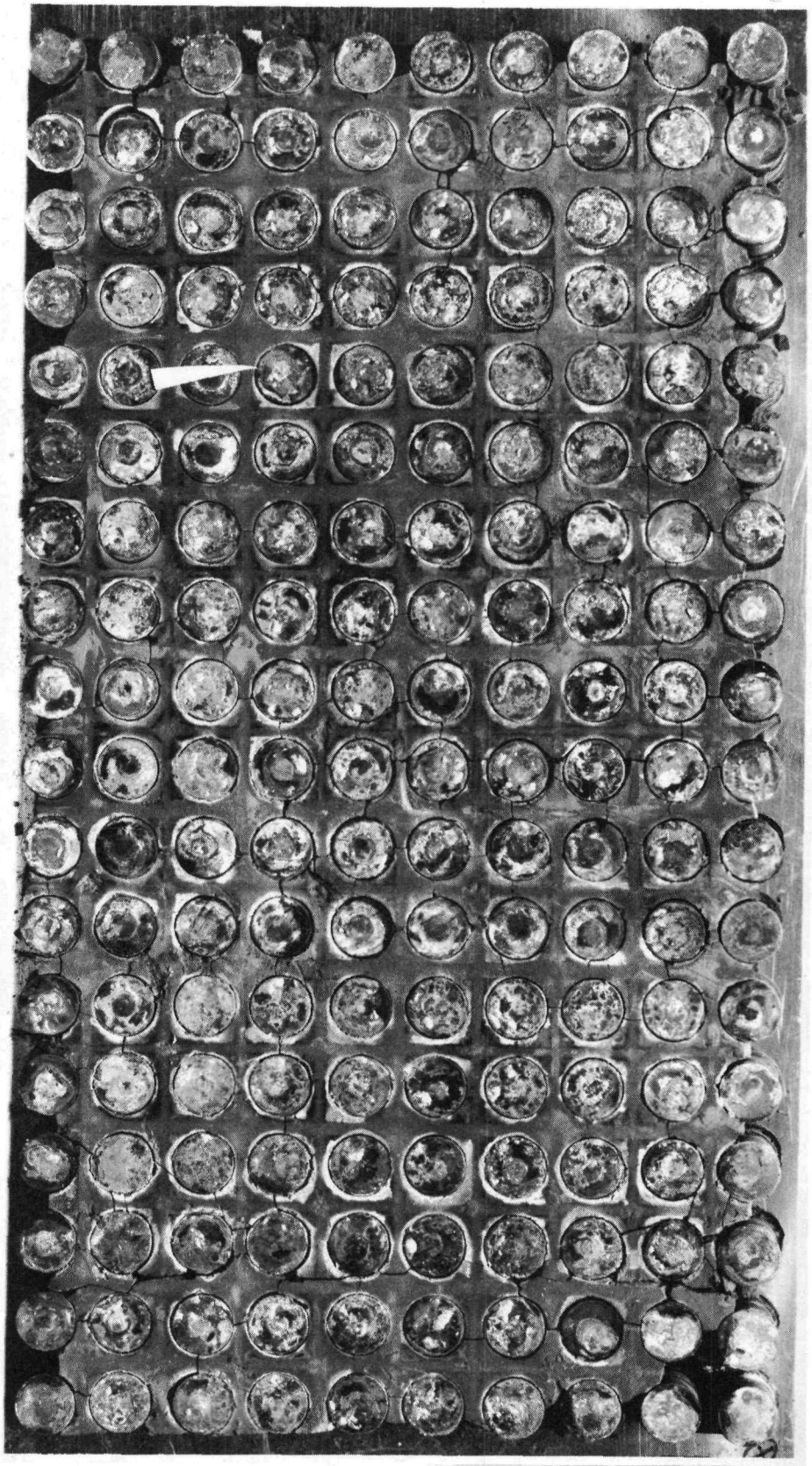

FIG. II-48a. PISTON HEAT SINK MODULE T/E CONVERSION ASSEMBLY AFTER DIAGNOSTIC DISASSEMBLY

FIG. II-48b. PISTON HEAT SINK MODULE T/E CONVERSION ASSEMBLY AFTER DIAGNOSTIC DISASSEMBLY

CONFIDENTIAL

CONFIDENTIAL

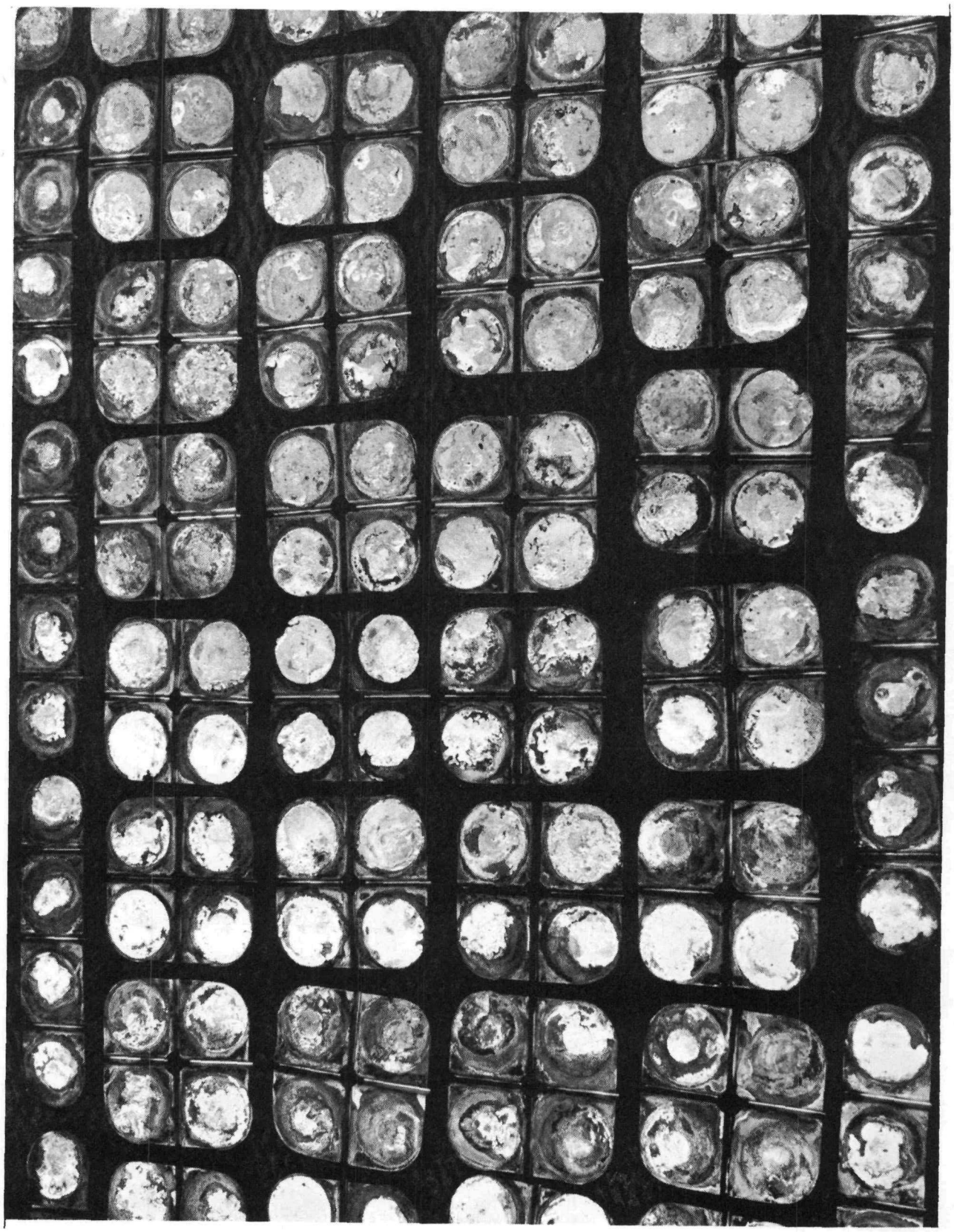

FIG. II-49. PISTON HEAT SINK MODULE S/N 002 COLD END STRAPS AFTER DISASSEMBLY

this problem, which will be incorporated on all future modules, is to pretin all solder bond surfaces in subassembly prior to mating the T/E conversion assembly to the cold end hardware.

Black carbon-like deposits were found on the hot end side of many of the couples in addition to a crystalline growth. This may have been caused by the use of Kester 817 flux which will not be used in the 2N-TAGS/SnTe couple assembly. It should be noted that during test these modules developed leaks which could have contributed to the discoloration revealed during examination. S/N 002 was subjected to dynamic testing in addition to the life performance testing. S/N 001 experienced a brief overtemperature during its test cycle, (~1125° F T_{HJ}, 420° F T_{CJ} for 15 minutes).

8. TAGS Material Property Data

The analytical data originally used to analyze TAGS performance (TEDP-00-10) was measured in May 1966. Recently these data have been revised to include a change in the resistivity values to conform to the data presented in the Summary of Advanced Technology Symposium, August 29-30, and the Thermoelectric Panel Meeting, October 10, 1967 (MND-3314, Martin Marietta). These new data will be labeled with a new material property identification TEDP-00-10A. A document entitled "Thermoelectric Data for TAGS (TEDP-00-10A) and SnTe (TEDP-00-27) Thermoelectric Elements," is included as Appendix B of this document.

A comparison of calculated results for the TEDP-00-10 and TEDP-00-10A data indicates no significant differences at SNAP 29 operating temperatures. Thermoelectric parameters such as thermoelectric efficiency, total generator resistance, normalized power output, normalized thermal input and leg diameter ratio for optimum efficiency are essentially unchanged. The SnTe (TEDP-00-27) thermoelectric data as used on the SNAP 29 project is also presented in Appendix B.

To complete the comparative analysis, E-I curves and heat rejection curves are parametrically being generated for the TEDP-00-10A material used in the SNAP 29 thermoelectric module. This task will be completed during the next reporting period.

During this period, a subcontract was let to Battelle Memorial Institute (BMI) to evaluate material properties of Isotopes TAGS thermoelectric material independently to obtain comparative data. Battelle will determine thermal conductivity, density, specific heat, thermal expansion coefficient, Seebeck voltage and electrical resistivity in the range of temperatures applicable to SNAP 29. These data will be available for inclusion in the 10th Quarterly Report.

9. 2N-TAGS/SnTe Thermoelectric Couple Development

During this reporting period, a large quantity of work has been performed in thermoelectric couple development for the SNAP 29 generator. Various groups of couples have been fabricated and put through a testing program to experimentally optimize fabrication techniques and material conditions for peak power generation. The testing program included two-hour power checks, nine-point resistance checks, tensile pull tests and metallographic examination. The bonding techniques, fabrication of the SnTe segment in the P leg, and heat treatment of elements and couples were among the variables which were investigated. The various groups of couples which were examined have been assigned code numbers. The code numbers are presented in Table II-19. The code number indicates the bonding procedure used on the couple and the defining conditions imposed upon the materials or couples.

TABLE II-19

Code Numbers

Code 1	Sn bond of P leg and 0.0004 to 0.0007 inch Ni-plated iron cups for N leg with a 0.0005 inch Ni wafer added in N leg hot cups.
Code 2	Exothermic bond of P leg (cast SnTe with step) and 0.0004 to 0.0007 inch Ni-plated Fe cups for N leg with 0.0005 inch Ni wafer added in N leg hot cup.
Code 3	Sn bond of P leg with 0.0007 to 0.0008 inch Ni-plated Fe cups for N leg.
Code 4	Sn bond of P leg with 0.0009 to 0.0010 inch Ni-plated Fe cups for N leg.
Code 5	Exothermic bond of P leg (cold pressed and sintered SnTe without step) and 0.0004 to 0.0007 inch Ni-plated Fe cups for N leg.
Code 6	Exothermic bond of P leg (cold pressed and sintered SnTe with step) and 0.0004 to 0.0007 inch Ni-plated Fe cups for N leg.
Code 7	Identical to Code 5 except elements Seebeck checked; TAGS element not heat treated.
Code 8	Identical to Code 5 except elements Seebeck checked; TAGS element heat treated*.
Code 9	Production couple--identical to Code 8 except couple as-fabricated was heat treated*.

*Heat treatment for TAGS element and couples: 890° F for 1 hour.

Appendix C presents an analysis of pertinent results from a series of 2N-TAGS/SnTe bonding technique experiments. The analysis compared the different bonding techniques (Code 1, 2, 3 and 4) between the N and P elements and their respective hot and cold cups by examining the power output from the thermoelectric couples, metallographic examination of the bonds and examination of the tensile pull test data for the N and P legs. The results of these tests indicated that no bonding technique showed significant advantage over the other techniques when comparing power output from the couple (Table II-20). Average power output from Code 2 couples = 1.473 watts (E_{oc} corrected). However, from the results of the pull tests, it was recommended that exothermic bonding (Code 2) be used on the P leg of the SNAP 29 couple and 0.0009 to 0.0010 inch nickel-plated iron cups be used in bonding the N leg. The basis of this analysis consisted of the description of the experiments and their detailed results as presented in Appendix D.

The problem of casting the SnTe segment into the P leg cup (as mentioned in Appendices C and D) has been eliminated by cold pressing a SnTe wafer in advance and pressing the wafer into the P cup screen at temperature and pressure during the fabrication step which bonds the N leg to the hot shoe.

TABLE II-20

Power Output from Thermocouples

Code	No. of Couples	Average Power		
		Measured	E_{oc} Corrected	Temperature Corrected
1	8	1.503	1.500	1.483
2	7	1.473	1.473	1.456
3	3	1.475	1.475	1.456
4	3	1.500	1.513	1.463
5	3	1.536	1.498	1.525
6	4	1.533	1.495	1.514
7	5	1.549	1.526	1.529
8	5	1.619	1.599	1.592
8 repeated	3	1.518	1.529	1.500
9	40	1.608	1.557	1.584

A study was performed to determine if the step in the SnTe segment could be eliminated without an appreciable effect on couple performance since cold pressing the wafers is greatly simplified if the stepped diameter is not required. A brief analysis showed that considering conduction heat transfer only, SnTe with a step exhibited a 94° F temperature difference across a 0.090-inch wafer, and SnTe without a step showed a temperature difference of 84° F. The Peltier effect reduces the thermal energy conducted through the element by approximately 20%. This reduces the temperature differences to ~75° for SnTe with a step and ~67° F for SnTe without a step. The difference in ΔT between the stepped and unstepped SnTe is 8° F. If an unstepped SnTe wafer is used in the P leg, the temperature of the interface between the SnTe and the TAGS-85 materials will be 983° F at the end of life when the hot shoe temperature is 1050° F. To experimentally evaluate the significance of the step on couple performance, two sets of two-hour power check data for the groups of couples under Codes 5 and 6 were examined for the 2N-TAGS/SnTe thermoelectric couple. The first set of data was for couples employing cold pressed and sintered SnTe, without any step, in the SnTe segment (Code 5). The other set of data was for couples employing cold pressed and sintered SnTe with a step in the SnTe segment (Code 6). Both sets of data were compared to the Code 2 couples presented in Appendix C which employed cast SnTe, with a step, in the SnTe segment. The new data indicated higher power output for the couples using cold pressed and sintered SnTe (Table II-20). Average power output on Code 5 and Code 6 couples = 1.497 watts (E_{oc} corrected). The step in the SnTe showed no effect on the test results and the step has been eliminated.

Past experience with the TAGS-85 material indicated that visible cracks were present after the completion of the Seebeck voltage measurement. Heat treatment of the TAGS-85 elements prior to the Seebeck voltage was proposed as an approach which should eliminate the cracks. Element Lot No. 29-003 was heat treated to evaluate this proposal. After heat treatment, the TAGS-85 elements were subjected to Seebeck voltage measurement and subsequently visually examined for cracks. No visual evidence of cracks was observed. Three of the TAGS-85 elements which had been heat treated and subsequently subjected to Seebeck voltage measurement were

subjected to metallographic examination. Results of the metallographic examination confirmed the visual observation. Therefore, heat treatment of the TAGS-85 elements was incorporated into the fabrication process.

The next step in examining the effect of heat treating the TAGS-85 elements was to examine the resultant thermoelectric couple performance. Two groups of couples were fabricated consisting of a control group (Code 7) which contained TAGS-85 elements which were not heat treated and a second group (Code 8) which contained heat treated TAGS-85 elements. No significant results could be drawn from this metallographic comparison concerning the cracked elements because both sets of fabricated couples, which were two-hour power checked and then subjected to metallographic examination, showed cracks in the TAGS-85 elements. At this point in time, the cracks were attributed to the thermal cycling which is experienced during two-hour power checks because metallography of fabricated couples which had not been power checked showed no cracks. The power output from the couples employing the heat treated elements had improved (Code 8 versus Code 7). To determine the effect of the cracks in the TAGS-85 element on the power output of the couple, three of the Code 8 couples were subjected to a second two-hour power check. The resulting power was down only 4% as shown in Table II-20.

Another attempt was made to solve the cracked TAGS element problem. Code 9 represents couples which have been heat treated as a couple assembly after they were fabricated according to the Code 8 process. It was hoped this would eliminate the cracks in the TAGS material. Two couples (Code 9) were two-hour power checked and then sent to metallography. The results showed cracks in each of the TAGS elements. At present more couples are being fabricated under Code 9 for the SNAP 29 qualification run. Metallographic examination of 10 couples fabricated (but not power checked) during the couple qualification run indicated no cracks in the 2N elements or nine of the TAGS elements. However, a small crack was observed in one TAGS element. These data, compared to the two couples power checked, confirm the belief that the two-hour power check is causing the cracks in the TAGS-85 element. The average power on the 40 qualification couples in this group compares favorably to the average power from the other groups of couples in Table II-20.

Preparations are presently underway to perform power checks on couples at substantially reduced heat up and cooldown rates (comparable to those used on assembled modules) in order to determine whether the cracking of the P leg in couples is the result of the power check operation.

10. Qualification of TAGS Element and 2N-TAGS/SnTe Couple Fabrication Process

During this period, process qualification was achieved for the TAGS element fabrication. Qualification of the 2N-TAGS/SnTe process is nearing completion and will be accomplished during the next reporting period. Figure II-50 shows the basic couple assembly steps. Figure II-51 shows typical metallographic samples of four of the 10 couples examined in accordance with process qualification procedures. Upon final qualification of the couple fabrication process, 20 couples will be subjected to life testing and couple fabrication for the T/E modules will proceed.

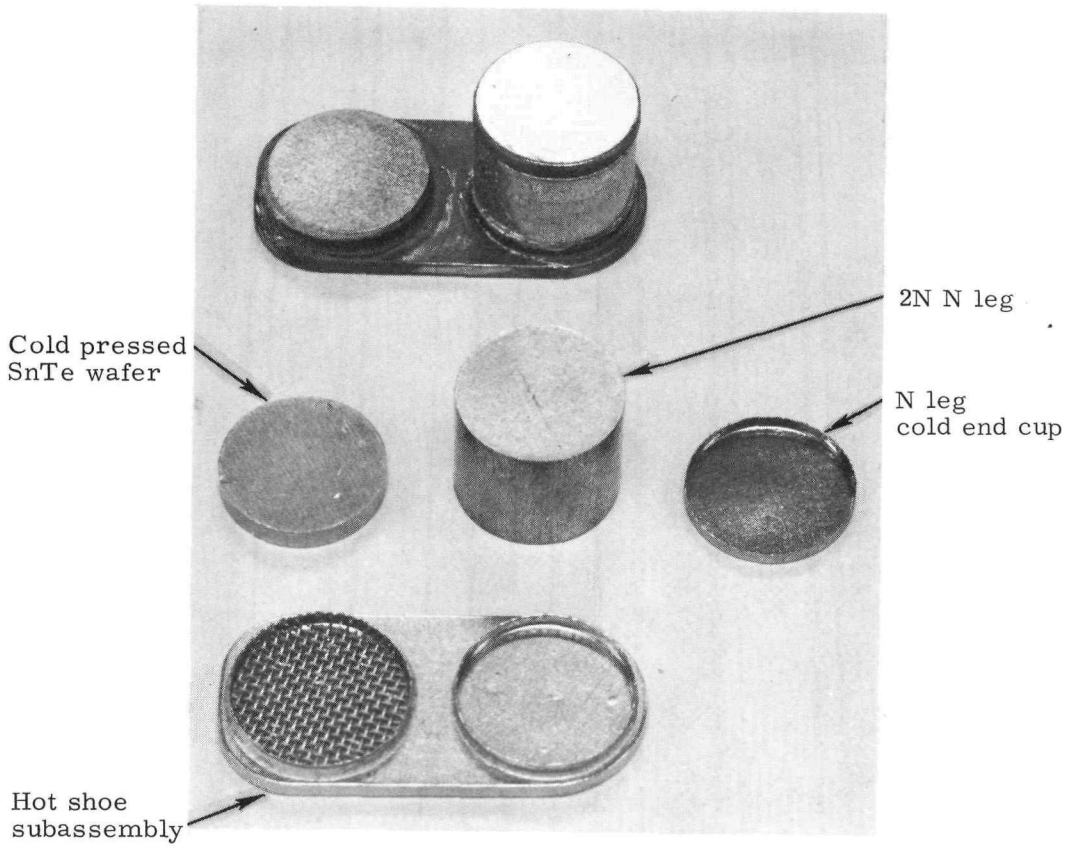

Step 1

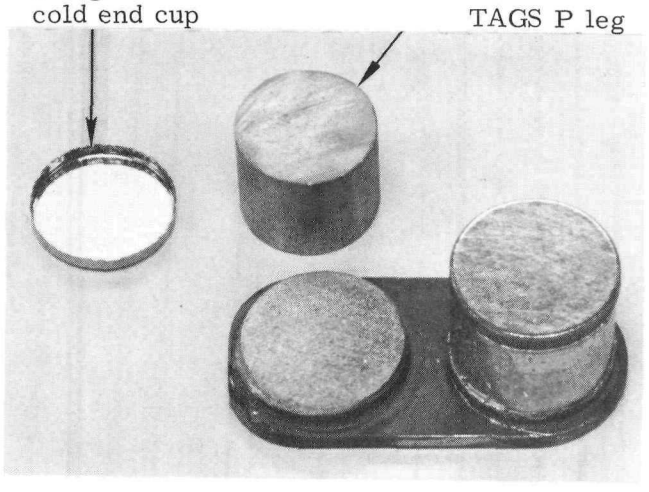

Step 2

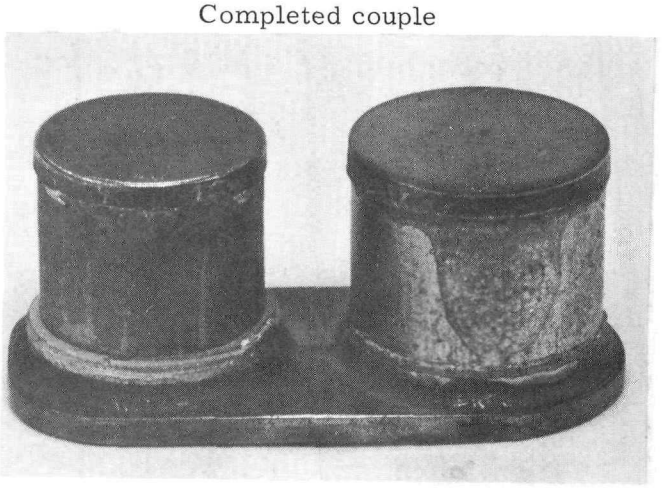

Step 3

FIG. II-50. BASIC 2N-TAGS/SnTe COUPLE ASSEMBLY STEPS

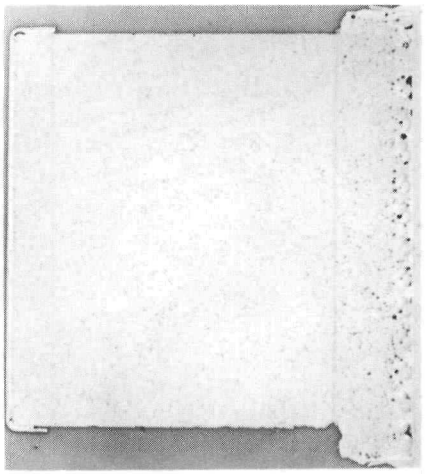

2N-TAGS S/N 08, P Element

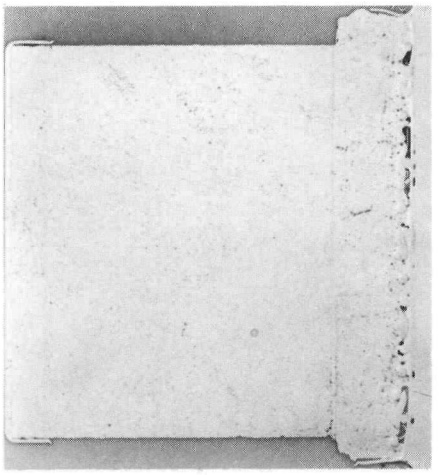

2N-TAGS S/N 29, P Element

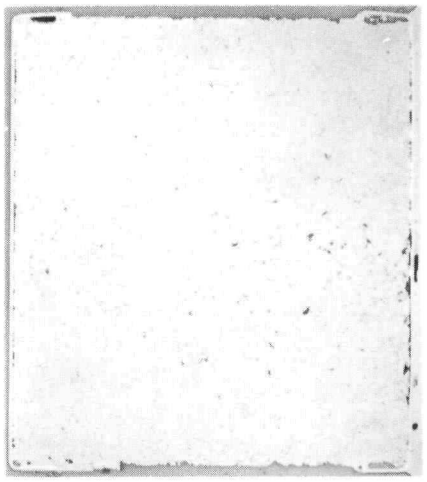

2N-TAGS S/N 29, N Element

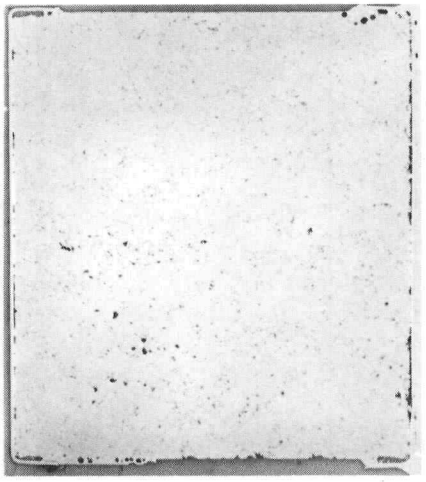

2N-TAGS S/N 20, N Element

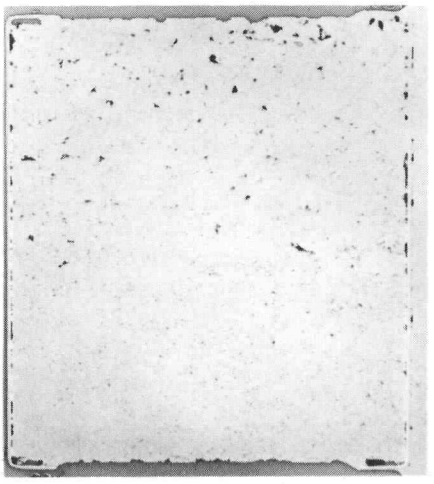

2N-TAGS S/N 08, N Element

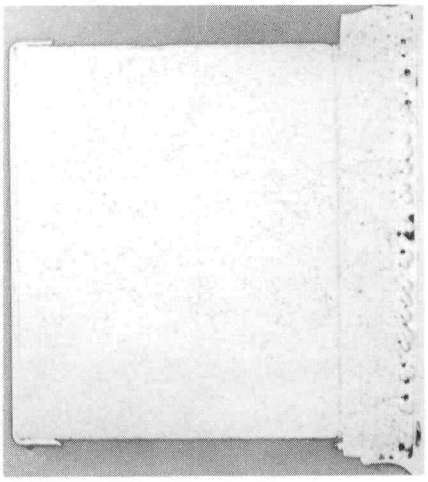

2N-TAGS S/N 12, P Element

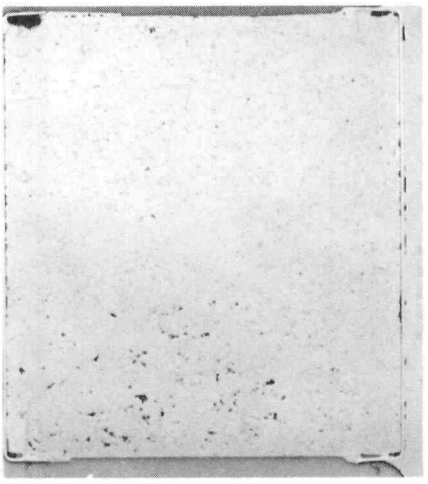

2N-TAGS S/N 12, N Element

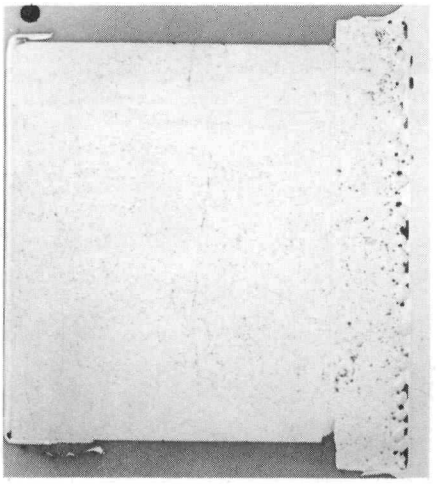

2N-TAGS S/N 20, P Element

FIG. II-51. METALLOGRAPHIC SAMPLES OF COUPLES FROM PROCESS QUALIFICATION RUN -LOT NO. 29-020

E. THERMAL CONTROL SUBSYSTEM--CONTROL POINT 1500

The objective of the effort within this control point is to develop a thermal control system which will maintain the thermoelectric module hot junction temperature within the prescribed limits during generator operation.

The thermal control system consists of a shutter assembly (six shutters); an actuator assembly (two sets, each consisting of an actuator, reservoirs, interconnecting tubing); and a linkage and bearing assembly which interconnects the actuators to the shutter. The system working fluid is the eutectic alloy of NaK.

Development of the complete system is achieved in the following sequence:

CP 1540--Thermal Control Subsystem, Component Development

CP 1530--Thermal Control Subsystem, Design Verification and Preprototype Units

WORK ACCOMPLISHED

A large portion of the engineering effort expended during this period was in Manufacturing liaison support, in which the following problem areas appeared:

(1) Brazed honeycomb shutter panels were completed during this period (Fig. II-52). Considerable difficulty existed in interpreting the ultrasonic traces. For future assemblies a control sample with known defects, will be included simultaneously with the shutter panels during ultrasonic inspection of the panels.

(2) A bowing condition occurred during brazing of all six shutter assemblies. The bowing was confined to the long sides of the frame assembly and was caused by insufficient support in the brazing fixture during brazing of the honeycomb panels. This problem was resolved by the addition of another bead on the side of the shutters which permits the accumulation of tolerances without causing an excessive clearance gap or without an interference which would prevent the shutters from closing. This is shown in Figs. II-53 and II-54. The addition of this bead will be considered for future shutter assemblies to permit larger manufacturing tolerances, thereby possibly reducing the costs. A final decision will be made after completion of the assembly and installation of all six shutters.

(3) An additional problem arose during final assembly of the shutters. After several shutters were assembled, they were placed together and it was found that the center to center distance of the shutter hinge points was being exceeded by approximately 1/16 inch per shutter, which would result in approximately 3/8 inch oversize for the whole assembly. An investigation disclosed that the condition is due to the Min-K which must be trimmed to contour prior to being encapsulated with the Haynes-25 foil. The design of the shutter support structure is such as to permit growth or shrinkage of individual shutters. Therefore, if the remaining shutters are made to the small side, a minimum amount of rework will be necessary to the completed shutters.

Additional work completed during this period consists of the revision to the titanium honeycomb brazing specification, 466A1533000. This includes the additional

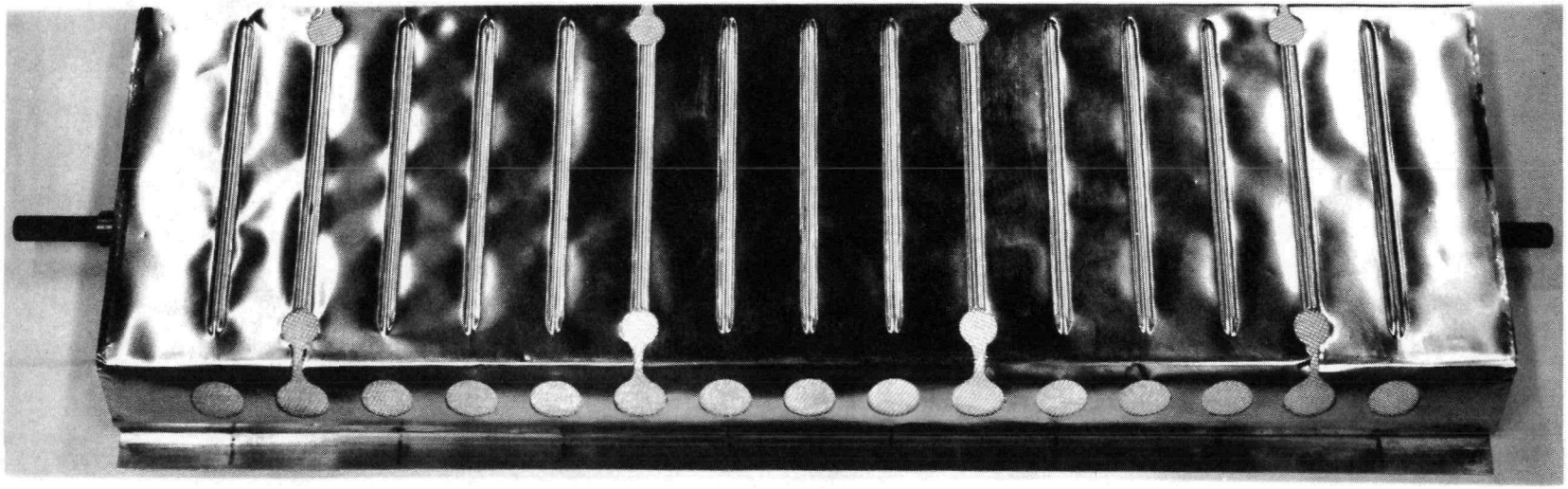

FIG. II-52. BRAZED HONEYCOMB SHUTTER ASSEMBLY

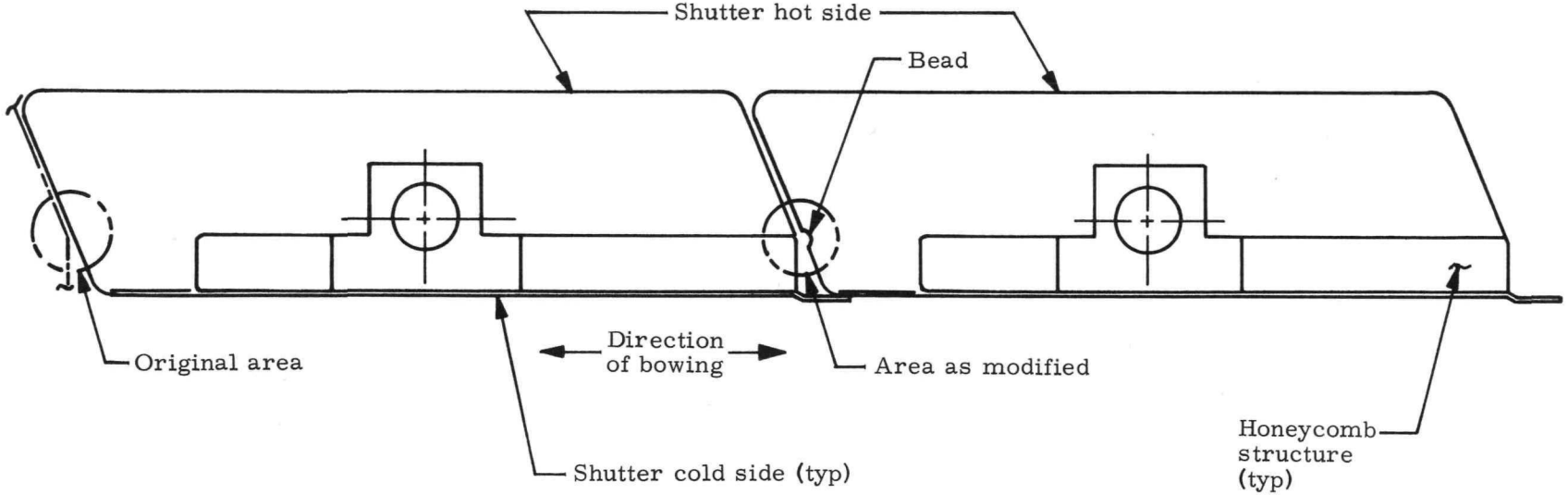

FIG. II-53. MODIFIED SHUTTER CONFIGURATION TO ELIMINATE TOLERANCE PROBLEM

CONFIDENTIAL

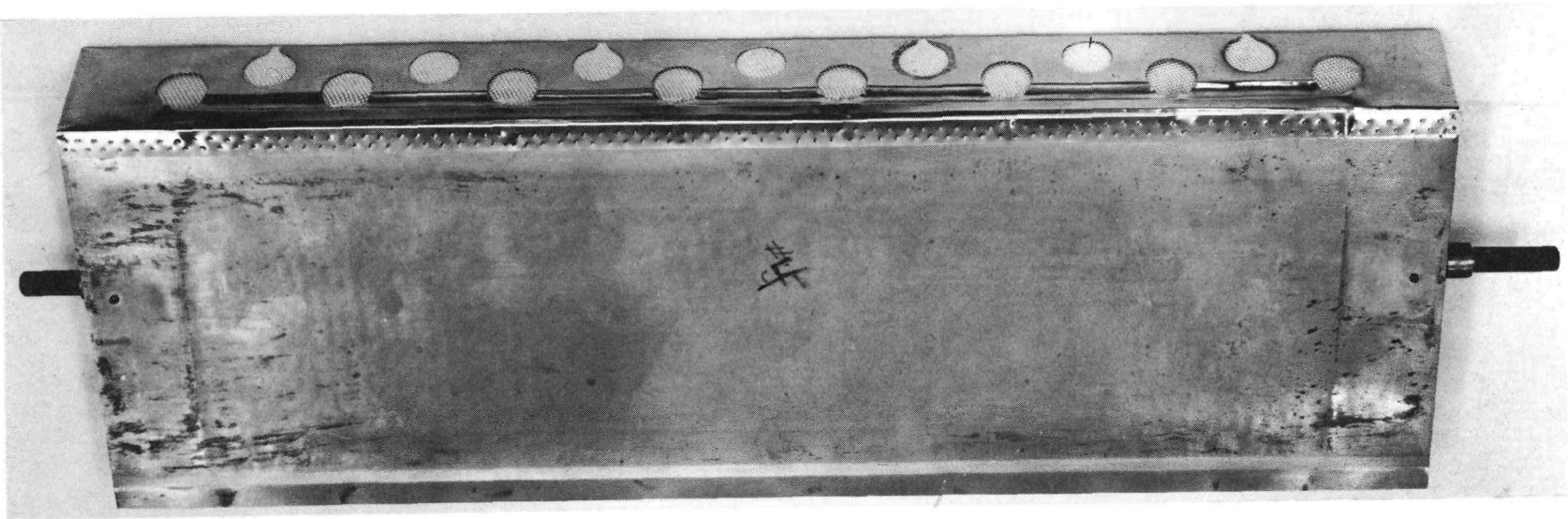

FIG. II-54. BEADED INSULATION COVER ON SHUTTER

CONFIDENTIAL

standard samples with known defects for ultrasonic inspection as described in Item (1). In addition, a series of honeycomb installation tolerances were added to the specification, based upon the results of the radiographic inspection of the existing shutters. This specification is currently in the release system and should be available early in the next reporting period.

1. Design Verification Test

The combined subsystems test (CP 1230, 1530, 1940) effort was delayed during this period as a result of the latest reprogramming effort. The proposed new approach would eliminate this test.

F. HEAT PIPE HEAT REJECTION SUBSYSTEM--CONTROL POINT 1800

The objective of this effort is to develop a static heat rejection subsystem capable of dissipating the waste heat from the thermoelectric module subsystem to a space environment over the life of the mission. Development has been divided into the following sequential efforts.

CP 1840--Heat Pipe Heat Rejection Subsystem, Component Development

CP 1830--Heat Pipe Heat Rejection Subsystem, Design Verification and Preprototype Models

WORK ACCOMPLISHED

Development testing on single, bent heat pipes was completed early this quarter. Extended life testing of selected heat pipes will continue. On the basis of these tests, previous development tests, and life tests still in progress, the corrugated condenser wick was selected together with the other features shown in Table II-21. All of the corrugated condenser wick designs meet the acceptance criteria set for the SNAP 29 heat pipes, i. e., 230 watts transport at transport temperatures from 300° to 370° F. In addition, life tests on the three corrugated, 15-foot, bent heat pipes have shown no apparent gas build-up problem to date (Table II-22). Each of these three pipes utilized distilled and outgassed water.

TABLE II-21

Features of Selected Heat Pipe Design

Tubing	15 feet 9 inches long 3/8 inch OD, 10-mil wall, Ni 200
Transport fluid	Water
Evaporator wick	3 layers, 30 mesh, Ni 200 screen
Condenser wick	1 layer, 200 mesh, Ni 200 screen Ten 35-mil corrugations
Evaporator bend	10- to 12-inch radius in transport section (in 3-30 portion)
Condenser bend	5-foot radius
Wick joint	Butt
Tube joint	Braze using sleeve coupling, Prema Braze 130
Cleaning method	Concentric nitric acid process
Oxidation method	775° F bake using flowthrough process

TABLE II-22

Status of Current Water Heat Pipe Life Tests
All Pipes Consist of Nickel Wicks and Tube

Configuration	No. of Days	Movement of Gas Interface from t = o (in.)	Comments
15 ft, 5-ft R, 3-30/corrugated HNO_3, 1000° F, weld	133	None	
HNO_3, 775° F, weld	80	None	
STD, 1000° F, weld	74	None	
8-ft St, 3-30 corrugated HNO_3, 775° F, braze	63	None	
HNO_3, 775° F, braze	57	None	
HNO_3, 775° F, braze	60	None	
15-ft St, 3-30 corrugated HNO_3, 775° F, weld Filled with boiling water	65	>4 in. <9 in.	Pipe previously run 118 days with outgassed water. During previous run built up gas also, oxidation probably not complete.
15-ft St, 3-30/annular HNO_3, tape baked, then 775° F FT baked	113	> 8 in. <12 in.	Pipe originally baked with electrical heating tapes built up gas; subsequent FT bake did not oxidize surfaces completely.

Because outgassing is time consuming, a 15-foot, straight heat pipe, which had been previously life tested for 118 days using outgassed water, was refilled with distilled and boiled water. This was placed on life test to compare boiled water with outgassed water. As noted in Table II-22, the gas build-up rate with boiled water is no greater than that in the same pipe using outgassed water. The composition of this gas will be determined to see if a portion of the small gas buildup could be accounted for as gas trapped initially in the nonoutgassed water.

The first six pipes listed in Table II-22 show no evidence of gas buildup. Since these were oxidized most recently, it appears that the process is under good control. Note that the difference between the weld joint and the braze joint appears to be nil as far as gas generation is concerned. Thermal analysis of the effects of up to six inches of gas buildup in each pipe has had very little effect on the overall heat rejection capability of the radiator. Documentation of this analysis is forthcoming in a report to be issued soon.

During this period a report was issued documenting the data upon which the heat pipe design configuration was based. This report is included as Appendix E.

2. Radiator Panel Development

A major portion of the quarter was devoted to checkout of the vacuum bonding retort tool which is being used to diffusion bond the 10 heat pipe condenser sections to the machined aluminum armor-fin radiator panel. Initially, a temperature survey of the bonding tool was conducted to assure adequate placement of the control thermocouples and to determine the power required for achieving bonding conditions. In conjunction with this effort, a transient thermal analysis of the bonding fixture was conducted.

The initial run in the bonding furnace was made without any heat pipes or armor in place in the die. Several problems were brought to light. On one run the bonding fixture had achieved a temperature of about 500° F with 180 volts ac across the heaters when the 50-ampere fuses blew out. Since the heater circuit to ground showed a very low resistance, the entire system was shut down. When the vacuum chamber was opened the cause of the trouble was obvious--the short circuit had been caused by plating out of some cadmium-plated washers used on the bonding fixture. These washers had originally been purchased as unplated and were subsequently replaced.

The temperature of the chamber shell had also been noted to be excessive and an aluminum liner was placed inside the carbon steel shell to decrease the heat loss. At the same time the thermocouple locations on the bonding fixture were changed to place the thermocouple within 1/2 inch of the armor/tube assembly for more accurate readout.

On the second run the bonding fixture was loaded with an aluminum panel and one nickel tube. The tube was pressurized to 4000 psig while cold and this pressure maintained until the temperature reached approximately 1000° F (about 10 hours after start). The temperature was held for 20 to 30 minutes when the pressure in the tube suddenly dropped. At the same time the chamber vacuum (5.6×10^{-4} mm Hg) began to deteriorate. Shortly thereafter the system short circuited due to the excessive helium in the chamber and blew out the fuses. Subsequent investigation of this problem revealed a crack in the weld bead around the tube end cap. The nickel tube was observed to be well bonded to the aluminum panel (Figs. II-55 and II-56). Due to an apparently inadequate quantity of Stop-Off some bonding occurred between the tool die bar and the aluminum panel.

On the third furnace run the decision was made to decrease the internal tube pressure but maintain the same temperature level and time span. This was done in an attempt to circumvent the weld bead failure problem while it was being investigated and prevent bonding between the aluminum and the tube die bars that had occurred during the previous run. It is also felt as a consequence that an adequate diffusion bond can be obtained at this pressure. The third run was made under 1500 psig internal tube pressure but using the same welded end caps. A fixture temperature of 780° F was attained on this run when the pressure was lost in the tube. Investigation revealed a fine crack in the weld bead. As a result of the weld bead cracking at high temperatures, it was decided to use a brazed plug for the bonding operation. This has been done and four nickel tubes will be bonded to an aluminum panel with this plug replacing the welded end cap.

The problem with the welded cap appears to be excess stresses in the weld due to tension forces developing in the bead (Fig. II-57). This could be due to an undersize cap or an oversize die bar which does not give the weld enough support at temperature. Closer tolerance parts are being prepared and tighter weld quality control will be imposed. Figure II-57 also shows a small pin hole in the weld bead which was thought to be the cause of the leak but metallurgical examination uncovered

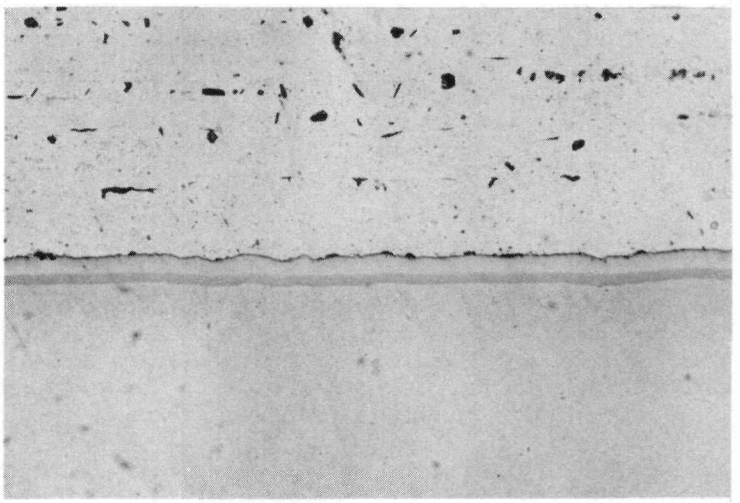

FIG. II-55. NICKEL-TO-ALUMINUM HEAT PIPE BOND

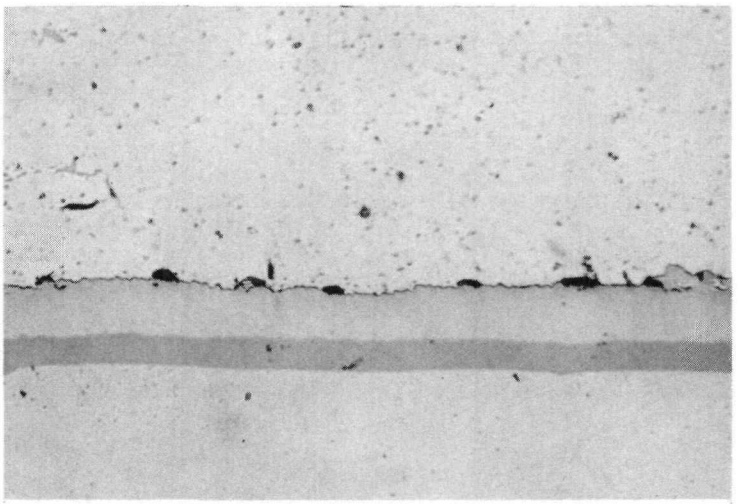

FIG. II-56. NICKEL-TO-ALUMINUM HEAT PIPE BOND

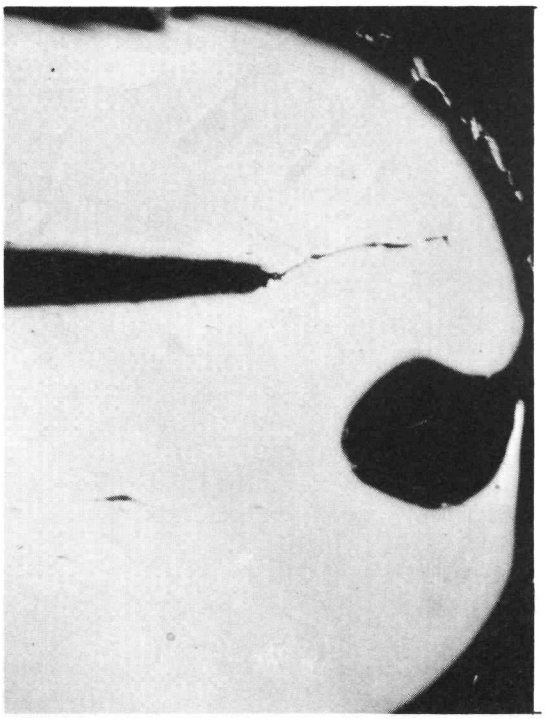

FIG. II-57. HEAT PIPE END CAP WELD DEFECT

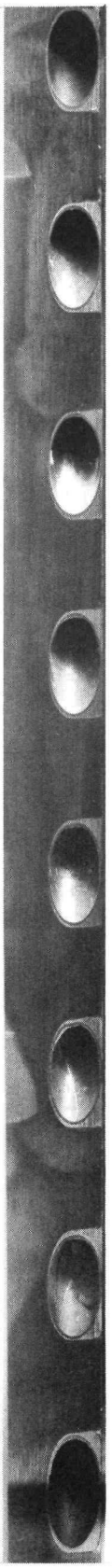

FIG. II-58. TYPICAL SOLDERED HEAT PIPE/HEAT SINK JOINT

the break as shown. This crack extended completely through the weld bead. The pin holes have been caused by surface contamination when welding. This problem is being corrected by changes in the welding fixture and method of coverage with the inert gas. During the next reporting period, heat pipe/radiator panel bonding processes will be modified as required in order to scale up the bonding process to the full-scale fixture and hardware requirements. Included in this area will be a review of cleaning processes, temperatures, pressures, exposure times, atmospheric controls and other process related parameters.

3. Manufacturing Checkout Test

Once an acceptable bonded panel is obtained, the next development step will be the Manufacturing checkout test series. For these tests the bonded radiator panel will be joined to the beryllium heat sink/heat pipe evaporator section subassembly. Currently, it is planned that the 10 evaporator sections are to be soldered into the beryllium heat sink using 40% Pb-60% Sn solder rather than using the high temperature brazing process originally planned.

Development effort has been performed to develop a practical soldering technique and consists of copper plating the grooves in the beryllium heat sink plate and pretinning both the copper clad beryllium and the nickel heat pipe evaporator section. The heat pipes will then be joined to the fully assembled module by preheating the module cold end to the solder melt temperature and filling each heat pipe hole in the heat sink with a predetermined quantity of solder. The 10 evaporator sections of the fully assembled heat pipe/radiator panel unit are then inserted into the heat sink, displacing the molten solder to fill the voids between the heat pipe and heat sink. Figure II-58 shows a section cut diagonally through a heat sink plate with soldered heat pipes. Photomicrographs of sections from the same development sample are presented in Fig. II-59. Results of development work to date indicate the method to be feasible and capable of producing a sound thermostructural joint. Farther refinements are under study to eliminate minor problems and assure a controllable process.

The tests planned for the radiator panel-Be heat sink assembly include thermal vacuum tests in the vacuum bonding chamber using a straight panel, and air performance tests with the straight panel and after bending the panel to a five-foot radius. Thermal analyses of the planned performance tests were conducted and the report documenting these results is included as Appendix F.

4. Zinc Oxide/Potassium Silicate Emissivity Coating for Low Temperature Space Radiators

The basic requirements of a surface coating designed for controlling the equilibrium temperature of RTG space radiators are low initial solar absorptivity (α_s), high emissivity (ϵ), thermal stability during ascent and photochemical stability to the environmental conditions in the upper atmosphere. The equilibrium temperature of an object in outer space is governed by the ratio α_s/ϵ. The lower the ratio, the more effective the coating.

Zinc oxide/potassium silicate coating (IITRI No. Z-93) was originally selected for the SNAP 29 program to obtain maximum heat rejection efficiency for the low temperature (150° to 350° F) RTG 6061 aluminum alloy radiator based on data available in the literature prior to 1967 (Refs. II-1 through II-5). The data for coating materials reported at that time resulted from studies, which for the most part, had been conducted at room temperature, with fewer studies at elevated and cryogenic temperatures. It had been a general observation that exposure to ultraviolet radiation degrades the properties of low α_s/ϵ surface materials by causing an increase in solar absorptance,

CONFIDENTIAL

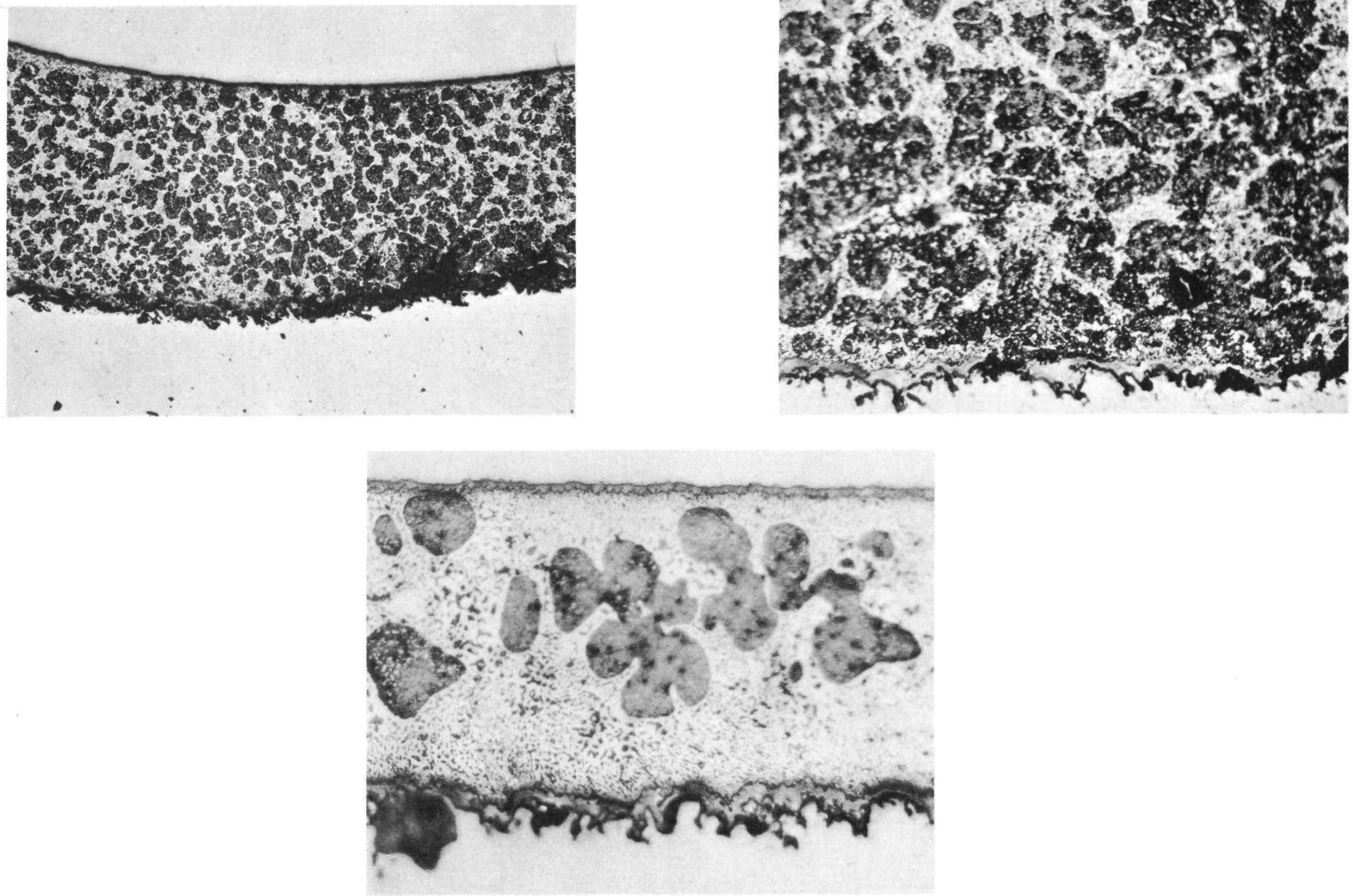

FIG. II-59. PHOTOMICROGRAPHS OF SOLDERED HEAT PIPE/HEAT SINK INTERFACE

CONFIDENTIAL

either by shifting the absorption band edge or by increasing the total absorption of the material in the solar wavelength region. The total hemispherical emittance of the more promising materials is not affected by this environment.

The criteria for selection of the IITRI Z-93 coating for the SNAP 29 program requirement were: initial solar absorptance = ≤ 0.20 and total hemispherical emittance = ≥ 0.80; long-term stability of optical properties, solar absorptance and total hemispherical emittance; and adhesion and compatibility with the substrate material, 6061 aluminum. In addition, studies had indicated that the thermal control coating (IITRI Z-93) would be optically and physically stable at temperatures up to 450° K (350° F) for extended periods of time in the space environment.

The major emphasis in the studies carried out during the latter quarter of 1968 by the SNAP 29 Materials Group was the conducting of a survey of the most recent literature to provide confirmation of the data used in the selection of the candidate coating. Also, formulation, application and Gier Dunkel tests of the candidate coating were performed to evaluate and compare findings from this program with those of other investigators.

The results of the literature and technology survey concluded that zinc oxide/potassium silicate coating (IITRI Z-93) offered the best choice at this time for a paint-type coating material to be used for a moderate temperature RTG radiator surface. Total hemispherical emittance is as high as any of the coatings tested (0.14), based upon absolute spectral reflectance measurements (Table II-23). For applications to 422° K (300° F), the solar absorptance after prolonged exposure is 0.20. For higher temperatures 450° K (350° F) and 534° K (500° F), the solar absorptances after prolonged exposure are 0.25 and 0.26, respectively (Ref. II-6). Comparison of radiative properties data for the materials tested is presented in Table II-24.

In situ absorptance data for zinc oxide/potassium silicate (Z-93) coating at 300°, 350° and 500° F in a vacuum at $< 1 \times 10^{-7}$ torr for the indicated exposure times are presented in Fig. II-60.

The spectral absorptance curves for the Z-93 coating as presented show an increase in the solar absorptance upon exposure in vacuum to ultraviolet radiation with increasing temperature. It has been postulated that during irradiation there is a liberation of oxygen from the zinc oxide pigment which, at elevated temperatures in vacuum, may then be physically desorbed from the surface. If the zinc oxide becomes substoichiometric (SnO_{2-x}), the presence of excess zinc will result in increased absorption and the observed degradation of solar absorptance (Ref. II-6). Under a NASA Marshall Space Flight Center contract (Ref. II-7), LMSC has investigated solar radiation-induced damage to the optical properties of zinc oxide. That program succeeded in demonstrating that the damage mechanism for zinc oxide pigments was based on a photochemical evolution of oxygen. Furthermore, on the basis of in situ measurements of ultraviolet radiation damage in vacuum, it was conclusively demonstrated that ultraviolet-degraded zinc oxide rapidly recovered its initial optical properties upon re-exposure to air. This recovery phenomena has made much of the earlier exposure data suspect as degradation was evaluated on the basis of post-test reflectance measurements in air.

The search for and investigation of the effects of variables such as pigment formulation and application techniques necessitated changes to the specifications for IITR thermal control coating Z-93 (Ref. II-1). Per a telecom between Isotopes

TABLE II-23

Initial Room Temperature Optical Properties

Sample	Source	Coating	Solar Absorptance		Emittance (Optical Surface Comparator)
			Cary	Gier-Dunkle	
1	LMSC	Titanium dioxide/	0.15 ± 0.02	0.17 ± 0.01	0.88 ± 0.03
2		methyl silicone	0.15 ± 0.02	0.16 ± 0.01	0.82 ± 0.03
3		(LMSC Thermatrol	0.15 ± 0.02		0.91 ± 0.03
4		2A-100)	0.18 ± 0.02*	0.19 ± 0.01	0.85 ± 0.03
5			0.15 ± 0.02		0.85 ± 0.03
6			0.15 ± 0.02		0.85 ± 0.03
7			0.15 ± 0.02		0.87 ± 0.03
8			0.15 ± 0.02		0.86 ± 0.03
9	LMSC	Zirconium silicate/	0.11 ± 0.02	0.11 ± 0.01	0.91 ± 0.03
10		potassium silicate	0.11 ± 0.02		0.87 ± 0.03
11		(LMSC)	0.14 ± 0.02	0.15 ± 0.01	0.90 ± 0.03
12			0.11 ± 0.02		0.90 ± 0.03
13			0.13 ± 0.02		0.91 ± 0.03
14			0.11 ± 0.02	0.11 ± 0.01	0.90 ± 0.03
15			0.14 ± 0.02		0.90 ± 0.03
16			0.10 ± 0.02		0.90 ± 0.03
19	Hughes	Aluminum silicate/	0.14 ± 0.02	0.14 ± 0.01	0.90 ± 0.03
20		potassium silicate	0.14 ± 0.02	0.14 ± 0.01	0.88 ± 0.03
21		(Hughes)	0.14 ± 0.02		0.90 ± 0.03
22			0.14 ± 0.02		0.90 ± 0.03
23			0.14 ± 0.02		0.89 ± 0.03
24			0.14 ± 0.02		0.88 ± 0.03
25			0.14 ± 0.02		0.90 ± 0.03
26			0.13 ± 0.02		0.90 ± 0.03
27	IITRI	Zinc oxide/	0.19 ± 0.02	0.20 ± 0.01	0.79 ± 0.03
28		Methyl silicone	0.19 ± 0.02	0.20 ± 0.01	0.79 ± 0.03
29		(S-13, IITRI)	0.19 ± 0.02		0.81 ± 0.03
30			0.19 ± 0.02		0.80 ± 0.03
31			0.19 ± 0.02		0.81 ± 0.03
32			0.19 ± 0.02		0.87 ± 0.03
33			0.18 ± 0.02		0.85 ± 0.03
34			0.19 ± 0.02		0.80 ± 0.03
35	IITRI	Zinc oxide/	0.14 ± 0.02	0.15 ± 0.01	0.92 ± 0.03
36		potassium silicate	0.14 ± 0.02	0.14 ± 0.01	0.96 ± 0.03
37		(Z-93, IITRI)	0.14 ± 0.02		0.96 ± 0.03
38			0.14 ± 0.02		0.91 ± 0.03
39			0.14 ± 0.02		0.96 ± 0.03
40			0.14 ± 0.02		0.96 ± 0.03
41			0.14 ± 0.02		0.97 ± 0.03
42			0.14 ± 0.02		0.95 ± 0.03
43	IITRI	Zinc oxide/	0.19 ± 0.02	0.20 ± 0.01	0.85 ± 0.03
44		methyl silicone	0.20 ± 0.02	0.20 ± 0.01	0.85 ± 0.03
45		(S-13G, IITRI)	0.20 ± 0.02	0.20 ± 0.01	0.85 ± 0.03
46			0.20 ± 0.02	--	0.85 ± 0.03
47			0.19 ± 0.02	--	0.85 ± 0.03
48			0.16 ± 0.02	--	0.86 ± 0.03
49			0.20 ± 0.02	--	0.84 ± 0.03
50			0.19 ± 0.02	--	0.86 ± 0.03

*Coating not of proper thickness (5 mil).

Based on Ref. II-6

TABLE II-24

Comparison of Radiative Properties Data

Coating	Spec No.	Time (hr)	Temperature (° K) (° F)	ϵ_{TH} i	ϵ_{TH} f	α_s Initial Cary	α_s Initial Cal	α_s Final Cary	α_s Final Cal	$\Delta\alpha_s$ Cary	$\Delta\alpha_s$ Cal
Titanium dioxide/ methyl silicone (Thermatrol 2A-100)	1	550	395/250	0.87	0.85	0.15	0.18	0.26	0.32	0.11	0.14
Zinc oxide/methyl silicone (S-13)	27	500	395/250	0.86	0.86	0.18	0.21	0.28	0.28	0.10	0.07
	28	636 (1)	395/250	0.85	0.87	0.19	0.20	0.31	0.30	0.12	0.10
Zinc oxide/methyl silicone (S-13G)	43	500	395/250	0.90	0.91	0.19	0.20	0.31	0.28	0.12	0.08
	44	520	395/250	0.91	0.91	0.20	0.19	0.27	0.25	0.07	0.06
Zirconium-silicate/ potassium silicate	9	100	534/500	0.80	0.71	0.12	0.13	0.36	0.36	0.24	0.23
	14	500	534/500	0.71	0.71	0.12	0.12	0.51	0.42	0.39	0.30
Aluminum silicate/ potassium silicate	19	122	534/500	0.72	0.72	0.14	0.20	0.41	0.46	0.27	0.26
	21	530	534/500	0.82	0.81	0.14	0.16	0.45	0.50	0.29	0.34
Zinc oxide/ potassium silicate	35	502	534/500	0.81	0.81	0.14	0.12	0.26	0.25	0.12	0.13
	36	331 (1)	534/500	0.81	0.81	0.14	0.11	0.42 (1)	0.30	(2)	0.19 (1)
	40	1004	450/350	0.87	0.87	0.14	0.12	0.23	0.26	0.12	0.14
	38	500	422/300	0.88	0.88	0.14	0.14	0.20	0.19	0.06	0.05
	39	4574 (1)	422/300	0.91	0.88	0.14	0.11	0.34 (1)	0.16	(2)	0.05 (1)
	59	6001	422/300	0.88	(3)	0.15	0.14	(3)	(3)	(3)	(3)
	56	2024	366/200	0.89	0.89	0.15	0.14	0.21	0.20	0.06	0.06
	42	2001	300/80	0.90	0.88	0.14	0.14	0.17	0.18	0.03	0.04
OSR	60	1032	339/150	0.80	(3)	0.06	0.06	(3)	(3)	(3)	(3)

(1) Vacuum system or instrumentation failure during test.

(2) Post-test Cary taken after vacuum failure; substantial change in absorptance observed due to test failure.

(3) Test in progress.

Based in Ref. II-6

CONFIDENTIAL

CONFIDENTIAL

CONFIDENTIAL

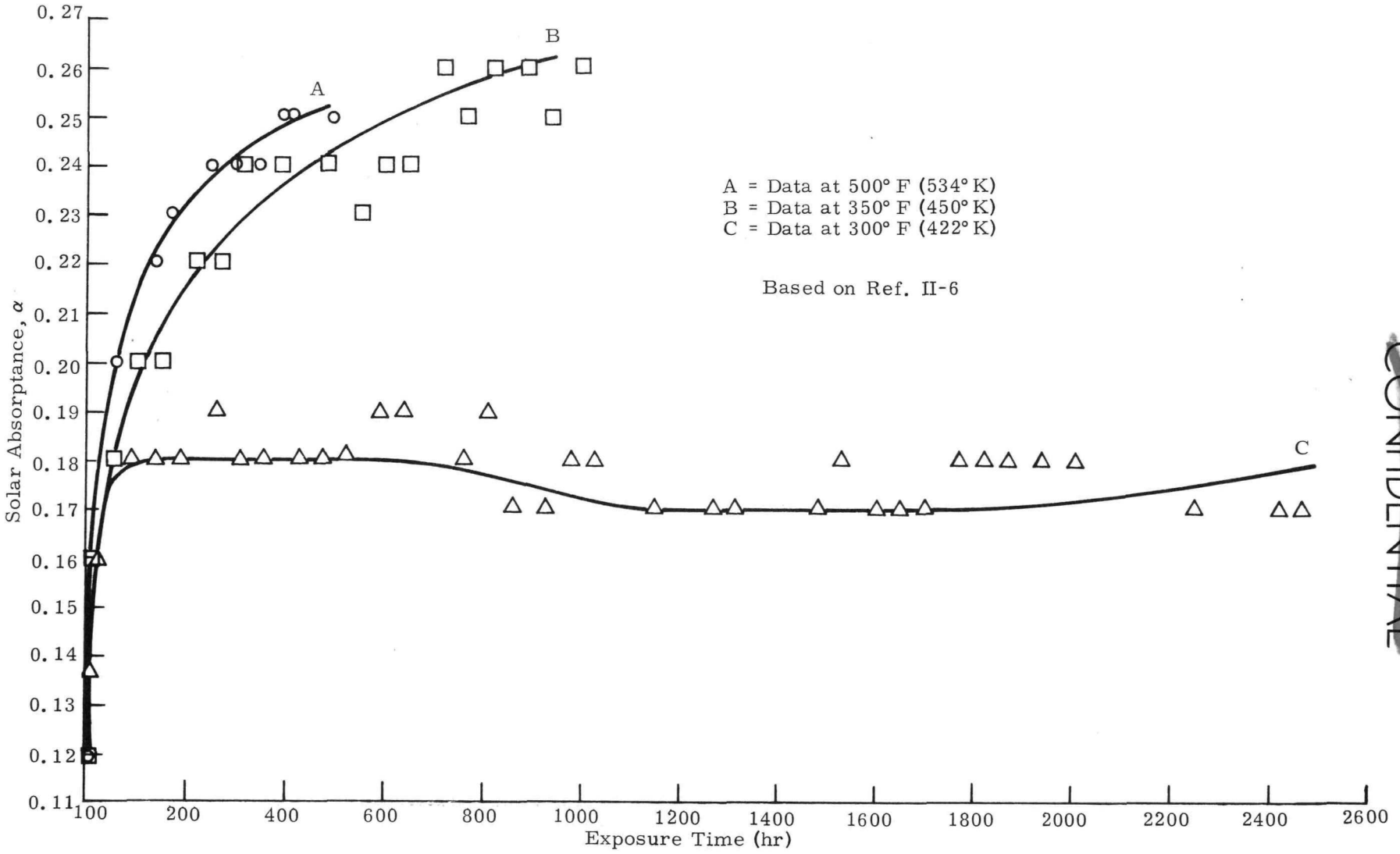

FIG. II-60. IN SITU ABSORPTANCE DATA FOR ZINC OXIDE/POTASSIUM SILICATE (Z-93) COATING AT 300°, 350° AND 500° F

CONFIDENTIAL

and IIT Research Institute personnel (Ref. II-8), recent available data indicated that calcination temperatures over 600° C or any degree of attritioning after calcination caused an increase in the initial solar absorptance. In addition, greater emphasis must be placed on cleanliness and the necessity to keep raw materials and the coated system free from contamination of degradable substances, such as, organics (especially acetone) and inorganics (especially sulfates). With regard to the Z-93 material preparation specification, a tentative specification has been written by the SNAP 29 Materials Engineering Group which will permit guidelines for trial coating applications. Sampling and testing procedures were written into the specification to permit one to ascertain optical property changes for the material during its preparation and after application.

Trial coating preparations and applications were conducted by the SNAP 29 Manufacturing Group for SP-500 zinc oxide material calcined at 650° C by the vendor (established manufacturing calcining temperature) and for material of the same lot which was calcined by the Isotopes Manufacturing Group at 600° C in accord with the tentative specification. Since initial preparation of the zinc oxide material by the vendor induces stresses into the crystal structure by attritioning, calcination is required to relieve those stresses so as to decrease the initial solar absorptance.

As of this date, the material calcined by the vendor (650° C) has been successfully applied to two test panels (1 x 2 ft) and two one-inch diameter discs required for Gier Dunkel testing. Test data at this time are not available. With regard to the material calcined at Isotopes (600° C), preliminary preparation trials have resulted in a nonapplicable spray mixture due to improper calcination techniques and/or requirements set forth in the tentative specification. First, the two hours at a calcining temperature of 600° C (recently suggested by IITRI per telecom, 10/68) appears to be insufficient for complete calcination of the material. Future preparation of this material will require that calcination be performed for 16 hours as initially reported (Ref. II-1) and at a temperature of 600° C. Second, the recommended containment configuration for the zinc oxide material prevented sufficient air exposure during calcination. To resolve this condition, agitation by stirring of the zinc oxide to effectively increase the surface area exposure during the heat treatment and/or substituting a flat open boat for the present cylindrical shaped container has been recommended. It is important to note that a sufficient oxidizing atmosphere is required during calcination to prevent the formation of substoichiometric zinc oxide (ZnO_{2-x}). Implementation of the aforementioned recommendations has been initiated and results of these most recent changes will be reported after evaluation and testing.

G. RTG HOUSING STRUCTURAL SUBSYSTEM--CONTROL POINT 1900

The objective of the effort within this control point is to develop a minimum weight housing structure which maintains the parasitic heat losses within acceptable limits, supports the various subsystems in their proper orientation, provides for remote loading of the fuel block, provides for ejection of the fuel block and provides a means of attaching the RTG to the vehicle supports.

Development of the complete structure is achieved in the following sequence:

CP 1940--RTG Housing Structural Subsystem, Component Development

CP 1930--RTG Housing Structural Subsystem, Design Verification

WORK ACCOMPLISHED

1. Dynamic Test Fixture

The dynamic test fixture for the subsystem interface test consists of a 10-foot diameter circular shell to be used as a support for the heat pipes and the RTG housing. This, in turn, is attached to an adapter providing interface to the shaker. The maximum shaker output of 28,000 force pounds was a limiting factor in the design of the fixture. To meet a random vibration level of 15 g rms, a maximum load of 28,000/15 = 1866 pounds is the limiting moving mass. Because of this weight restriction, a separate adapter for each of the three test axes are necessary and have been designed.

In axial or boost direction; four 3/4-inch thick bungee cables of less than 3 cps will suspend the fixture. The new fixture weight is provided per Table II-25.

TABLE II-25

Weights and Loads (lb)

	Boost Direction	Y-axis	Y-axis
Test specimen	420	420	420
C-210 armature	350	350	350
Stand and truss support	320	320	320
Drag of four team tables	--	300	300
Adapter	567	372	431
Totals	1657	1762	1821

For the lateral direction normal to the fuel block (y axis), four hydrostatic beams support the test fixture adapter. This removes all overturning moments from the shaker head and stabilizes the system during vibration testing.

In the lateral direction parallel to the fuel block (x-axis), the four beams or team tables, will be utilized to eliminate eccentric loadings.

The test stand for the RTG and heat pipe panel support was designed for a natural frequency of less than 20 cps whereas all components have natural frequencies equal to or in excess of 360 cps. The truss support for the RTG housing was designed such that the stiffness corresponds to a natural frequency of 500 cps.

The guide lines for the design of the three adapters were:

(1) Provide the shaker input loading area for a limit load of 1866 pounds.

(2) Natural frequency of all components equal or greater than 300 cps.

2. Cracked W Frame Weldments

At the end of the last quarter, several cracks were discovered in the ends of the fuel block support beam assembly (466A1941006). This is a welded assembly of René 41 nickel base superalloy. An investigation was conducted to determine the cause of these cracks, which included a literature survey, an investigation of the material history and the fabrication and evaluation of two test specimens. The results of this investigation are included as Appendix G of this report and will also be released as an informal topical report. The principal cause of the cracks was apparently the combination of an improper heat treatment (for welded René 41) and a constrained weld joint.

3. Fabrication Status of RTG Structure

During this quarter, RTG structure components were fabricated for RTG S/N 1. Photographs of completed parts are shown in Figs. II-61 through II-64. Figures II-65 through II-67 show views of assembled structural components.

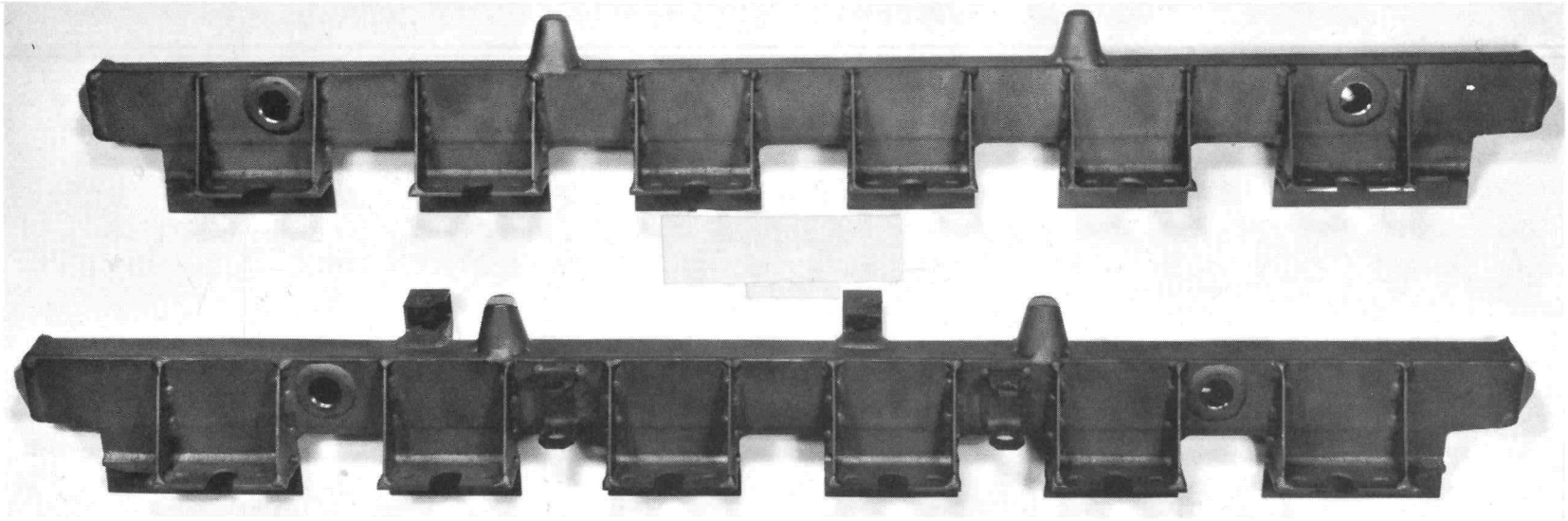

FIG. II-61. SHUTTER SUPPORT BEAMS

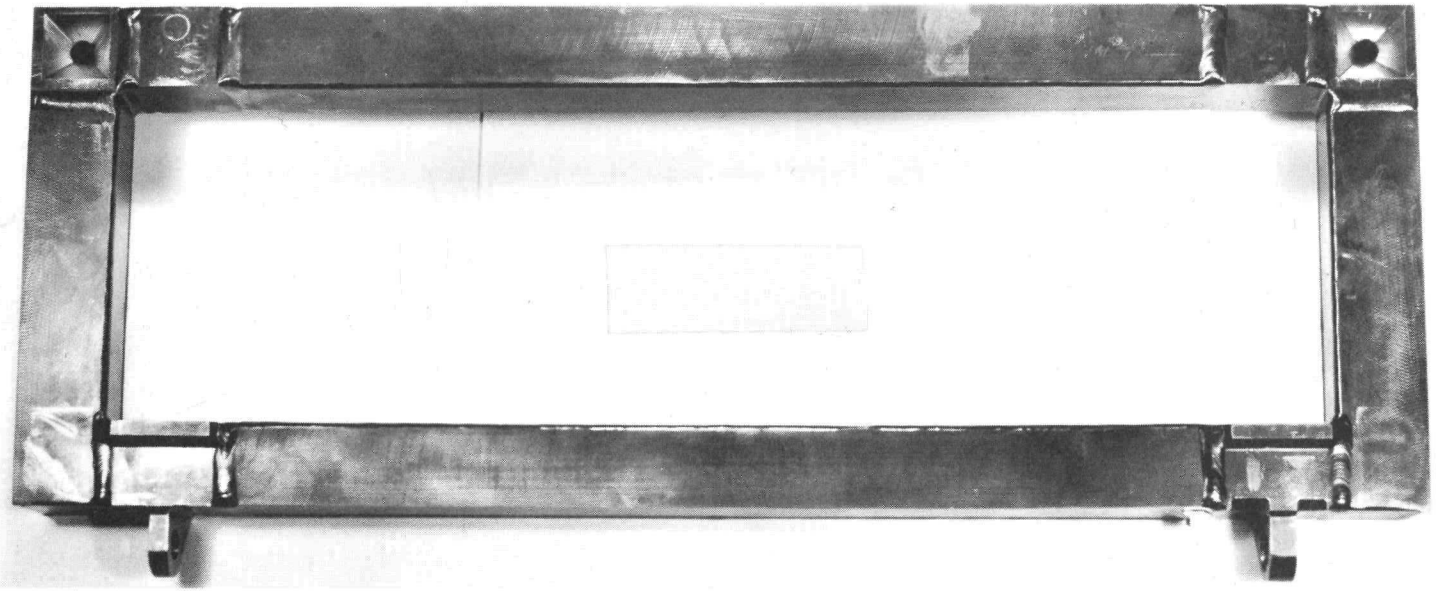

FIG. II-62. SIDE FRAME ASSEMBLY

CONFIDENTIAL

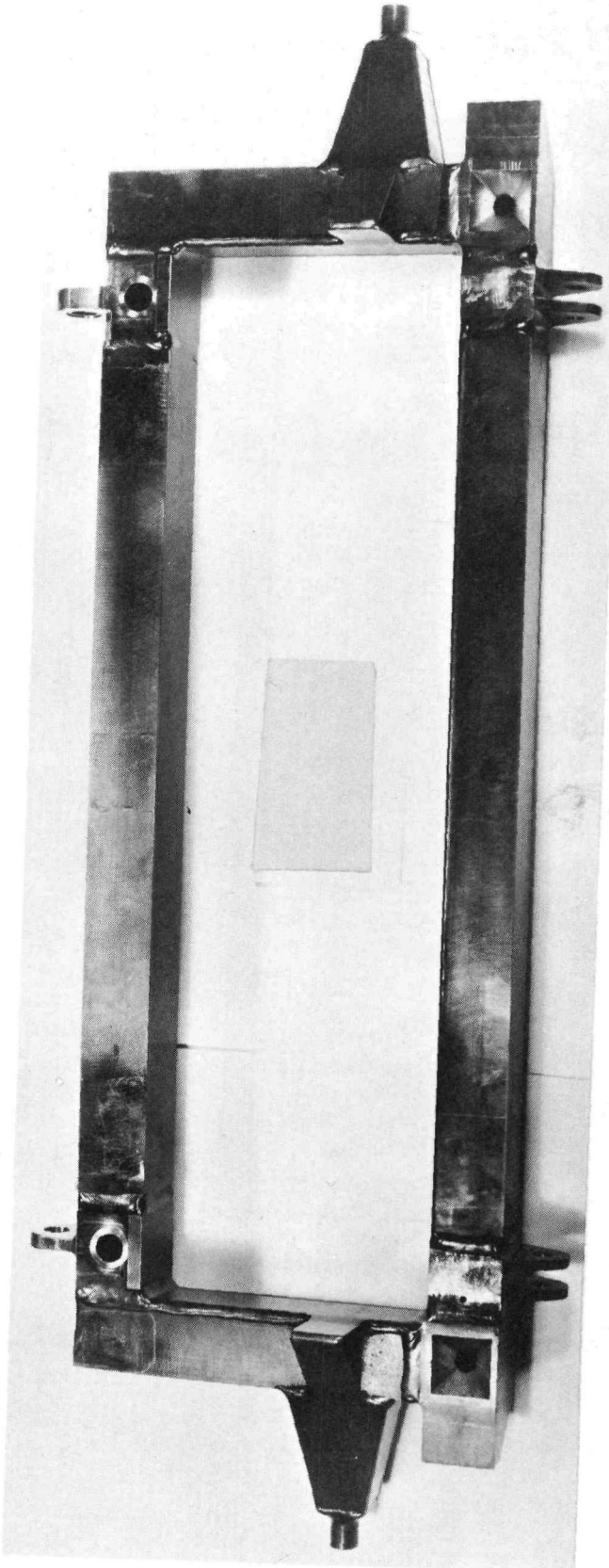

FIG. II-63. SIDE FRAME ASSEMBLY SHOWING HEAT SOURCE LOADING SIDE

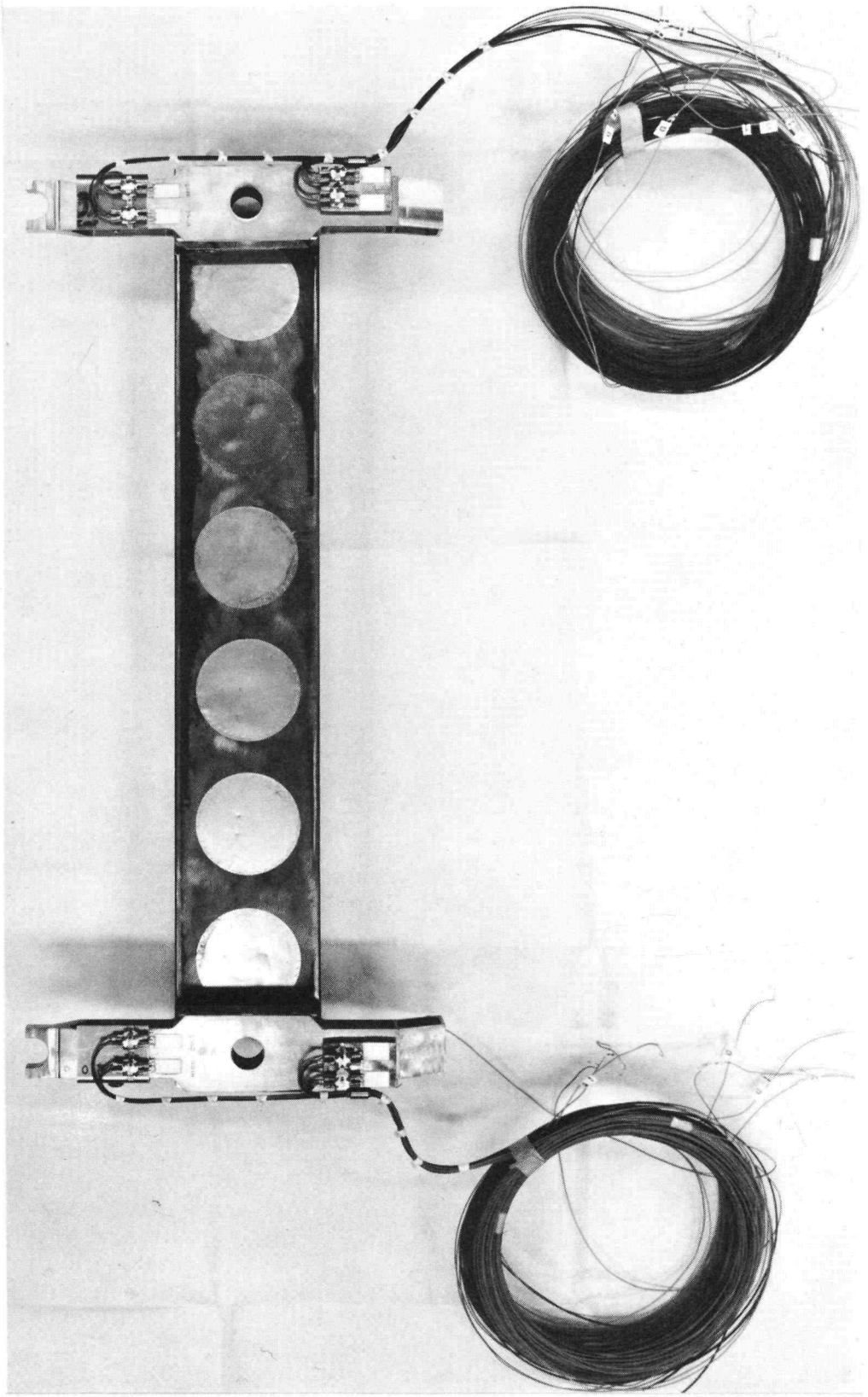

FIG. II-64. W FRAME AND HINGE ON HEAT SOURCE LOADING SIDE

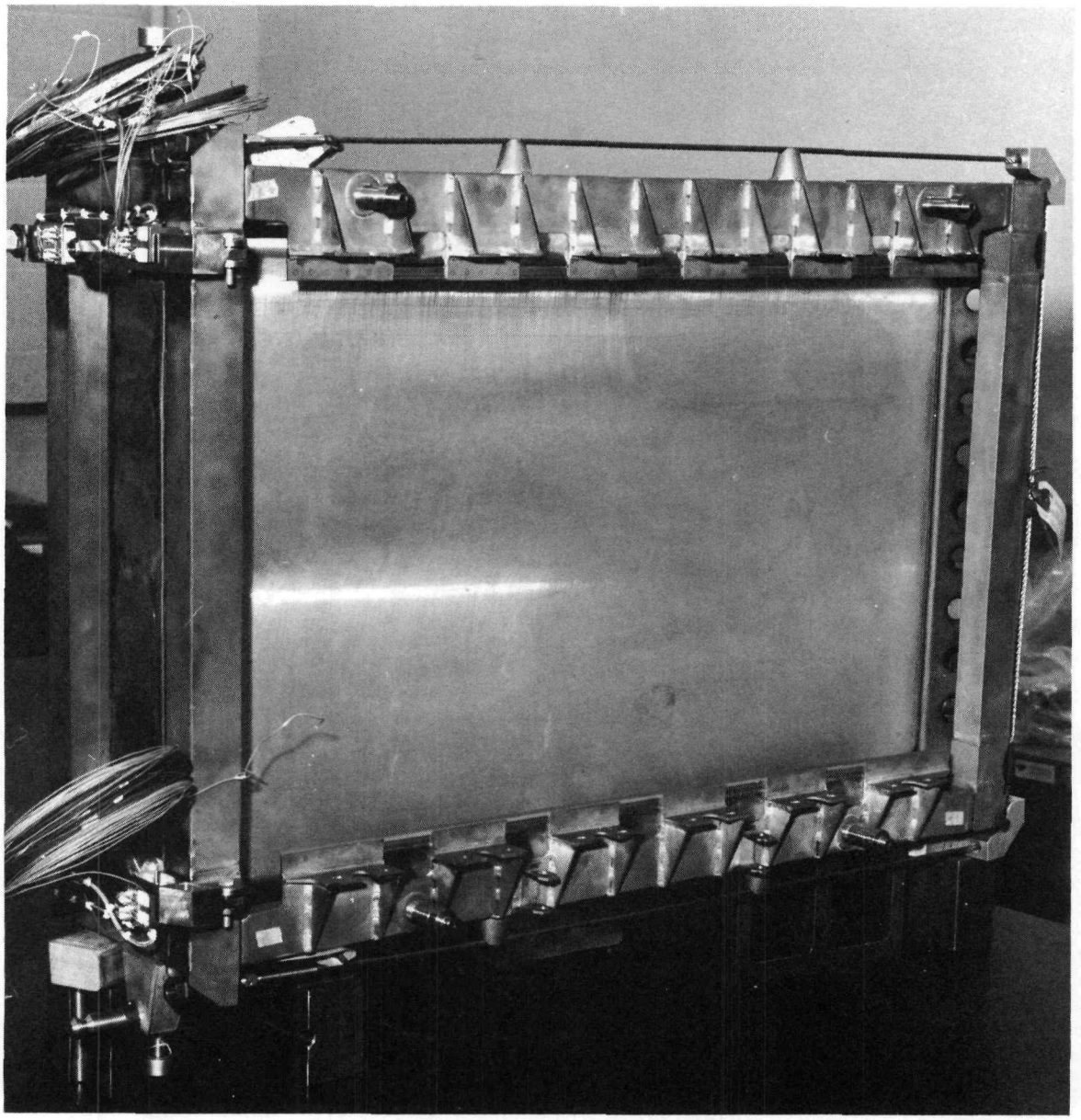

FIG. II-65. ASSEMBLED STRUCTURE FRAME WITH DUMMY ALUMINUM FUEL BLOCK

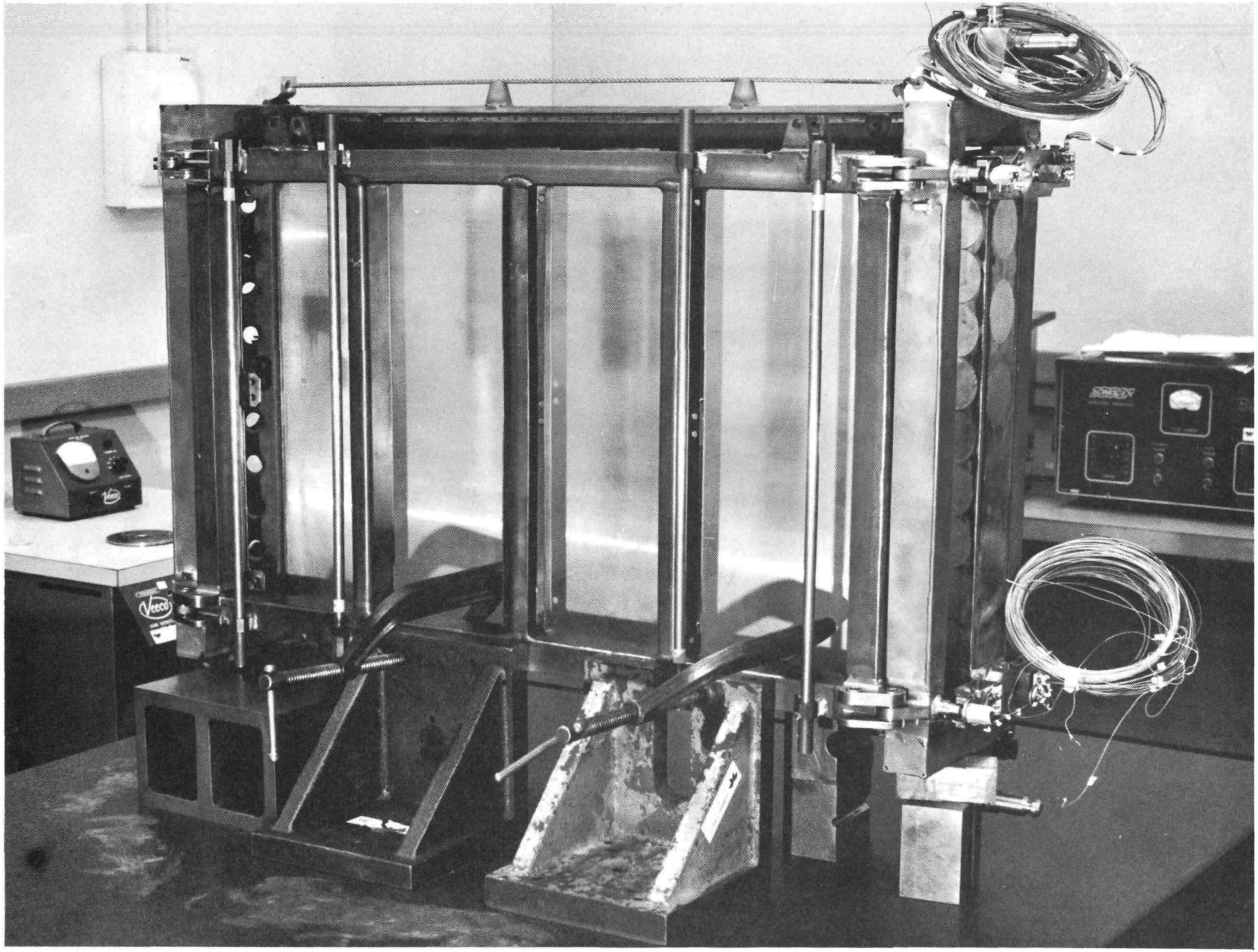

FIG. II-66. THREE-QUARTER REAR VIEW OF ASSEMBLED STRUCTURE FRAME WITH DUMMY FUEL BLOCK

CONFIDENTIAL

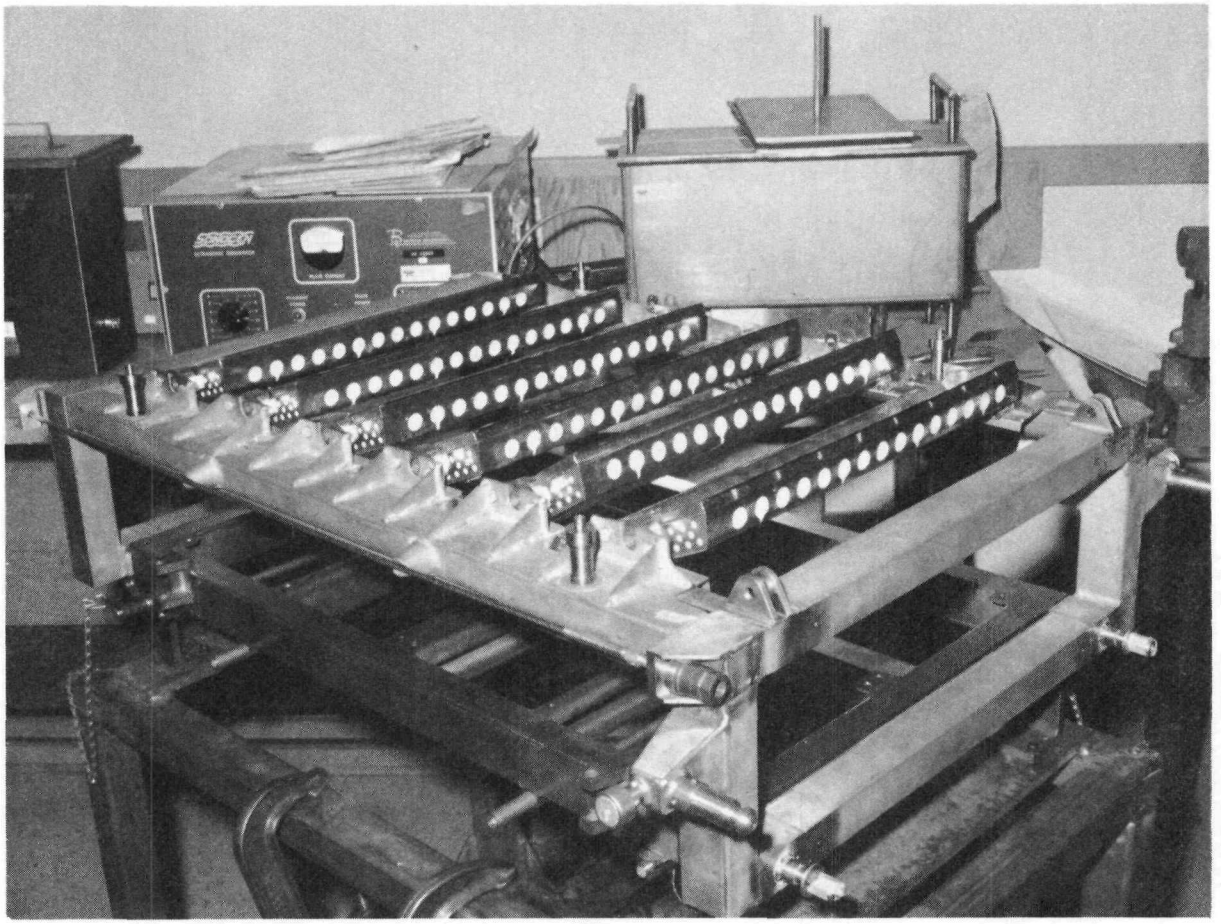

FIG. II-67. RTG STRUCTURE FRAME WITH THERMAL CONTROL SHUTTERS

H. REFERENCES

II-1. Zerlaut, G. A. and Harada, Y., "Stable White Coatings, Summary Report." IITRI-C 207-25, IIT Research Institute, Chicago, Ill., August 27, 1963.

II-2. Diedrich, J. H. and Curtis, H. B., "Experimental Investigation of Total Emittance and Solar Absorptance of Several Coatings Between 300° and 575° K." NASA TN D-3381, Lewis Research Center, Cleveland, Ohio, April 1966.

II-3. Smith, F. J., et al., "Emissivity Coatings for Low-Temperature Space Radiators." QPR-1, NASA - CR - 54807, Lockheed Missles & Space Company, Sunnyvale, Calif., September 1965.

II-4. IBID QPR-2, December 1965.

II-5. IBID QPR-3, June 1966

II-6. Grammer, J. R. and Cunnington, G. R., "Emissivity Coatings for Low-Temperature Space Radiators." L-23-68-1, Interim Progress Report for period ending June 1,1968, Contract NAS-3-7630, Lockheed Missiles & Space Company, Sunnyvale, Calif.

II-7. "Solar Radiation-Induced Damage to the Optical Properties of ZnO-Type Pigments." NAS 8-11266, M-50-65-2, Lockheed Missiles & Space Company, Sunnyvale, Calif., September 1965.

II-8. Telecom between Neal P. Strazza, Isotopes, Inc. and C. A. Zerlaut and Y. Harada, IIT Research Institute, Chicago, Ill., October 1968.

BLANK

III. SYSTEMS EVALUATION AND INTEGRATION--CONTROL POINT 3200

Control of the overall system baseline design, coordination and integration of SNAP 29 RTG system and its associated AGE into the simulated launch complex and demonstration of system performance and reliability objectives are conducted under this task. Three subtasks were involved in performing this effort during the reporting period:

CP 3210--Systems Interface Evaluation

CP 3230--Reliability (Reported in Chapter IV)

CP 3240--Systems Test Integration

A. SUMMARY OF SIGNIFICANT ACCOMPLISHMENTS

The GFE survey was completed and a letter summarizing the transfer action was transmitted to the AEC.

The three systems test consoles for checking out the four-module RTG were completed.

B. SYSTEM INTERFACE EVALUATION--CONTROL POINT 3210

The objectives of the system interface evaluation include the dissemination of design constraint criteria and disciplines to control RTG/AGE systems design, development, fabrication, test and reporting to properly satisfy program requirements.

Additionally, the functions pertinent to engineering scheduling, drawing release control, drawing change control, material release and control, monthly and quarterly reporting, still photography control and GFE requirements coordination are performed hereunder.

1. Drawing Control

One hundred and forty drawings and/or revisions were reviewed and released during this quarter.

2. Material Control

One hundred twenty eight Purchase Requests were processed by Engineering during the current period.

3. Reports

The Eighth Quarterly Report (MND2062-9-8) and Monthly Reports 31, 32 and 33 were prepared during October, November and December. The control numbers of the latter were MND 2062-3110-10-68, MND 2062-3110-11-68 and INSD 2062-3110-12-68.

4. Photography

Approximately 35 8-1/2 x 11 black and white photos were processed to document hardware development highlights.

5. GFE Coordination

The Government-furnished equipment assigned to Contract AT(30-1) 3067 (SNAP 19) was reviewed for application to SNAP 29 requirements since some of the equipment is common to both contracts. This task was completed. Requests for transfer of accountability of required equipment was forwarded to the AEC by Isotopes Letter No. 3213-53 on December 16, 1968.

C. SYSTEM TEST INTEGRATION--CONTROL POINT 3240

1. Systems Test Consoles

The instrumentation and electrical power design, construction and checkout for three portable test consoles was completed. The intended use for these consoles will be the checkout and performance tests of a four-module RTG assembly.

Figures III-1 through III-3 show the front view of these three instrumentation consoles.

The portable instrumentation and power console (Fig. III-1) is planned for use during testing of SNAP 29 generators. It is designed as a versatile unit to accommodate a maximum number of different heater blocks and RTG configurations. Provisions have been made to enable tests of modules in an RTG assembly as well as to test T/E modules as separate units. The console is capable of supplying heater power and providing load circuits for one to eight T/E modules simultaneously.

The basic functions of the console are then to supply controlled electrical heater power to the heater block in the RTG assembly, serve as an electrical matched load for the generated power from the RTG and provide alarms and automatic controls to protect the RTG in the event of associated equipment malfunctions.

Power from a 480-volt, 3-phase, 60-cycle line is transformed within the console to three single-phase circuits of 120 volts ac or 240 volts ac as required by the particular electrical heaters in the RTG heater block. Each of the three power output circuits is conduction-angle controlled by a 10-kva SCR controller which governs the power applied to the heater circuits. Each of these three output circuits is further divided into nine output branch lines, with each line protected by a circuit breaker. Thus, the console provides 27 power output lines which can be used in various combinations to provide up to 30 kva of electrical heater power to RTG heaters.

The RTG or individual T/E module load banks consist of eight separate load circuits which can be adjusted to match the internal impedance of the RTG or the individual T/E module to achieve maximum power transfer. Eight power rheostats within the console provides this capability.

Arrangements are included in each load circuit for measurement of load and open circuit voltages and load current. Front panel controls for matching load resistances and for the measurement functions are one of the salient features of this console.

Front panel selection of control thermocouples for the heater power temperature controllers and for the overtemperature alarm controls are provided. Selected thermocouples from the hot shoes of the T/E modules are routed to thermocouple selector switches for Controllers 1, 2 and 3. The position of these switches then determines which of these selected thermocouples are actually applied to the controllers.

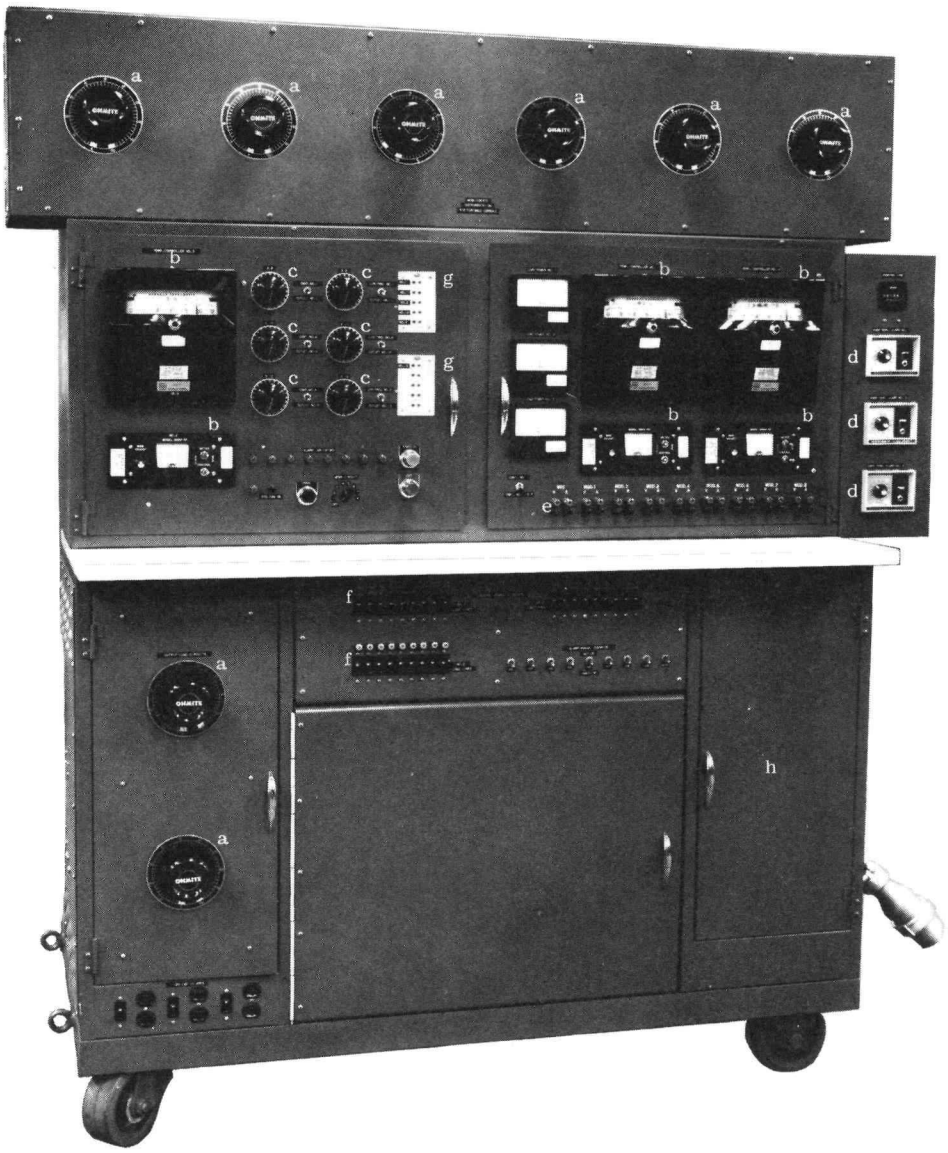

FIG. III-1. POWER CONSOLE

Legend:

a = T/E modules or RTG load circuit control
b = Heater power temperature controller
c = T/C selector switches
d = Overtemperature alarm control
e = Load and open circuit terminals
f = Heater power branch line circuit breakers
g = T/C panel outlets
h = Storage compartment

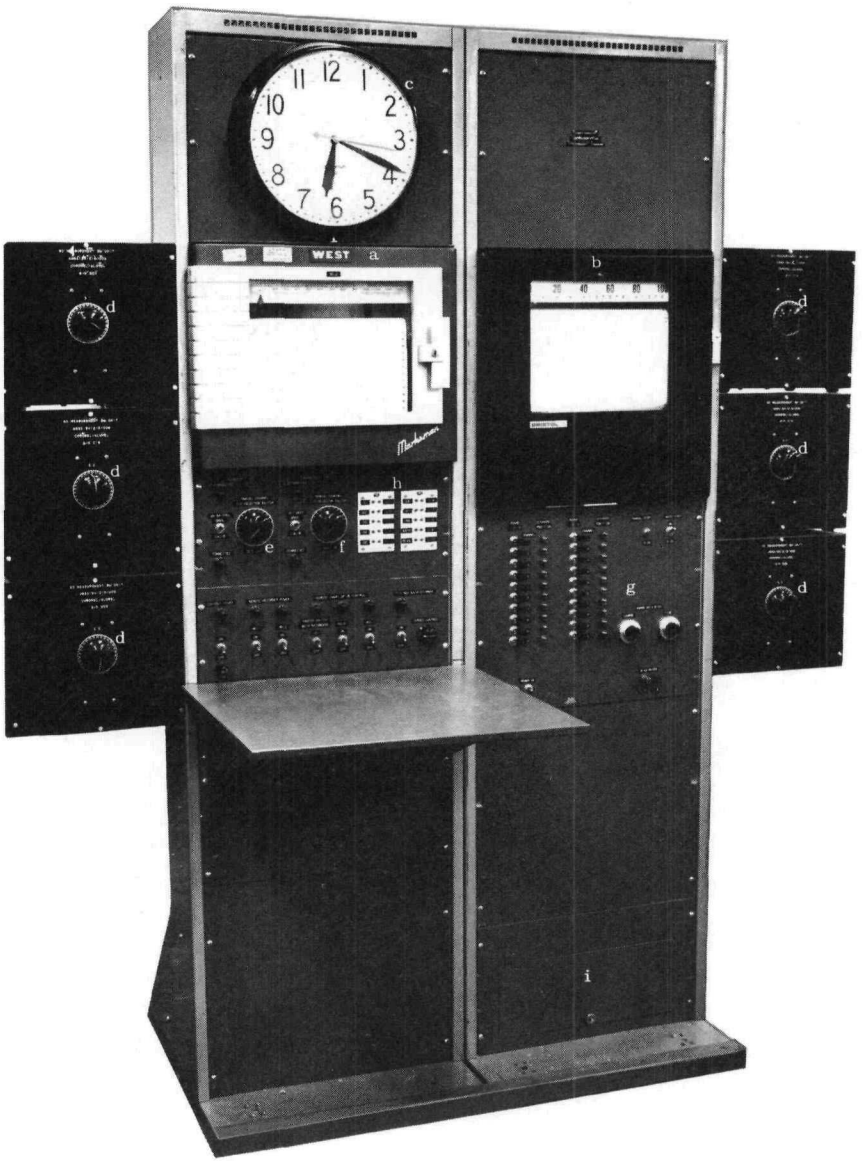

Legend:

a = Recorder 2

b = Recorder 1

c = SNAP 29 test master time clock

d = 60-position T/C selector switches

e = 24-position T/C selector switch for input channels of Recorder 1 (manual readout)

f = 24-position T/C selector switch for input channels of Recorder 2 (manual readout)

g = Signal conditioning unit for Recorder 1

h = T/C panel outlets for input channels of Recorders 1 and 2 and reference ice bath temperature measurement

i = Storage compartment

FIG. III-2. THERMODOUPLE READOUT CONSOLE

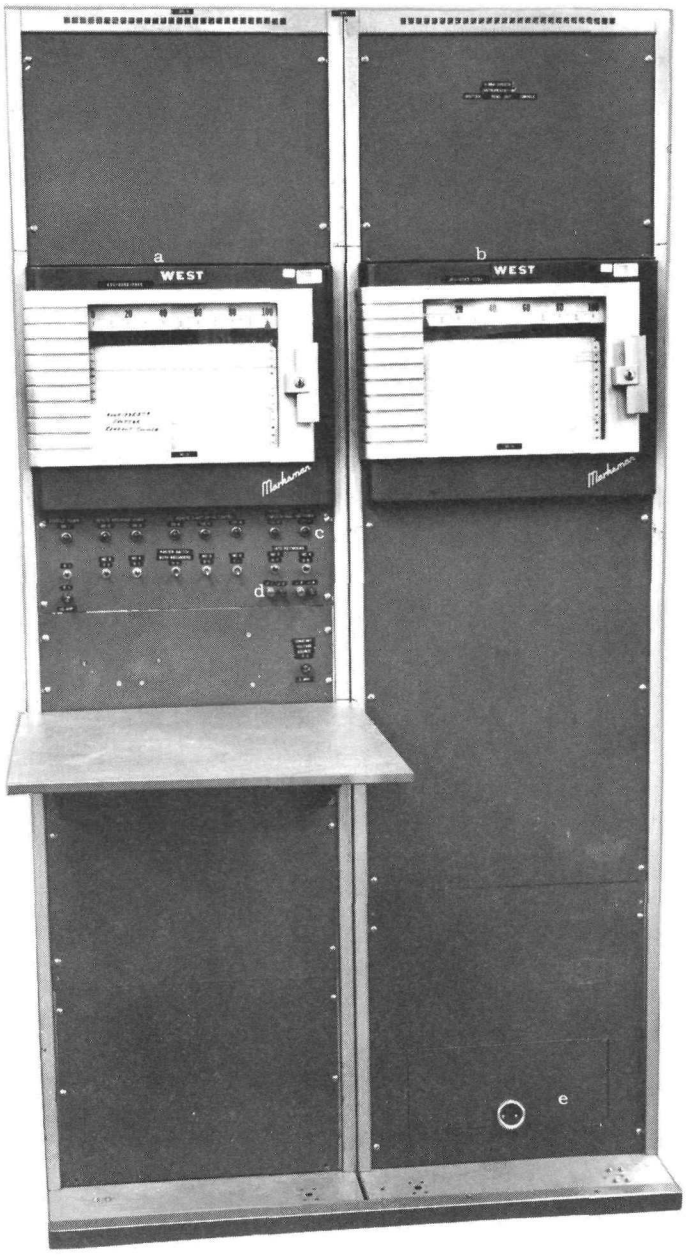

Legend:

a = Recorder 3

b = Recorder 4

c = Remote controls

d = Signal conditioning unit calibration output terminals

e = Storage compartment

FIG. III-3. SHUTTER CONSOLE

Provisions are also included for manual readout of all thermocouples connected to these T/C selector switches by connecting a thermocouple precision potentiometer to respective thermocouple panel outlets.

The same arrangement is designed for the control thermocouples for the over-temperature alarms.

The portable T/C readout console (Fig. III-2) is intended for use during testing of SNAP 29 generators and associated equipment. It was specifically designed for the monitoring of large temperature sensor measurement systems where only a relatively slow readout is required and consequently does not justify the costs of a high speed electronic multiplexer or an electromechanical commutation data acquisition system. The console will be especially useful where a large number of thermocouples can be read out at periodic intervals manually but at the same time selected T/C measurement channels must be continuously recorded.

Basically, the console consists of switching circuits, signal conditioning circuits, manual precision readout instruments and two medium speed recorders. The console is designed to facilitate manual measurements of chromel/alumel thermocouple outputs as well as to provide for signal conditioned recording of significant and/or critical measurement prints.

The console includes switching provisions to accommodate 392 chromel/alumel thermocouples for readout directly in terms of temperature. Two potentiometer-type readout instruments with 1/4% accuracy are provided, making it possible for two operators to take readings simultaneously. The scales of these T/C potentiometers are calibrated from 0° to 2000° F in temperature directly.

Two chart-type recorders, each with an 11-inch scale band, are included, providing the capability to continuously record a total of 32 chromel/alumel thermocouple channels. Console Recorder 1 handles 20 channels, processing all of these in 19 seconds. All inputs to this recorder are referenced to an ice bath and processed by a signal conditioning unit which permits any channel to be switched on any of the following full-scale ranges, at the operators option:

Range No.	Scale Band (°F)	Value of Each Scale Division (°F)
1	32 to 2032	20
2	1000 to 1300	3
3	32 to 532	5

Console Recorder 2 handles 12 channels, processing all of these in 33 seconds. This recorder is directly compensated for thermocouple reference. The measurement bandwidth of this recorder extends from 0° to 1300° F for chromel/alumel thermocouple inputs.

High precision switching provisions are included to permit manual readout of all 32 recorder input channels. The operation of the recorders is automated by remote control and both recorders are synchronized with respect to time.

The portable shutter readout console (Fig. III-3) is intended for use during testing of SNAP 29 generators and shutter assemblies. Specifically, it is to be used to record the angular position of the RTG shutter blades during RTG operation to

record continuously a selected function or functions related to operation of the RTG and/or the SNAP 29 fuel handling machine. As shutter console, one of the prime functions for this unit will be the determination of the thermal response time of the RTG thermal control system.

Basically, the console consists of a number of chart-type recorders with remote front panel control and time synchronization units. A signal conditioning unit consisting of a constant voltage power supply and associated equipment is included to provide excitation for the angular position sensor of the RTG shutter mechanism.

The recorders are single-channel units, each with an 11-inch scale band. Their direct input range is 0 to 5 millivolts.

Recorder 3, which is used to record shutter angular position, receives its input signal from a temperature-stabilized precision potentiometer that is mechanically linked to the RTG shutter assembly. The 0- to 5-millivolt input signal corresponds to 0- to 100-degree angular movement of the shutter blades. Therefore, this signal provides a continuous direct angular readout of 1-degree angular increment per one chart division on the recorder.

The goal of the instrumentation systems design is to achieve a 16.8-minute (angular) resolution of shutter rotation under optimum conditions; under worst conditions, an accuracy of $\pm$ 1/2-degree angular data recording of the RTG shutter position is expected.

BLANK

IV. RELIABILITY--CONTROL POINT 3230

The SNAP 29 reliability program has been proceeding in accordance with the tasks and schedule presented in the SNAP 29 Program Plan. The plan establishes the management and technical reliability controls necessary to implement an effective and economically planned and integrated reliability program in support of design, procurement, fabrication and test. To accomplish this overall program most effectively, three major work areas have been established. These are:

CP 3231--Planning and System Analysis

CP 3232--Design Evaluation and Approval

CP 3233--Test Program Definition and Evaluation

The three work areas are further subdivided into tasks for planning and control purposes. The task breakdown follows that developed in the Program Plan and is used for presenting the information under Sections B through D.

A. SUMMARY OF SIGNIFICANT ACCOMPLISHMENTS

A reduction in the total amount of test data available as a result of program redefinition will reduce the ability to verify the reliability prediction for the RTG.

The ability of the RTG four-module configuration to meet the load voltage requirements specified by contract documents has been substantiated through preparation of voltage-current and power-current characteristics for the generator at beginning and end of life.

An analysis and reliability prediction for the heat rejection subsystem has been initiated. The failure mode effects analysis and apportionment of the overall subsystem reliability to the individual constituents has been completed and is reported here.

The analysis of the qualification lot of the selected SNAP 29 2N-TAGS/SnTe couple has been completed. It showed an increase in electrical power and reduction in variance of the TAGS leg over that obtained with the development couple.

B. RELIABILITY PLANNING AND SYSTEM ANALYSIS--CONTROL POINT 3231

1. Program Planning

The reliability program is being implemented in accordance with the tasks and schedule established in the SNAP 29 Program Plan. A listing of the tasks were presented in the Seventh Quarterly Report.

The effect of program redefinition is expected to limit the scope and level of testing at the subsystem level. This, in turn, will significantly reduce the amount of data that would be available to substantiate reliability predictions. The impact of program redefinition is still under evaluation. The redefinition is also expected to shift the emphasis placed on the reliability requirements and on the individual tasks which make up the reliability program. The most obvious impacts are expected to result in the elimination of the confidence level portion of the reliability requirements and increased dependance on analytical verification for the assessment of the generator reliability.

The primary effort of the reliability activity during the next reporting period is to implement the reliability prediction plan. This includes the establishment of an apportionment, analysis and prediction for each subsystem of the RTG.

2. System Analysis

a. RTG subsystem apportionment

Apportionment is the allocation or assignment of the overall system numerical requirements, be it volume, weight, reliability, etc., among its subdivision or constitutent elements in such a manner that their quantitative values bear some relationship to the overall numerical requirements. This reliability apportionment has been developed using inputs from failure mode and effects analyses coupled with engineering judgment and knowledge of the functions, characteristics and relationships, between the parts and materials in their respective operating environments.

The reliability requirement, from which the apportionment is formulated, has been stated in previous quarterly reports and repeated for convenience. "The SNAP 29 preprototype RTG which consists of four T/E modules, shall have a predicted probability of 0.98 at a confidence level of 50% of delivering 400 watts(e) throughout a period of 114 days of which 90 days shall be in a space environment." This requirement has been allocated to the subsystem level for the RTG configuration with an intact re-entry heat source. A corresponding allocation for the RTG with a burn-up heat source has not been completed. It is expected that meteoroid penetration will be more significant for the burn-up configuration than for the intact re-entry configuration.

Figure IV-1 presents the allocation based on the physical breakdown of the RTG by control points. The appropriate mathematical models and block diagrams are shown for both the catastrophic and noncatastrophic type failures. The physical breakdown is oriented to the hardware configuration of the subsystem. Figure IV-2 presents the identical information except for the functional breakdown. The functional breakdown, as the term implies, is oriented to functions. It simplifies analyses and predictions which interrelate subsystems and thus far more adaptable where predictions are made using variables data.

b. RTG power output characteristics

The RTG is comprised of four T/E modules connected in series. Within each module are 90 thermoelectric couples connected in a series/parallel ladder configuration. The voltage-current (E-I) and power-current (P-I) characteristics are determined by the T/E couple and electrical parameters. The parameter values in turn are influenced by the temperature difference across them and by the change in their electrical characteristics with time. The variation of these characteristics determine the slope of the E-I curves and the shape of the P-I curve. The E-I curve is also utilized to verify that the load voltage will be 14% $\pm$10 volts at matched load which occurs when the internal generator resistance equals the external load resistance. The results of the analysis show the load voltage to be 13.84 and 14.27 volts at BOL and EOL, respectively. These values are well within the specified requirements.

An initial prediction of the beginning of life(BOL) power output was established as 434.64 watts based on the diaphragm-type T/E module using 2N-TAGS/SnTe type thermoelectric couples and operating at couple junction temperatures of T_H = 1050° F and T_C of 373° F. This value was developed and presented in the Eighth Quarterly Progress Report.

Math Model/Allocation

System -

$R_T = R_C \times R_{NC}$

$0.98 = 0.9928 \times 0.9872$

Catastrophic -

$R_C = R_{HSS} \times R_{TMS} \times R_{TCS} \times R_{HRS} \times R_{STS}$

$0.9928 = 1.000 \times 0.9978 \times 0.9995 \times 0.9958 \times 0.9997$

Noncatastrophic -

$R_{NC} = R_{HSS} \times R_{TMS} \times R_{TCS} \times R_{HRS} \times R_{STS}$

$0.9872 = 0.9997 \times 0.9986 \times 0.9970 \times 0.9920 \times 0.9999$

Block Diagrams

Catastrophic

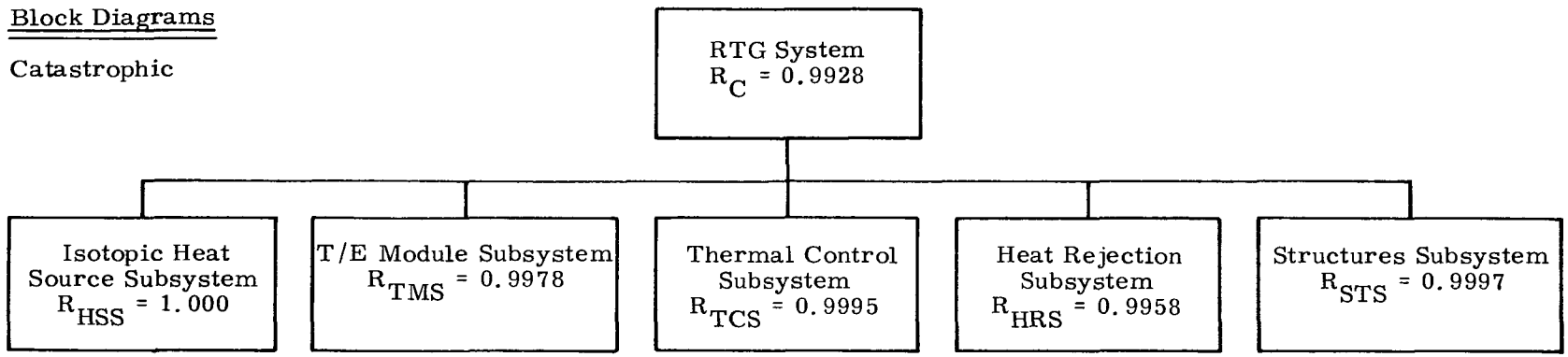

Noncatastrophic

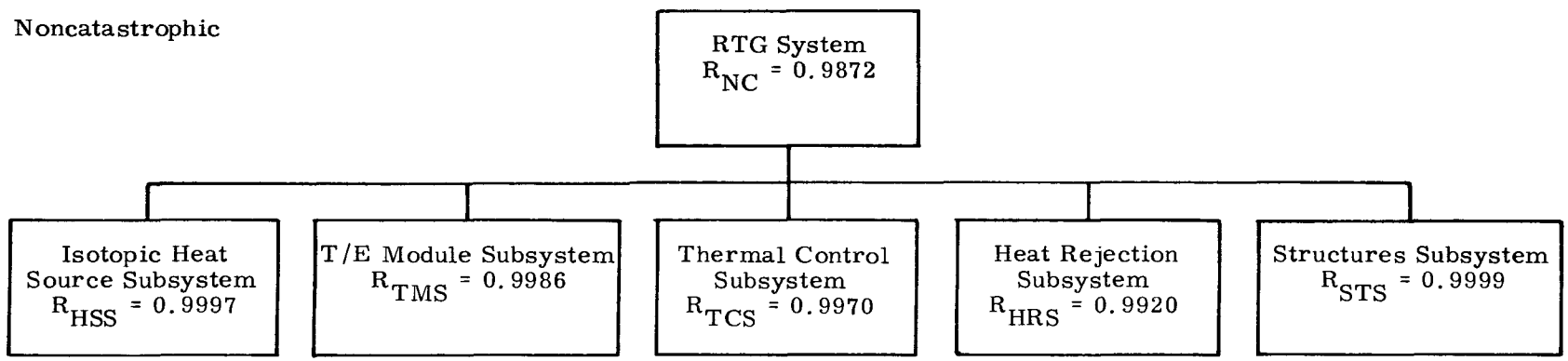

FIG. IV-1. SNAP 29 RTG RELIABILITY APPORTIONMENT (PHYSICAL BREAKDOWN)

CONFIDENTIAL

Math Model

$R_{TOT} = R_M \times R_E \times R_T \times R_P$

$0.98 = 0.9943 \times 0.9985 \times 0.9876 \times 0.9996$

Block Diagram

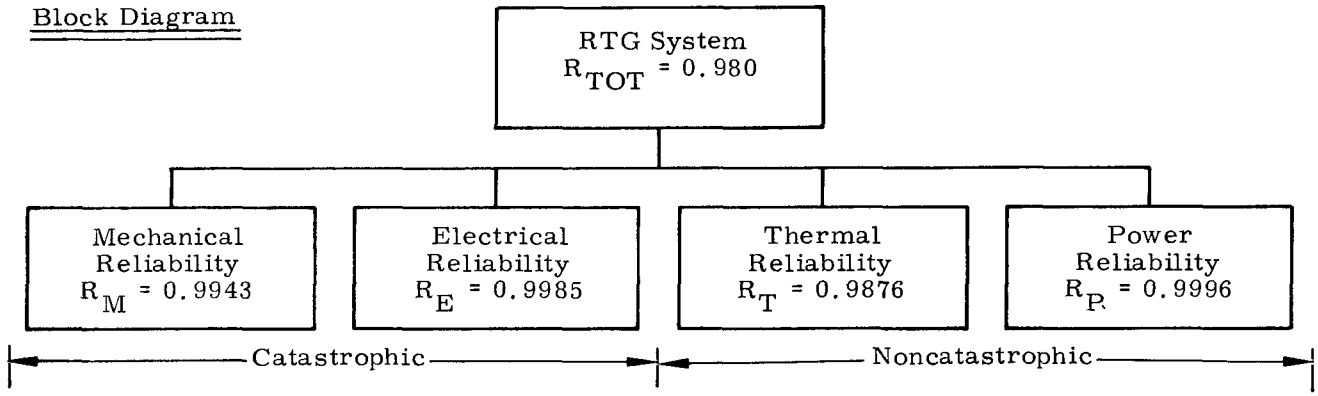

FIG. IV-2. SNAP 29 RELIABILITY APPORTIONMENT (FUNCTIONAL BREAKDOWN)

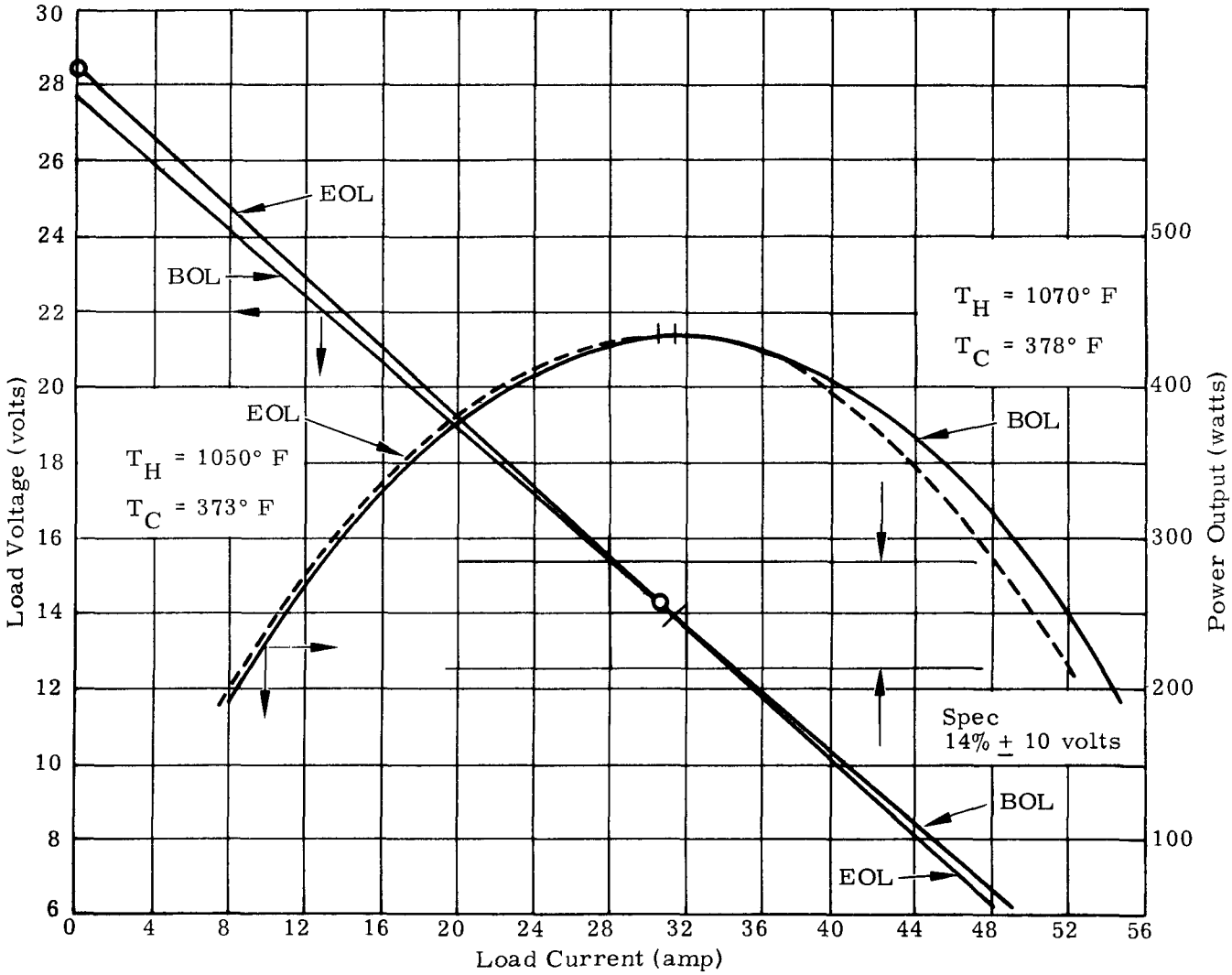

FIG. IV-3. PREDICTED ELECTRICAL PARAMETRIC OF FOUR-MODULE SNAP 29 RTG

This analysis has been based on the characteristics of the SNAP 29 development couple P/N 466A1341071-009. A corresponding analysis based on the production couple design, P/N 466A1331005-009, has not been completed. A review of the couple data for the selected design, presented in Section C-2 indicates that the net power output of the RTG will be increased. All data indicate that the maximum power output remains substantially constant (within two watts) throughout the life of 114 days based on results obtained from the large TAGS module (LTM) and T/E couple tests. There is, however, a shift in the current value at which the maximum power output occurs and the slope of E-I curves between BOL and EOL due to a change in the basic electrical parameters of the T/E couples and a difference in operating temperature encountered at these two time periods.

The 2N-TAGS/SnTe type T/E couples exhibit an increase in open circuit voltage (E_{oc}) and an increase in resistance (R_c) with elapsed time. This increase is estimated to be 5.37% for E_{oc} and 10.04% for R_c between BOL and EOL. In addition, the T/E couple hot junction temperature drops from 1070° F at BOL to 1050° F at EOL due to a temperature differential inherent in the thermal control (shutter) subsystem. The couple cold junction temperature, which is affected by the change in the hot junction temperature, exhibits a corresponding decrease of 378° to 373° F during this same period.

Figure IV-3 presents, in a graphical format, the E-I and P-I curves for the RTG at beginning and end of life. The values used for plotting the E-I curves were obtained from Tables IV-1 and IV-2. The P-I curves were calculated by multiplying the load voltage by the load current.

TABLE IV-1

Summary of Voltage Calculations

	T/E Module				RTG	
Operating Time	Open Circuit Voltage (E_{oc}) (volts)	Temperature Correction Factor (T_{CF})	Drift Correction Factor (D_{CF})	Open Circuit Voltage ($E_{oc_{(M)}}$) (volts)	Open Circuit Voltage ($E_{oc_{(G)}}$) (volts)	Load Circuit Voltage (LV_G) (volts)
BOL	7.002	0.9885	1.0000	6.920	27.68	13.84
EOL	7.002	0.9671	1.0537	7.133	28.53	14.27
	1	2	3	4	5	6

TABLE IV-2

Summary of Current Calculations

	T/E Module					RTG			
Operating Time	T/E Couple Resistance 1050/350° F (R_C) (ohms)	Temperature Correction Factor (T_{CF})	Drift Correction Factor (D_{CF})	Strap and Wire Resistance (R_S) (ohms)	Total Module Resistance (R_M) (ohms)	Module Resistance (R_{4M}) (ohms)	Wiring Resistance (R_W) (ohms)	Total Generator Resistance (R_G) (ohms)	Load Current (I_G) (amps)
BOL	0.09104	1.0120	1 000	0.01136	0.10713	0 42852	0.01220	0 4407	31 40
EOL	0.09104	1 0174	1 1004	0.01136	0.1133	0.4531	0 01220	0.4653	30 37
	1	2	3	4	5	6	7	8	9

Table IV-1 presents a summary of the calculation steps related to voltage characteristics of the RTG. The equations used, the sources of data and the resulting values are tabulated. The numbered heading of the following paragraphs correspond to the respective column number in the table.

1. The module open circuit voltage (E_{oc}) has been calculated to be 7.002 volts at a hot junction temperature of 1050° F and a cold junction temperature of 350° F.

2. A temperature corrector factor (T_{CF}) is applied to the E_{oc} to convert the voltage to the application temperatures of the RTG at BOL and EOL, namely:

T_H/T_C of 1070°/378° F and 1050°/373° F. Open circuit voltage is, in the range of temperatures involved, directly proportional to delta temperature. The correction factors thus become for:

$$\text{BOL} = \frac{T_{H(1070)} - T_{C(378)}}{T_{H(1050)} - T_{C(350)}} = \frac{692}{700} = 0.9885$$

$$\text{EOL} = \frac{T_{H(1050)} - T_{C(373)}}{T_{H(1050)} - T_{C(350)}} = \frac{677}{700} = 0.9671$$

3. A drift correction factor (D_{CF}) is applied to account for a 5.37% increase in open circuit voltage of the couples between BOL and EOL. This value has been substantiated by T/E module and couple test data.

4. The module open circuit voltage (E_{oc_M}) is calculated from the equation

$$E_{oc_{(M)}} = E_{oc} \times T_{CF} \times D_{CF}$$

$$E_{oc_{(M)}}\ \text{BOL} = 7.002 \times 0.9885 \times 1.000 = 6.920 \text{ volts}$$

$$E_{oc_{(M)}}\ \text{EOL} = 7.002 \times 0.9671 \times 1.0537 = 7.133 \text{ volts}$$

5. The RTG open circuit volts (E_{oc_G}) is calculated by multiplying the E_{oc_M} times the number (4) of modules connected in series.

6. The RTG load voltage (LV_G) is calculated as the $E_{oc_G}/2$ or that point which maximum power is realized. This point occurs when the internal generator resistance equals the external load resistance.

Table IV-2 presents a summary of the calculation steps related to the current characteristics of the RTG. The equations used, the sources of data and the resulting values are tabulated. The numbered headings of the following paragraphs correspond to the respective column numbers in the table.

1. The rssistance of all couples (R_C) in the T/E module has been calculated to be 0.9104 ohm at a hot junction temperature of 1050° F and a cold junction temperature of 350° F, Ref. (b).

2. A temperature compensating factor (T_{CF}) is applied to convert the resistance to the requirements of the RTG at BOL and EOL, namely: T_H/T_C of 1070°/373° F. This factor has been developed using the change in resistivity (σ) of the T/E couple elements with temperature. An error, which has been determined to be small, exists in this method since the resistance of the hot shoe of the couple is ignored.

3. A drift correction factor (D_{CF}) is applied to compensate for a 10.04% increase in resistance of the T/E couples during the 114 days. This increase has been developed from test data.

4. The resistance of the internal wire leads, copper straps, cold end bonds and solder connections (R_S) is assumed to be identical to that calculated for the piston-heat sink module design. This value is 0.01136 ohm. Resistance variations in the copper, etc., materials for the range of temperatures covered by this analysis, are considered negligible.

5. The resistance of the module (R_M) is calculated from the equation:

$$R_M = R_C \times T_{CF} \times D_{CF} + R_S$$

$$R_M = 0.9104 \times 1.0520 \times 1 + 0.01136 = 0.10713 \text{ ohm}$$
BOL

$$R_M = 0.9104 \times 1.0174 \times 1.1004 + 0.01136 = 0.11327 \text{ ohm}$$
EOL

6. The RTG resistance due to the contribution of the modules (R_{4M}) is calculated by multiplying R_M times the number (4) of series-connected modules.

7. The resistance of the inter-module wiring (R_W) has been calculated considering material, gage, length and average operating temperatures. This value is established at 0.01220 ohm.

8. The total generator resistance (R_G) is the sum of the module resistance (R_{4M}) plus the internal wiring resistance (R_W).

9. The current is calculated from the equation $I_G = \sqrt{\frac{P_G}{R_G}}$

where

I_G = generator line current (amp)

P_G = generator power output of 434.64, Ref. (b).

The values are:

$$I_{BOL} = \frac{434.64}{0.4407} = 31.40 \text{ amperes}$$

$$I_{EOL} = \frac{434.64}{0.4653} = 30.57 \text{ amperes}$$

C. DESIGN EVALUATION AND APPROVAL-- CONTROL POINT 3232

1. Heat Rejection Subsystem Analysis

A portion of the reliability analysis of the heat rejection subsystem configuration, representative of the design verification phase of the program, CP-1830, has been completed. The failure mode and effects analysis and its accompanying reliability apportionment are presented herein. A reliability analysis and prediction of the subsystem is currently in process of preparation.

The function of the heat rejection subsystem is to dissipate the waste heat from the T/E module subsystem to an air or space environment throughout the operating life of the generator. The subsystem consists of two basic component groups--space radiator and heat pipes. The space radiator contains the structural framing for mounting four radiator panels and the thermal insulation to minimize the heat transfer from the panels to the satellite vehicle. The meteoroid armor protection and emissivity coating complete the space radiator assembly. The space radiator wraps around the satellite vehicle in a band the height of which does not exceed that of the T/E module building block. The curvature of the space radiator is one-half the diameter of the vehicle and the wrap length approaching one-half the circumference of the vehicle.

The heat pipe is a static device for absorbing, transmitting and radiating heat through a closed tube containing a wick and liquid. The heat pipe design selected for the SNAP 29 is 3/8 inch in diameter, 15 feet long and curved to a radius of five feet. It is fabricated from a nickel tube of 200 material with a 0.010 inch wall thickness. The heat pipe is fabricated in two sections which are jointed using a butt-type joint and a brazed coupling sleeve. The condenser end of the pipe, which is bonded onto the radiator panel, has a wick made from a nickel 200 mesh screen formed into a 0.035 inch deep corrugated configuration. The evaporator end of the pipe, which is soldered into the T/E module heat sink, has a wick composed of three layers of 30 mesh nickel screen. The interior surfaces are oxidized at a temperature of 750° F using a flow through process. The completed assembly is cleaned with nitric acid, charged with the specified amount of water and sealed. The pipe is hydrostatic pressure and helium leak tested prior to filling. It is performance tested subsequent to sealing but prior to assembly to the module/radiator panel.

a. Failure mode and effects analysis

A failure mode and effects analysis is a basic tool for discovering critical design areas. It identifies:

(1) Probable modes of failure

(2) Potential failure mechanisms that contribute to these failure modes

(3) And projects the effect on mission performance resulting from such failures.

In addition, the analyses permit identification of the importance of each failure mode and its probability of occurrence so that the capability of the design to overcome, counteract or resist the mode of failure may be established.

The identification of the failure modes and the effect of these failures on the power output characteristics of the RTG are tabulated in Table IV-3 and IV-4 for the heat pipes and space radiator, respectively. The heat pipe group includes those functions related to the transfer of heat from the heat sink of the T/E module to the space radiator. It consists of the heat pipe tube, evaporator wick, condenser wick and coupling sleeve. The attachment of the tube by soldering into the hot plate and bonding to the radiator completes this group. The space radiator group includes the radiator structure radiator panel, emissivity coating and meteoroid armor. The latter is incorporated directly into the basic structure.

The results show that the most critical catastrophic-type failure is associated with the loss of a heat pipe(s) due to meteroid penetration. This type failure may be reduced through the addition of armor or an increase in the thickness of the radiator panel or the heat pipe tube wall. The most noncatastrophic-type failure is related to internal gas buildup within a heat pipe. The gas buildup does not effect the thermal transport capability of the heat pipe, only the radiating surface area. A preliminary inspection of this effect indicates a minor reduction of the heat rejection capability of the radiator.

Definitions and codes applicable to Tables IV-3 and IV-4 are:

Failure category:

F_1--failure results in a rapid degradation of performance or catastrophic loss of the function

F_2--failure may result in a reduction in performance of the system

F_3--no system failure by itself although it may combine with another to produce failure.

Failure probability:

P_1--high probability of occurrence during operating life

P_2--average probability of occurrence during operating life

P_3--low or remote probability of occurrence during operating life.

Criticality ranking:

$C_{(x)}$--catastrophic

$NC_{(x)}$--noncatastrophic

The subscript (x) is determined by a ranking method that is based on comparison by pairs of the relative importance among a number of events; the higher the subscript the more critical the failure.

TABLE IV-3

Failure Mode and Effects Analysis, Heat Pipes

Math Model Symbol	Probable Failure Mode	Potential Failure Mechanism	Effect On Performance	Compensating Factor	Design and/or Fabrication Assurance	Failure Category	Failure Probability	Criticality Ranking
R_{HP} Heat pipes	Catastrophic loss of heat transfer capability	Leak at end cap weld, coupling sleeve braze or fill tube crimp	Failure of heat pipe to transfer heat	Heat pipes - redundant except for those in edge of radiator panel	Hydrostatic pressure and helium leak test prior to changing	F_3	P_2	C(2)
		Leak due to micro meteoroid penetration of tube			Armor thickness is a design variable determined by mission requirements	F_3	P_1	C(4)
		Dryout of pipe (fails to transport heat)			Performance test prior to assembly to module or radiator panel	F_3	P_2	C(3)
		Discontinuity of wick at transition area or gap between wick and tube				F_3	P_2	C(0)
	Degradation of heat transfer capability	Vapor bubbles or chemical deposits in wick restricts water flow to evaporator	Reduction in heat pipe transfer capability	Heat pipes are redundant except for those in edge of radiator panel	Tube finish, part cleaning and water purification processes	F_3	P_2	NC(0)
		Gas accumulation at cold end of evaporator			Design compensates for gas buildup	F_3	P_1	NC(3)

CONFIDENTIAL

CONFIDENTIAL

TABLE IV-4

Failure Mode and Effects Analysis, Space Radiator

Math Model Symbol	Probable Failure Mode	Potential Failure Mechanism	Effect On Performance	Compensating Factor	Design and/or Fabrication Assurance	Failure Category	Failure Probability	Criticality Ranking
R_{SR} Space radiator	Catastrophic loss of heat rejection	Failure of radiator, support structure, radiator panel or mounting devices	Minor reduction in heat radiation capability unless heat pipe seal(s) is broken	Some degree of redundance of mounting hardware and heat pipes	Manufacturing and quality control of processes Vibration acceptance test of system	F_2	P_3	C(1)
		Failure of braze or solder between heat pipe and radiator panel and/or T/E module heat sink						
	Degradation of heat rejection	Deterioration of emissivity coating due to thermal cycling, salt air, humidity, booster propellants, bending and twisting during installation	Reduction in heat radiation capability	Surface may be cleaned, repaired or refinished	Re-inspection prior to launch	F_3	P_2	NC(1)
		Deterioration of emissivity coating due to shock and vibration during launch or vacuum vaporization, meteoroid errosion and ultraviolet light in space.		None	Design compensates for loss of emissivity	F_3	P_2	NC(2)

b. Apportionment

The initial reliability apportionment for the SNAP 29 heat rejection subsystem, CP 1830 has been completed for the catastrophic-type failures only. Noncatastrophic (degradation)-type failures will be covered in a subsequent report.

The reliability of 0.9958, apportioned to the heat rejection subsystem for catastrophic-type failures, by the previous paragraph, has been allocated among the assemblies, components and elements of the subsystem using best estimate reliability predictions supported when available, by test data. Where such sources were not available, engineering judgment was applied.

Table IV-5 presents the results of the apportionment. The table follows the breakdown of failure modes identified in the failure mode and effects analysis. The use of unreliability (Q), expressed in parts per million (ppm) has been adapted along with the conventional reliability (R). Two benefits derive from this scheme: computations are simplified and comparisons are more readily envisioned. For example, the comparison of two items haveing a R of 0.999985 and 0.999997 has little meaning. However, comparing the equivalent Q in ppm (15 with 3) shows the latter to be five times more reliable. The relationship of R, Q and ppm is developed using the allocated R of 0.9958.

Q = 1 - R = 1 - 0.9958 = 0.0042 which becomes 4200 when expressed in ppm.

The code number column provides an identification for the mathematical model(s). It also functions similar to the next assembly on drawings, i.e., the next assembly of all items with a code (4) is the code (3) immediately above it.

2. T/E Couple Electrical Characteristics

The results of an analysis of the qualification lot for the selected SNAP 29 2N-TAGS/SnTe couple have been prepared based on 40 samples. The couple is identified by P/N 466A1331005-009. The analysis shows that the net power output has increased approximately 6% over the development couple P/N 466A1341071-009. In addition, the variance factor, ratio of standard deviation to mean expressed in percent, has been reduced approximately one half. The result of these two factors is to greatly enhance and possibly exceed the attainment of the RTG power output reliability. The mean power output is 1.585 watts when operated at the rated hot/cold junction temperatures of 1050°/350° F. The corresponding standard deviation is 0.0421 watt.

The input data were obtained from measurements recorded during conduction of the two-hour power test. The input data include hot and cold junction temperatures, open circuit and load voltages and load current. The corrected power output and, open circuit voltages and resistance were calculated using established procedures for couple data reduction.

Table IV-6 is the summary of the mean, standard deviation and variance factor for the corrected power output (P_C cor), open circuit voltage (E_{oc} cor) and resistance (R_C cor) for the total couple, N and P legs.

The analysis of various types and designs of T/E presented in the previous quarterly progress report, showed that the TAGS-type offered the greatest potential for increased power output. However, the variance associated with the TAGS leg was higher than that experienced with the 3P leg. This analysis has shown that the selected design has recorded both an increase in power output and a reduction in P leg variance.

TABLE IV-5

Heat Rejection Subsystem Reliability Apportionment

Code No.	Item	Quan/ NA	Code Number 1	2	3	4	Math Model
1	Heat Rejection System		0.995800 4200				$R_1 = R_{2a} \times R_{2b}$
2a	Heat Pipe Subsystem	40		0.995960 4040			$R_{2a} = R_{3a}^{32} \times R_{3a}^{8} + 8R_{3a}^{7}(1 - R_{3a})$
3a	Heat Pipe Assembly	1			0.999875 125		$R_{3a} = R_{4a} \times R_{4b} \times R_{4c}$
4a	Meteoroid Penetration	1				0.999910 90	
4b	Performance (dry out)	1				0.999980 20	
4c	Structural (leak)	1				0.999985 15	
2b	Radiator Panel Subsystem	1		0.99840 160			$R_{2b} = R_{3b}^{4}$
3b	Radiator Panel Assembly	4			0.999960 40		$R_{3b} = R_{4d} \times R_{4e}$
4d	Structure	1				0.999980 10	
4e	Mounting Hardware	1				0.999970 30	

CONFIDENTIAL

CONFIDENTIAL

Using SNAP 29 development couple P/N 466A1341071-009 for comparison, the power increased approximately 6% from 1.496 to 1.585 watts and the variancefactor for the TAGS leg, $(s/\bar{x})$ expressed in percent, decreased from over 7% to approximately 3.6%. This 3.6% is comparable with that experienced with the 3P leg of other couple designs.

TABLE IV-6

Electrical Characteristics of SNAP 29 2N-TAGS/SnTe T/E Couples

Item	No. of Samples	Total Couple $\bar{x}$	Total Couple s	Total Couple $\frac{s}{\bar{x}} \times 100$	N Leg $\bar{x}$	N Leg s	N Leg $\frac{s}{\bar{x}} \times 100$	P Leg $\bar{x}$	P Leg s	P Leg $\frac{s}{\bar{x}} \times 100$
Power R_C cor (watts)	40	1.585	0.0423	2.67	0.760	0.0220	2.89	0.822	0.0295	3.58
Resistance 1 R_C cor (ohms)	40	0.00412	0.0000 917	2.23	0.00306	0.0000 826	2.70	0.00128 406	0.0000	3.17
Open circuit voltage E_{oc} cor (volts)	40	0.1615	0.00168	1.04	0.0964	0.00113	1.17	0.0649	0.000 927	1.43

V. AEROSPACE GROUND EQUIPMENT SYSTEM-- CONTROL POINT 2000

The AGE system for the SNAP 29 consists of the equipment necessary to service, test, check out and transport the RTG system.

The objective of the AGE system is to develop equipment which will demonstrate the AGE capability of checking out and transporting the RTG and heat source and loading and unloading the heat source in the RTG.

Tasks to be conducted are:

CP 2200--Fuel Handling Machine

CP 2400--Transportation and Handling Equipment

CP 2600--Field Test Equipment

Preliminary design work on the fuel handling machine, which was scheduled to begin during this reporting period, was postponed until a decision can be reached on the configuration of the isotopic heat source (CP 1100), that is, intact re-entry or burnup re-entry configuration.

BLANK

VI. SAFETY EVALUATION AND INTEGRATION--CONTROL POINT 3300

A. SUMMARY OF SIGNIFICANT ACCOMPLISHMENTS

There was one major item of work accomplished during this period. Re-entry and abort trajectory and heating rates were obtained for various burn-up element configurations and a fuel matrix.

A summary of this item follows; the detailed description of this and other accomplishments will be discussed under separate control point headings.

Final wind tunnel test reports in the intact heat source have either been issued or completed on the following tests: free flight, low density, force and moment, forced oscillation and the rotating force and damping.

B. SAFETY EVALUATION AND INTEGRATION--CONTROL POINT 3310

1. Downwind Diffusion

DELFIC Richardson numbers and turbulence intensities near ground were compared with reported observations from Project Great Plains and documented by SNAP 29 Monthly Report, MND-2062-3110-10-68. Lateral gustiness for positive stability was correlated successfully to wind speed and stability and documented by SNAP 29 Monthly Report, MND-2062-3110-11-68. Initial experience with actual winds indicated a need for interpolation on shear and lapse rate, instead of wind speed components and temperature, and necessary modifications were checked out. The remaining effort during this quarter was applied to obtaining dose predictions for actual wind data.

2. High Altitude Release Transport and Removal

The STREAK computer program, a high-altitude release transport and deposition code, was applied to the SNAP 9A release and results compared with measurements of surface air concentrations and ground deposition. The SNAP 9A comparison is necessary to establish the validity of the code for SNAP 29 releases. Various combinations of parameters of the code were found to improve agreement.

The STREAK code was applied to a SNAP 29 release to determine if the resulting air concentrations were capable of being measured. The peak surface air concentration occurs about 1-1/2 years after release and reaches about 5×10^{-17} curies/cubic meter of air. This is an order of magnitude lower than the Po-210 natural background concentrations reported by Barton and Stewart. (Nature, May 1960).

Natural background in the normal high altitude sampling range (50,000 to 70,000 feet) is several orders of magnitude above the lower limits of detectability. STREAK calculations indicate air concentrations on the order of background would result (at 50,000 feet) from the burnup of 500,000 curies of polonium-210. A doubling of background would be relatively easy to detect. At an altitude of 100,000 feet, the polonium background will be lower while the injected polonium concentration would be about two orders of magnitude greater. Thus, at 100,000 feet, the presence of injected polonium would be obvious. Detection at ground level of a SNAP 29 burnup would be difficult because of natural polonium background variability.

A detailed report of findings from known high altitude releases and their application to SNAP 29 will be presented in the next reporting period.

3. Error Analysis

Standard computer subroutines have been developed to facilitate the programming of a specific error analysis study. The use of these subroutines tends to minimize the effort required to write a master program as reported in SNAP 29 Monthly Report INSD-2062-3110-10-68.

A study was performed which compared the results of the Monte Carlo technique with a known analytic solution. Results are documented in Report 3312-24.

The master program for the launch pad abort error analysis was completed and checked out. Thermal analyses are required to complete this study.

4. Fuel Release Characterization

Recommendations for a proposed fuel release test program were prepared and presented to the AEC in a meeting at Germantown. Conclusions reached as a result of this effort are summarized in Report 3313-81 (a summary is also found in the SNAP 29 November Monthly Progress Report, INSD-2062-3110-11-68).

5. Internal Dosimetry

A parametric analysis of the body model was completed. Results are presented in the November Monthly Progress Report. The results were reviewed at meetings with experts in the field at Battelle Northwest (see Report 3313-86). A detailed report on this effort is in progress and will be presented in the next reporting period.

6. External Dosimetry

The regulations pertinent to the mechanical and radiobiological shield design were compiled. A detailed list is presented in the December Monthly Progress Report INSD-2062-12-68.

Unshielded capsule and element dose rate calculations were initiated and will be completed during the next reporting period.

7. Failure Mode Analysis

Recommendations for the proposed solid propellant tests were prepared and transmitted to Sandia (Report 4002-36A). Meetings were attended at Sandia to assist in the planning of an accelerated solid propellant burn test program designed to be completed by February 1, 1969. Continued assistance of this test program is planned.

C. AERODYNAMIC ANALYSES AND TESTS--CONTROL POINT 3320

1. Parameter Effects on Drag of Right Circular Cylinders

Extensive source data were utilized to determine the effects of angle of attack, fineness ratio, flow regime and motion on the hypersonic drag coefficient values for right circular cylinders. Re-entry trajectories were computed for typical cylindrical burn-up configurations. The resulting average surface heating rate values, which include the effect of flow regime, were determined according to the techniques described by Klett in SC-RR-64-2141.

The continuum hypersonic drag coefficient as a function of cylinder fineness ratio (ℓ/d) and angle of attack is shown in Fig. VI-1. The values presented were obtained assuming modified Newtonian flow (pressure coefficient equal to 1.84) with empirical corrections applied according to Hoerner. This results in the equation for drag coefficient being written as

$$C_D = 1.23 \sin^3 \alpha + 1.3 (d/l) \cos^3 \alpha$$

where the reference area is equal to (ℓ) (d). It can be observed from the figure that fineness ratio effects are negligible near an angle of attack of 90 degrees (or else with the cylinder in a near side-on orientation with respect to the free stream). This is important since a cylinder is statically stable in a side-on orientation. It is also reasonable to expect a side-on, rolling re-entry mode to be a minimum heating rate configuration. If so, fineness ration effects will not need to be considered, thus greatly reducing the required data and analyses.

Figure VI-2 presents a comparison of available data with the theory. Excellent agreement was obtained between the pressure measurements in a wind tunnel and those values resulting from the modified Newtonian theory for a cylinder without a face (ℓ/d$\rightarrow\infty$). The force measurements from the wind tunnel indicate higher values of drag coefficient which are attributed to viscous effects. In the case of the low aspect ratio cylinder (AR$\approx$2.0), the data values are substantially higher than the theoretical ones at the intermediate angles of attack. This can be the result of a corner effect on the flow field which the theory does not predict. Later, it will be shown that the test conditions are possible within the vicinity of transitional flow which would explain the higher test values.

A comparison of the continuum values of drag coefficient with free molecular values (derived according to Hoerner and Klett) are shown in Fig. VI-3. This information is presented for fineness ratio values of two and infinity and as a function of angle of attack. It can be seen that the free molecular values of drag coefficient are substantially higher than those for continuum flow. The averaging effect of motion on both the free molecular and continuum values of drag coefficient is shown in Fig. VI-4. The average drag values were obtained by integrating the coefficient values of Fig. VI-3 over the angle-of-attack range of the motion assuming an angle-of-attack value of 90 degrees to be the mean of that motion. The results of Fig. VI-4 emphasize the relative large changes in drag coefficient with flow regime when compared with those due to fineness ratio and angle of attack. Since a large portion of the significant re-entry time (when the aerodynamic heat pulse is high) occurs during the transition phase between free molecular and continuum flow, the variation of drag coefficient with flow regime is an important part of the configuration burn-up analyses.

Figure VI-5 presents the value of drag coefficient for a cylinder in a side-on re-entry mode as a function of altitude. It can be seen that the limits of flow regime vary substantially for the various theories identified. Available test data values are also shown in the figure. The most conservative curve shown (the one yielding the higher drag coefficients) is being used for all heating rate estimates of the burnup configuration.

2. Fuel Element Re-entry Trajectories and Heating Rates

Figures VI-6 through VI-18 present values of average surface heating rate versus altitude as well as corresponding trajectory values in the form of altitude-velocity and altitude-time graphs for various element burnup design values of weight and dimension. Results are presented for initial flight path angles of -0.1 and -3.0 degrees

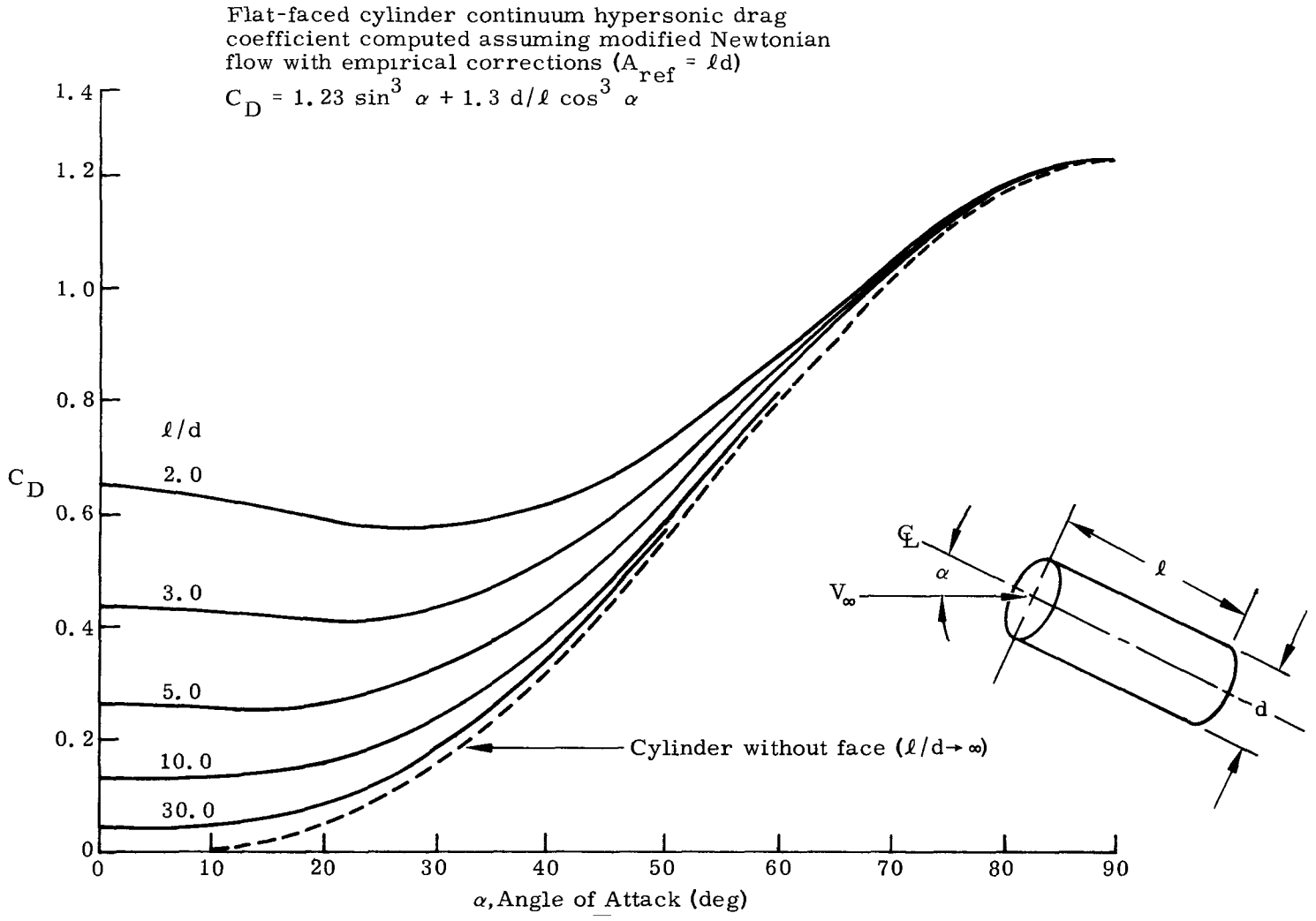

FIG. VI-1. EFFECT OF LENGTH TO DIAMETER RATIO

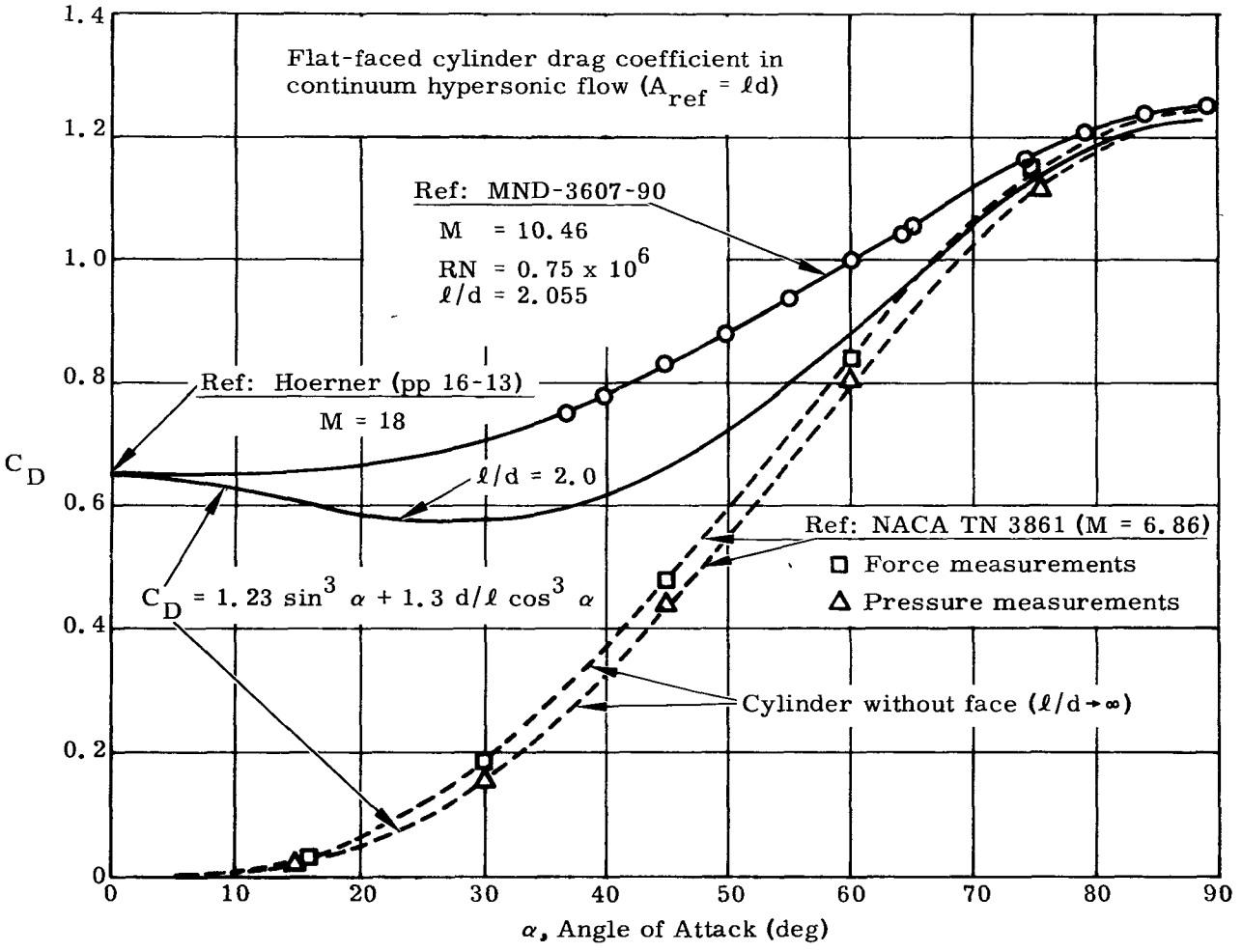

FIG. VI-2. COMPARISON OF DATA WITH THEORY

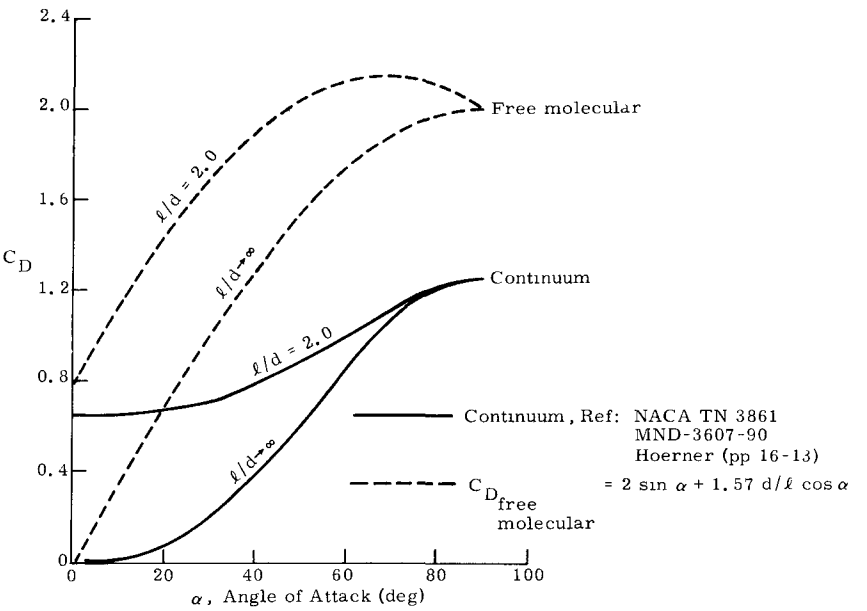

FIG. VI-3. COMPARISON OF CONTINUUM HYPERSONIC AND FREE MOLECULAR DRAG COEFFICIENTS FOR FLAT FACED CYLINDERS ($A_{ref} = \ell d$)

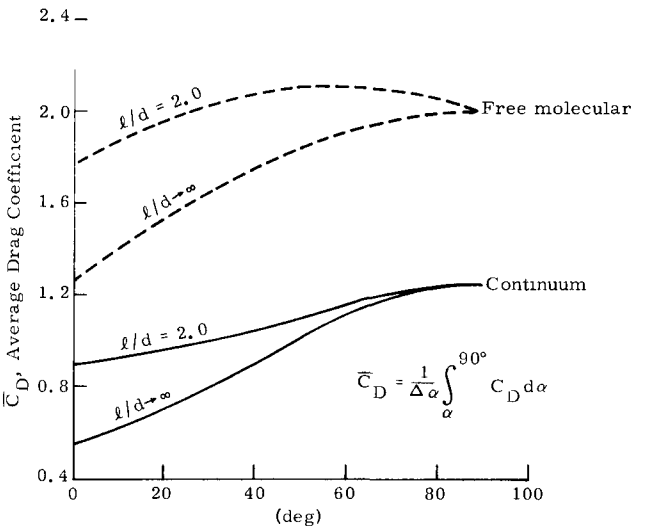

Note: When $\alpha' = 0$, cylinder is tumbling end-over-end.
α' - Minimum angle of attack resulting from oscillating or coning motion about α = 90 degrees (α' 90 - $\Delta\alpha$)

FIG. VI-4. COMPARISON OF AVERAGE CONTINUUM HYPERSONIC AND FREE MOLECULAR DRAG COEFFICIENTS FOR FLAT FACED CYLINDERS AS FUNCTION OF ANGLE OF ATTACK DEVIATION ABOUT TRIM VALUE OF 90 DEGREES ($A_{ref} = \ell d$)

CONFIDENTIAL

$W/C_D A_{ref} \approx 10$ lb/ft^2
$V_{entry} = 25,690$ fps

1962 U. S. Standard Atmosphere

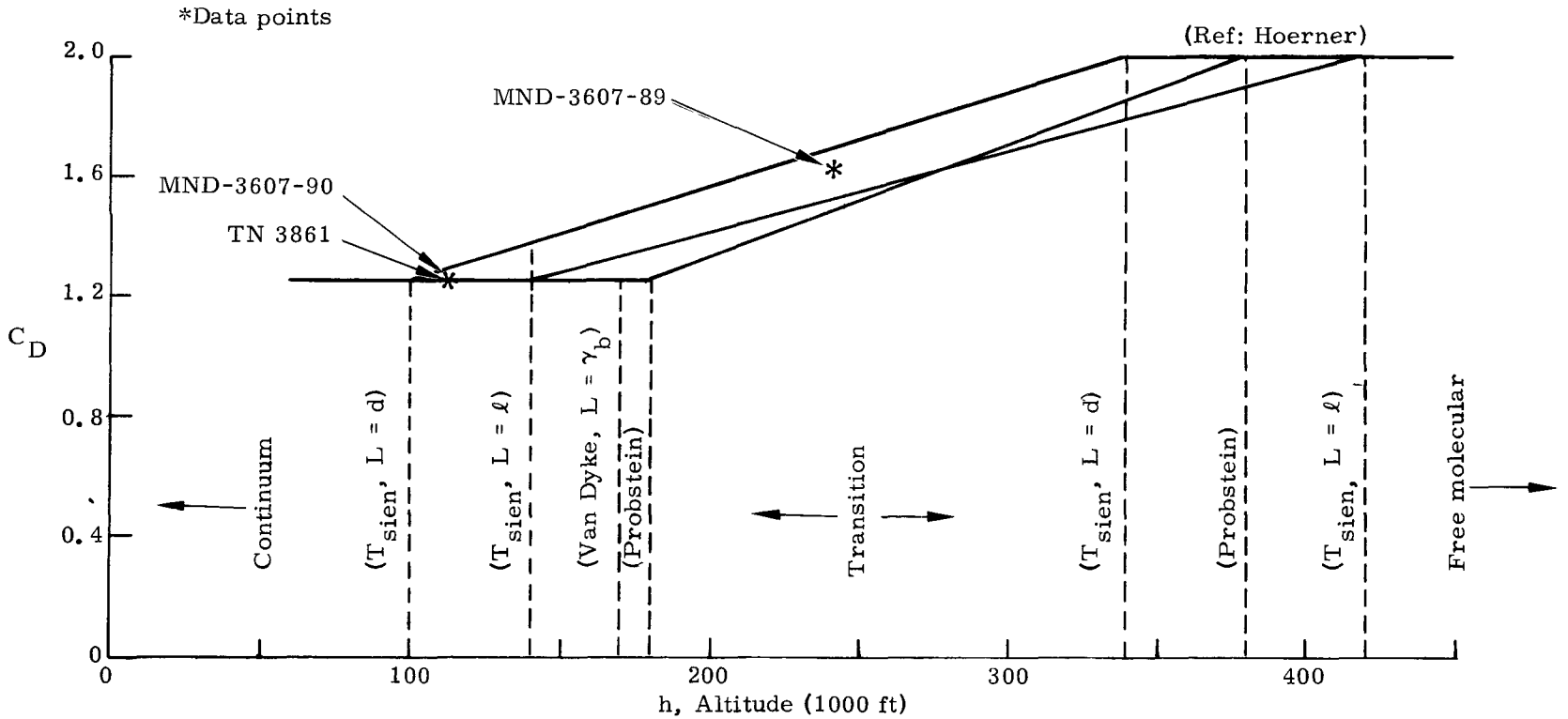

FIG. VI-5. CYLINDER SIDE-ON DRAG COEFFICIENT VERSUS ALTITUDE

CONFIDENTIAL

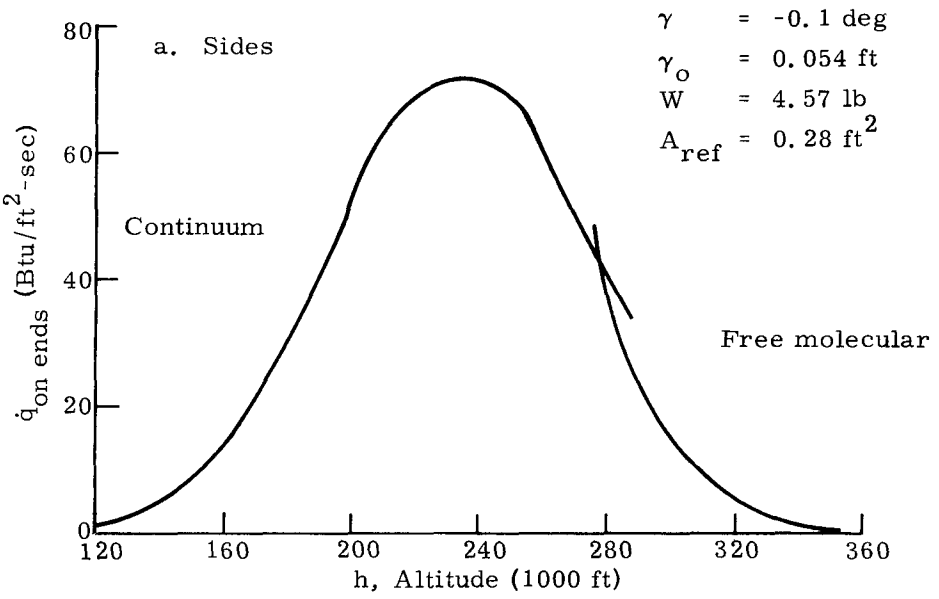

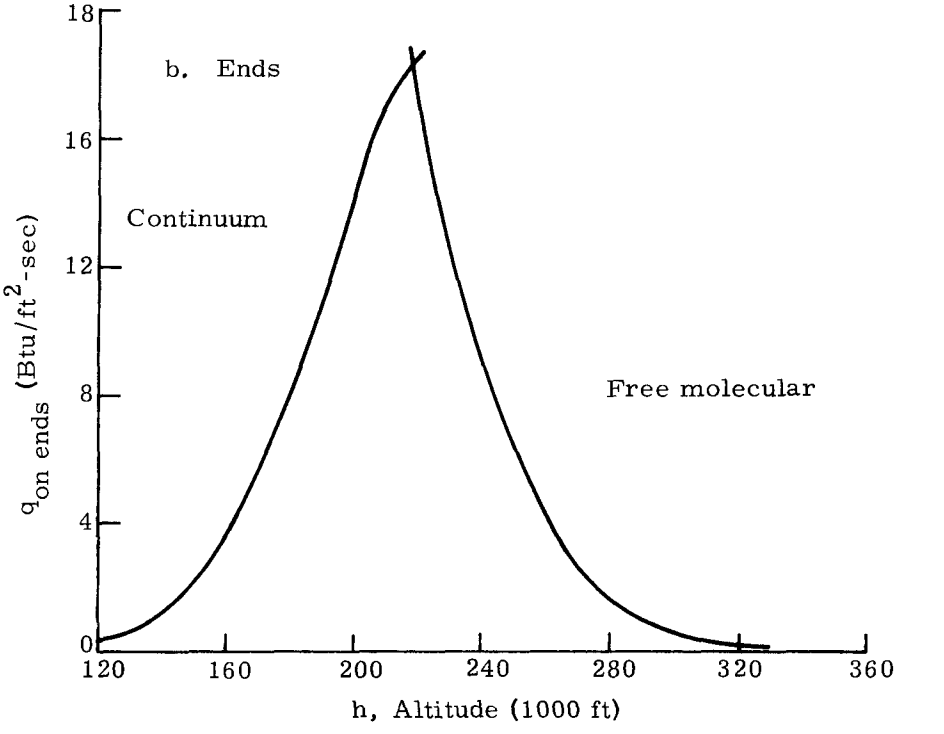

FIG. VI-6. AVERAGE SURFACE HEATING RATE VERSUS ALTITUDE FOR CYLINDER RE-ENTERING WITH SIDE-ON ROLL

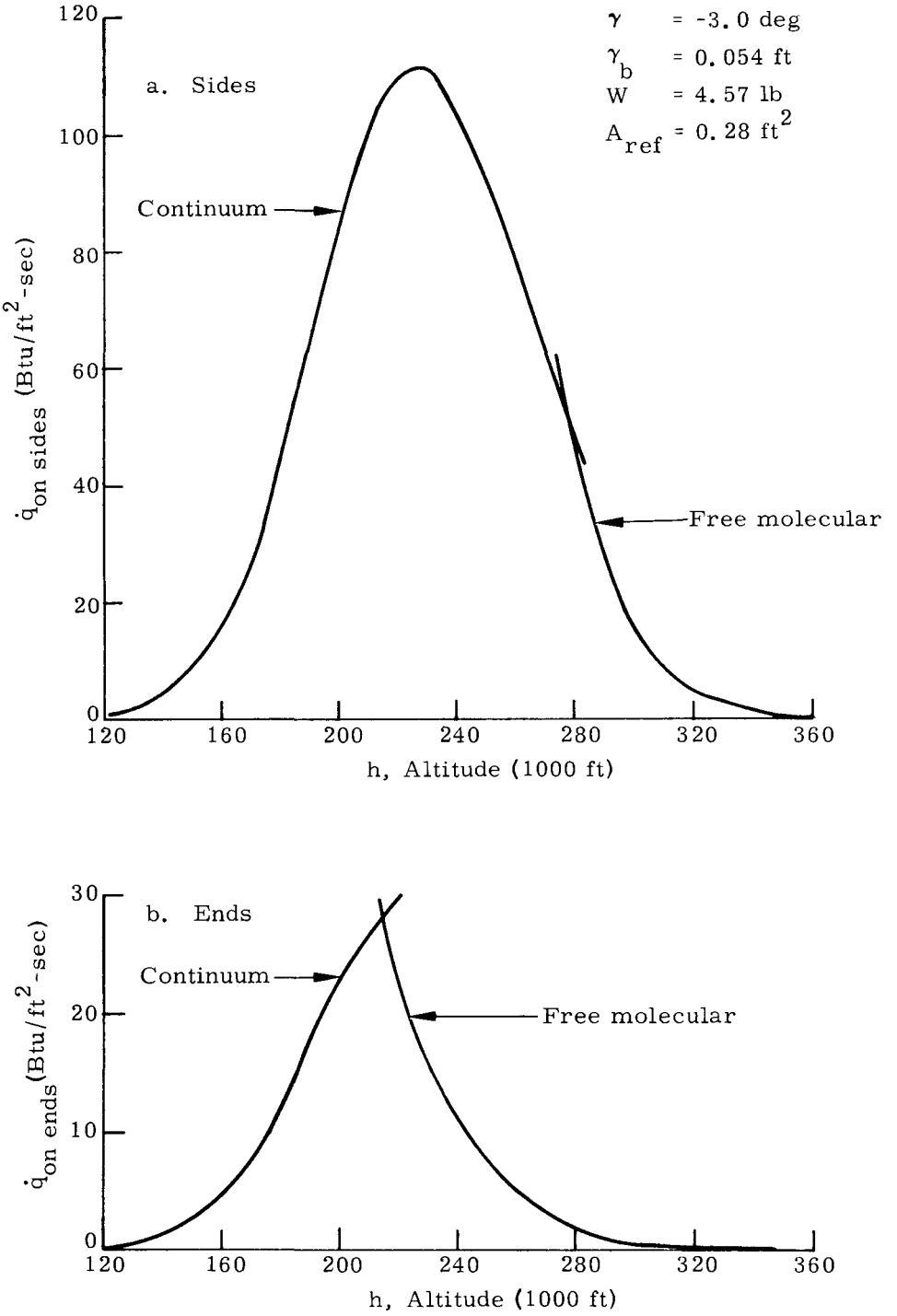

FIG. VI-7. AVERAGE SURFACE HEATING RATE VERSUS ALTITUDE FOR CYLINDER RE-ENTERING WITH SIDE-ON ROLL

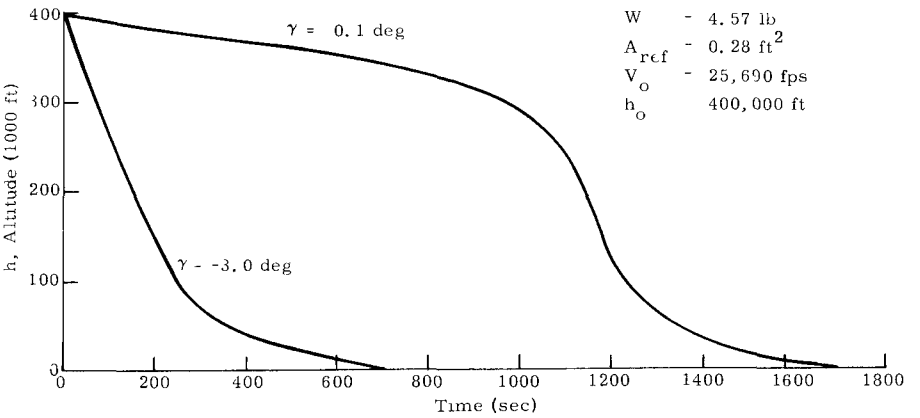

FIG. VI-8. ALTITUDE VERSUS TIME CYLINDERS RE-ENTERING WITH SIDE-ON ROLL

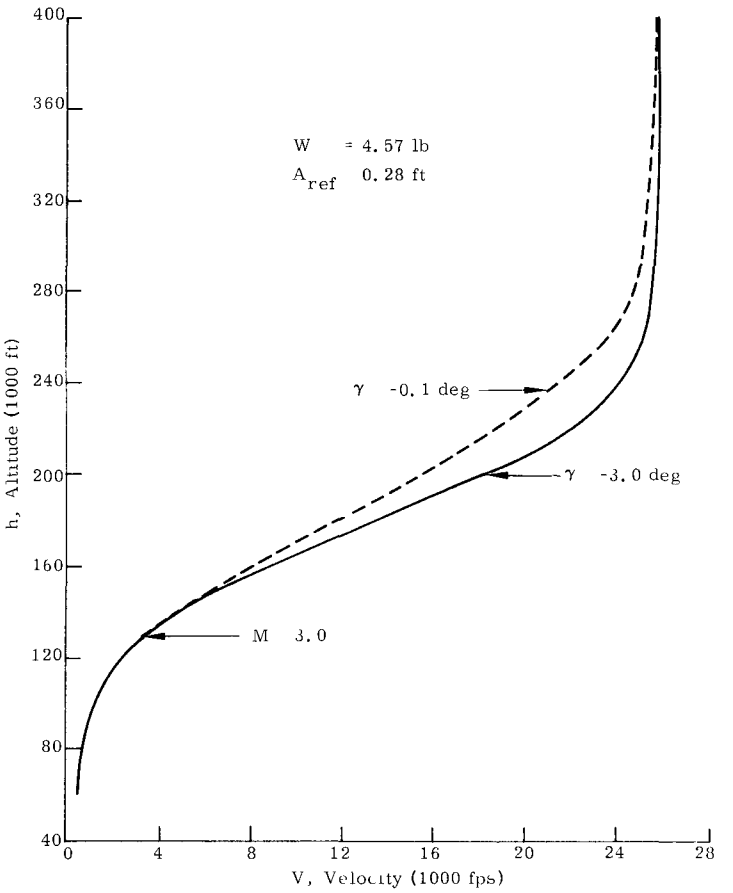

FIG. VI-9. ALTITUDE VERSUS VELOCITY PROFILE FOR CYLINDER RE-ENTERING WITH SIDE-ON ROLL

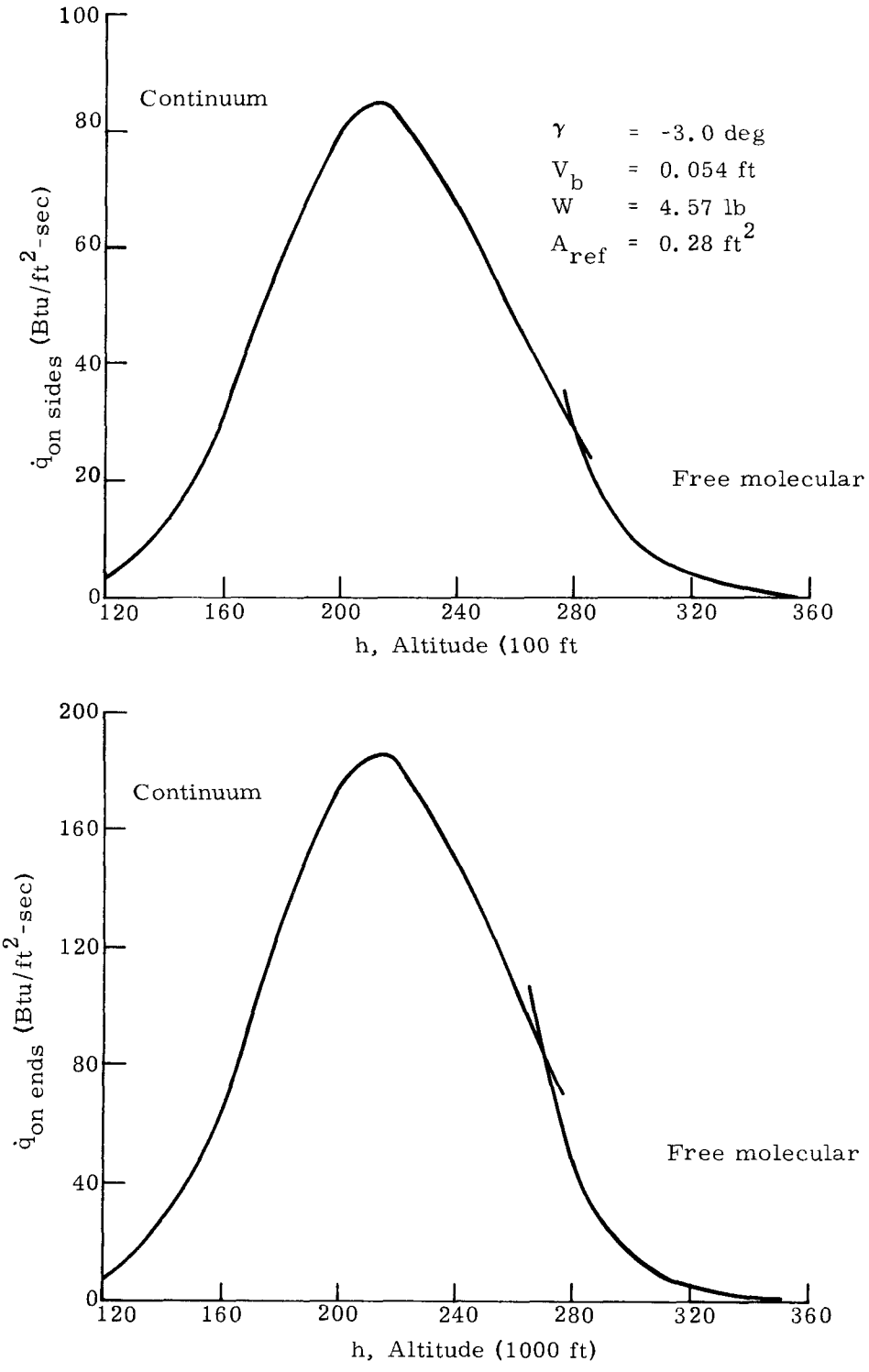

FIG. VI-10. AVERAGE SURFACE HEATING RATE VERSUS ALTITUDE FOR CYLINDER, ℓ/d = 23.9, RE-ENTERING WITH ROLLING END-OVER-END TUMBLE

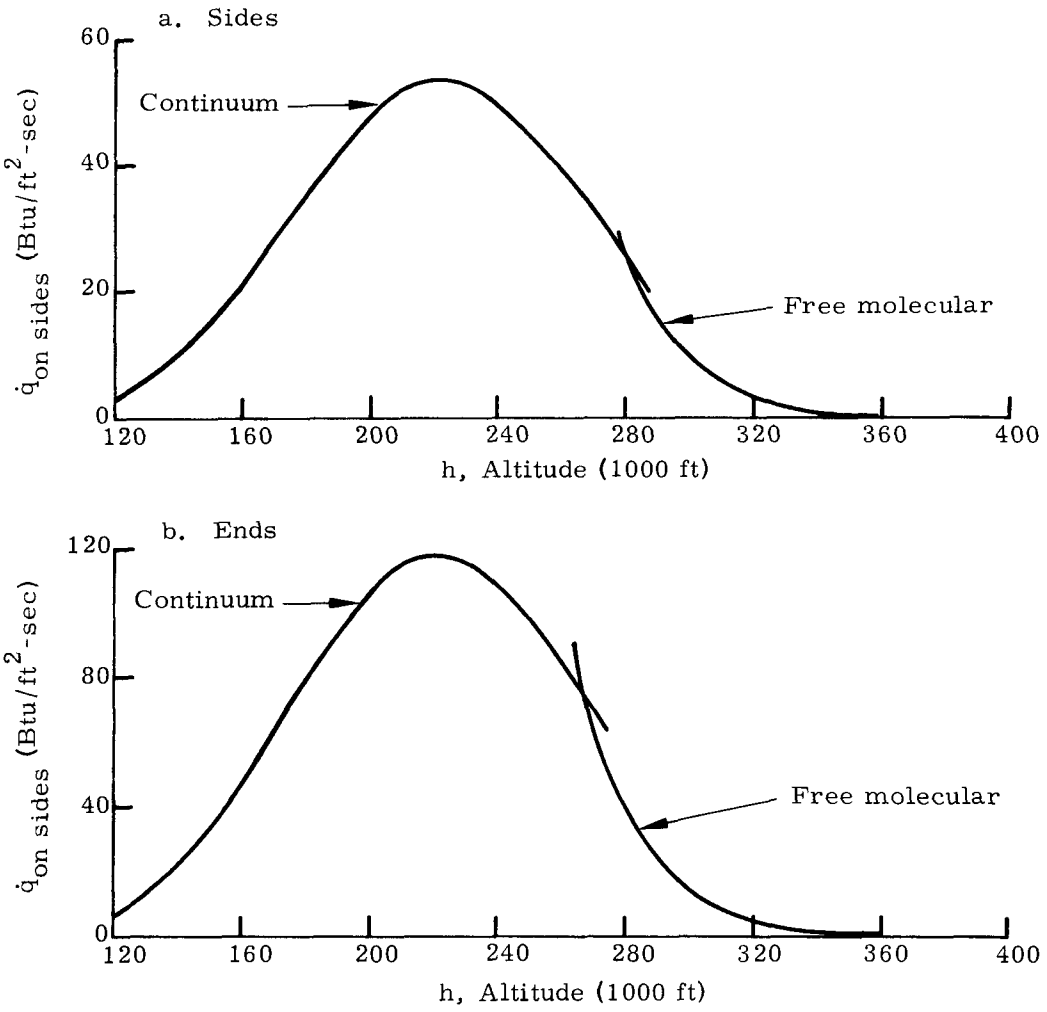

FIG. VI-11. AVERAGE SURFACE HEATING RATE VERSUS ALTITUDE FOR CYLINDER, ℓ/d = 23.9, RE-ENTERING WITH ROLLING END-OVER-END TUMBLE

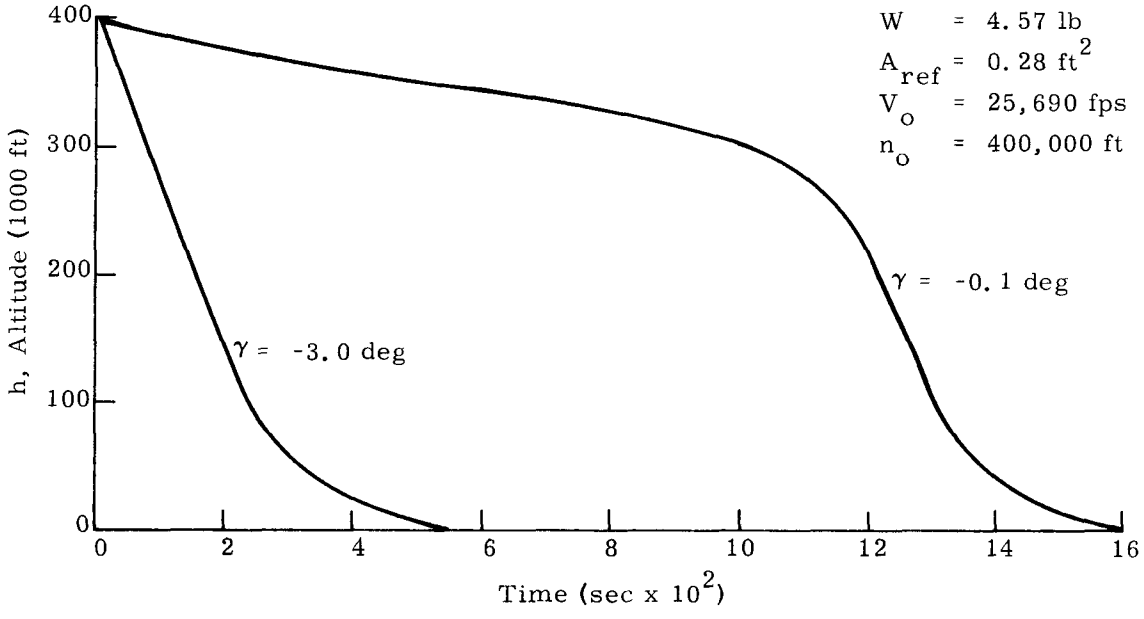

FIG. VI-12. ALTITUDE VERSUS TIME FOR CYLINDER RE-ENTERING WITH ROLLING END-OVER-END TUMBLE

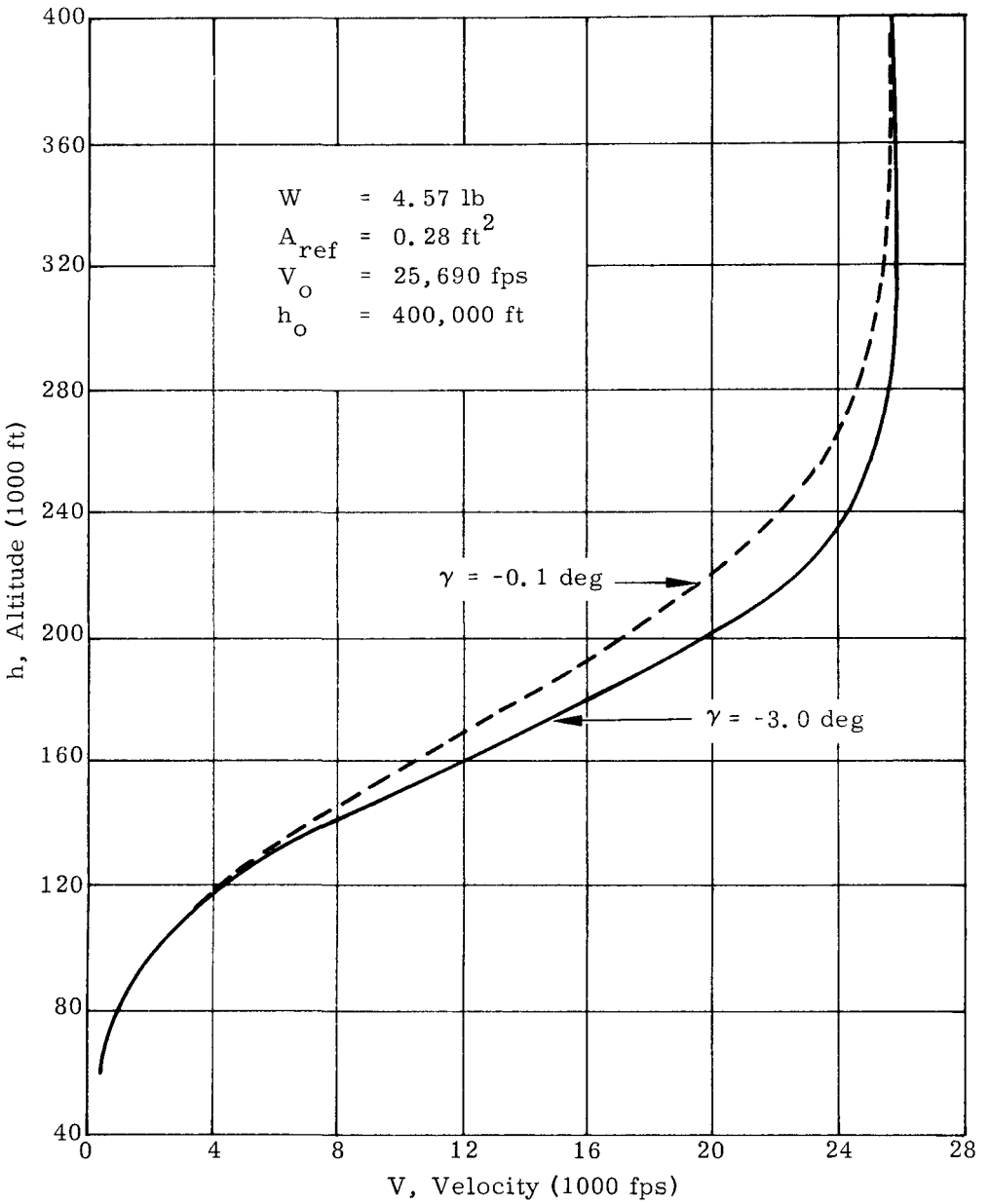

FIG. VI-13. ALTITUDE VERSUS VELOCITY FOR CYLINDER RE-ENTERING WITH ROLLING END-OVER-END TUMBLE

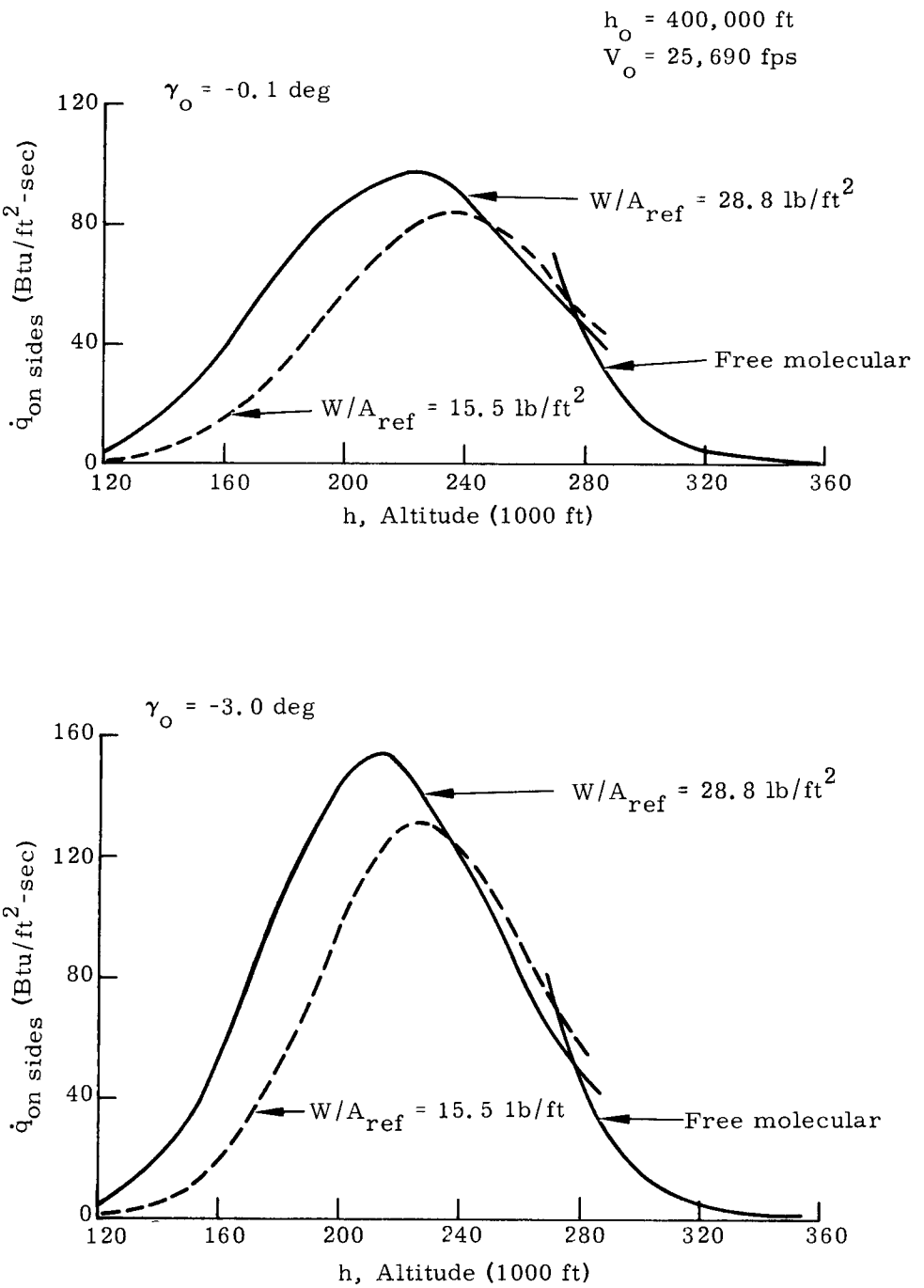

FIG. VI-14. AVERAGE SURFACE HEATING RATE OVER SIDE OF CYLINDER RE-ENTERING WITH SIDE-ON ROLL

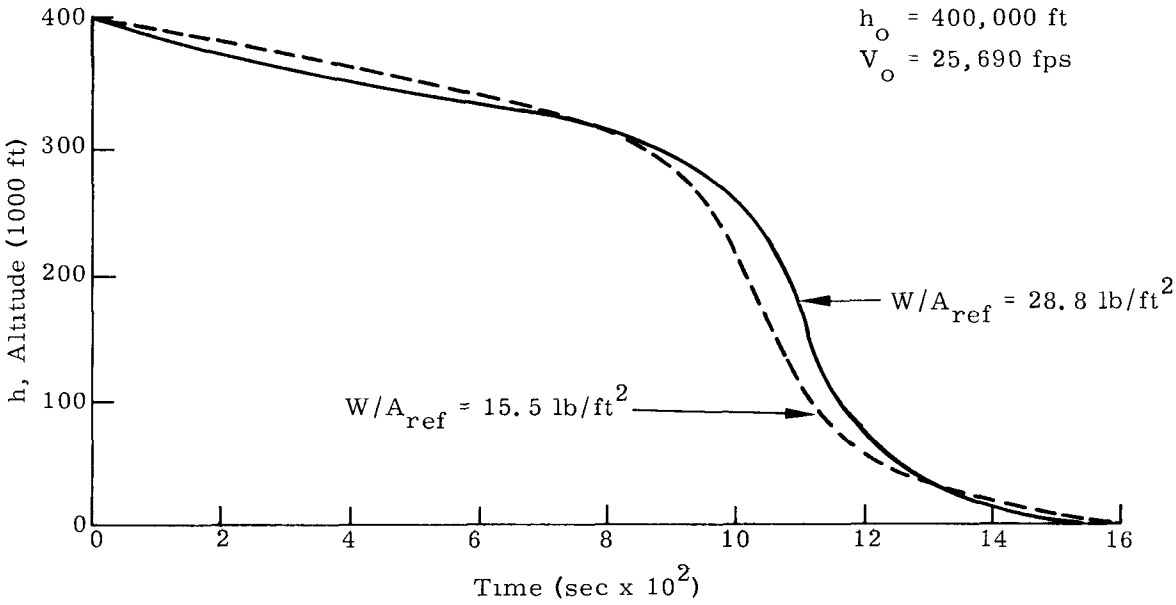

FIG. VI-15. ALTITUDE VERSUS TIME FOR CYLINDER RE-ENTERING WITH SIDE-ON ROLL, γ = -0.1 DEGREE

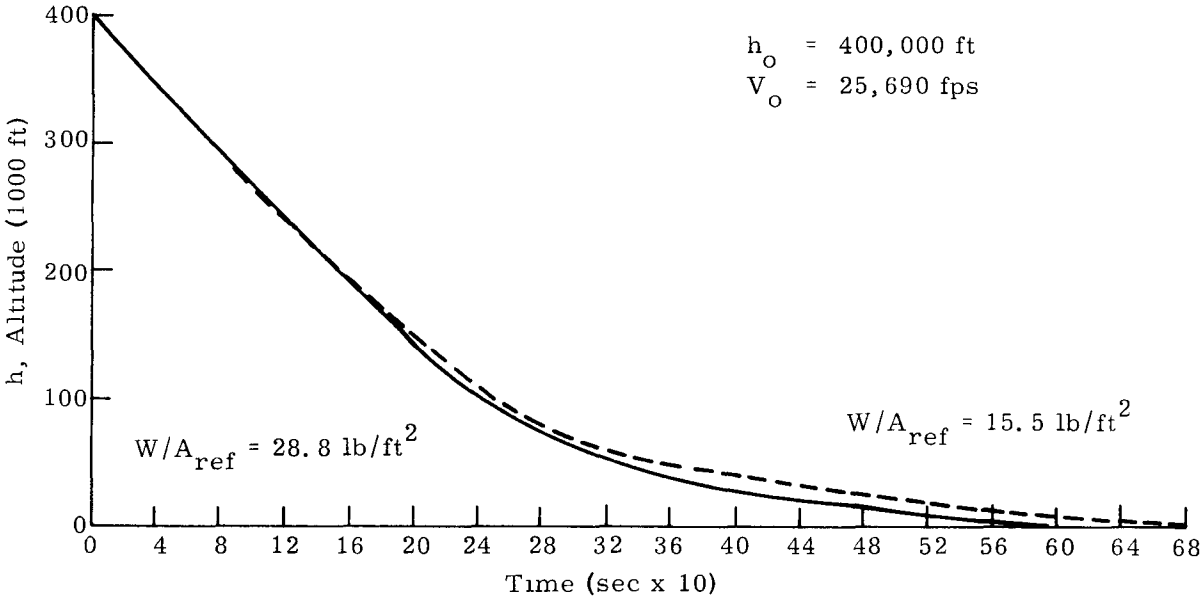

FIG. VI-16. ALTITUDE VERSUS TIME FOR CYLINDER RE-ENTERING WITH SIDE-ON ROLL, γ = -3.0 DEGREES

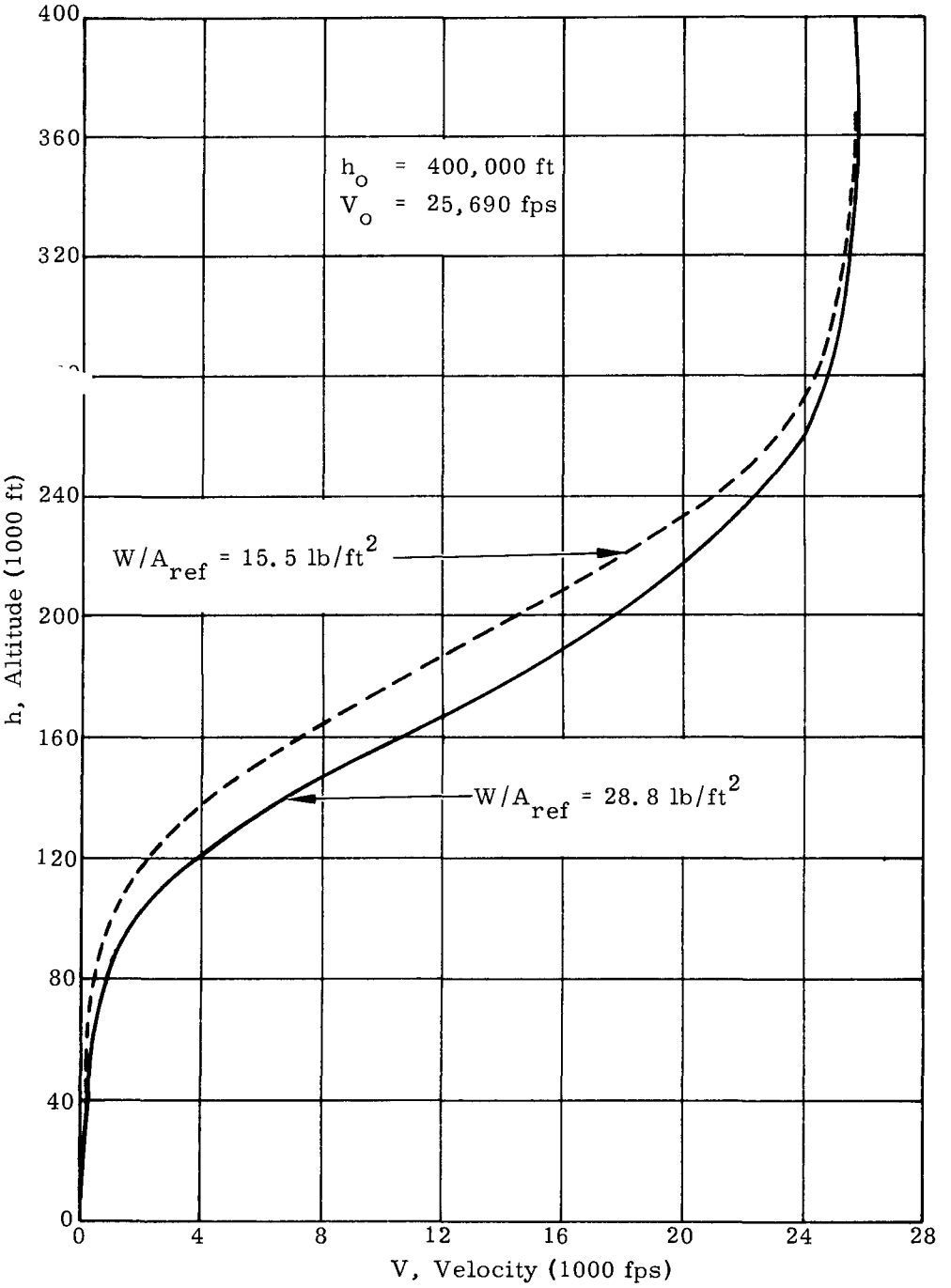

FIG. VI-17. ALTITUDE VERSUS VELOCITY FOR CYLINDER RE-ENTERING WITH SIDE-ON ROLL

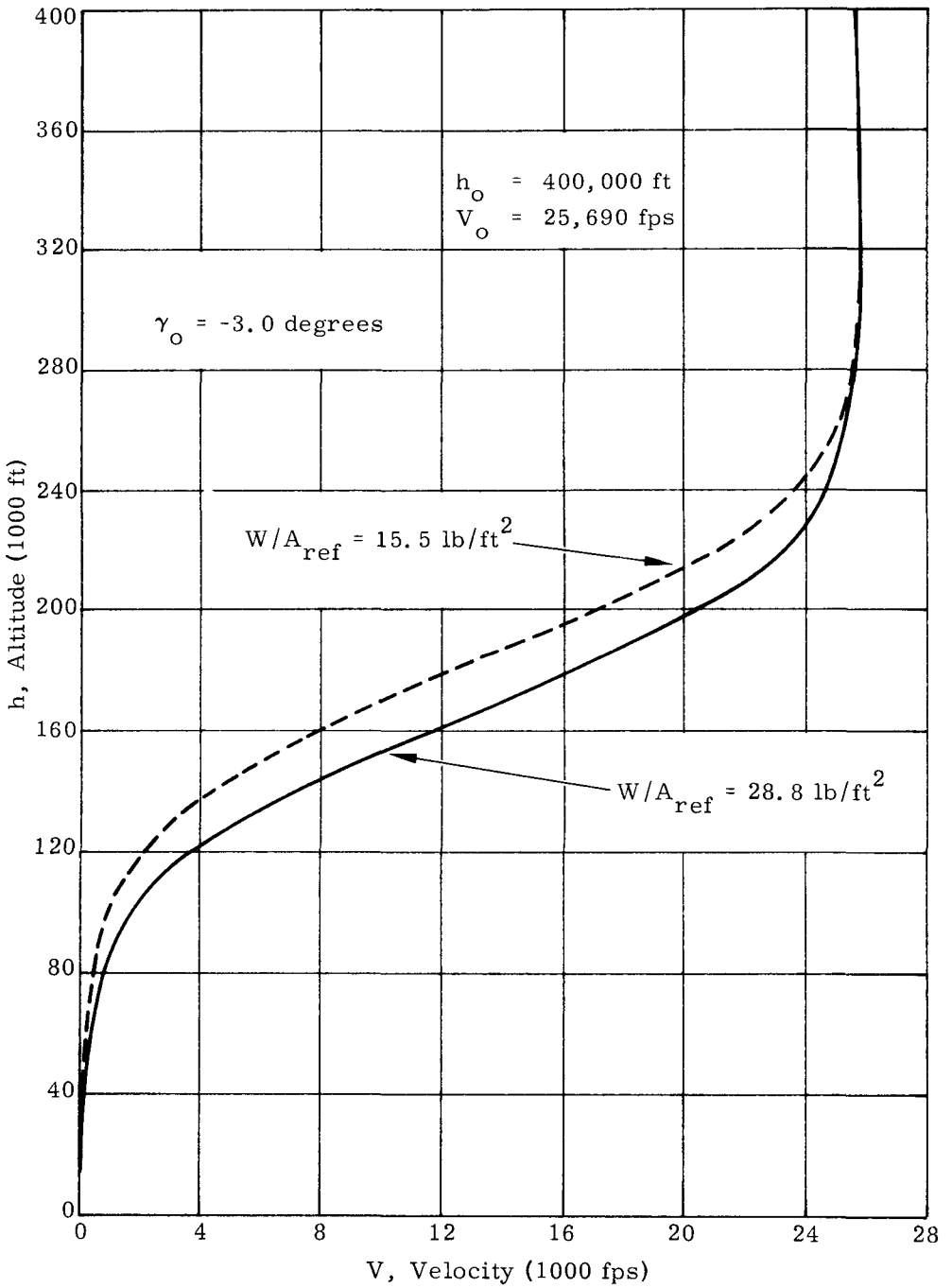

FIG. VI-18. ALTITUDE VERSUS VELOCITY FOR CYLINDER RE-ENTERING WITH SIDE-ON ROLL

corresponding to initial re-entry altitude and velocity conditions of 400,000 feet and 25,690 fps. Heating rate values for both free molecular and continuum flow were computed. The free molecular values were treated according to Klett in SC-RR-64-2141.

Figures VI-6 through VI-13 present data for a beryllium fuel element (Configuration II.C.1(e)) for both the side-on roll and tumbling modes of re-entry. This configuration has a weight of 4.57 pounds and a diameter of 1.3 inches. In the case of a side-on roll mode of re-entry, the heating on the ends of the element is shown to be relatively low when compared to the sides. However, for the tumbling mode, the heating on the ends increases and is higher than that over the sides. Figures VI-14 through VI-18 give data for a stainless steel fuel element (weight = 7.45 pounds; diameter = 1.2 inches) when re-entering with a side-on roll motion. Two heating rate curves are presented to show the limits of heating rate between the initial element configuration (solid line) and that configuration which exists just prior to the exposure of the capsules (dashed line). The largest differences in heating rate for the two configurations considered occur at the lower altitude levels.

3. Ascent Abort Study

Ascent abort conditions were simulated by assuming a typical Titan III boost trajectory with an Agena stage. A southward launch from the Western Test Range was assumed, with Titan stages 0, I, and II burning prior to first orbital injection. The Agena is ignited at suborbital velocities, and orbital injection occurs at about 100 nautical miles (perigee). A coast in a transfer orbit follows. Re-ignition of the Agena provides injection into the final orbit. A typical sequence of events is shown in Table VI-1. Altitude as a function of ground range along with velocity and altitude time history traces are shown in Fig. VI-10 for the ascent trajectory.

Six assumed abort points, usually at the time of a discrete functional event during the ascent, were chosen and are designated in Table VI-1. In each abort the complete element was assumed to be thrown completely free of the launch vehicle. The ground range traces of the abort element are shown in Fig. VI-19. Continuum stagnation point heating rates and trajectory values of altitude and velocity are presented as a function of time in Figs. VI-20 through VI-22. These data were computed for an element weight of 8.2 pounds and reference area of 0.25 ft^2.

4. Fuel Matrix Trajectories, Heating Rates and Pressures

Re-entry trajectories and surface heating rates and pressures were determined for a fuel matrix that was assumed to have been thrown free from the fuel element during re-entry of the burn-up configuration. Two sets of initial conditions were selected as being representative of where melting of the fuel element inner liner occurs when entering the Earth's atmosphere at initial flight path angles of -3.0 and -0.1 degrees. The element was assumed to re-enter in a side-on rolling mode relative to the air stream to provide a conservative analysis of the burnup concept. The corresponding initial conditions for the fuel matrix were computed to be as follows:

h_o (ft)	230,000	260,000
V_o (fps)	23,000	23,500
γ_o (deg)	-3.2	-1.35

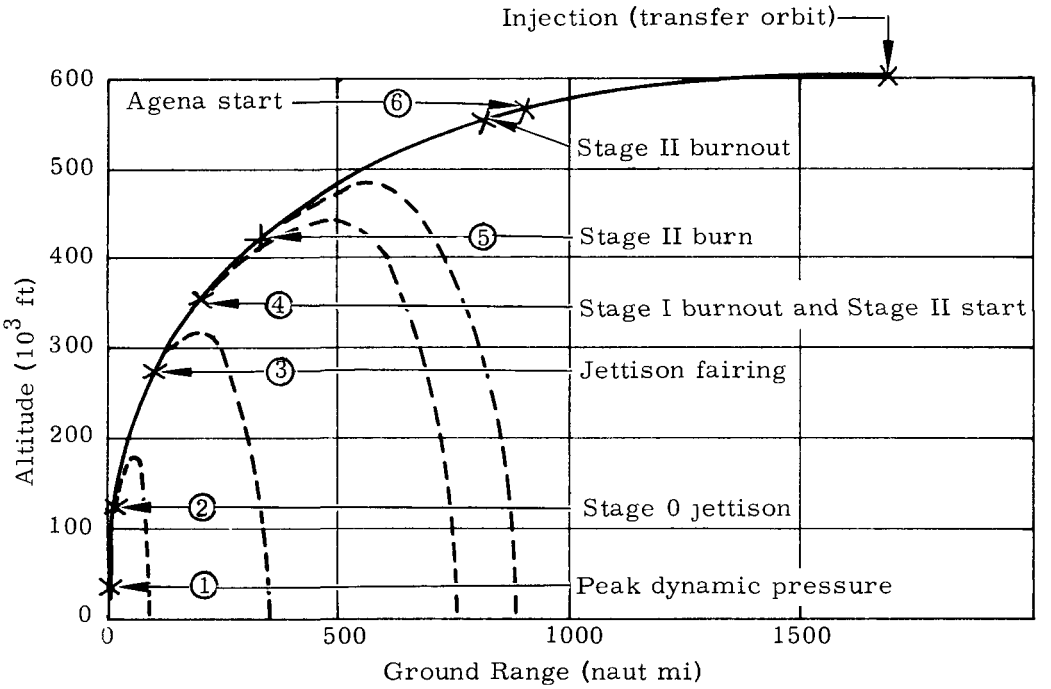

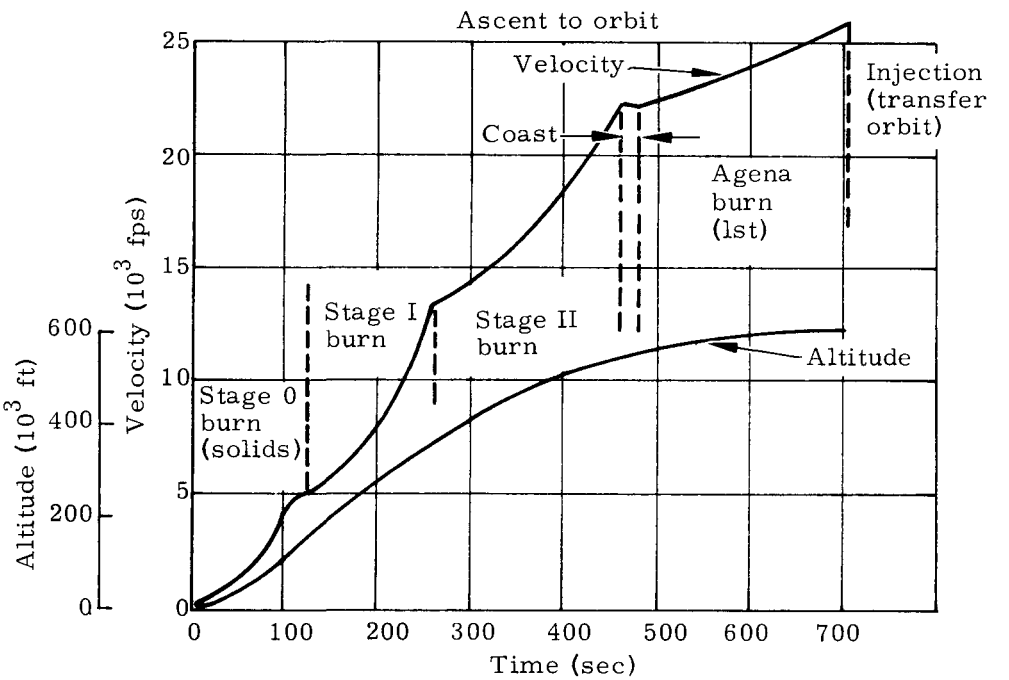

FIG. VI-19. GROUND RANGE TRACES OF ABORT ELEMENT

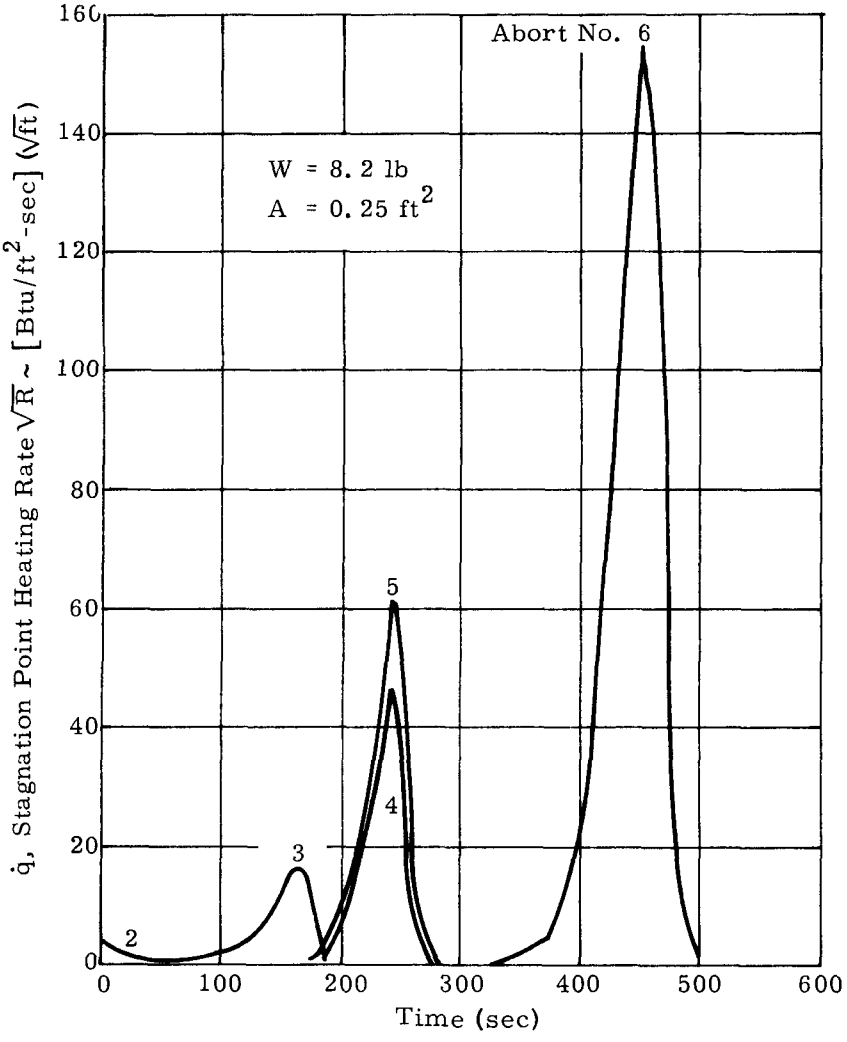

FIG. VI-20. CONTINUUM STAGNATION POINT HEATING RATE SNAP 29 BURN-UP ELEMENT

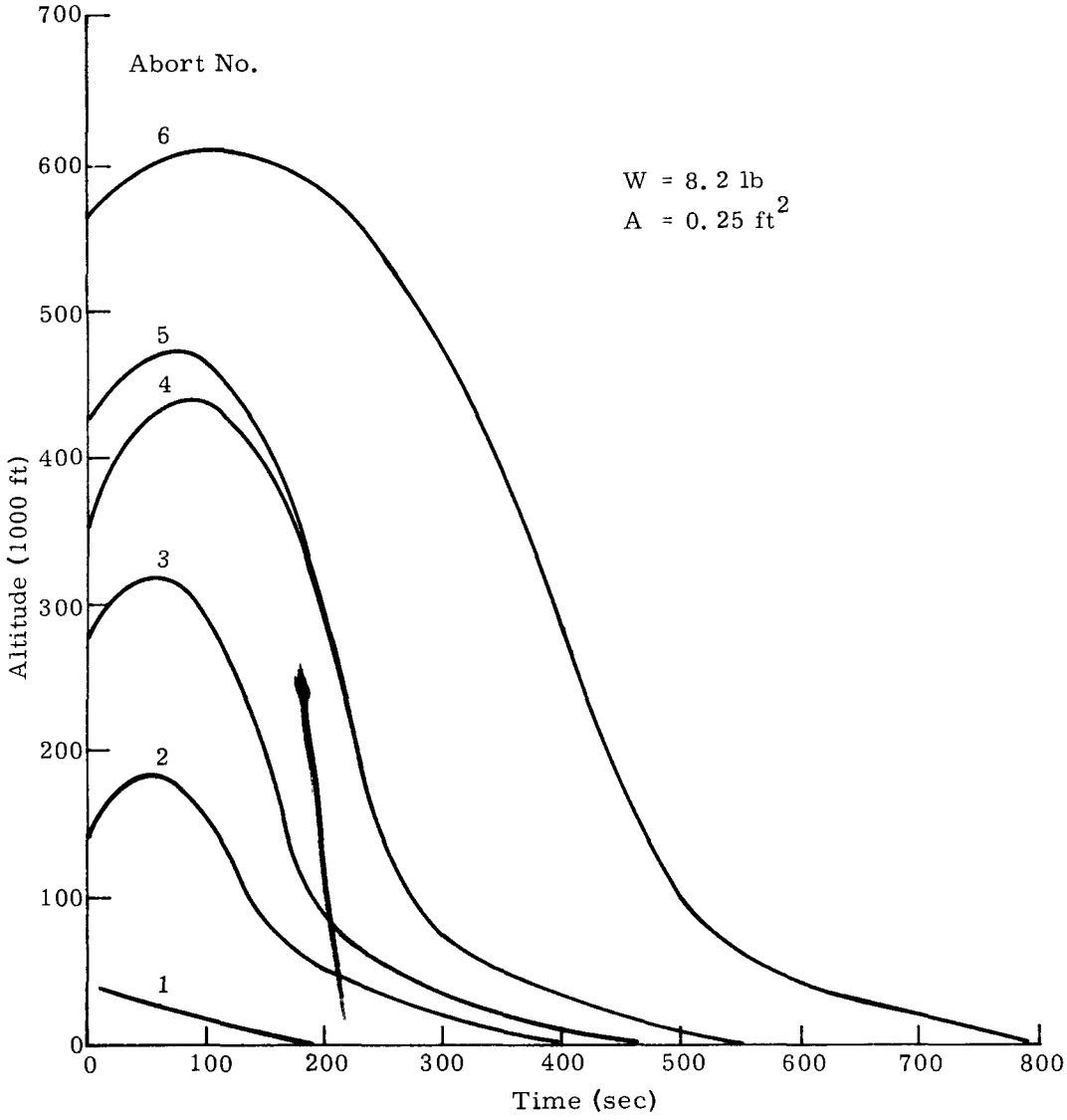

FIG. VI-21. ALTITUDE VERSUS TIME--SNAP 29 BURN-UP ELEMENT

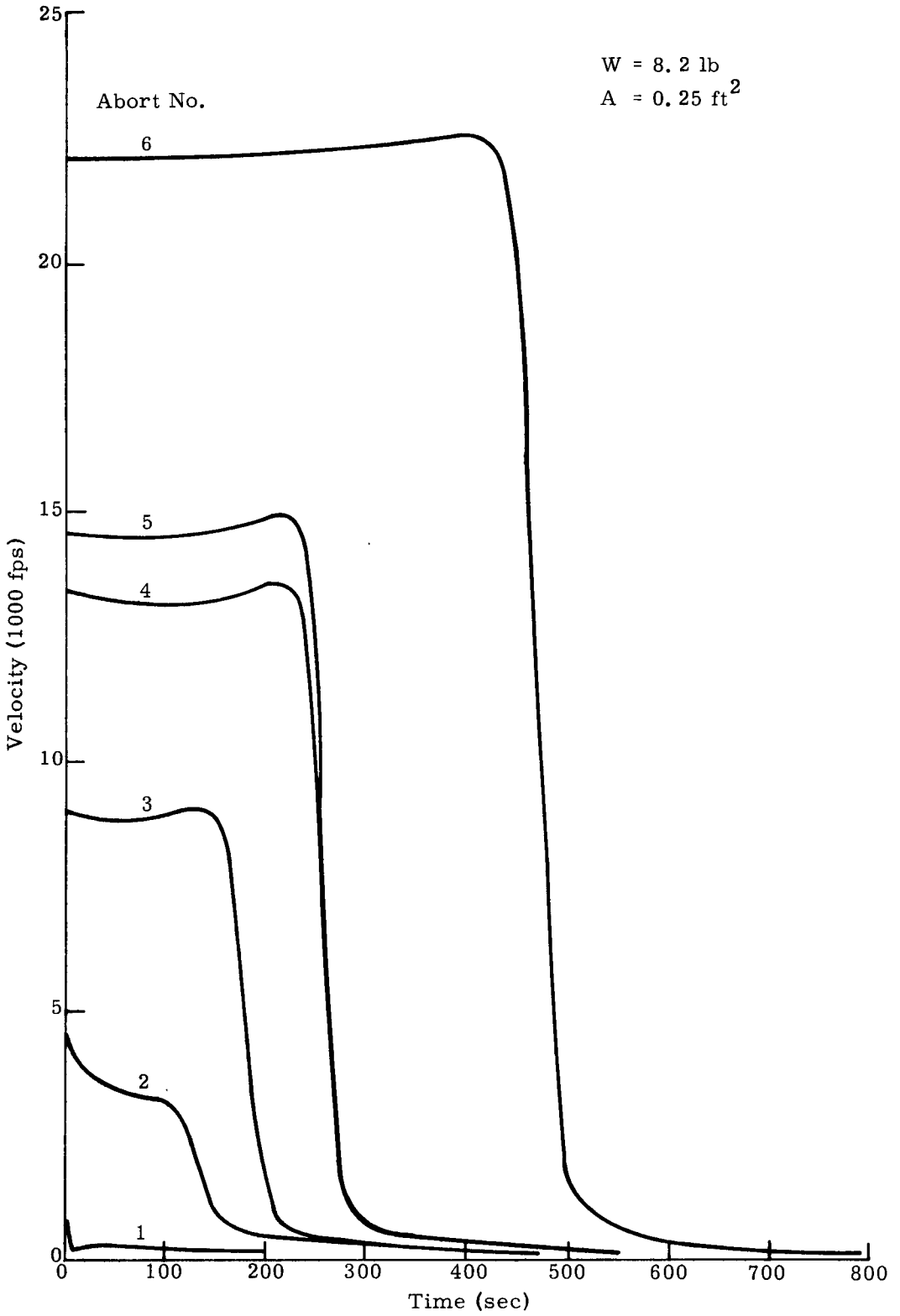

FIG. VI-22. VELOCITY VERSUS TIME--SNAP 29 BURN-UP ELEMENT

TABLE VI-1

Ascent to Orbit

Abort No.	Event	Comments	Time (sec)	Velocity (fps)	Flight Path Angle (deg)	Altitude (1000 ft)	Range (naut mi)	Weight (1000 lb)	Designation
	Liftoff	Stage 0 (solids)	0	0	90	0	0	1409	A
			12	259	89.6	1.89	0	1293	
		$Q = 664$ lb/ft^2	40	1006	65.3	18.5	1	1041	
1		$Q = 846$ lb/ft^2	56	1503	53.3	35.5	2.55	914	
		$Q = 501$ lb/ft^2	80	2575	37.9	69	8.1	738	
			104	4125	28.0	111	19.1	578	
2	Stage 0 jettison		119.26	4750	23.2	140	26.2	524	B
	Stage I start	Stage I	119.26	4750	23.2	140	26.2	360	
			160	6248	14.4	209	63.6	291	
3		Jett Fair T-IIID	210	9008	9.2	281	123	206	
	Stage I burnout		258.23	13324	8.2	357	207	125	C
4	Stage II start	Stage II	258.23	13324	8.2	357	207	109	
5			300	14596	5.6	423	309	96.7	
			352	16497	3.4	482	444	79.6	
			400	18680	2.2	519	589	63.8	
	Stage II burnout		461.2	22280	2.0	558	795	43.5	D
6	Stage III separate	Coast	461.2	22280	2.0	558	795	37.2	
	Stage III start	Agena	481.2	22180	2.0	570	868	37.2	
			585.2	23720	1.0	600	1259	31.3	
		Circular velocity	689.2	25560	0	607	1638	25.6	
	Stage III shutdown	Injection	701.9	25820	0	608	1692	24.9	E
	Start transfer	Transfer orbit	701.9	25820	0	608	1692	24.9	
	Finish transfer		3422	24783	0	1520	12492	24.9	
	Stage III start (2)	Agena apogee	3422	24783	0	1520	12492	24.9	F
	Stage III shutdown	Circular orbit	3434.7	25043	0	1520	12545	24.2	

CONFIDENTIAL

CONFIDENTIAL

The fuel matrix had the following physical characteristics:

Shape	Ring
Inner diameter (in.)	0.642
Outer diameter (in.)	0.746
Width (in.)	0.25
Weight (lb)	0.01
Reference area (ft^2)	0.0013

Continuum values of drag coefficient were used, resulting in a hypersonic ballistic coefficient of 6.15 lb/ft^2.

The fuel matrix trajectory data for an element initial flight path angle of -3.0 degrees are shown in Fig. VI-23 while the associated average surface heating rates and pressure time histories are shown in Fig. VI-24. Comparable data for an element initial flight path angle of -0.1 degree are presented in Figs. VI-25 and VI-26, respectively.

5. Wind Tunnel Test Program--Burn-Up Design

A program of proposed aerodynamic-aerothermodynamic tests was prepared. A tentative selection of test facilities, model scales, material requirements and instrumentation locations was made. Test schedules and manpower and travel estimates were made for the projected program plan.

6. Wind Tunnel Test Programs--Intact Design

The final report on the free flight test of the four-module fuel block was completed (Drawing 466A3322682) as was the final report on the low density force and moment test (Drawing 466A3322681). The principal results of these tests were presented and discussed in the Eighth Quarterly Progress Report.

Some typical aerodynamic damping data from the forced oscillation test are shown in Fig. VI-27. Measurements were made at total angles of attack from 74 to 90 degrees and all test data show the fuel block to be dynamically stable and statically unstable in this angle range. Static aerodynamic instability in this near edge-on angle range agrees with earlier force and moment testing. The region of static stability is, of course, near the side-on flight condition. The aerodynamic damping parameter increases with increasing Reynolds number and also increases as the fuel block moves away from the edge-on attitude. The final test report on the forced oscillation test has been completed in draft form and has been reviewed.

The final report on the rotating force and pitch, roll and yaw damping tests has been completed in draft form. The aerodynamic damping coefficients that were measured during these tests were presented and discussed in the Eighth Quarterly Progress Report.

Scorch models bearing representative aerodynamic heating patterns are shown in Figs. VI-28 and VI-29. It can be seen from these figures that rotation very effectively distributes the heat load over the fuel block. However, whether rotating or not, the highest heating is on or near the edges. High speed motion pictures, taken during the scorch test, are being analyzed to obtain some quantitative heating data from the scorch test.

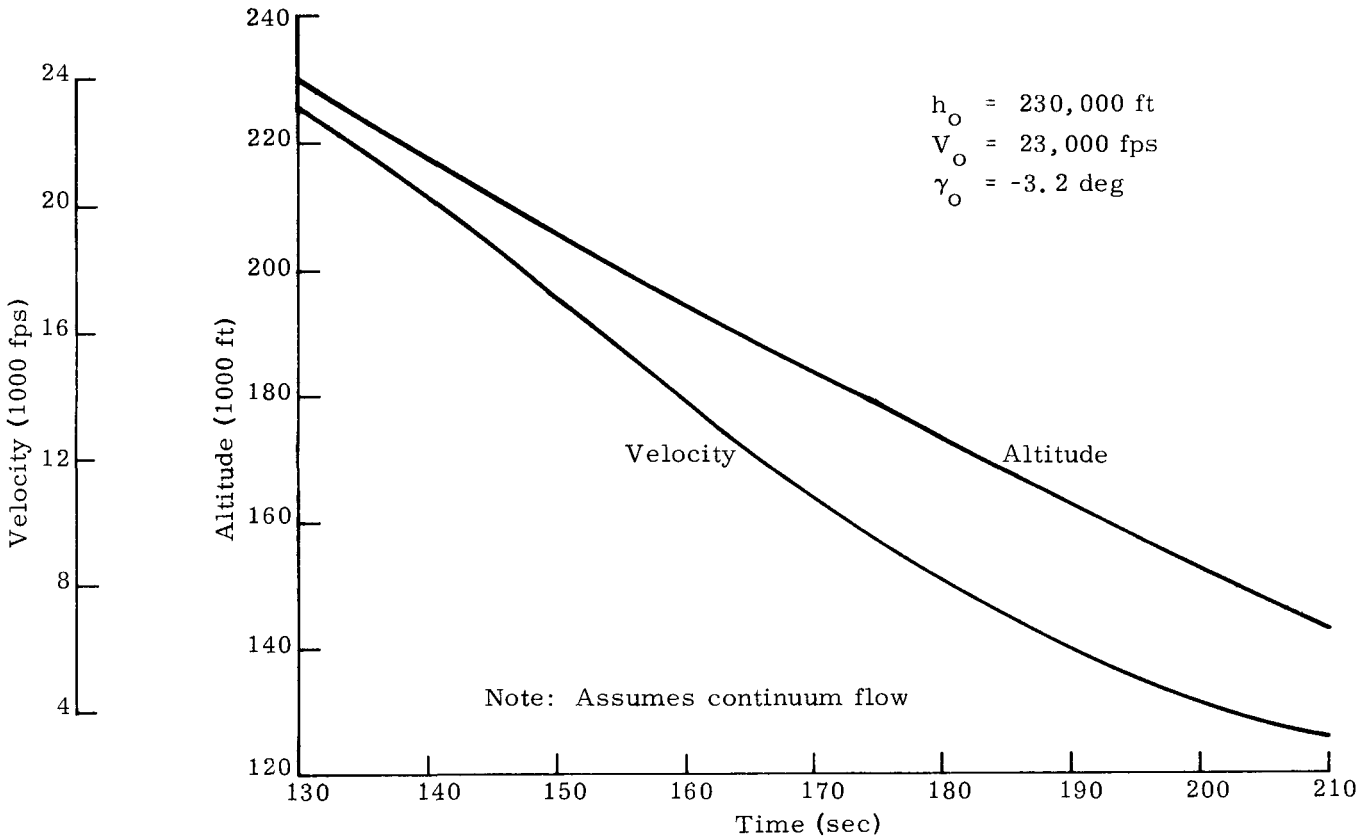

FIG. VI-23. VELOCITY AND ALTITUDE TIME HISTORIES--SNAP 29 FUEL MATRIX COMPONENT DURING RE-ENTRY

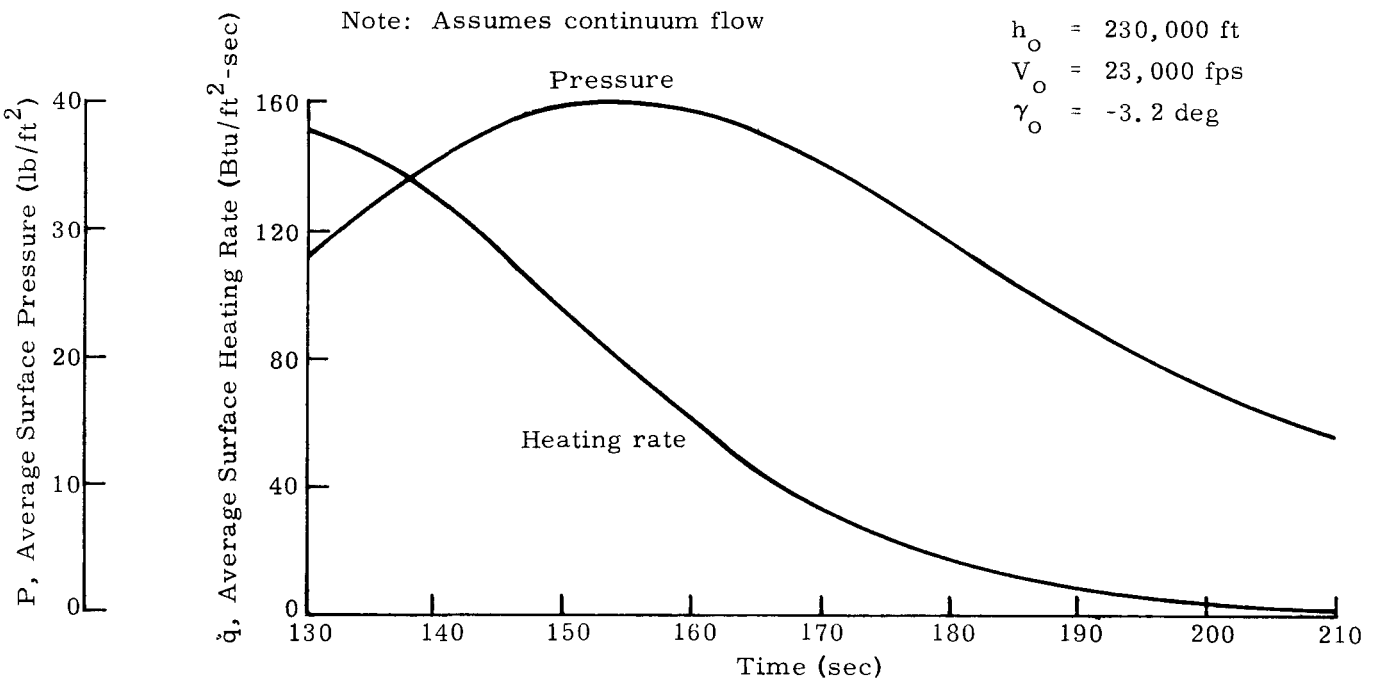

FIG. VI-24. PRESSURE AND HEATING RATE TIME HISTORIES--SNAP 29 FUEL MATRIX COMPONENT DURING RE-ENTRY

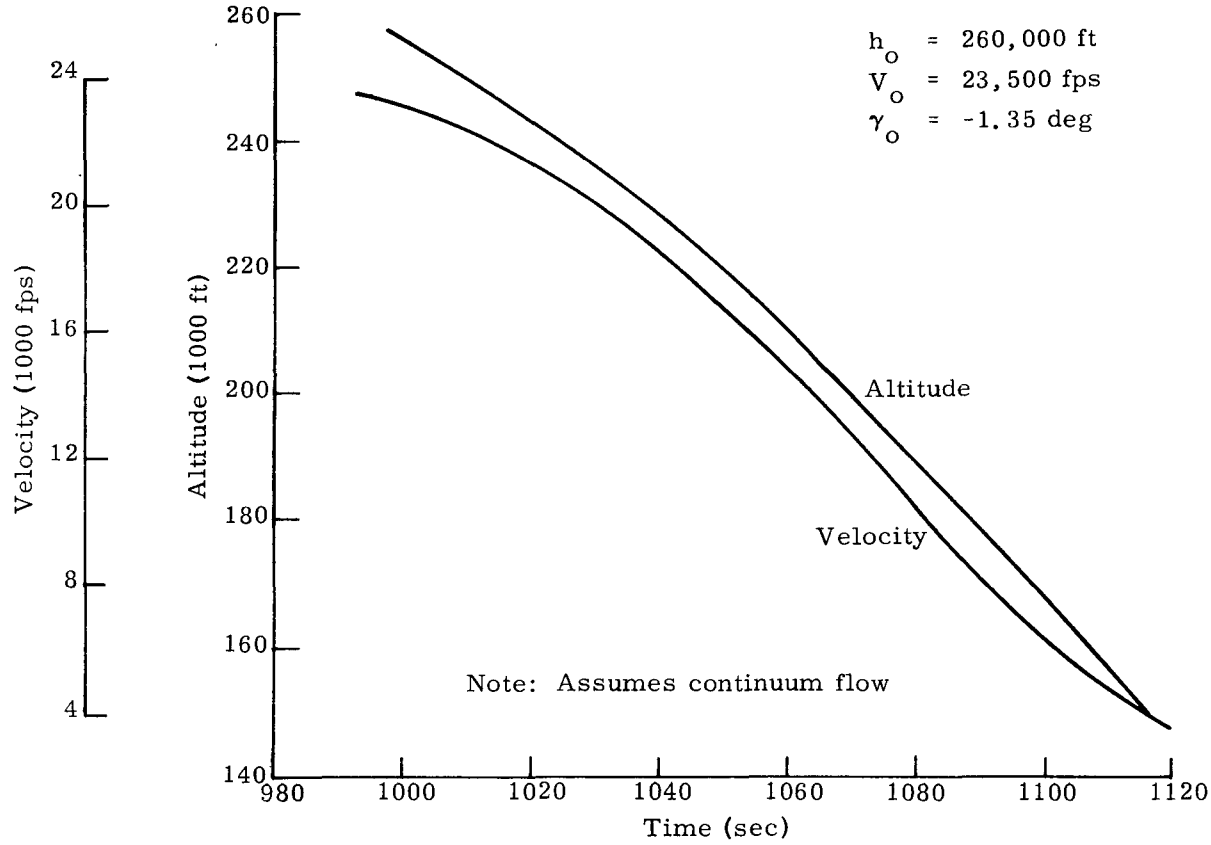

FIG. VI-25. VELOCITY AND ALTITUDE TIME HISTORIES--SNAP 29 FUEL MATRIX COMPONENT DURING RE-ENTRY

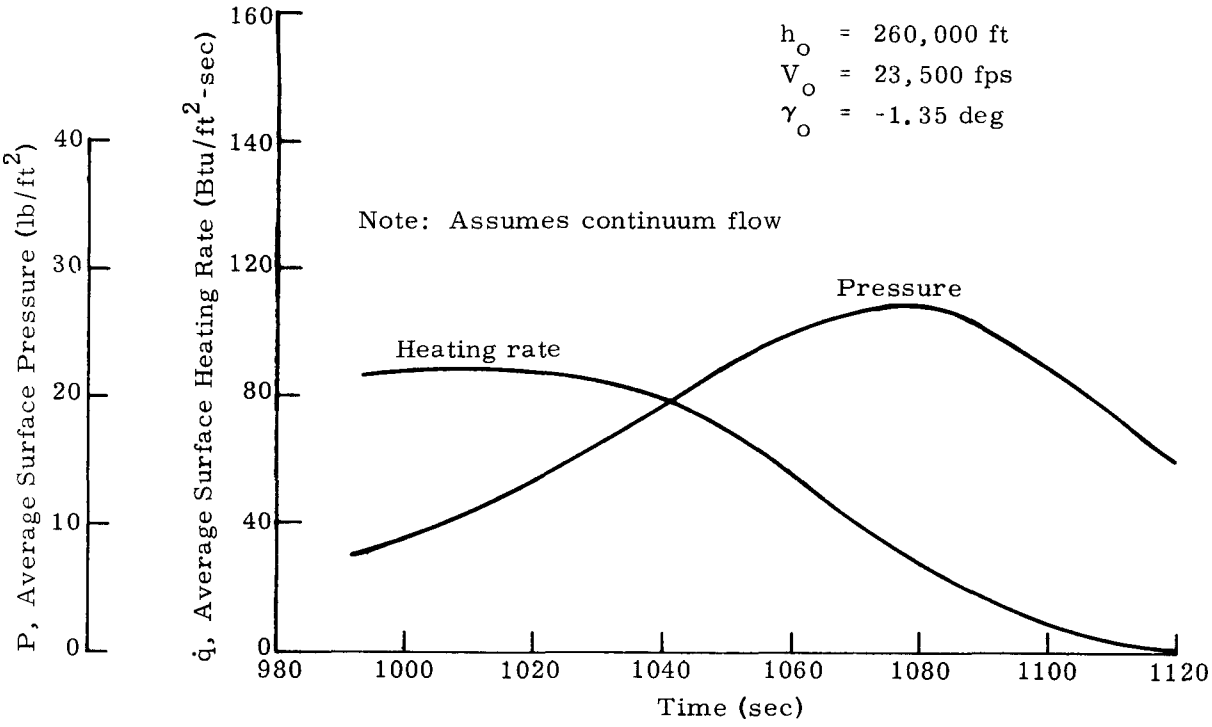

FIG. VI-26. PRESSURE AND HEATING RATE TIME HISTORIES--SNAP 29 FUEL MATRIX COMPONENT DURING RE-ENTRY

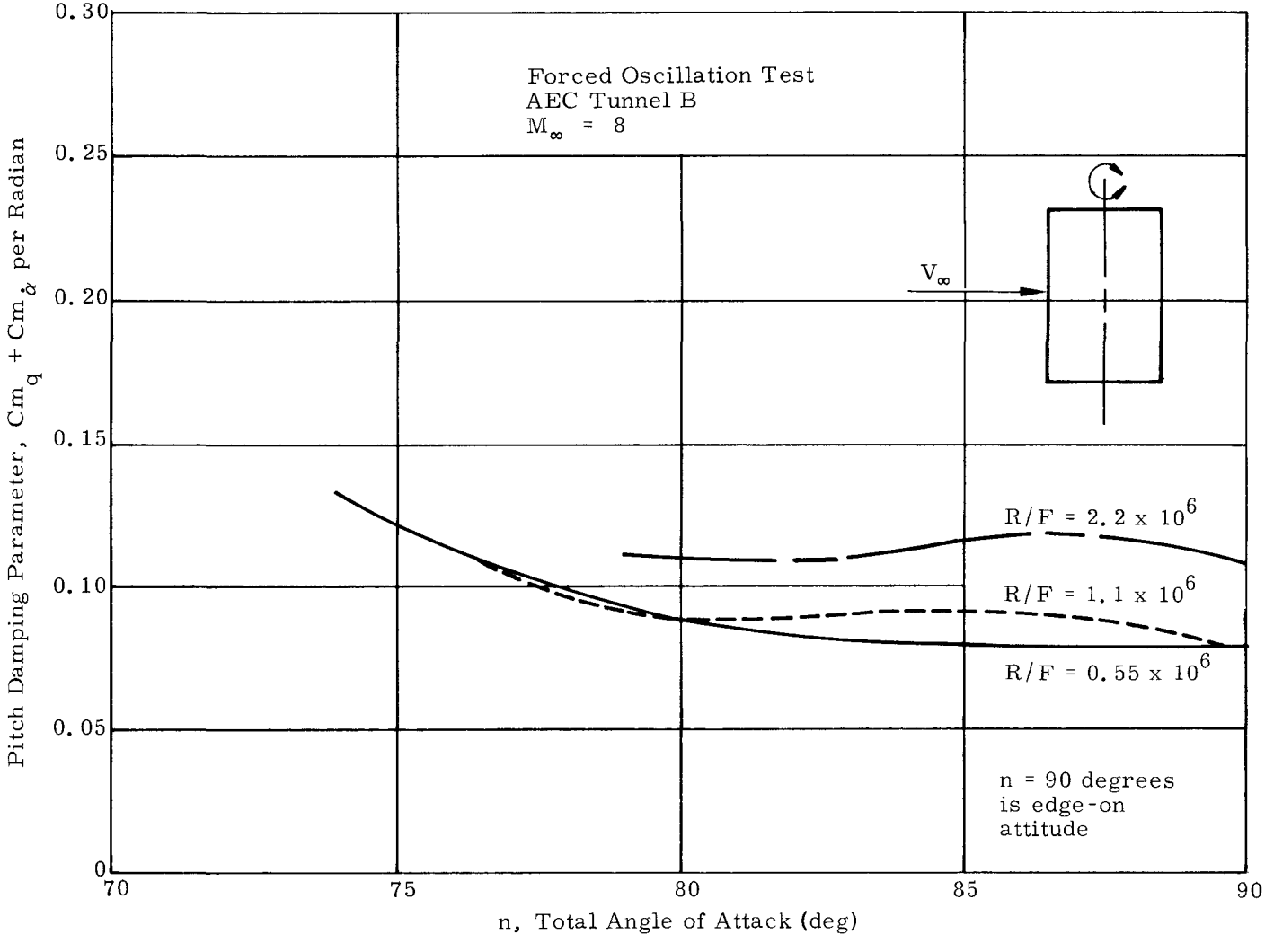

FIG. VI-27. FORCED OSCILLATION TEST RESULTS

CONFIDENTIAL

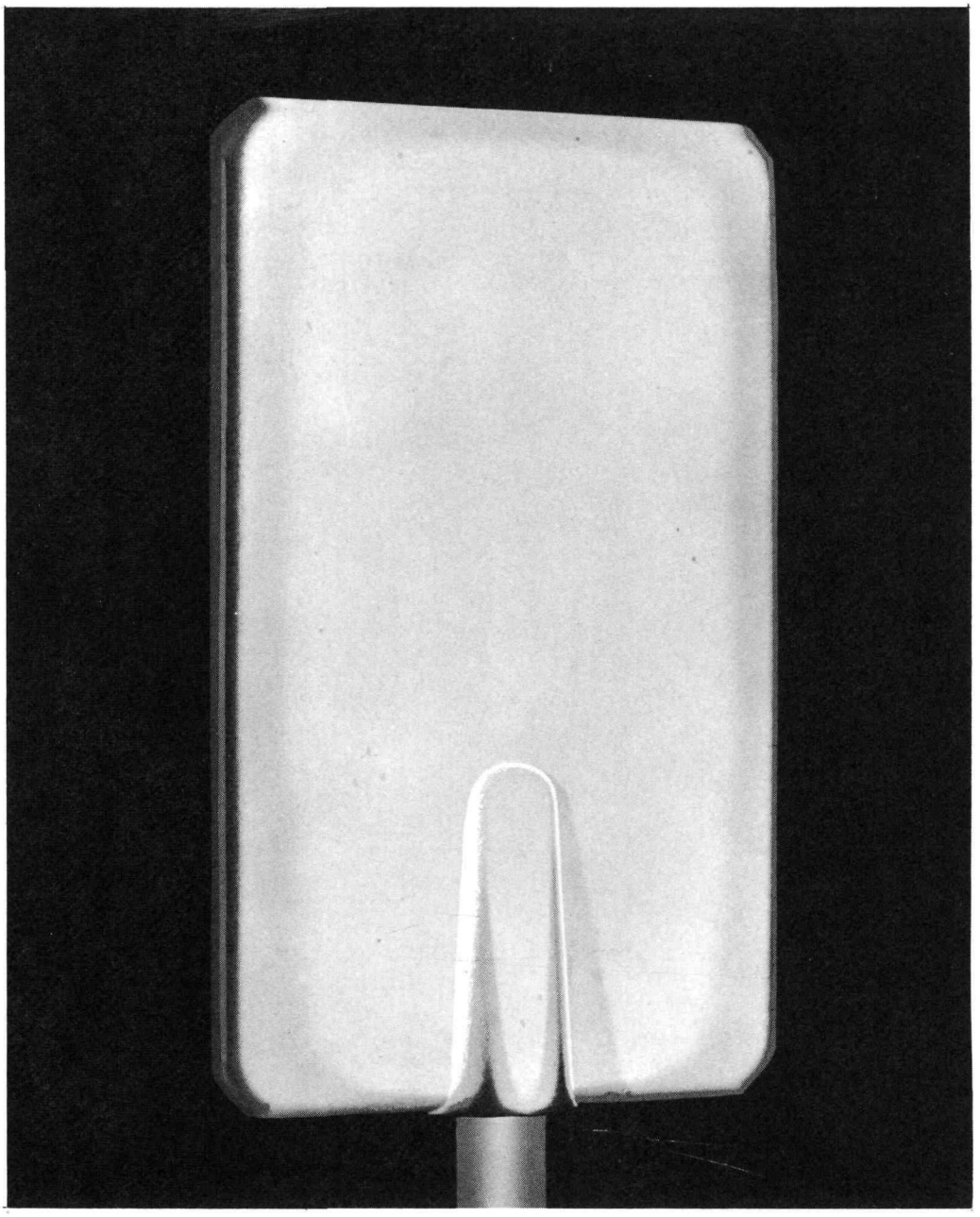

FIG. VI-28. SCORCH MODEL HEATING PATTERNS AFTER CONTINUOUS ROTATION RUN

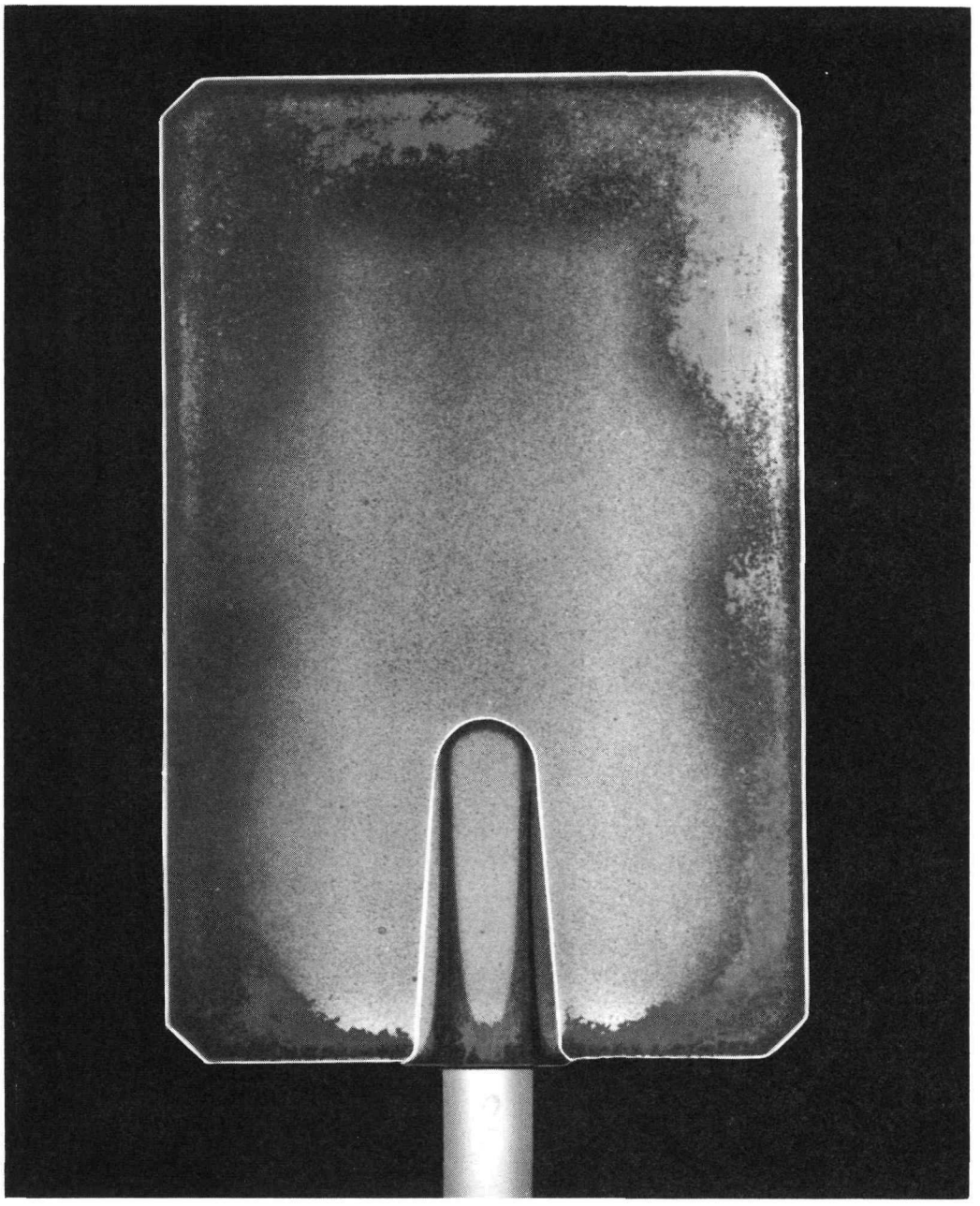

FIG. VI-29. SCORCH MODEL HEATING PATTERNS AFTER NONROTATING (SIDE-ON HEATING) RUN

D. IMPACT AND BURIAL TESTS AND ANALYSES -- CONTROL POINT 3330

1. Earth Penetration

The SNAP 29 Earth penetration study, initially reported in the November Monthly Progress Report, was completed. Analytical results correlated to test results indicate that burial of the SNAP 29 fuel element will not occur.

2. Impact Evaluation

A literature search was completed for impact test data. Data from about 1000 specimens was obtained. Of this number, about 300 were made from Haynes-25. Analysis of these data and their possible SNAP 29 application was initiated.

3. Planning and Reporting

Scheduling of the impact program was completed. The impact program consists of two test programs, the helicopter drop test and impact evaluation. A total of 40 fuel elements will be tested.

VII. MOUND LABORATORY EFFORT IN SUPPORT OF SNAP 29

As part of an extensive radioisotope fuels development effort being conducted at Mound Laboratory, A Po-210 program has been defined and implemented in support of the total SNAP 29 effort. This program comprises the radioisotope fuel and fueled heat source fabrication for the SNAP 29 RTG. Interface responsibilities among Isotopes, Inc., Mound and the AEC are identified in Specification MN-2062-4, Rev. A, "RTG Nuclear Fuel and Fuel Encapsulation Interface Plan, SNAP 29 Power Supply System."

A. PROGRAM SUMMARY

Two capsulette mechanical seal designs have been found to produce a gas-tight seal. They are the metal O-ring design and a compression type seal (Clydlok) similar in construction to the flareless-type tube fitting. The latter seal has been successfully leak-tested at 1500° F and an internal helium pressure of 700 psig.

Two polonium metal distribution tests were completed. In these tests small containers of polonium metal were allowed to attain elevated temperatures by suspending them in a vacuum. Three containers were fueled with about one gram each of polonium using the distillation fueling process. No prominent hot spots were detected on the surfaces of the containers during the two tests. The three fueled containers are being subjected to metallographic examination.

Compatibility tests are being performed at 880° and 1000°C to study possible reactions between a gadolinium polonide/tantalum matrix fuel form and Haynes-25 containers.

B. WORK ACCOMPLISHED

1. Capsulette Mechanical Seal

Design of the capsulette (primary fuel container) for the SNAP 29 dispersal heat source requires a mechanical seal. Mound is evaluating several seal designs which are discussed in the following.

a. Metal O-ring seal

In initial tests performed with nickel-plated Haynes-25 O-rings, the bottle-neck of the capsulette yielded before sufficient torque could be applied to compress the O-ring. (Forces of approximately 4000 and 1200 pounds are necessary to compress Haynes-25 and Inconel-X O-rings, respectively.)

The bottle-neck section of the capsulette was, therefore, strengthened by increasing the thread diameter and by increasing the original 0.04-inch thick top section to 0.07 inch. Figure VII-1a illustrates these modifications. It was also found that the surfaces contacting the O-ring required a surface finish of less than 8 rms to obtain an effective seal.

A gastight seal has been achieved with a metal O-ring made of platinum-plated Inconel-X. The O-ring used had a 5/8-inch OD by 1/2-inch ID and was manufactured from tubing 1/16 inch in diameter having a 0.01-inch thick wall. The effectiveness of this seal was evaluated with a helium leak detector. No leaks were found at a sensitivity setting in which a standard leak of 2.25×10^{-8} cc/sec is readily detected.

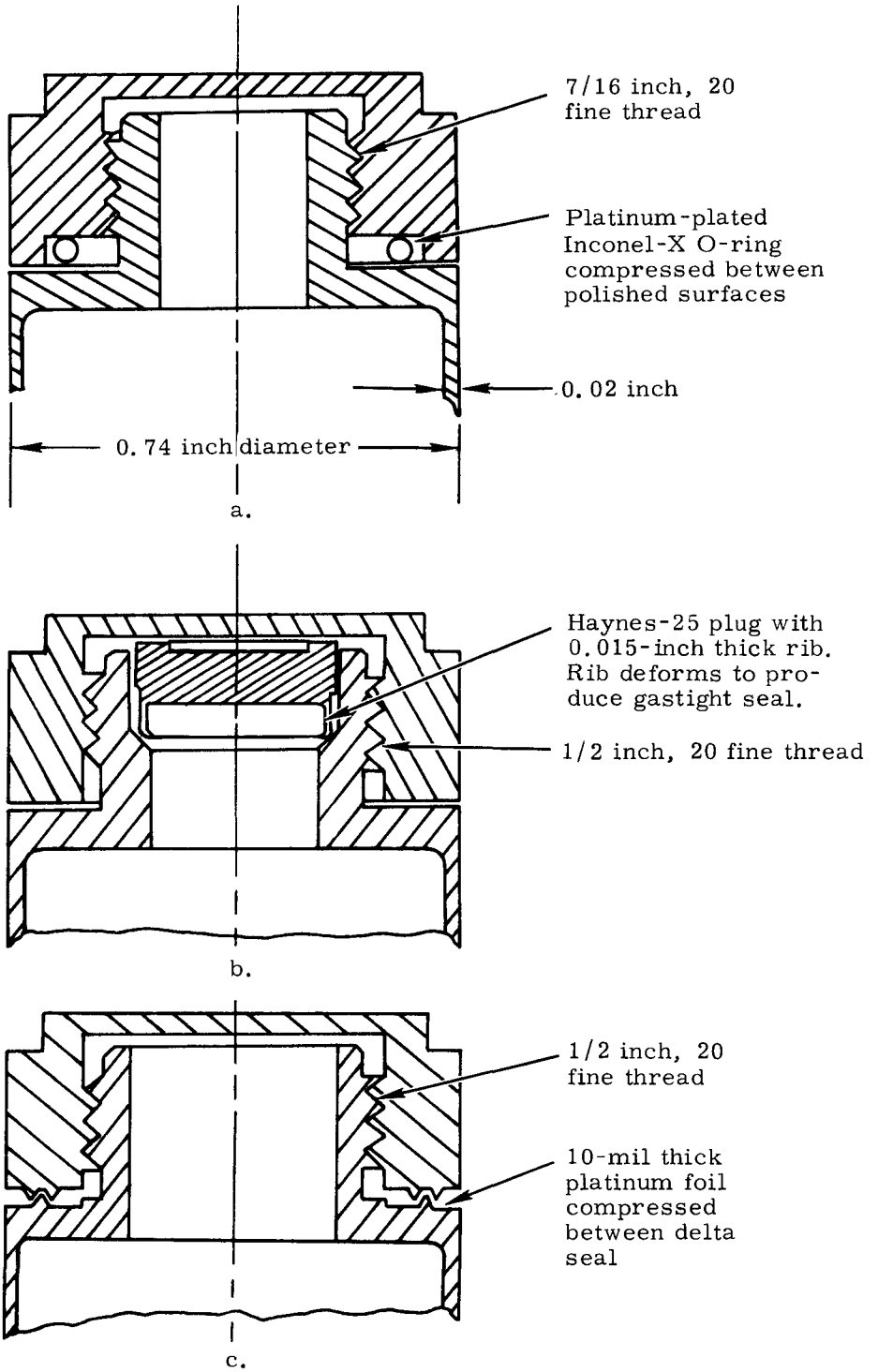

FIG. VII-1. MECHANICAL SEAL DESIGNS FOR THE HAYNES-25 CAPSULETTE

b. Plastically deformed compression seal

Successful mechanical seals were also obtained using a variation of the flareless tube fitting seal. Figure VII-1b illustrates this assembly. As the threaded cap is tightened, the 0.015-inch thick rim on the plug deforms to the shape of the conical bearing surface and forms the seal.

Room temperature leak checks showed that this Clydlok seal could be released and recompressed as many as six times without loss of its effectiveness. The seal was also successfully subjected to two high temperature, high pressure tests. The high temperature test assembly consisted of a Clydlok seal machined from Haynes-25 and welded to a two-foot length of stainless steel tubing. A pressurized helium line was attached to the assembly. Heating was performed in an argon-filled stainless steel muffle furnace. No helium was detected when the Clydlok seal was subjected to the following tests:

(1) Test 1

(a) Pressurize capsule to 60 psig and heat to 780° F

(b) Heat to 1450° F in one hour, increasing the internal helium pressure to 650 psig

(c) Cool to 300° F in 1/2-hour at an internal pressure of 650 psig.

(2) Test 2

(a) Pressurize capsule to 600 psig and heat to 1500° F in one hour

(b) Increase pressure to 700 psig while at 1500° F

(c) Cool to room temperature in 1-1/2 hours at an internal pressure of 650 psig.

After Test 2 was completed, the threaded cap was removed from the assembly, leaving the plug in position. A helium leak test showed that the plug remained sealed (pressure differential). The bonded plug was readily removed from the conical seat by a light tap.

c. Delta seal

Figure VII-1c illustrates a delta-sealed capsulette that was evaluated. An annealed 0.01-inch thick platinum gasket was used for this assembly. This design did not produce a gastight seal. Apparently, the rotating motion of the cap fails to result in proper seating of the platinum gasket. A two-component cap that permits the delta seal to remain stationary as the threaded component is tightened would probably be required for a satisfactory seal of this design.

d. Other seals

Two other types of seals were examined using stainless steel tubing as stand-in material. These included a polished tapered plug forced into the tubing and a mechanical crimping of the tubing. Neither of these types of mechanical seals was found to be leak-tight.

e. Conclusions

The Clydlok seal appears most attractive for obtaining the required gastight, mechanical closure. The seal is constructed of Haynes-25; therefore, the use of materials for which compatibility data are not available is avoided. An effective seal can be obtained without the need for a polished metal surface. Furthermore, the torque required to seat the Haynes-25 plug is about 50 in. -lb, as compared to the 100 to 200 in. -lb required to seat a superalloy O-ring. This lower torque requirement will make it easier to obtain a seal during remote control assembly operations.

2. Polonium Metal Distribution Tests

Polonium metal is being considered as an alternative fuel for the SNAP 29 generator. In the current design concept, the fuel form would consist of a mechanically sealed capsulette of Haynes-25 containing approximately 0.8 gram of polonium at launch. Seven capsulettes would be encapsulated in a liner of Haynes-25 to form the primary fuel capsule. If the polonium did not become evenly distributed in the capsulette, hot spots could develop which could at worst result in melting of the capsulette and, ultimately, the rest of the capsule members.

A series of polonium distribution tests is being made to study the temperature profiles of capsules containing polonium. The objectives of these tests were:

(1) To determine the temperature profile in a vacuum environment of a capsulette containing approximately one gram of polonium metal.

(2) To develop basic fueling data and procedures for subsequent tests with prototype SNAP 29 capsulettes.

(3) To examine the test containers metallographically for evidence of attack by the fuel.

a. Distribution Test 1

The primary test facility is depicted in Figs. VII-2 and VII-3. The tests were performed in a vacuum chamber constructed from an eight-inch section of a four-inch diameter Pyrex pipe. The top of the chamber was a stainless steel plate fitted with a thermocouple feedthrough, a valve for backfilling and two hooks by which the test assembly could be suspended. The chamber was positioned in an argon atmosphere glove box over a four-inch diameter opening to a vacuum pumping system. The opening was covered by a stainless steel screen. Neoprene O-rings were used at each end of the chamber, and a wire mesh guard was placed around the wall of the chamber.

The capsulette used in the first test was one of the stainless steel cans normally used as a receiver in the polonium still. Dimensions of the can and its cap are shown in Fig. VII-4. A copper gasket is used for sealing. Major dimensions of the sealed can are:

	(in.)
OD	0.870
ID	0.770
Wall thickness	0.050
External height	2.157
Internal height	1.426
Volume	11.0 cm^3

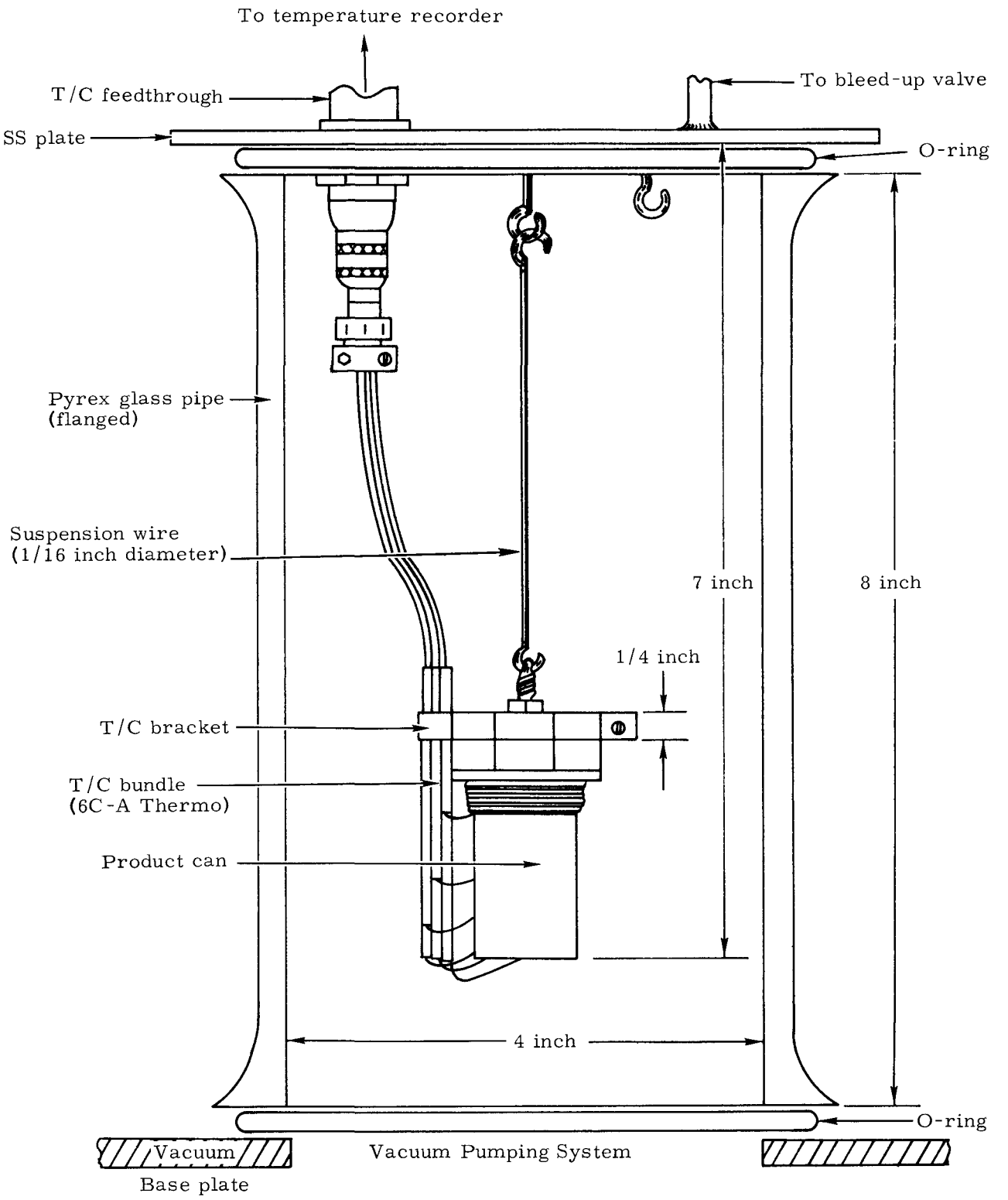

FIG. VII-2. SCHEMATIC OF TEST CHAMBER FOR Po DISTRIBUTION TEST

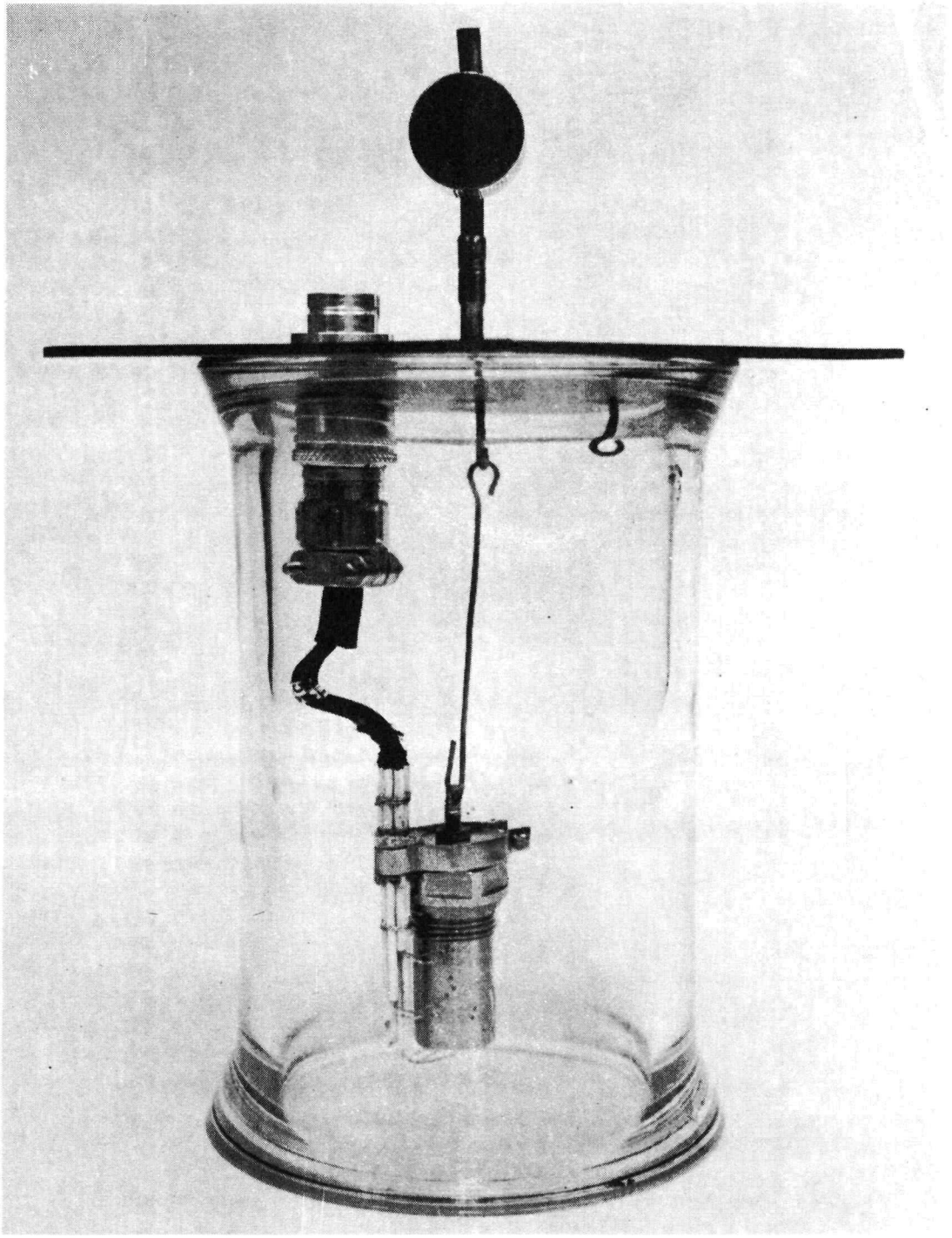

FIG. VII-3. TEST CHAMBER WITH STAND-IN CAPSULE FOR Po DISTRIBUTION TEST

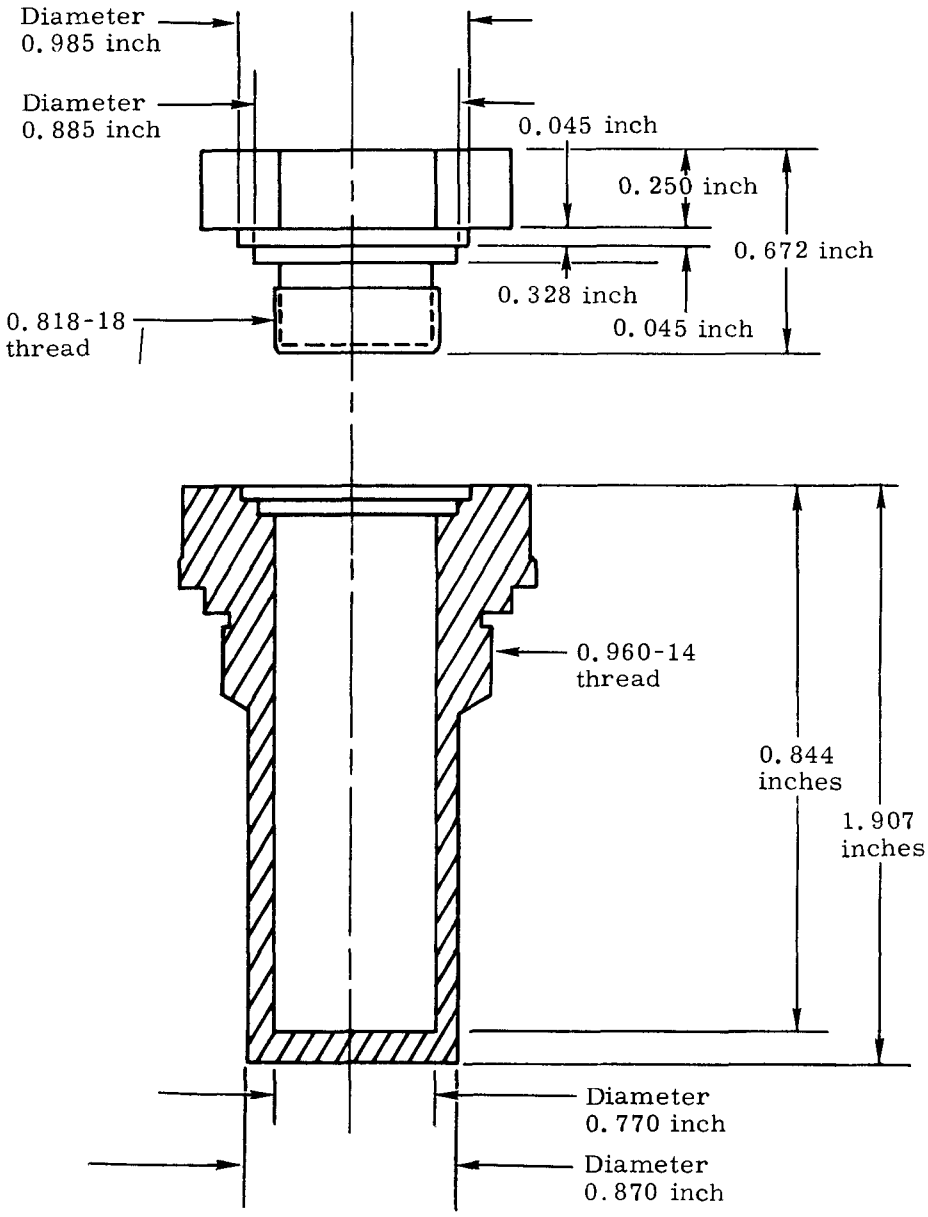

FIG. VII-4. STAINLESS STEEL CAPSULE AND CAP USED IN DISTRIBUTION TEST

For this test the center of the cap was tapped to receive a threaded plug containing an eye by which the can could be suspended.

A pre-assembled bundle of six chromel-alumel thermocouples separated by alumina sheathing was prepared for attachment to the fueled can by a stainless steel clamp fitted around the top of the can (Fig. VII-5). The six thermocouples were later spot welded to the can in the locations indicated in Figs. VII-6 and VII-7. The temperature of each location was indicated by a six-point recorder. The can with the attached thermocouple bundle was suspended from the top of the chamber by a 1/16-inch diameter stainless steel wire. The can could be positioned vertically under a hook in the center of the end plate or tilted approximately 25 degrees from the vertical by the use of a second hook located 1-3/8 inches from the center.

The soundness of the vacuum chamber was checked prior to transfer of the fueled can to the glove box and again when it was placed in position for the test. The order of connection of the thermocouples to the feedthrough plug was verified, and operation of the temperature recorder was completely checked before the test. Since final joining and attachment of the thermocouples were made immediately prior to the test, the thermocouples were not calibrated.

The stainless steel can was fueled with 4370 curies of polonium on 9/16/68 according to the procedures normally used in operation of the polonium still. The cap used to seal the can was tapped for an eyed plug so that a suspension wire could be attached later.

The fueled can was calorimetered, and the neutron flux was determined by standard procedures. The can was then transferred to argon atmosphere glove box facilities where the thermocouple bundle was attached to the can by securing the clamp around the cap. The six thermocouples were attached by resistance welding.

The plug of the thermocouple bundle was attached to the feedthrough in the vacuum chamber end plate and the can was attached to the center hook in the end plate by the suspension wire. The assembly was then lowered into the vacuum chamber. Operation of the temperature recorder was initiated, the vacuum pump was turned on, and the chamber was evacuated slowly by closing the backfill valve. The pressure in the system was monitored at all times by an ion gauge installed in the foreline to the pump.

An additional thermocouple was welded to the top plate of the vacuum chamber near the thermocouple feedthrough so that a temperature correction for this junction could be determined. The measurement was made with a potentiometer.

Data recorded at various times during the test are given in Table VII-1. The temperature of the thermocouple feedthrough was found to be 136° F; this value should be added to the recorded temperatures listed in Table VII-1 to obtain actual temperatures.

Throughout the test, the temperatures indicated by Thermocouple 6, located near the top of the capsule, were 500° to 600° F lower than at the other five points. When the assembly was moved during the latter part of the test, it was found that insulation on this thermocouple had become damaged by heat when the thermocouple bundle was attached to the source, allowing the leads to become shorted. Malfunctioning of the thermocouple was assumed from the beginning of the investigation, since a temperature differential between the top and bottom of the capsule could not be detected visually. Evacuation of the chamber was delayed about two hours while minor repairs were made on the temperature recorder. When the mechanical pump was activated, the recorded temperatures increased about 100° F. The maximum temperatures recorded

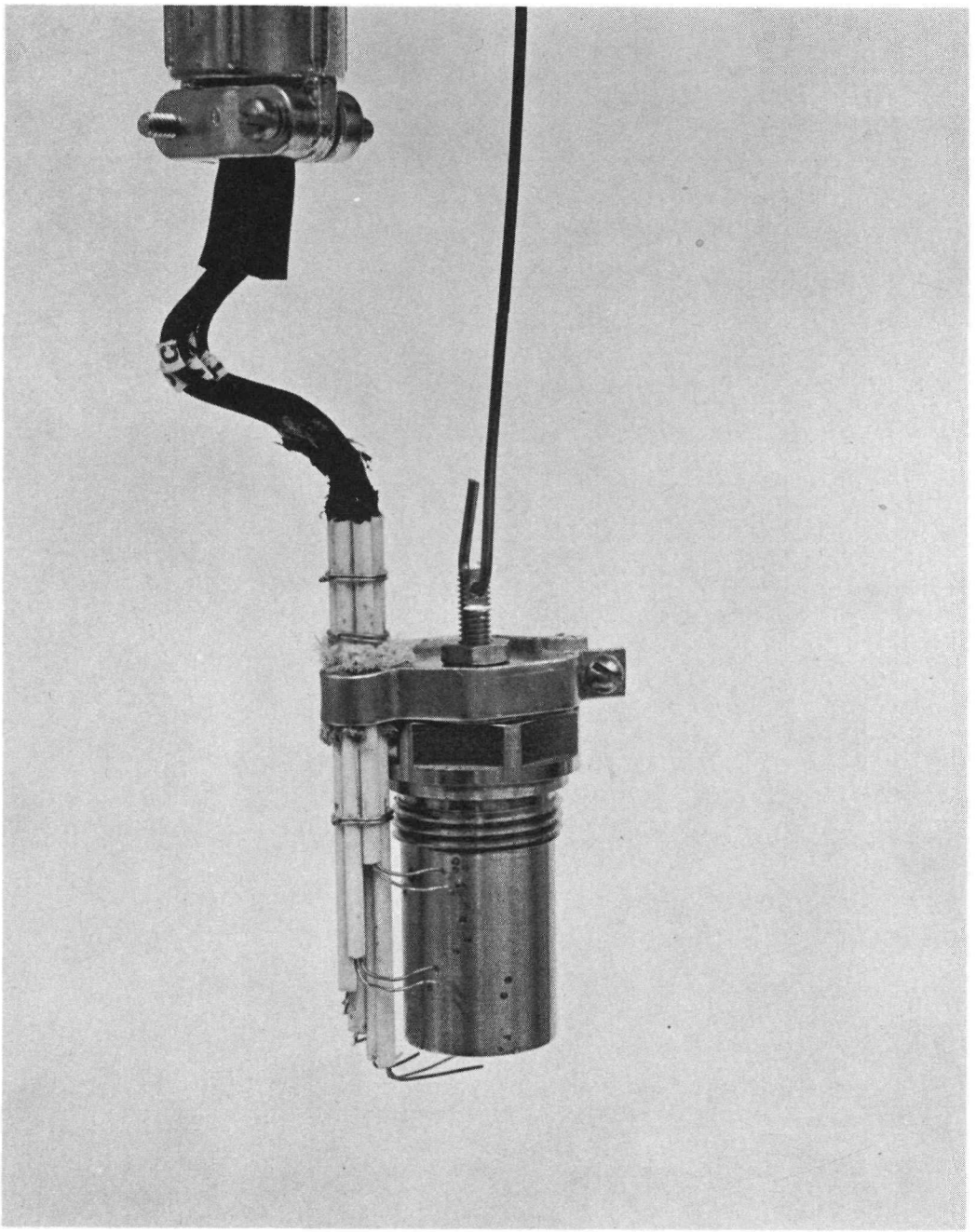

FIG. VII-5. THERMOCOUPLE BUNDLE WITH STAND-IN CAPSULE USED IN Po DISTRIBUTION TEST

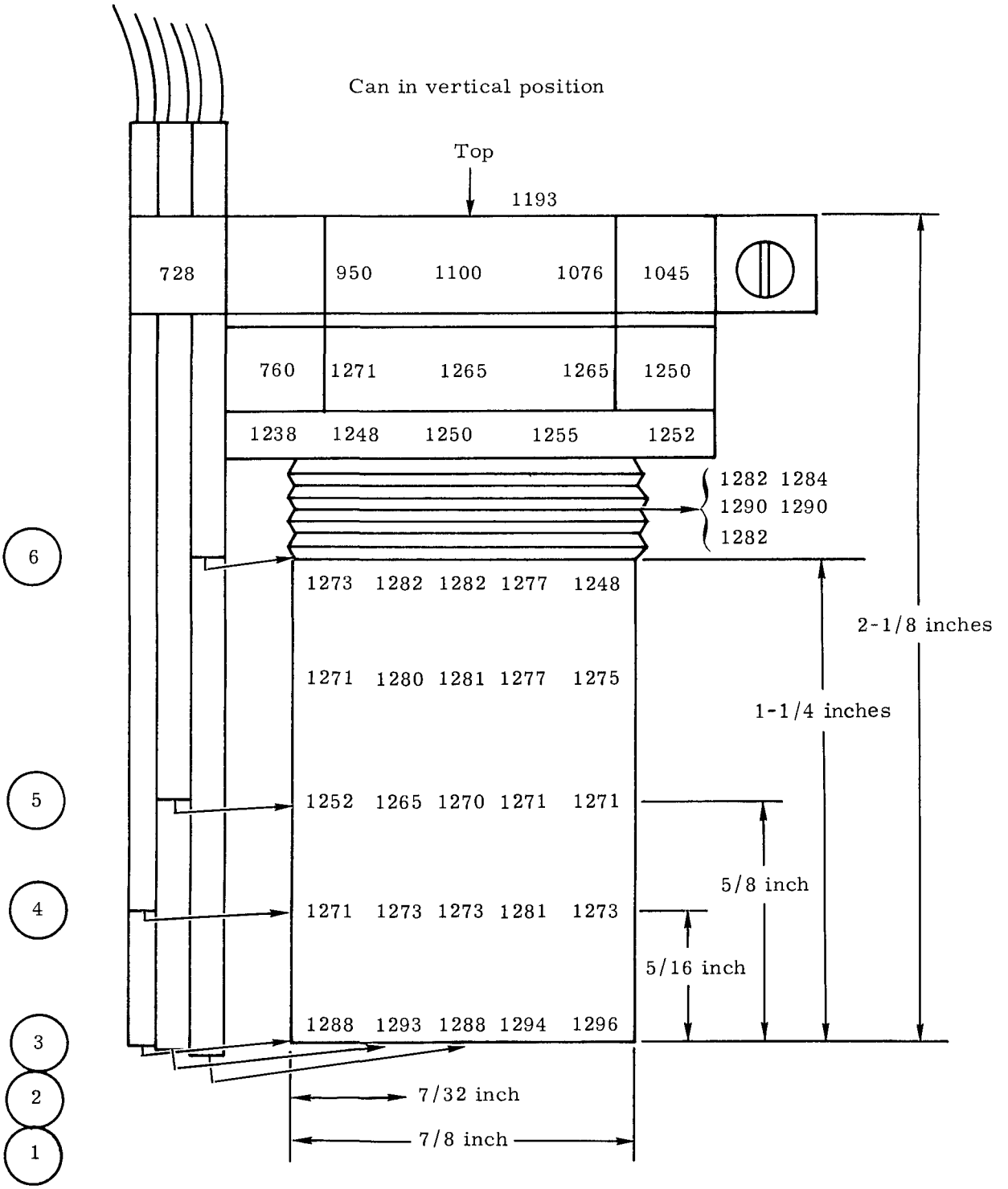

FIG. VII-6. TEMPERATURE DISTRIBUTION ESTIMATED FROM RADIATION THERMOMETER READINGS

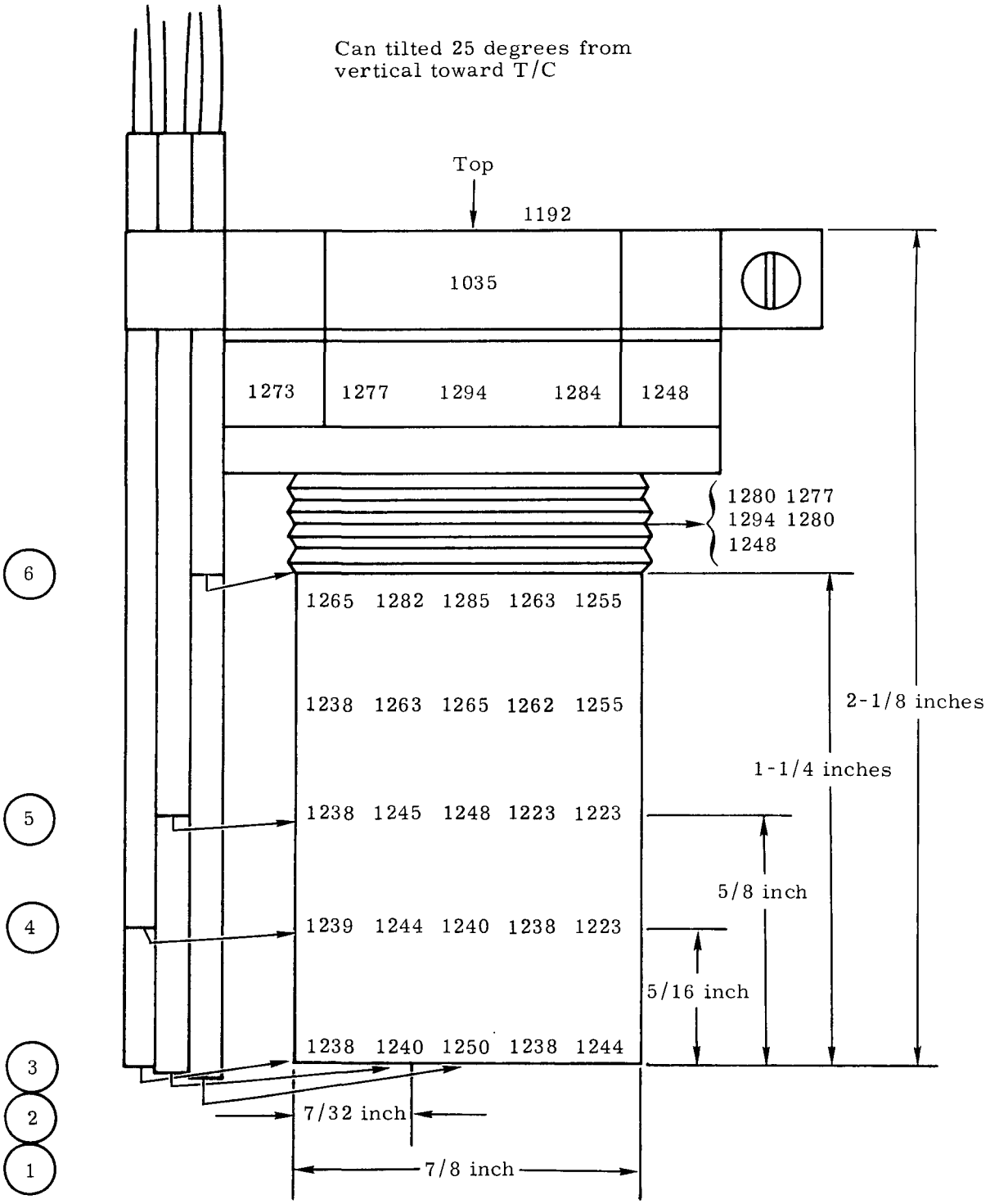

FIG. VII-7. TEMPERATURE DISTRIBUTION ESTIMATED FROM RADIATION THERMOMETER READINGS

TABLE VII-1

Selected Data from Polonium Distribution Test No. 1

Date	Time	T/C Temperatures (° F) 1	2	3	4	5	6	Glove Box Temperature (°F)	Chamber Pressure (torr)	
9/17	1335	1265	1240	1245	1245	1205	685	88	Argon atm	First readings with source in place (vertical).
	1605	1225	1185	1190	1185	1140	700	93	Argon atm	Immediately before evacuation of chamber started.
	1625	1320	1285	1300	1275	1220	730	95	8×10^{-3}	Maximum readings observed.
	1633	1311	1272	1288	1262	1215	720	95	7×10^{-3}	
	1730	1281	1250	1255	1235	1175	695	95	5×10^{-3}	
	1930	1260	1222	1227	1202	1149	673	95	5×10^{-3}	
	2330	1245	1195	1202	1180	1130	663	96	5×10^{-3}	
9/18	0630	1235	1179	1186	1160	1110	652	95	5×10^{-3}	
	0925	1238	1175	1185	1160	1112	655	94	1×10^{-4}	Diffusion pump on.
	1230	1235	1175	1185	1158	1112	653	93	1×10^{-5}	
9/19	0030	1229	1165	1175	1150	1102	648	97	1.2×10^{-5}	
	1030	1214	1153	1163	1138	1094	640	97	1.4×10^{-5}	
	1615	1205	1143	1148	1132	1045	615	98	5×10^{-3}	35 minutes after capsule was tilted.
	1730	1205	1145	1154	1132	1052	608	98	8×10^{-5}	
	2130	1195	1137	1145	1128	1045	605	97	0.5×10^{-6}	
	2430	1190	1133	1141	1124	1042	602	97	0.8×10^{-6}	
9/20	1325	1170	1118	1125	1112	1035	600	99	0.8×10^{-6}	
	1830	1145	1101	1109	1099	1025	598	98	0.7×10^{-6}	
	2400	1115	1083	1095	1083	1015	595	93	0.7×10^{-6}	
9/21	0700	1088	1059	1069	1060	995	590	91	1.5×10^{-5}	
9/23	0850	800	723	830	760	750	500	100	Argon atm	Source in chill can

*As-recorded temperatures.

CONFIDENTIAL

CONFIDENTIAL

occurred 20 minutes after evacuation was started. Thereafter temperatures slowly decreased, with minor fluctuations occurring when the pressure in the chamber was changed. The chamber pressure was maintained at about 5×10^{-3} torr for 17.5 hours by means of the mechanical pump. A diffusion pump was then activated and the pressure thereafter was generally 10^{-5} to 10^{-6} torr. The chamber was occasionally backfilled briefly with argon to determine whether polonium was escaping from the capsule.

By the end of the first day of the test it was apparent that the surface of the capsule had darkened considerably. It was estimated that the emissivity increased to 0.8 to 0.9. Surface oxidation apparently occurred during preparation of the test assembly and before the diffusion pump was activated. (The argon atmosphere in the glove box contained 100 to 200 ppm oxygen.)

After the first few hours of the test, the temperature of the capsule was below the range of the optical pyrometer, and supplemental temperature data were obtained with a Thermodot Model TD-6 radiation thermometer. On the third day (9/19/68), after it was determined by a cathetometer that the capsule was truly vertical, signals from the radiation pyrometer were tabulated by scanning one side of the capsule. The data from this scanning are shown in Fig. VII-6.

Suspension of the capsule was then changed so that it was tilted 25 degrees from the vertical toward the thermocouples. No unusual changes were noted in subsequent thermocouple data. On the fourth day (9/20/68), a visible change in the incandescence of the capsule occurred. Within a four-hour period, it was noted that the upper part of the capsule became brighter. A second scan with the radiation pyrometer was made (Fig. VII-7) which indicated that the top section was slightly hotter than the base section.

Actual temperatures could not be directly calculated from these data due to the filtering effect of the plexiglass window in the glove box.

Signals from the radiation thermometer were converted to temperature data by relating the signal obtained in the vicinity of Thermocouple 4 with the corrected temperature indicated by the recorder. A correlation curve was constructed from a slide rule temperature calculator supplied with the Thermodot instrument, and all signals were converted to temperature readings by reference to this curve.

At 8 AM on 9/21/68, the chamber was backfilled with argon so that contamination of the pumping system would not result if polonium leakage occurred during the weekend. Five hours later, fluorescence, indicating the presence of polonium, was observed in the test chamber. The capsule was then removed from the chamber, placed in a metal container and surrounded with copper shot to lower its temperature. Temperature recordings were continued until 9/24/68, when the assembly was dismantled and the capsule was sealed in protective containers. After calorimetry, the capsule was returned to the polonium still. The cap was easily opened, and it was found that the copper gasket was severely corroded. After polonium was removed from the capsule components by distillation, they were removed from the still and are being retained for metallographic examination.

Components of the test chamber and the copper shot were later leached with nitric acid. As shown in Table VII-2, approximately 200 curies of polonium was not recovered and presumably was dispersed in the glove box facilities.

TABLE VII-2

Material Balance for Polonium Distribution Test 1

	(Ci)
Po in capsule at start of test (9/16/68)	4370
Original loading decayed to 9/26/68	4157
Recovered values as of 9/26/68	
Po remaining in capsule	3857
Recovered from apparatus	78
Total	3935
Po unaccounted for	204

b. Distribution Test 2

The first container to be fueled for the second test was a Haynes-25 capsulette as shown in Fig. VII-8. This fueling operation was the first attempt to distill polonium metal into a container of this design and size.

Approximately 95% polonium transfer efficiency was obtained in distilling 1.2 grams into the capsulette. The neutron flux from the fueled capsulette was less than 50 n/Ci-sec, which indicates a low level of light element impurities.

The capsulette was scheduled to be used for a second polonium distribution test; however, when it was removed from the transfer container after two days storage, a crack was present about 0.06 inch above the bottom weld. The crack direction was parallel to the weld direction. Polonium was visually observed to be escaping from the crack.

Since the capsulette was helium leak-checked prior to the distillation test and no polonium leak was detected immediately after fueling, it is assumed that propagation of the crack through the 0.02-inch thick wall occurred during the two-day storage period. The polonium was immediately leached from the capsulette and metallographic analysis begun.

A second Haynes-25 capsulette was prepared for fueling. This capsulette was very similar to the first one with the exceptions that it was shorter and employed a Clydlok seal (see Capsulette Mechanical Seals) rather than an O-ring seal. Prior to fueling, the capsulette was checked with a helium leak detector and examined for cracks by dye penetrant testing. The capsulette was fueled on 11/19/68, in the polonium process development still with 3440 curies of polonium metal (correcting for decay, 3423 curies of polonium remained on 11/20 when the test was initiated). The neutron emission rate of the fuel was found to be 35 n/Ci-sec. Following calorimetric assay, the capsulette was transferred into the glove box where the test facility was located.

The capsulette was removed from the transfer container and mounted in an aluminum support assembly which also held the 12 alumina-sheathed, chromel-alumel thermocouples. A 1/16-inch diameter wire hook which had previously been tack-welded to the capsulette top cap was used to secure the Haynes-25 container to the support assembly. The thermocouples were attached to the capsulette by spot welding. Figures VII-9 and VII-10 show the locations of the thermocouples which were attached at four levels and positioned 30 degrees apart around the circumference. For example, Thermocouple 1 was at the bottom, No. 2 was located

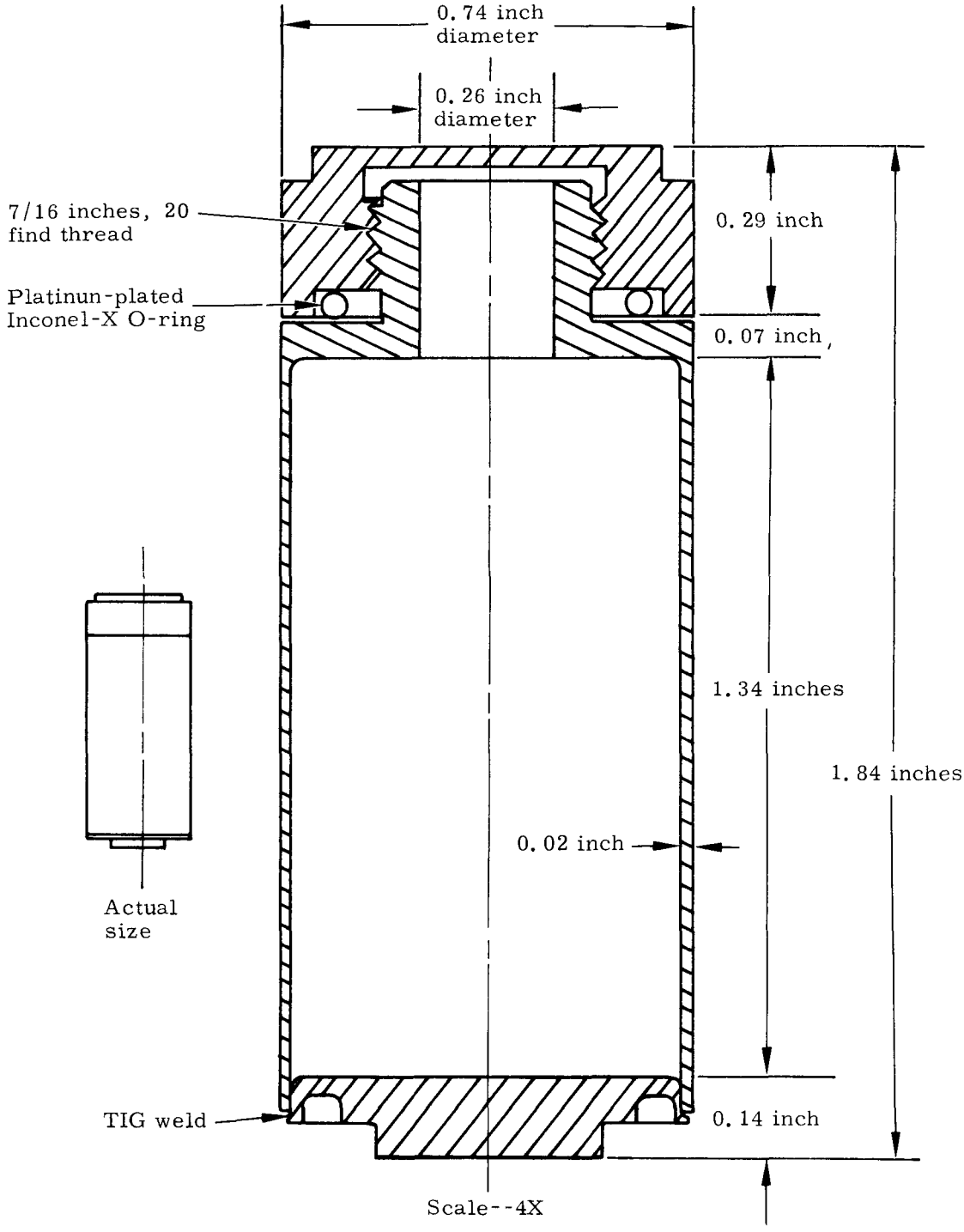

Note: Actual capsulette length = 1.61 inches.

FIG. VII-8. CAPSULETTE DESIGN USED FOR Po DISTILLATION TEST

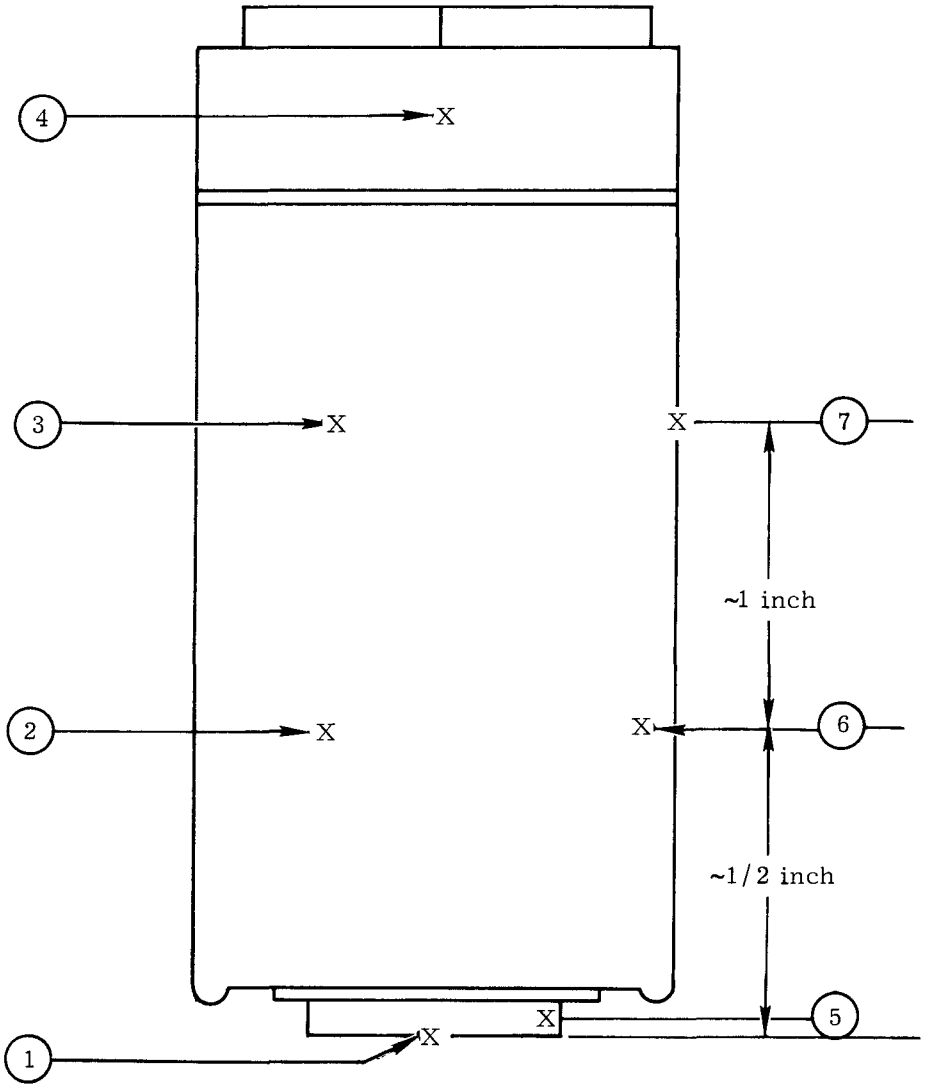

FIG. VII-9. THERMOCOUPLE LOCATIONS ON HAYNES-25 CAPSULETTE USED IN Po DISTRIBUTION TEST

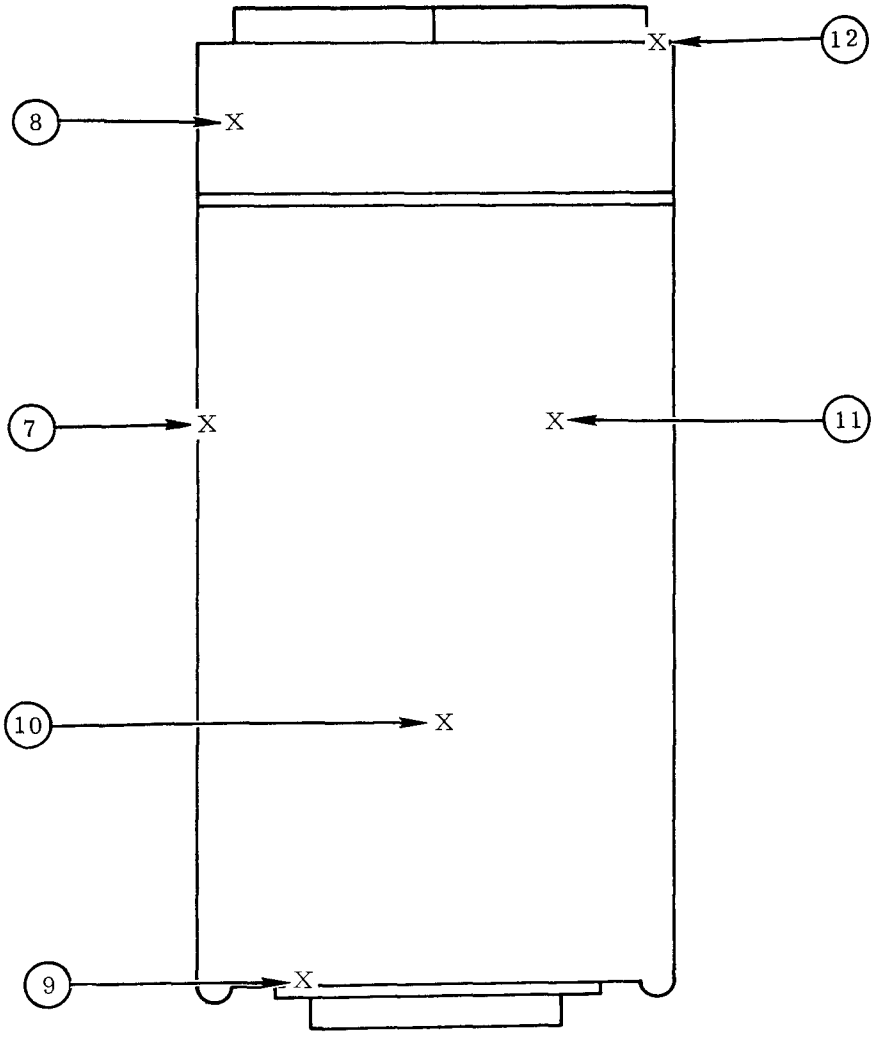

Capsulette rotated 180 degrees from Fig. VII-9 orientation

FIG. VII-10. THERMOCOUPLE LOCATIONS ON HAYNES-25 CAPSULETTE USED IN Po DISTRIBUTION TEST

approximately one-half inch above the bottom on the side wall, with No. 3 approximately one inch above the bottom and No. 4 on the side of the top cap. This same sequence was repeated with Nos. 5 through 8 and 9 through 12.

Difficulty was encountered in attaching the thermocouple junctions to the capsulette due to the large number of wires involved, the relatively confined area, the heat from the capsulette and the frangible nature of the junctions. Several attempts were made to affix all 12 thermocouples on the capsulette; however, only eight were attached. Two of these later failed. A thermocouple was also attached to the top plate of the vacuum chamber near the thermocouple lead wire feedthroughs so that a temperature correction for this junction could be determined.

Continuous temperature data were recorded by a L & N Speedomax, Type W 12-point recorder. In addition, supplemental readings were periodically taken with a Thermodot radiation thermometer. The thermocouple temperature data which were recorded at selected times during the test are presented in Table VII-3. A 37° to 40° C correction must be added to the temperatures listed in the table to compensate for the lead wire junction temperature. At the beginning of the test, the capsulette temperature ranged from 745° C (corrected) on the bottom to 690° C (corrected) on the top cap with the side wall temperature at 705° to 710° C (corrected). After rough vacuum was applied to the chamber the temperature of each thermocouple increased by an average of approximately 40° C. The temperature at the bottom of the capsulette rose to 795° C (corrected) which was the highest temperature observed at any time during the test. No additional temperature increase was observed after a high vacuum was attained. Periodic temperature readings at about one-half hour intervals showed a slight decrease of ~20° to 25° C at all locations monitored during the following five hours. (A similar temperature decrease was also observed in the first polonium distribution test and was attributed to a change in the emissivity of the capsule due to tarnishing.)

As a supplement to the thermocouple temperature data, periodic readings were tabulated with the aid of the radiation thermometer. Since direct temperatures could not be determined with the instrument due to partial absorption by the window of the glove box, estimated values were obtained by relating the radiation thermometer data to Thermocouple 4 temperature. The results of these estimated temperature readings are shown in Fig. VII-11. Estimates ranged from approximately 740° C at the bottom to approximately 700° C on the top cap and compared with thermocouple temperatures of 770° and 700° C (corrected), respectively, taken at the same time.

Approximately five hours after initiation of the distribution test a slight deposit was observed on the walls of the glass vacuum chamber. The chamber was backfilled with argon from the glove box and an intense ionization glow became visible, which indicated release of polonium from the capsulette. The capsulette was removed from the vacuum chamber, detached from the thermocouple and support fixture, and sealed in a transfer container to prevent any further leakage. Calorimetric assay revealed that 3336 curies of polonium (11/20/68) were still present in the capsulette; the loss was 87 curies. Visual examination of the capsulette showed no evidence of cracks similar to those found in the first polonium-fueled Haynes-25 capsulette. The cap was tightened further, and the capsulette was again suspended in the vacuum chamber. Upon evacuation the chamber was immediately plated with a substantial deposit of polonium. A second visual inspection was made and, again, no cracks were found. When the top was loosened in preparation for defueling, an intense ionization glow was observed on the inside surfaces of the cap, indicating that the compression seal had failed. The capsulette was transferred to the polonium recovery facility so that the fuel could be removed by nitric acid leaching.

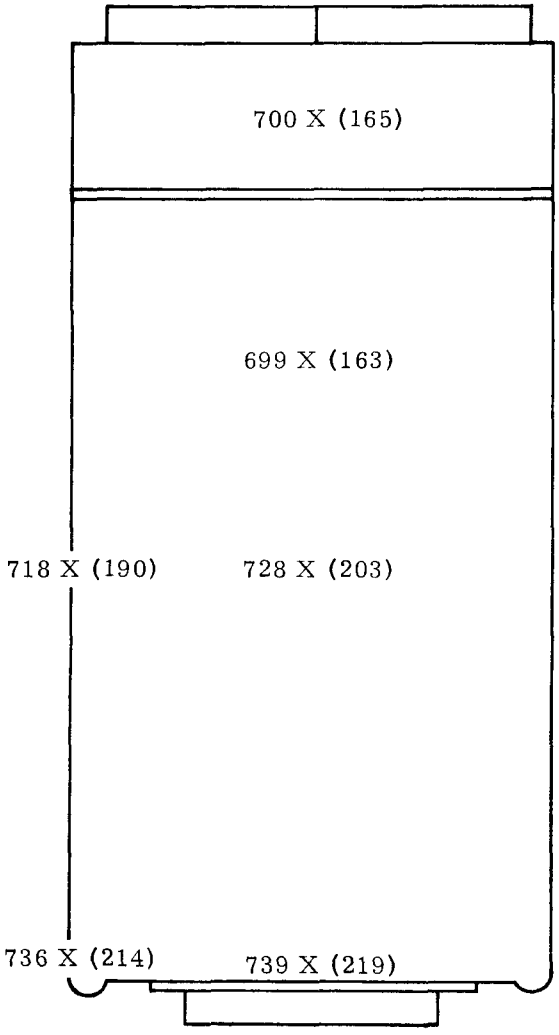

FIG. VII-11. ESTIMATED TEMPERATURES BASED ON THERMODOT RADIATION THERMOMETER READINGS FOR Po DISTRIBUTION TEST (°C)

TABLE VII-3

Selected Data from Polonium Distribution Test 2

Time	T/C Temperatures As-Recorded (°C) 1	2	3	4	5	6	7	8	9	10	11	12	Chamber Pressure (torr)	Top Plate Temperature (°C)
1057	705	665	670	650	X	650	X	630	685	655	X	X	Atm	--
1110	750	690	720	680	X	675	X	Failed	740	680	X	X	1×10^{-2}	--
1140	755	685	720	685	X	Failed	X	X	735	680	X	X	2×10^{-4}	--
1235	735	670	705	665	X	X	X	X	715	665	X	X	3×10^{-5}	37
1300	735	670	700	660	X	X	X	X	710	665	X	X	2×10^{-5}	37
1330	730	670	695	660	X	X	X	X	710	665	X	X	4×10^{-5}	37
1445	730	670	690	660	X	X	X	X	710	655	X	X	5×10^{-5}	40
1535	725	670	685	655	X	X	X	X	705	650	X	X	1.4×10^{-5}	--
1610*	725	668	683	655	X	X	X	X	702	650	X	X	--	--
1613	668	630	638	617	X	X	X	X	643	610	X	X	Atm	--
1631	668	630	638	617	X	X	X	X	643	610	X	X	Atm	--

All readings on 11/20/68.

*--deposit observed on chamber walls.

X--denotes nonfunctioning thermocouple.

Note: Corrected temperatures = as-recorded temperature plus top plate temperature.

CONFIDENTIAL

CONFIDENTIAL

c. Metallographic examination of containers

Metallographic examination of the stainless steel container from Polonium Distribution Test 1 showed that surface corrosion was present throughout the interior. The depth of attack varied from less than 0.001 to 0.005 inch in localized regions. The appearance and depth of corrosion were similar in all the metallographic sections which were examined.

Figures VII-12a through 12e illustrate these similarities. The regions in Fig. VII-12 are shown in the unetched condition. This was possible since polonium was removed from the surfaces by vacuum distillation, not by the usual nitric acid leaching operation.

Figure VII-13 shows the section through a deposit which was present on the base of the capsule. This particular section of the capsule had been leached in concentrated nitric acid prior to metallographic examination. The deposit was very porous and 0.02 inch thick in some regions. It appeared to consist of more than one phase. A small sample of the deposit was found by emission spectroscopy to contain only constituents of the stainless steel and lead.

The copper gasket used to seal the container was severely corroded by the polonium. This corrosion resulted in breach of the seal and loss of polonium after four days of testing at approximately 650° C.

Figure VII-14 is a photomicrograph of the first fueled Haynes-25 capsulette showing a large fracture in the side wall. The length of the fracture was slightly less than one-half the circumference of the cylinder.

As can be seen from Fig. VII-14, the fracture occurred just above the weld zone. This photomicrograph indicates that the wall is 0.014-inch thick in this base region, not 0.020-inch thick, as designed. The difference is a result of a weld dressing operation.

In addition to the large fracture, a number of smaller cracks were found in the capsulette. At least three of these smaller cracks were observed along a 1/4-inch length of the 0.020-inch thick cylindrical wall. Sections were not prepared from material farther away than 1/4 inch from the base. The smaller cracks appear to have initiated at regions of intergranular attack, then progressed in a transgranular manner across the wall.

Figure VII-15 shows localized corrosion which was observed on the base of the capsulette. The depth of the localized penetration was 0.0015 inch. The corrosion occurred during a two-day period in which the capsulette was stored under water. It is estimated that the temperature did not exceed 540° C for more than a few minutes.

There are several factors which could have contributed to the capsulette failure. First, prior to fueling, the capsulette had some undesirable characteristics. The starting bar stock had a large grain size (ASTM 1 to 2). A cold-worked surface layer was also present on the capsulette walls as the result of the machining operation. These conditions have, in the past, caused problems in obtaining crack-free welds. In this particular case, the bottom cap had to be rewelded before a leak tight capsulette was obtained. The extensive amount of heat dissipated in the metal would be expected to further aggravate the embrittlement problems. The welded capsulette was helium leak-checked, but not inspected for surface cracks.

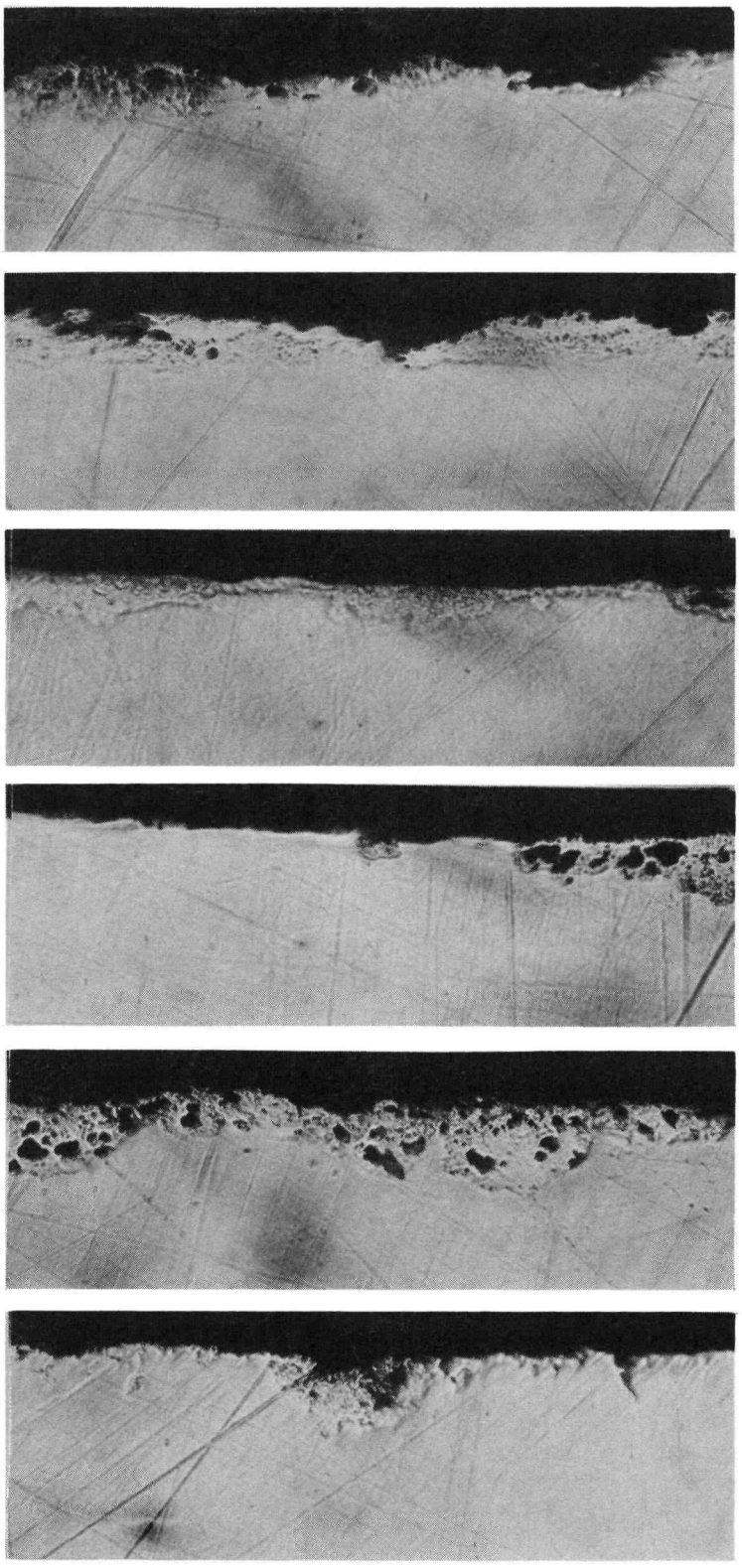

a. Cap

b. Above Bottom--
1-1/4 Inches

c. Above Bottom--
15/16 Inch

d. Above Bottom--
5/8 Inch

e. Side Wall Just
Above Bottom

f. Bottom

FIG. VII-12. UNETCHED INTERIOR SURFACES OF SS CONTAINER FROM Po DISTRIBUTION TEST. MAGN. 125X

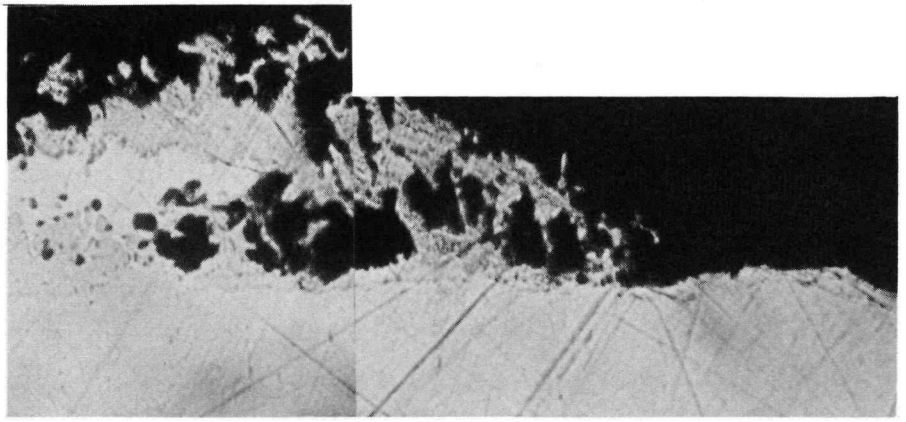

FIG. VII-13. SECTION THROUGH DEPOSIT ON BASE OF SS CONTAINER. MAGN. 125X

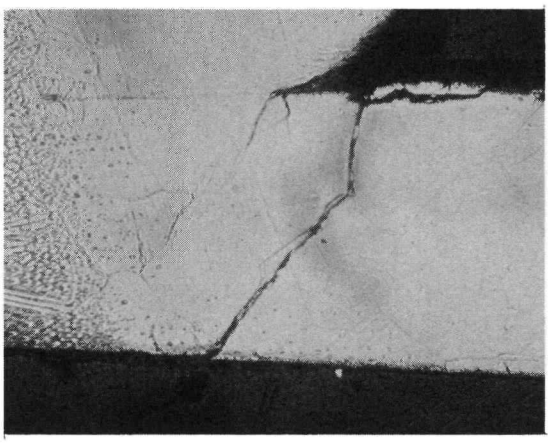

FIG. VII-14. FRACTURE IN CYLINDRICAL WALL OF HAYNES-25 CAPSULETTE, SECTION $\overline{OA}$. MAGN. 125X

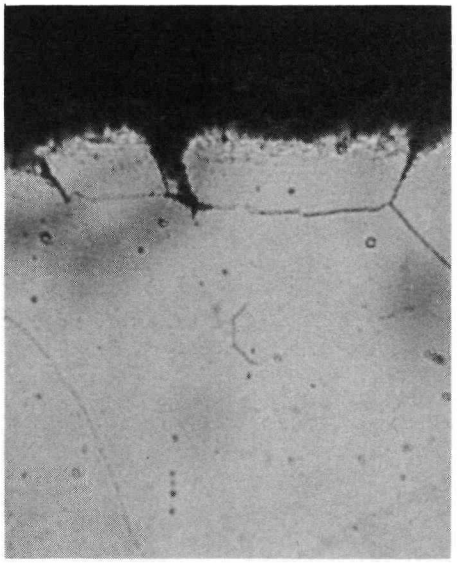

FIG. VII-15. BASE OF HAYNES-25 CAPSULETTE SHOWING LOCALIZED ATTACK TO A DEPTH OF 1-1/2 MILS. MAGN. 460X

Second, handling of the polonium-fueled capsulette presented some problems. The chill fixture used to hold the capsulette failed to secure it tightly enough to permit the metal O-ring seal to be torqued down. The capsulette had to be removed from the chill block to be sealed. Self-heating to red heat was very rapid under these conditions and the capsulette was cooled several times by partial submersion in water before it was sealed. (A force of approximately 200 in.-lb is required to compress the O-ring. A maximum shear stress of less than 30,000 psi would be imparted on the capsulette wall by this moment, a value much less than the tensile strength of solution-annealed Haynes-25.)

Third, metallographic examination showed surface corrosion and localized penetration on the internal surface of the capsulette. Corrosion can, of course, compromise mechanical properties, and the localized attack presents possible stress concentration sites.

Fourth, geometric factors could have contributed to the formation of the fractures near the base. The path of the large fracture shown in Fig. VII-14 closely follows the internal surface of the bottom cap. The junction between the cap and cylindrical wall would be a stress concentration site. Variations between the heating and cooling rates of the 0.014-inch thick base region and the remainder of the 0.02-inch thick capsulette side walls could also be a source for thermal stresses. The presence of fine cracks away from the base region indicates that geometry was not the sole cause of the capsulette failure, however.

Upon opening the second fueled Haynes-25 capsulette, a readily visible deposit of polonium was observed on the inside of the cap. It was then leached in nitric acid and subjected to a visual and dye penetrant inspection. No cracks were found on the external surface of the capsulette, indicating that leakage had occurred at the mechanical seal. The capsulette is now being prepared for metallographic examination.

d. Conclusions

Fueling of three small containers with quantities of approximately one gram of polonium metal shows that the distillation process is feasible.

There was no evidence of any prominent hot spots on the container surfaces during either of the tests. Since the polonium was essentially all in the bottom of the container just after fueling, it is assumed it tends to redistribute, thereby equalizing the surface temperature. As expected, the copper gasket in the first test was completely decomposed on exposure to polonium. It is assumed that this was the cause of the leak. The extent of attack on the stainless steel was also not unexpected.

The cracks which developed in the first fueled Haynes-25 capsulette cannot be assigned a specific cause. The mechanical and thermal stress, as well as the prior condition of the metal, probably played an important part in the failure.

The capsulette used in the second distribution test leaked through the Clydlok seal. The cause of this leak was probably closely associated with the corrosion of the Haynes-25 seen in both the first and second fueled capsulettes. This corrosion was more extensive than expected from the C-capsule compatibility data.

4. Compatibility Testing

Polonium metal contained in a Haynes-25 capsulette is the primary candidate for the SNAP 29 dispersal heat source; however, gadolinium polonide-fueled

tantalum matrices in Haynes-25 containers are being considered as a possible alternate. Since no compatibility data exist for this fuel-container combination, the N-series tests were initiated.

Six Haynes-25 capsules were loaded with pellets of the matrix fuel form. Table VII-4 summarizes the loading results. Nominal capsule and matrix dimensions are also given in the table.

TABLE VII-4

Summary of Haynes-25/GdPo/Ta Matrix Capsule Loadings

Specimen No.	Amount of Polonium on 10/31/68 (Ci)	Power Densities		Neutron Emission Rate (n/Ci/sec)
		Capsule (watts/cc)	Matrix (watts/cc)	
N-1	87.8	17.7	37.6	340
N-2	107.8	21.7	46.2	310
N-3	83.6	17.0	35.8	200
N-4	Control	--	--	--
N-5	107.3	21.6	46.0	130
N-6	70.4	14.2	30.2	140
N-7	98.6	20.0	42.2	210
N-8	Control	--	--	--

Compatibility Capsule Dimensions

OD = $\frac{0.250}{0.249}$ inch ID = $\frac{0.171}{0.169}$ inch

External height = $\frac{0.501}{0.499}$ inch Base thickness = 0.040 inch
Cap thickness = 0.030 inch

Outer Capsule Dimensions

OD = $\frac{0.502}{0.498}$ inch ID = $\frac{0.252}{0.251}$ inch

External height = $\frac{0.726}{0.724}$ inch Base thickness = 0.125 inch
Cap thickness = 0.100 inch

Matrix Dimensions

Diameter = 0.159 inch; height = 0.23 inch
Theoretical density = 61 to 64%
Ta/GdPo volume ratio = 10:1

The test temperature originally designated was 1000° C, but this was changed due to the following considerations.

(1) The SNAP 29 dispersal heat source operating temperature is anticipated to be approximately 880° C.

(2) Haynes-25 aging effects (grain boundary precipitation, embrittlement) are most rapid and extensive at about 880° C.

The tests were modified to run Nos. N-1, 4, 5 and 6 at 880° C and Nos. N-2, 3, 7 and 8 at 1000° C. These test temperatures refer to the wall temperature of the Haynes-25 outer strength body, as measured by a thermocouple attached to the surface. Heating tests began on 11/26/68. It is planned to examine the capsules from the 880° C test after 50 days. The other set will be heated for 150 days so that data can be compared with results obtained in the 1000° C C-series tests.

An additional type of control specimen will be included in the N-series tests. It will consist of a pressed pellet of tantalum powder contained in a Haynes-25 capsule. Additional fueled capsules may also be included in these tests at a later date.

5. Polonium Fuels Properties

Table VII-5 presents a list of polonium fuels properties. A summary of the available properties data, corresponding by number to the Table VII-5 list, is presented in Table VII-6. Additional property information is available in the "Polonium-210 Isotopic Fuel Form Data Sheets." MLM-1563.

TABLE VII-5

Polonium Fuels Property List

1. Neutron spectrum and emission rate
2. Half-life
3. Alpha spectrum and emission rate
4. Gamma spectrum and emission rate
5. X-ray spectrum and emission rate
6. Impurities in fuel form
7. Chemical reactions and rates in air as a function of pressure
8. Chemical reactions and rates in fresh water
9. Chemical reactions and rates in seawater or equivalent
10. Chemical reactions and rates in soil (model to be specified by Isotopes, Inc.)
11. Chemical reactions and rates with capsule materials
12. Chemical reactions and rates with graphite
13. Solubility constants of reaction products
14. Density of predominant reaction products
15. Vapor pressure of GdPo and PoO
16. Melting point
17. Boiling point
18. Heat of fusion
19. Heat of vaporization
20. Specific heat
21. Thermal conductivity of matrix
22. Heat of reaction of GdPo with oxygen
23. Reactions and reaction rates with propellants and propellant reaction products to be specified by Isotopes, Inc.
24. Fuel state as a function of environmental conditions to be determined by Isotopes, Inc.
25. Density of GdPo
26. Stoichiometry of GdPo
27. Specific activity of Po
28. Matrix density (final product)
29. Volume ratio of GdPo to matrix material

TABLE VII-6

Polonium Fuels Properties

Property No.	Presently Available Data		Date for New Data	Comments
1	1.0 to 2.5 Mev 0		5/69	Available in Po metal data sheet New data for encapsulated fuel
2	138.375			Available in Po metal data sheet
3	5.298 Mev	1.155×10^{12} alpha/watts-sec		Available in Po metal data sheet
	4.5 Mev	1.410×10^{7} alpha/watts-sec		
4	0.804 Mev	1.41×10^{7} photons/watts-sec		Available in Po metal data sheet
5	0.077 to 0.090 Mev	1.7×10^{6} photons/watts-sec		Available in Po metal data sheet
	0.01 to 0.015 Mev	3.3×10^{8} photons/watts-sec		
6	Te 0.6 ± 0.2% Se <0.05% O_2 2 to 4% Pb Time dependent	Po metal		Available in Po metal, GdPo and GdPo in Ta matrix data sheets
	(ppm) N_2 10 Re 250	Gd metal		(Pb impurity increases at rate of ~0.5% of Po content/day)
	C 100 O_2 100 H_2 150 N_2 1000 B 5 Na 50 Ni 50 Ca 50 Cr 30 Sn 20 Zr 20 Ti 30 Si 100 W 100 Fe 100 Mn 20 Al 20 Mo 20 Nb 50 Other 45	Ta matrix impurities		All data maximum impurities of components. To find maximum impurities in GdPo-Ta matrix fuel add impurities in ratio
7	Rate of oxidation of Po in a GdPo-Ta matrix ~50 Ci/hr		7/69	Data maximum rate during 1st hour of Air Exposure Test 2
8			4/69	
9			4/69	
10				Property will not be determined
11				Compatibility data available in Mound SNAP 29 Monthly Reports
12				Property will not be determined

TABLE VII-6 (continued)

Property No.	Presently Available Data	Date for New Data	Comments
13		4/69	
14		9/69	
15	For: Po vapor over GdPo ~10^{-4} atm at 1400° C For: GdTe→Gd(g) + Te(g) $\text{Log } P_{total} = \frac{-2.4372 + 0.1253 \times 10^{-4}}{T_{°K}} + 7.37 \pm 0.76$	2/68	Data available in GdPo data sheets Data for PoO_2 as function of T available in Mound SNAP 29 Monthly Reports for 2 through 5/68
16	Melting point Po 254° C GdPo 1675° C Ta 2996° C		Data available in Po metal and GdPo Ta matrix data sheets Data for GdPo Pb system available in GdPo data sheets
17	Boiling point Po 962° C		Data available in Po metal data sheets. GdPo data not available.
18	For Ta: $\Delta H_{(f)}$ = 34.6 to 41.5 cal/gm at ≈ 3000°C		Data available in GdPo in Ta matrix data sheets. GdPo data not available
19	For: Po(1)→Po (gm) $\Delta H_{(v)} = 24.597 \pm 0.031$ kcal/(gm-atm) For: GdTe (s)→Gd (gm) + Te (gm) $\Delta H = 223 \pm 11$ kcal/mole For Ta: $\Delta H_{(v)}$ = 0.995 to 1.021 kcal/gm		Estimates available in Po metal, GdPo and GdPo Ta matrix data sheets
20	Sp H GdPo at 25° C = 12.5 cal/mole-°C Sp H GdPo at 1000° C = 14 cal/mole-°C Sp H Ta at 25° C = 0.034 cal/gm-°C		Estimates available in GdPo and GdPo in Ta matrix data sheets. Enthalpy not available. Data for Po metal as function of T in Po metal data sheets
21	For 50:1 Ta: GdPo weight ratio at 293° K $Q = 8.2 \times 10^{-2}$ cal (sec-cm-°C)$^{-1}$ For 10:1 Ta: GdPo weight ratio at 293° K $Q = 7.2 \times 10^{-2}$ cal		Estimate available in GdPo in Ta matrix data sheets
22			Data not available
23			Property will not be determined
24			Gd-Po-Pb phase diagram available in GdPo data sheet. Thermal profile test provides more data. Adequate environmental conditions not defined for thermal profile test.
25	For GdPo: density = 9.78 gm/cc		Data available in GdPo data sheet
26	1:1		Data available in GdPo data sheet
27	4500 Ci/gm		Data available in Po metal data sheets
28	For 50:1 Ta: GdPo weight ratio: 10.4 gm/cc at 63% theoretical density For 10:1 Ta: GdPo weight ratio: 10.3 gm/cc at 64% theoretical density For 10:1 Ta: GdPo volume ratio: 9.91 gm/cc for 62% theoretical density		Data available in GdPo in Ta matrix data sheets
29	Minimum Ta volume/GdPo volume = 10/1		Smaller ratio than 10/1 may require further testing of fueling technique

APPENDIX A

I^2R LOSSES FOR COPPER FLAME-SPRAYED PADS

A. LIST OF SYMBOLS

A	Surface area of top of pad	$in.^2$
b	Width of pad	inches
I	Electric current	amperes
ℓ	Length of pad through which current flows	inches
m	Weight	pounds
N	Number of pads/module	--
M	Number of pairs of straps/module	--
P	Power	watts
P_{sp}	Specific power	watts/lb
R	Electric resistance	ohms
t	Pad thickness	inches
V	Voltage drop across plate	volts
η	Number of modules	--
ρ	Weight of density	$lb/in.^3$
R	Electrical resistivity	ohms-inch

Subscripts

opt	Optimum
P	Pad
s	Strap
sys	System
T	Total

B. INTRODUCTION

Dielectric and circuit resistance tests have been completed for copper flame-sprayed stainless steel plates. A description of the tests along with test results is presented in Ref. A-1. A schematic of the test module is shown in Fig. A-1. Details of a single copper pad and strap are shown in Fig. A-2. The purpose of this study is to analyze the test results and to determine the difference in I^2R losses between the 0.012- and 0.020-inch thick copper flame-sprayed pads. The optimum pad thickness is also determined as a function of SNAP 29 system weight for the nominal TAGS operating condition.

CONFIDENTIAL

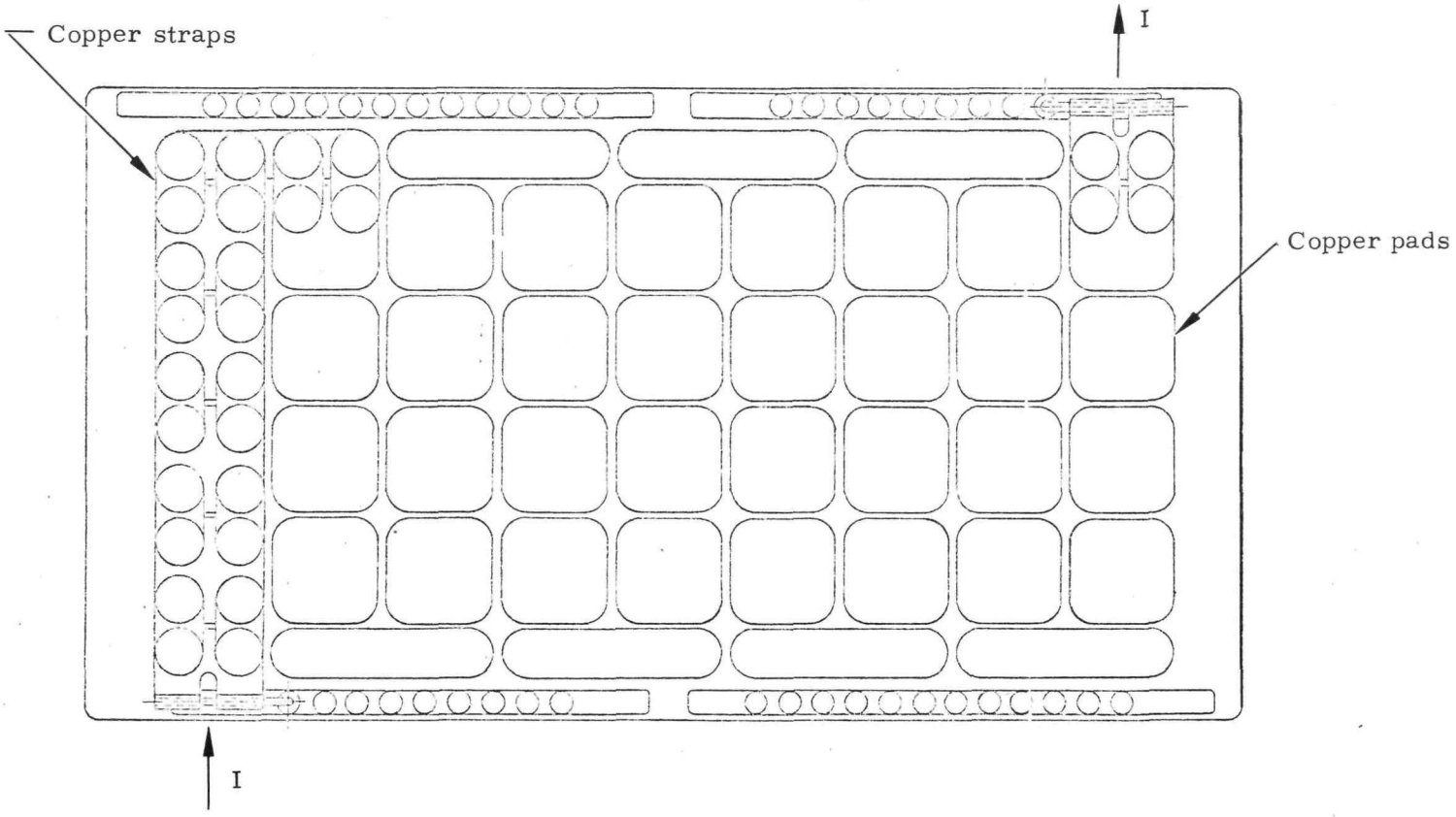

*Although not shown in the drawing, copper straps connect all pads on the plate in order to complete the electric circuit.

FIG. A-1. COLD END MODULE TEST PLATE*

CONFIDENTIAL

CONFIDENTIAL

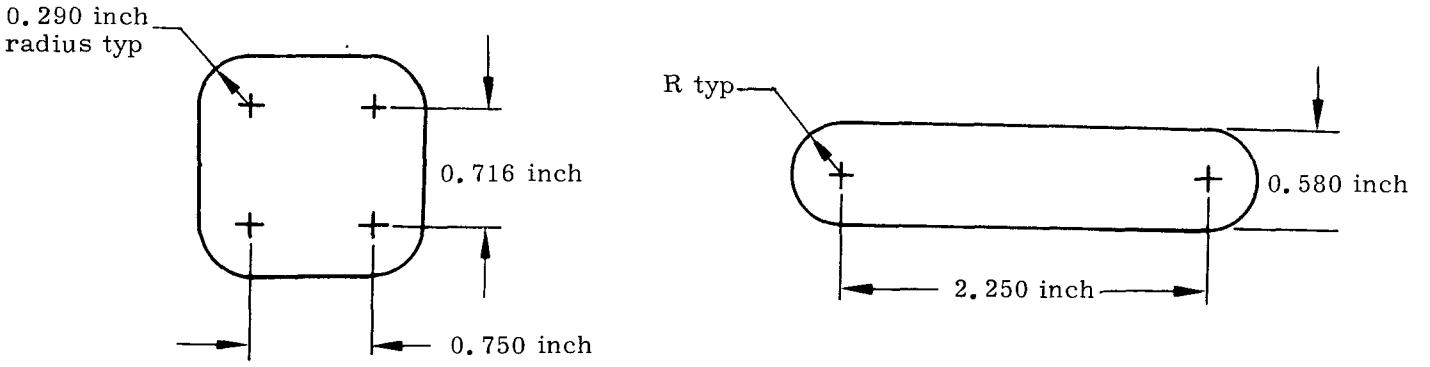

Typical Pad Configuration

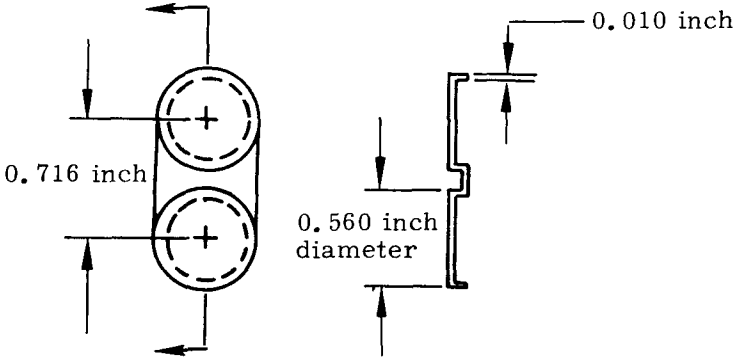

Copper Straps

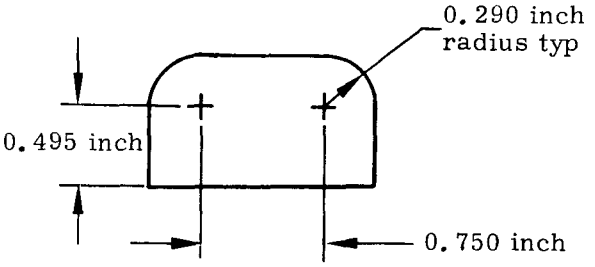

Power Lead Pad
(0.002 inch thick)

FIG. A-2. DETAILS OF COPPER PADS AND STRAPS

CONFIDENTIAL

C. DESCRIPTION OF ANALYSIS

Results of the circuit resistance tests obtained from Ref. A-1 are listed in Table A-1. The I^2R losses of the plate were calculated from the test data as

$$(I^2R)_T = IV \tag{A-1}$$

where

I = current through the plate (amp)

V = voltage drop across the plate (volts)

TABLE A-1

Results of Circuit Resistance Tests of Copper Flame-Sprayed Pads

I (amp)	Voltage Drop Across Plate (volts) -0.012 In. Pad	-0.020 In. Pad
T = 72° F		
25	0.1065	0.086
30	0.1276	0.103
35	0.1490	0.120
T = 350° F		
25	0.160	0.135
30	0.1923	0.160
35	0.2231	0.187
T = 400° F		
25	0.1740	0.125*
30	0.2065	0.149*
35	0.2410	0.174*

*The data for the 0.020-inch pads indicate a decrease in voltage drop as the plate temperature is increased from 350° to 400° F. This is inconsistent with the rest of the data and also the fact that the resistivity of copper increases with temperature. This inconsistency can probably be attributed to an experimental error such as having one of the voltage probes come loose, etc.

The difference in I^2R losses between the 0.012- and 0.020-inch thick pads was then calculated from

$$\Delta(I^2R)_p = (I^2R)_{T_{0.012}} - (I^2R)_{T_{0.020}} \tag{A-2}$$

The I^2R losses of the pads were determined by first calculating the I^2R losses of the copper straps.

$$(I^2R)_s = M\, I^2 R_{s_e}$$

where

M = number of pairs of straps = 45

R_{s_e} = resistance of a pair of straps (ohms)

Since the straps are in parallel

$$R_{s_e} = \frac{R_s}{s} \qquad \text{(A-3)}$$

where

R_s = resistance of a single strap (ohms)

The current is assumed to flow in the straps through the 0.716-inch length designated in Fig. A-1. The resistance of a single strap which was measured across this length was 0.1 mΩ at room temperature. The resistance of the copper straps was assumed to have the same variation with temperature as the resistivity of copper. This variation is shown in Table A-2.

TABLE A-2

Temperature Variation of Electrical Resistivity of Cu and Resistance of Cu Strap

T (°F)	ρ_R* (μohms-cm)	$\rho_R/\rho_{R_{T = 72° F}}$	R_s (mohms)
72	1.6	1.0	0.1
300	2.3	1.43	0.143
350	2.45	1.53	0.153
400	2.6	1.63	0.163

*Ref. A-2.

Having determined the I^2R losses of the straps, the I^2R losses of the pads were calculated from

$$(I^2R)_p = (I^2R)_T - (I^2R)_s \qquad \text{(A-4)}$$

Since at present the thickness of the copper pads is a variable parameter, it is desirable to know what pad thickness will optimize the specific power of the SNAP 29 system at its nominal operating conditions. As derived in the Appendix, the specific power of a four-module system at the nominal TAGS operating condition (T_{CJ} = 375° F, I = 28 amperes) is expressed in terms of the pad thickness as

$$P_{sp} = \frac{441 - 0.108\,\frac{1}{(t)}}{m^1 + 74\,t} \qquad \text{(A-5)}$$

where

$$m_{sys} = m^1 + \eta m_p \quad \text{(A-6)}$$

m_{sys} = weight of the system (lb)

m_p = weight of the pads (lb)

η = number of modules

The optimum pad thickness for the same conditions is

$$t_{opt} = \frac{0.027\, m^1}{-2 + \sqrt{4 + 220.5\, m^1}} \quad \text{(A-7)}$$

D. RESULTS

The results of the analysis are listed in Tables A-3 through A-5. The difference in I^2R losses between the 0.012- and 0.020-inch pads is also shown in Fig. A-3. At the nominal TAGS operating condition this difference is approximately 1.17 watts/module. The I^2R losses of the pads are also shown in Figs. A-4 to A-6. The optimum pad thickness is shown in Fig. A-7 as a function of m^1. The system weight of the SNAP 29 is approximately 375 pounds. Since the weight of the pads will be very small ($m_p \sim 2$-3 lb), m^1 can be assumed equal to the system weight. From Table A-5 the optimum pad thickness is approximately 0.035 inch.

E. DERIVATION OF OPTIMUM PAD THICKNESS

The specific power of a system is defined as

$$P_{sp} = \frac{P_{net}}{m_{sys}} \quad \text{(A-8)}$$

where

m_{sys} = weight of the system

$$m_{sys} = m^1 + \eta m_p \quad \text{(A-6)}$$

with η = number of modulus/system

The weight of the pads can be expressed in terms of the pad thickness as

$$m_p = N \rho A t \quad \text{(A-9)}$$

where

A = surface area of the top of the pad (in.^{2})

N = number of pads/module

TABLE A-3

I^2R Losses Associated with Copper Flame-Sprayed Pads

	0.012-Inch Thick Pads		0.020-Inch Thick Pads		
I (amp)	$(I^2R)_T$ (watts)	$(I^2R)_P$ (watts)	$(I^2R)_T$ (watts)	$(I^2R)_P$ (watts)	$(I^2R)_P$ (watts)
T = 72° F					
25	2.67	1.26	2.15	0.74	0.52
30	3.83	1.6	3.09	1.06	0.74
35	5.22	2.46	4.20	1.44	1.02
T = 350° F					
25	4.0	1.85	3.37	1.22	0.63
30	5.76	2.66	4.8	1.7	0.96
35	7.81	3.6	6.55	2.34	1.26
T = 400° F					
25	4.31	2.02	3.13	0.84	1.18
30	6.2	2.9	4.47	1.17	1.73
35	8.47	3.98	6.09	1.60	2.38

TABLE A-4

Specific Power of SNAP 29*

Pad Thickness t (in.)	(m^1 = 375 lb) P_{sp} (watt/lb)	$P_{sp}/P_{sp_{opt}}$
0.035	1.16	1.0
0.020	1.157	0.997
0.012	1.149	0.99

TABLE A-5

Optimum Copper Flame-Sprayed Pad Thickness*

m^1 (lb)	t_{opt} (in.)
350	0.0342
375	0.0354
400	0.0365

*Nominal TAGS operating condition (T_{CJ} = 375° F, I = 28 amperes)

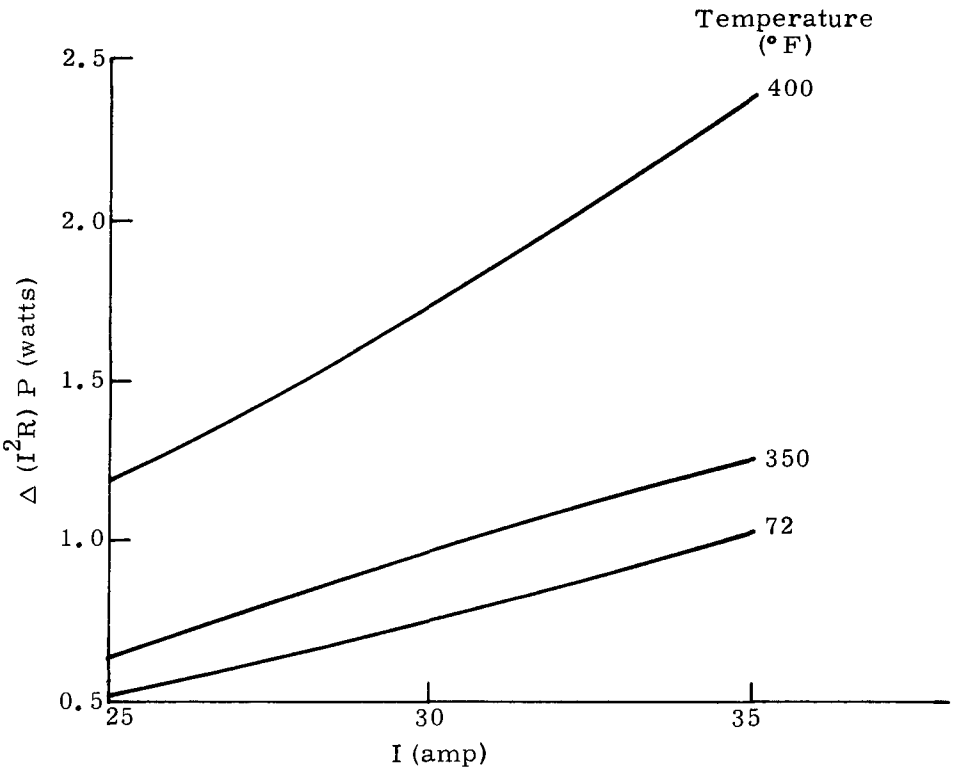

FIG. A-3. INCREASE IN I^2R LOSSES--0.012 VERSUS 0.020 INCH THICK COPPER FLAME-SPRAYED PADS

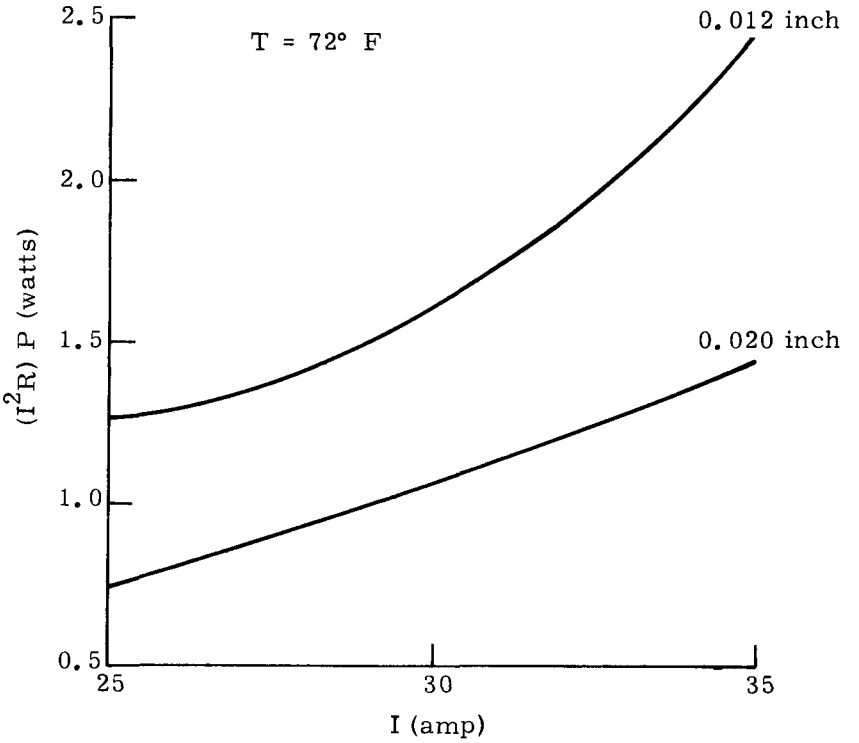

FIG. A-4. I^2R LOSSES OF COPPER FLAME-SPRAYED PADS--ONE MODULE

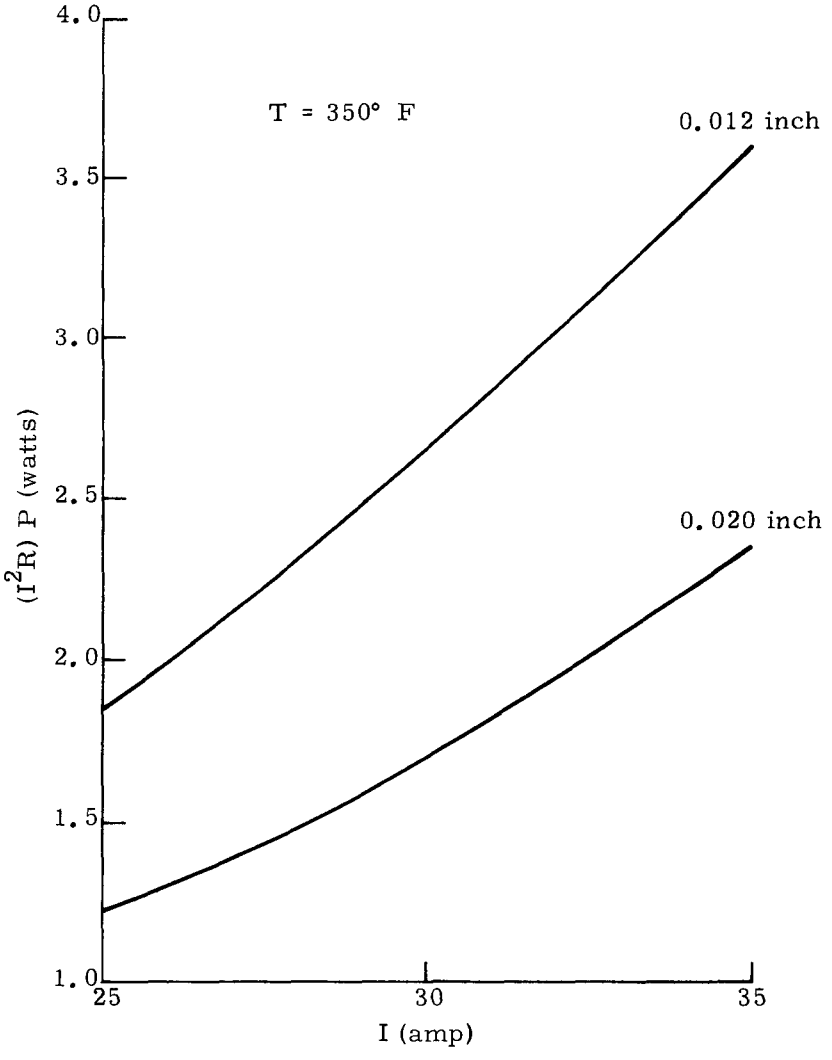

FIG. A-5. I^2R LOSSES OF COPPER FLAME-SPRAYED PADS--ONE MODULE

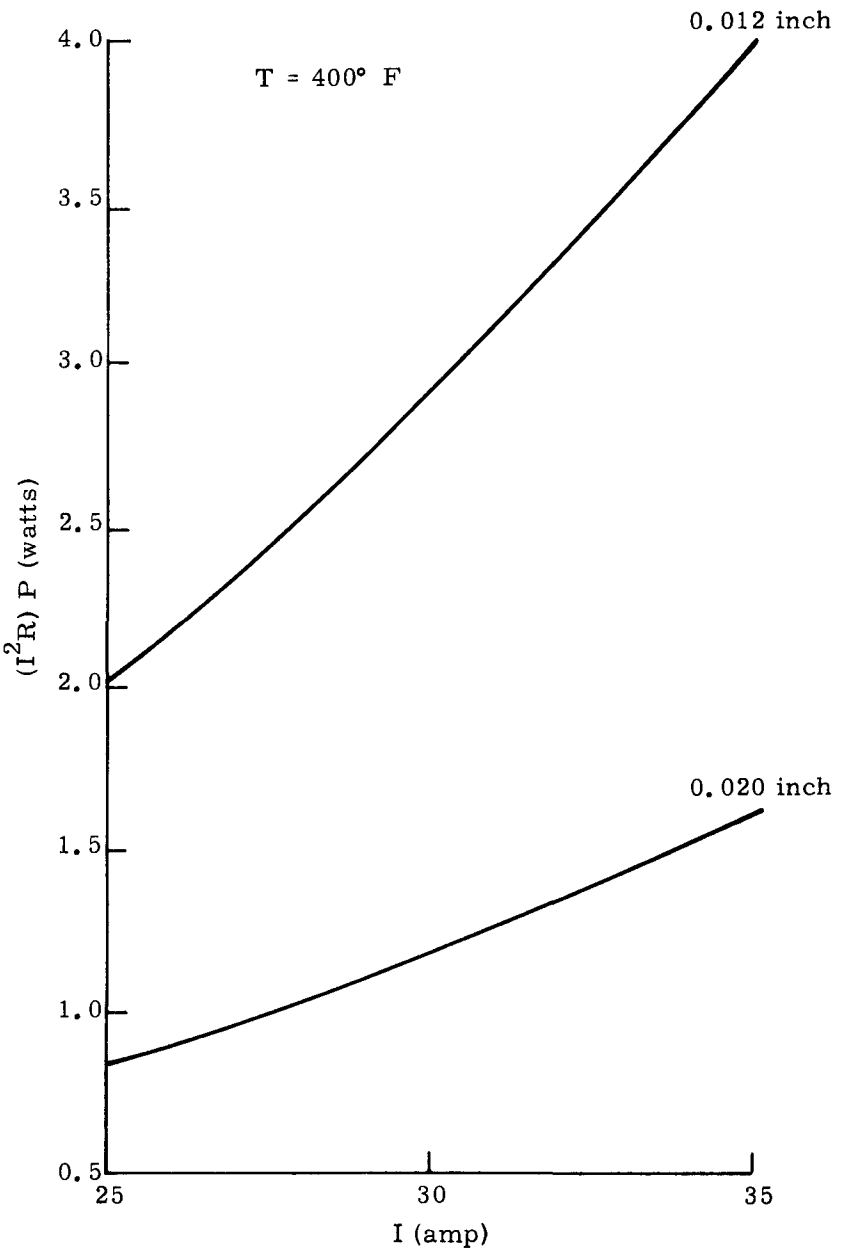

FIG. A-6. I^2R LOSSES OF COPPER FLAME-SPRAYED PADS--ONE MODULE

t = thickness of the pads (in.)

ρ = weight density of the pads (lb/in.^{3})

Also, the net power is given by

$$P_{net} = P_{in} - P_L \tag{A-10}$$

with P_{in} = total power input (watts)

and P_L = total power loss of the system (watts)

$$P_L = p_L^1 + \eta (I^2R)_p \tag{A-11}$$

The I^2R losses of the pads can be written in terms of the pad thickness as

$$(I^2R)_p = I^2 \frac{(\rho_R \ell)}{bt} \tag{A-12}$$

where

b = width of pad (in.)

ℓ = length of pad through which current flows (in.)

t = thickness of pad (in.)

ρ_R = electrical resistivity of pad material (ohms-in.)

If the following parameters are defined,

$$\gamma = N \rho A \tag{A-13}$$

$$\mathfrak{t} = I^2 \rho_R \frac{\ell}{b} \tag{A-14}$$

Equation (A-8) for the specific power can be expressed in terms of the pad thickness as

$$P_{sp} = \frac{P_{in} - P_L^1 - \eta \mathfrak{t} (\frac{1}{t})}{m^1 + \eta \gamma t} \tag{A-15}$$

To optimize the specific power with respect to the pad thickness, one must have

$$\frac{dP_{sp}}{dt} = 0 \tag{A-16}$$

or

$$m^1 \mathfrak{t} (\frac{1}{t})^2 + 2 \eta \gamma \mathfrak{t} (\frac{1}{t}) - \gamma (P_{in} - P_L^1) = 0 \tag{A-17}$$

Since all the parameters involved are physical quantities and therefore must be positive, the solution of this quadratic equation which gives the optimum pad thickness is

$$t_{opt} = \frac{m^1}{-\eta\gamma \quad + \quad (\eta\gamma \quad)^2 + m^1\gamma \quad (P_{in} \; P_L^2)} \tag{A-18}$$

From Ref. A-3, the net power for a SNAP 29 system consisting of four TAGS modules was 436 watts. The pads in this module design were 0.020 inch rolled copper as opposed to the flame-sprayed copper pads being considered. The I^2R losses for 0.010-inch rolled copper pads were determined in Ref. A-4 to be 3 watts/module. Since the I^2R losses of the pads are inversely proportional to the pad thickness, the losses for the 0.020-inch rolled copper pads is 1.5 watts/module, thus for the four-module system

$$P_{in} - P_L^1 = P_{net} + P_P = 436 + 6 = 442 \text{ watts}$$

From Ref. A-2

for

$t = 0.012$ inch, $m_p = 98$ grams $\rightarrow \gamma = 18$ lb/in.

$t = 0.020$ inch, $m_p = 172.5$ grams $\rightarrow \gamma = 19$ lb/in.

hence, the arithmetic average of γ is

$\bar{\gamma} = 18.5$ lb/in.

At the nominal TAGS operating condition from Figs. A-5 and A-6

for

$t = 0.012$ inch, $(I^2R)_P = 2.41$ watts $\rightarrow$ $= 0.029$ watt-in.

$t = 0.020$ inch, $(I^2R)_P = 1.25$ watts $\rightarrow$ $= 0.025$ watt-in.

thus, the arithmetic average of $\frac{1}{t}$ is

$\overline{\frac{1}{t}} = 0.027$ watt-in.

Using these average values, the specific power for a four-module system at the nominal TAGS operating condition is given by

$$P_{sp} = \frac{442 - 0.108\left(\frac{1}{t}\right)}{m^1 + 74\,t} \tag{A-19}$$

Similarly, the optimum pad thickness is

$$t_{opt} = \frac{0.027}{-2.0 + \sqrt{4.0 + 220.5\,m^1}} \tag{A-7}$$

F. CONCLUSIONS

The difference in I^2R losses between the 0.012- and 0.020-inch thick copper flame-sprayed pads is approximately 1.17 watts/module at the nominal TAGS operating condition. The optimum pad thickness for maximum specific power is approximately 0.035 inch for the SNAP 29 system. Although this optimum thickness is nearly triple that of the 0.012-inch pads, as shown in Table A-2, the specific power of the 0.012-inch pads is just 1% less than the optimum specific power. Thus, only a very slight penalty in the specific power of the SNAP 29 system will result if fabrication or some other factor dictates using copper flame-sprayed pads significantly thinner than the optimum thickness.

G. SUMMARY

The increase in I^2R losses between 0.020- and 0.012-inch thick copper flame-sprayed pads has been determined. This increase is 1.17 watts/module at the nominal TAGS operating condition. The I^2R losses of the copper pads have also been determined for both pad thicknesses. In addition, the pad thickness which optimizes the specific power of the SNAP 29 system has been determined. This optimum thickness is approximately 0.035 inch. The specific power of the 0.012-inch pads is only 1% less than the optimum power. It can be concluded that little or no penalty in specific power will result if the thickness of the copper flame-sprayed pads is less than the optimum thickness but greater than 0.012 inch.

H. REFERENCES

A-1. Chryst, G., Report, August 19, 1968.

A-2. Lyon, W., "Isotopes Nuclear Systems Division Physical Properties Compilation."

A-3. Young, C. and Christenbury, S. T., "SNAP 29 RTG System Weight and Specific Power Utilizing an Intact Heat Source Design." IDC-1100-55A, August 1968.

A-4. Sellevaag, P., "Electrical Circuit Tradeoff Study." IDC-1340-135B, December 1967.

BLANK

APPENDIX B

THERMOELECTRIC DATA FOR TAGS (TEDP-00-10A) AND SnTe (TEDP-00-27) THERMOELECTRIC ELEMENTS

A. INTRODUCTION

The SNAP 29 thermoelectric couple is made up of a PbTe (TEDN-00-34) 2N leg and a TAGS-85/SnTe (TEDP-10A-27) segmented P leg. Analytical studies are made for this thermoelectric couple with the aid of the VINCE TOM (KN-125D) computer program and experimental thermoelectric property data. The T/E property data for a given material consists of the Seebeck coefficient, resistivity and thermal conductivity as a function of temperature.

B. TAGS-85 THERMOELECTRIC PROPERTY DATA

The TAGS-85 (TEDP-00-10) thermoelectric property data were a result of research data taken in May 1966. These data are no longer recommended. Present research data indicate a change in the resistivity of the TAGS-85 material data. The material is still TAGS-85 but the property data will be associated with a new thermoelectric element identification, TEDP-00-10A. The thermoelectric property data for TEDP-00-10 and 10A are presented in this report.

C. COMPARISON OF TEDP-00-10 AND TEDP-00-10A DATA

Two typical SNAP 29 thermoelectric couples were analyzed using the VINCE TOM computer code. The couples were analyzed under SNAP 29 conditions: T_H = 1050° F, T_C = 350° F, C_T = 125 $\mu\Omega$-cm^2, length of elements = 0.5 inch, diameter of the N leg = 0.56 inch and diameter of the P leg = 0.5 inch. Both couples had N legs made of TEDN-00-34 (PbTe) and 0.090 inch TEDP-00-27 (SnTe) segments in the P leg. (Thermoelectric property data for TEDP-00-27 (SnTe) is presented in this report.) For comparison, one couple employed TEDP-0010 for the TAGS portion of the P leg, and the other couple used TEDP-0010A. The results of the VINCE TOM runs indicate no significant difference in the calculated T/E parameters between the two thermoelectric couples. These T/E parameters are presented in Table B-1.

TABLE B-1

Comparison of TEDP-00-10 and TEDP-00-10A T/E Parameters

T/E parameter	TEDP-00-10	TEDP-00-10A
Thermoelectric efficiency (%)	7.971	7.966
Total generator resistance (Ω)	5.795	5.802
Normalized power = P/NA = power/total cross sectional area of couples (watts(e)/in.^{2})	3.143	3.141
Normalized heat = Q/NA = thermal input/total cross sectional area of couples (watts(t)/in.^{2})	39.429	39.427
Diameter ratio for optimum efficiency N leg/P leg	1.483	1.482

Looking at the plot of resistivity for TEDP-00-10 and 10A, it can be visualized that the insignificant difference between the couples is attributed to the fact that the area between the two curves for the temperature range of 600° to 840° F nullifies the area between the two curves for the temperature range of 840° to 950° F. This makes the areas under the two curves approximately equal for the SNAP 29 temperature range. It is important to realize that only the SNAP 29 temperature range is being examined, 350° to ~950° F for the TAGS-85 (~950° to 1050° F is through the SnTe segment because ~950° F is the upper limit for TAGS-85 operation). Therefore, if the TAGS-85 material (TEDP-00-10A) is employed at a hot junction temperature below the 950° F limit, an advantage may be realized due to the lower resistivity between 600° and 840° F. This will be most prominent when the hot junction temperature is near 840°. Below 600° F there is no difference in data between the two materials.

D. CONCLUSIONS

In the future the TEDP-00-10 thermoelectric data will be disregarded and the TEDP-00-10A data should be given preference. Past analysis for the thermoelectric couples in the SNAP 29 system will be reviewed on the basis of the prementioned TAGS-85 data comparison.

E. TEDP-00-10 AND TEDP-00-10A THERMOELECTRIC PROPERTY DATA

Reference: B-1 TEDP-00-10 Data

B-2 TEDP-00-10A Data--Supplied by Dr. D. Evans as published in "Summary of the Advanced Technology Symposium," August 29-30, 1967, and the Thermoelectric Panel Meeting, October 10, 1967, MND-3314 by Martin Marietta Corporation.

TAGS-85 T/E Property Data

TEDP-00-10

Temperature (°F)	Seebeck (volts/°F)	Resistivity (ohm-in.)	Conductivity (Btu/hr-ft-°F)
0.0			
50.0			
100.0	45.0E-06	281.0E-06	0.868*
150.0	53.7E-06	297.0E-06	0.872*
200.0	62.2E-06	312-0E-06	0.878
250.0	68.8E-06	326.0E-06	0.882
300.0	74.5E-06	340.0E-06	0.886
350.0	79.5E-06	354.0E-06	0.890
400.0	84.5E-06	368.0E-06	0.894
450.0	89.1E-06	382.5E-06	0.898
500.0	93.2E-06	398.0E-06	0.902
550.0	97.0E-06	415.0E-06	0.906
600.0	100.5E-06	434.0E-06	0.910
650.0	103.5E-06	453.0E-06	0.915
700.0	106.2E-06	471.0E-06	0.923
750.0	108.5E-06	481.0E-06	0.933
800.0	109.9E-06	485.0E-06	0.948
850.0	110.1E-06	480.0E-06	0.970
900.0	109.8E-06	468.0E-06	1.006
950.0	109.0E-06	450.0E-06	1.043

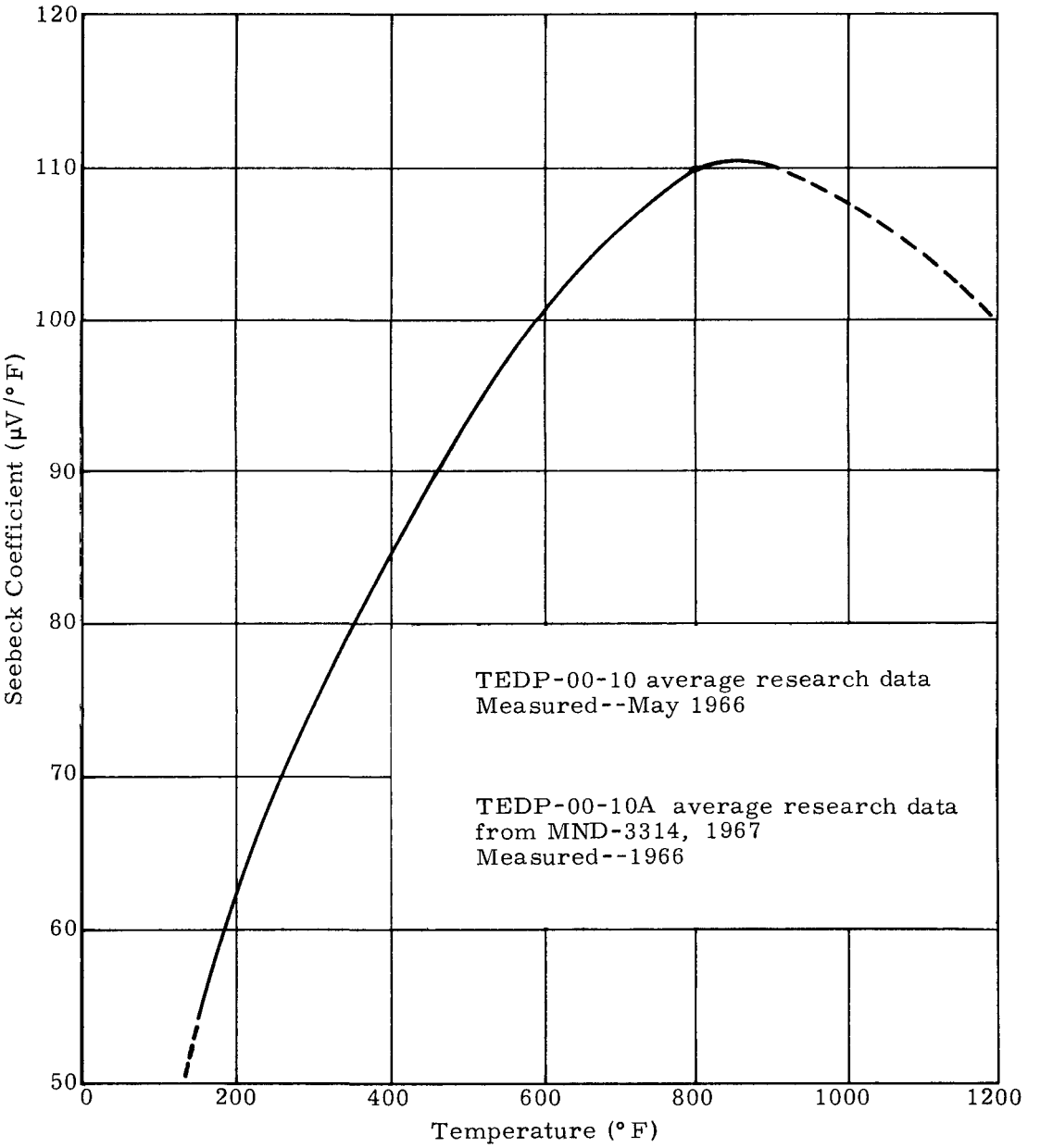

FIG. B-1. TEDP-00-10 AND 10A TAGS-85 P TYPE ELEMENT

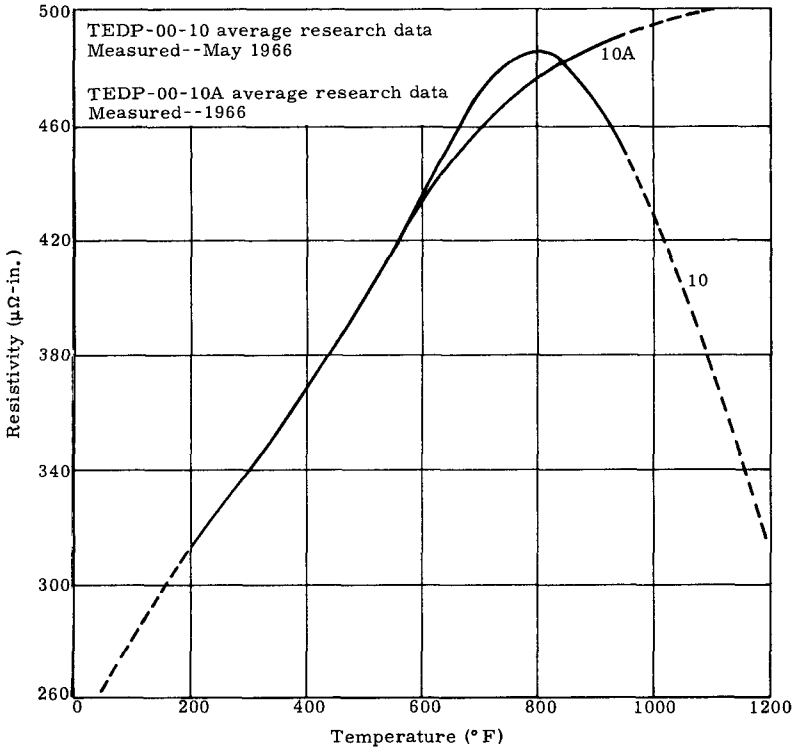

FIG. B-2. TEDP-00-10 AND 10A TAGS-85 P TYPE ELEMENT

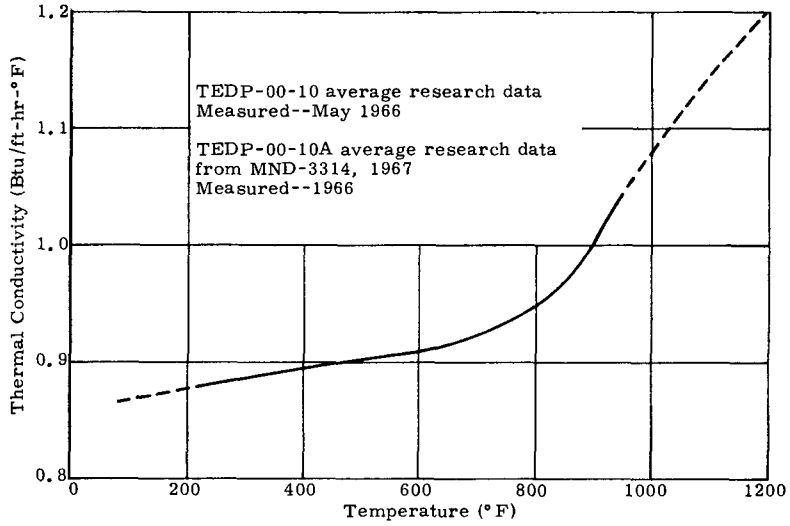

FIG. B-3. TEDP-00-10 AND 10A TAGS-85 P TYPE ELEMENT

TEDP-00-10 (continued)

Temperature (°F)	Seebeck (volts/°F)	Resistivity (ohm-in.)	Conductivity (Btu/hr-ft-°F)
1000.0	107.9E-06	429.0E-06	1.080*
1050.0	106.3E-06	403.0E-06	1.116*
1100.0	104.3E-06	375.0E-06	1.146*
1150.0	102.0E-06	345.0E-06	1.175*
1200.0	99.6E-06	311.0E-06	1.201*

Temperature Distribution Used in Data Pack for VINCE TOM (°R)

1660.0	1610.0	1560.0	1510.0	1460.0	1410.0
1360.0	1310.0	1260.0	1210.0	1160.0	1110.0
1060.0	1010.0	960.0	910.0	860.0	810.0
760.0	660.0				

/&

*Extrapolated data for code input only

Recommended TAGS-85 T/E Property Data

TEDP-00-10A

Temperature (°F)	Seebeck (volts/°F)	Resistivity (ohm-in.)	Conductivity (Btu/hr-ft-°F)
0.0			
50.0			
100.0	45.0E-06	281.0E-06	0.868*
150.0	53.7E-06	297.0E-06	0.872*
200.0	62.2E-06	312.0E-06	0.878
250.0	68.8E-06	326.0E-06	0.882
300.0	74.5E-06	340.0E-06	0.886
350.0	79.5E-06	354.0E-06	0.890
400.0	84.5E-06	368.0E-06	0.894
450.0	89.1E-06	382.5E-06	0.898
500.0	93.2E-06	398.0E-06	0.902
550.0	97.0E-06	415.0E-06	0.906
600.0	100.5E-06	432.5E-06	0.910
650.0	103.5E-06	446.0E-06	0.915
700.0	106.2E-06	457.0E-06	0.923
750.0	108.5E-06	467.0E-06	0.933
800.0	109.9E-06	475.0E-06	0.948
850.0	110.1E-06	482.0E-06	0.970
900.0	109.8E-06	486.5E-06	1.006
950.0	109.0E-06	490.5E-06	1.043
1000.0	107.9E-06	494.2E-06	1.080*
1050.0	106.3E-06	498.0E-06	1.116*
1100.0	104.3E-06	501.0E-06	1.146*
1150.0	102.0E-06	504.0E-06	1.175*
1200.0	99.6E-06	506.0E-06	1.201*

Temperature Distribution Used in Data Pack for VINCE TOM (°R)

1660.0	1610.0	1560.0	1510.0	1460.0	1410.0
1360.0	1310.0	1260.0	1210.0	1160.0	1110.0
1060.0	1010.0	960.0	910.0	860.0	810.0
760.0	660.0				

/&

*Extrapolated data for code input only

F. TEDP-00-27 THERMOELECTRIC PROPERTY DATA

Reference: B-3 TEDP-00-27 Data

"24th Progress Report from Thermoelectric Research Program for Reporting Period Nov. 1 - Dec. 1, 1966" by C. Eicheldinger, January 16, 1967.

Recommended SnTe Property Data

TEDP-00-27

Temperature (°F)	Seebeck (volts/°F)	Resistivity (ohm-in.)	Conductivity (Btu/hr-ft-°F)
0.0			
50.0			
100.0			
150.0			
200.0	13.9E-06	98.4E-06	4.364
250.0	15.0E-06	107.0E-06	4.27
300.0	16.7E-06	118.1E-06	4.15
350.0	18.5E-06	128.0E-06	4.023
400.0	20.6E-06	137.8E-06	3.873
450.0	22.8E-06	149.6E-06	3.734
500.0	25.3E-06	161.4E-06	3.572
550.0	28.3E-06	173.2E-06	3.367
600.0	31.7E-06	189.0E-06	3.191
650.0	35.0E-06	206.0E-06	2.98
700.0	38.9E-06	228.4E-06	2.751
750.0	43.3E-06	253.9E-06	2.52
800.0	47.2E-06	275.6E-06	2.295
850.0	52.2E-06	299.2E-06	2.092
900.0	57.0E-06	322.8E-06	1.919
950.0	61.7E-06	348.4E-06	1.786
1000.0	66.1E-06	376.0E-06	1.682
1050.0	71.1E-06	405.5E-06	1.59
1100.0	76.1E-06	433.1E-06	1.538
1150.0	81.6E-06	464.6E-06	1.468
1200.0	86.3E-06	495.0E-06	1.40

Temperature Distribution Used in Data Pack for VINCE TOM (°R)

1660.0	1610.0	1560.0	1510.0	1460.0	1410.0
1360.0	1310.0	1260.0	1210.0	1160.0	1110.0
1060.0	1010.0	960.0	910.0	860.0	810.0
760.0	660.0				

/&

*Extrapolated data for code input only

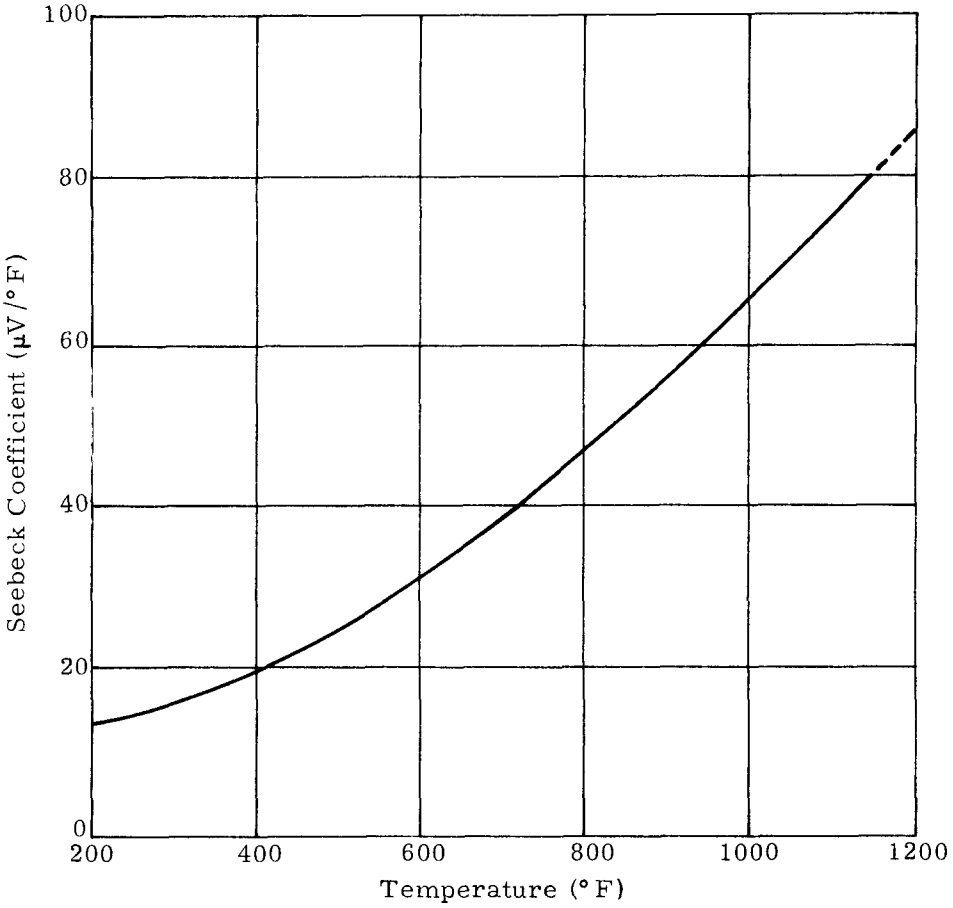

FIG. B-4. TEDP-00-27 SnTe P TYPE ELEMENT DATA MEASURED 12/66

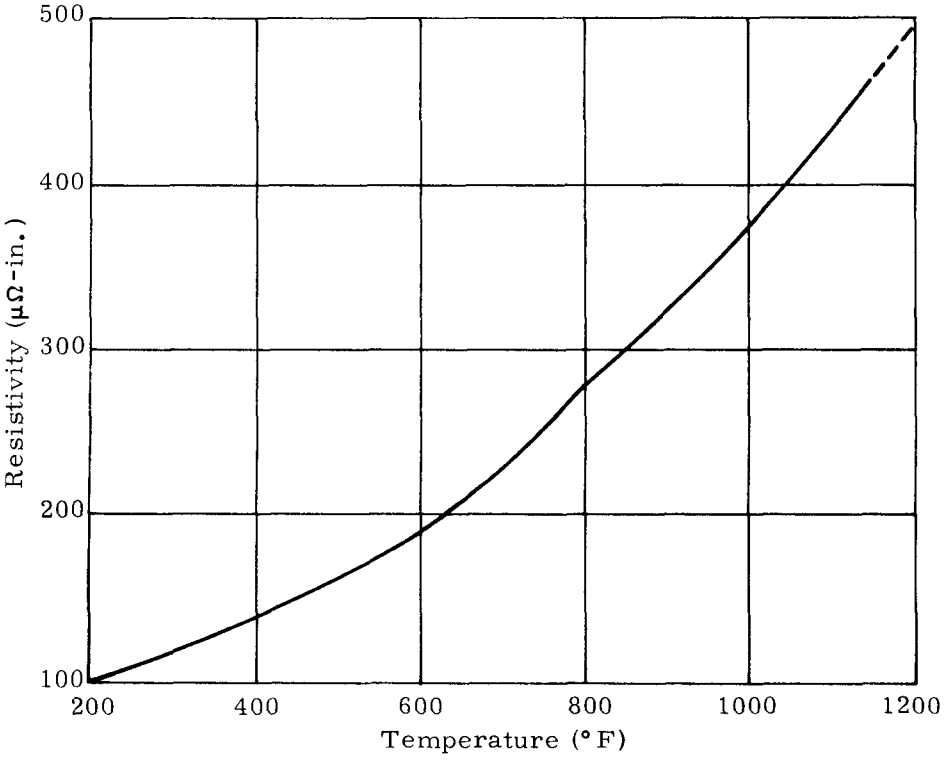

FIG. B-5. TEDP-00-27 SnTe P TYPE ELEMENT DATA MEASURED 12/66

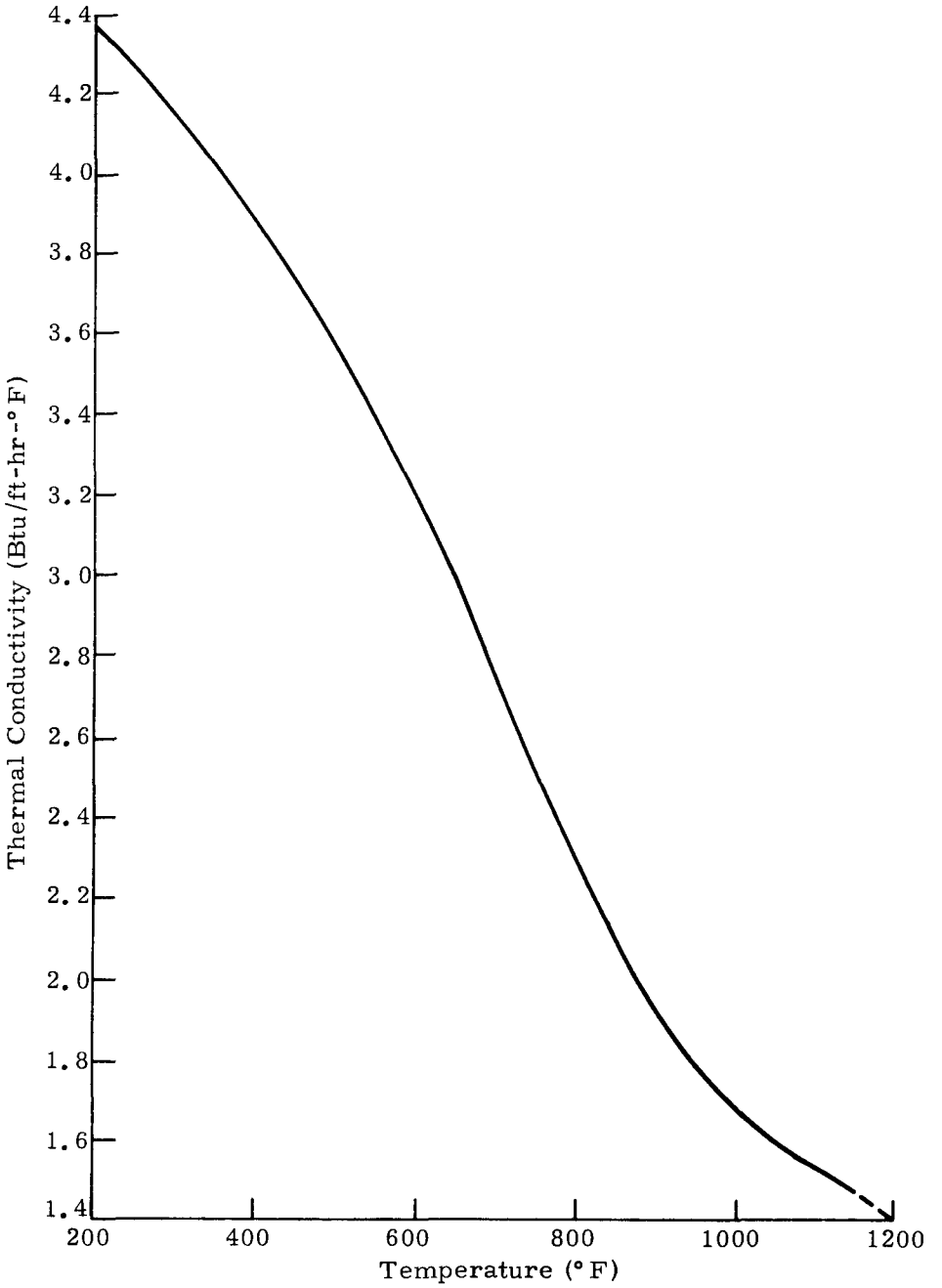

FIG. B-6. TEDP-00-27 SnTe P TYPE ELEMENT DATA MEASURED 12/66

APPENDIX C

SELECTION OF 2N-TAGS/SnTe THERMOELECTRIC COUPLE BONDING PROCEDURE

A. INTRODUCTION

One of the major questions in the SNAP 29 thermoelectric couple development is the technique to be used to bond the 2N-TAGS/SnTe elements into the hot and cold shoe cups. For this reason a number of thermoelectric couples were bonded in various ways and put through a series of performance and strength tests to determine, if possible, an element suited to the hot and cold cup bonding technique. The purpose of this document is to present and compare the pertinent results of the bonding technique experimentation.

B. DESCRIPTION OF TESTING

A number of experiments were initiated on a series of SNAP 29 2N-TAGS/SnTe thermoelectric couples to determine a preferred bonding technique for the N and P elements. These experiments, in chronological order, were as follows:

(1) Nine point resistance check

(2) Two-hour power check

(3) Nine point resistance check

(4) Life power check, ~100 hours

(5) Nine point resistance check

(6) Tension pull test

(7) Metallography (low magnification and high magnification).

Not all of the thermoelectric couples tested went through the complete series of experiments. Table C-1 identifies the thermoelectric couples tested and indicates the experiments applied to each.

The bonding techniques which were used in these thermoelectric couple experiments were coded as follows:

Code 1: Sn bond of the P leg, and 0.0004 to 0.0007-inch Ni-plated Fe cups for the N leg with a 0.0005-inch Ni wafer added in the N leg hot cups.

Code 2: Exothermic bond of the P leg, and 0.0004 to 0.0007-inch Ni-plated Fe cups for the N leg with a 0.0005-inch Ni wafer added in the N leg hot cup.

Code 3: Sn bond of the P leg with 0.0007- to 0.0008-inch Ni-plated Fe cups for the N leg.

Code 4: Sn bond of the P leg with 0.0009- to 0.0010-inch Ni-plated Fe cups for the N leg.

Identical bonds were used for the cold and hot sides of the elements.

TABLE C-1

Flow Chart for T/E Couple Experimentation

Thermoelectric Couple Identification	Bonding Code	Nine Point	Two-Hr Power	Nine Point	Life Power	Nine Point	Pull Test	Metallography LM	Metallography HM
29-36-97	Code 2	X	X	X			X		
-98		X	X	X				X	
-99		X	X	X	X			X	
-100		X	X	X			X		
-101		X	X	X	X		X		
-102		X	X	X				X	
-103		X	X	X			X		
-104		X	X	X			X		
-105		X	X	X	X		X		
-106		X	X	X			X		
-107		X	X	X				X	X
-108	Code 2	X	X	X			X		
29-38-01	Code 1	X	X	X			X		
-02		X	X	X			X	X	X
-03		X	X	X					
-04		X	X	X	X	X	X		
-05		X	X	X			X		
-06		X	X	X				X	
-07		X	X	X	X	X		X	
-08		X	X	X			X		
-09		X	X	X				X	
-10		X	X	Couple damaged			X		
-11		X	X	X			X		
-12	Code 1	X	X	X			X		
29-38-13	Code 4	X	X	Couple damaged			X		
-14		X	X	X			X		
-15	Code 4	X	X	X			X		
29-38-16	Code 3	X	X	X			X		
-17		X	X	X			X		
-18	Code 3	X	X	X			X		

LM = Low magnification

HM = High magnification

The main tests performed on the thermoelectric couples were the power tests because power output is a major concern. The nine-point resistance checks are used as an indication of expected power. The nine-point resistance check, in theory, is a suitable method for finding thermoelectric couples which will not produce an acceptable power, and is a means of pin pointing faulty construction of the thermoelectric couple. Figure C-1 indicates the points on the thermoelectric couple where resistances are checked. In theory any resistance deviating above an established norm indicates a potential loss in power for the thermoelectric couple.

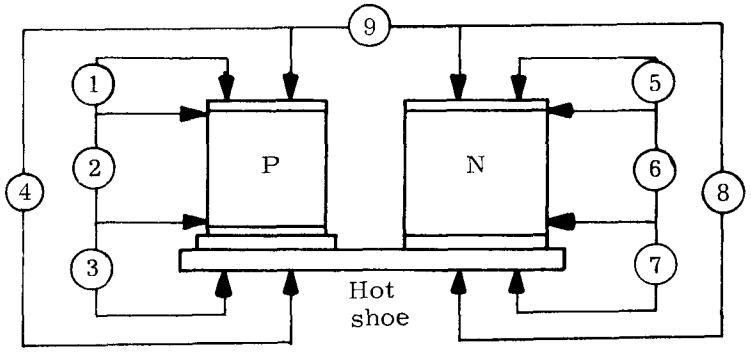

FIG. C-1. NINE-POINT RESISTANCE CHECK POSITIONS FOR THERMOELECTRIC COUPLE

The tensile pull test attempts to remove the cold or hot cup from the element. For a given test, one of three things can happen:

(1) The cold cup can break loose--this gives the strength of the cold bond and indicates that the hot bond and element have strengths of greater magnitude.

(2) The element breaks--this gives the strength of the element and indicates the hot bond and cold bond have strengths of greater magnitude.

(3) The hot bond breaks loose--this gives the strength of the hot bond and indicates the cold bond and element have strengths of greater magnitude.

It is not customary to perform a retest after the first failure, but this was done for a number of N leg elements which lost their cold cups on the first test. The pull test data for couple 29-38-12 gives warning that misleading data can be obtained when a second pull test is made after the first failure. In this case, if the strength of the element was only 185 psi, then it should have broken on the first test which indicated 285 psi for the cold bond break.

Metallography was performed on various thermoelectric couples to enable a visual inspection of the quality of the bonding techniques.

C. DISCUSSION OF RESULTS

A complete set of resulting data from the experimentation performed on the thermoelectric couples has been documented in Appendix D. The more pertinent results are presented here.

The nine-point resistance check is used as a guide to indicate expected power from the thermoelectric couple. Table C-2 presents the resistance ranges encountered in these thermoelectric couple experiments. These ranges are a good indication of the norm for each resistance check. Table C-3 presents three-point data from the nine-point resistance check before and after the two-hour check along with the measured power of the thermoelectric couple. It can be seen for the most part, that high

TABLE C-2

Range of Nine-Point Resistance Check

	As-Fabricated			After Two-Hour Power Check		
Resistance	Bonding Code 2	Bonding Code 1	Bonding Code 3 and 4	Bonding Code 2	Bonding Code 1	Bonding Code 3 and 4
1	0.060→0.080	0.040→0.080 -01 at 0.110	0.06→0.09	0.05→0.095	0.05→0.120 -01 at 0.15	0.09→0.120 -14 at 0.24
2	0.300→0.360 -105 at 0.420	0.300→0.360	0.280→0.350	0.420→1.05	0.390→0.500 -06 at 0.550	0.34→0.50
3	0.055→0.085 -105 at 0.040	0.050→0.080	0.070→0.090	0.069→0.170	-01 & 09 at 0.15 0.060→0.100 -02 & 11 at 0.22	0.100→0.150
4	-101 at 0.510 0.420→0.460 -105 at 0.570	0.430→0.510	0.430→0.500	0.540→0.800 -104 at 1.10	0.620→0.780 -10 at 1.45	0.670→0.750
5	-97 at 0.095 0.055→0.08 -108 at 0.115	-01 & 05 at 0.10 0.050→0.090 -02 at 0.550	0.040→0.080	0.060→0.150	-07 at 0.110 0.040→0.090 -10 at 1.60	0.040→0.040
6	0.305→0.365	0.290→0.370	0.300→0.390	0.305→0.370	0.320→0.360 -10 at 0.250	0.320→0.380
7	0.040→0.090	0.030→0.080	0.040→0.085	0.060→0.090	0.040→0.080	0.050→0.060
8	0.420→0.470 -108 at 0.510	0.400→0.490 -02 at 0.895	0.400→0.420	-103 at 0.530 0.440→0.485 -108 at 0.615	0.390→0.490 -10 at 1.80	0.400→0.420
9	0.910→1.05 -97 at 1.75	0.875→1.00 -02 at 1.37	0.880→0.960	1.10→1.68	1.02→1.22 -10 at 3.35	1.05→1.15

CONFIDENTIAL

CONFIDENTIAL

TABLE C-3

Nine-Point Resistance Check Data

Thermoelectric Couple Identification	Bonding Code	First Nine-Point Resistance Check R_4	R_8	R_9	Two-Hour Power Check Measured (watts)	Second Nine-Point Resistance Check R_4	R_8	R_9	Remarks on Nine-Point Resistance Check
29-36-97	2	0.420	0.470	1.05	1.344	1.150	0.500	1.75	First 9-point high before rework; N cold, ⑤, still high afterwards.
-98		0.450	0.440	0.93	1.480	0.800	0.460	1.30	
-99		0.440	0.430	0.92	1.440	0.600	0.480	1.12	Life tested afterwards--116.0 hours.
-100		0.460	0.430	0.93	1.480	0.620	0.485	1.17	
-101		0.510	0.430	0.995	1.480	0.720	0.440	1.20	Life tested afterwards--100.4 hours.
-102		0.460	0.440	0.950	1.480	0.610	0.475	1.13	
-103		0.450	0.470	0.945	1.464	0.750	0.530	1.31	
-104		0.460	0.420	0.940	1.488	1.100	0.470	1.68	
-105		0.570	0.445	1.05	1.464				First 9-point showed high P element, ②, and P_{total}, ④, couple stayed on test for 67 hours.
-106		0.435	0.425	0.91	1.504	0.540	0.470	1.10	
-107		0.445	0.435	0.92	1.520	0.670	0.465	1.16	
-108	2	0.460	0.510	1.00	1.326	0.705	0.615	1.40	First 9-point showed high N cold, ⑤, and N_{total}, ⑧; total couple, ⑨, was marginal
29-38-01	1	0.435	0.485	1.00	1.343	0.710	0.480	1.22	First 9-point showed high P cold, ①, and N cold, ⑤; total couple, ⑨, was marginal
-02		0.400	0.450	0.92	1.365	0.780	0.410	1.20	First 9-point was high before rework of N cold bond; acceptable afterwards.
-03		0.440	0.450	0.98	1.488	0.730	0.390	1.13	
-04		0.430	0.465	0.975	1.520	0.650	0.440	1.10	Life tested afterwards--139.8 hours.
-05		0.440	0.480	1.00	1.472	0.620	0.460	1.10	First 9-point showed high N cold, ⑤; total couple, ⑨, was marginal.
-06		0.510	0.400	0.95	1.424	0.700	0.410	1.12	
-07		0.470	0.470	0.98	1.488	0.730	0.490	1.22	Life tested afterwards--117.1 hours
-08		0.450	0.435	0.97	1.520	0.650	0.450	1.10	
-09		0.500	0.490	0.93	1.528	0.690	0.390	1.10	
-10		0.430	0.440	0.90	0.908	1.450	1.800	3.35	P leg and N hot side damaged during test; resulted in high values for 2nd 9-point.
-11		0.430	0.415	0.875	1.611	0.700	0.430	1.15	
-12	1	0.460	0.420	0.91	1.444	0.580	0.420	1.02	
29-38-13	4	0.430	0.420	0.88	1.536				Couple damaged when removed from couple tester.
-14	4	0.500	0.420	0.96	1.496	0.680	0.400	1.08	
-15	4	0.460	0.420	0.90	1.469	0.750	0.400	1.15	
29-38-16	3	0.450	0.410	0.90	1.496	0.670	0.420	1.10	
-17	3	0.500	0.420	0.95	1.456	0.670	0.410	1.12	
-18	3	0.450	0.400	0.89	1.472	0.610	0.410	1.05	

CONFIDENTIAL

CONFIDENTIAL

TABLE C-4

Summary of Two-Hour Power Tests

P_m = Average power; σ = standard deviation

Bonding Code	Couples (No.)		Measured Power (watts)			ΔT^2 Corrected Power (watts)			E_{oc}^2 Corrected Power (watts)		
			Total	N Leg	P Leg	Total	N Leg	P Leg	Total	N Leg	P Leg
1	12		All of couples considered.								
		P_m	1.4259	0.6730	0.7492	1.4105	0.6735	0.7327	1.4324	0.7003	0.7189
		σ	0.1787	0.1094	0.0806	0.1744	0.1110	0.0735	0.1716	0.1032	0.0702
1	10		Exclude Couple -02 because couple was reworked and power was low. Exclude Couple -10 because couple was damaged and power was low.								
		P_m	1.4838	0.7101	0.7691	1.4644	0.7103	0.7488	1.4852	0.7327	0.7376
		σ	0.0714	0.0537	0.0454	0.0776	0.0591	0.0376	0.0603	0.0314	0.0402
1*	8		Exclude Couples -02 and -10 as above. Exclude Couple -01 because 9-point resistance check was marginal and power was low. Exclude Couple -05 because 9-point resistance check was marginal.								
		P_m	1.5029	0.7194	0.7779	1.4826	0.7209	0.7551	1.5004	0.7372	0.7444
		σ	0.0574	0.0516	0.0457	0.0749	0.0585	0.0395	0.0522	0.0327	0.0414
2	12		All of couples considered.								
		P_m	1.4558	0.7167	0.7373				1.4572	0.7274	0.7290
		σ	0.0600	0.0346	0.0477				0.0568	0.0265	0.0387
2	9		Exclude Couple -97 because 9-point resistance check was high and power was low. Exclude Couple -105 because 9-point resistance check was high. Exclude Couple -108 because 9-point resistance check was marginal, power was low and temperature data insufficient.								
		P_m	1.4818	0.7303	0.7533				1.4818	0.7369	0.7397
		σ	0.0225	0.0195	0.0343				0.0225	0.0193	0.0299
2*	7		Exclude Couples -97, -105 and -108 as above. Exclude Couples -106 and -107 due to insufficient temperature data.								
		P_m	1.4731	0.7366	0.7364	1.4560	0.7204	0.7359	1.4731	0.7409	0.7263
		σ	0.0163	0.0172	0.0077	0.0267	0.0296	0.0069	0.0163	0.0201	0.0157
3*	3		All of couples considered.								
		P_m	1.4747	0.6820	0.7927	1.4560	0.6756	0.7801	1.4747	0.7056	0.7431
		σ	0.0201	0.0095	0.0106	0.0287	0.0143	0.0173	0.0201	0.0135	0.0099
4*	3		All of couples considered								
		P_m	1.5003	0.7470	0.7473	1.4631	0.7300	0.7286	1.5128	0.7618	0.7558
		σ	0.0337	0.0518	0.0316	0.0266	0.0584	0.0489	0.0207	0.0356	0.0330

*Recommended set of data for each bonding process.

Blank spaces due to insufficient data.

resistance values do indicate a low power performance from the thermoelectric couple. A value of 1.0 for R_9 was taken to be marginal. There is one piece of data which indicates the nine-point resistance check is not infallible. Thermoelectric Couple No. 29-38-02, after reworking, shows acceptable resistance values, but the power output is one of the four lowest values.

A summary of the two-hour power tests is presented in Table C-4. The measured power output from each thermoelectric couple is presented in Table C-5 for the two-hour power check data. Table C-6 gives those for the life power data. Along with the measured powers are the temperature corrected powers and the open circuit voltage (using the N leg open circuit voltage for life data) corrected powers. The temperature corrected power was determined from Eq. (C-1).

$$P\Delta_T{}^2 = P_{measured} \cdot \left(\frac{T\ standard}{T\ measured}\right)^2 \qquad (C-1)$$

where ΔT standard = 1050° - 350 = 700° F

The open circuit voltage corrected power was determined from Eq. (C-2).

$$P_{E_{oc}} = P_{measured} \cdot \left(\frac{E_{oc}\ standard}{E_{oc}\ measured}\right)^2 \qquad (C-2)$$

where E_{oc} standard = 0.0160 volt for total couple

= 0.099 volt for N leg

= 0.061 volt for P leg

A comparison of the measured power data in Tables C-4 through C-6 does not indicate any appreciable difference in thermoelectric couple power output due to the differences in the bonding techniques. This remains true for a comparison of the corrected power data. In Table C-6 the change in output power over the time of the test is presented (initial data are not used in this evaluation). For the most part, the thermoelectric couples employing the exothermic bonding in the P leg, Code 2, show an increase in power while the thermoelectric couples employing Sn bonding in the P leg, Code 1, show a decrease in power. This could be a definite advantage for the exothermic bonding technique. It should be noted that it is only ~100-hour life power data on only a limited number of samples; longer life tests would be needed on a larger number of test specimens to bear this out.

Another means of evaluating a given bonding technique is its physical strength. The results of the tensile pull tests are presented in Table C-7. Examination of the pull test data can be divided into two parts:

(1) P leg--comparing Sn bond and exothermic bond

(2) N leg--comparing regular Ni plating on the iron cups with added Ni wafers and heavy Ni plating on the iron cups.

For the P leg, the pull test results show in general that using the exothermic bond, Code 2, the P elements break before the P hot cup bonds. On the other hand, using the Sn bond in the hot cup, Codes 1, 3 and 4, the P hot cup bonds break before

TABLE C-5

Couple Power Output for Two-Hour Power Check

Thermoelectric Couple Identification	Bonding Code	Measured Power (watts)			ΔT^2 Corrected Power (watts)			E_{oc}^2 Corrected Power (watts)		
		Total	N Leg	P Leg	Total	N Leg	P Leg	Total	N Leg	P Leg
29-36-97	2	1.344	0.705	0.638	1.3250	0.6853	0.6380	1.344	0.7195	0.6380
-98	↕	1.48	0.740	0.740	1.4550	0.7193	0.7358	1.48	0.7552	0.7163
-99		1.44	0.702	0.738	1.4057	0.6635	0.7444	1.44	0.7020	0.7380
-100		1.48	0.740	0.740	1.4695	0.7295	0.740	1.48	0.740	0.740
-101		1.48	0.758	0.721	1.4949	0.7624	0.7314	1.48	0.758	0.6979
-102		1.48	0.740	0.740	1.4591	0.7193	0.740	1.48	0.740	0.740
-103		1.464	0.732	0.732	1.4515	0.7156	0.7362	1.464	0.732	0.732
-104		1.488	0.744	0.744	1.4566	0.7335	0.7232	1.488	0.7595	0.7202
-105		1.464	0.695	0.750	1.4745	0.6950	0.7608	1.464	0.7093	0.7260
-106		1.504	0.714	0.808				1.504	0.7286	0.7821
-107	↕	1.52	0.703	0.817				1.52	0.7174	0.7909
-108	2	1.326	0.628	0.680				1.3427	0.6679	0.7269
29-38-01	1	1.343	0.629	0.714	1.3624	0.6290	0.7348	1.3772	0.6977	0.6912
-02	↕	1.365	0.595	0.770	1.3709	0.5950	0.7766	1.4177	0.6890	0.7219
-03		1.488	0.613	0.855	1.4026	0.6095	0.7651	1.488	0.7098	0.7087
-04		1.52	0.741	0.779	1.5464	0.7539	0.7925	1.520	0.7562	0.7541
-05		1.472	0.717	0.754	1.4208	0.7069	0.7127	1.472	0.7317	0.7299
-06		1.424	0.694	0.729	1.3649	0.6746	0.6891	1.424	0.7082	0.7057
-07		1.488	0.725	0.762	1.4795	0.7209	0.7577	1.488	0.7399	0.7376
-08		1.52	0.741	0.779	1.5309	0.7626	0.7680	1.520	0.7562	0.7541
-09		1.528	0.783	0.745	1.5324	0.7989	0.7345	1.528	0.7991	0.7212
-10		0.908	0.380	0.529	0.9106	0.3833	0.5275	0.9195	0.3878	0.5290
-11	↕	1.611	0.756	0.836	1.5704	0.7390	0.8126	1.591	0.7264	0.8360
-12	1	1.444	0.702	0.738	1.4337	0.7081	0.7214	1.444	0.7020	0.7380
29-38-13	4	1.536	0.768	0.7680	1.493	0.7361	0.7571	1.536	0.7527	0.7938
-14	4	1.496	0.785	0.7110	1.4542	0.7850	0.6720	1.496	0.8011	0.7349
-15	4	1.469	0.688	0.7630	1.4421	0.6688	0.7565	1.5064	0.7317	0.7386
29-38-16	3	1.496	0.692	0.804	1.4875	0.6920	0.7949	1.4960	0.7208	0.7538
-17	3	1.456	0.673	0.783	1.4314	0.6692	0.7611	1.4560	0.7010	0.7341
-18	3	1.472	0.681	0.791	1.4491	0.6657	0.7843	1.4720	0.6950	0.7416

Some corrections not made because of insufficient data.

CONFIDENTIAL

CONFIDENTIAL

TABLE C-6

Couple Power Output for the 100-Hour Life Power Check

Thermoelectric Couple Identification and Time (hr)	Bonding Code	Measured Power (watts)			ΔT^2 Corrected Power (watts)			E_{oc}^2 Corrected Power (watts)		
		Total	N Leg	P Leg	Total	N Leg	P Leg	Total	N Leg	P Leg
29-36-99	2									
Initial		1.423	0.847	0.644						
2.0		1.45	0.866	0.6560	1.4377	0.8635	0.6467	1.407	0.8403	0.6366
25.0		1.454	0.876	0.6490	1.4582	0.8760	0.6527	1.4053	0.8467	0.6273
116.0		1.45	0.855	0.6670				1.4183	0.8363	0.6524
ΔP		+0.00			+0.0205			+0.0113		
29-36-101	2									
Initial		1.548	0.792	0.756						
8.1		1.564	0.81	0.754				1.4734	0.7631	0.7102
25.8		1.697	0.839	0.839				1.5986	0.7904	0.7904
70.3		1.36	0.697	0.663				1.5085	0.7731	0.7354
100.4		1.428	0.722	0.688				1.4875	0.7521	0.7167
ΔP		-0.136						+0.0141		
29-36-105	2									
1.4		1.44	0.702	0.738	1.44	0.6921	0.7487	1.4695	0.7164	0.7531
3.4		1.464	0.695	0.75	1.4745	0.6950	0.7608	1.4940	0.7093	0.7654
67.3		1.514	0.673	0.822	1.48	0.6579	0.8035	1.5451	0.6868	0.8389
ΔP		+0.074			+0.04			+0.0756		
29-38-04	1									
Initial		1.469	0.781	0.758						
2.0		1.529	0.826	0.782	1.5203	0.8284	0.7709	1.4604	0.7889	0.7469
19.5		1.519	0.835	0.765						
49.7		1.524	0.842	0.764						
73.8		1.515	0.836	0.758	1.515	0.8384	0.7558	1.4498	0.8	0.7254
139.8		1.511	0.827	0.766	1.5088	0.8270	0.7638	1.4489	0.7930	0.7345
ΔP		-0.018			-0.0115			-0.0115		
29-38-07	1									
Initial		1.452	0.801	0.720						
2.0		1.462	0.804	0.726	1.4558	0.7949	0.7281	1.4709	0.8089	0.7304
26.8		1.479	0.813	0.732	1.4960	0.8107	0.7512	1.4971	0.8229	0.7410
50.6		1.485	0.819	0.732	1.5043	0.8190	0.7512	1.4971	0.8257	0.7380
117.1		1.502	0.831	0.737	1.515	0.8286	0.7520	1.4662	0.8112	0.7195
ΔP		+0.04			+0.0592			-0.0047		

Some corrections not made because of insufficient data.
Initial points not used to determine ΔP values.

CONFIDENTIAL

CONFIDENTIAL

anything else and with relatively low strength values. This indicates that the exothermic technique yields stronger bonds for the P element. Note that there is no effect of the bonding technique for the cold bond.

TABLE C-7

Pull Test Results

Thermoelectric Couple Identification	Bonding Code	N Leg (psi) Hot Bond Broke	N Leg (psi) Element Broke	N Leg (psi) Cold Bond Broke	P Leg (psi) Hot Bond Broke	P Leg (psi) Element Broke	P Leg (psi) Cold Bond Broke	Couple Life Power Tested
29-36-97	Code 2		308*	55		20		
-98								
-99								Yes
-100			260*	138	102			
-101			398		32			Yes
-102								
-103			373*	24		332		
-104			>276*	65		16		
-105		49				103		Yes
-106			532*	138		250		
-107								
-108	Code 2		>415*	8		123		
29-38-01	Code 1				0			
-02			258*	127	87			
-03								
-04		305			0			Yes
-05			>333*	40	204			
-06								
-07								Yes
-08			>512*	90	102			
-09								
-10			248*	15		48		
-11			>575*	125	26			
-12	Code 1		185*	285	174			
29-38-13	Code 4	188			0			
-14		315					92	
-15	Code 4		>315*	285	62			
29-38-16	Code 3	220			0			
-17		430			82			
-18	Code 3		428*	413	38			

*Retest after first failure

Examination of the results for the N leg hot bond reveals that the heavy Ni-plated iron cups, Bonding Codes 3 and 4, broke loose in the same range of strength values as the normal Ni-plated iron cups with added Ni wafers, Codes 1 and 2. On the other hand, examination of the cold bond for the N leg shows the heavy Ni-plated cups, bonding Code 3 and 4, have a definite increase in strength over the regular Ni-plated cups, Bonding Code 1 and 2. Therefore heavy Ni-plated cups should be used in bonding the cold end of the N leg. They should also be used on the hot end of the N leg for manufacturing simplicity.

Photomicrographs were made on a number of elements as indicated in Table C-1. These photomicrographs are presented in Appendix D and are supplemented by additional photos of Sentinel TAGS elements after 1000 hours. Appendix D points out that there existed a manufacturing problem in casting of the SnTe in the P leg cup. This was solved by using a cold pressed wafer in place of casting.

After a two-hour power test, the exothermically bonded P elements show good fusion of the exothermic bond region with both the thermoelectric element and the tin telluride step. There are few voids in the bond region and the well-distributed minor phase may be primary tellurium remaining after the exothermic reaction stops.

After a 100-hour power test a few voids have appeared on the thermoelement side of the bond region while the amount of primary phase has decreased. After a 1000-hour power test, the void size has increased slightly. In no case is any unbonding apparent.

D. RESULTS AND RECOMMENDATIONS

The thermoelectric couple experimentation shows that the various bonding techniques did not appreciably affect the power output. Also, the exothermic hot bond exhibited more strength than the Sn hot bond for the P leg. On the N leg, the data indicated heavy Ni-plated iron cups produced the strongest bond at the cold end.

It is recommended that the SNAP 29 thermoelectric couples be fabricated employing 0.0009- to 0.0010-inch Ni-plated iron cups on the N element and exothermic bonding on the P element (identical bonds on both ends of elements). These recommendations are made primarily on the bases of structural strength.

E. SUMMARY

A quantity of 30 2N-TAGS/SnTe thermoelectric couples were manufactured employing different bonding techniques between the N and P elements and their respective hot and cold shoe cups. The thermoelectric couples were subjected to a series of performance tests to determine the characteristics of the different bonding techniques. In chronological order the tests included:

(1) As-fabricated nine-point resistance check

(2) Two-hour power check

(3) Nine-point resistance check

(4) One hundred-hour life power check

(5) Nine-point resistance check

(6) Tensile pull test

(7) Metallography.

The results of these tests indicated that no bonding technique showed significant advantage over the other techniques when comparing the BOL power output of the thermoelectric couple. On the other hand, the pull tests indicated that the exothermic bond had a greater tensile strength then the Sn bond for the bond between the

P leg and its hot shoe cup. Results of the tensile pull test for the N leg hot bond showed no appreciable difference between the normal Ni-plated iron cup with a Ni wafer added, and the heavy Ni-plated iron cup. For the cold bond, the heavy Ni-plated iron cups form stronger bonds than the normal Ni-plated iron cups.

There were a number of photomicrographs made of the P leg of the 2N-TAGS/SnTe thermoelectric couple. These photomicrographs indicated good fusion of the exothermic bond regions.

From the results of the pull tests, it is recommended that exothermic bonding be used on the P leg of the SNAP 29 couple, and 0.0009- to 0.0010-inch Ni-plated iron cups be used in bonding the N leg.

APPENDIX D

T/E COUPLE DEVELOPMENT, EXPERIMENTAL DATA

Twelve couples were fabricated with an exothermic bond of the P leg with a wafer bond of the N hot shoe and a standard bond of the N cold cup. The couples nine-point resistance measurements of the as-fabricated couples are:

Couple Identification	1 P	2 P	3 P	4 P	5 N	6 N	7 N	8 N	9 P/N
36-97	0.070	0.340	0.060	0.420	0.095	0.310	0.090	0.470	1.05
-98	0.070	0.360	0.060	0.450	0.075	0.320	0.070	0.440	0.930
-99	0.075	0.310	0.070	0.440	0.065	0.310	0.070	0.430	0.920
-100	0.065	0.300	0.085	0.460	0.075	0.365	0.050	0.430	0.930
-101	0.080	0.350	0.065	0.510	0.060	0.360	0.060	0.430	0.995
-102	0.070	0.340	0.060	0.460	0.060	0.360	0.060	0.440	0.950
-103	0.070	0.340	0.060	0.450	0.080	0.320	0.060	0.470	0.945
-104	0.070	0.340	0.070	0.460	0.080	0.340	0.040	0.420	0.940
-105	0.060	0.420	0.040	0.570	0.065	0.350	0.050	0.445	1.05
-106	0.075	0.310	0.055	0.435	0.065	0.315	0.065	0.425	0.910
-107	0.070	0.320	0.060	0.445	0.070	0.350	0.050	0.435	0.920
-108	0.070	0.320	0.060	0.460	0.115	0.340	0.060	0.510	1.00

The twelve couples were subjected to a two-hour power test with the following results:

Couple Identification	N		P	Total Couple		N Leg		P Leg	
	T_C(° F)	T_H(° F)	T_C(° F)	E_o	P	E_{oc}	P	E_{oc}	P
36-97	350	1050	350	160	1.344	0.098	0.705	0.061	0.638
-98	350	1060	358	160	1.480	0.098	0.740	0.062	0.740
-99	340	1060	363	160	1.440	0.099	0.702	0.061	0.738
-100	355	1060	360	160	1.480	0.099	0.740	0.061	0.740
-101	357	1055	360	160	1.480	0.099	0.758	0.062	0.721
-102	350	1060	360	160	1.480	0.099	0.740	0.061	0.740
-103	350	1058	360	160	1.464	0.099	0.732	0.061	0.732
-104	355	1060	350	160	1.488	0.098	0.744	0.062	0.744
-105	355	1055	360	160	1.464	0.098	0.695	0.662	0.750
-106	355	1048		160	1.504	0.098	0.714	0.062	0.808
-107	354	1056		160	1.520	0.098	0.703	0.062	0.817
-108	358	1058		159	1.326	0.096	0.624	0.059	0.680

After two-hour power testing, the couples were again nine-point resistance checked.

Couple Identification	1 P	2 P	3 P	4 P	5 N	6 N	7 N	8 N	9 P/N
36-97	0.200	0.920	0.070	1.15	0.100	0.380	0.090	0.500	1.75
-98	0.095	0.710	0.070	0.800	0.070	0.340	0.080	0.460	1.30
-99	0.06	0.460	0.090	0.600	0.070	0.330	0.08	0.480	1.12
-100	0.065	0.430	0.120	0.620	0.070	0.330	0.090	0.485	1.17
-101	0.070	0.560	0.075	0.720	0.06	0.320	0.090	0.440	1.20
-102	0.06	0.470	0.095	0.610	0.08	0.320	0.085	0.475	1.13
-103	0.09	0.670	0.080	0.750	0.15	0.305	0.070	0.530	1.31
-104	0.05	1.05	0.060	1.10	0.08	0.340	0.060	0.470	1.68
-105				Not available					
-106	0.08	0.420	0.070	0.540	0.070	0.350	0.060	0.470	1.10
-107	0.07	0.540	0.080	0.670	0.08	0.330	0.07	0.465	1.16
-108	0.06	0.550	0.120	0.705	0.150	0.370	0.08	0.615	1.40

T/E couple 36-105 was selected for the 67-hour power test. The couple was not removed from the couple test at the end of the initial two-hour power test, but had been tested continuously for the full 67 hours. The couple performance is as follows:

Couple Identification	Elapsed Time (hr)	N		P	Total Couple		N Leg		P Leg	
		T_C(° F)	T_H(° F)	T_C(° F)	E_o	P	E_o	P	E_o	P
36-105	2	355	1055	360	160	1.464	0.098	0.695	0.062	0.750
	67.3	340	1048	340	162	1.514	0.098	0.673	0.069	0.822

Couples 36-99 and 36-101 were subjected to a 100-hour power test. Both couples were thermocycled, that is, two-hour tested, cooled, then retested at 100 hours. Couple 36-101 was tested in Manufacturing's bell jar tester and Couple 36-099 in the Engineering console tester. In both tests hot junction thermocouples were inoperative at the beginning of the tests. Manufacturing's data reflect measurements taken at the 100 hours, by maintaining open circuit voltage. Both 100-hour measurements are:

Couple Identification	Total Couple		N Leg		P Leg	
	E_o	P	E_o	P	E_o	P
36-99	167.7	1.450	0.100	0.855	0.069	0.667
36-101	166	1.428	0.097	0.722	0.068	0.688

Tensile tests were performed on couples with the following results:

Couple tensile test after two-hour power test:

Couple Identification	Leg/Load (psi) N	P	Fracture/Failure			Descriptions
36-97		20		P	Fracture element	~1/3 length from cold cup
	55			N	Failure cold cap bond	~60% bond
	308			N	Fracture element	~100% bond
36-100		102		P	Failure hot shoe bond	~30% bond
	138		1st	N	Failure cold cap bond	~70% bond
	260		2nd	N	Failure hot shoe bond	~80% bond
36-103		332		P	Fracture element	Just above bond reaction zone
	24		1st	N	Failure cold cap	~30% bond
	373		2nd	N	Fracture element	Just above bond
36-104		16		P	Fracture element	~1/3 length from hot shoe
	65		1st	N	Failure cold cap bond	~40% bond
	>276		2nd	N	*No fracture/ failure	Maximum load that could be applied because of epoxy failure
36-106		250		P	Fracture element	Just above bond reaction zone
	138		1st	N	Failure cold cap	~75% bond
	532		2nd	N	Fracture element	Just above bond
36-108		123		P	Fracture element	~in 1/2
	8		1st	N	Fracture cold cap	~10% bond
	>415		2nd	N	*No fracture/failure	Maximum load that could be applied because of epoxy failure

*To apply tensile load, hex nuts are attached to couple cold caps with an epoxy cement. Maximum loads represent failure of epoxy after several attempts.

Couple tensile test after 67-hour power test:

36-105		103		P	Fracture element	Just above bond
	49			N	Failure	Hot shoe bond
36-101		32		P	Failure hot shoe bond	~40% bond
	398			N	Fracture element bond	~85% bond

Figures D-1 through D-4 are couples submitted to metallography. Couples 36-98, 36-102 and 36-107 (Figs. D-1, D-2 and D-3 were from the beginning, middle and end of the Fabrication, after two-hour power test. Couple 36-99 (Fig. D-4) was tested 100 hours. From observing the photomicrographs, Manufacturing recognized a potential problem area, namely, the casting of the SnTe in the P leg cup. However, during the fabrication of these and following samples, make-shift tooling was employed. Corrective action in the form of new tooling should eliminate any further problems in this area. By comparing the voids in the SnTe, it was found that Couple 36-107 had the least void areas. Correlating this to couple two-hour performance data, Couple 36-107 produced 1.52 watts, Couples 36-98 and 36-102 were 1.48 watts each. 36-99 had SnTe voids greater than 36-107, but less than 36-98 and 36-102. Couple 36-99 produced power of 1.44 watts. However, the metallography of Couple 36-99 is after 100 hours, not the two hours as in the other couples. Therefore, a direct comparison of the photomicrographs of the 100- and 2-hour tests is not possible.

Figure D-5 is of Couple 36-105 after 67 hours of performance and tensile testing.

In addition to the data collected on SNAP 29 TAGS-type couples, Figs. D-6 and D-7 are of couples fabricated as development work for the Sentinel TAGS. Both of the Sentinel couples were fabricated using the same manufacturing techniques used in the fabrication of SNAP 29 TAGS, Lot 36, except the N leg was Isotopes T/E 2000. However, Couples XO-01-59 and XO-01-61 (Sentinel) had life data collected covering 1038 and 1124 hours, respectively. After removal from life test, a tensile test was performed on each couple as follows:

Couple Identification	Test Time (hr)	Leg/Load N (psi)	Leg/Load P (psi)	Description
XO-01-59	1038		18	P Fracture element Just above bond
		160		N Fracture element
XO-01-61	1124		70	P Fracture element Just above bond
		45		N Fracture Hot shoe bond

Additional couples were fabricated with a Sn wafer bonded P leg and 0.0007- to 0.001-inch Ni-plated cups of the N leg. All couples were submitted to a nine-point resistance test after bonding.

Couple Identification	1 P	2 P	3 P	4 P	5 N	6 N	7 N	8 N	9 N/P
36-13	0.070	0.300	0.080	0.430	0.070	0.370	0.080	0.420	0.880
-14	0.090	0.340	0.090	0.500	0.075	0.350	0.075	0.420	0.960
-15	0.090	0.350	0.085	0.460	0.080	0.300	0.085	0.420	0.900
-16	0.070	0.320	0.070	0.450	0.050	0.320	0.070	0.410	0.900
-17	0.060	0.320	0.080	0.500	0.040	0.390	0.040	0.420	0.950
-18	0.070	0.280	0.080	0.450	0.040	0.340	0.040	0.400	0.890

Couples 36-13, 36-14 and 36-15 had actually 0.0009- to 0.001-inch Ni plate on both hot and cold shoes. Nickel platings used on Couples 36-16, 36-17 and 36-18 were of 0.0007- to 0.0008-inch thicknesses.

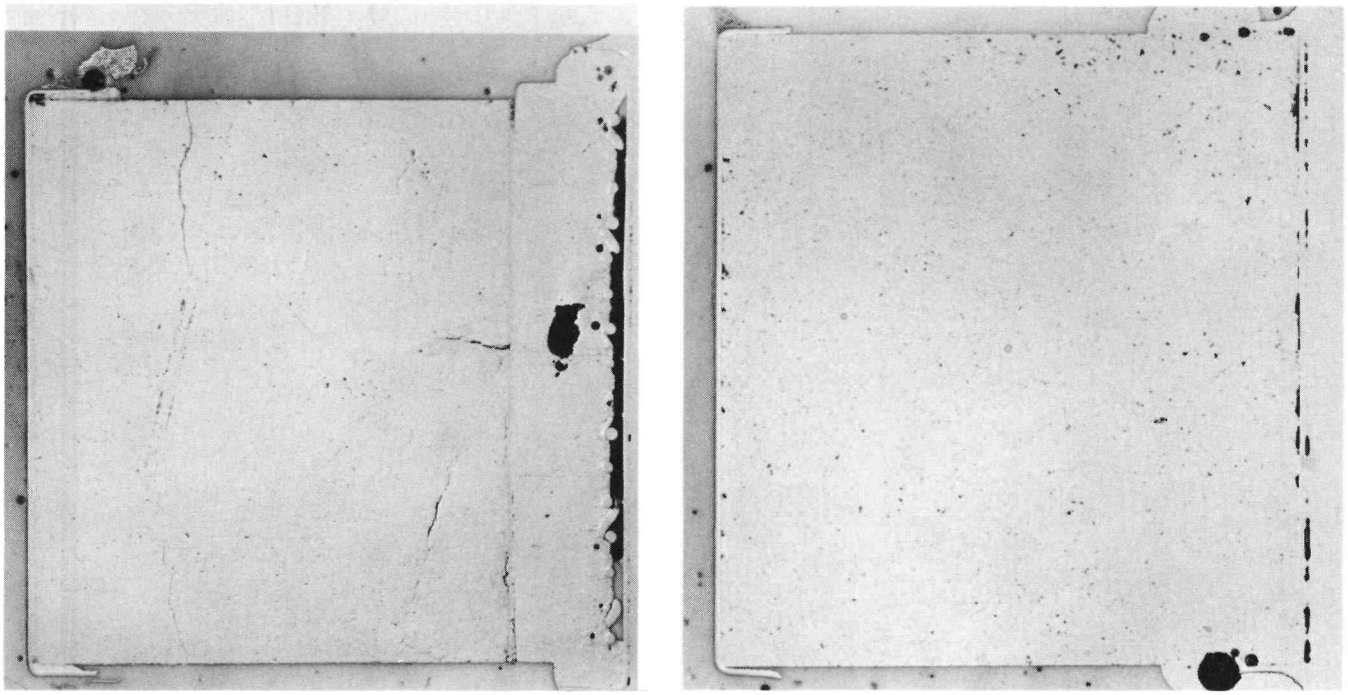

a. P Element b. N Element

FIG. D-1. AS-POLISHED SNAP 29 COUPLE 29-36-98 ELEMENTS AFTER TWO-HOUR POWER

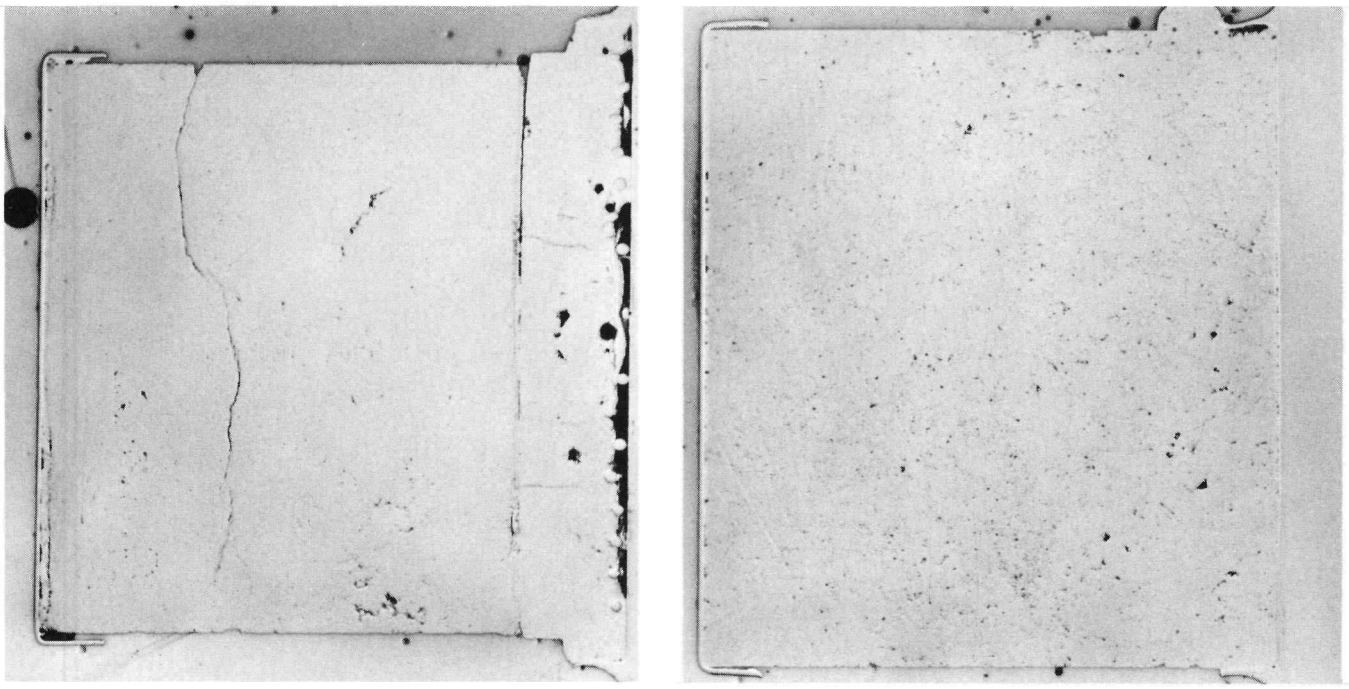

a. P Element b. N Element

FIG. D-2. AS-POLISHED SNAP 29 COUPLE 29-26-102 ELEMENTS AFTER TWO-HOUR POWER TEST

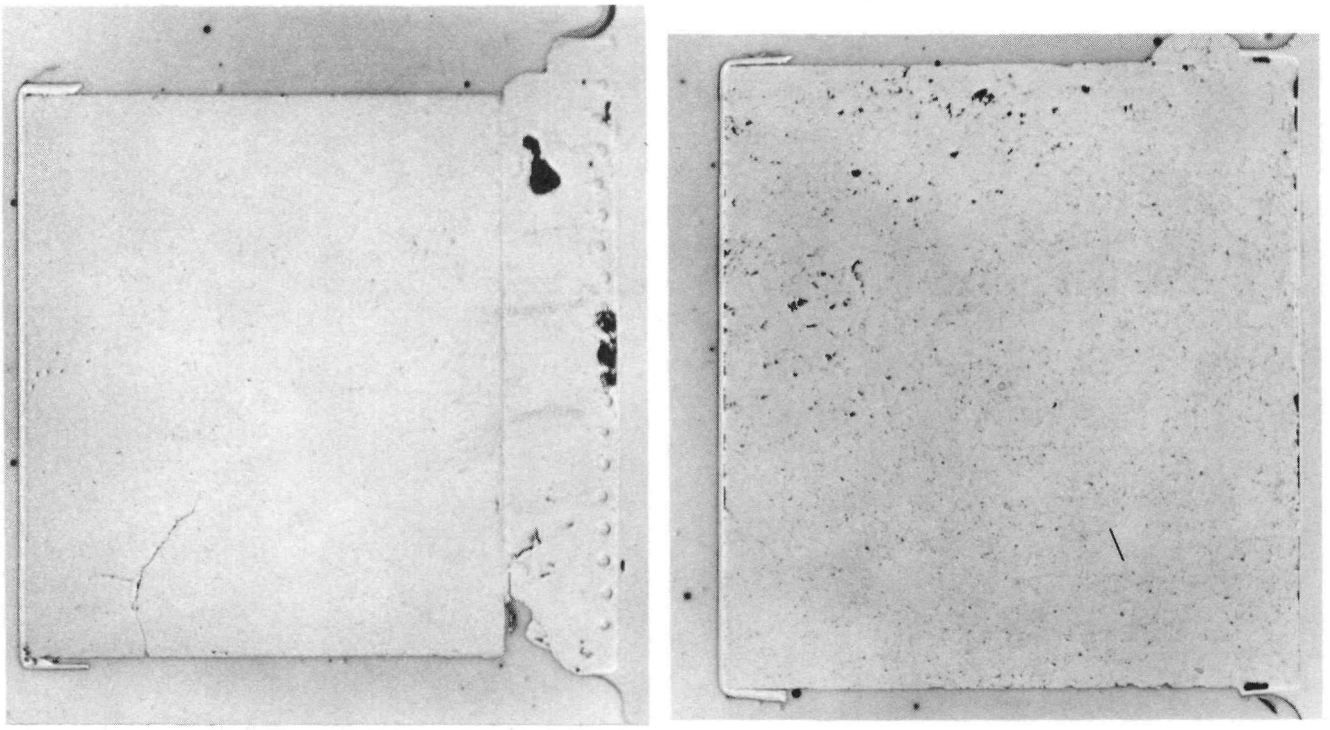

a. P Element b. N Element

FIG. D-3. AS-POLISHED SNAP 29 COUPLE 29-36-107 ELEMENTS AFTER TWO-HOUR POWER TEST

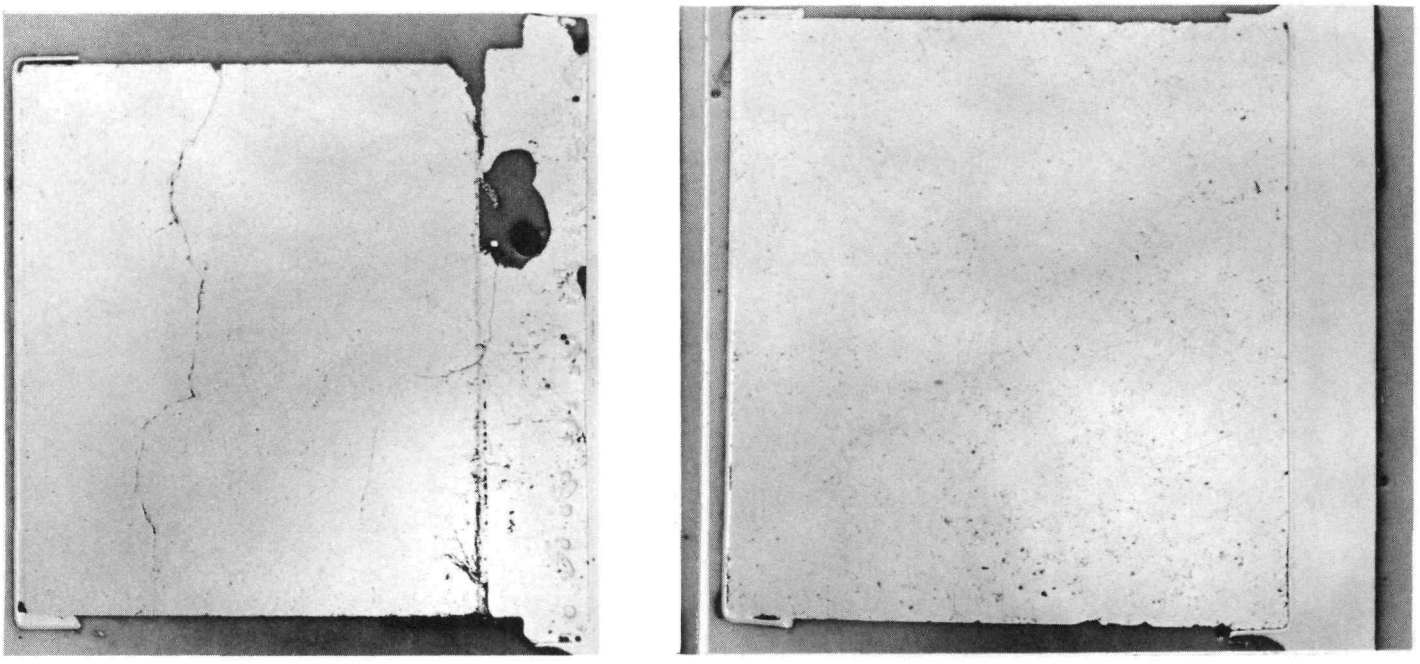

a. P Element b. N Element

FIG. D-4. AS-POLISHED SNAP 29 COUPLE 29-36-99 ELEMENTS AFTER TWO-HOUR POWER TEST

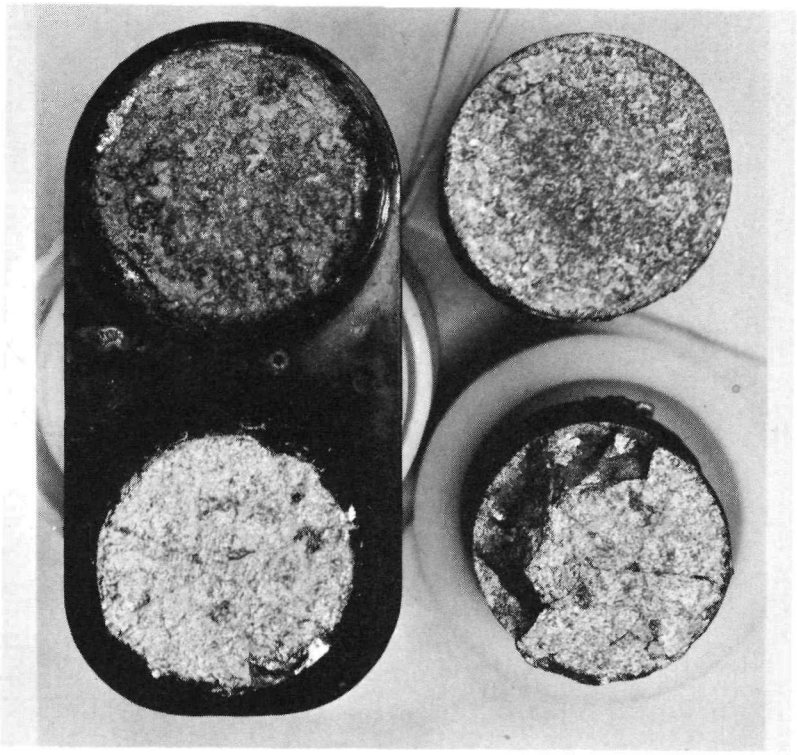

FIG. D-5. COUPLE 29-36-105 AFTER 67 HOURS OF PERFORMANCE AND TENSILE TESTING

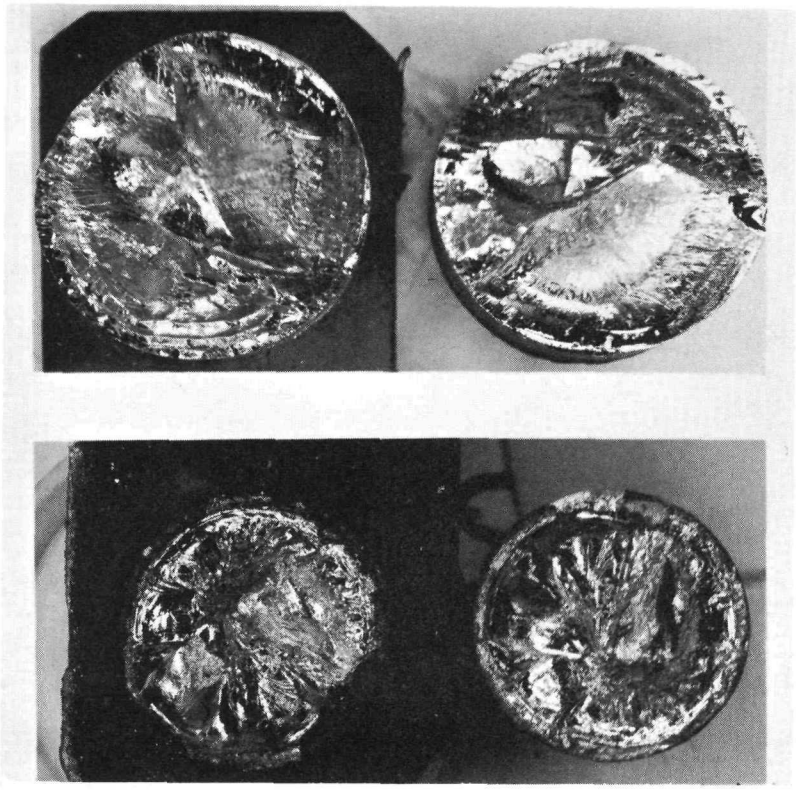

FIG. D-6. SENTINEL TAGS DEVELOPMENT COUPLE X0-01-59

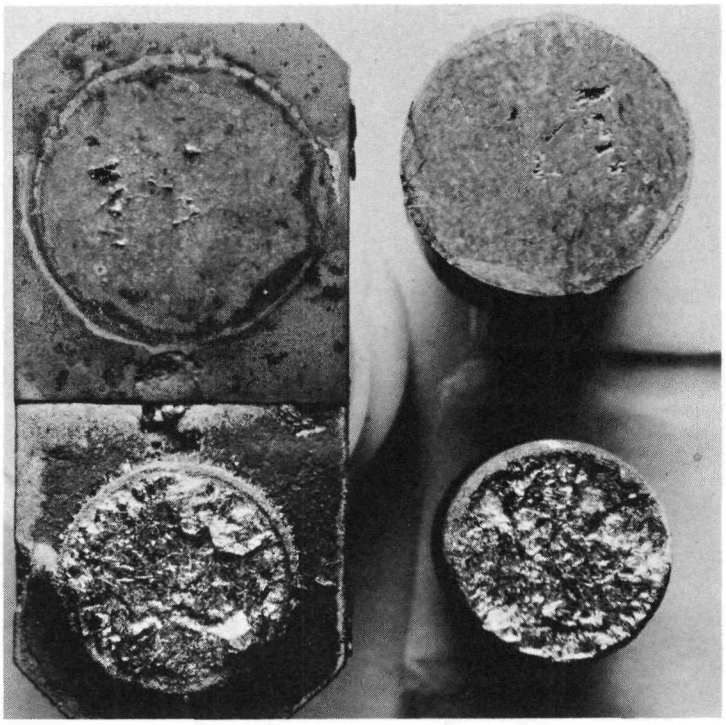

FIG. D-7. SENTINEL TAGS DEVELOPMENT COUPLE X0-01-61

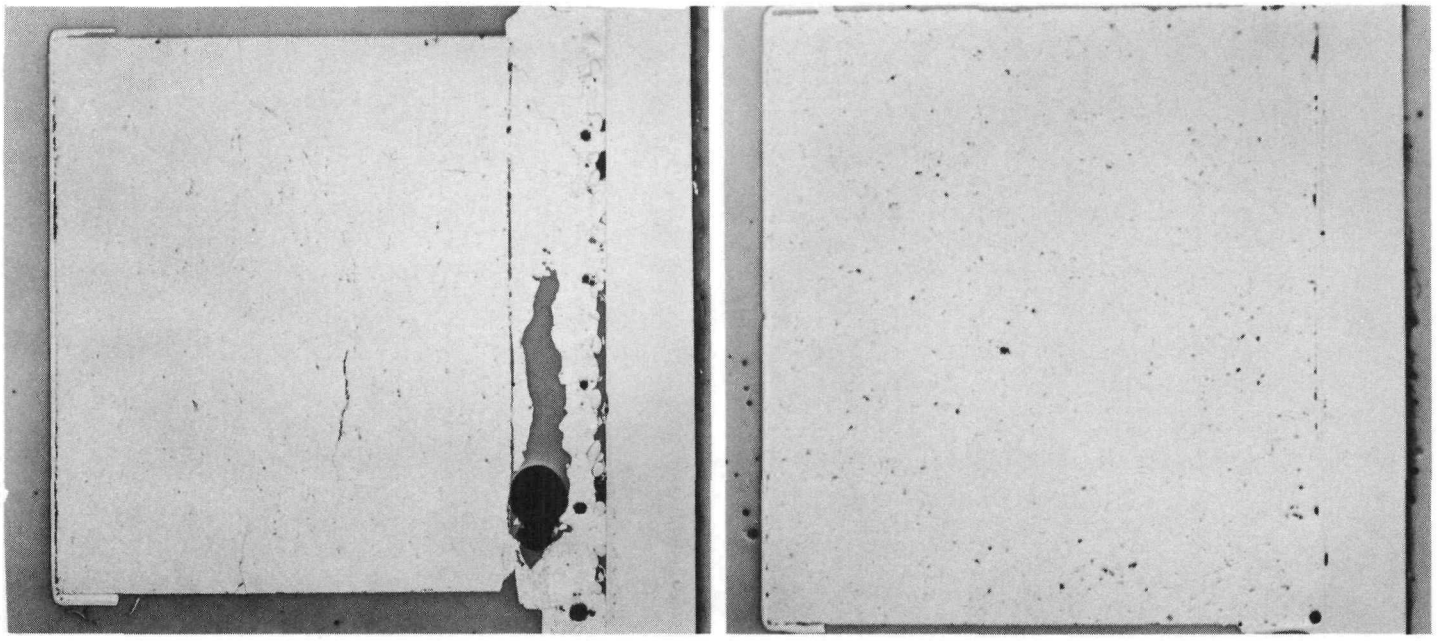

a. P Element

b. N Element

FIG. D-8. SNAP 29 COUPLE 29-38-03 AFTER TWO-HOUR TEST

Power test results (two-hour) of the 0.0007- to 0.001-inch Ni-plated couples were:

Couple Identification	N		P	Total Couple		N Leg		P Leg	
	T_C(°F)	T_H(°F)	T_C(°F)	E_o	P	E_o	P	E_o	P
36-13	340	1055	350	160	1.536	0.100	0.768	0.060	0.768
-14	360	1060	340	160	1.496	0.098	0.785	0.060	0.711
-15	350	1060	357	160	1.469	0.096	0.688	0.062	0.763
-16	352	1052	348	160	1.496	0.097	0.692	0.063	0.804
-17	358	1060	350	160	1.456	0.097	0.673	0.063	0.783
-18	350	1058	355	160	1.472	0.098	0.681	0.063	0.791

The six couples were submitted to a nine-point resistance test following the power testing:

Couple Identification	1 P	2 P	3 P	4 P	5 N	6 N	7 N	8 N	9 N/P
36-13	Not available								
-14	0.24	0.340	0.10	0.680	0.040	0.340	0.350	0.400	1.08
-15	0.09	0.500	0.15	0.750	0.040	0.320	0.060	0.400	1.15
-14	0.120	0.400	0.140	0.670	0.040	0.380	0.050	0.420	1.10
-17	0.090	0.500	0.120	0.670	0.040	0.330	0.06	0.410	1.12
-18	0.090	0.370	0.110	0.610	0.050	0.330	0.050	0.410	1.05

Tensile tests were performed on the couples following the two-hour power and nine-point tests.

Couple Identification	Leg/Load (psi) N	Leg/Load (psi) P		Fracture/Failure	Descriptions
36-13		0	P	Leg fell off when removed from power test	
	188		N	Fracture element	Failure hot shoe bond
36-14		92	P	Failure	Cold cup bond
	315		N	Fracture element	Failure hot shoe bond
36-15		62	P	Failure	Hot shoe bond
	285		N	Fracture element	Failure cold cap bond
	>315		N*	No fracture failure	
36-16		0	P	Leg fell off while setting up for tensile test	
	220		N	Fracture element	Failure hot shoe bond
36-17		82	P	Failure	Hot shoe bond
	430		N	Fracture element	Failure hot shoe bond
36-18		38	P	Failure	Hot shoe bond
	413		N	Fracture element	Failure cold cup bond
	428		N	Fracture element	Failure hot shoe bond

* Maximum load applied due to epoxy failures.

Twelve couples were fabricated utilizing a Sn bond P leg with a wafer bond of the N hot shoe and a standard cold cup bond. Couple resistance (nine-point) was taken of each couple after fabrication.

Couple Identification	1 P	2 P	3 P	4 P	5 N	6 N	7 N	8 N	9 N/P
38-01	0.110	0.350	0.050	0.435	0.10	0.360	0.030	0.485	1.00
-02									
-03	0.060	0.350	0.050	0.440	0.08	0.300	0.08	0.450	0.920
-04	0.040	0.310	0.050	0.430	0.08	0.310	0.08	0.465	0.975
-05	0.075	0.320	0.060	0.440	0.100	0.370	0.05	0.480	1.00
-06	0.080	0.340	0.080	0.510	0.050	0.350	0.05	0.400	0.950
-07	0.07	0.360	0.070	0.470	0.090	0.370	0.050	0.470	0.980
-08	0.065	0.340	0.060	0.450	0.070	0.320	0.050	0.435	0.970
-09	0.05	0.340	0.07	0.500	0.05	0.300	0.060	0.490	0.930
-10	0.075	0.300	0.06	0.430	0.075	0.320	0.050	0.440	0.900
-11	0.050	0.310	0.05	0.430	0.05	0.330	0.050	0.415	0.875
-12	0.080	0.340	0.075	0.460	0.070	0.350	0.070	0.420	0.910

After bonding the N leg, a four-point resistance measurement was taken. Couple 38-02 had an extremely high cold cup resistance at this point.

5 N	6 N	7 N	8 N
0.550	0.290	0.065	0.895

The cold cup was removed and a 0.001-inch thick plated cup was rebonded to the N leg with the following leg and total couple resistance.

Couple Identification	1 P	2 P	3 P	4 P	5 N	6 N	7 N	8 N	9 N/P
38-02	0.050	0.340	0.050	0.400	0.080	0.320	0.070	0.450	0.920

Couple 38-09 also had a 0.001-inch thick plated cold cup but this cup was used on the initial N leg bond.

Two-hour power test results of the Sn bonded TAGS couples were as follows:

Couple	N		P	Total Couple		N Leg		P Leg	
Identification	T_C(° F)	T_H(° F)	T_C(° F)	E_o	P	E_o	P	E_o	P
38-01	348	1048	358	158	1.343	0.094	0.629	0.062	0.714
-02	353	1053	356	157	1.365	0.092	0.595	0.063	0.770
-03	358	1060	320	160	1.488	0.092	0.613	0.067	0.855
-04	356	1050	356	160	1.520	0.098	0.741	0.062	0.779

Couple Identification	T_C(° F)	T_H(° F)	T_C(° F)	Total Couple E_o	Total Couple P	eg E_o	eg P	eg E_o	eg P
38-05	355	1060	340	160	1.472	0.098	0.717	0.062	0.754
-06	350	1060	340	160	1.424	0.098	0.694	0.062	0.729
-07	348	1050	348	160	1.488	0.098	0.725	0.062	0.762
-08	360	1050	345	160	1.520	0.098	0.741	0.062	0.779
-09	357	1050	345	160	1.528	0.098	0.783	0.062	0.744
-10	358	1055	354	159	0.908	0.098	0.379	0.061	0.529
-11	350	1058	348	161	1.611	0.101	0.756	0.061	0.836
-12	353	1050	342	160	1.444	0.099	0.702	0.061	0.738

After two-hour power testing, the couples resistances (nine-point) were taken:

Couple Identification	1 P	2 P	3 P	4 P	5 N	6 N	7 N	8 N	9 N/P
38-01	0.15	0.390	0.150	0.710	0.090	0.350	0.05	0.480	1.22
-02	0.090	0.460	0.220	0.780	0.040	0.340	0.05	0.410	1.20
-03	0.120	0.500	0.100	0.730	0.040	0.320	0.05	0.390	1.13
-04	0.07	0.490	0.08	0.650	0.04	0.350	0.05	0.440	1.10
-05	0.09	0.420	0.06	0.620	0.08	0.340	0.05	0.460	1.10
-06	0.09	0.550	0.06	0.700	0.05	0.360	0.04	0.410	1.12
-07	0.10	0.470	0.095	0.730	0.110	0.330	0.06	0.490	1.22
-08	0.10	0.440	0.08	0.650	0.09	0.340	0.04	0.450	1.10
-09	0.05	0.480	0.150	0.690	0.05	0.320	0.05	0.390	1.10
-11	0.06	0.420	0.220	0.700	0.06	0.330	0.06	0.430	1.15
-12	0.07	0.400	0.07	0.580	0.04	0.320	0.065	0.420	1.02

Concerning Couple 38-10, it is evident from the nine-point data after power test, that the reason for a low power yield is a result of a cracked P leg and a high resistance cold cup bond. Both of these facts are substantiated by the tensile test data. Following is the tensile data of all couples from Lot 38.

Couple Identification	Leg/Load (psi) N	Leg/Load (psi) P	Fracture/Failure	Description
38-01		0	P Leg fell off while preparing for tensile test	
	432		N Fracture element	Failure bond hot shoe
38-02		87	P Fracture element	Failure of hot shoe ~80% bond
	127		N Failure	Cold cup bond
	258		N Fracture element	
38-05		204	P Failure	Hot shoe bond
	40		N Failure	Cold cup bond
	333		N* No fracture or failure	

Couple Identification	Leg/Load (psi) N	P		Fracture/Failure	Description
38-10		48	P	Fracture element	Crack heavy oxide
	15		N	Failure	Cold cup bond
	248		N	Fracture element	Failure bond
38-11		26	P	Failure	Hot shoe bond
	125		N	Failure	Cold cup bond
	575		N*	No fracture or failure	
38-12		174	P	Failure	Hot shoe bond
	285		N	Failure	Cold cup bond
	185		N	Fracture element	
38-08	90	102			
	>512				

*Maximum load applied due to epoxy failures.

Couples 38-04 and 38-07 were submitted to Engineering for the 100-hour power tests after completing a two-hour power test. Results are as follows:

Couple Identification	Elapsed Time	N		P	Total Couple		N Leg		P Leg	
		T_C(° F)	T_H(° F)	T_C(° F)	E_o	P	E_o	P	E_o	P
38-04	2.0	350	1048	350	164.5	1.529	101.3	826	65.8	782
	139.8	350	1050	350	169.0	1.511	101.1	827	69.5	766
38-07	2.0	351	1055	349	163.6	1.462	98.7	804	66.7	726
	117.1	350	1051	350	169.0	1.502	100.2	831	70.3	737

Couple resistance (nine-point) was secured on both Couples 38-04 and 38-07 after removal from their 100-hour tests.

Couple Identification	1 P	2 P	3 P	4 P	5 N	6 N	7 N	8 N	9 P/N
38-04	0.81	0.78	0.21	1.84	0.05	0.300	0.07	0.430	2.40
38.07	0.10	1.0	0.63	1.83	0.070	0.290	0.07	0.440	2.41

Tensile test was performed on Couple 38-04 after the 100-hour test.

Couple Identification	Leg/Load (psi) N	P		Fracture/Failure	Description
38-04		0	P	Failure	Hot shoe bond
	305		N	Failure	Hot shoe bond
				Fracture element	

Figures D-8 through D-10 are metallographic photographs after the two-hour power tests of couples fabricated during the beginning, middle and end of fabrication. Again, the problem of the poor SnTe casting is evident. Photomicrograph, Fig. D-11, is of Couple 38-08 after 100-hour performance testing.

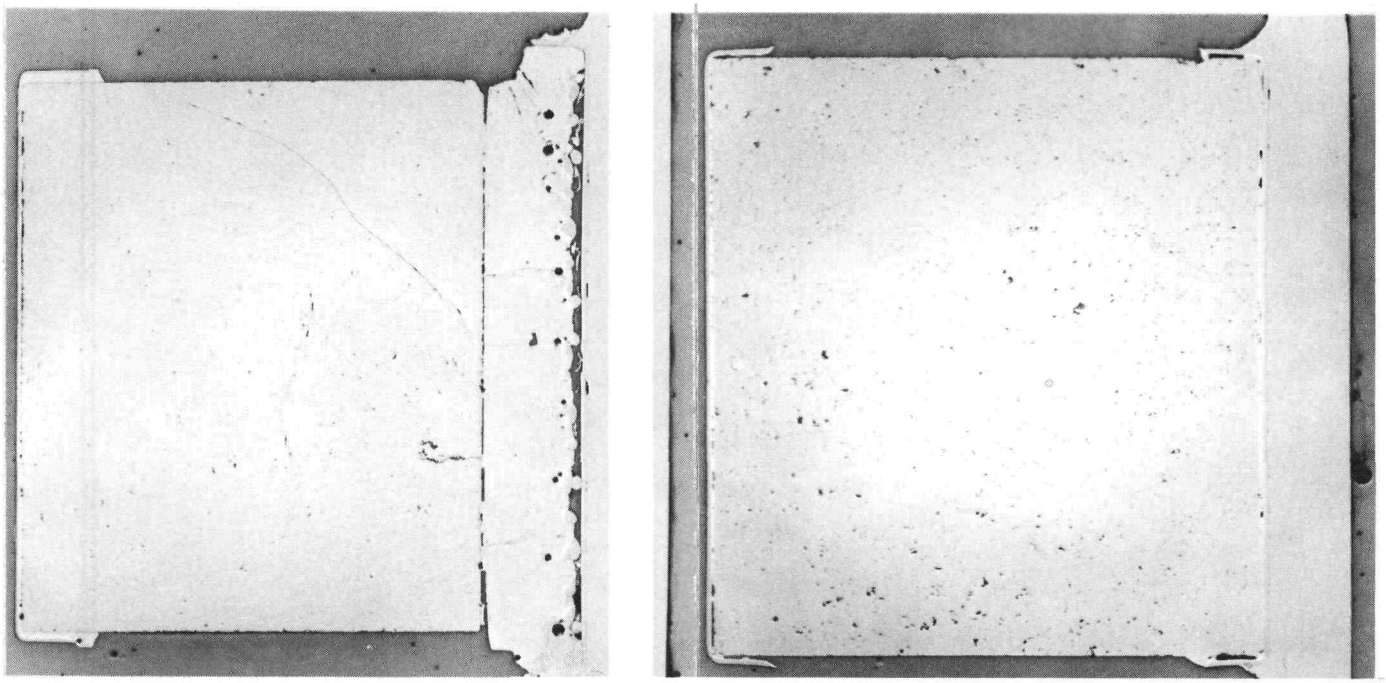

a. P Element b. N Element

FIG. D-9. SNAP 29 COUPLE 29-38-06 AFTER TWO-HOUR TEST

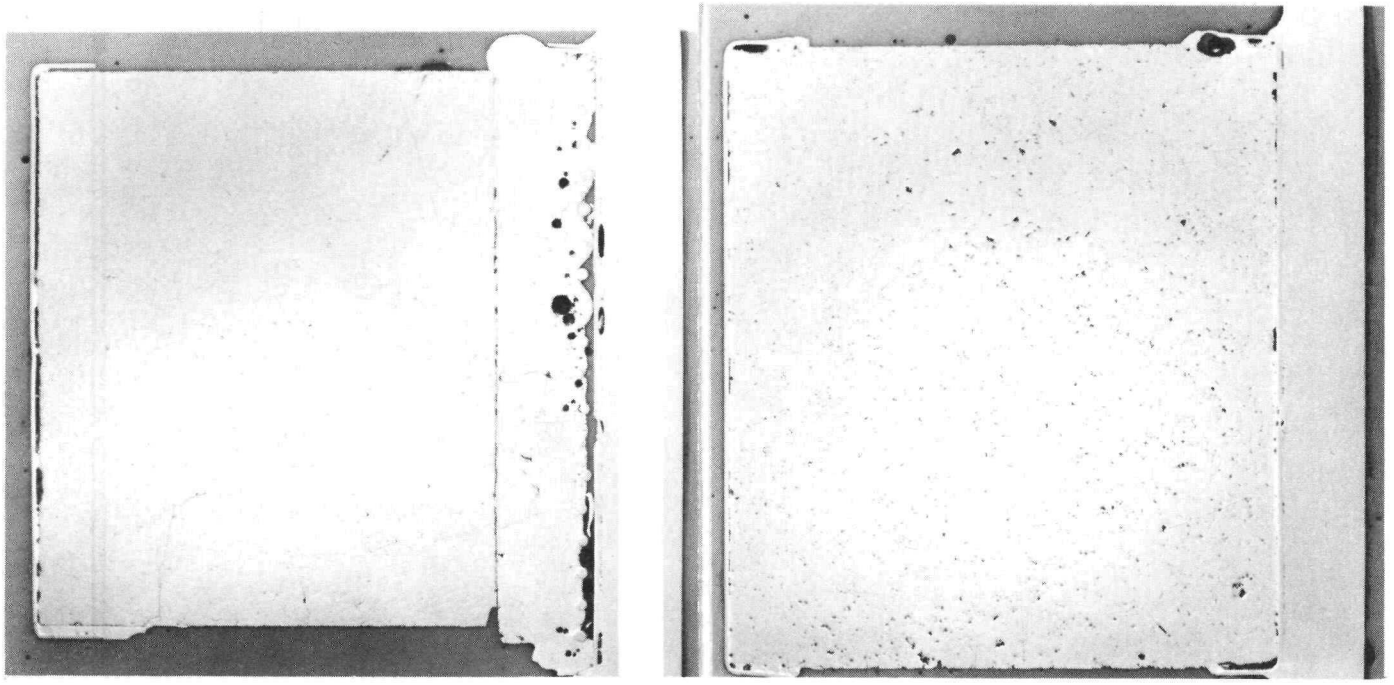

a. P Element b. N Element

FIG. D-10. SNAP 29 COUPLE 29-38-09 AFTER TWO-HOUR TEST

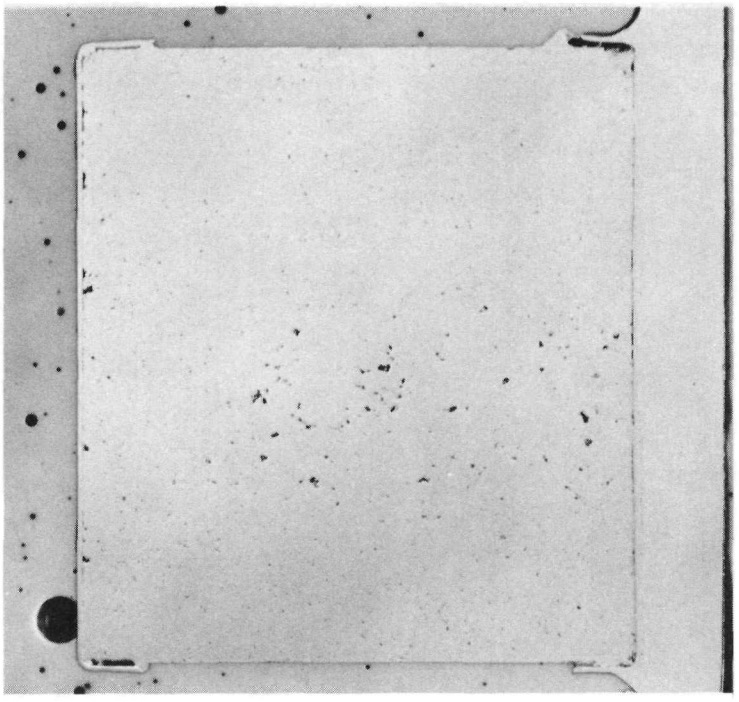

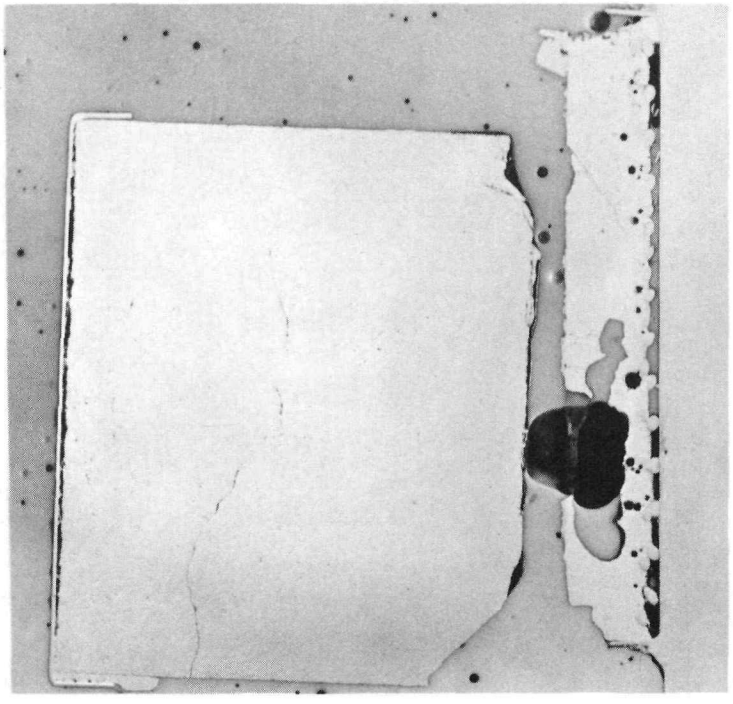

b. N Element

FIG. D-11. SNAP 29 COUPLE 29-38-07 AFTER 100-HOUR TEST

APPENDIX E

HEAT PIPE DESIGN SELECTION

A. INTRODUCTION

With the decision to use heat pipes for the SNAP 29 heat rejection system that was made in June 1967, a program was initiated to investigate heat pipe systems which would be satisfactory for this application from thermodynamic, reliability and manufacturing considerations. Various designs were tested and primary and backup configurations were selected in January 1968 as discussed in Ref. E-1. From February to September 1968, tests have been conducted on about 20 heat pipes of the primary and back-up designs. These tests units differed in that cleaning methods, surface preparation and/or fabrication techniques were varied from unit to unit. Data from these tests have been studied and used as a base to recommend the preferred design to be used in the heat rejection subsystem.

The heat pipe development test program is shown in Table E-1. This indicates the numerous variables investigated as well as quantities of heat pipes fabricated during this study.

Table E-2 shows a summary of heat pipes with different combinations of variables tested. Those test units listed above the broken line are the ones which most closely conform to the recommended design.

B. DISCUSSION

The water-filled heat pipes tested for the heat rejection system have been sized from thermo-structural analyses of the module and radiator and heat pipe fabrication limitations. The wick geometry and surface preparations are predicated on maximum heat transport capability of the heat pipe.

The configurations tested had the same evaporator section, namely, three layers of 30 mesh nickel screen and either an annulus or corrugated condenser. The annulus condenser geometry is formed from a single layer of 200 mesh nickel screen using 0.020 inch diameter nickel wire running axially with the screen between it and the inside diameter of the tube. The corrugated condenser section utilizes a 200 mesh screen having triangular corrugations approximately 0.035 inch high running lengthwise. This screen is placed directly against the inside diameter of the tubing.

Five nickel heat pipes were made for the final evaluation tests. These were 15 feet long with a 3/8-inch diameter and a 0.010-inch wall thickness. The condenser section had a five-foot radius contour in it. Four of these heat pipes were oxidized at 1000° F (two annulus and two corrugated configurations), and one was oxidized at 750° F (corrugated condenser). Q (max) versus temperature for these pipes is shown in Fig. E-1.

In as much as the evaporator design for both heat pipes was selected to provide the heat transport capability at a low temperature gradient across the evaporator wick by previous screening tests, the discussion herein will be limited to the condenser wick considerations.

1. Annulus Condenser

The advantages of the annulus condenser design are that the control of the annulus dimension is assured by the spacer wires with the internal helical spring to maintain

TABLE E-1

Heat Pipe Selection Development Summary

Step Variable	Types Fabricated Tested	Fabrications and Tests of Selected Feature	Types of Tests on Selected Feature	Manufacturing Control Over Variable	Results of Testing and Manufacturing Development*	Basis for Selection of Feature	Selection
Evaporator wick	13 types: Annular (1); Corrugated (1); Single artery (1); Dual artery (2); 5-100 (1); 4-100 (1); 3-30 (44); 1-30, 1-40 (3); Modif corr (1); 2-20 (1); 2-20 (1); 2-30, 1-60 (1); 1-40 (1); 3-30, 1-200 (1)	3-30 14 SS; 44 fabrication 30 Ni 200 Techniques evaluated: 1/2 in. OD tube drawn (tight tolerance) (loose tolerance nondrawn)	>200 performance tests with 3-30 Vibration tests-sine (3 g) Shock (40 g); random (29 g rms) Acceleration--15 g, 8 min Boost recovery tests--11 Freeze tests--3 Tolerance control tests--3 Bend tests--1 ft R Life tests--12 (2 SS, 10 Ni)	X-ray of wick Borescope Tube drawn down over mandrel	No fabrication control problem. Easy to bend W/O degradation Performance--ΔT: Good compromise	Provides required Q (max) Low wick ΔT. Excellent fabrication control. Rugged. Can be bent or kinked W/O degradation. Withstands dynamic environment.	3 layers 30 mesh Ni 200
Condenser wick	Tests with 3-30 3 types: Annular 19; Corrugated 24; Dual artery 1	Corrugated 10 SS; 28 fabricated 18 Ni 200 Lengths fabricated: 7 ft--1; 8 ft--13; 15 ft--14 Techniques evaluated: Draw form die; Punch die	>60 performance tests with corrugated Vibration tests--sine 3 g; random 29 g Shock tests--40 g Acceleration tests--15 g, 8 min Boost recovery tests--6 Freeze tests--3 Bend tests: 4 ft R--1; 5 ft R--4 Life tests--6	X-ray of wick Borescope Corrugated shape, height and numbers not critical	Easy to fabricate. Low flow resistance--based on 8 ft vs 15 ft. No fabrication control problem. Degrades least after bend. Good recovery characteristics. Withstand dynamic environment.	Ease of fabrication. Performance relatively insensitive to length with 3-30. Low wick ΔT. No internal spring required. Bending degradation performance only slight. Stiff cross section. High Q (max) vs annular after bending.	200 mesh 35-mil Corrugated Ni 200
Evaporator bend	1 type: 3-30, 8 ft, 12 in. R Related test: 3-30, 15 ft, Large kink in evaporator 5 ft R bend in condenser	Performance test: Temperature elevation, No degradation Performance tests: Temperature elevation, No degradation	9 performance tests (1 additional test planned) 7 performance tests	X-ray of bend and wick joint	No degradation in performance due to bending or kinking.	Rugged. Can be bent or kinked W/O performance degradation. 1 ft R required for application.	3 layers 30 mesh 1 ft R bend
Condenser bend	9 types: Annular--4 Ni and SS; Corrugated--5 Ni and SS Bend radii: Annular: 45° mitre joint 2 ft--1; 4 ft--1; 5 ft--2 Corrugated: 4 ft--1; 5 ft--4	Corrugated bend 5 fabricated: 4 ft R (8 ft); 5 ft R (15 ft)	15 performance tests with corrugated bent Dynamic tests Acceleration Corrugated 4 ft R Annular 4 ft R	X-ray of bend and wick joint	Corrugated performance degradation least after bending. Wick joint interface after bend is better with corrugated. Can be bent without mandrel. Cannot bend after evaporator and condenser sections are joined.	Corrugated performance degrades least; meets Q (max) requirements. Stiff cross section at joint interface. No internal spring required. 5 ft R bend required for application.	Corrugated 5-ft R bend
Wick joint	2 types: 56 butt: 3-30/corrugated--24 (5 bent, 19 straight); 3-30/annular--20 (5 bent, 15 straight) Overlap--dual artery/DA--1	56 butt joints fabricated: 56 test series with butt joints. (>200 tests)	Performed Dynamic Life Freeze 10 tests of remade joints	X-ray of joint Alignment tooling	Interface gap control required but not extremely critical. Joint bent with straight sections requires good alignment.	Provides required Q (max). Very few problems. Easiest to fabricate and remake.	Butt
Tube joint	2 types: 46 butt weld (Ni 20, SS 26); 11 braze coupling (Ni only)	11 braze joints: 9 corrugated, 2 annular	Performance tests--11 series Life tests--3 Compatibility--5 samples Remade joints--6	X-ray of joint Coupling design Alignment tooling	Braze material has insignificant effect on gas generation. Braze penetration controlled by coupling design. Joints remade relatively easily.	Braze of 10 heat pipes at once easier than welding. Coupling provides stronger joint. Easier to control braze penetration with proper coupling design.	Braze coupling Prema-braze 130
Cleaning method	HNO_3 + HF: 30 SS: 7 ft--5; 8 ft--17; 15 ft--8 Std: 9 Ni: 15 ft HNO_3: 20 Ni: 8 ft--13; 15 ft--7 Mixed--1 Ni, 15 ft acids	20 HNO_3 Ni: 14--3-30/corrugated; 6--3-30/annular	Performance tests--20 series Dynamic tests--4 std SS Life tests (3) HNO_3, Ni--104d (1) HNO_3, Ni--120d (1) HNO_3, Ni--116d (1) HNO_3, Ni--40d (1) HNO_3, Ni--57d (1) HNO_3, Ni--7d 3 std SS--62d	Process specification	Any cleaning method W/O oxidation generates gas. Std Ni gives poor wetting. HNO_3 leaves smooth surface, thus easier to completely oxidize. HNO_3 gives better performance than std cleaning. Mixed acids generates excess gas.	Leaves smooth surface. Easier to completely oxidize. In combination with bake, generates minimum gas. Improves performance over std cleaning.	HNO_3 clean
Oxidation method	Passive 750° F air-bake--6 Ni: 4 std, 2 HNO_3 775° F ± 25 flowthru--8: Ni-HNO_3 1000° F modified FT--4 Ni: 2 std, 2 HNO_3 500° F vacuum--1 SS std	8 775° F ± 25--8 corrugated: 8-ft--6; 15-ft--2 Flowthru bakeout	Performance tests 19 series with Life tests bakeout (1) HNO_3--pass. 750--116d (2) HNO_3--FT 775--120d, 7d (1) HNO_3--rebaked--40d, FT 775 (1) HNO_3--1000 mod FT--57d (1) Std--1000 mod FT--just initiated (1) HNO_3--FT 775--planned	Flowthru assures complete oxidation. Temperature control 750° F assures stable oxide process specification	Oxidation above 750° F required for stable oxide surface. Complete oxidation required to eliminate gas generation. HNO_3 cleaned surface easier to completely oxidize.	Flowthru 775 process in combination with HNO_3 clean gives generation. Flowthru 775 + HNO_3 clean gives best performance.	Flowthru 775° F ± 25 bakeout

CONFIDENTIAL

CONFIDENTIAL

TABLE E-2

Combinations of Selected Heat Pipe Variables Tested

All pipes 3/8 in. diameter
Ten-mil wall
Nickel 200 materials
All evaporator wicks 3 layer, 30 mesh
Wick joint--butt

Length (ft)	Cond Wick	Evap Bend 1 ft (R) Reqd (1)	Cond Bend 5 ft (5) Reqd	Tube Joint (2)	Clean Method	Oxidation Method (3)	Number Perf Tested	Number Life Tested	Acceptable Perf
15	Corr	1 ft (R)	5 ft (R)	Braze	HNO_3	775 FT	0	0	
15	Corr	None*	5 ft (R)	Braze	HNO_3	775 FT	0	0	
15	Corr	None*	5 ft (R)	Welded*	HNO_3	775 FT	1	1	Yes
15	Corr	None*	5 ft (R)	Welded*	HNO_3	1000 FT*	1	1	Yes
15	Corr	None*	5 ft (R)	Welded*	Std*	1000 FT*	1	1	Yes
15	Ann*	None*	5 ft (R)	Welded*	HNO_3	1000 FT*	1	0	Marginal
15	Corr	None*	St*	Welded*	HNO_3	775 FT	1	1	Yes
8*	Corr	None*	St*	Braze	HNO_3	775 FT	1	1	Yes
8*	Corr	None*	St*	Braze	HNO_3	775 FT	1	1	Yes
8*	Corr	None*	St*	Braze	HNO_3	775 FT	1	1	Yes
15	Ann*	None*	St*	Welded*	HNO_3	775 FT (rebaked)	1	1	Yes

Notes: (1) Evaporator wick (3-30) can be bent or kinked severely without performance degradation as proved by tests.
(2) Welded (butt) tube joint judged to be more difficult alignment and weld penetration problem than brazed collar joint.
(3) The 1000° F flowthrough process in combination with HNO_3 clean is not expected to produce significant different results than the 775° F FT + HNO_3 process since both should produce a stable oxide surface.

*Items not recommended for selected heat pipe design.

CONFIDENTIAL

CONFIDENTIAL

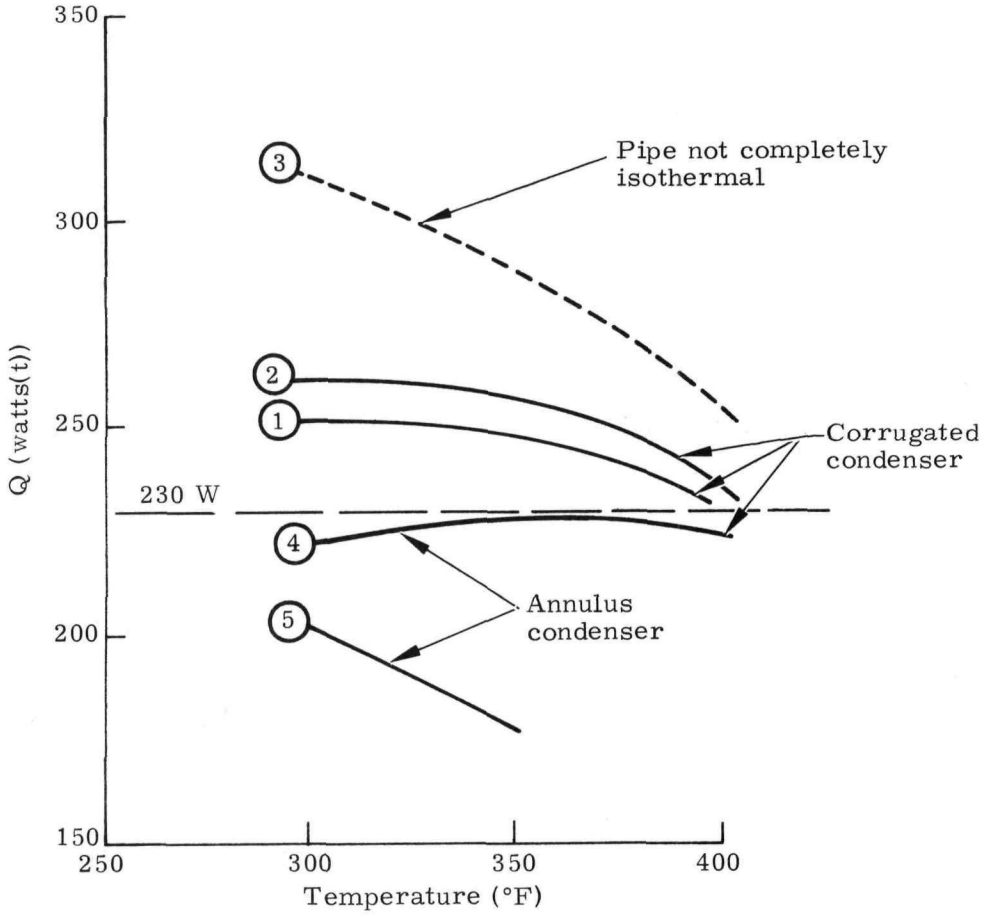

Heat Pipes:

3/8 in. OD x 0.010 wall Ni-200
5-ft bend radius in condenser
Evaporator--3 layers, 30 mesh screen
Wick joint--butt-type

1 750° F + bakeout, HNO_3 cleaned
2 1000° F + bakeout, HNO_3 cleaned
3 1000° F + bakeout, HNO_3-HF cleaned
4 1000° F bakeout, HNO_3 cleaned
5 1000° F bakeout, HNO_3-HF cleaned

Heat pipes tested in level position.

FIG. E-1. Q (MAX) VERSUS TEMPERATURE--15-FOOT PIPES

radial pressure against the wall of the tube and better configuration control during bending. This geometry has its disadvantages such as a larger temperature gradient through the water-filled annulus (temperature drop now becomes a function of the conductivity of the fluid), lower heat transport capability and poor configuration control of the wick at the joint interface and at screen overlap between pitch intervals of the internal spring. Also, this type is more difficult to fabricate.

The advantage gained by the spacer wires is offset by the fabrication problems associated with attaching these wires in position on the screen while the configuration control afforded by the internal spring during bending is lost at the joint interface where the spring terminates.

2. Corrugated Condenser

The condenser design using the corrugated wick is judged to be superior to other condenser wick designs investigated in that there is only one apparent disadvantage which arises during fabrication. A certain amount of wick geometry control is lost at the time the formed screen is inserted into the tube. The process of drawing the wick into the tube tends to deform it and thus the final shape and fit to the wall of the condenser tube relies only on the small spring rate of the screen material, since this design precludes the use of an internal spring which would deform the corrugations.

The corrugated condenser section is easier to fabricate since the corrugations are all formed at the same time in one die set. No additional work is required before assembly of the wick into the tube.

The corrugated condenser section has consistently shown a smaller temperature drop across the wick than the annulus. In the corrugated wick the metal screen helps to conduct some of the heat through the water film. This has a two-fold effect. First, it conducts some of the heat directly to the tube wall and second, it tends to minimize the temperature gradient through the water film. The temperature drop across the annulus condenser has been found to be 3° to 10° F, while that of the corrugated condenser has been 1° to 3° F.

Figure E-1 shows a comparison of Q (max) versus temperature for the five bent heat pipes mentioned earlier. As can be seen, both annulus condenser pipes show a Q (max) which is below the 230-watt acceptance level as recommended by Ref. E-2. Briefly, this heat transport of 230 watts(t) is based on meeting the system requirements of a short term off-design condition (high current and low voltage) as well as a design maximum power requirement. This design power level is approximately 16% below the acceptance level and thus assures a system in which the individual heat pipes are operating at a suitable margin below their maximum capacity.

The heat pipe represented by Curve 5 had an exceptionally low Q, and no attempt was made to test this at 400° F. X-rays of this heat pipe clearly show a screen deformation between the spring helix. The heat pipe shown as Curve 3 has an excess of water in it and is not isothermal for its full length, i.e., effectively increasing the heat transport capacity.

Curve 1 shows data from a heat pipe which was oxidized at 750° F +, while Curve 2 pipe was oxidized at 1000° F. Pipes oxidized at the higher temperature generally have shown a tendency to generate some gas, although insufficient life test data are available currently with 1000° F bakeout pipes to permit valid comparison with 750° F + bakeout pipes.

3. Cleaning and Surface Treatment

Two methods of cleaning have been investigated. Both methods consist of degreasing and cleaning for gross contaminants followed by an acid etch. In one method, nitric-hydrofluoric acid is used, and in the other the etch is done with nitric acid only. The nitric-hydrofluoric acid produces a rough, pitted surface, whereas the nitric acid treated material is smoother in appearance. Oxidation after acid etch has been done at 1000° and 750° F.

The nitric-hydrofluoric acid etching has shown a pattern of being susceptible to gas generation after being in operation for a period of time. This is probably due to the extensive area exposed on the spongy surface which may not be completely oxidized. Lack of an oxide coating even in the small crevices produced by this acid etch will set up a nickel/nickel oxide electrochemical cell which produces hydrogen gas.

Tests on heat pipes with the two acid treatments and with different oxidation temperatures have shown better performance (i.e., high Q and no gas buildup) by using the nitric acid with a 750° F + oxidation temperature (Table E-3). These test units have been undergoing performance testing for approximately three months and have now been placed on a steady-state life test.

TABLE E-3

Performance Data

	Type	Method of Cleaning	Oxidation Temperature (°F)	Q (watts)	Gas	T (°F) Evaporator	T (°F) Condenser
1.	Corrugated	HNO_3	750	252	No	8	2
2.	Corrugated	HNO_3	1000	262	No	9	1
3.	Corrugated	HNO_3-HF	1000	312	Yes	9	-
4.	Annulus	HNO_3	1000	222	No	10	5
5.	Annulus	HNO_3-HF	1000	202	Test terminated	10	4

All heat pipes level and transport temperature at 300° F.

C. CONCLUSIONS

For a water heat pipe having a minimum temperature drop through the system, adequate heat transport capacity throughout its operating spectrum, minimum degradation during its operating life and with few fabrication problems, the use of a hybrid heat pipe consisting of a multilayer screen wick in the evaporator coupled with the corrugated 200 mesh screen wick in the condenser section is recommended (Table E-4).

TABLE E-4

Recommended Design

Three-layer, 30 mesh evaporator wick

Thirty-five-mil corrugated condenser wick (200 mesh)

Material: Nickel 200 for tube and wicks

Three-eights-inch OD by 10-mil wall tubing

Joints: Wick--butt
Tube--braze with coupling

Cleaning: Nitric acid

Preconditioning: 750° F + flowthrough process backout

NOTES FOR HEAT PIPE SELECTION DEVELOPMENT CHART

1. Documentation of heat pipe analyses, test results and manufacturing and development evaluations may be found in the following reports:

   (1) IDC 4000-2, "Study to Evaluate the Feasibility of Using Heat Pipes in the Heat Rejection System of SNAP 29." From W. B. Bienert to M. Scheve, June 23, 1967.

   (2) IDC 1840-2, "Heat Rejection Subsystem Radiator Requirements for a 6 T/E Module RTG SNAP 29 Configuration." From R. Hannah to A. LaPorte, September 26, 1967.

   (3) IDC 1840-6, "Selection of Primary and Back-up Water Heat Pipe Design Configurations." From R. Hannah and J. Peters to A. LaPorte, February 26, 1968.

   (4) IDC 1840-7, "Evaluation of the Effects of Heat Pipe Failures on SNAP 29 System Design and Performance." From R. Hannah to A. LaPorte, May 15, 1968.

   (5) Memo 1840-9, "Heat Transport Acceptance Level for SNAP 29 Heat Pipes." From R. Hannah and J. Peters to A. LaPorte, September 11, 1968.

   (6) Memo 1840-8, "Steady State Heat Pipe Analysis and Correlation of SNAP 29 Heat Pipe Test Data." From P. Brennan and R. Hannah to A. LaPorte, September 17, 1968.

   (7) SNAP 29 Monthly and Quarterly Progress Reports from June 1967.

2. Boost Recovery Tests: Refer to deliberate dryout tests of heat pipes for periods simulating boost times with subsequent attempts to recover. See SNAP 29 7th Quarterly Report, April-June 1968.

3. Heat Pipe Performance Tests: See Nuclear Test Directive NTD-1840-01, Rev. A, November 7, 1967.

4. Heat Pipe Dynamic Tests: See NTD 1840-02, Rev. A, December 1967.

5. Freeze Tests: See February 1968 Monthly.

6. Ref: Condenser Bend Section

   Forty-five degree-mitre joint pipe mated two condenser sections having an annular wick configuration. It is judged that this accomplishment is much more difficult than, for example, mitre joining of two sections of three layer, 30 mesh wick, which could be considered in lieu of a one-foot radius bend.

BLANK

APPENDIX F

PRETEST THERMAL ANALYSES OF HEAT REJECTION SUBSYSTEM MANUFACTURING CHECKOUT UNIT TEST SERIES

A. INTRODUCTION

Since the incorporation of the heat pipe into the heat rejection subsystem design, all development effort has centered about the selection of a heat pipe configuration which would adequately meet all the design and mission requirements for the SNAP 29 system. With this development step virtually completed; the next step is to uncover the manufacturing and assembly problems associated with the incorporation simultaneously of 10 heat pipes into the aluminum radiator panel and into the T/E module beryllium heat sink. A vacuum bonding retort (chamber ~16 inches in diameter and 18 feet long) has been fabricated for the purpose of diffusion bonding the 10 Nickel 200 heat pipe condenser sections to the machined aluminum armor-fin panel. In addition, development of the techniques for brazing the 10 Nickel 200 heat pipe evaporator sections into the module beryllium heat sink is in progress. Following the successful development of these two joining techniques, a series of tests will be conducted with the manufacturing checkout test unit for the purpose of determining the thermal efficiency of these bonded units after they are joined together using the heat pipe braze couplings.

The test series will consist of thermal vacuum testing of the heat sink-radiator panel assembly in the vacuum bonding retort (after removal of the bonding tool) and air performance tests of the assembly both before and after the radiator panel is bent to a five-foot radius.

Because the vacuum bonding retort was not designed specifically for thermal vacuum testing, the interior walls of the chamber are not coated with a high infrared absorbing coating. In addition, because the chamber walls are water cooled, the lowest temperature to which the radiator panel can reject heat will be on the order of 60° F or higher. The thermal analyses reported herein were undertaken to establish the required electrical power inputs to the evaporator heater block in order to achieve design temperatures at the radiator panel and to serve as a means of evaluating and comparing the test results with the expected results.

B. TEST ASSEMBLY AND ANALYTICAL MODEL

A sketch of the insulated evaporator section and the radiator panel (backside insulated) as installed in the vacuum retort (chamber) is presented in Fig. F-1. A cross section of the evaporator-beryllium heat sink assembly is presented in Fig. F-2 which shows the potential parasitic heat loss paths from the aluminum heater block-beryllium heat sink assembly. Figure F-3 shows a cross sectional view of the insulated radiator panel.

Referring to Fig. F-1, power is supplied to the test model by means of electrical heaters installed in an aluminum heater block (Fig. F-2). Heat then flows to the T/E module beryllium heat sink to which the evaporator sections of the heat pipes are attached. This evaporator section is insulated with Johns Manville Thermobestos block insulation. Heat is then transported by means of 10 3/8-inch OD, 10-mil thick wall, 15-foot long, Nickel 200 hybrid heat pipes to the aluminum radiator where the heat is rejected to the surrounding medium. However, in the test model, heat losses occur through the insulated backface of the radiator and through the insulation surrounding the evaporator and transport sections (Fig. F-2 and F-3). For tests in a

CONFIDENTIAL

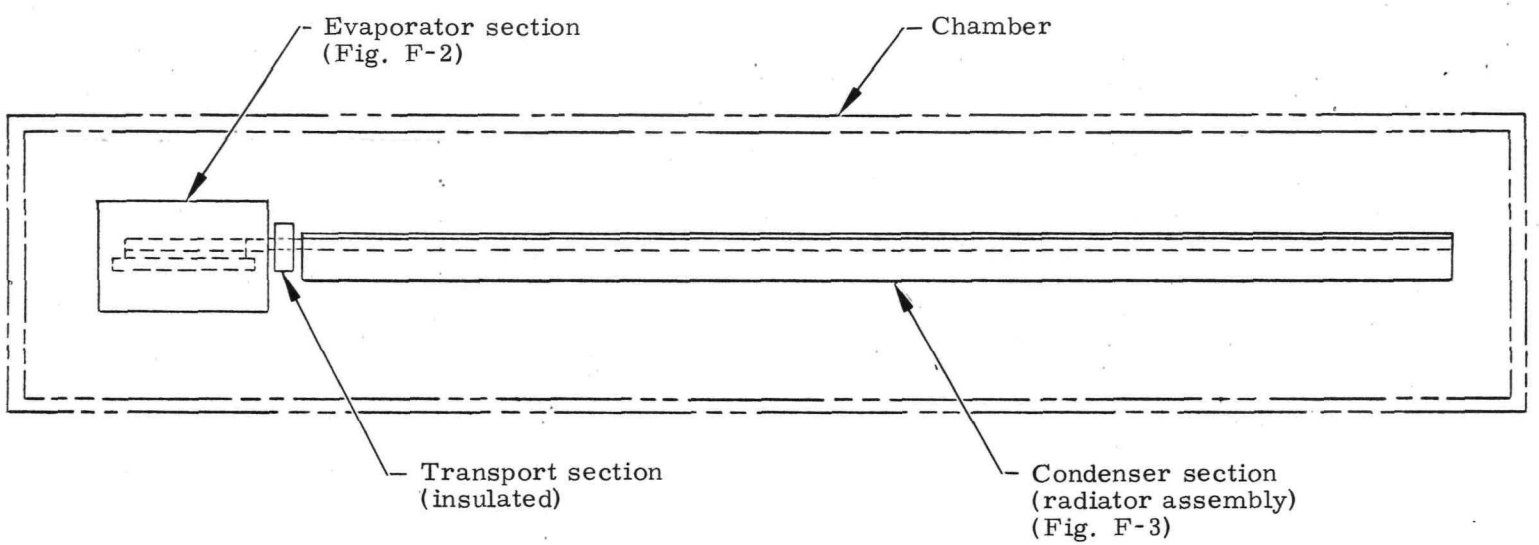

FIG. F-1. SNAP 29 HEAT PIPE TEST MODEL

CONFIDENTIAL

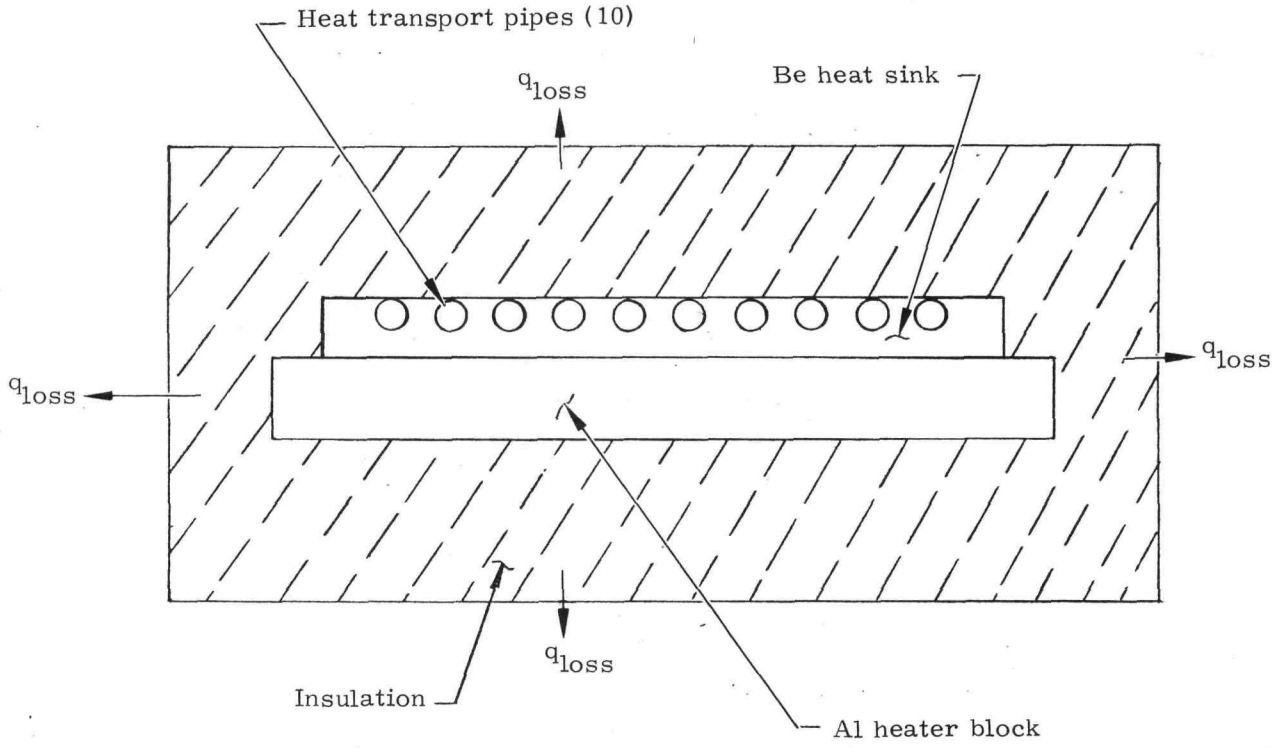

FIG. F-2. CROSS SECTION VIEW OF EVAPORATOR SECTION

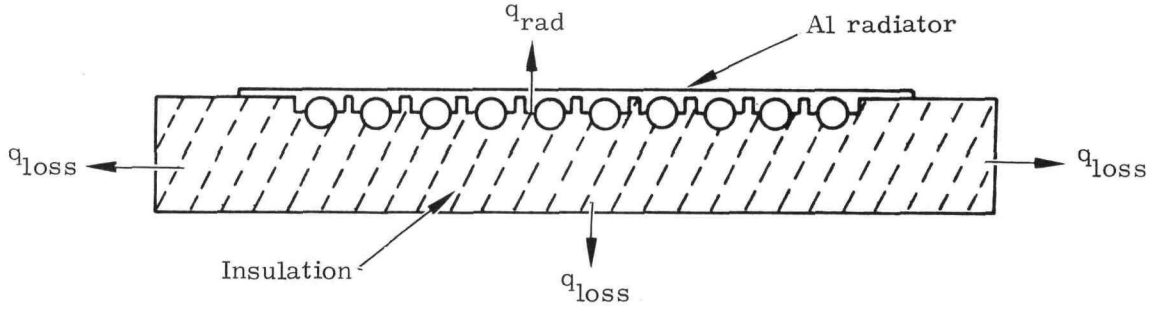

FIG. F-3. CROSS SECTION VIEW OF RADIATOR ASSEMBLY

vacuum, the model is enclosed in a 16-inch diameter by 18-foot long, water-cooled steel vacuum bonding retort which will be employed as a vacuum chamber of these tests.

The thermal model which represents the test assembly and which was the basis for the analyses is given in Figs. F-4 through F-8.

The test assembly thermal model was analyzed using the linearized inversion matrix digital computer program. The analysis was performed for various test conditions both inside the vacuum retort (chamber) and in room temperature air. Since the inside surface of the chamber is uncoated, the surface emissivity was assumed to be between 0.3 and 0.8. In addition, it was assumed that the chamber walls could be held between 60° and 200° F by cooling. This range provides a sufficient envelope within which the actual results should lie. For tests to be conducted in room temperature air, analyses were performed for both free and low level forced convection using heat transfer coefficients of 1.0 and 2.0 Btu/hr-ft^2-°F, respectively, for all external surfaces of the model.

It was assumed that perfect contact existed at the interface between the heat pipes and the radiator panel and the heat pipes and the beryllium heat sink. The various test conditions studied are summarized in Table F-1.

TABLE F-1

Test Conditions Analyzed of SNAP 29 Heat Pipes

Power Input (watts)	Test Media	Boundary Temperature (°F)	Emissivity of Surrounding Surface	Convective Heat Transfer Coefficient (Btu/hr-ft^2-°F)
2500	Vacuum	60	0.3	--
2500	Vacuum	60	0.8	--
2500	Vacuum	200	0.3	--
2500	Vacuum	200	0.8	--
2500	Air	70	1.0	1.0
2500	Air	70	1.0	2.0
2000	Vacuum	60	0.3	--
2000	Vacuum	60	0.8	--
2000	Air	70	1.0	1.0
2000	Air	70	1.0	2.0
1500	Vacuum	60	0.3	--
1500	Vacuum	60	0.8	--
1500	Air	70	1.0	1.0
1000	Vacuum	60	0.3	--
1000	Vacuum	60	0.8	--
1000	Vacuum	200	0.3	--
1000	Vacuum	200	0.8	--
1000	Air	70	1.0	1.0
1000	Air	70	1.0	2.0

CONFIDENTIAL

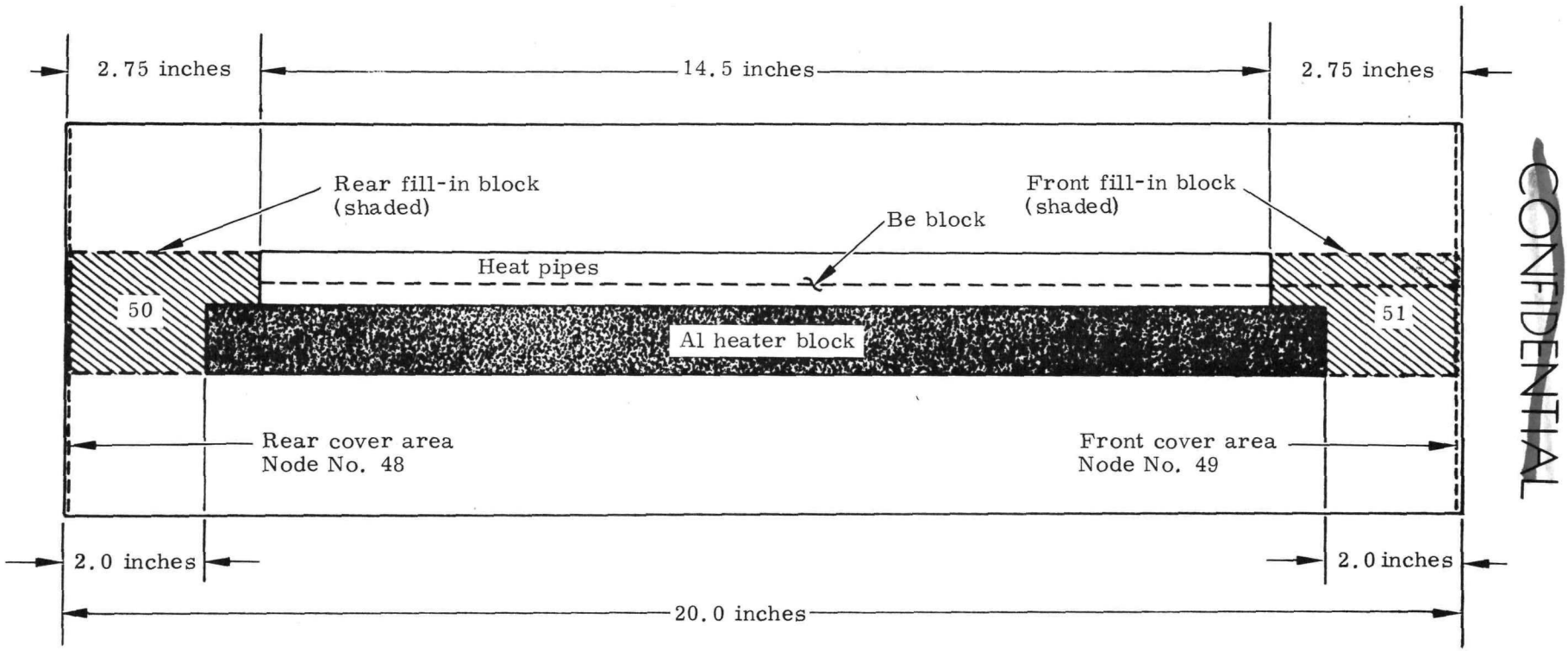

FIG. F-4. SIDE VIEW OF EVAPORATOR SECTION

CONFIDENTIAL

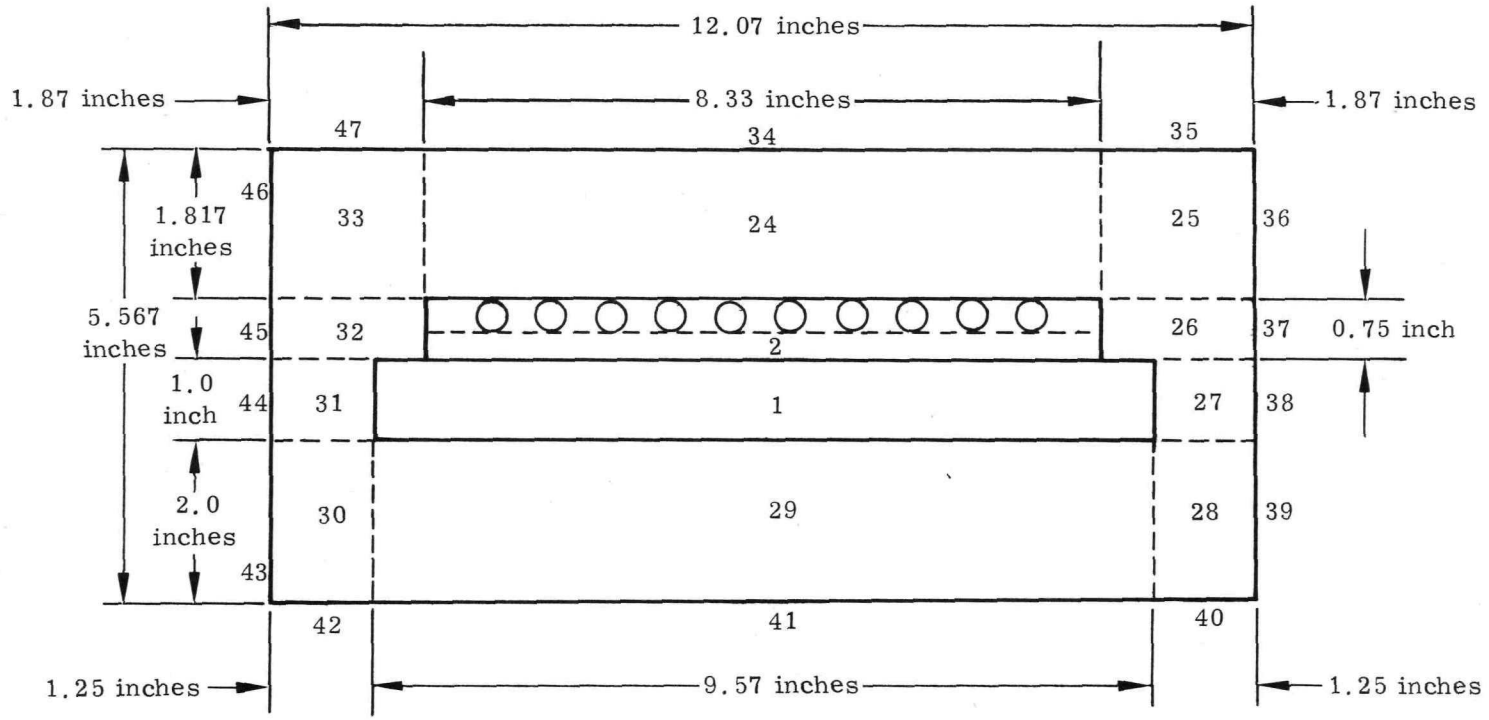

FIG. F-5. NODAL ARRANGEMENT IN EVAPORATOR

CONFIDENTIAL

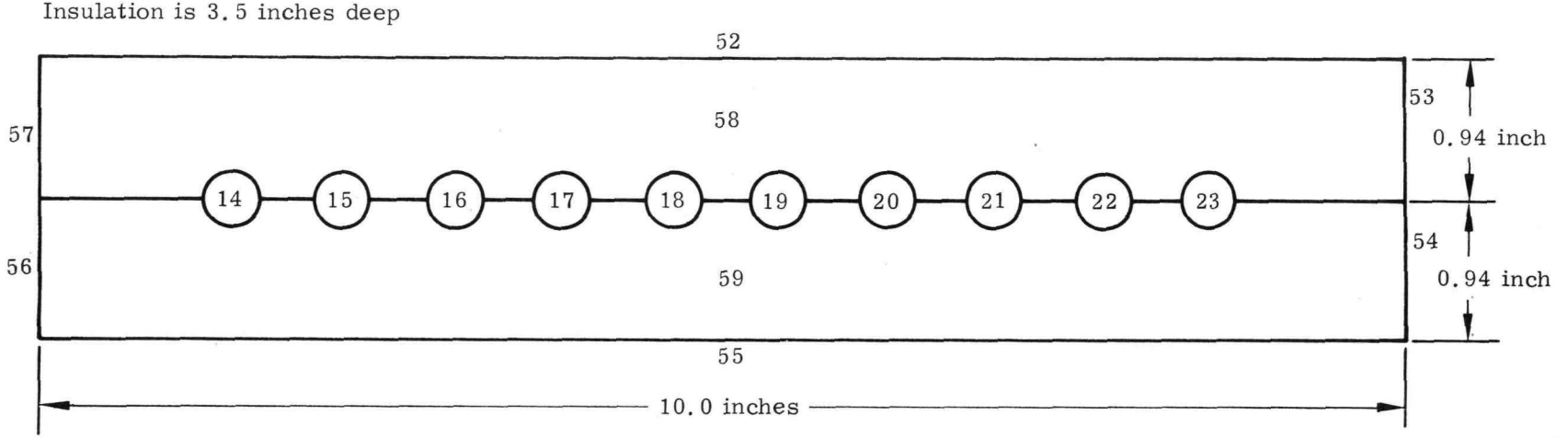

FIG. F-6. NODAL ARRANGEMENT IN TRANSPORT SECTION

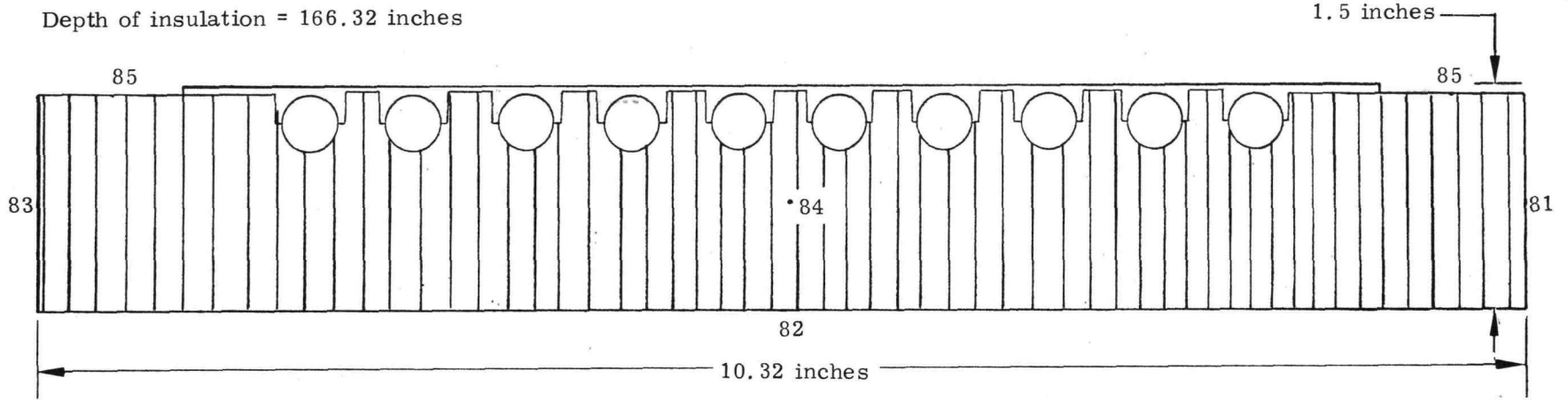

FIG. F-7. NODAL ARRANGEMENT OF INSULATION ON BACKFACE OF RADIATOR PANEL

CONFIDENTIAL

CONFIDENTIAL

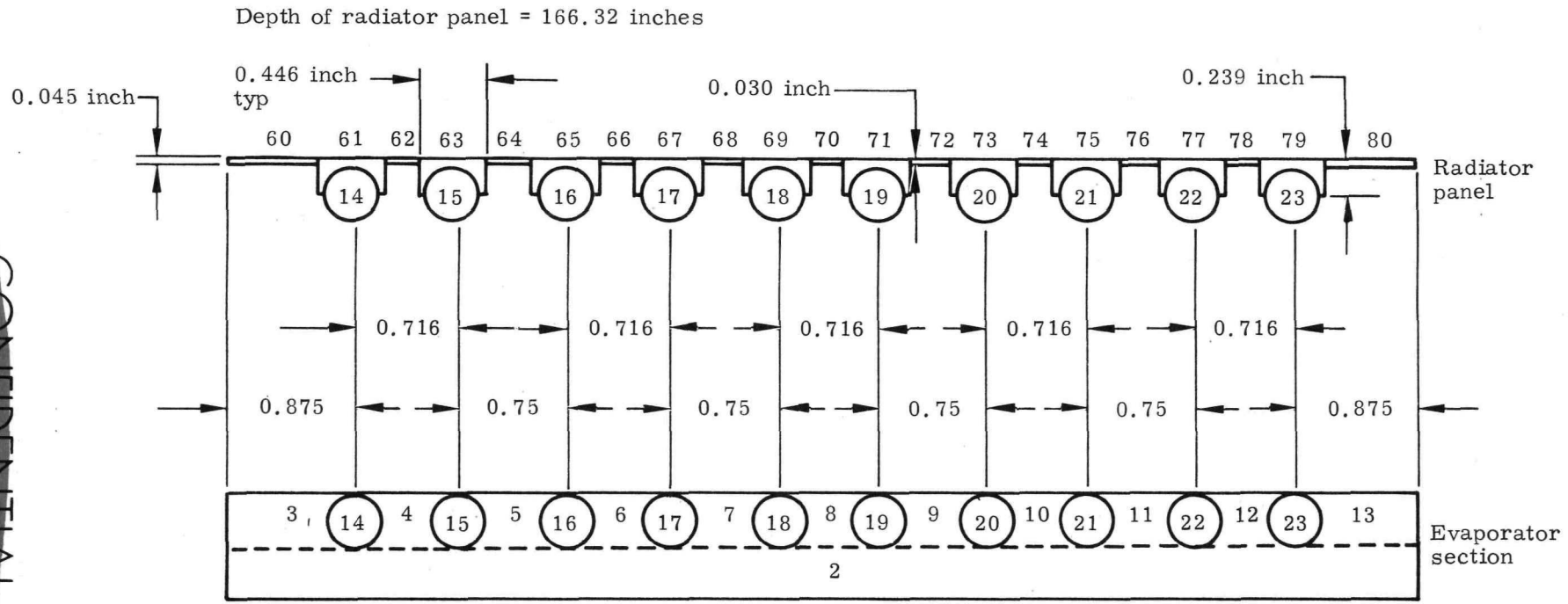

	(in.^{2})		(in.^{2})
Area 3 =	0.2729	Area 60 =	108.44064
Area 4 =	0.15805	Area 61 =	74.17872
Area 5 =	0.1708	Area 62 =	44.9064
Area 14 =	0.11045	Area 64 =	50.56128

FIG. F-8. NODAL ARRANGEMENT OF Be HEAT SINK HEAT PIPES AND RADIATOR PANEL

CONFIDENTIAL

C. DISCUSSION OF RESULTS

Figure F-9 presents the peak radiator temperature as a function of the electrical power input to the heater block for the various boundary conditions analyzed. The test specification currently requires a 2000-watt(e) power input. For the vacuum test, radiator temperatures ranging from 390° to 520° F are predicted at this power input, depending on the chamber wall emittance and temperature. The predicted parasitic heat losses at the evaporator end range from 45 to 65 watts (or ~2 to 3%) as shown in Fig. F-10. The resultant heat transported through the heat pipes under the vacuum conditions is thus predicted at 1935 to 1955 watts for a 2000-watt(e) input. However, as shown in Fig. F-9, an estimated 105 to 145 watts is expected to be lost from the backside of the radiator. This heat loss could be appreciably less depending upon the extent to which the multilayer-type insulation becomes evacuated during the test.

Based on a SNAP 29 RTG system composed of a NaK diaphragm 2N-TAGS couples, the heat rejection requirements have been estimated at 1680 watts at a transport temperature of ~335° F for the normal operating conditions in space. The implications of the analysis are that in the proposed test it will not be possible to simulate both the design heat flux and the design temperature because of lack of control over the boundary conditions. In addition, the 2000-watt(e) power input specified in the test specification for the vacuum test may result in radiator and thus transport temperatures exceeding the 400° F limit quoted therein.

Since the primary objective of these tests is to determine the thermal efficiency of the bonds, it is not absolutely necessary to simulate the design heat flux and temperature conditions exactly, but test personnel should be cautioned to be prepared to reduce the electrical power input during heatup of the test assembly to prevent excessive overheating of the panel.

D. RECOMMENDATIONS

It is recommended that during the vacuum thermal test in the bonding retort the chamber walls be cooled to as low a temperature as possible with the existing test facility. It is also recommended that test personnel be advised that the 200-watt(e) power input will probably result in heat pipe transport and radiator temperatures exceeding the 400° F maximum specified in the Nuclear Test Directive for the heat rejection subsystem Manufacturing checkout tests.

E. SUMMARY

A thermal analysis of the Manufacturing checkout tests indicates that system design heat fluxes and temperatures cannot be obtained simultaneously during the thermal vacuum phase of the test series. This imposes no serious problems, however, since the main objective of these tests is to determine the thermal efficiency of the radiator-heat pipe and beryllium heat sink-heat pipe bonds. Test personnel are cautioned herein that the 2000-watt(e) power input indicated in the test directive for the vacuum test phase will probably result in heat pipe transport and radiator temperatures exceeding the 400° F maximum specified in the test directive.

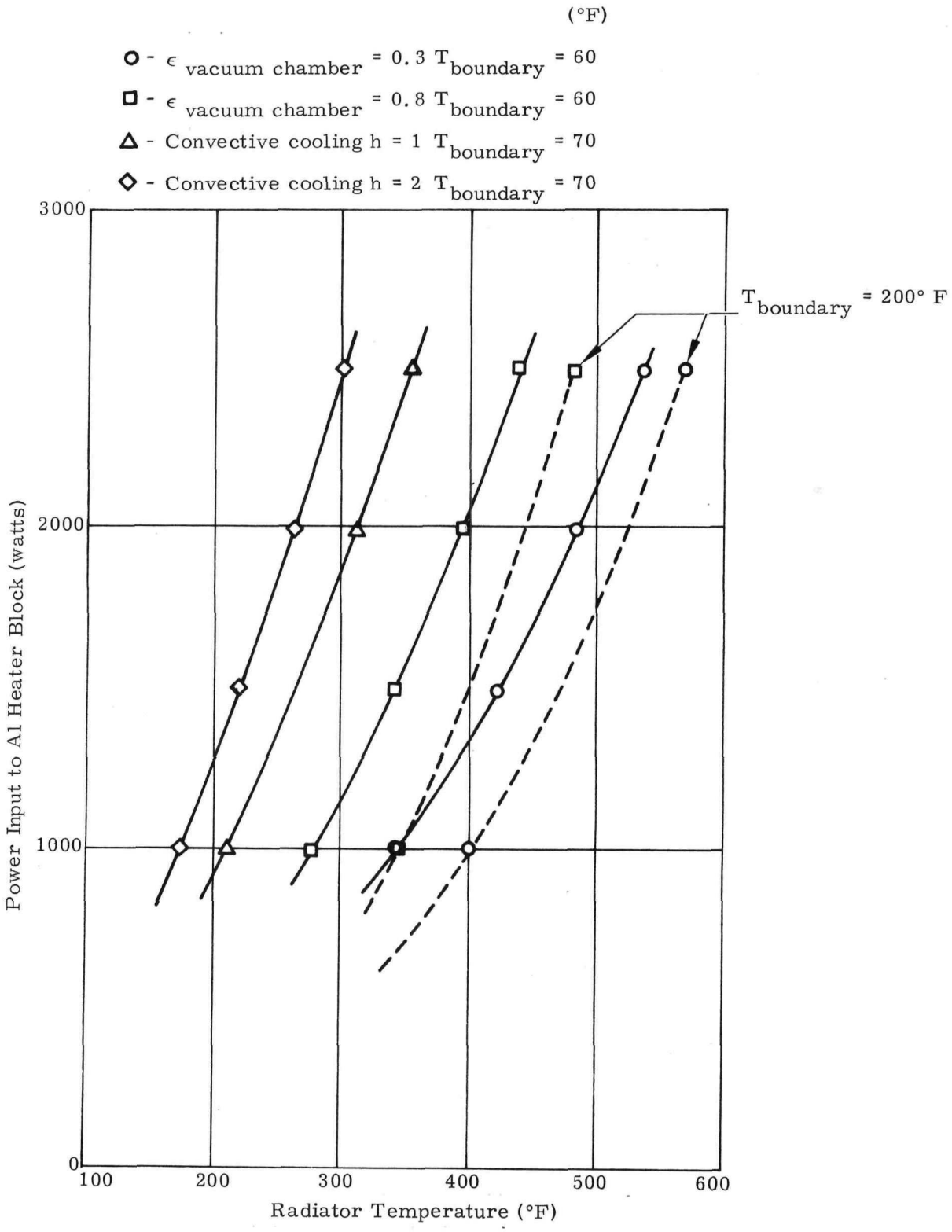

FIG. F-9. ANALYTICAL RESULTS FOR REQUIRED POWER FOR SNAP 29 MANUFACTURING CHECKOUT TEST ASSEMBLY

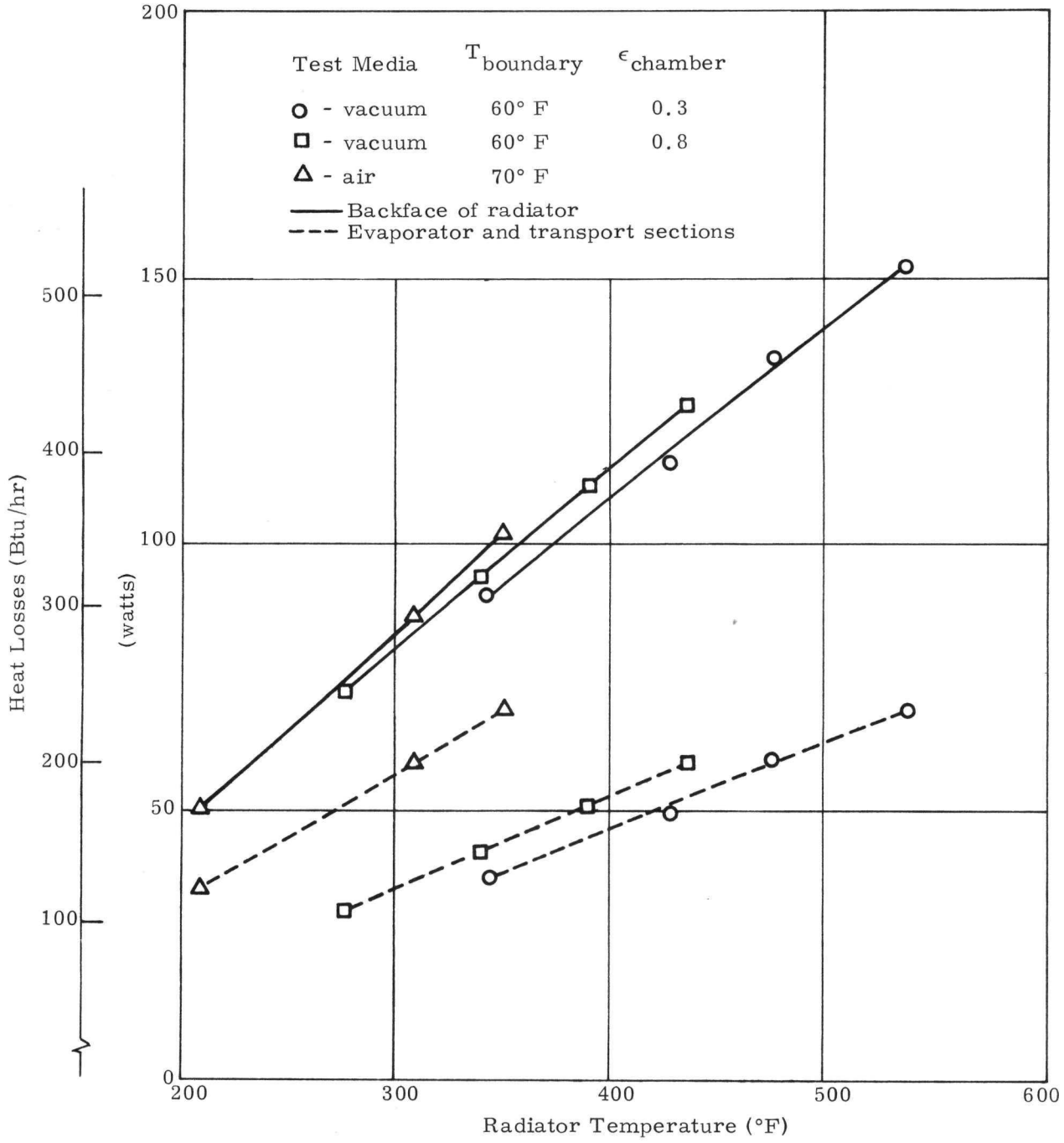

FIG. F-10. PREDICTED HEAT LOSSES FROM MANUFACTURING CHECKOUT TEST ASSEMBLY

BLANK

APPENDIX G

DESIGN EVALUATION OF RENÉ 41 FUEL BLOCK SUPPORT BEAMS

A. INTRODUCTION

The purpose of this study is to evaluate the design and fabrication techniques, as well as to document the results of an investigation into the causes of several cracks which appeared on the edges of the fuel block support beams, Drawing 466A1941006.

The results of a literature survey, an investigation into the material history and the results of a program in which two specimens were fabricated, heat treated and evaluated are included. In addition, the hardware functional design background will be discussed.

B. FUNCTIONAL DESCRIPTION

1. Function

The SNAP 29 isotopic heat source is supported in the RTG housing by two beams, one along each side as shown in Fig. G-1. The function of these beams is to provide a structural (load carrying) support for the isotopic heat source in three axes during static ground, launch and orbital conditions. In addition, it must permit remote loading of the heat source, compensate for differential thermal expansion and permit unrestricted ejection of the fuel block from the RTG assembly. These functions must be performed at a minimum possible cost in both heat losses and weight.

2. Material Selection

The material selected for use in the construction of the beam is the nickel base superalloy, René 41. The use of a superalloy for this application is justified by the high operating temperature of the most highly stressed portions of the design (1500° F temperature range). A comparison of physical properties of several candidate high temperature alloys which were considered is presented in Table G-1.

TABLE G-1

Physical Properties

Material	Ft_y at 1500° F	Ft_u at 1500° F	K*	ρ (lb/in^3)
Inconel X-750	42,000	51,100	13.1	0.300
Inconel 600	13,200	24,800	14.95	0.307
René 41	92,200	103,800	12.9	0.298
L-605 (Haynes-25)	25,900	39,000	14.35	0.330

*Btu/ $\left[(hr)(ft^2)(°F/ft)\right]$

These data were obtained from MIL-HDBK-5A (Ref. G-7). As can be seen, the use of René 41 results in a considerable weight saving. This is due to the thinner sections which can be utilized as well as to the lower density of the René 41. The use of René 41 also results in a smaller heat loss (by conduction) because of the combination of lower thermal conductivity and thinner net section thickness.

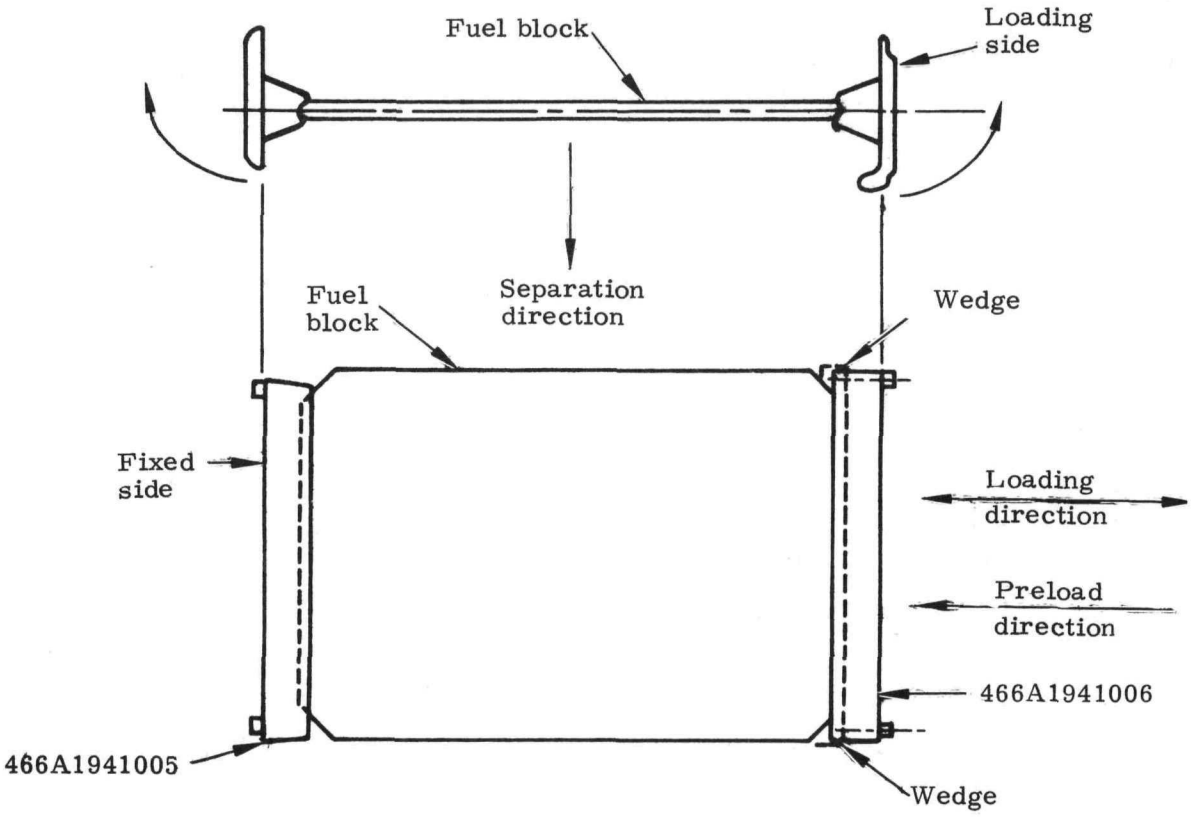

FIG. G-1. GENERAL ARRANGEMENT FUEL BLOCK SUPPORT

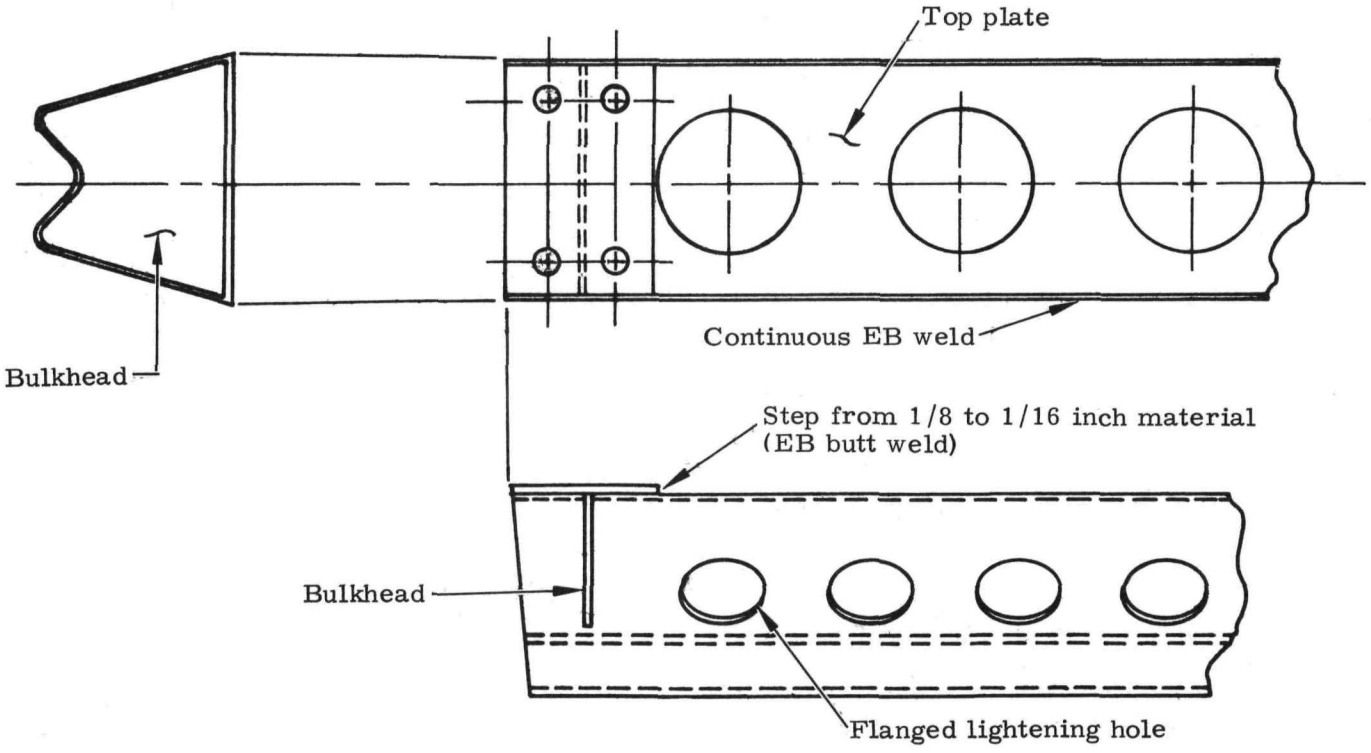

FIG. G-2. CONFIGURATION OF FIXED SIDE SUPPORT BEAM (466A1941005)

The composition of René 41, as reported by several sources, is presented in Table G-2. Metallurgically, the René 41 is a precipitation hardening alloy, which requires a solution heat treatment followed by an aging heat treatment. The strength and ductility of the alloy are affected by complex intermetallic compounds, $Ni_3(Al, Ti)$, (gamma prime) dispersed in a face-centered cubic matrix of a nickel-rich solid solution and by two complex carbides, $M_{23}C_6$ and M_6C. Annealing is almost identical to solution treatment except that it requires a very rapid quench, thereby preventing any precipitation from occurring. Some precipitation (aging) occurs during the solution treating process because of the time involved in progressing through the aging temperature range (~1700° to 1200° F) when air quenching. Aging may be accomplished from either condition. The two metallic carbides, M_6C and $M_{23}C_6$ have been found to have a considerable effect on the final properties of the heat treated and aged material (Refs. G-2 and G-3). (The M represents a metallic radical, usually chromium, molybdenum and possibly titanium.)

TABLE G-2

Composition of Rene 41

Source, Reference and Material Form	Elements (%)											
	C	Mn	Si	S	Cr	Co	Mo	Fe	Ti	Al	B	Ni
AMS 5545, Ref. G-1 Sheet and Strip	0.12 Max	0.10 Max	0.50 Max	0.015 Max	18.0 to 20.0	10.0 to 12.0	9.0 to 10.5	5.00 Max	3.0 to 3.3	1.40 to 1.60	0.003 to 0.010	Balance
Aerospace Structural Metals Handbook, Ref. G-8	0.12 Max	0.10	0.50 Max	0.015 Max	18.0 to 20.0	10.0 to 12.0	9.0 to 10.5	5.00 Max	3.0 to 3.3	1.40 to 1.80	0.003 to 0.010	Balance
Haynes Stellite Co. Ref. G-9 Wrought Alloy	0.05 to 0.12	0.10	0.50 Max	0.015 Max	18.0 to 20.0	10.0 to 12.0	9.0 to 10.5	5.00 Max	3.0 to 3.30	1.40 to 1.80	0.003 to .010	Balance
Haynes Stellite Co. Ref. G-9 Cast alloy	0.06 to 0.12	0.50 Max	0.50 Max	--	18.0 to 20.0	10.0 to 12.0	9.0 to 10.5	5.00 Max	3.0 to 3.30	1.50 to 1.80	0.010 Max	Balance

3. Support Beam Design

The detail design of the support beams was evolved after coordination with the Manufacturing Department to determine the suitability of a preliminary design to be fabricated from René 41. The design was continually reviewed for simplicity because of the relative difficulty of fabricating the superalloys. The basic structure consists of a sheet metal form, with three parallel bends to form a W section as shown in Fig. G-2. The top of the W is closed by a flat plate which is welded to the sides. The fixed side beam is attached to the housing door frame by two titanium fittings which are bolted to the René 41 beam at each end. A torque box is provided by an internal bulkhead under each fitting. The sides of the W are stiffened (and lightened) by a series of flanged lightening holes.

The design of the loading side support beam (Drawing 466A1941006) is almost identical to that of the fixed side. The major design variation occurs in the ends, where it was necessary

to provide a cavity for the fuel block support wedges which react the vertical fuel block loads. This cavity required the use of two bulkheads and two interconnecting members (intercostals) as shown in Fig. G-3.

Electron beam welding was selected for fabricating both beams wherever possible because it provided a good joint (demonstrated on samples to the satisfaction of the Stress Group) with a minimum amount of heating of the joint. Several weld samples were made prior to final design release. In addition, the fact that it is accomplished in a vacuum provides a clean weld configuration, relatively free of oxides.

Machining pads are provided on the top surfaces as well as on the insides of the W (shown in Figs. G-2 and G-3) to permit the relatively close tolerances on straightness and parallelism established by the requirements to maintain uniform contact on the fuel block.

4. Heat Treatment of Rene 41

The basic heat treatment of the René 41 consists of a solution heat treatment followed by an aging heat treatment. Annealing (solution annealing) is similar to the solution treatment except that it requires a very rapid quench. Two basic heat treatments are presented in the literature (Ref. G-2).

For optimum short time tensile properties, a 1950° F (nominal) solution treating temperature is recommended (Ref. G-2). This allows the dissolution of the $M_{23}C_6$ carbides but has little effect on the M_6C carbides. These carbides restrict grain growth and their presence results in a fine grain structure. This, combined with a 1400° F aging temperature, results in a fine dispersion of small gamma-prime (Ni_3Al compound) particles and provides the optimum short time tensile properties, with minimum grain sizes.

For optimum creep and stress-rupture properties, a 2150° F solution temperature is recommend (Ref. G-2). At this temperature both carbides are in solution, and also some grain growth occurs. A 1650° F aging temperature results in the formation of $M_{23}C_6$ carbides at the grain boundaries. This, together with a somewhat coarser gamma-prime particle size and larger grain size, provides the optimum stress-rupture properties.

These are in substantial agreement with the heat treatments recommended by MIL-HDBK-5A (Reg. G-7) which are as follows:

(1) For optimum strength at 1400° F and and below:

   (a) Solution treat at 1950° F for 1/2 hour and air cool (air blast) or water quench

   (b) Age at 1400° F for 16 hours and air cool

(2) For better dimensional stability above 1400° F:

   (a) Solution treat at 2050° F for 1/2 hour and air cool

   (b) Age at 1650° F for four hours and air cool.

The Aerospace Structural Metals Handbook (Ref. G-8) includes the range of 1950° to 2150° F for annealing or solution treating. It recommends a 2150° F solution treatment temperature for high creep-rupture strength.

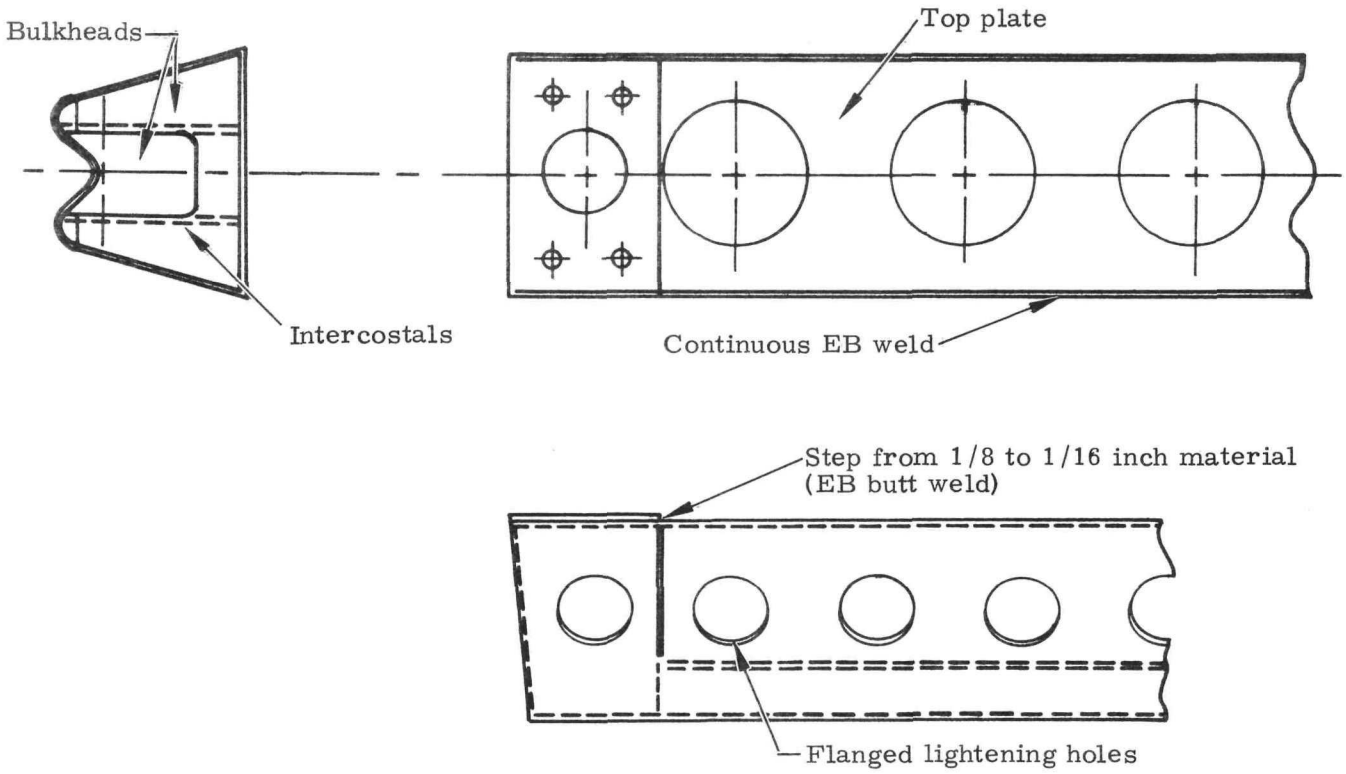

FIG. G-3. CONFIGURATION OF LOADING SIDE BEAM (466A1941006)

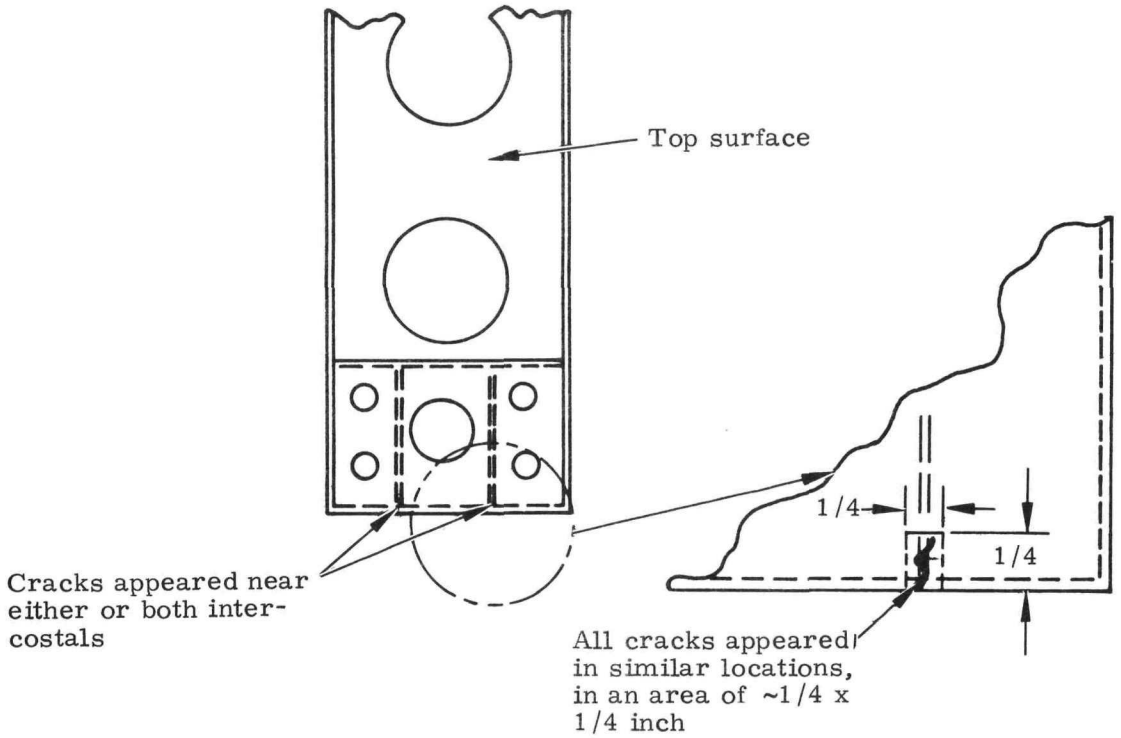

FIG. G-4. LOCATION OF CRACKS

The heat treatment to which the original W frames were subjected represented a compromise between optimum short term tensile strength and optimum creep-rupture properties, and was as follows:

(1) Solution treat at 2025° /2050° F for 1/2 hour, air cool

(2) Age at 1650° F for 1 hour, furnace cool to 1400° F, and hold for 10 hours. Air cool.

The duplex aging treatment was recommended specifically to reduce the possibility of cracking during aging (Ref. G-3).

C. CRACKS IN SUPPORT BEAMS

Upon completion of the support beams a routine Quality Control inspection disclosed the appearance of cracks on the two loading side support beams (Drawing 466A1941006) as shown in Fig. G-4.

Because of the relatively low stress level in the immediate area of the cracks, it was decided that the parts could be saved by machining out the cracks with an end mill. Of the two cracked parts, one was to be used for a test in which it would not be exposed to large vibration loads; the other was to be dynamically loaded. Upon further reflection it was decided to hold back the W beam which was to be exposed to large vibration loads until the cause of the cracks was determined.

An investigation to determine the cause of the cracks was directed toward three major areas, namely, a literature survey, an investigation of the material history of the parts and the manufacture of two test specimens. One of these test specimens was to be manufactured in accordance with the original procedures; the other in accordance with the results of the literature survey.

1. Literature Survey

The results of the literature survey indicated that the occurrence of cracking in the welds of the parts as originally manufactured was a possibility. This is based on statements in Refs. G-2, G-3, G-4 and G-5 which state that René 41 structures, welded under a high degree of restraint, have cracked upon subsequent thermal treatments, due to brittleness associated with the precipitation of large amounts of the $M_{23}C_6$ carbides at the grain boundaries. This occurs principally when the solution treating (or annealing) temperature is in excess of 2000° F. Beyond this temperature, the M_6C carbides as well as the $M_{23}C_6$ carbides are taken into the solution. The resultant availability of the extra carbon in solution results in the precipitation of an excessive amount of $M_{23}C_6$ in the grain boundaries during cooling from the solution treatment temperature. This carbon markedly decreases ductility. When followed by internal stresses, this can result in cracks. A solution treating temperature of 1975° F is recommended to help overcome this situation (Refs. G-3 and G-5).

The following general recommendations are made in Ref. G-12 for producing consistantly sound welds:

(1) "René 41 must be in the 1975° F mill annealed condition prior to forming or welding."

(2) "Welding on cold worked parts should be avoided. Any necessary in-process anneals should be a 1975° F treatment followed by a rapid quench."

(3) "Strain age cracking can be avoided by changing welded components into a hot furnace (1970° F maximum) to reach the solution temperature as rapidly as possible. This minimizes the time in the aging range."

(4) "Weld designs and procedures that minimize weld restraint and heat input are most important for the consistent fabrication of good parts."

. . . "Good fit-up is absolutely necessary."

. . . "Copper and argon backing should be used whenever possible."

. . . "Gas coverage on both sides is mandatory on all butt joints."

. . . "Joint edges should be ground to remove burrs before welding."

. . . "Control of arc length and current is helpful for minimum heat input."

. . . "Automatic welding is preferred to manual welding."

2. Material History

An investigation of the material history was undertaken to ensure that the material met original specifications and to determine if it was improperly heat treated prior to being received at Isotopes. This investigation proved to be inconclusive; the material was traced back to the mill, and no indications of improper treatment could be found. The material was purchased to Specification AMS 5545 (Ref. G-1), and no deviations to the requirements of this specification could be determined. However, during examination of the original 1/8-inch sheet material from which some of the parts were fabricated, a large variation in grain size was noted. The average grain size near the edge of the sheet was ASTM No. 4. The average grain size near the area from which the parts were made was ASTM No. 8. These are shown in Figs. G-5 and G-6. While these grain sizes are within the limitations of the specification, the larger grain sizes are undesirable for welded parts since the welding will result in a further increase in local grain size with a consequent reduction in ductility. This leads to the conclusion that the AMS specification is too general for material which is to be subsequently welded, and that a more specific requirement be written for Rene 41 material which is to be welded as part of its fabrication. No grain size variations of this magnitude were noted in the 1/16-inch sheet material which is shown in Fig. G-7.

3. Test Specimens

It appeared evident, from the repetitive nature of the cracks and from the results of the literature survey, that the cracks were due to a condition where a constrained weldment was subjected to a temperature in excess of 2000° F. This made it appear that the cracks were therefore due to strain-age effects.

To verify this, it was decided to manufacture two test specimens, each identical to the end portion of the support beams (Drawing 466A1941006). One of the specimens was subjected to the original heat treatment solution treat at 2025° / 2050° F and aged at 1650° F for 1 hour and at 1400° F for 10 hours. It was intended that this specimen be used to duplicate the cracks. The second specimen was subjected to an improved heat treatment specifically recommended by the literature to minimize cracking. This

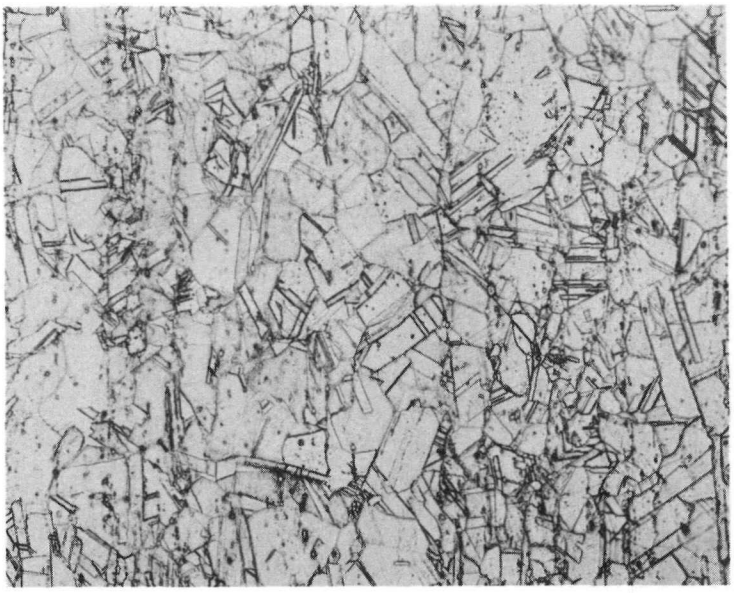

FIG. G-5. ONE-EIGHTH INCH RENÉ 41 SHEET MATERIAL; AVERAGE GRAIN SIZE ASTM NO. 4; MAGN 85X

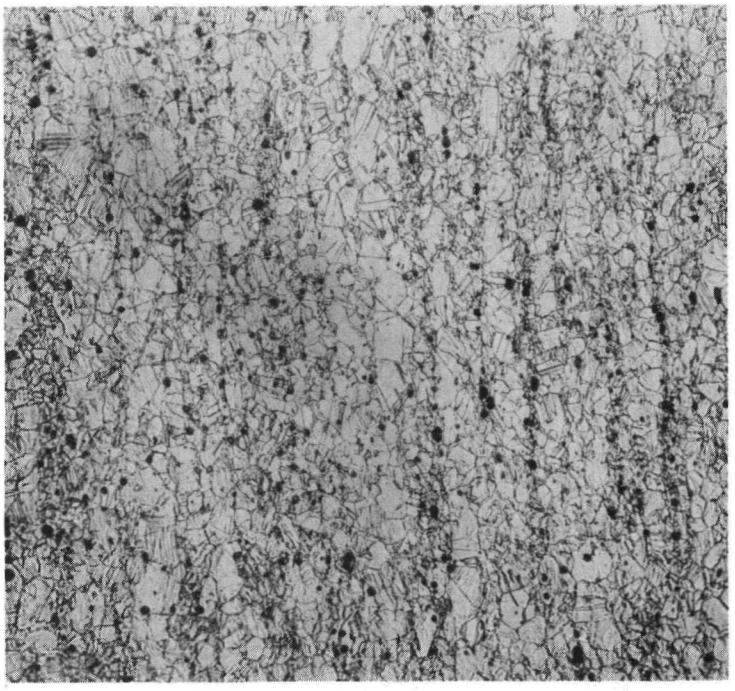

FIG. G-6. ONE-EIGHTH INCH RENÉ 41 SHEET MATERIAL; AVERAGE GRAIN SIZE ASTM NO. 8; MAGN 85X

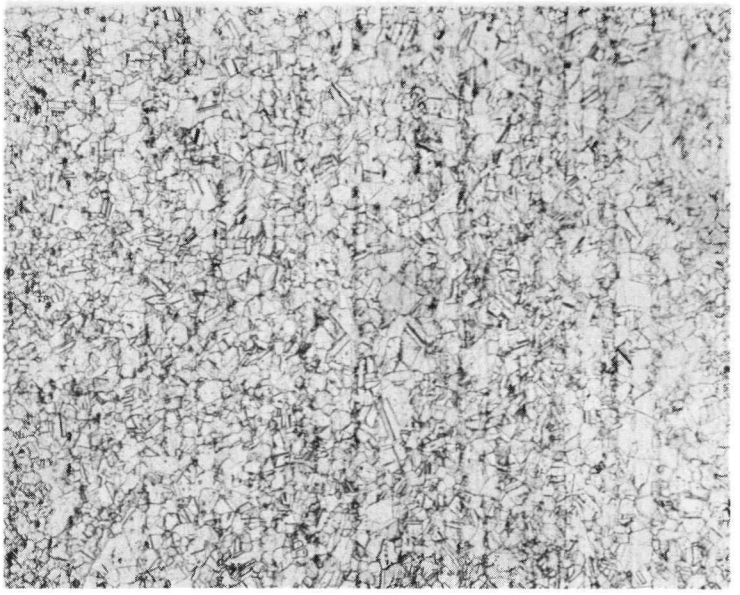

FIG. G-7. ONE-SIXTEENTH INCH RENÉ 41 SHEET MATERIAL; AVERAGE GRAIN SIZE ASTM NO. 8; MAGN 85X

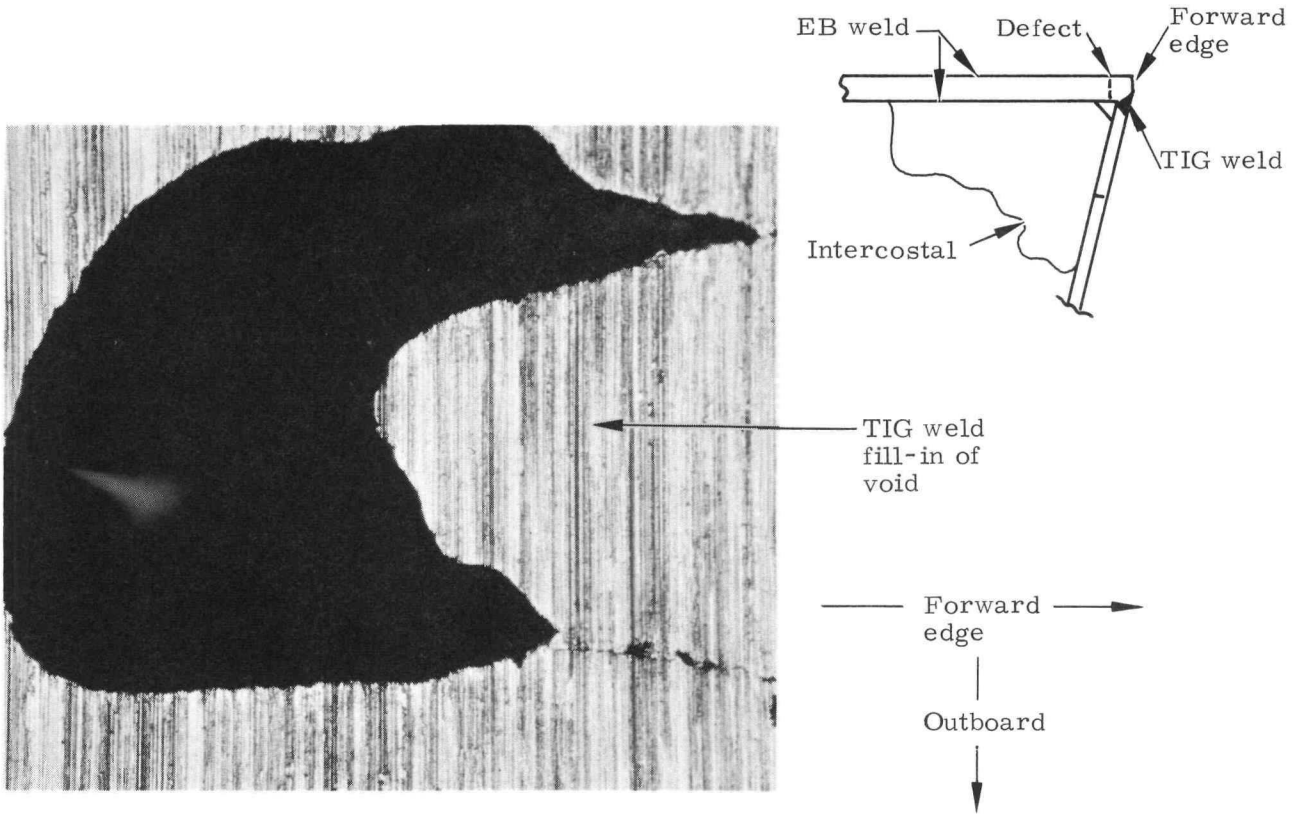

FIG. G-8. VOID DEFECT IN EB WELD OF RENE 41 SPECIMEN 2; MAGN 64X

consists of a 1975° F ± 25 solution anneal (quench to less than 1200° F in 4 seconds maximum) followed by the 1650° F for 1 hour and 1400° F for 10 hours duplex aging treatment. This was accomplished in accordance with Reg. G-10. Aside from the appearance of several minor cracks and flaws (in other locations) which were related to welding technique, no other cracks occurred. These are shown in Figs. G-8, G-9, G-10, G-11 and G-12. Figures G-11 and G-12 indicate typical conditions caused by ending an EB weld. These conditions can be avoided on future parts by running the weld into the edge of a hole. For the same reason, it is recommended that a starting tab be provided for the EB weld which can then be machined off. The weld defect shown in Fig. G-9 was a local defect which disappeared when polished with emery cloth. The defect shown in Fig. G-10 appeared in the fillet of the joint shown. This area had been built up with weld metal to fill a localized gap caused by an undersized detail.

Since the original type of cracks did not appear in either of the parts it was decided to permit them to age prior to undergoing further evaluation. The purpose of this was to allow sufficient time for a crack to develop in the event that it was a time-dependent phenomena. Therefore, the specimens were retained in storage for a period of four weeks. (The specimens were kept in an environment of 70° F ± 1° F during this period.)

a. Specimen evaluation

The specimens were re-examined after the four-week period in accordance with Ref. G-11. The initial examination, prior to polishing and cutting, disclosed no new additional flaws with the exception of an inclusion (Fig. G-13). Figure G-14 is a view of one of the electron beam weld beads (etched and polished) in the upper surface of Specimen No. 2. Following this, the specimens were sectioned to permit evaluation of all the basic welds involved in the ends of the parts. This disclosed weld flaws in almost every TIG weld (fusion weld) involved. In addition, several of the electron beam weld joints indicated poor fit-up and some misalignment of the weld with respect to the parts. These conditions were prevalent in both specimens. Figures G-15 through G-25 are typical of these flaws.

4. Support Beam

During the evaluation period of the test specimen it was decided to re-instate the support beam assembly which had been held back for approximately six to eight weeks. This part was examined with fluorescent dye penetrant, prior to its release, in order to determine if any of the cracks had reappeared during storage. This beam originally had cracks in three of the four locations. Machining out of one of these cracks was not completed prior to the part being placed in storage. The dye penetrant inspection revealed the appearance of an additional crack in the fourth location (previously sound). This is shown in Fig. G-26. This crack is approximately 0.087 inch long and is located almost in the center of the EB weld bead. Figure G-27 is a photograph of the uncompleted machine cut which shows a breakthrough in the material.

D. CONCLUSIONS AND RECOMMENDATIONS

1. Conclusions

The appearance of similar cracks in the eight locations of the 466A1941006 beams, but in none of the 466A1941005 beams which were made of the same original materials and received the same heat treatment as the others, leads to the conclusion that the cracks were related to the configuration. This is evidenced by comparing Figs. G-2 and G-3. The only difference between the two parts is in the boxed-in end construction of 466A1941006. This conclusion is supported by the literature (Refs. G-2, G-3, G-4, G-5, G-12 and G-13). For the most part, the literature is somewhat general in reference to a definition of a constrained weldment, however, the boxed-in ends of the beams which developed cracks are considerably more restrained than those of the parts which did not crack.

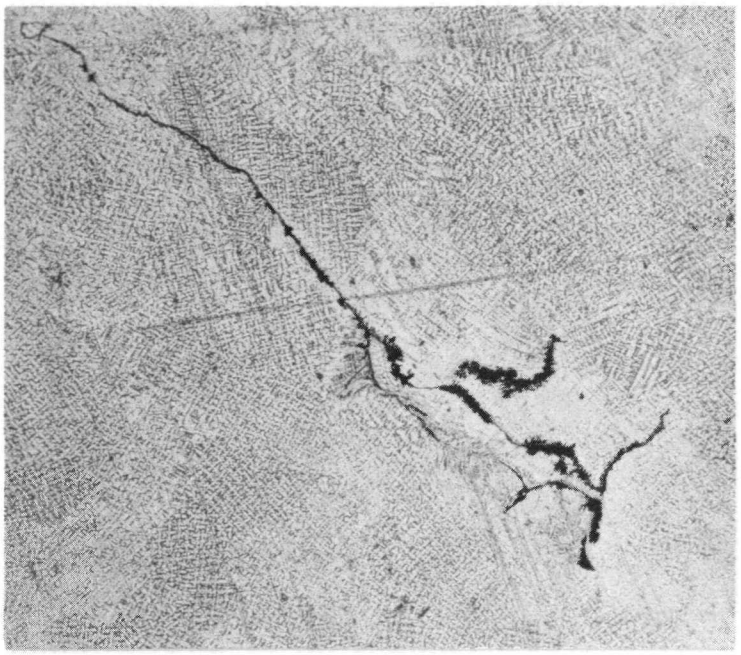

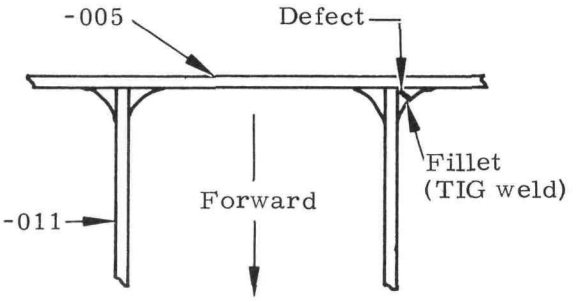

Subassembly (-005 and -011)

FIG. G-9. TIG WELD DEFECT IN RENÉ 41 SPECIMEN 2; MAGN 128X

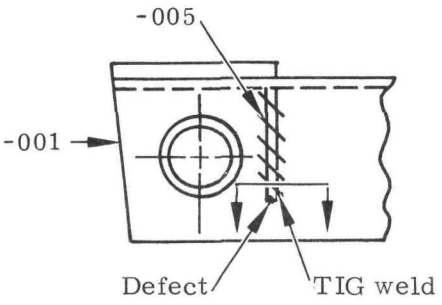

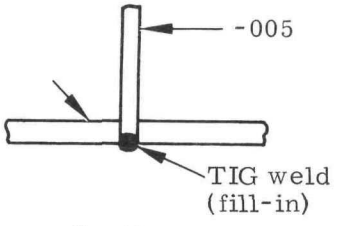

Section

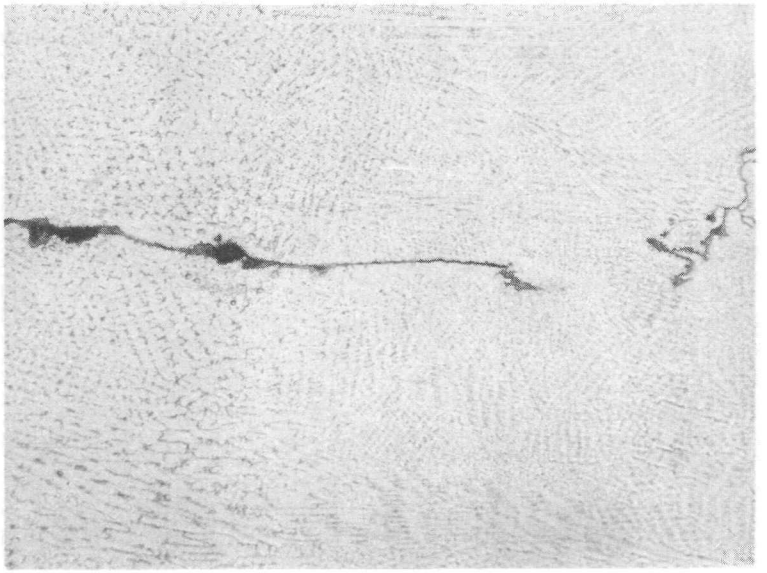

FIG. G-10. TIG WELD DEFECT IN RENÉ 41 SPECIMEN 1; MAGN 64X

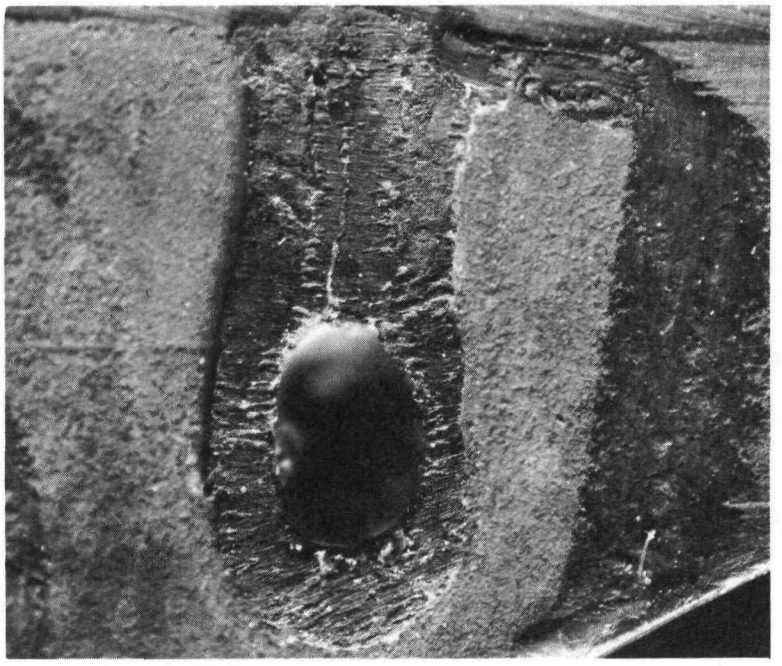

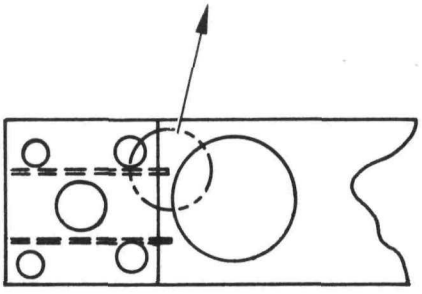

Plan View

FIG. G-11. EB WELD DEFECT AT END OF WELD BEAD OF RENÉ 41 SPECIMEN 2; MAGN 17X

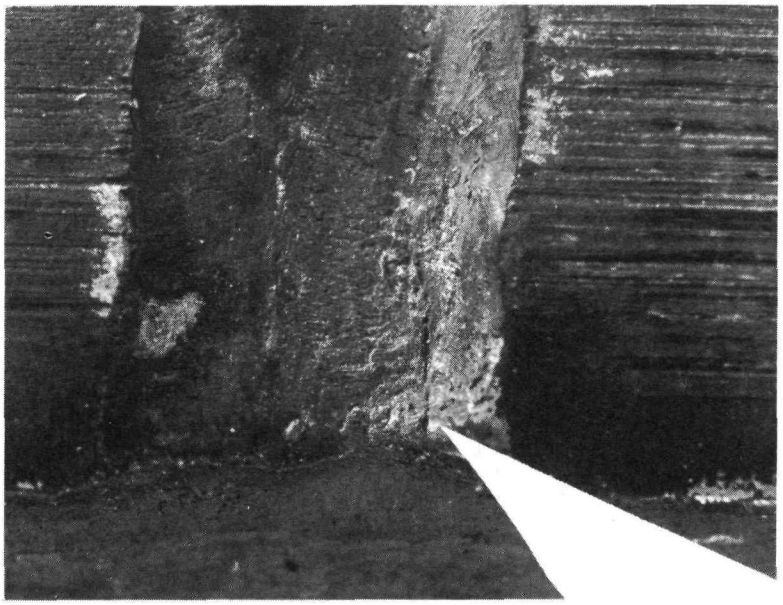

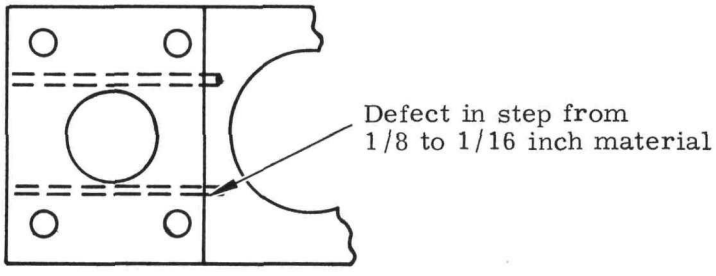

FIG. G-12. EB WELD DEFECT IN WELD RUNOFF OF RENÉ 41 SPECIMEN 2; 1/8 to 1/16 INCH MATERIAL; MAGN 17X

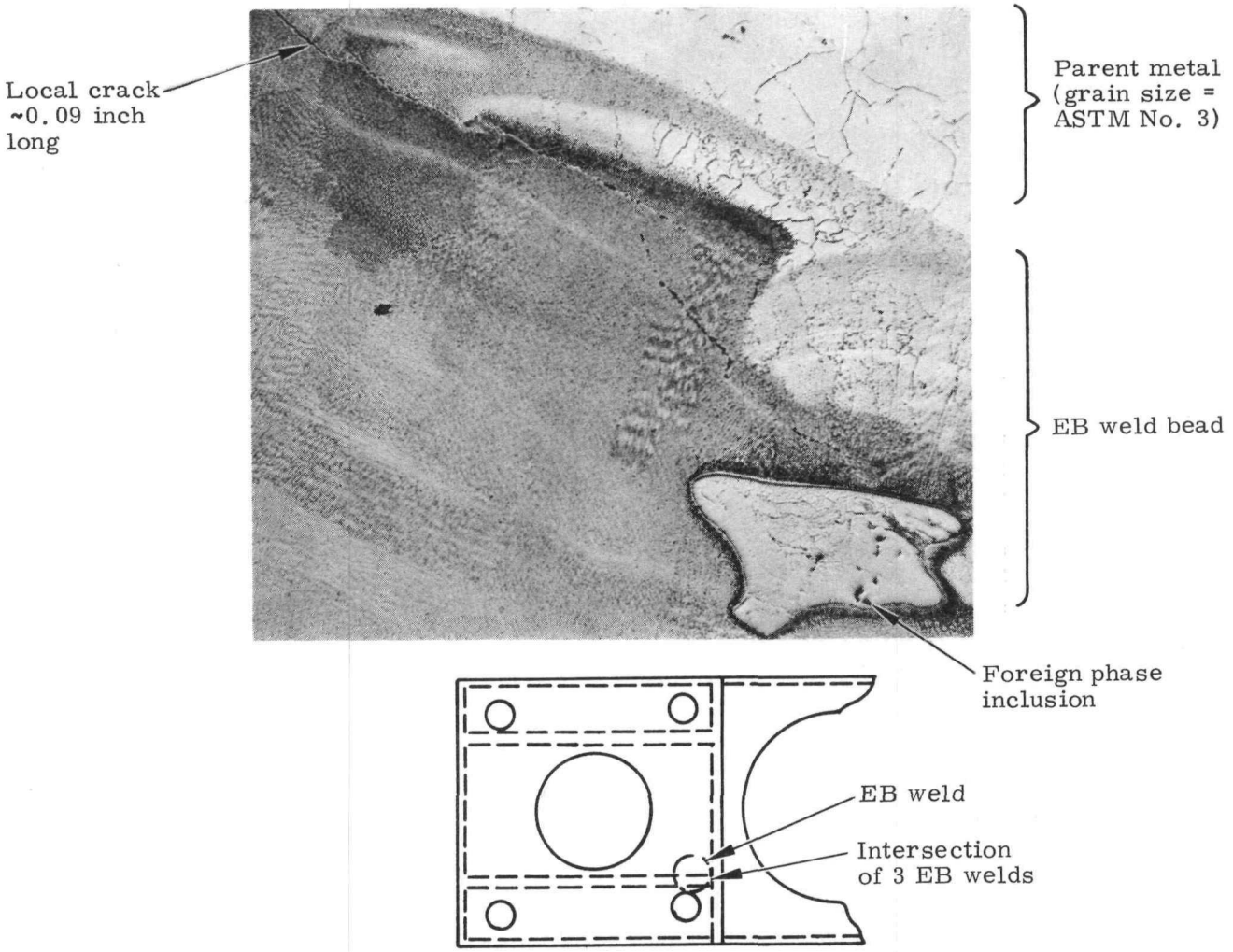

FIG. G-13. UPPER SURFACE OF SPECIMEN 2 SHOWING EB WELD DEFECT IN RENÉ 41; MAGN 64X

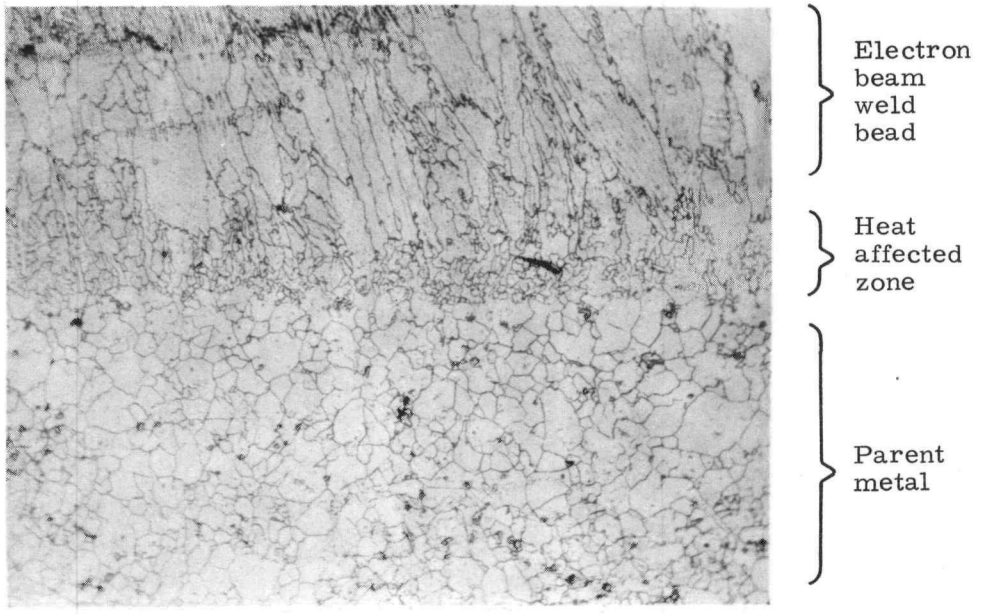

FIG. G-14. UPPER SURFACE OF SPECIMEN 2 SHOWING TYPICAL EB WELD IN RENÉ 41; MAGN 64X

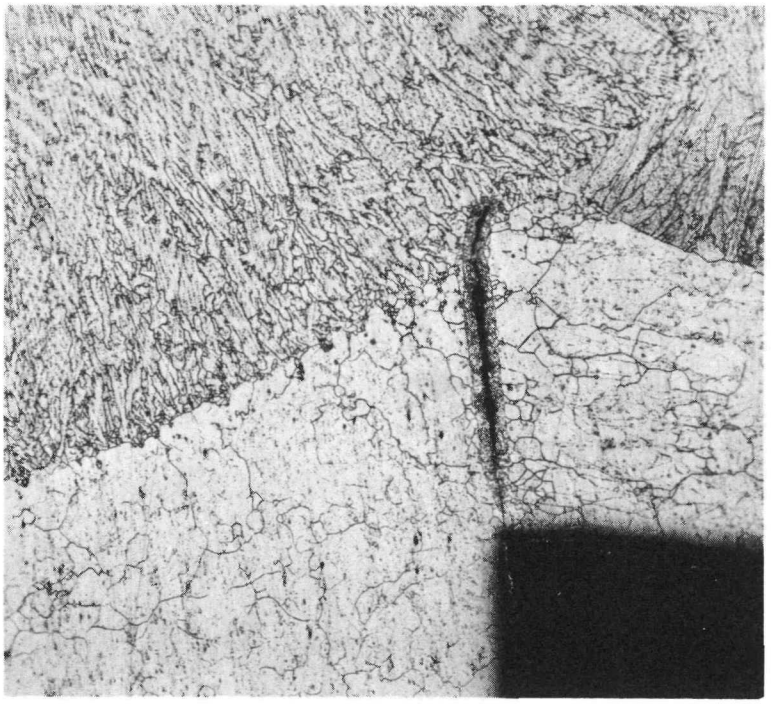

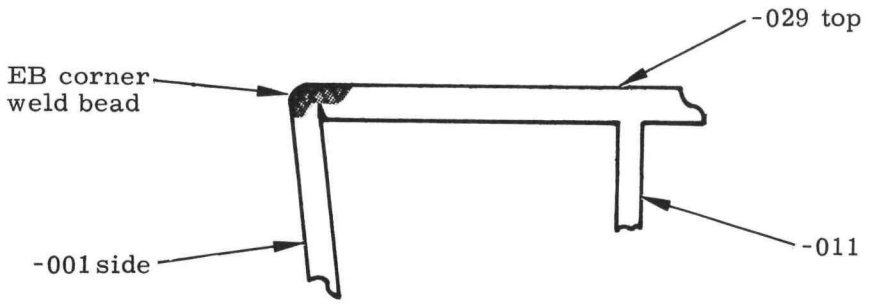

FIG. G-15. ELECTRON BEAM WELD ON SPECIMEN 1; MAGN 64X

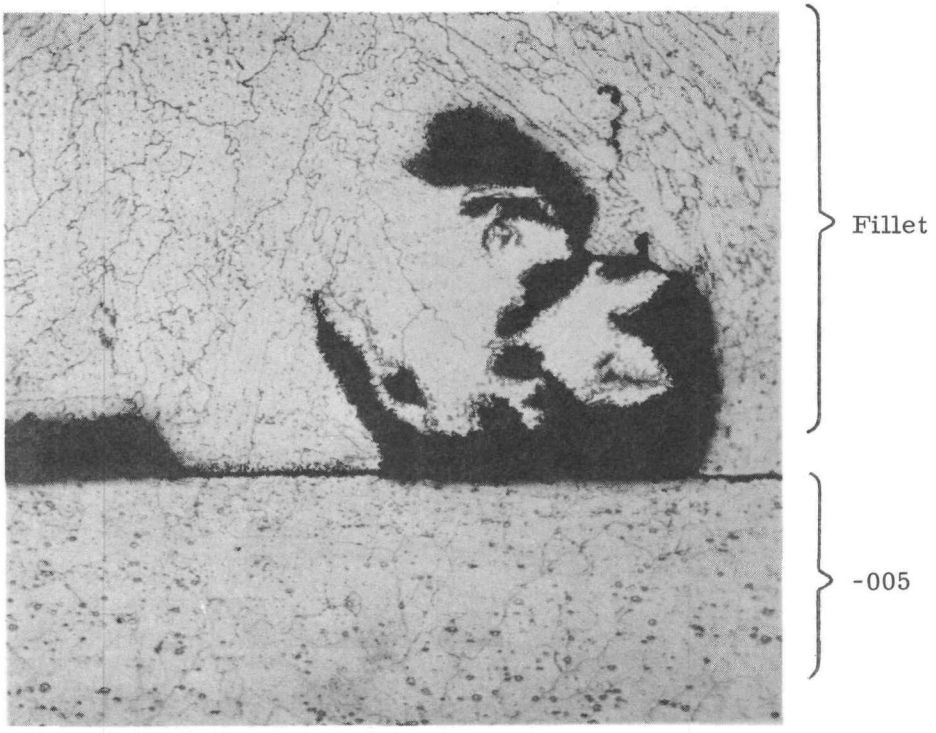

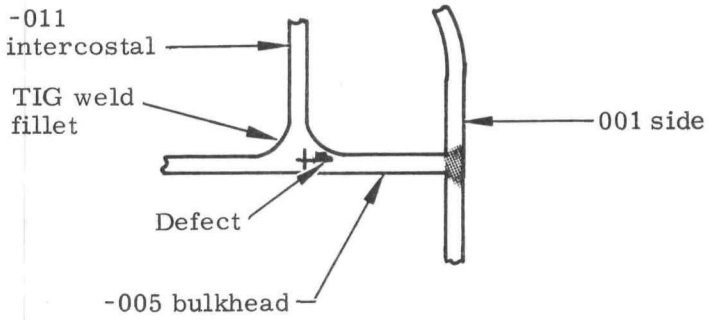

FIG. G-16. TIG WELD DEFECT IN SPECIMEN 1; MAGN 64X

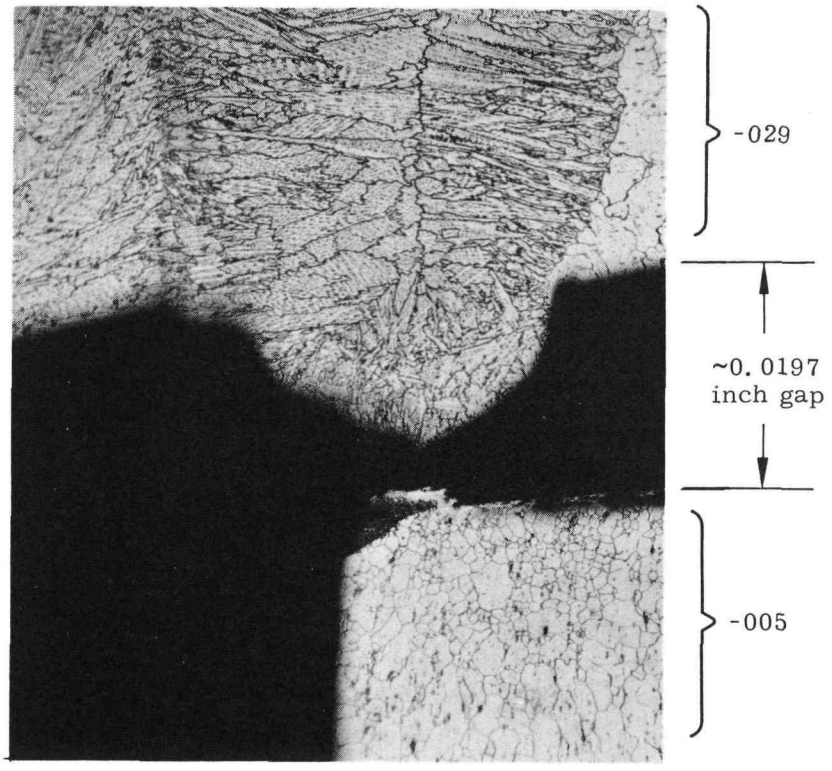

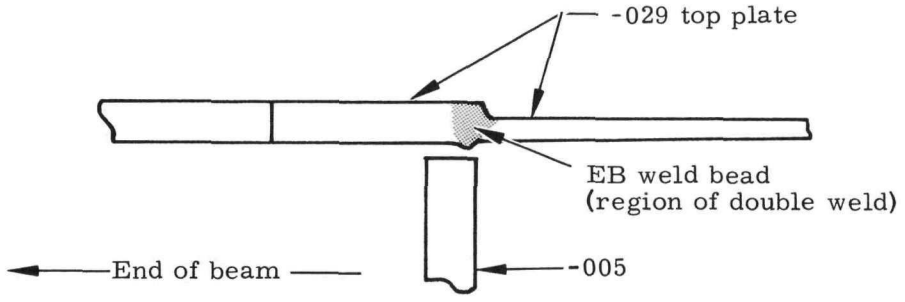

FIG. G-17. EB WELD DEFECT SHOWING POOR FIT-UP IN SPECIMEN 1; MAGN 64X

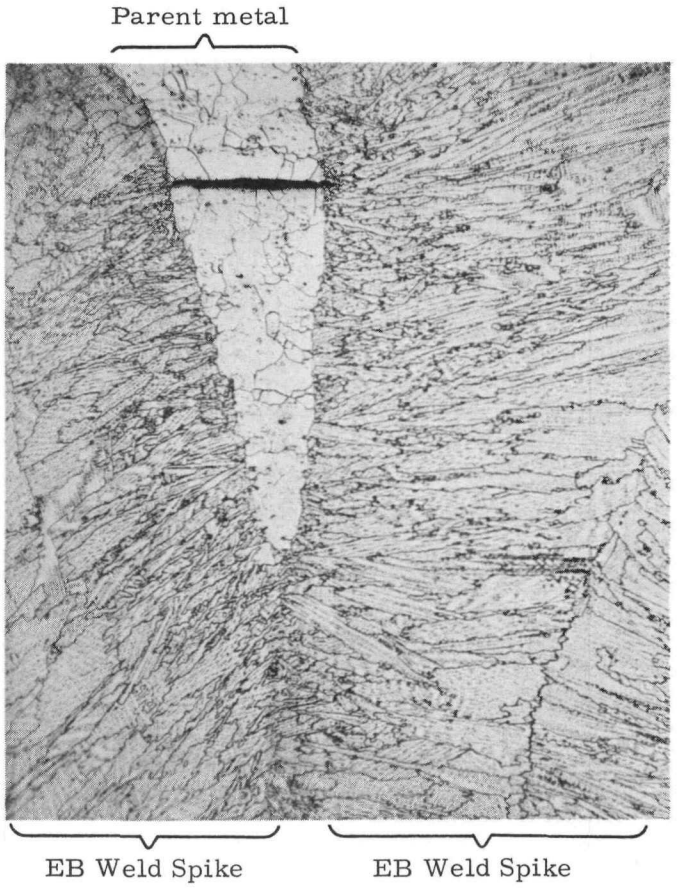

FIG. G-18. DOUBLE EB WELD ON SPECIMEN 1; MAGN 64X

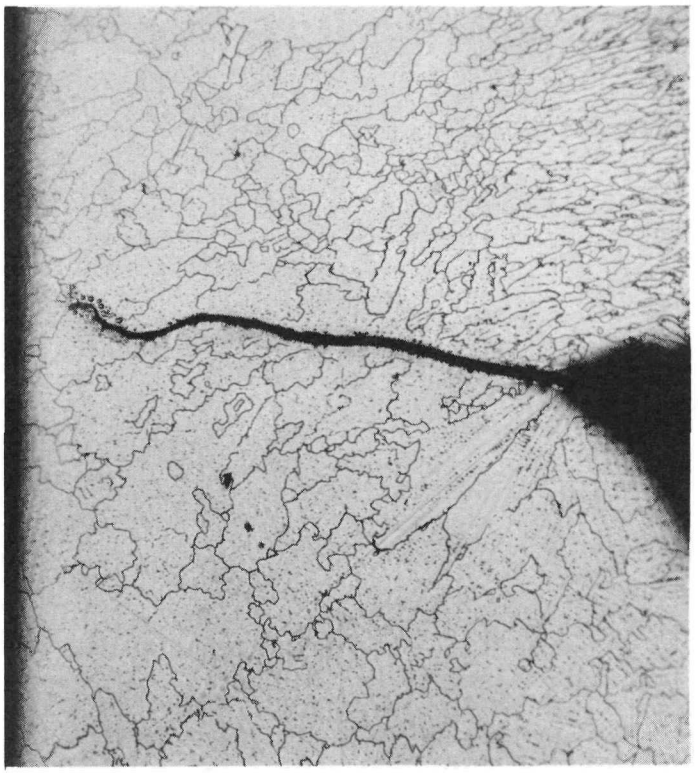

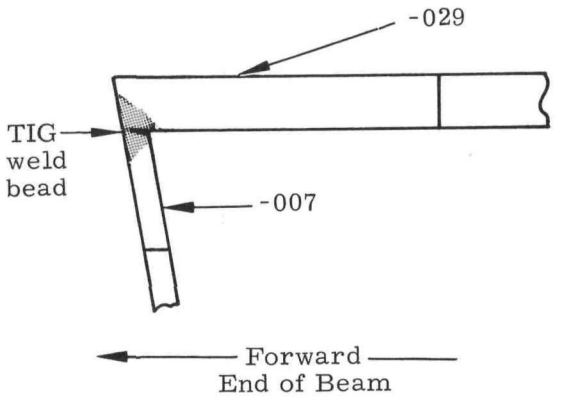

FIG. G-19. TIG WELD BEAD SHOWING 0.005 INCH FUSION ON SPECIMEN 1; MAGN 64X

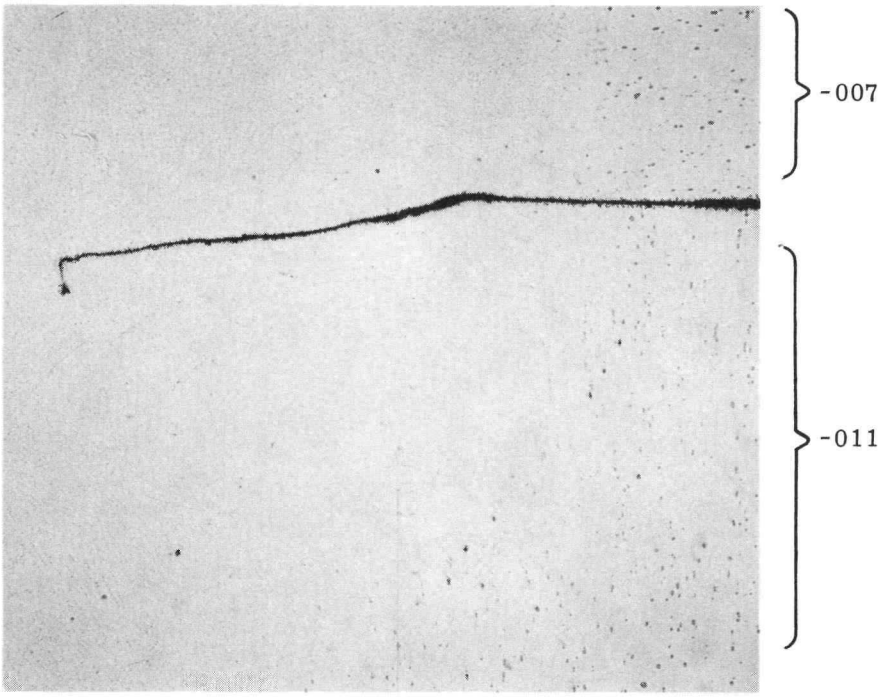

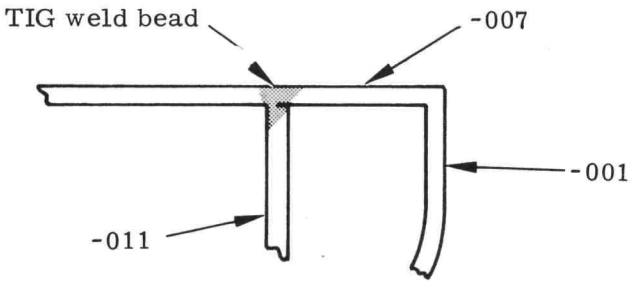

FIG. G-20. TIG WELD BEAD SHOWING INCOMPLETE FUSION IN SPECIMEN 1; MAGN 64X

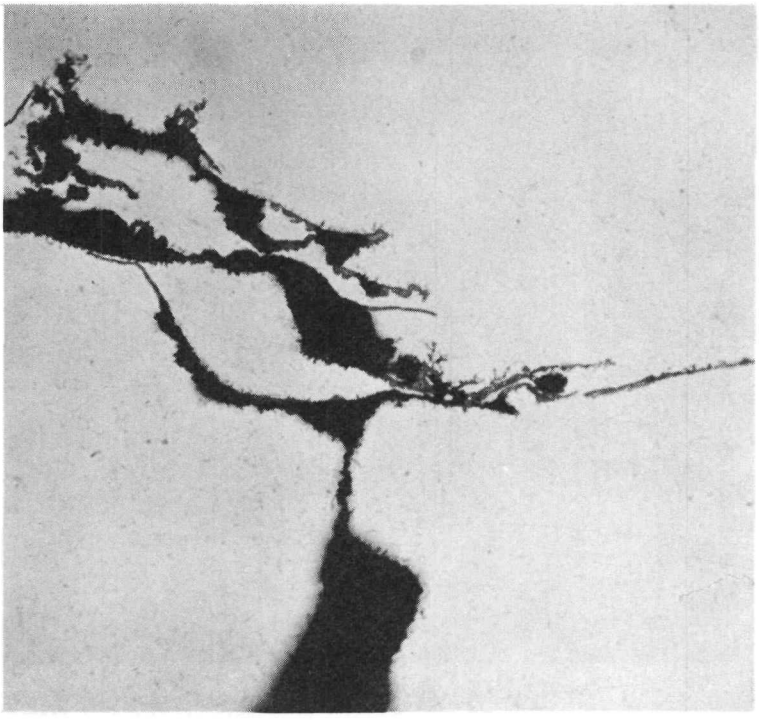

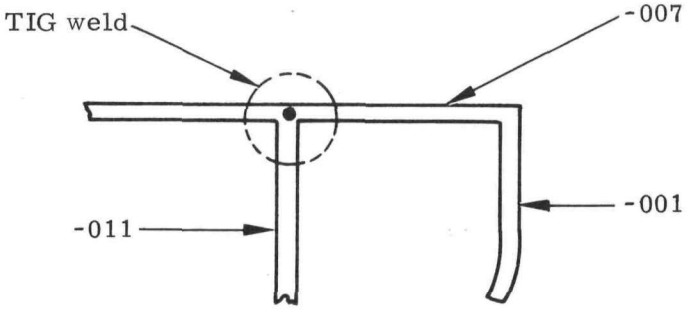

FIG. G-21. TIG WELD DEFECT IN SPECIMEN 1; MAGN 128X

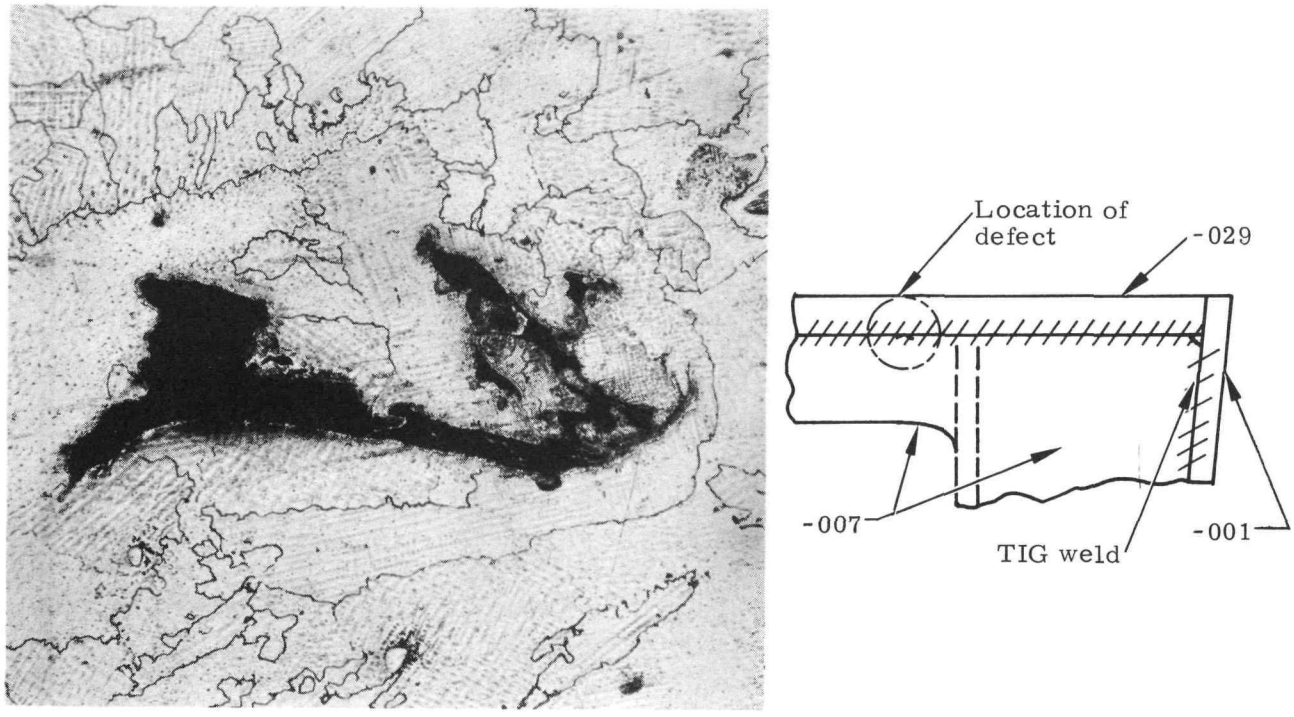

FIG. G-22. TIG WELD DEFECT ON FACE WELD ON SPECIMEN 2; MAGN 85X

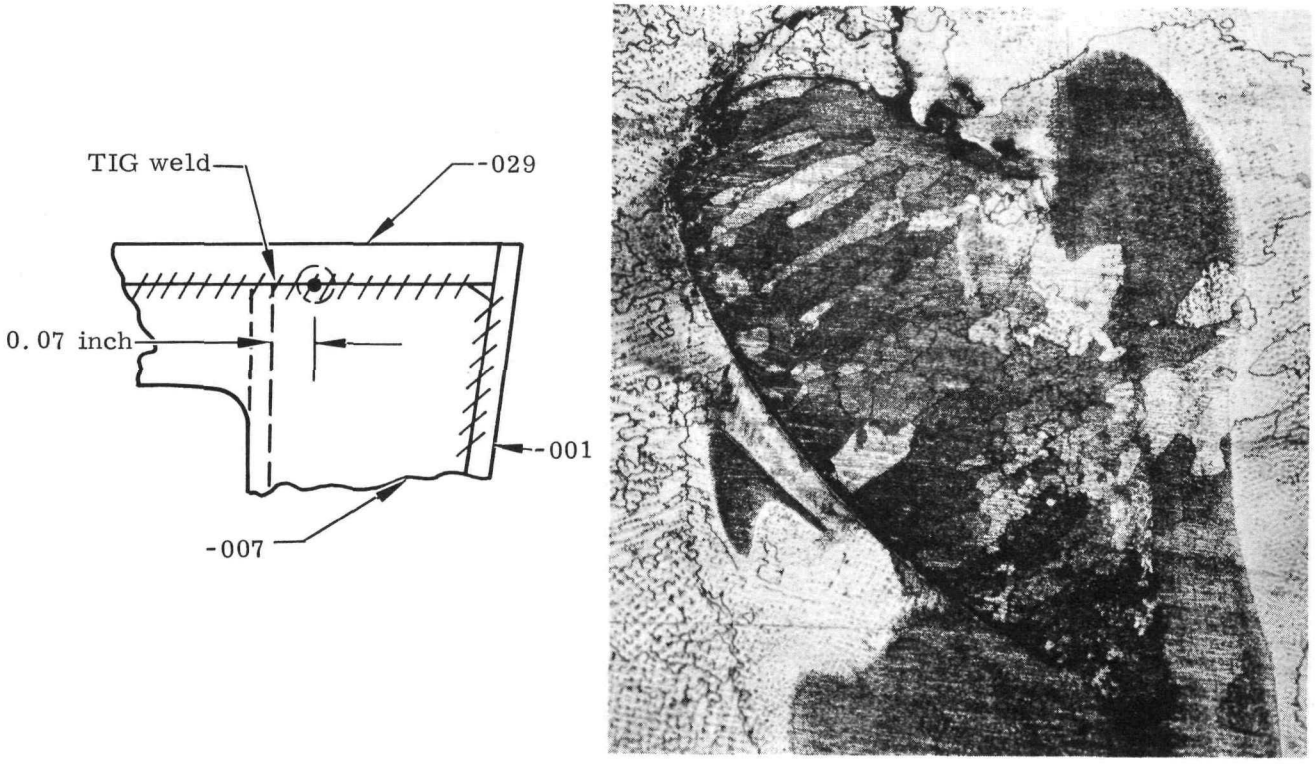

FIG. G-23. TIG WELD DEFECT IN UNMELTED AREA OF SPECIMEN 2; MAGN 85X

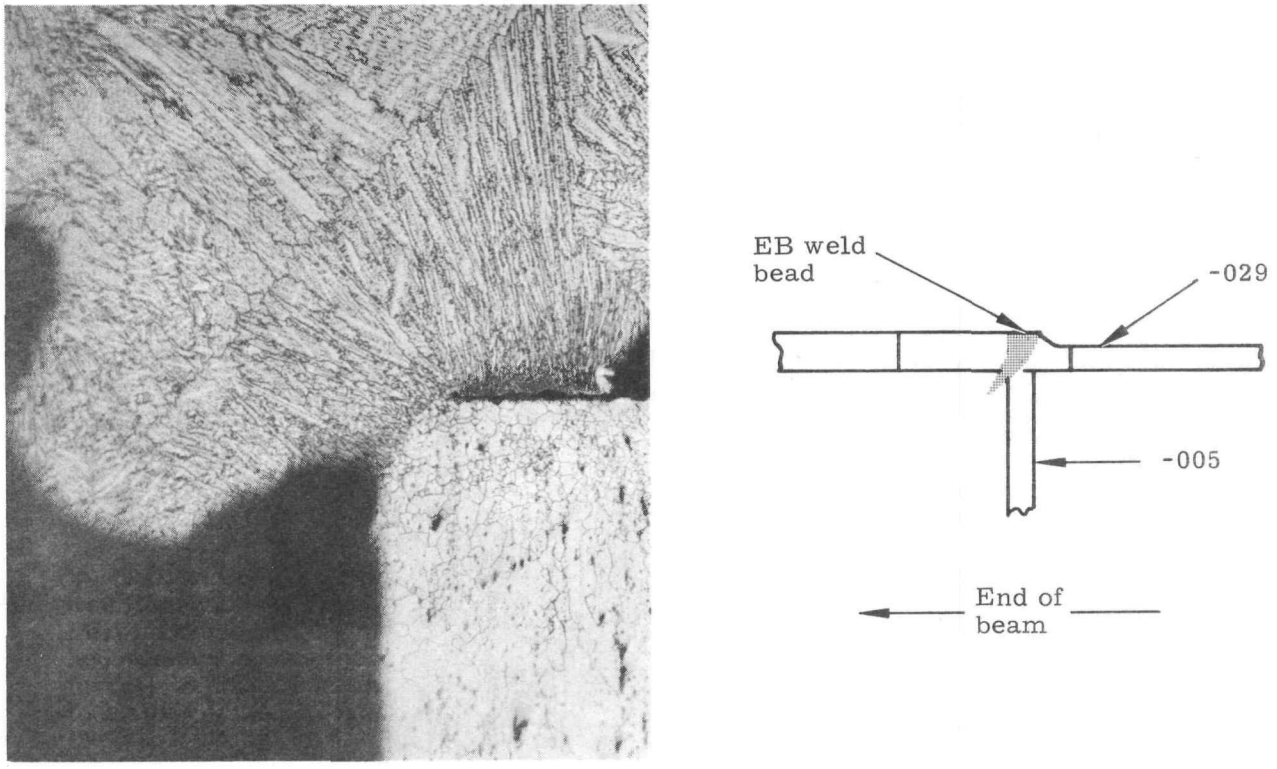

FIG. G-24. EB WELD BEAD SHOWING 0.008 INCH FUSION IN SPECIMEN 2; MAGN 64X

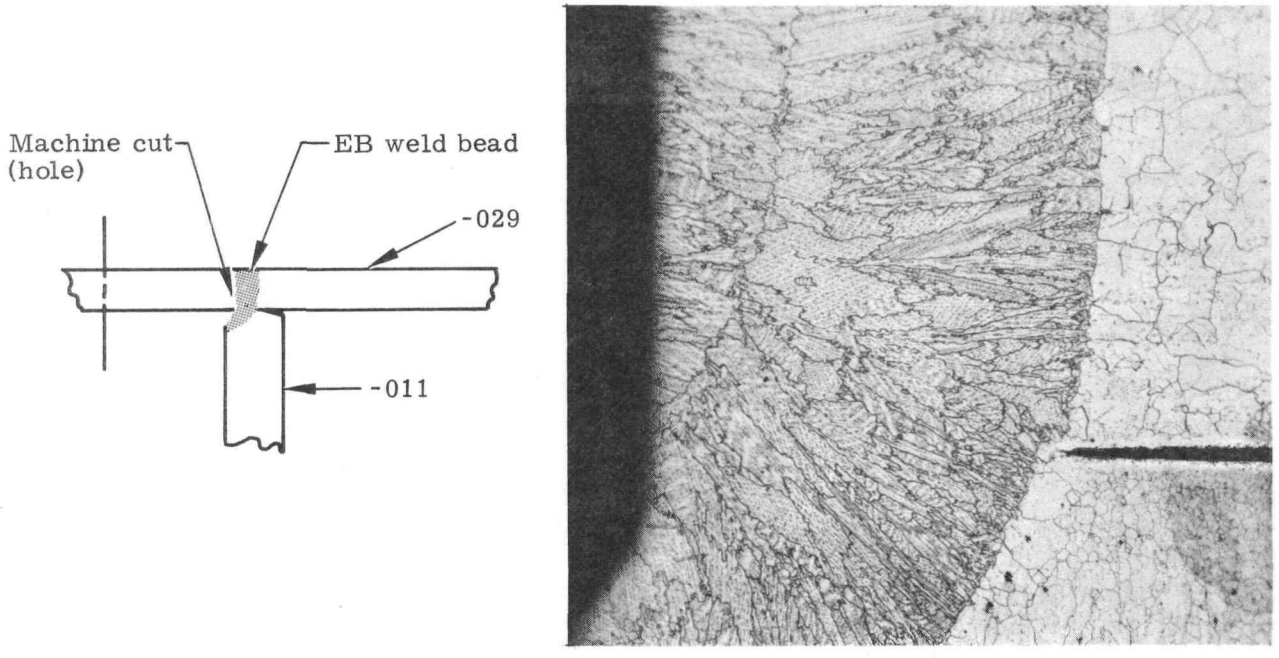

FIG. G-25. OFF-CENTER EB WELD BEAD ON SPECIMEN 2; MAGN 64X

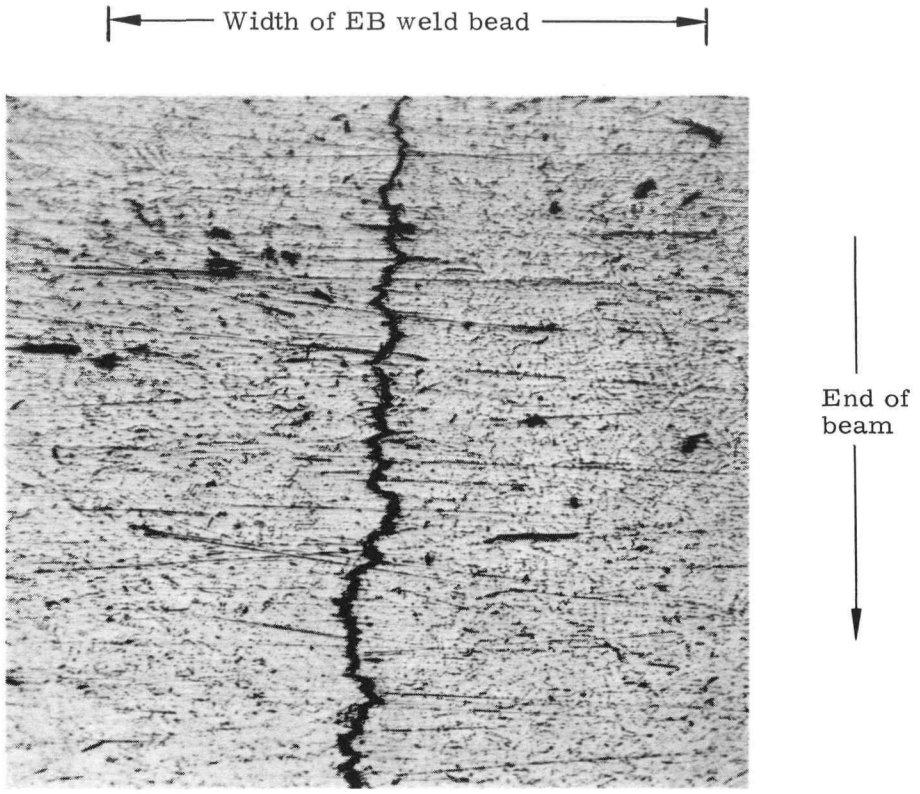

FIG. G-26. UPPER SURFACE OF 466A1941006 BEAM, S/N 2 SHOWING TYPICAL APPEARANCE OF CRACKS THAT WERE ~0.087 INCH LONG; MAGN 128X

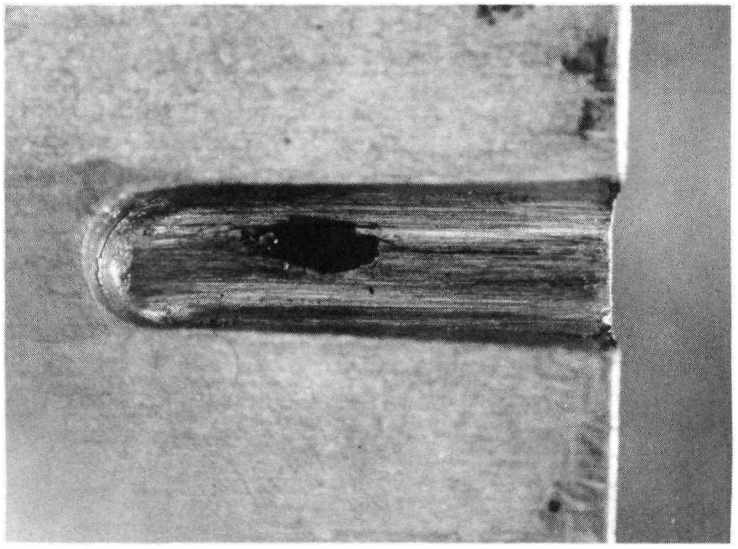

FIG. G-27. UPPER SURFACE OF 466A1941006 BEAM, S/N 2 SHOWING PARTIALLY MACHINED OUT CRACK; MAGN 9X

The literature cited is almost unanimous in placing the blame for the cracks upon the presence of an excessive amount of the $M_{23}C_6$ at the grain boundaries, resulting in a loss of ductility at the grain boundary. A crack ensues when this is combined with a constrained weldment. This condition is brought about by a heat treatment in excess of 2000° F.

Unfortunately, this condition could not be demonstrated by the test specimens which were manufactured to two different heat treatments. The reason for this is not completely clear, however the large number of weld defects, poorly fitted joints and lack of fusion, may have resulted in too much freedom and lack of constraint in the specimens, especially if the design was initially only marginally constrained.

The original path of the cracks may be deduced by inspection of Fig. G-28, G-29, G-30 and G-31 which are sections of EB weld beads on Specimens No. 1 and 2. As can be seen, the microstructure of the bead is dendritic in nature and consists of two rows of well-ordered grains which are oriented from the center out to the sides. This is caused by the natural heat flow path during cooling. This results in what appears to be a long grain boundary at the center which runs almost the entire depth of the weld bead. A larger magnification of this area, Fig. G-30, reveals this to be the intersection of the individual grain boundaries, and while it is broken up (zigzag) in nature, it could conceivably provide the basis for a long (depth) crack. If the part is subsequently heat treated beyond 2000° F, this grain boundary will contain an excessive amount of the $M_{23}C_6$ carbide, which because of its relative size, will make it susceptible to strain-age cracking. A heat treatment below this temperature will reduce the amount of $M_{23}C_6$ carbides, thereby increasing the ductility of the grain boundary.

The aging heat treatments for both specimens resulted in satisfactory average hardness values for all details. The average grain structure of welded areas was somewhat greater in Specimen No. 1 than in No. 2 (average maximum of 3 for No. 1 to 4 for No. 2). This is probably due to the less abundant M_6C carbides in No. 1 than in No. 2. The grain size of both welded specimens was within the limits of Ref. G-1 (AMS 5545) for raw material. The grain sizes of both were therefore acceptable after welding.

2. Recommendations

The following recommendations are based upon the results of the literature survey, test specimen evaluation, and the material history investigation.

(1) The raw material certifications, for parts to be welded, must be verified to ensure that at no time prior to arrival at Isotopes did the material receive a heat treatment in excess of 2000° F. The material must be controlled during handling and fabrication to ensure that it does not accidentally receive an in-house heat treatment in excess of 2000° F. These requirements should appear on the drawings as well as in any applicable process or procurement specifications. Note that material for parts which are not to be welded are acceptable with heat treatments in excess of 2000° F.

(2) Good fit-up of the parts to be welded, particularly in the case of electron beam welding, is essential. This should be reflected on the drawing as well as in any applicable process specifications. All joint edges should be ground to remove burrs and fins prior to welding.

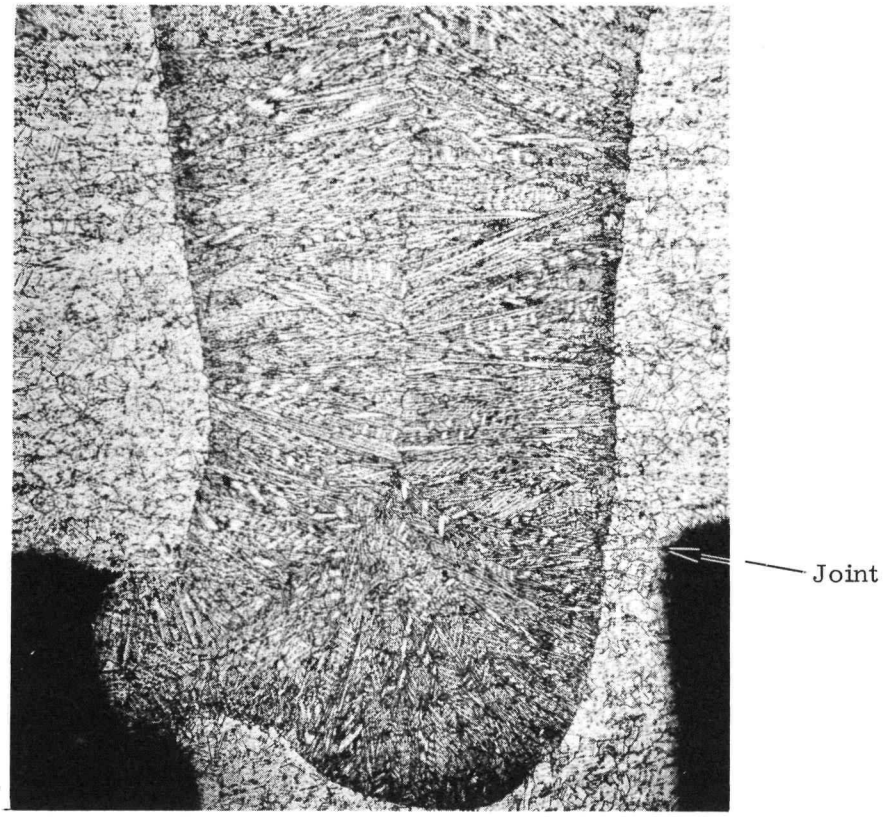

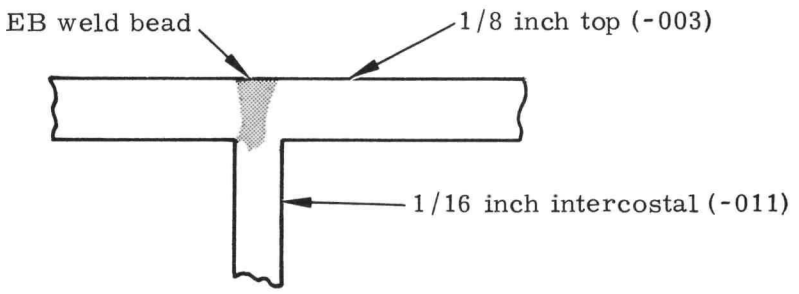

View Looking Aft

FIG. G-28. TYPICAL EB TEE JOINT WELD ON SPECIMEN 1; MAGN 43X

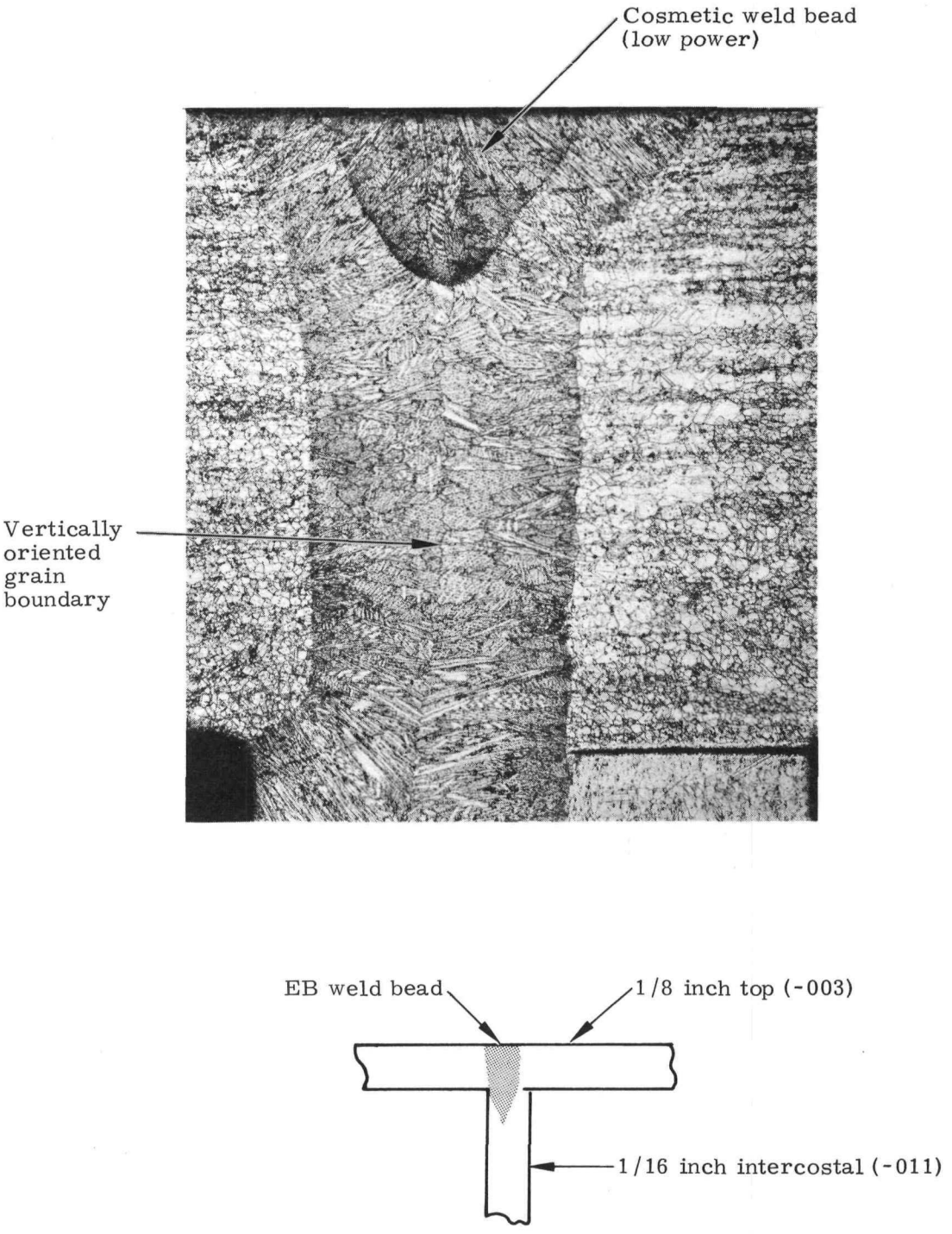

FIG. G-29. TYPICAL EB TEE JOINT WELD OF SPECIMEN 2; MAGN 43X

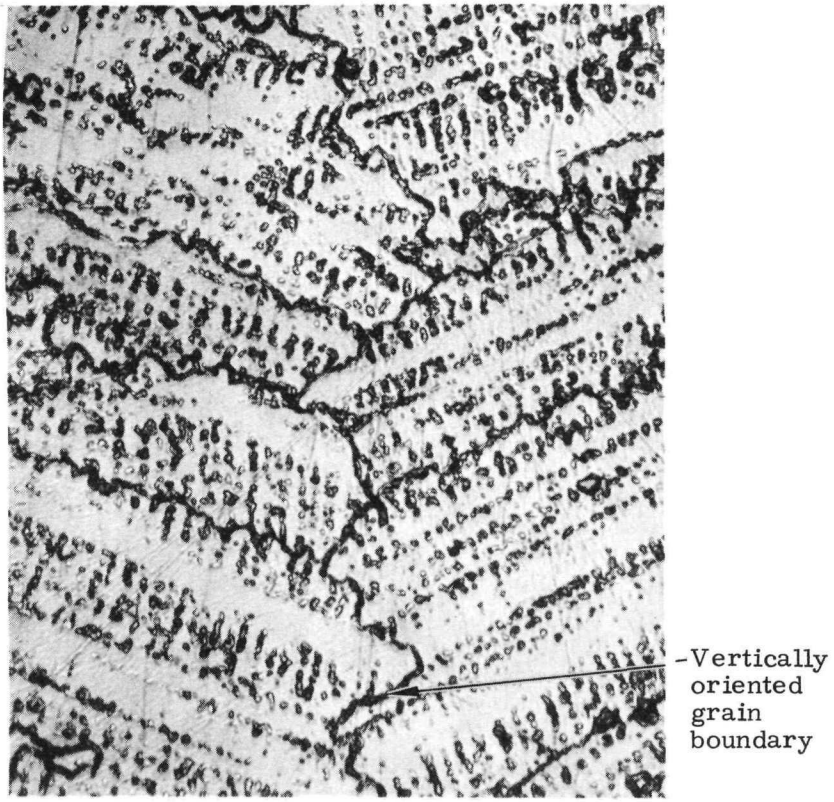

FIG. G-30. VERTICAL GRAIN BOUNDARY OF EB WELD TEE JOINT OF SPECIMEN 2; MAGN 638X

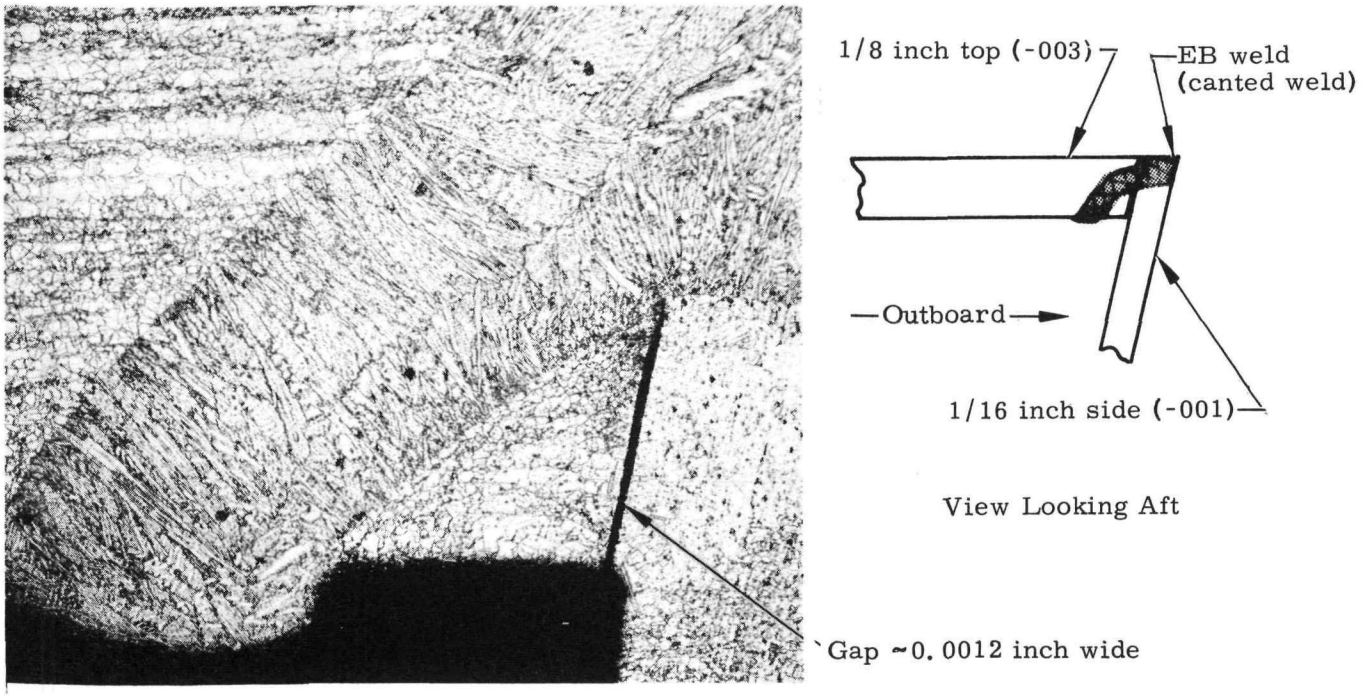

FIG. G-31. TYPICAL EB CANTED WELD ON SPECIMEN 2; MAGN 43X

(3) Parts that have been severely cold worked should be annealed at 1975° F ± 25 prior to welding (see Item (6)). A maximum of two in-process anneals prior to the final anneal are acceptable.

(4) Copper and argon backing should be used wherever possible when fusion welding. Gas coverage is mandatory on both sides of butt weld joints. These requirements should appear in all applicable process specifications.

(5) Starting tabs and either finishing tabs or holes should be provided to start and stop EB welds. These tabs should be machined off after welding.

(6) The following heat treatment is recommended for all welded parts:

> Solution anneal at 1975° F ± 25 for 1/2 hour minimum. Water quench to 1200° F or less within 4 seconds. Cool to room temperature by air or water quenching. Age at 1650° F ± 25 for 1 hour. Furnace cool to 1400° F ± 25 and hold for 10 hours. Air cool to room temperature.

All aging is to be accomplished in either an argon atmosphere or in a vacuum furnace. When solution treating or annealing, the parts should be charged into a hot, preheated furnace to reduce the time the material is in the aging range (1200° to 1800° F). Caution should be exercised when doing this to prevent heating the parts above 2000° F. The design of the parts involved should be reviewed to ensure that consideration is given to permitting good access to the water quenching medium during the solution annealing process with its 4-second quench limitation.

(7) All welded joints should be designed to permit a minimum heat input to the weld. For this reason the use of EB welds should be continued. The applicable process specification, or the drawing, should be revised to include a better definition of the EB weld joint, including maximum bead size, centering requirements of bead to joint, specific edge preparation and fit-up requirements and test or certification sample requirements.

(8) Either a separate material specification for parts to be welded on an addendum to AMS 5545 (Ref. G-1) should be added to the purchase requisition to emphasize that the material should not be heat treated above 2000° F and that the grain size shall not be coarser than ASTM No. 5.

(9) The use of additional cosmetic EB weld passes over the original bead (Fig. G-29) is not recommended for René 41. In addition, the design of the assembly should be reviewed to correct the condition which results in double EB welds (Fig. G-18).

(10) Future parts will be welded only by qualified personnel, how have demonstrated their ability to produce acceptable welds on sample parts.

E. REFERENCES

G-1. "Alloy, Sheet and Strip, Corrosion and Heat Resistant." Aerospace Material Specification, Society of Automotive Engineers, Inc., AMS 5545, New York, New York, January 15, 1961.

G-2. Lund, C. H., "Physical Metallurgy of Nickel-Base Superalloys." DMIC Report No. 153, Defense Metals Information Center, Battelle Memorial Institute, Columbus, Ohio, May 5, 1961.

G-3. "Heat Treatment, Cleaning, and Finishing." Metals Handbook, Vol. 2, AMS, Metals Park, Ohio, 8th Edition, 1964.

G-4. Kaprielyan, S. P., "Working René 41 into Your Design." Aircraft and Missiles, November 1960.

G-5. Thompson, E. G., Nunez, S. and Prager, M., "Practical Solutions to Strain-Age Cracking of René 41." Welding Research Supplement, July 1968.

G-6. Gischlar, G., "Cracks in 466A1941006-019 W Beams." IDC 1940-60, Isotopes, October 1968.

G-7. "Metallic Materials and Elements for Aerospace Vehicle Structures." MIL-HDBK-5A, Department of Defense, Washington, D. C., February 8, 1966.

G-8. Sessler, J. G. and Weiss, V., Ed., Supplement 4, "Non-Ferrous Heat Resistant Alloys." Aerospace Structural Metals Handbook, ASD-TDR 63-741 Vol. II-A, Air Force Systems Command, Wright-Patterson AFB, Ohio, March 1967.

G-9. Data Sheet, "Haynes Alloy No. R-41." Union Carbide Stellite Company, April 1963.

G-10. Gischlar, G., "Weld and Heat Treat Evaluation--René 41." Engineering Work Order No. 149, Isotopes, September 24, 1968.

G-11. Gischlar, G., "Evaluation of René 41 Weld Joints." Engineering Work Order No. 174, Isotopes, November 19, 1968.

G-12. Weisenberg, L. A. and Morris, R. J., "How to Fabricate René 41." Metal Progress, November 1960.

G-13. Slunder, C. J., and Hall, A. M., "Thermal and Mechanical Treatments for Nickel and Selected Nickel-Base Alloys and Their Effect on Mechanical Properties." NASA TM X-53443, April 20, 1966.

G-14. 466A1941005, "Support Beam Assembly-RTG Housing, (Fixed Side)."

G-15. 466A1941006, "Support Beam Assembly-RTG Housing, (Loading Side)."

APPENDIX H

TRW PLATINUM-RHODIUM CLAD DEVELOPMENT PROGRAM

The work performed by TRW Systems from October through December 1968 under subcontract (Contract 8E350) to the Martin Marietta Corporation (now Isotopes, Inc.) on the SNAP 29 program is described in this appendix. TRW efforts are directed at the systematic evaluation of the SNAP 29 intact capsule cladding-emittance coating system under both operational and abort conditions. The three primary tasks involved are as follows:

(1) Consulting Services--In this task, the basic material and inspection criteria needed for the preparation of a material specification for the SNAP 29 Pt-20% Rh capsule cladding system were established. This task was completed during the first quarterly reporting period.

(2) Post-Impact Compatibility--The objective of this task is to determine the long-term chemical and metallurgical behavior of the SNAP 29 capsule system from the liner outward. Stacked disc assemblies of interdiffusion couples heated in vacuum for periods of 1.8, 18 and 180 days at 1600°, 2000° and 2200° F will be used to determine the rates of interdiffusion of liner elements into the Pt-20% Rh cladding and platinum into the liner. Using subscale cylindrical specimens with the SNAP 29 liner, cladding and coatings, the capsule material system integrity will be determined in representative post-impact air/soil environments.

(3) Emissive Coating Verification--This task is aimed at evaluating, under both operational and abort conditions, the physical and chemical stability of three candidate high emittance coatings--iron titanate, calcium titanate and platinized alumina applied to the Pt-20% Rh cladding.

A. POST-IMPACT COMPATIBILITY TESTING

Work performed during the past quarter on this task included:

(1) Startup, in October, of the flat disc interdiffusion test at 2000° F for 180 days in vacuum.

(2) Completion of the electron microprobe analyses of the 1.8- and 18-day, flat disc interdiffusion tests at 1600°, 2000° and 2200° F.

(3) Initiation of quality assurance tests on the Pt-20% Rh cladding for the composite capsules.

1. Flat Disc Interdiffusion Testing

Testing of flat disc interdiffusion stack No. 6 (Ref. Table 2-3, SNAP 29 Development Program Plan, 2/9/68) at 2000° F for 180 days in vacuum was begun. The configuration of the stacked discs is the same as the stacks previously tested for 1.8 and 18 days at 1600°, 2000° and 2200° F (Ref. Fig. 1, SNAP 29 Development Program Plan, Revisions and Modifications, dated 12/20/68). On completion of this test in April 1969, electron microprobe analyses will be used to correlate and confirm the analyses of the short-term tests discussed in the following.

2. Flat Disc Interdiffusion Analyses

Electron microprobe analyses were conducted on cross sections of interfaces between stacked flat disc specimens which were contained in metal holders during thermal exposure in vacuum. Six stacks were analyzed, representing tests at 1600°, 2000° and 2200° F for 1.8 and 18 days. Two sets of analyses were conducted on each stack at longitudinally sectioned planes approximately 0.020-inch apart. The procedures followed are outlined.

Spatial scans (specimen moving at controlled rate under stationary electron beam) were run across the thicknesses of plasma arc sprayed Al_2O_3 applied as a potential diffusion barrier between the liner material and Pt-20% Rh discs. The intensities of characteristic X-rays of platinum and liner material elements were monitored during these scans.

Quantitative analysis of the liner/Pt-20% Rh interfaces were conducted at selected locations at the edges of the intermetallic zones and in the solid solution regions. The precise locations of the intermetallic edges were determined by spectral scans across each interface. A photomicrograph, illustrating a typical area on which microprobe analyses were conducted, is shown in Fig. H-1.

In the initial series of microprobe analyses, only the liner material element concentrations in the Pt-20% Rh side of the interface were determined. In the second series, the liner side was also analyzed for platinum to provide data for estimating the rate at which the liner material is modified by interdiffusion. Rhodium concentrations were not determined due to interference between principal rhodium characteristic X-ray wavelengths and those of the other elements in the system.

Microprobe intensity data were converted to quantitative elemental concentrations by applying corrections for X-ray absorption and fluorescence. A computer program (ØØ4, as described in Section D) was prepared to determine diffusion coefficients from quantitative data by the method of Wagner-Vasileff-Smoluchowski.

Although the thickness of each disc placed in the stacks was carefully measured prior to assembly, longitudinal compressive forces on the discs during the thermal exposure caused plastic deformation. The resulting reduction in thicknesses of the discs made it impossible to determine the exact location of the original interfaces. It was thus necessary to assume that the interfaces were located at the center of the intermetallic zones and that intermetallic zone propagation rates were equal on the cladding and liner sides of the interfaces. Rate constants for propagation of the intermetallic boundary were derived on the basis of a parabolic rate law. Results of the analyses are summarized:

(1) The diffusion barrier (0.005-inch thick plasma arc sprayed Al_2O_3) was effective in all cases in preventing interdiffusion between the Pt-20% Rh and liner material.

(2) Careful microprobe examination of the Pt-20% Rh adjacent to a defect (0.020-inch diameter hole) intentionally placed in the Al_2O_3 layer indicated the presence of a small quantity of liner material elements in some cases. However, no correlation could be established between the quantity of liner materials and test temperature or time. Detection of the liner material elements was not reproducible when duplicate analyses were conducted on sections which were ground and repolished subsequent to the initial analyses. It is thus suspected that the presence of these elements may be due to

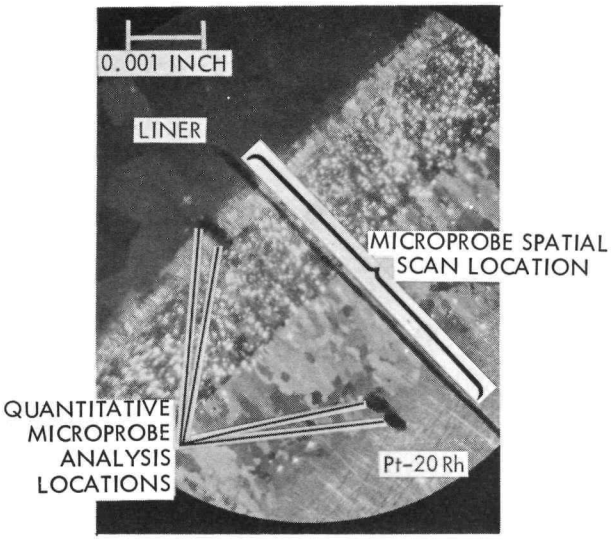

POLARIZED LIGHT 500X
NO. 8

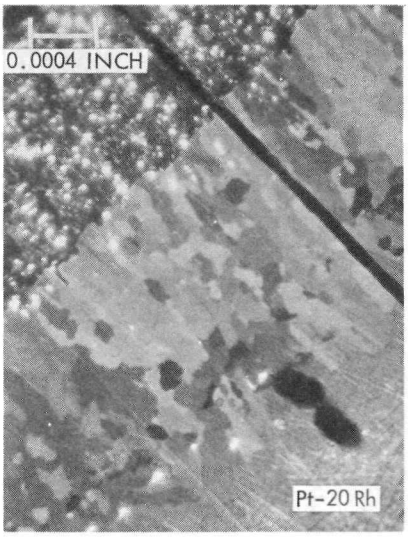

POLARIZED LIGHT 1100X
NO.8

FIG. H-1. PHOTOMICROGRAPHS OF Pt-20% Rh/LINER INTERFACE AREA OF STACK 8 WHERE MICROPROBE ANALYSES WERE CONDUCTED

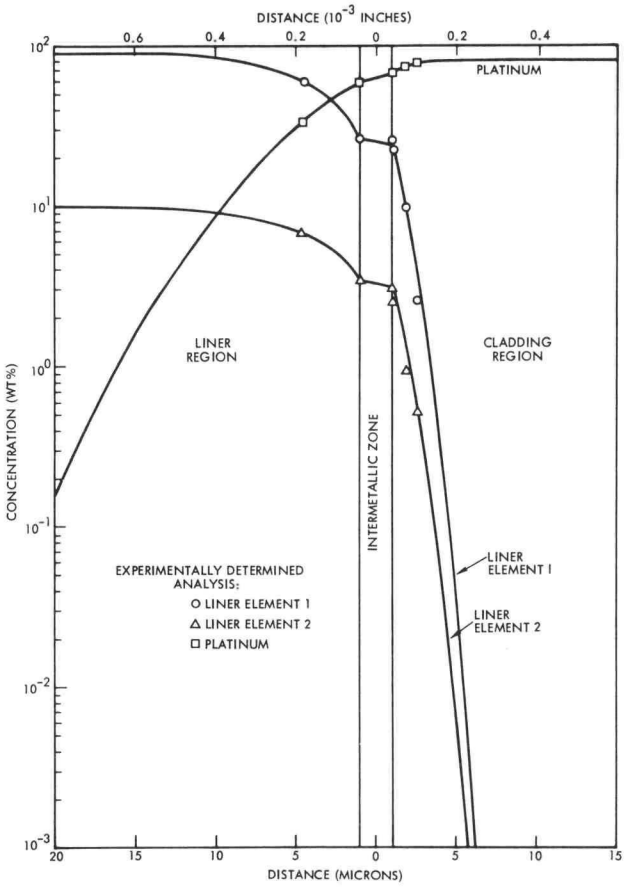

FIG. H-2. CONCENTRATION PROFILE ACROSS Pt-20% Rh/LINER INTERFACE AFTER 1.8 DAYS AT 1600° F

smearing during metallographic surface preparation rather than migration during thermal exposure.

(3) Values of the diffusion coefficients, D, of the principal liner material elements in the Pt-20% Rh and of the rate constant, b, for propagation of the intermetallic boundary into the Pt-20% Rh, based on data from the initial analyses are given in Table H-1. Values of D for all elements analyzed and b, based on the second analyses, are given in Table H-2.

TABLE H-1

Experimentally Determined Diffusion Parameters--First Microprobe Analysis

Stack Number	Thermal Exposure (days)	(°F)	Intermetallic Boundary Propagation Rate Constant $b\ (cm \cdot sec^{-1/2})$*	Diffusion Coefficients Liner Element 1 $D_1\ (cm^2 \cdot sec^{-1})$	Liner Element 2 $D_2\ (cm^2 \cdot sec^{-1})$
1	1.8	1600	2.8×10^{-7}	7.6×10^{-14}	7.5×10^{-14}
2	18	1600	2.2×10^{-7}	6.3×10^{-14}	7.0×10^{-14}
4	1.8	2000	1.7×10^{-6}	9.4×10^{-13}	6.2×10^{-14}
5	18	2000	1.2×10^{-6}	8.5×10^{-13}	4.0×10^{-14}
7	1.8	2200	3.7×10^{-7}	2.6×10^{-12}	1.1×10^{-12}
8	18	2200	3.0×10^{-7}	2.9×10^{-12}	1.3×10^{-12}

*Propagation rate of intermetallic zone assumed equal on both sides of each interface.

TABLE H-2

Experimentally Determined Diffusion Parameters--Second Microprobe Analysis

Stack Number	Thermal Exposure (days)	(°F)	Intermetallic Boundary Propagation Rate Constant $b\ (cm \cdot sec^{-1/2})$*	Diffusion Coefficients Liner Element 1 $D_1\ (cm^2 \cdot sec^{-1})$	Liner Element 2 $D_2\ (cm^2 \cdot sec^{-1})$	Platinum $D_{Pt}\ (cm^2 \cdot sec^{-1})$
1	1.8	1600	2.9×10^{-7}	8.2×10^{-14}	8.9×10^{-14}	1.7×10^{-12}
2	18	1600	2.3×10^{-7}	6.5×10^{-14}	8.4×10^{-14}	1.2×10^{-12}
4	1.8	2000	1.5×10^{-6}	9.2×10^{-13}	5.8×10^{-13}	1.3×10^{-11}
5	18	2000	1.4×10^{-6}	8.9×10^{-13}	5.5×10^{-13}	9.8×10^{-12}
7	1.8	2200	3.6×10^{-6}	3.0×10^{-12}	1.2×10^{-12}	3.4×10^{-11}
8	18	2200	4.0×10^{-6}	3.3×10^{-12}	1.4×10^{-12}	3.7×10^{-11}

From the experimentally determined values of b and D, based on 1.8- and 18-day data, the recession rates of remaining unmodified cladding and liner material can be determined. A computer program (ØØ5, described in Section E) was prepared to facilitate concentration profile determination for operating durations up to 1800 days at temperatures between 1600° and 2200° F. The diffusion parameters used in these computations are based on both sets of microprobe analyses and are given in Table H-3. A proportional relationship between diffusion parameters and reciprocal of absolute temperature was used to calculate the values for 1850° F.

TABLE H-3

Diffusion Parameters Used for Determining Concentration Profiles

Temperature (°F)	Intermetallic Boundary Propagation Rate Constant $b\ (cm \cdot sec^{-1/2})$*	Diffusion Coefficients: Liner Element $D_1\ (cm^2 \cdot sec^{-1})$	Liner Element 2 $D_2\ (cm^2 \cdot sec^{-1})$	Platinum $D_{Pt}\ (cm^2 \cdot sec^{-1})$
1600	2.6×10^{-7}	7.4×10^{-14}	8.2×10^{-14}	1.5×10^{-12}
1850	8.7×10^{-7}	3.2×10^{-13}	2.4×10^{-13}	6.4×10^{-12}
2000	1.5×10^{-6}	9.1×10^{-13}	5.7×10^{-13}	1.1×10^{-11}
2200	3.8×10^{-6}	3.2×10^{-12}	1.3×10^{-12}	3.6×10^{-11}

*Propagation rate of intermetallic zone assumed equal on both sides of each interface.

The relationships between elemental composition and distance from the original interface after thermal exposure to 1600° F for 1.8 days is shown in Fig. H-2 and for 18 days in Fig. H-3. The quantitative microprobe analyses data points are included in these figures. The predicted concentration profile after exposure to 1600° F for 180 days is shown in Fig. H-4, and for 1800 days in Fig. H-5. Corresponding composition versus distance curves at 1850° F are shown in Figs. H-6 to H-9, at 2000° F in Figs. H-10 to H-13, and at 2200° F in Figs. H-14 to H-17.

The extrapolated data thus show that after 1800 days at the anticipated operating temperature of 1850° F, 60% of the original 500-micron (0.020-inch) thick Pt-20% Rh protective cladding would be modified by interdiffusion to contain at least 0.1 wt% liner material elements. After operating at 2000° F for 1800 days, the entire cladding thickness would be affected to this extent.

The extent of diffusion of the platinum into the liner side is more severe. After 1800 days at 1850° F, the liner would contain 0.1 wt % or more platinum to a distance of 1300 microns (0.052-inch) from the cladding interface. After 1800 days at 200° F, this distance would be 1800 microns (0.072-inch).

3. Quality Assurance Tests of the Pt-20% Rh Cladding for Composite Cylinder Test Specimens

The quality assurance tests of the Pt-20% Rh cladding (1/4-inch OD tubing with 0.020-inch thick wall) included measurements of its microhardness, metallographic examination of its structure and nondestructive tests for surface defects.

a. Microhardness tests

Microhardness measurements were made on a full transverse cross section of tubing (~1/4-inch long) mounted in plastic and polished for metallographic examination. The testing machine used was a Leitz Mini-Load Microhardness Tester with a 136-degree Vickers diamond indenter. The microhardness of the tubing was 289 kg/mm^2 with a 50-gram test load. Since fully annealed Pt-20% Rh has a microhardness of 130 kg/mm^2 or less, the tubing as-received from Engelhard Industries was obviously in a wrought condition.

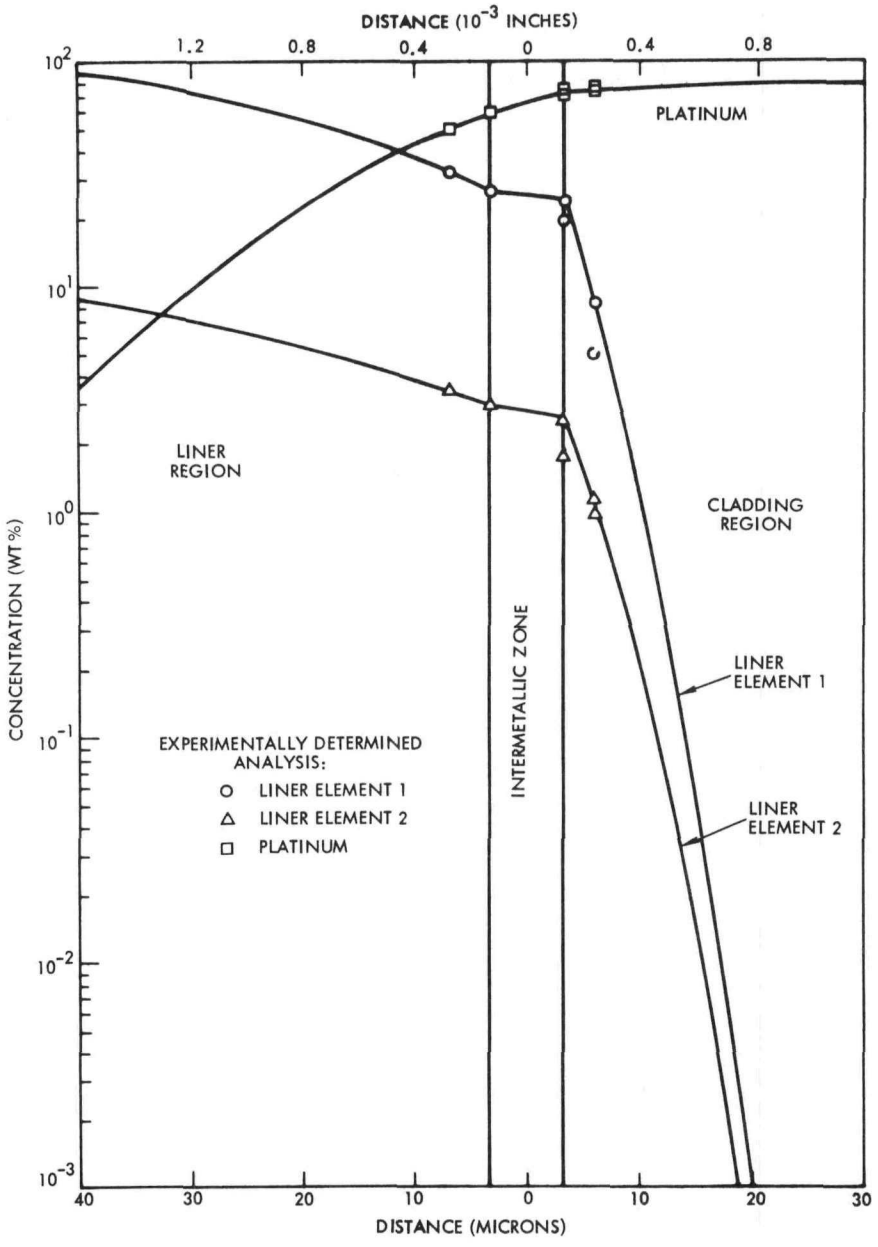

FIG. H-3. CONCENTRATION PROFILE ACROSS Pt-20% Rh/LINER INTERFACE AFTER 18 DAYS AT 1600° F

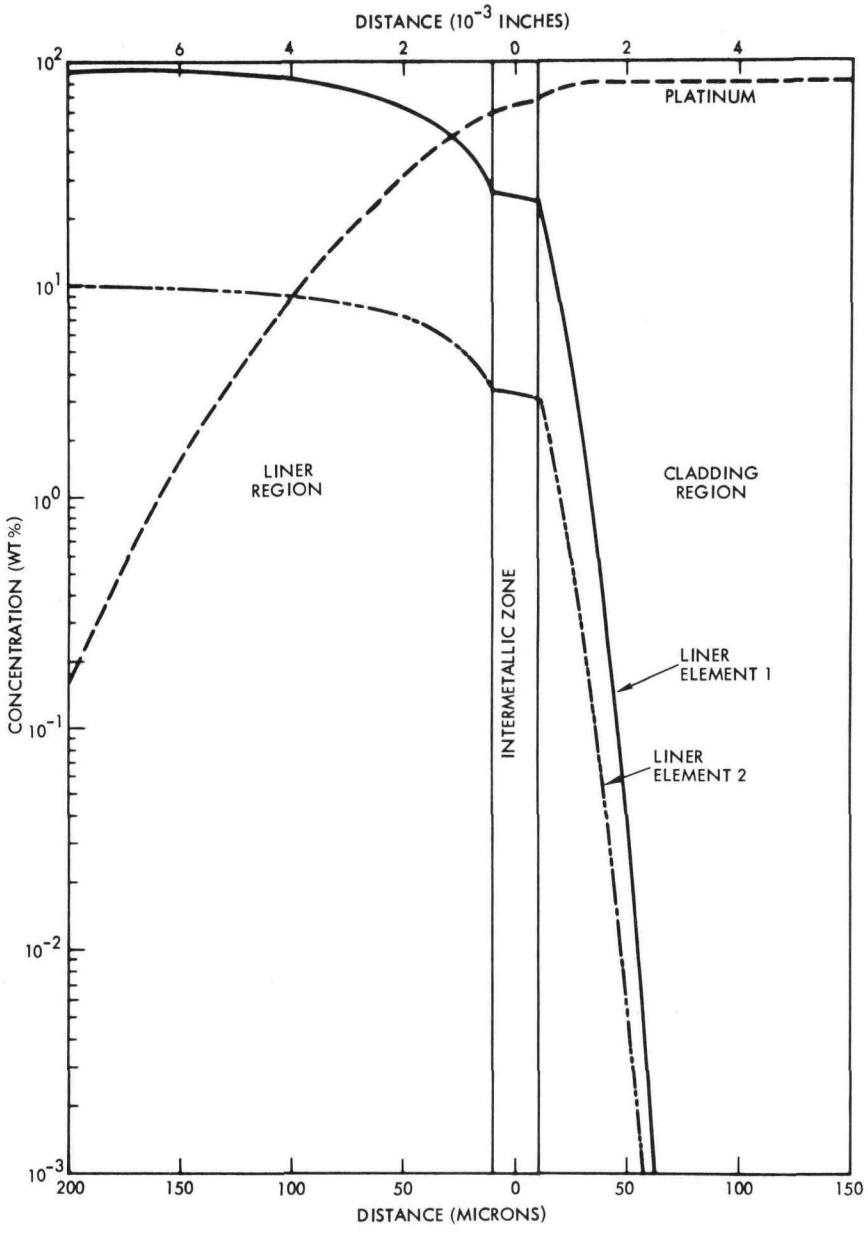

FIG. H-4. PREDICTED CONCENTRATION PROFILE ACROSS Pt-20% Rh/LINER INTERFACE AFTER 180 DAYS AT 1600° F

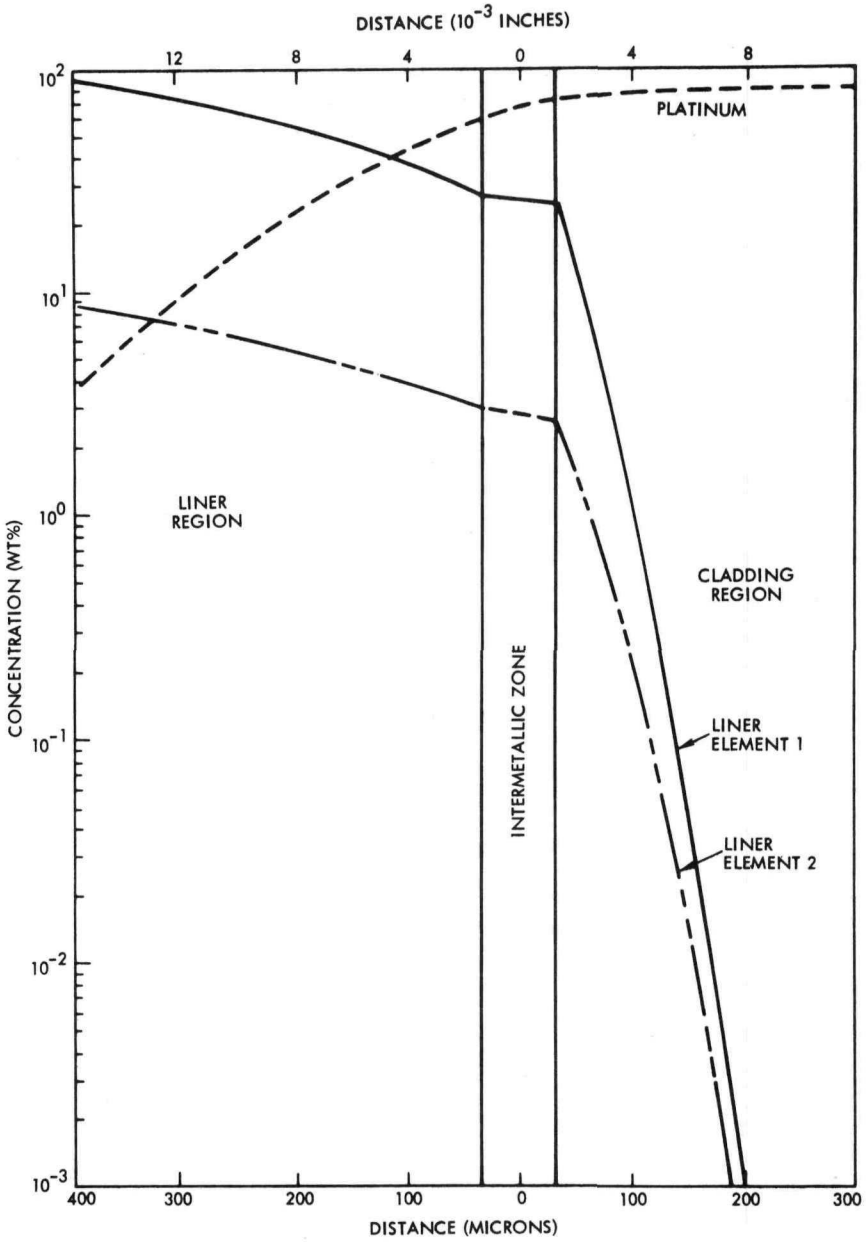

FIG. H-5. PREDICTED CONCENTRATION PROFILE ACROSS Pt-20% Rh/LINER INTERFACE AFTER 1800 DAYS AT 1600° F

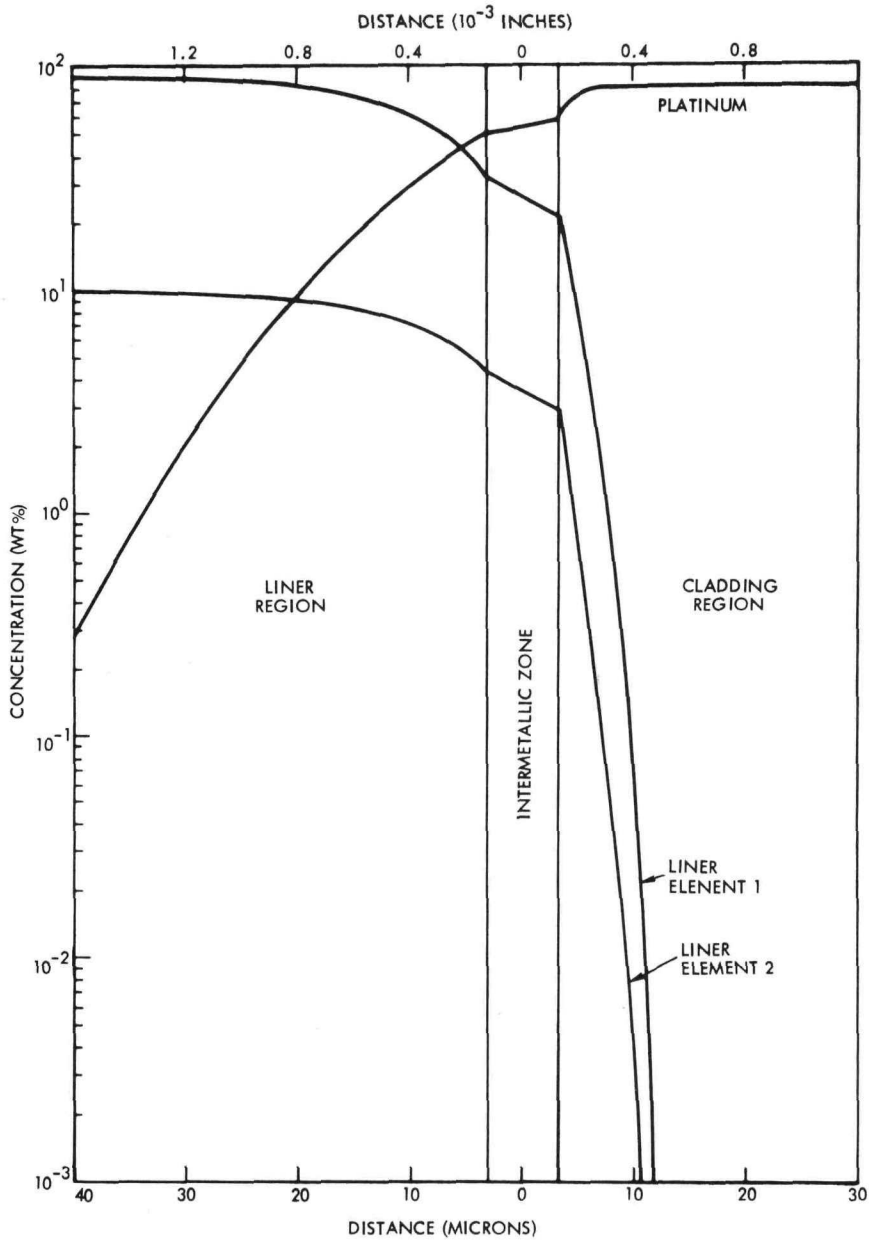

FIG. H-6. PREDICTED CONCENTRATION PROFILE ACROSS Pt-20% Rh/LINER INTERFACE AFTER 1.8 DAYS AT 1850° F

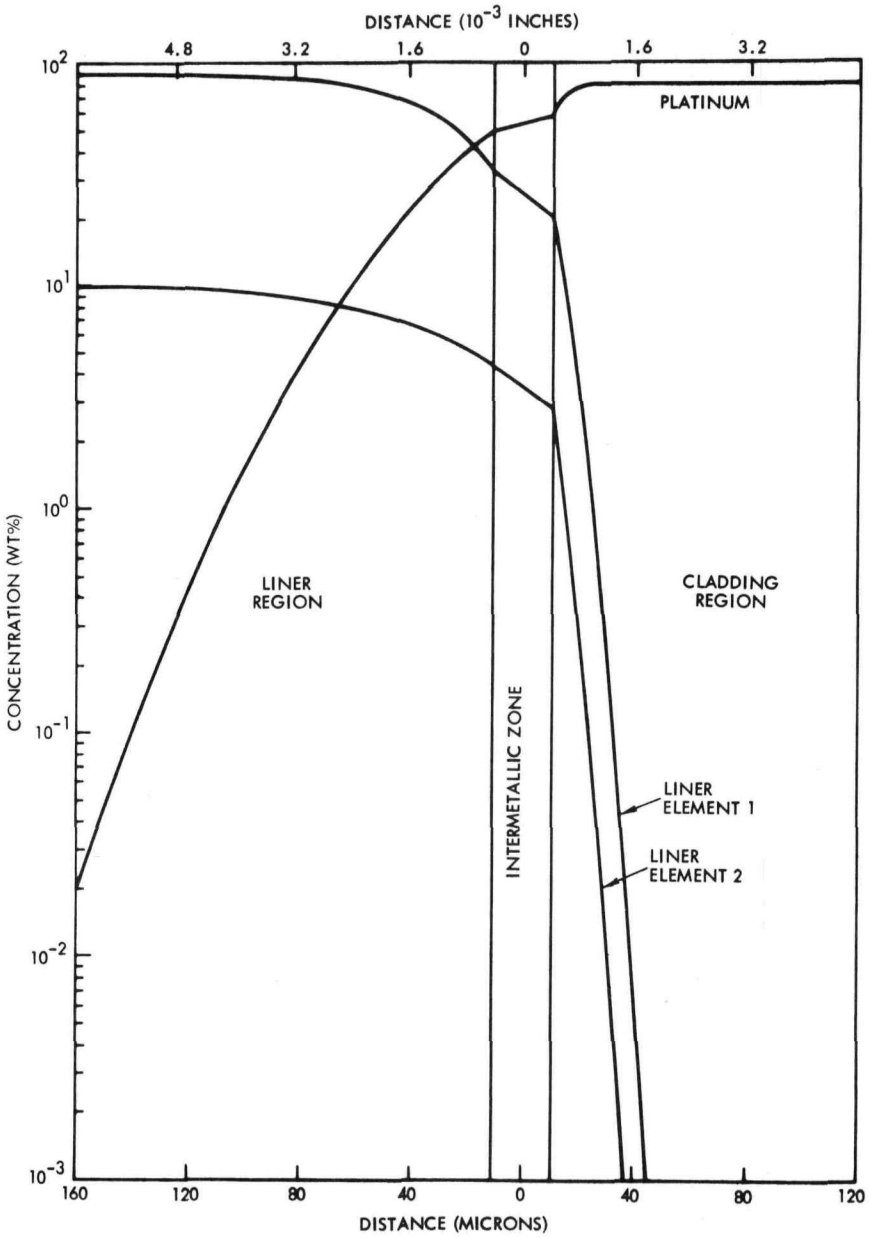

FIG. H-7. PREDICTED CONCENTRATION PROFILE ACROSS Pt-20% Rh/LINER INTERFACE AFTER 18 DAYS AT 1850° F

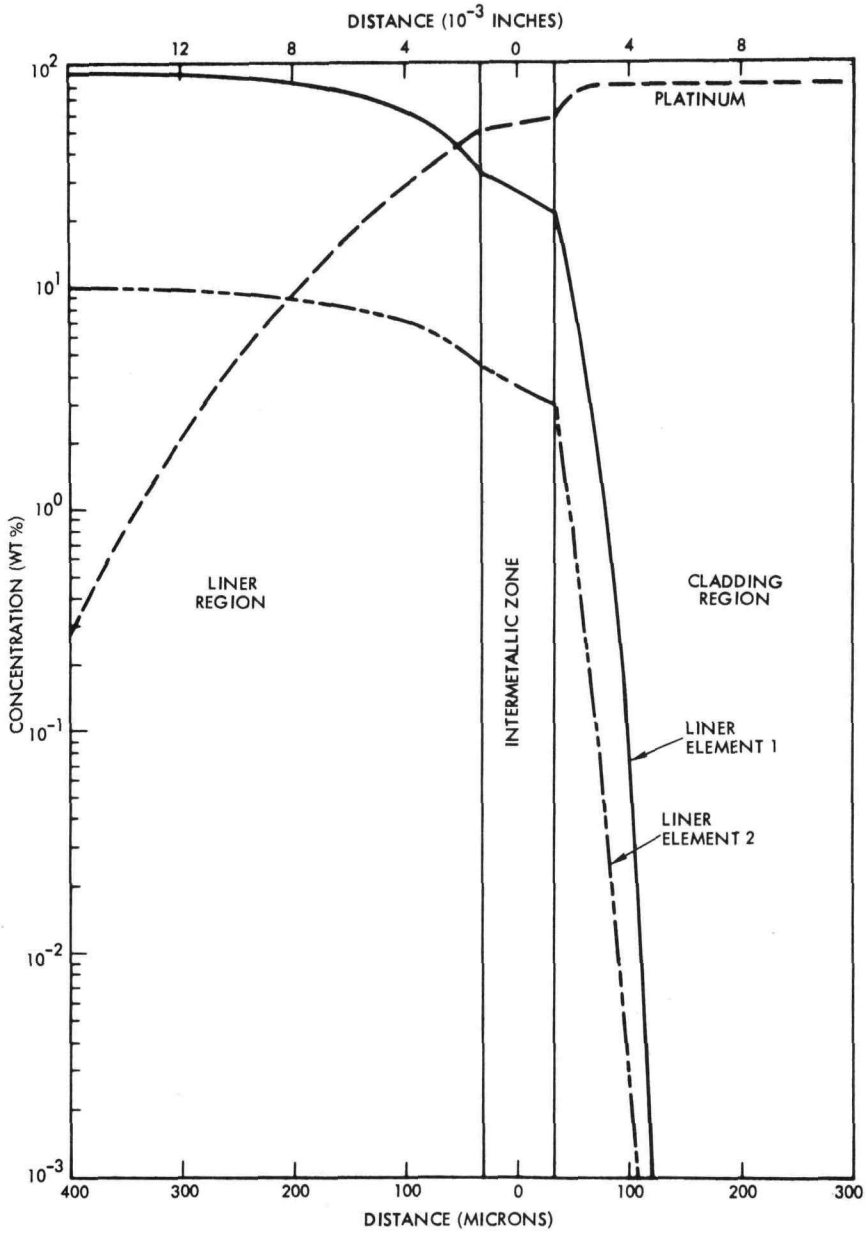

FIG. H-8. PREDICTED CONCENTRATION PROFILE ACROSS Pt-20% Rh/LINER INTERFACE AFTER 180 DAYS AT 1850° F

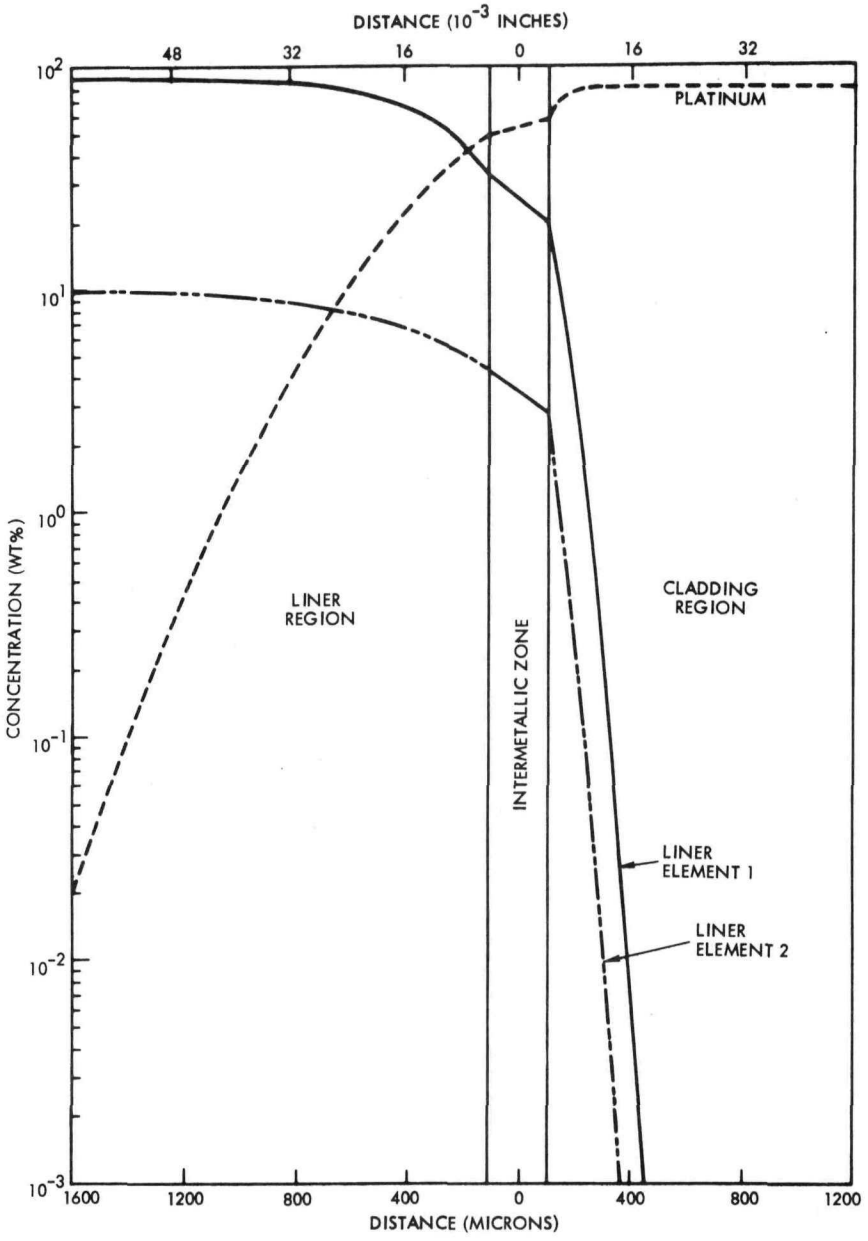

FIG. H-9. PREDICTED CONCENTRATION PROFILE ACROSS Pt-20% Rh/LINER INTERFACE AFTER 1800 DAYS AT 1850° F

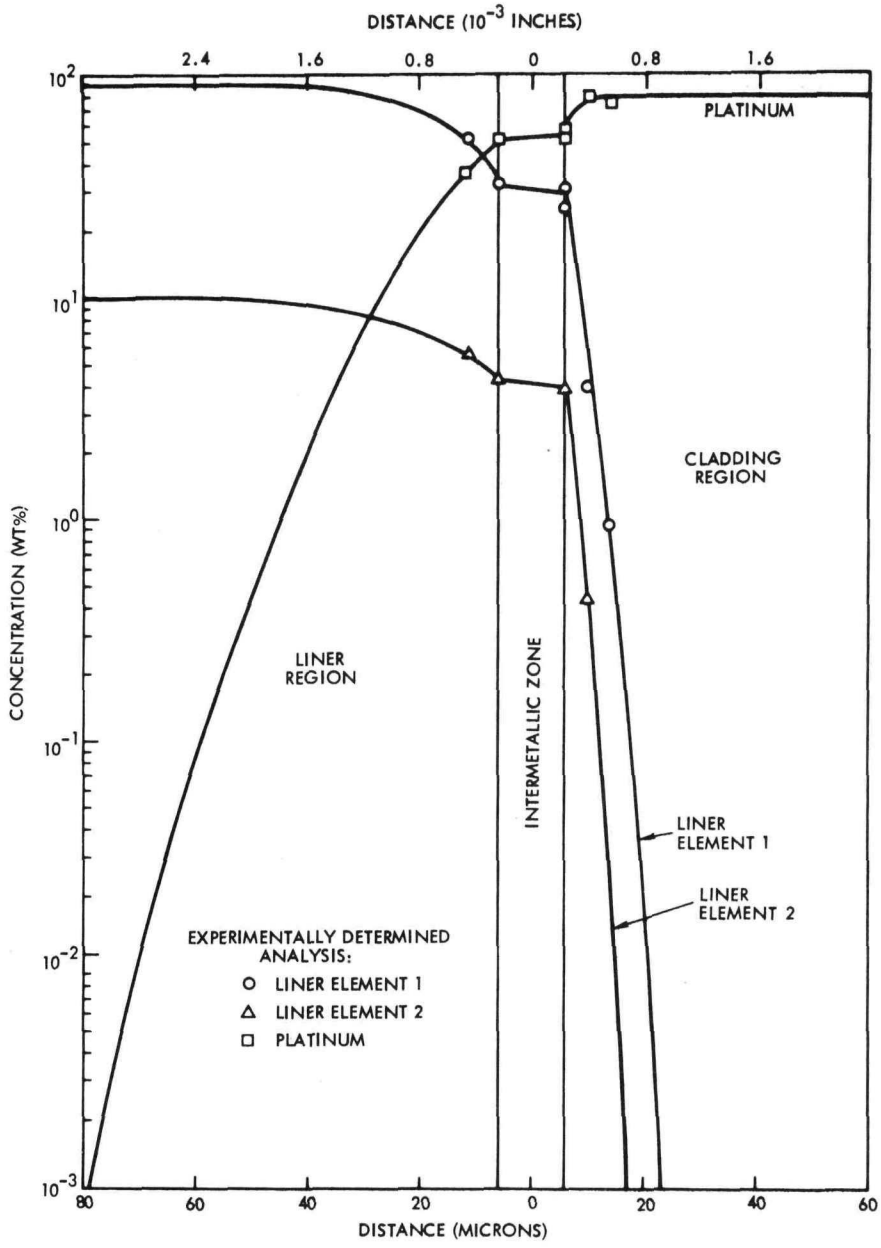

FIG. H-10. CONCENTRATION PROFILE ACROSS Pt-20% Rh/LINER INTERFACE AFTER 1.8 DAYS AT 2000° F

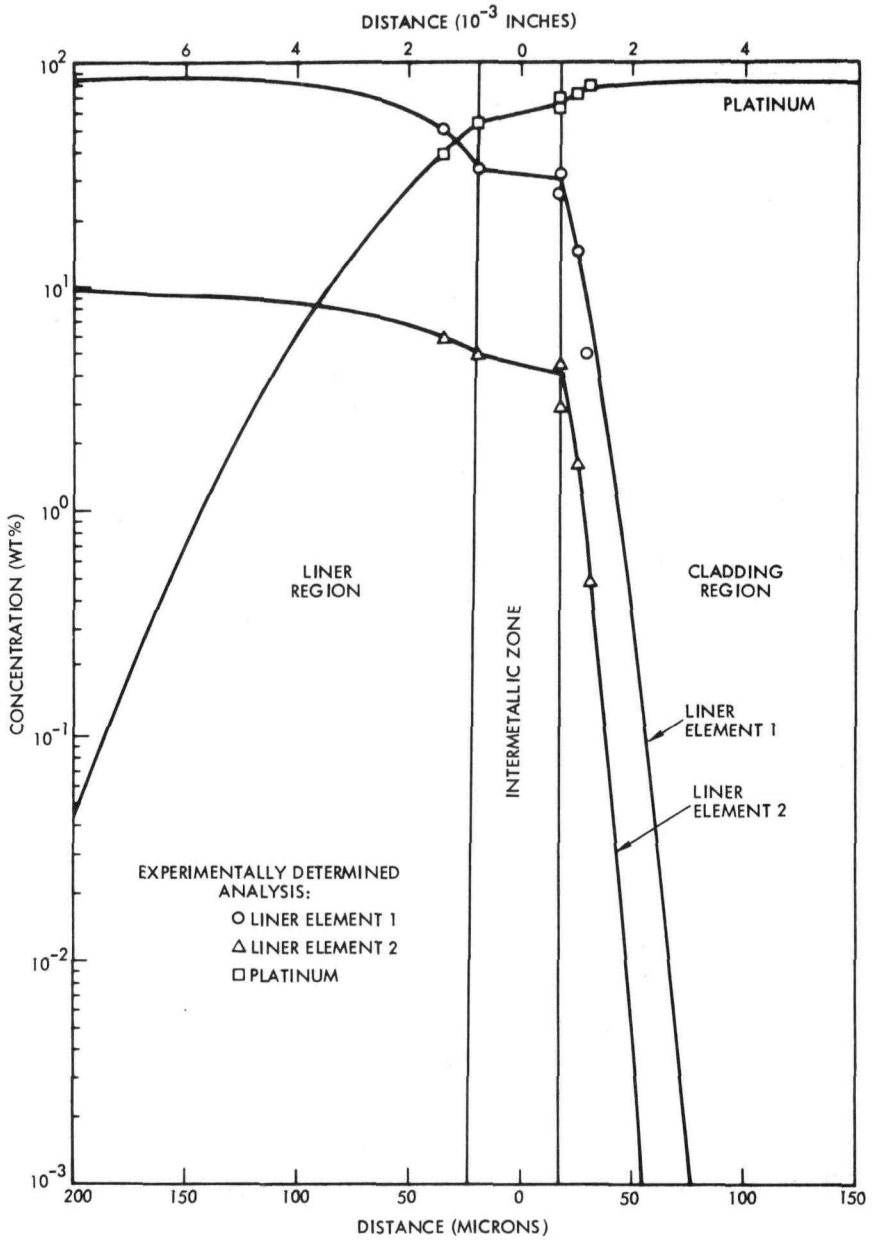

FIG. H-11. CONCENTRATION PROFILE ACROSS Pt-20% Rh/LINER INTERFACE AFTER 18 DAYS AT 2000° F

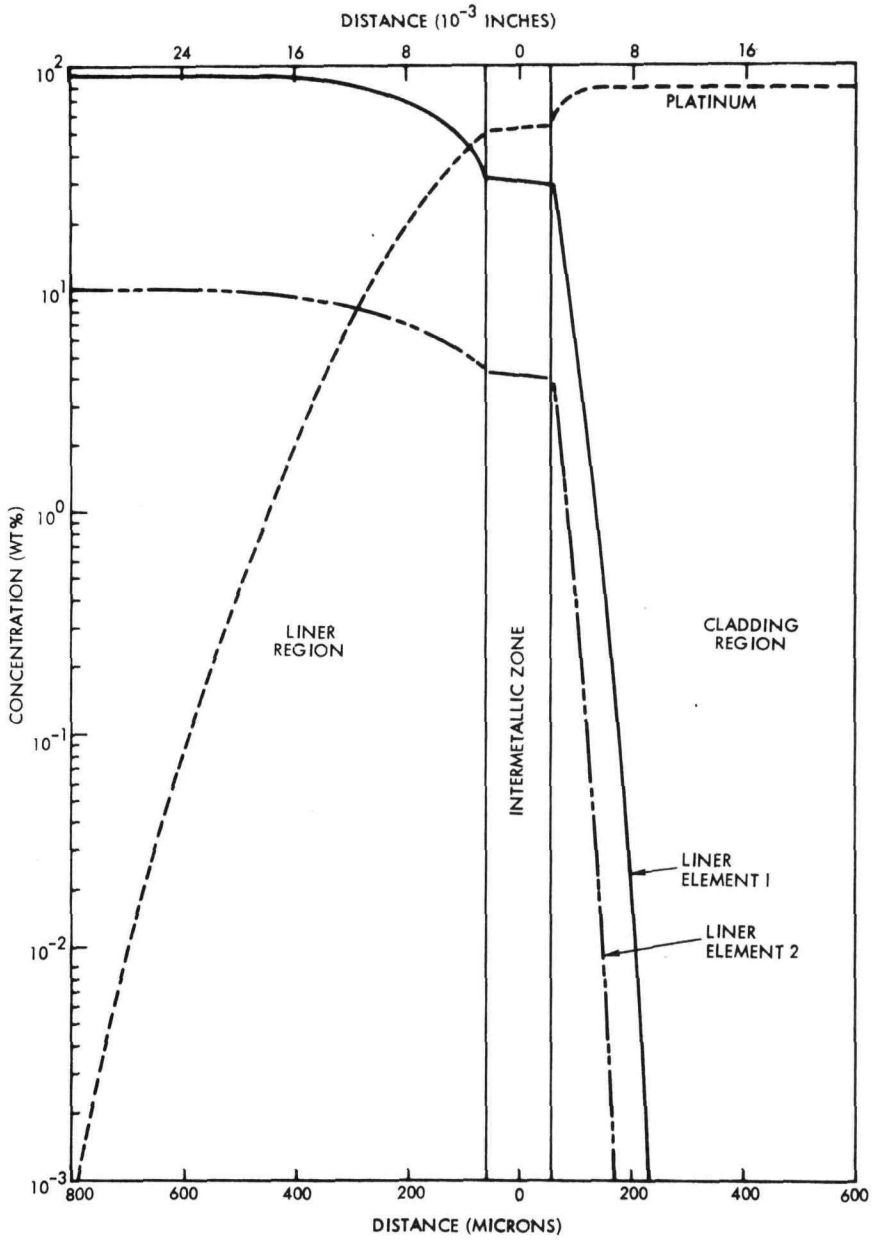

FIG. H-12. PREDICTED CONCENTRATION PROFILE ACROSS Pt-20% Rh/LINER INTERFACE AFTER 180 DAYS AT 2000° F

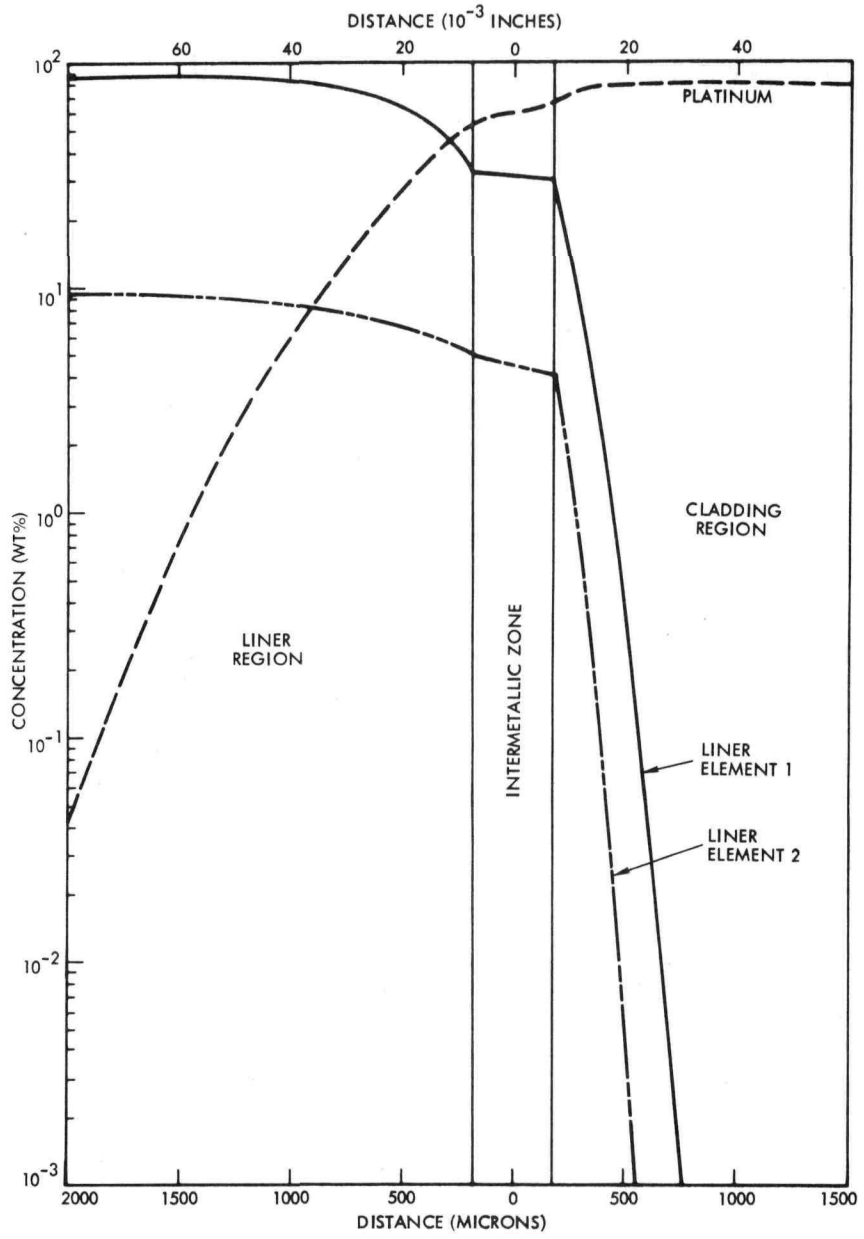

FIG. H-13. PREDICTED CONCENTRATION PROFILE ACROSS Pt-20% Rh/LINER INTERFACE AFTER 1800 DAYS AT 2000° F

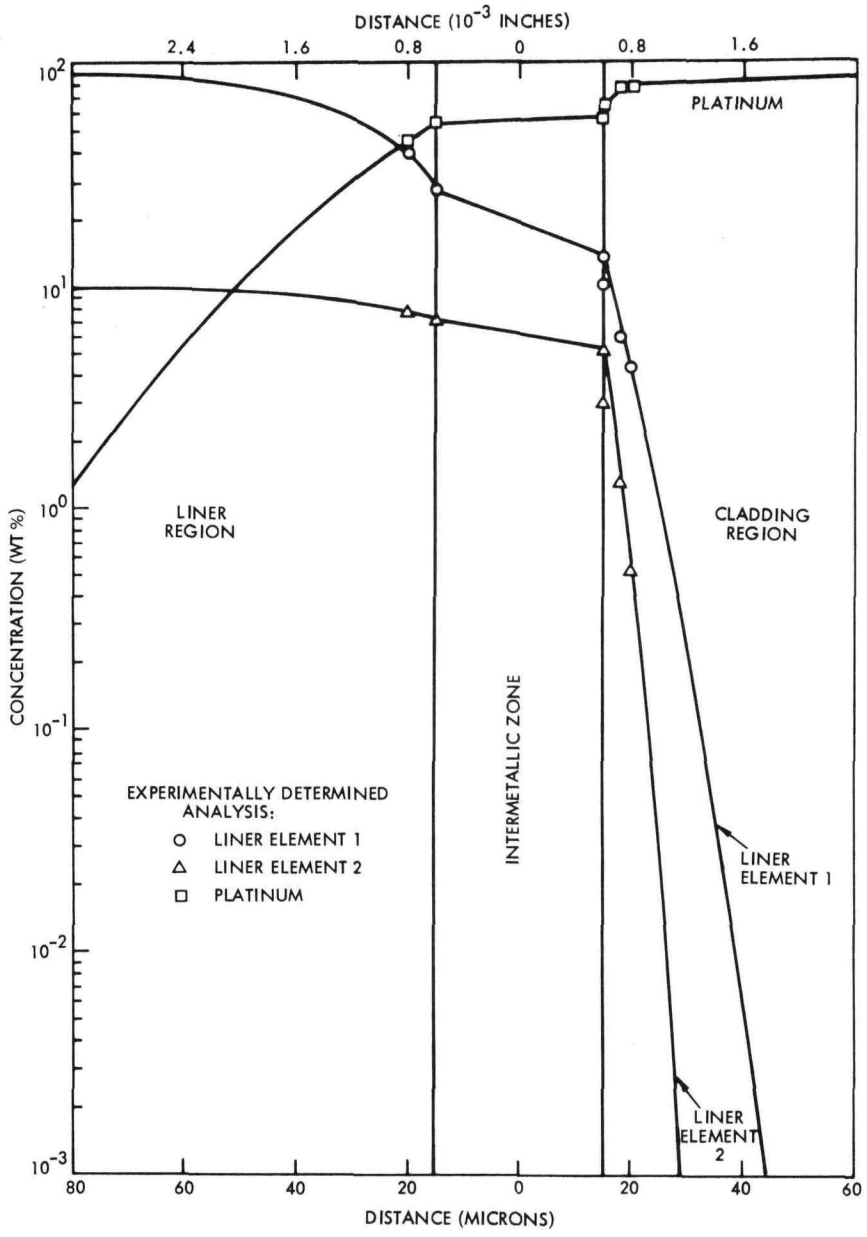

FIG. H-14. CONCENTRATION PROFILE ACROSS Pt-20% Rh/LINER INTERFACE AFTER 1.8 DAYS AT 2200° F

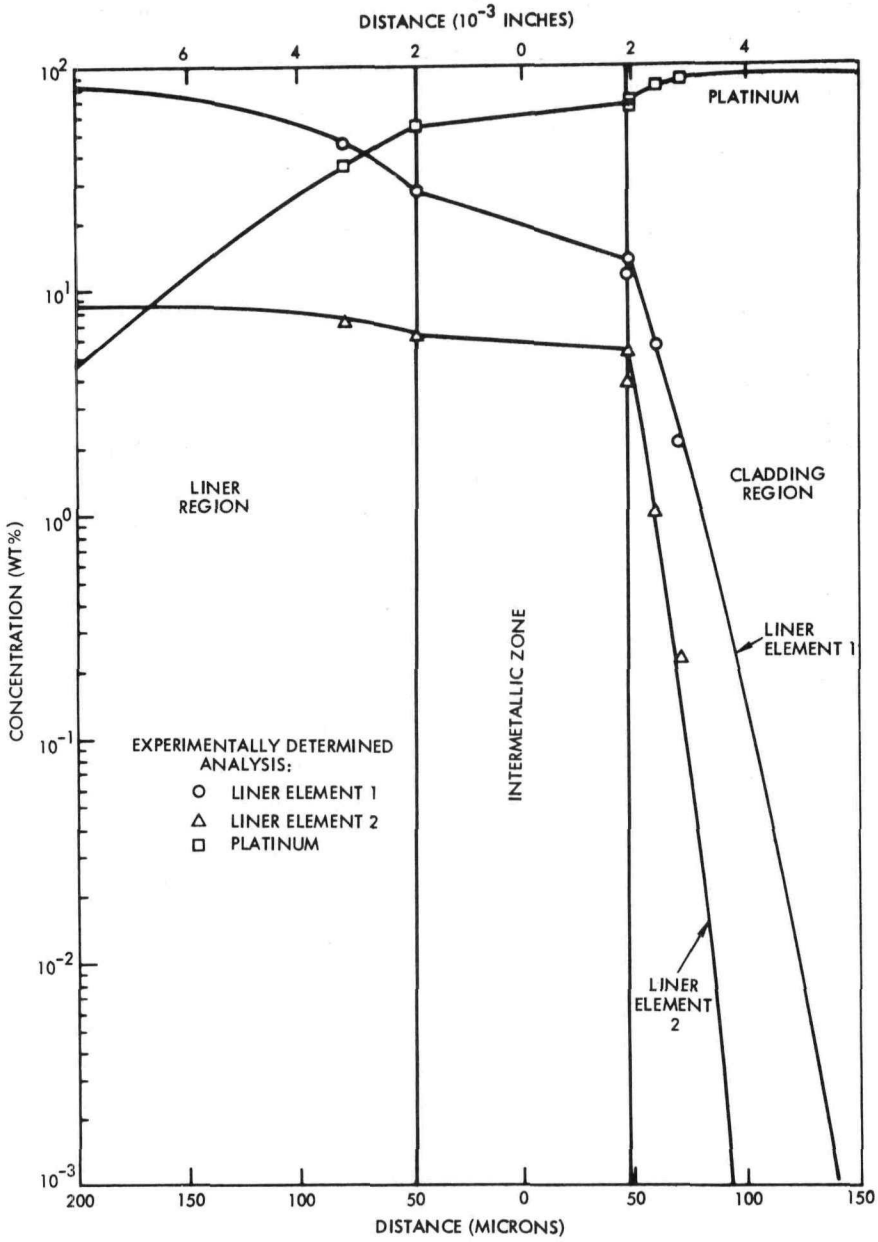

FIG. H-15. CONCENTRATION PROFILE ACROSS Pt-20% Rh/LINER INTERFACE AFTER 18 DAYS AT 2200° F

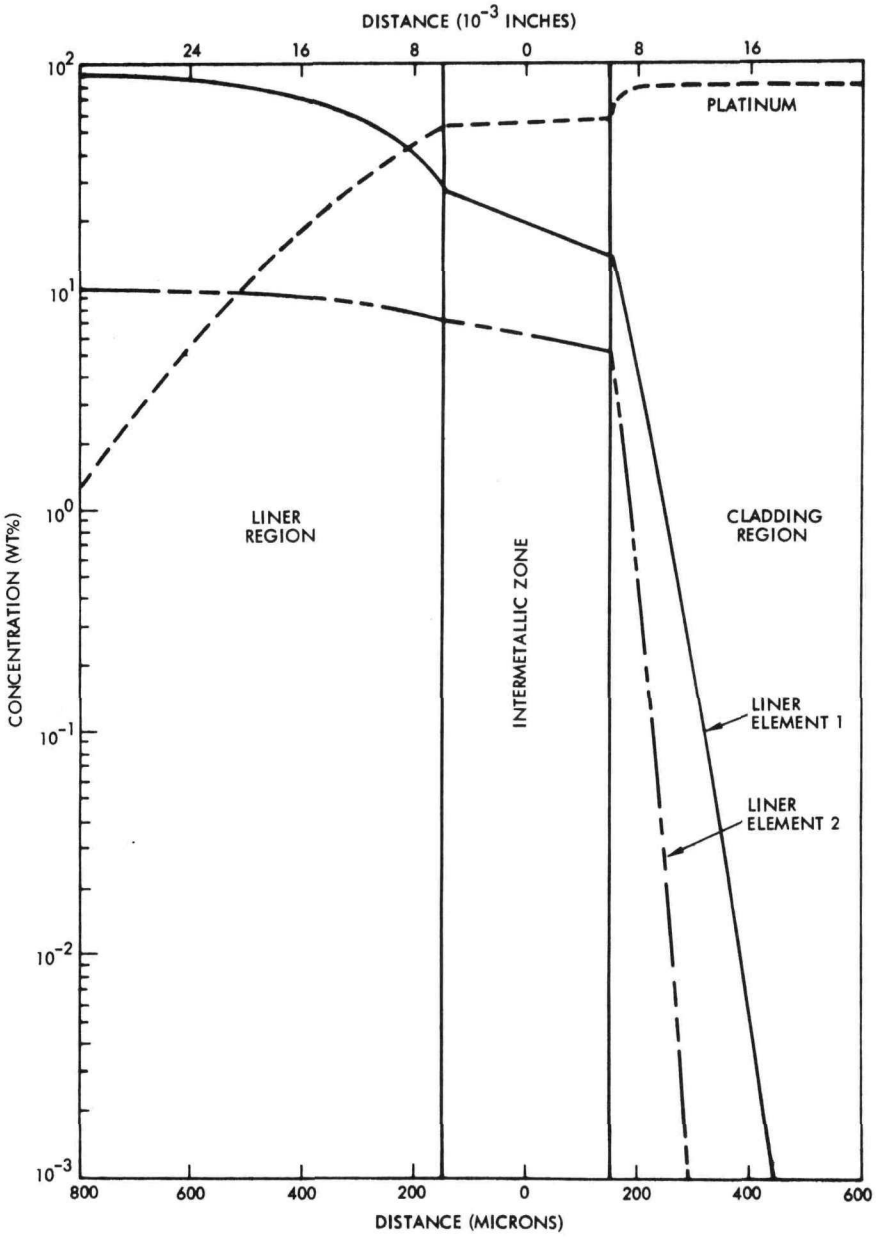

FIG. H-16. PREDICTED CONCENTRATION PROFILE ACROSS Pt-20% Rh/LINER INTERFACE AFTER 180 DAYS AT 2200° F

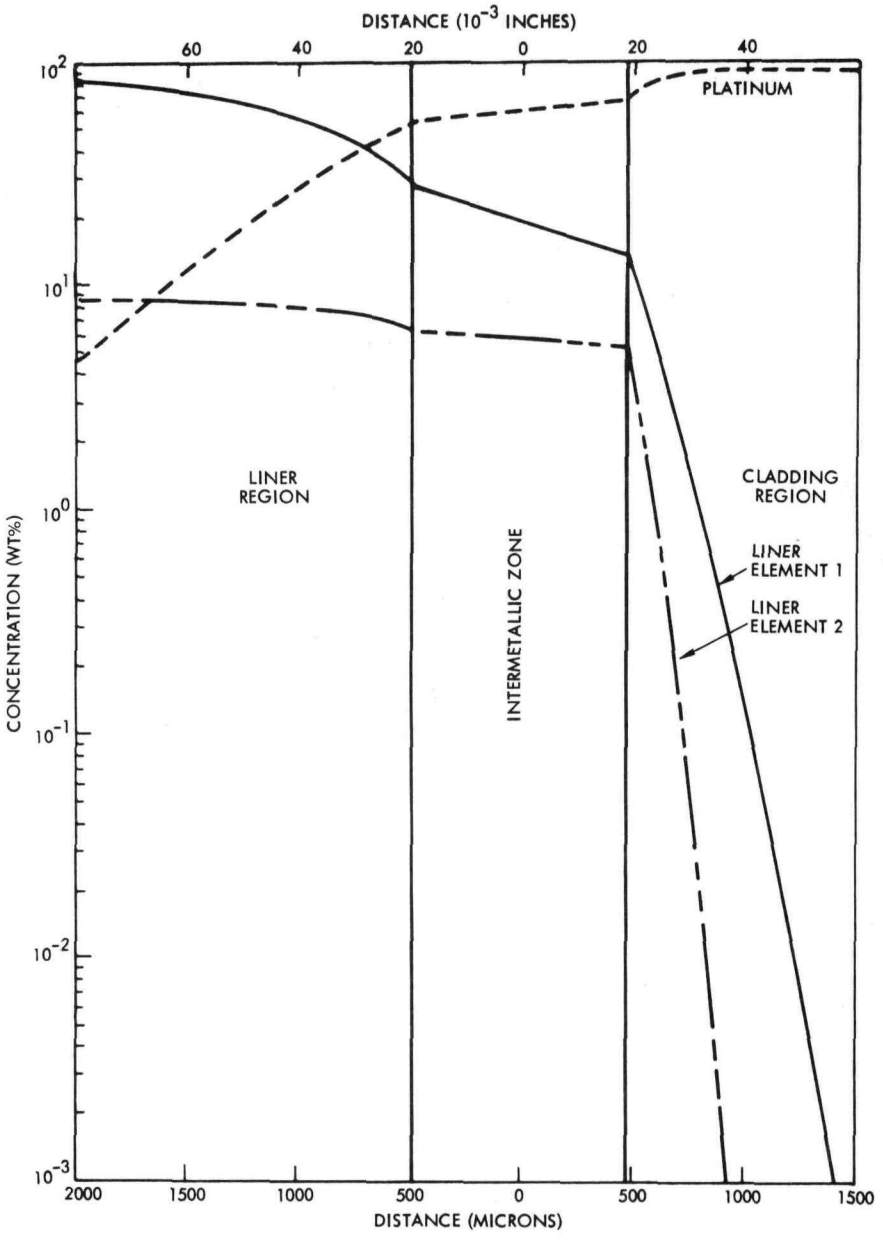

FIG. H-17. PREDICTED CONCENTRATION PROFILE ACROSS Pt-20% Rh/LINER INTERFACE AFTER 1800 DAYS AT 2200° F

b. Metallographic examination

Metallographic examination of the microhardness test specimen after etching revealed a fine-grained wrought structure (Fig. H-18). Prior to final assembly of the composite capsules, the Pt-20% Rh will be fully annealed by a 16-hour heat treatment at 2000° F in vacuum.

c. Nondestructive testing

An ultrasensitive fluorescent penetrant inspection was performed on 100% of the OD surface of the tubing using HM-400 penetrant (Sherwin Incorporated, Los Angeles). No surface defects were detected. Scratches running the length of the tubing were noted, but were not classified as defects because of their shallow depth. It is hypothesized that the shallow scratches were incurred during the tubing fabrication process.

Prior to cutting, the 36-inch long Pt-20% Rh tubes will be helium leak checked for defects extending through the tubing wall. Leaks greater than 1×10^{-9} scc/sec will be a cause for tubing rejection.

C. EMISSIVE COATING VERIFICATION TASK

The following subtasks were performed during this reporting period:

(1) Evaluated iron titanate and calcium titanate as emissive coatings for Pt-20% Rh after a 90-day operational exposure at 1950° F.

(2) Evaluated iron titanate and calcium titanate as emissive coatings for Pt-20% Rh after a two-minute re-entry exposure at 3000° F.

(3) Investigated the high temperature chemical stability of iron titanate in air in contact with ATJ graphite and Pt-20% Rh.

(4) Investigated the hemispherical total emittance stability of calcium titanate as a function of air exposure at elevated temperatures.

(5) Replaced iron titanate as an emissive coating candidate for Pt-20% Rh with plasma arc sprayed platinized alumina.

(6) Started the 18-day abort environmental exposure tests at 1600° and 2000° F.

(7) Designed an emissive coating shear strength test.

1. Evaluation of Iron and Calcium Titanates as Emissive Coatings for Pt-20% Rh After 90-Day Operational Exposure

The Pt-20% Rh strips (1/4-inch wide x 6-inches long x 0.020-inch thick), coated on both sides with iron titanate and calcium titanate, completed a 90-day exposure to vacuum in an ATJ graphite block at 1950° F. Hemispherical emittance measurements were made on the strips in vacuum after exposure. Both coating materials had previously been shown to be stable through nine days exposure; however, after 90 days, the iron titanate clearly indicated a condition of instability (Tables H-4 and H-5). Not only had the emittance of iron titanate dropped below the established minimum value of 0.8, its adherence to the substate was extremely poor (Fig. H-19). In addition to chipping and pealing, the iron titanate appeared to have sintered and

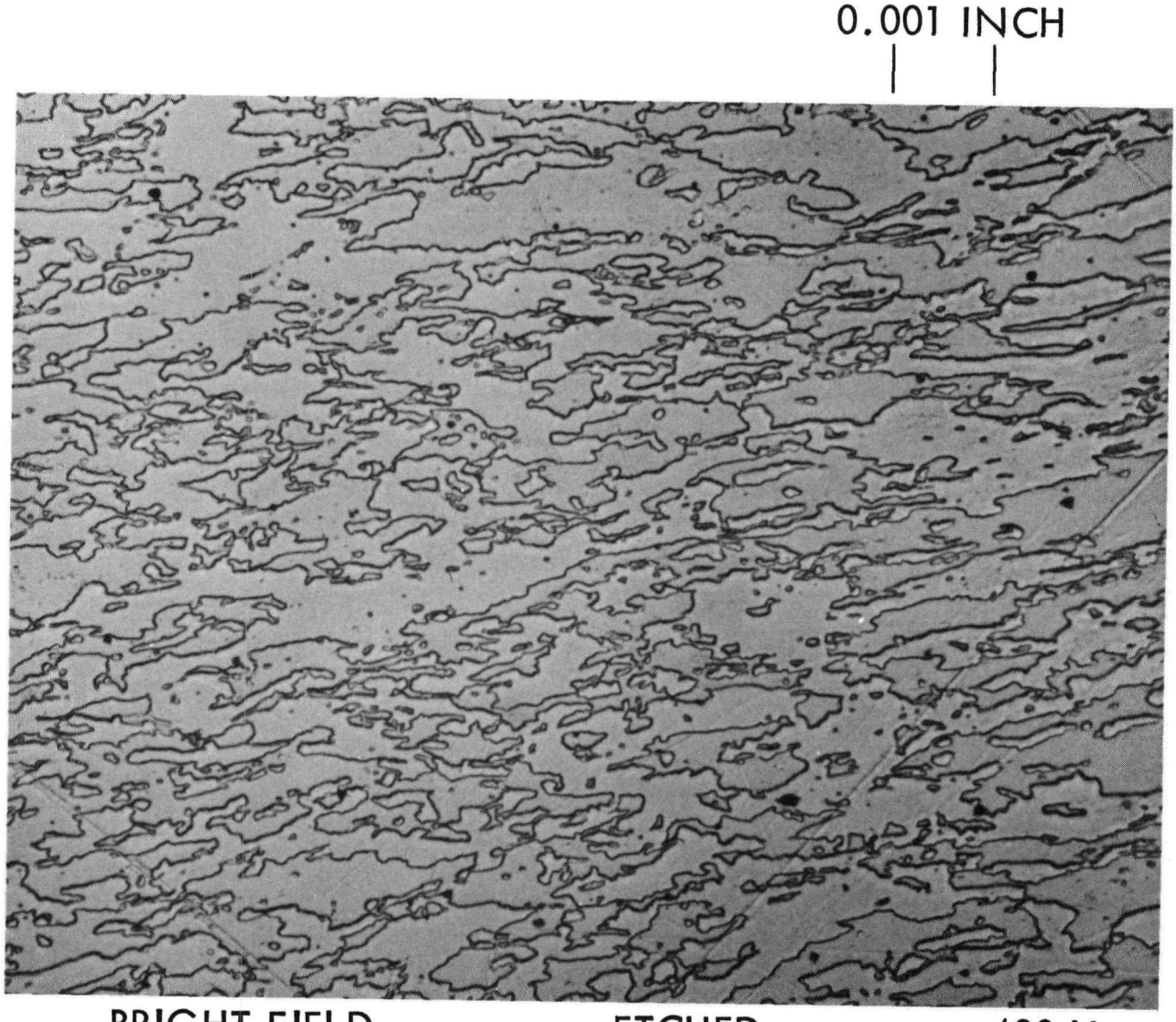

FIG. H-18. MICROSTRUCTURE OF AS-RECEIVED Pt-20% Rh TUBING

left small uncoated areas (~0.003-inch diameter) distributed uniformly over the entire strip so as to leave ~15% of the strip bare. Also, there were areas at the edges of the strips of iron titanate which had the appearance of pure TiO_2 (white colored).

TABLE H-4

Hemispherical Total Emittance--Iron Titanate Coated Pt-20% Rh
Specimen 1

Temperature (°F)	As Plasma Arc Sprayed	Space Operational (1950° F vacuum in contact with graphite) 1.0 Day	9.0 Days	90 Days	Re-entry (3000° F air in contact with graphite) 2 Minutes	On-the-Ground Abort (1600° F) 18 Days	180 Days
1000	0.080*	0.89	0.86	0.77	0.48		
	0.83	0.89	0.86	0.78	0.47		
1400	0.82	0.87	0.84	0.78	0.53		
	0.83	0.88	0.86	0.77	0.49		
1850	0.83	0.87	0.86	0.78	0.53		
	0.83	0.87	0.86				
2000	0.83	0.87	0.86				

*If two emittance values are shown for any given test point, the first was obtained on heating the specimen and the second on cooling the specimen.

TABLE H-5

Hemispherical Total Emittance--Iron Titanate Coated Pt-20% Rh
Specimen 2

Temperature (°F)	As Plasma Arc Sprayed	Space Operational (1950° F vacuum in contact with graphite) 1.0 Day	9.0 Days	90 Days	Re-entry (3000° F air in contact with graphite) 2 Minutes	On-the-Ground Abort (2000° F) 18 Days	180 Days
1000	0.80*	0.84	0.83	0.69	0.52		
	0.80	0.84	0.83	0.69	0.52		
1400	0.79	0.84	0.83	0.67	0.53		
	0.81	0.83	0.83	0.67	0.53		
1850	0.81	0.84	0.84	0.67	0.56		
	0.81	0.84	0.85	0.66	0.55		
2000	0.81	0.84	0.86	0.67	0.56		

*If two emittance values are shown for any given test point, the first was obtained on heating the specimen and the second on cooling the specimen.

In contrast to iron titanate, the adherence of the exposed calcium titanate was unchanged; no chipping or pealing was seen (Fig. H-19). The only apparent change was in color; areas of calcium titanate which had apparently been in intimate contact with the ATJ graphite were dark gray compared with areas on the same strip which were

CONFIDENTIAL

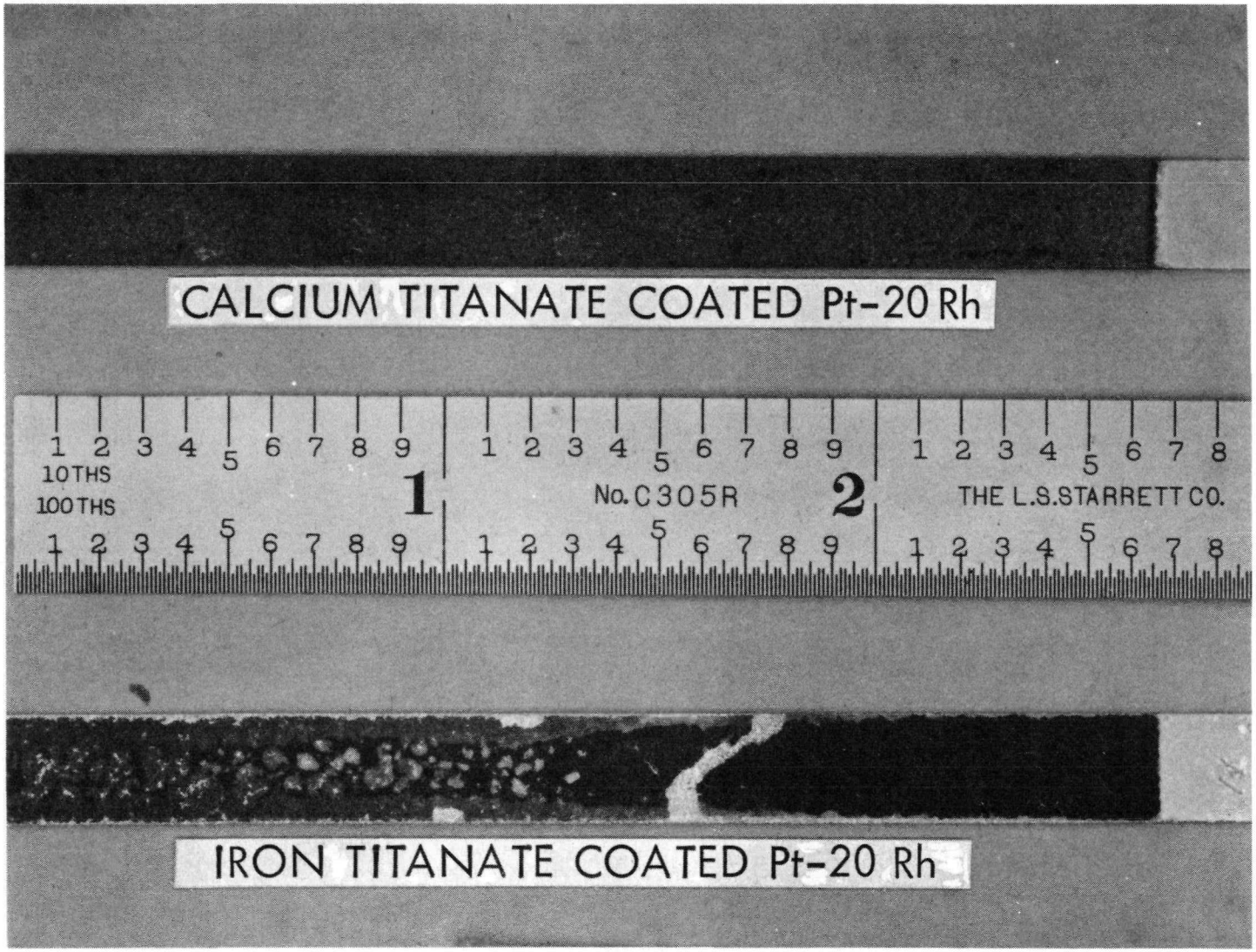

FIG. H-19. EMISSIVE COATINGS AFTER 90-DAY OPERATIONAL EXPOSURE IN CONTACT WITH ATJ GRAPHITE

CONFIDENTIAL

light colored. Hemispherical total emittance measurements in vacuum showed the calcium titanate to be highly stable (Tables H-6 and H-7). Within experimental error (±0.02-0.03), the emittances were unchanged from the measurements previously made after the nine-day exposures.

TABLE H-6

Hemispherical Total Emittance--Calcium Titanate Coated Pt-20% Rh
Specimens 3 and 6

Temperature (°F)	As Plasma Arc Sprayed	Space Operational (1950° F vacuum in contact with graphite) 1.0 Day	9.0** Days	90 Days	Re-entry (3000° F air in contact with graphite) 2 Minutes	On-the-Ground Abort (1600° F) 18 Days	180 Days
1000	0.80*	0.85	0.86	0.86	0.63		
	0.81	0.85	0.87	0.86	0.73		
1400	0.81	0.84	0.85	0.86	0.60		
	0.81	0.85	0.86	0.84	0.72		
1850	0.82	0.85	0.86	0.85	0.74		
	0.81	0.84	0.86	0.84	0.82		
2000	0.82	0.85	0.87	0.86	0.82		

*If two emittance values are shown for any given test point, the first was obtained on heating the specimen and the second on cooling the specimen.
**Specimen 6 was substituted for Specimen 3 after the 1.0-day run because of the oxidation of Specimen 3.

TABLE H-7

Hemispherical Total Emittance--Calcium Titanate Coated Pt-20% Rh
Specimens 4 and 8

Temperature (°F)	As Plasma Arc Sprayed	Space Operational (1950° F vacuum in contact with graphite) 1.0 Day	9.0** Days	90 Days	Re-entry (3000° F air in contact with graphite) 2 Minutes	On-the-Ground Abort (2000° F) 18 Days	180 Days
1000	0.87*	0.83	0.87	0.82	0.70		
	0.82	0.84	0.86	0.82	0.73		
1400	0.82	0.83	0.84	0.82	0.67		
	0.81	0.84	0.84	0.80	0.73		
1850	0.83	0.84	0.84	0.81	0.80		
	0.82	0.84	0.84	0.80	0.80		
2000	0.82	0.84	0.84	0.80	0.82		

*If two emittance values are shown for any given test point, the first was obtained on heating the specimen and the second on cooling the specimen.
**Specimen 8 was substituted for Specimen 4 after the 1.0-day run because of the oxidation of Specimen 4.

Electron beam microprobe analyses were performed on other coated Pt-20% Rh strips which had been heated to 1950° F in vacuum for 90 days in the same graphite block as the emittance specimens. Figure H-20 shows the electron microprobe data in the form of back scattered electron scans and elemental X-ray pictures. The iron titanate was coated with electroless nickel after the high temperature testing to help preserve the iron titanate coating edge during metallographic specimen grinding and polishing. The back scattered electron scans in Fig. H-20 show the gross distribution of elements as a function of average atomic number; the lighter a given area is the higher is the average atomic number. The Pt-20% Rh cladding is therefore the lightest area on the back scattered electron scans. The X-ray pictures show the distribution of the elements iron, titanium and calcium. Note that all of the detectable iron has diffused from the iron titanate into the Pt-20% Rh. Qualitative microprobe analyses (line profile data more sensitive than the X-ray pictures) showed high concentrations (several percent) of iron extending into the substrate, a distance of 0.008-inch from the two iron titanate/Pt-20% Rh interfaces (both sides of the strip were coated). The X-ray pictures of the calcium titanate coated Pt-20% Rh in Fig. H-20 show no interaction between the coating and substrate; the more sensitive line profile data on strip charts also revealed no interaction.

2. Evaluation of Iron and Calcium Titanates as Emissive Coatings for Pt-20% Rh After Two-Minute Re-entry Exposure

The same Pt-20% Rh strip specimens which had undergone the 90-day operational exposure were placed in tight-fitting slots cut in ATJ graphite blocks and pushed rapidly into a tube furnace preheated to 3000° F in air and held for two minutes after temperature equilibration (7 minutes total time in furnace). Stereo microscopic examination of the exposed strips showed a gross iron titanate/Pt-20% Rh interaction. In one case 70% of the iron titanate had flaked off the substrate. Any adhering iron titanate (in contact with graphite) had reacted extensively with the substrate. Total hemispherical emittance measurements on two specimens (Tables H-4 and H-5) clearly showed the effect of the loss of coating material on emittance; in one case, the emittance dropped from 0.77 to 0.48.

The calcium titanate coating remained very adherent and was not even slightly cracked. The only visible change in the calcium titanate was that it appeared glassy and large areas (up to 95%) were dark gray; other areas had bleached white. It is hypothesized that the burning graphite and the resultant reducing atmosphere (carbon monoxide) is responsible for the reduction, as evidenced by the dark color, of the calcium titanate. Hemispherical total emittance measurements (Tables H-6 and H-7) showed that the bleaching of calcium titanate in air at high temperatures with a resultant loss of emittance was a reversible phenomenon. A careful scrutiny of the data in Tables H-6 and H-7 will reveal that the hemispherical emittance of calcium titanate after re-entry exposure increases with measurement temperature; e.g., it is highest at 2000° F. The reason for this increase is not measurement temperature, but a result of time at elevated temperature in vacuum. The high temperature vacuum treatment converts stoichiometric calcium titanate, $CaTiO_3$, to a substoichiometric form, $CaTiO_{2-x}$. Substoichiometric or oxygen deficient calcium titanate is the high emittance form.

Other coated Pt-20% Rh strips which had been exposed to a 3000° F re-entry environment were analyzed by electron beam microprobe and metallographic techniques. Figure H-21 shows the electron microprobe data in the form of back-scattered electron scans and elemental X-ray picutres. No difference was seen between these data for iron titanate after re-entry and those after the 90-day operational exposure (Fig. H-20). The reasons no further reaction was detected after re-entry are: all of the

90-DAY OPERATIONAL
1950°F

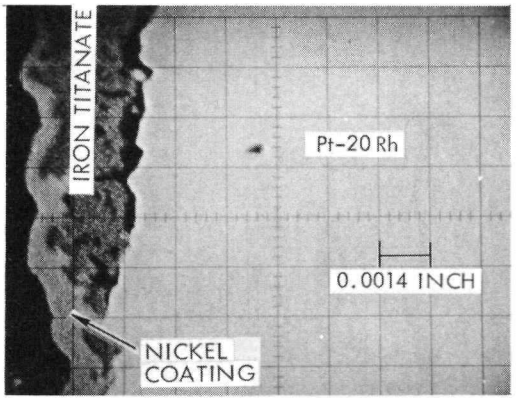

BACK SCATTERED ELECTRON NO. 11

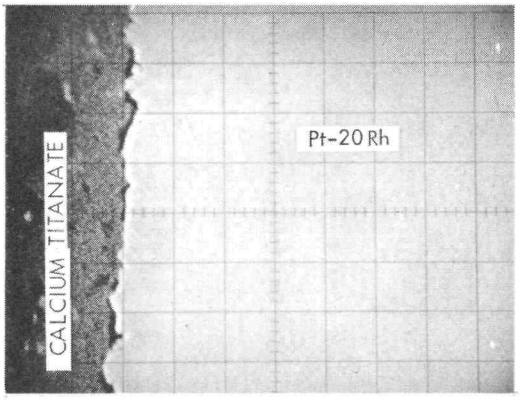

BACK SCATTERED ELECTRON NO. 12

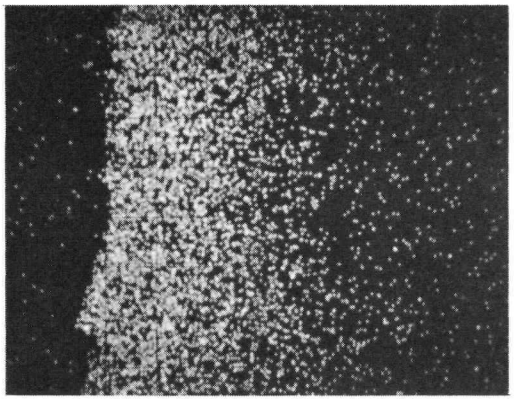

Fe X-RAY

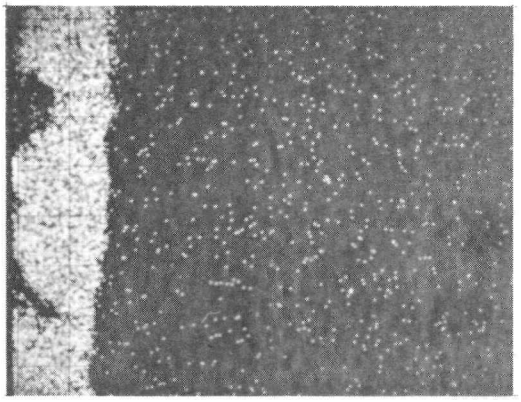

Ca X-RAY

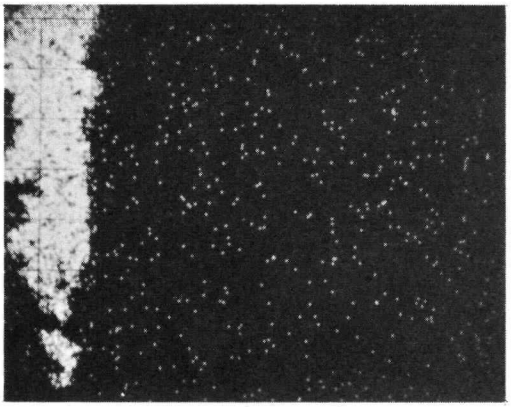

Ti X-RAY

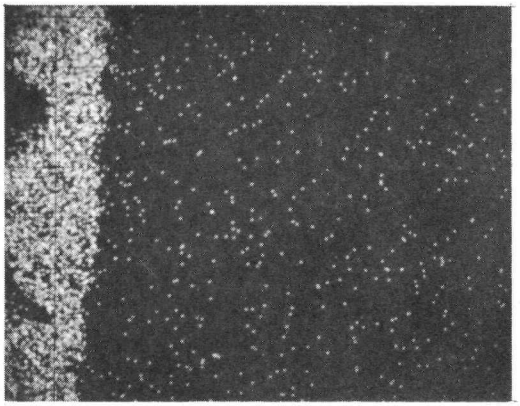

Ti X-RAY

FIG. H-20. ELECTRON MICROPROBE DATA

REENTERED
3000°F

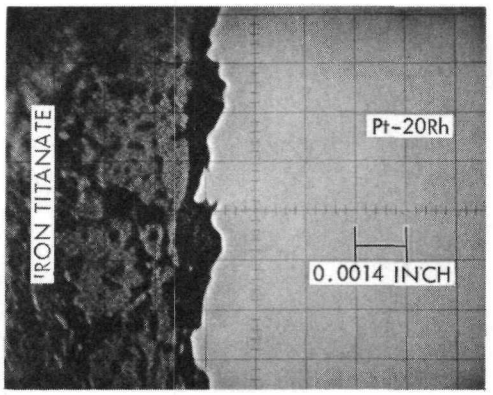

BACK SCATTERED ELECTRON NO. 13

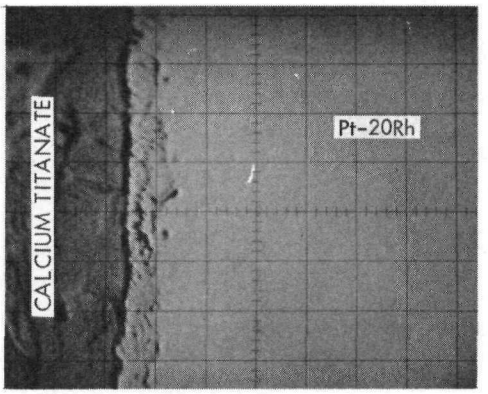

BACK SCATTERED ELECTRON NO. 14

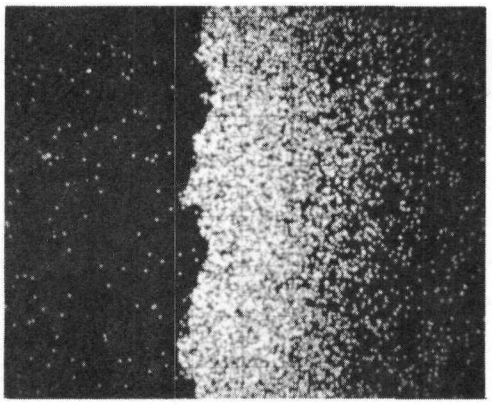

Fe X-RAY

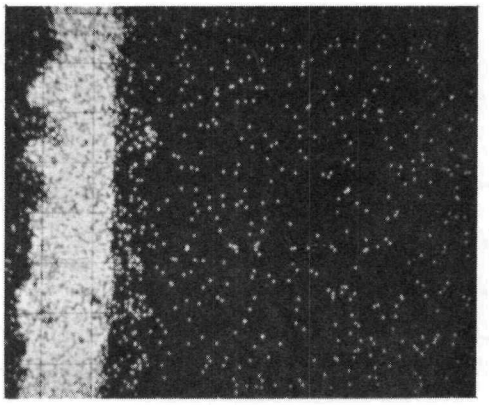

Ca X-RAY

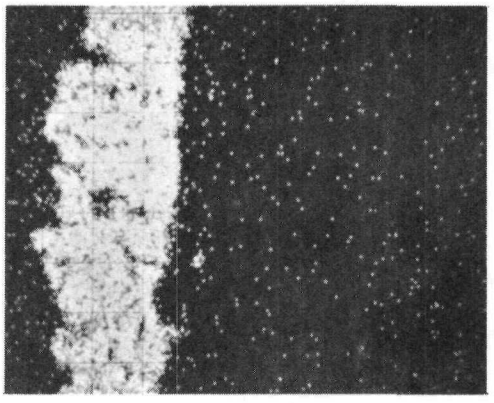

Ti X-RAY

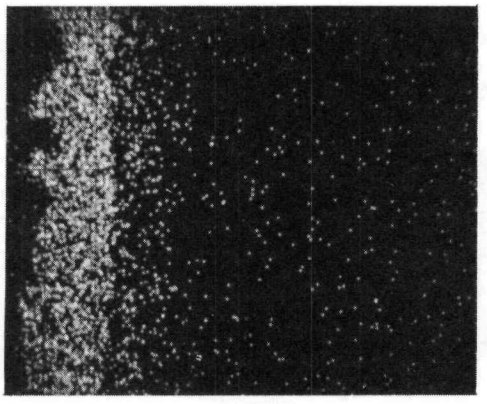

Ti X-RAY

FIG. H-21. ELECTRON MICROPROBE DATA

iron in the iron titanate had already diffused into the Pt-20% Rh during the 90-day operational exposure; and there was actually very little contact between the coating and substrate after the 90-day operational exposure. The electron microprobe data for calcium titanate coated Pt-20% Rh in Fig. H-21 show that some chemical interaction occurred between the coating and substrate. The calcium and titanium X-ray pictures show that both elements diffused into the Pt-20% Rh substrate; calcium was detected a distance of 0.7 mil from the coating/substrate interface and titanium a distance of 1.5 mils. The photomicrograph in Fig. H-22 clearly shows the interaction zone. A second re-entry experiment at 2800° F was performed with calcium titanate coated Pt-20% Rh which had undergone the 90-day operational exposure. Results of the electron microprobe analyses of the 2800° F re-entered specimen showed no calcium diffusion into the substrate; titanium, however, had diffused a distance of 1.4 mils.

3. *High Temperature Chemical Stability of Iron Titanate in Contact with ATJ Graphite and Pt-20% Rh in Air*

In addition to the long term emittance stability tests with coated strips, experiments were performed to determine the maximum permissible re-entry temperature of iron titanate coated Pt-20% Rh. That temperature was obviously below 3000° F if one used the criterion that no gross interaction should occur between the coating and substrate.

The Pt-20% Rh strips (1/4 inch wide x 0.020 inch thick x 2 inches long), coated on both sides with plasma arc sprayed iron titanate (0.004-inch thick), were placed in tight-fitting slots cut in ATJ graphite blocks and heated to 2600° and 2800° F for three minutes in air at atmospheric pressure. The graphite blocks (~3/4-inch square x 3 inches long) were pushed rapidly into furnaces preheated to 2600° and 2800° F to simulate re-entry conditions. Metallographic and electron microprobe analyses showed the following:

(1) Simulated re-entry at 2600° F caused only a slight amount of iron titanate/Pt-20% Rh interaction. Metallographic examinations revealed no interactions (Fig. H-23); electron microprobe analyses showed detectable iron diffusion from the iron titanate into the Pt-20% Rh to a depth of ~0.002 inch. The detectable limit for iron in this case was in the 0.2 to 0.3 wt % range.

(2) Simulated re-entry at 2800° F caused a massive iron titanate Pt-20% Rh interaction (Fig. H-23). Metallographic examination showed an interaction zone extending 0.017 inch through the 0.020-inch Pt-20% Rh strip. Electron microprobe analyses showed detectable iron diffusion (no titanium) through 0.0185 inch of the Pt-20% Rh strip. The major interaction occurred from one side only, apparently because of a lack of good graphite contact with the iron titanate coating on the opposite side. The iron penetrated from the opposite side to a depth of 0.0005 inch leaving only ~0.001 inch of the original 0.020-inch thick Pt-20% Rh strip with an iron content less than ~0.25 wt %.

Since the high purity Cerac Special iron titanate coating used in these tests is marginal for a 2600° F re-entry and entirely inadequate for a 2800° F re-entry, it was decided to compare the high temperature behavior of the Cerac Special material with iron titanate from two other sources, Continental Coatings and TRW Systems. Although the Cerac Special material was selected early in the program because of its high purity, there was a remote chance that iron titanate from a different supplier would be more chemically stable in contact with graphite and Pt-20% Rh than the Cerac Special iron titanate.

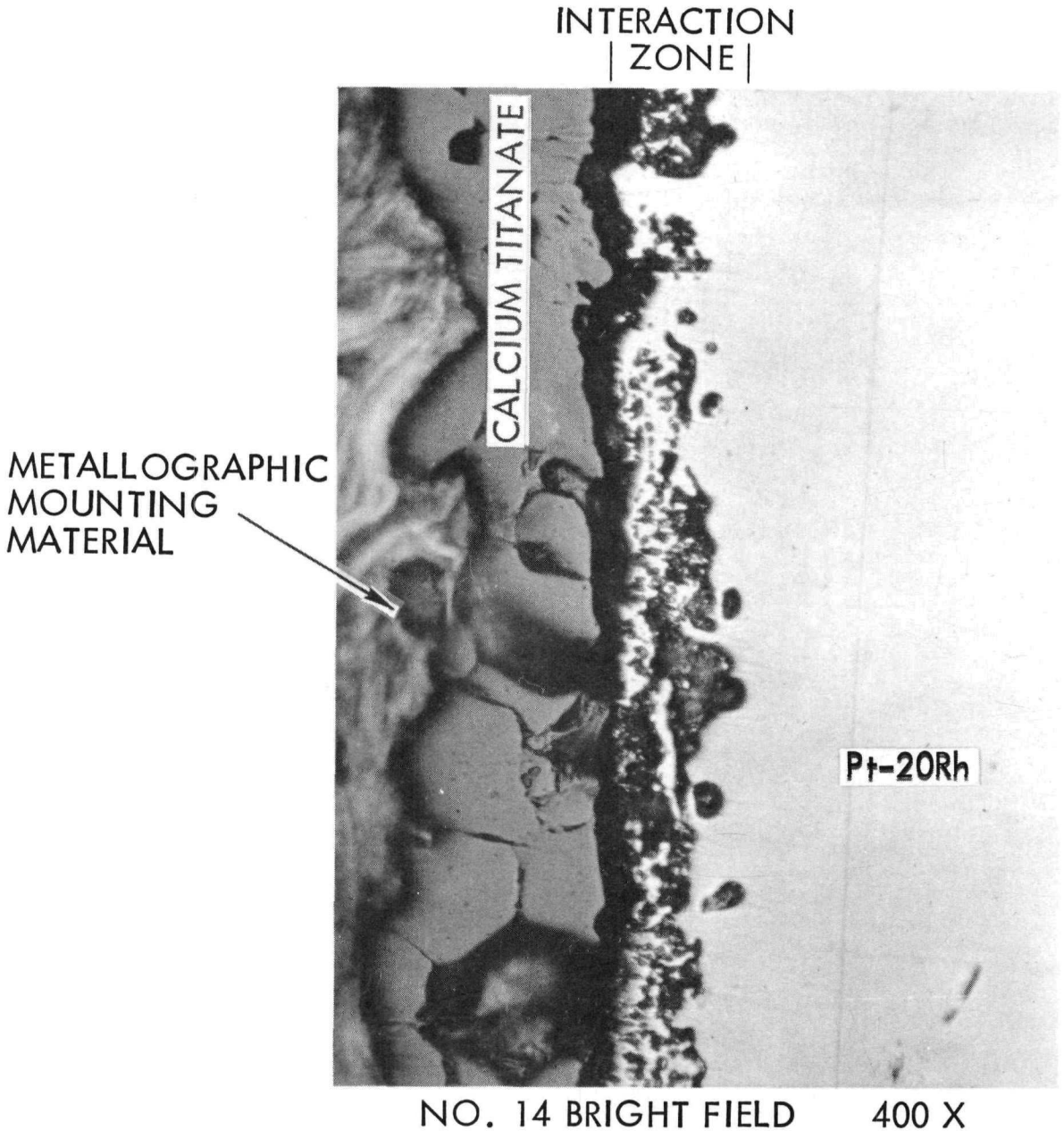

FIG. H-22. CALCIUM TITANATE COATED Pt-20% Rh AFTER RE-ENTRY EXPOSURE AT 3000° F

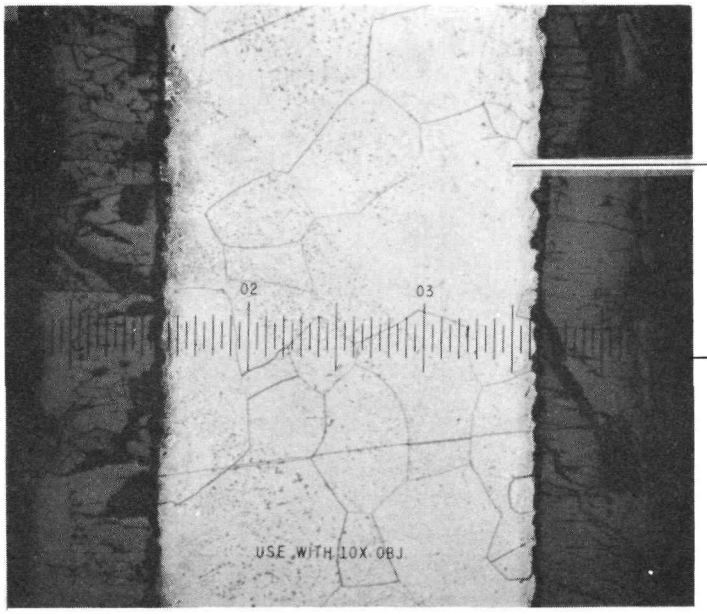

BRIGHT FIELD ETCHED

2600°F

REACTION ZONE

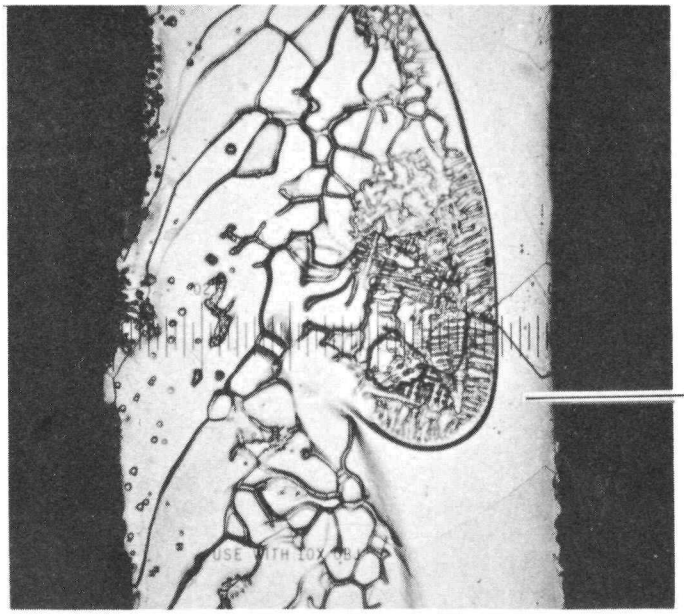

BRIGHT FIELD ETCHED

2800°F

FIG. H-23. RE-ENTERED IRON TITANATE COATER Pt-20% Rh

Iron titanate powder from three sources--Cerac, Continental Coatings, and TRW--was heated in air at atmospheric pressure in a graphic boat from 2400° F to progressively higher temperatures until complete melting of each iron titanate was observed under a stereo microscope at 30X. New iron titanate specimens in a graphite boat were inserted into an electric furnace after each step rise in temperature. The specimens were held for approximately three minutes at temperature prior to removal from the furnace and microscopic examination. Temperatures were measured with a Pt/Pt-13% Rh thermocouple inserted in the graphite block. The following observations were made concerning the iron titanate during the course of the experimentation:

a. TRW iron titanate

The material appeared single-phased at 30X in the as-prepared condition and throughout the stepwise heating until it completely melted.

Complete melting in air in contact with ATJ graphite occurred in the 2505° to 2525° F temperature range.

b. Continental coating iron titanate (FCT-11H)

This material is the natural mineral ilmenite and has been studied for almost a decade by Pratt and Whitney Aircraft under a contract from NASA. At 30X, the material appears multiphased (six or more different chemical species) until it completely melts. Prior to melting, the particles have the appearance at 30X of multicolored, smooth stones; this appearance contrasts sharply with the sintered particle appearance of the other two iron titanates studied (Fig. H-24).

Complete melting in air in contact with ATJ graphite occurred in the 2606° to 2635° F temperature range.

c. Cerac special iron titanate

This material, as was the case with the TRW material, was synthesized by reacting equimolar quantities of iron oxide (Fe_2O_3) and titanium (TiO_2) in the solid state. Although the synthesis details are proprietary to Cerac Incorporated, it is obvious that their material was reacted at a much lower temperature than the 2600° F reaction temperature used by TRW. The Cerac material at 30X appears two-phased until heated to 2459° F in air in contact with ATJ graphite. Three minutes at 2459° F is enough time for the two phases to react and form a single phase as observed microscopically at 30X.

Complete melting in air in contact with ATJ graphite occurred in the 2492° to 2505° F range.

Since the experiments discussed in this section showed a slight interaction between the Cerac iron titanate (in contact with graphite) and Pt-20% Rh at 2600° F and gross interaction at 2800° F, the next logical step was to investigate and compare the chemical compatibility of all three iron titanates with Pt-20% Rh in contact with ATJ graphite in air at 2800° F.

Three holes (1/2-inch diameter x 1/2-inch deep) were drilled in an ATJ graphite block (3/4-inch square x 2-1/2 inches long), and each hole was half filled with a different iron titanate than TRW, Continental Coatings or Cerac. A Pt-20% Rh end cap (0.2-inch diameter x 0.040-inch thick), fabricated for the cylinder environmental tests, was placed in each half-filled hole and covered with ~1/4-inch of iron titanate. The ATJ graphite block with end caps and iron titanate were inserted into an electric

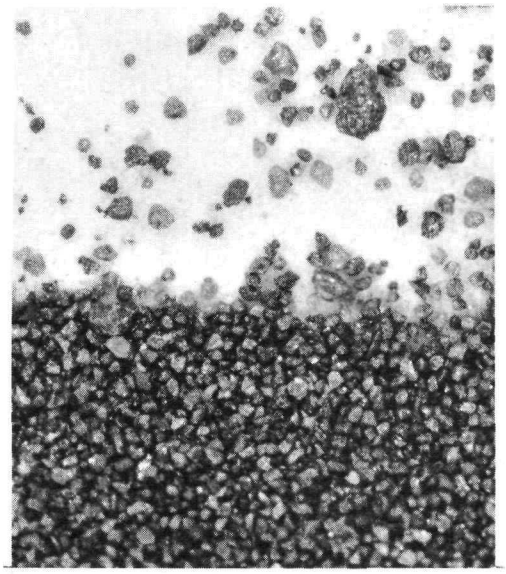

CERAC SPECIAL
PARTICLE SIZE: 44-105 MICRONS

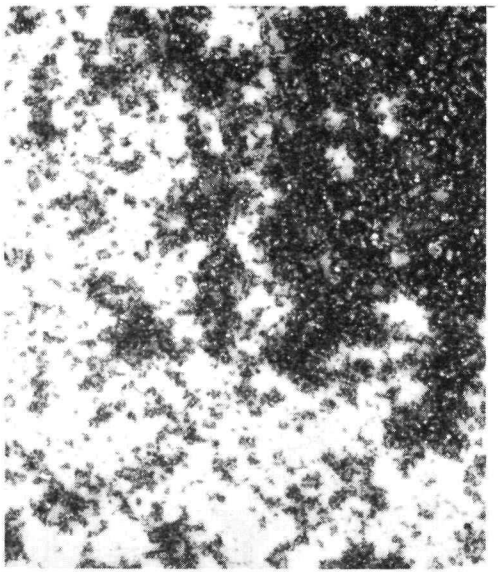

TRW SYNTHESIZED
PARTICLE SIZE: <44 MICRONS

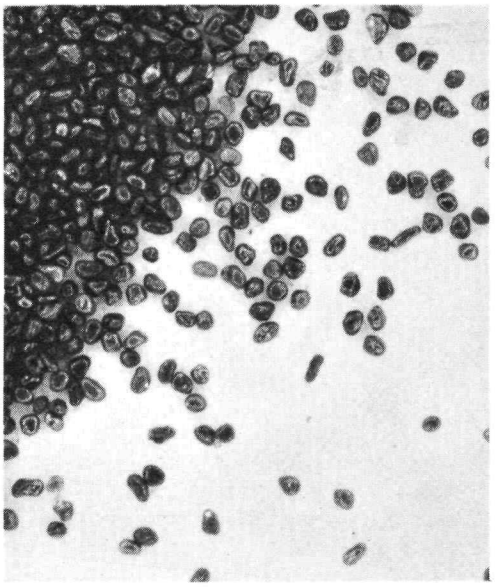

CONTINENTAL COATINGS FCT-11H
PARTICLE SIZE: 44-105 MICRONS

FIG. H-24. IRON TITANATE POWDERS IN THE AS-RECEIVED CONDITION

furnace and held at 2800° F for three minutes in air at atmospheric pressure. The result was a gross interaction between each of the iron titanates and the buried Pt-20% Rh end caps. Metallographic examination of the end caps revealed a metal structure riddled with holes with an appearance much like lacework (Fig. H-25).

Throughout the SNAP 29 program, it has been observed that graphite drastically lowers the melting point of iron titanate in air. Therefore, an investigation was carried out to determine the high temperature behavior of iron titanate in contact with Pt-20% Rh without graphite.

Two Pt-20% Rh plates (1/2 inch wide x 2 inches long x 0.040 inch thick) were dimpled in order to form three hemispherical-shaped depressions 1/4 inch in diameter by 1/16 inch deep spaced 1/2 inch apart. The three depressions were filled with iron titanate from Continental Coatings, TRW and Cerac. In air, each of the three iron titanates completely melted in the 2750° to 2800° F range; evidence of complete melting was not apparent by microscopic (30X) examination after the three specimens were heated to 2700° F.

Chemical compatibility tests between each of the three molten iron titanates (no graphite in system) and Pt-20% Rh were conducted at 2800° F and 3000° F for three minutes in air at atmospheric pressure. Metallographic examinations revealed no interactions between the iron titanates and Pt-20% Rh at 2800° F (Fig. H-26). At 3000° F, no interactions between the TRW or Continental Coatings iron titanate were detected; a very localized interaction (cross-section shows a zone with a ~0.010-inch diameter centered on the iron titanate/Pt-20% Rh interface) was seen between the Cerac material and the Pt-20% Rh (Fig. H-27). Based on the metallographic examinations, it is concluded that both the TRW synthesized iron titanate and the Continental Coatings iron titanate would be compatible with a Pt-20% Rh substrate during a 3000° F re-entry if no graphite was in contact with the coating. The cause of the Cerac incompatibility is not known, but the unusual local attack suggests the presence of an impurity such as carbon at that point. Other cross sections of the same specimen showed no interactions between the Cerac iron titanate and Pt-20% Rh.

4. Emittance Stability of Calcium Titanate as Function of Exposure to Air at Elevated Temperatures

Early in the SNAP 29 program at TRW, it was learned that the visible color (black, white or gray) of calcium titanate was a function of its exposure to oxidizing or reducing gases at elevated temperature. The importance of this observation is the fact that the total hemispherical emittance was found to vary with the visual color, the blacker the coating, the higher its emittance. Since it was observed that the coating bleached when heated in air (except when in intimate contact with graphite), the emittance stability of calcium titanate exposed to air at elevated temperatures was questioned. The effects of short-term air exposure at the capsule fabrication temperature (300° F), and fuel block loading storage shipment temperature (1600° F) on stability were studied by means of thermogravimetric analysis, high temperature X-ray diffraction and total hemispherical emittance measurements.

a. Thermogravimetric analysis of calcium titanate

Specimens of plasma arc sprayed, black colored calcium titanate (1/4 inch x 1/2 inch x 0.050 inch) weighing ~0.4 gram were held at 300°, 1400° and 1600° F for one hour on a thermobalance. The air flow rate past the porcelain crucible in which each specimen was placed was ~10 ft/hr. A summary of the information learned is given here:

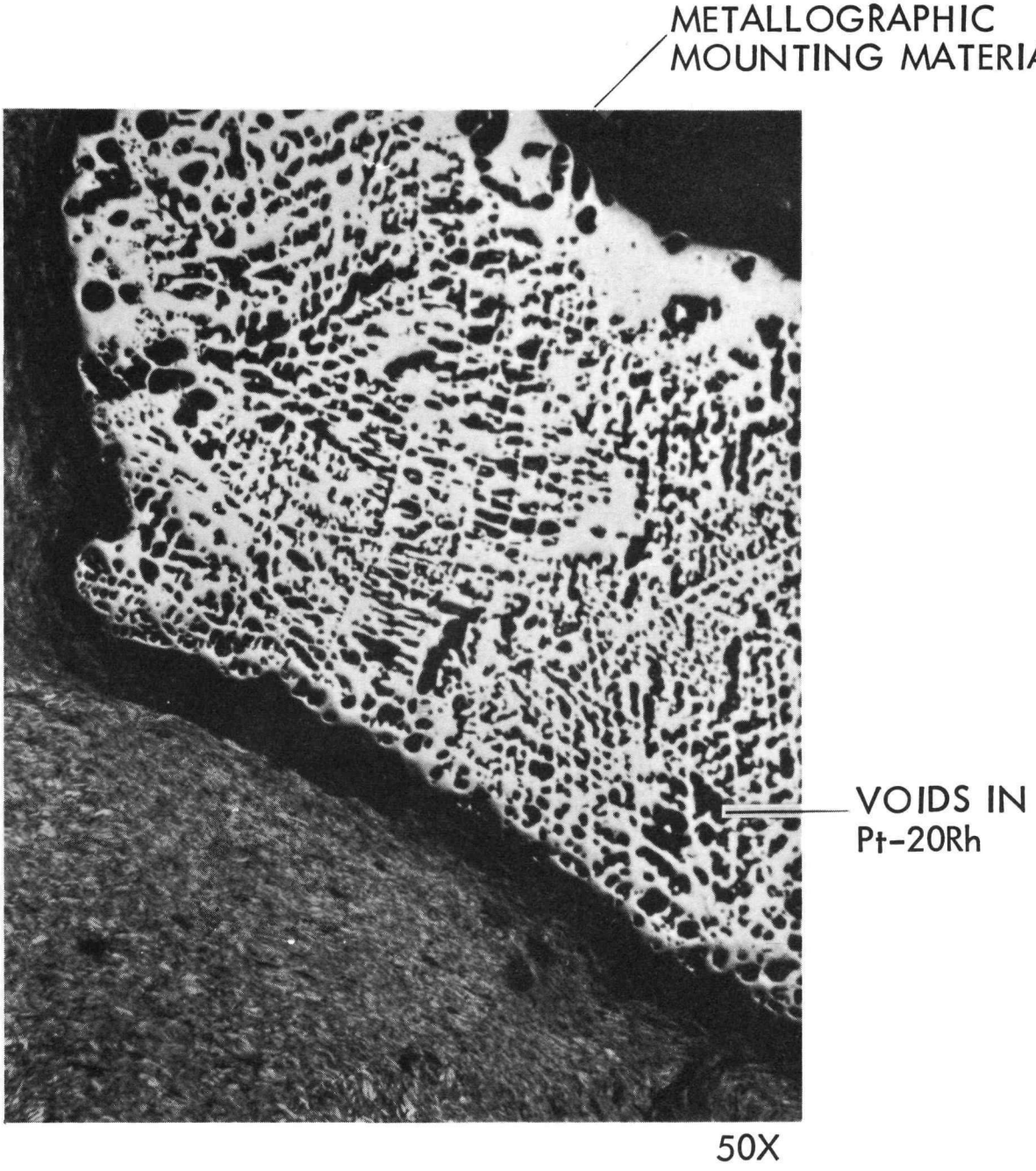

FIG. H-25. Pt-20% Rh HEATED TO 2800° F IN AIR FOR THREE MINUTES IN CONTACT WITH ATJ GRAPHITE AND IRON TITANATE

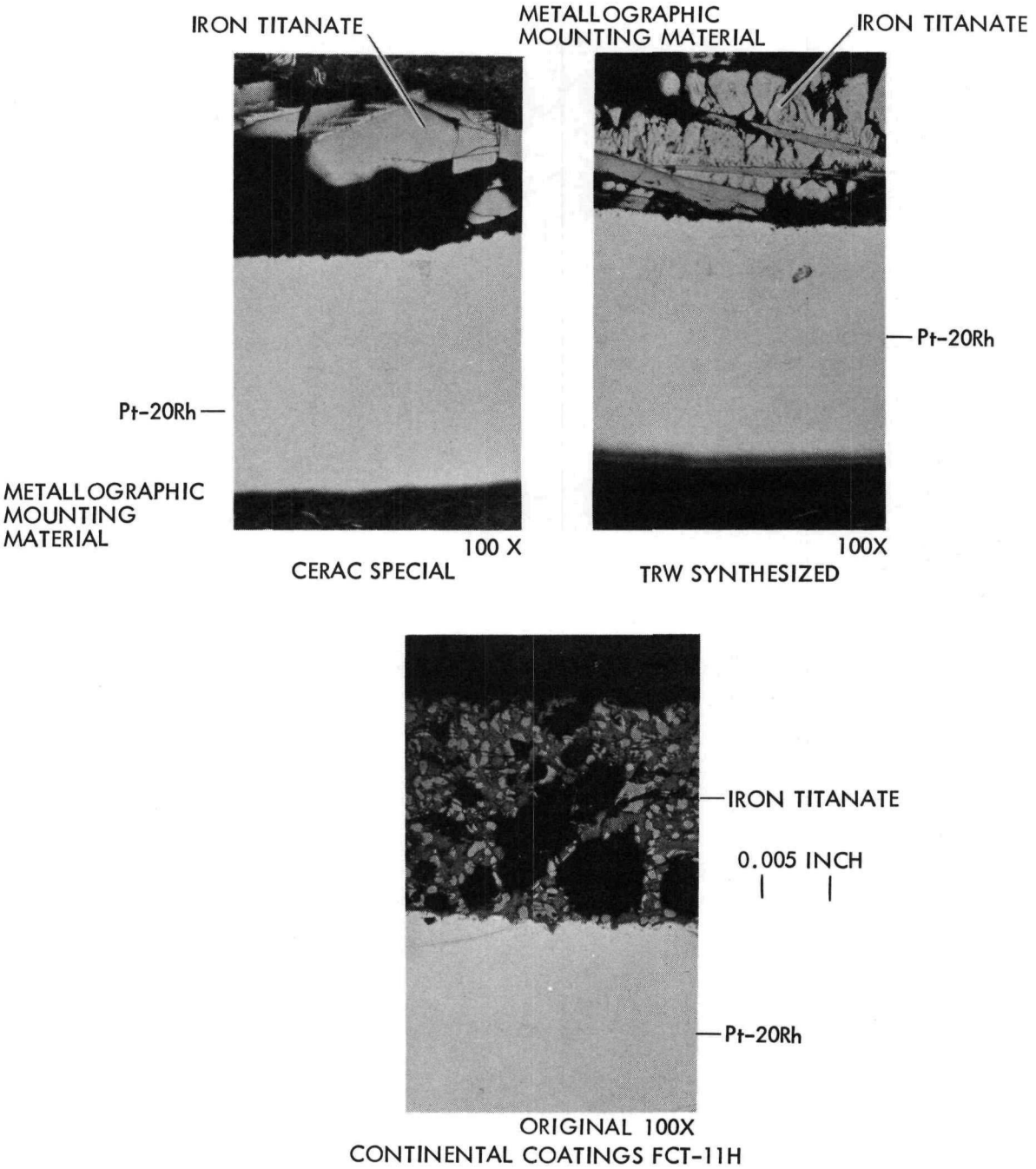

FIG. H-26. IRON TITANATE HEATED TO 2800° F IN AIR FOR THREE MINUTES WITHOUT GRAPHITE

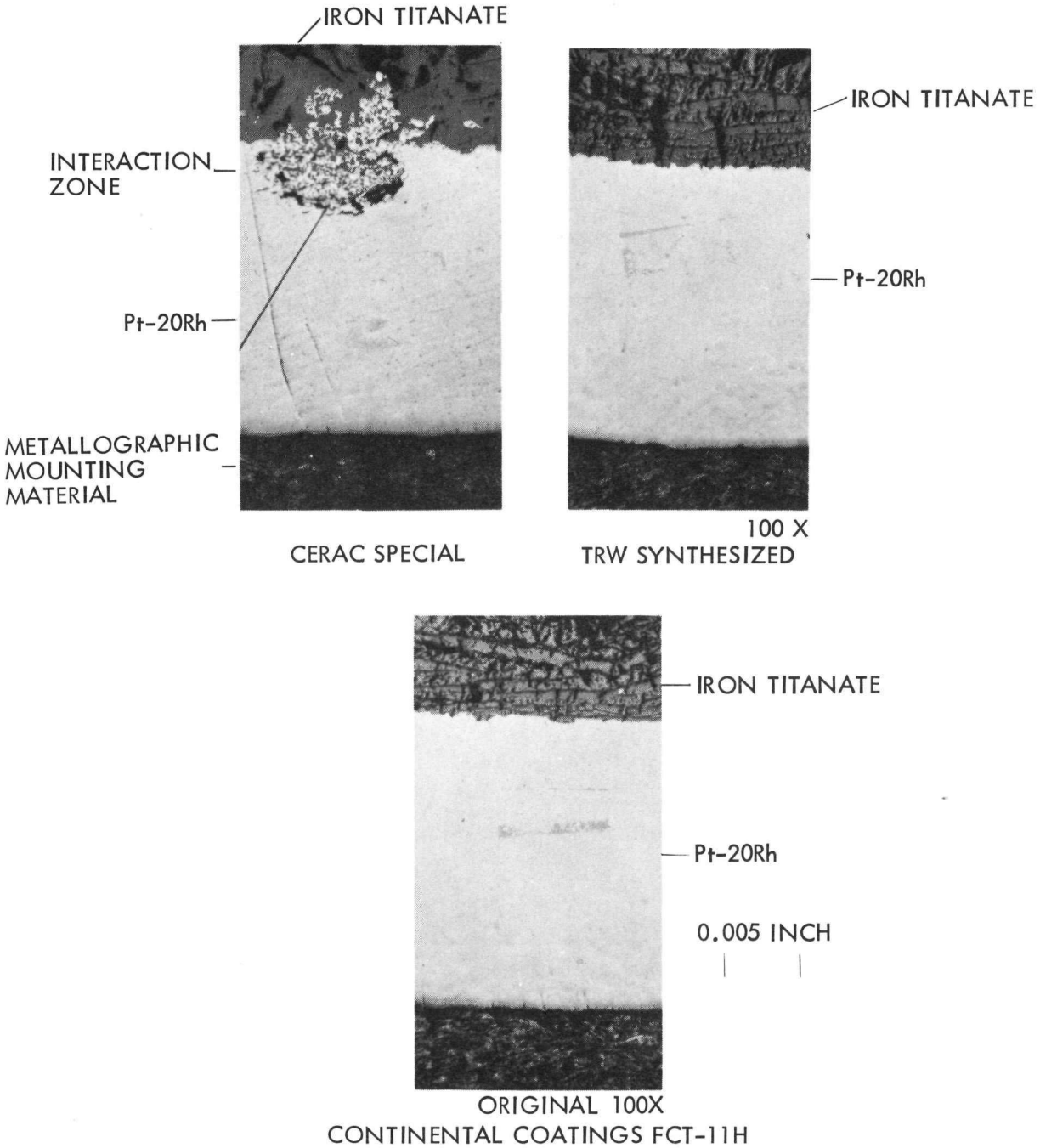

FIG. H-27. IRON TITANATE HEATED TO 3000° F IN AIR FOR THREE MINUTES WITHOUT GRAPHITE

(1) Exposure to 300° F air at atmospheric pressure for one hour caused no color or weight changes in the black calcium titanate.

(2) Exposure to 1400° and 1600° F air at atmospheric pressure caused the black calcium titanate to bleach to white or a light cream color. A weight gain of 6% occurred within a few seconds and increased to 10% after one hour.

(3) Assuming that $CaTiO_3$ is the highest oxidation state of calcium titanate, and 10% is its maximum possible weight gain in air after plasma arc spraying, the stoichiometry of plasma arc sprayed calcium titanate (black colored) is $CaTiO_{2.23}$. This represents an oxygen reduction of 7 at .%, from 60 at .% to 53 at .% during the plasma arc spraying process.

b. X-ray diffraction analyses of calcium titanate

X-ray diffraction analyses in air using a high temperature diffractometer attachment were performed on calcium titanate plasma arc sprayed on a platinum substrate. X-ray patterns of calcium titanate were obtained at room temperature before and after oxidation; a pattern was also obtained at 1850° F. The only crystallographic change noted, other than that attributable to thermal expansion of the crystal lattice (1850° F data), was the appearance of two additional lines in the room temperature pattern of the white colored oxidized specimen. The interplanar spacings of the lines were d = 0.93451Å and d = 0.93267Å. Although the meaning of these extra crystallographic lines or planes is not entirely clear, it is hypothesized that the lack of these lines in the black, as plasma arc sprayed specimens is a result of the oxygen deficiency in the crystal lattice.

c. Hemispherical total emittance measurements

The experiments described showed in detail how heating plasma arc sprayed calcium titanate in air affected its visual color, oxygen stoichiometry and crystal structure. To study the effect of air oxidation on hemispherical total emittance, a Pt-20% Rh strip (1/4 inch wide x 0.020 inch thick x 5 inches long) coated on both sides with 0.004-inch thick plasma arc sprayed calcium titanate was heated for 10 minutes in air at 300°, 1400° and 1500° F; emittance measurements were made in vacuum before and after each air heat treatment. The hemispherical total emittances measured are shown in Table H-7. The important conclusions to be drawn from the emittance data measured in vacuum are:

(1) Air exposure at 300° F for 10 minutes did not change the hemispherical total emittance of plasma arc sprayed calcium titanate on Pt-20% Rh.

(2) Air exposure at 1400° and 1600° F for 10 minutes reduced the hemispherical total emittance of plasma arc sprayed calcium titanate on Pt-20% Rh by ~ 25% (from 0.8 to 0.6).

(3) Exposure of oxidized plasma arc sprayed calcium titanate on Pt-20% Rh (oxidized at 1400° and 1600° F) to a vacuum of 1×10^{-6} torr at 1850° to 2000° F for one hour increased its emittance by ~33% (from 0.6 to 0.8).

The ability of calcium titanate to rejuvenate its emittance by high vacuum oxygen reduction at an elevated temperature removes one of the principal objections against its selection as the primary high emittance coating for Pt-20% Rh claddings.

TABLE H-7

Hemispherical Total Emittance of Calcium Titanate Measured in Vacuum

Exposure (same specimen each time)	1000° F	1850° F	2000° F
9 days in vacuum at 1950° F	0.84/0.82*	0.81/0.81	0.82
10 minutes in air at 300° F	0.84/0.83	0.81/0.82	0.83
10 minutes in air at 1400° F	0.67/0.84	0.82/0.82	0.83
10 minutes in air at 1600° F	0.63/0.82	0.80/0.80	0.81

*The first value was obtained on heating and the second on cooling. The specimen was exposed to high vacuum at 1850° to 2000° F for a period of about one hour prior to the cooldown remeasurements.

5. Deletion of Iron Titanate as Emissive Coating Candidate

Based on the experimental results obtained to date, much of which is described in the previous sections, iron titanate will be dropped as an emissive coating for the SNAP 29 Pt-20% Rh/graphite intact re-entry heat source system. The principal concern is that plasma arc sprayed iron titanate in contact with graphite chemically reacts with Pt-20% Rh. This interaction seriously degrades the oxidation resistance of the Pt-20% Rh and thereby negates its usefulness as an oxidation protective cladding for the radioisotope capsule outer liner or strength member. The poor adherence of iron titanate to Pt-20% Rh after the 90-day operational test was also a factor considered in making the decision to drop it as a coating candidate. Table H-8 summarizes the key experimental results obtained with the iron titanate and calcium titanate coatings and presents the available data on a platinized alumina coating which is an attractive alternative to the iron titanate coating. A platinized alumina coating will be initially evaluated (preliminary characterizations) and, if promising, will be tested in accordance with the original program plan. A platinized yttria coating will also undergo preliminary characterization. This coating would appear to be from thermodynamic and crystallographic considerations more stable than the platinized alumina coating, but has the disadvantage that no development work has been performed on it. With the exception of an apparently minor interaction between calcium titanate and the Pt-20% Rh substrate in a 2800° F simulated re-entry test, the calcium titanate coating has, to date, passed all tests satisfactorily.

6. Abort Environmental Exposure of Long Term Emittance Stability Specimens

The same strips (1/4 inch wide x 6 inches long x 0.020 inch thick) of Pt-20% Rh coated with calcium titanate that had undergone a 90-day vacuum operational exposure at 1950° F and a two-minute re-entry exposure at 3000° F were placed on alumina supports in air furnaces (lineal flow rate over the specimens ~1 mph) at 1600° and 2000° F. After 18 days exposure, hemispherical total emittance measurements will be made in vacuum at 1000°, 1400°, 1850° and 2000° F.

7. Emissive Coating Shear Strength Test

The emissive coating mechanical vibration tests will be replaced with a coating/substrate bond shear strength test. The test specimens will be Pt-20% Rh, open-ended, right cylinders, 0.928-inch OD x 0.885-inch ID x 4 inches long. One cylinder will be coated with 0.004-inch thick calcium titanate and one cylinder with 0.004-inch thick platinized alumina. One end of each coated tube will be cemented (3M 2214 epoxy)

TABLE H-8

Summary of Properties of Emissive Coating Candidates

Exposure	Calcium Titanate	Platinized Alumina	Iron Titanate
Material as plasma arc sprayed	*E_{ht} = 0.84 (average 1000° to 2000° F range)	E_{ht} = 0.70 (average 1000° to 2000° F range)	E_{ht} = 0.82 (average 1000° to 2000° F range)
	Adherence to Pt-20% Rh substrate excellent with a bond tensile strength of 6300 psi	Adherence to Pt-10% Rh good.	Adherence to Pt-20% Rh substrate good with bond tensile strength of 4000 psi
	Single phase crystalline compound	Two-phase composite crystalline material	Multiphase crystalline material
Space operational	E_{ht} = 0.85 after 90 days vacuum, 1950° F with ATJ graphite	E_{ht} = 0.71 after 10 days at 1800° F and 10 minutes at 2550° F in vacuum with ATJ graphite	E_{ht} = 0.70 after 90 days vacuum, 1950° F with ATJ graphite
	Adherence to Pt-20% substrate was excellent	Adherence to Pt-10% Rh substrate good	Adherence to Pt-20% Rh substrate very poor
	No chemical interaction with Pt-20% Rh detected by electron microprobe analyses	No chemical interaction with Pt-10% Rh detected by metallography	Gross chemical interaction with Pt-20% Rh. Iron diffused from coating into substrate
Re-entry	Above specimen heated for 2 minutes in air at 3000° F with ATJ graphite	Experiments to be performed later	Above specimen heated for 2 minutes in air at 3000° F with ATJ graphite
	E_{ht} decreased to 0.63 (1000° F measurement). E_{ht} increased to 0.74 (1850° F) and 0.82 (2000° F) during measurements in vacuum		E_{ht} = 0.51
	Coating has glassy appearance. No evidence of liquid flow.		Coating melted at 2500° F and flowed along surface of Pt-20% Rh
	Adherence to Pt-20% Rh substrate excellent		Adherence to Pt-20% Rh substrate very poor
	Chemical interaction with Pt-20% Rh detected by electron microprobe analyses. Both calcium and titanium diffused into substrate 0.001-inch		Gross chemical interaction with Pt-20% Rh
Ground abort	Experiments to be performed later	Experiments to be performed later in the program	Further iron titanate experimentation will not be performed

*E_{ht} = Hemispherical total emittance.

into a one-inch deep, close-fitting hole drilled in a steel tensile bar. The other end of each coated tube will have a steel tensile bar cemented into its ID. The tensile bars with the coated Pt-20% Rh tube will then be pulled until shear failure of the coating/Pt-20% Rh substrate bond (the epoxy bond between the coating and tensile bars is assumed to be stronger than the coating/Pt-20% Rh substrate bond). The shear strength of the PAS calcium titanate/Pt-20% Rh bond and the PAS platinized alumina/Pt-20% Rh bond will be calculated by dividing the load at shear failure by the area of the coating pulled away from the substrate. The shear strengths obtained are a measure of the abrasion resistance of each coating relative to the other. A high shear strength indicates a high resistance to abrasion.

D. PROGRAM ØØ4

1. Program Description

Program ØØ4 is designed to compute the diffusion coefficient D_β^i for the Wagner-Vasileff-Smoluchowski solution of Fick's second law given as follows:

$$C_\beta^i(x,t) = C_\beta^{i,o}\left[1 - \Phi\left(\frac{x}{2\sqrt{D_\beta^i t}}\right)\right]$$

where

$$C_\beta^{i,o} = C_\beta^i\left[1 - \Phi\left(\frac{b_{\beta\gamma}}{2\ D_\beta^i}\right)\right]$$

and

$$\Phi(z) = \text{error function} = \frac{2}{\sqrt{\pi}}\int_o^z e^{-s^2}\,ds$$

D_β^i = diffusivity of element i in the terminal solid solution (cm^2/sec)

C_β^i = maximum concentration of the element i in the terminal solid solution (wt %)

x = distance from the initial dissimilar metal interface (cm)

$b_{\beta\gamma}$ = rate constant which describes the motion of the interface between the solid solution and adjacent intermetallic compound = $\lambda/t^{1/2}$ ($cm/sec^{1/2}$)

λ = distance from the initial dissimilar metal interface to interface of intermetallic compound with solid solution (cm)

t = annealing time (sec)

$C_\beta^i(x,t)$ = concentration of the element i within the solid solution phase as a function of distance and time

The solution of the equation, given all parameters but the diffusivity, is obtained using Newton's method. For estimate D_{j+1}

$$D_{j+1} = D_j - (C_j - C_{obs}) (\partial C / \partial D)_{D_j}$$

where

D_j = jth value of D

C_j = C(x, t) corresponding to D_j

C_{obs} = C(x, t) observed

and $(\partial C / \partial D)_{D_j}$ is defined by

$$\left(\frac{\partial C}{\partial D}\right)_{D_j} = \frac{C_\beta^i}{\left[1 - \Phi\left(\frac{b_{B\gamma}}{2\sqrt{D_\beta^i}}\right)\right]^2} \left[-\left(1 - \Phi\left(\frac{x}{2\sqrt{D_\beta^i t}}\right)\right)(-1)\frac{2}{\sqrt{\pi}} * \right.$$

$$\exp\left(-\left(\frac{b_{\beta\gamma}}{2\sqrt{D_\beta^i}}\right)^2\right)\left(\frac{-b_{\beta\gamma}}{4\sqrt{D_\beta^{i3}}}\right) + \left(1 - \Phi\left(\frac{b_{\beta\gamma}}{2\sqrt{D_\beta^i}}\right)\right)(-1)\frac{2}{\sqrt{\pi}} *$$

$$\left. \exp\left(-\left(\frac{x}{2\sqrt{D_\beta^i t}}\right)^2\right)\left(\frac{-x}{4\sqrt{D_\beta^{i3} t}}\right)\right]$$

The program flow is given in Fig. H-28.

2. Use of the Program

Program ØØ4 operates under the F2R system on the in-house time sharing system from file /ØØ4B/. It is designed for use by an individual knowledgeable of the diffusion process. The parameter values are input together with an initial estimate for the D_β^i value. The program computes and outputs C_j, C_{obs}, and $D_{j+1} - D_j = \Delta D$. New estimates of D_j are given until ΔD is less than 0.5D in absolute value. (Normally new estimates are 1.5D or 0.5D depending on whether the sign of ΔD is positive or negative, respectively.) When the $\Delta D < 0.5D$ a value of zero is input for the new estimate and the program automatically continues the computation, outputting each step. When the calculation has converged to the user's satisfaction, it is halted by depressing the ESC key once.

A description of the input data format follows.

Line 1

Program types: DIST, TIME, RATE, MAX. CØNC =

User inputs: DIST(1), T(1), BBG(1), CBI(1) (Cr) FØRMAT (4E12.6, /)

CONFIDENTIAL

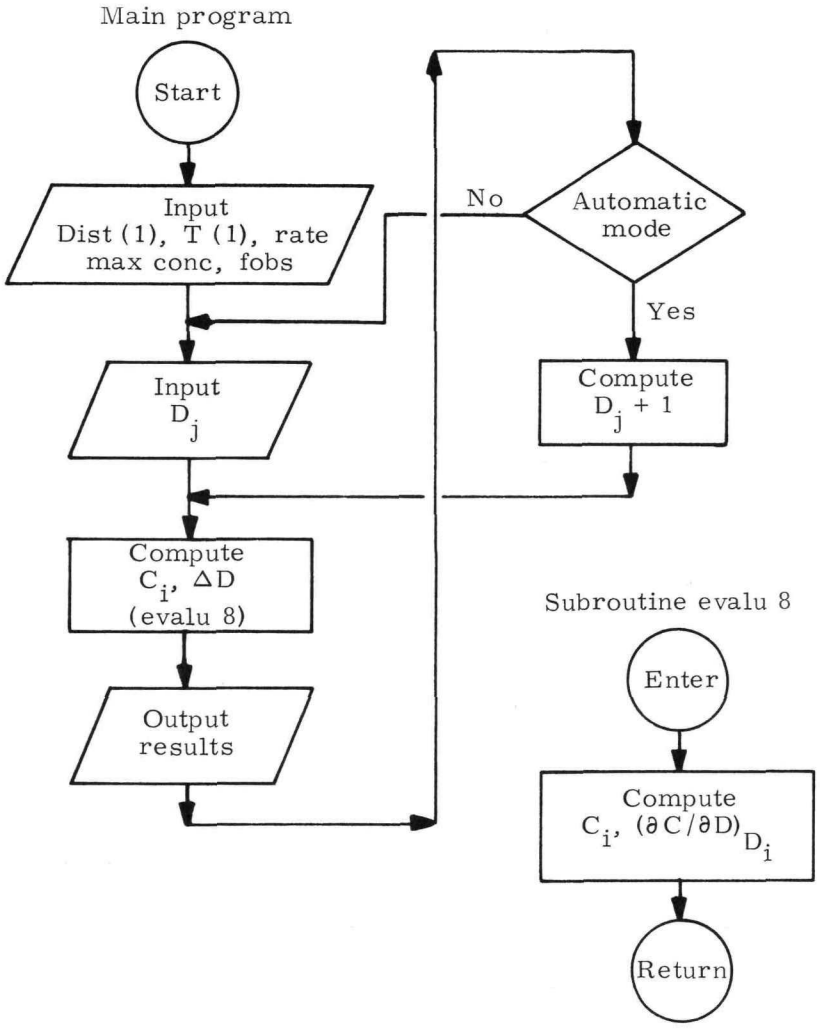

FIG. H-28. FLOW CHART FOR PROGRAM ØØ4

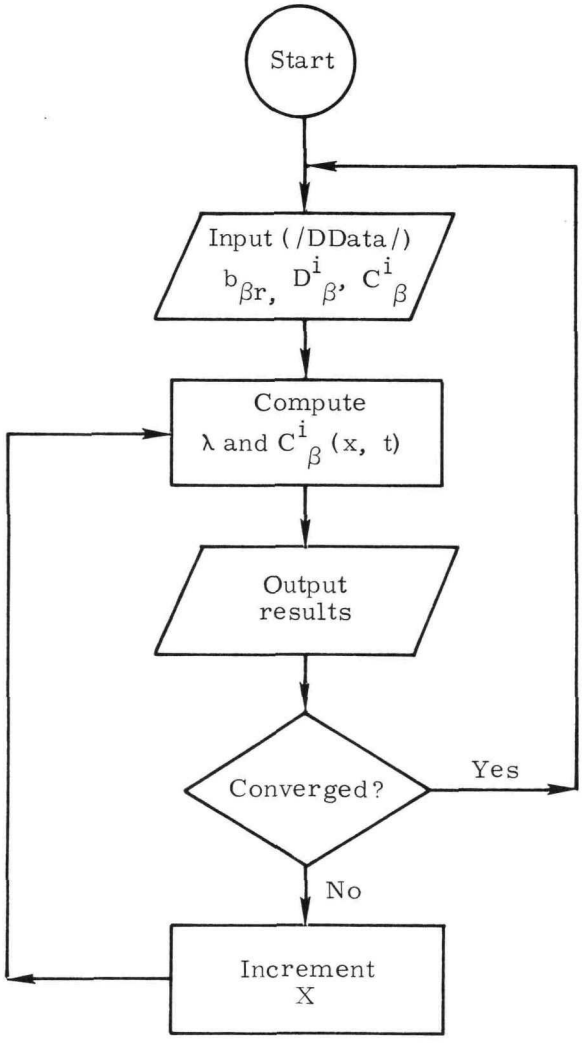

FIG. H-29. PROGRAM ØØ5 FLOW DIAGRAM

CONFIDENTIAL

Line 2

Program types: CBI(X, T) =
User inputs: FOBS (Cr)
FORMAT (E12.6, /)

where

DIST(1) = x
T(1) = t
BBG(1) = $b_{\beta\gamma}$
CBI(1) = C^i
FØBS = $C_{\beta(x,t)}$

At this point the program types a heading, stops, rings the bell and awaits the input of the initial D estimate.

Line 3

User inputs: D (Cr)
FØRMAT (E12.6, /)

Program computes corresponding function values, Line 3 is repeated until $|\Delta D| < 0.5D$ when the following is given

Line 4

User inputs: 0. (Cr) or (Cr)
FØRMAT (E12.6, /)

Program prints iterations of D

Line 5

ESC returns control to FORTRAN monitor.

E. PROGRAM ØØ5

1. Program Description

Program ØØ5 is designed to compute concentration as a function of distance and time for the equation

$$C_\beta^i(x,t) = C_\beta^{i,o}\left[1 - \Phi\left(\frac{x}{2\sqrt{D_\beta^i t}}\right)\right]$$

where

$$C_\beta^{i,o} = C_\beta^i\left[1 - \Phi\left(\frac{b_{\beta\gamma}}{2\sqrt{D_\beta^i}}\right)\right]$$

The various parameters are described in the PRØGRAM ØØ4 document.

Values for the parameters $b_{\beta\gamma}$, D^i_β, and C^i_β are input to the program from the data file /DDATA/. The program computes the position of the intermetallic compound-solid solution interface and the composition in the solid solution as a function of distance for 1.8, 18, 180 and 1800 days. Concentrations are computed and output until $C^i_\beta(x,t) \leq 0.015$ wt % and $x > 0.05$ centimeter or until $C^i_\beta(x,t) = 0$.

A program flow diagram is given in Fig. H-29.

2. Use of the Program

Program ØØ5 operates under the F2R system on the in-house time sharing system from file /ØØ5B/. The data necessary to the calculations are stored in the data file /DDATA/, prepared under the QED operating system.

A description of the input data format follows.

Line 1

BBG(1), X(1), CBI(1)

FORMAT (3E12.6, /)

where

BBG(1) = $b_{\beta\gamma}$

X(1) = D^i_β

CBI(1) = C^i_β

Line one is repeated for each data set.

BLANK